



Greenwich Academic Literature Archive (GALA)
– the University of Greenwich open access repository
<http://gala.gre.ac.uk>

Citation:

[Masroor, Ahmad \(1983\) Bond strength history in prestressed concrete reactor vessels. PhD thesis, Thames Polytechnic.](#)

Please note that the full text version provided on GALA is the final published version awarded by the university. “I certify that this work has not been accepted in substance for any degree, and is not concurrently being submitted for any degree other than that of (name of research degree) being studied at the University of Greenwich. I also declare that this work is the result of my own investigations except where otherwise identified by references and that I have not plagiarised the work of others”.

*Masroor, Ahmad (1983) Bond strength history in prestressed concrete reactor vessels.
##thesis type##, ##institution## .*

Available at: <http://gala.gre.ac.uk/8723/>

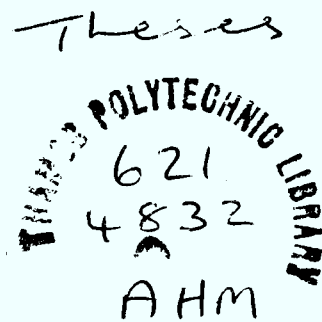
Contact: gala@gre.ac.uk

BOND STRENGTH HISTORY IN PRESTRESSED CONCRETE REACTOR VESSELS

A THESIS SUBMITTED TO THE
COUNCIL FOR NATIONAL ACADEMIC AWARDS (CNAА)
for the
DOCTOR OF PHILOSOPHY DEGREE

by

Masroor Ahmad B.Sc. (Eng), M.Sc. (Eng)



SCHOOL OF CIVIL ENGINEERING
THAMES POLYTECHNIC, LONDON

May 1983

ABSTRACT

BOND STRENGTH HISTORY IN PRESTRESSED CONCRETE REACTOR VESSELS

M. Ahmad

An attempt has been made to study bond strength history in Prestressed Concrete Reactor Vessels (PCRV) which house the Advanced Gas-cooled Reactors.

Three-dimensional non-linear analytical model has been developed in which the effect of bond is included. A finite element computer program is written in which solid, membrane, line and bond-linkage elements have been used to represent vessel concrete, steel liner, prestressing tendons and bond (between steel and concrete) respectively. Concrete is assumed to be non-linear material in compression and linear brittle (tension cut-off) material in tension, and the steel as elasto-plastic material with strain hardening. Provision is also made for concrete cracking, crushing and visco-elastic creep.

Two experiments have been carried out during this research. The purpose of the first experiment was to determine bond coefficients required for the analysis. This was achieved by pull-out tests on prestressing specimens using 5 mm and 7 mm diameter prestressing wires. The second experiment was performed on an octagonal prestressed concrete slab representing a top cap of a reactor vessel. The experimental results obtained from this slab are corroborated with the analytical results.

A typical Prestressed Concrete Reactor Vessel with boilers and circulators housed within the vessel wall thickness has been analysed for bond strength under increasing gas pressure at suitable intervals of its 30 year life. A comparison is made between the unbonded and bonded vessels. All analytical results compare well with those obtained from the experiments and available published data.

ACKNOWLEDGEMENTS

The author wishes to express his gratitude and appreciation to Dr. Y. Bangash for his supervision and support throughout the course of the present study. He is also grateful to Mr. A.A. Alexandrou for helpful discussion on the experimental side. In addition, valuable advices on creep side by Dr. G.L. England of King's College, London, are also acknowledged.

The author thanks the School of Civil Engineering, Thames Polytechnic, London, for providing financial assistance and computer facilities.

The technical staff of the Civil Engineering Laboratory are also acknowledged, without whose experience and technical skill the experimental part of this work would not have been possible. Special mention must be made of Mr. J. Humphreys for his technical assistance and of Mr. William Clegg for his skilled and continuous assistance during the laboratory work.

The author thanks Miss Julie Thorpe for typing this thesis.

CONTENTS

	Page
ABSTRACT	2
ACKNOWLEDGEMENTS	3
CONTENTS	4
NOTATION	10
CHAPTER 1 - GENERAL INTRODUCTION	12
1.1. Bonded and Unbonded Tendons	13
1.2. Scope of the Present Research	14
CHAPTER 2 - LITERATURE REVIEW	16
2.1. Introduction	16
2.2. Step-by-step Review	16
2.2.1. Methods of Analyses	16
2.3. Model Techniques and Model Testing	19
2.4. Bond and Bond-slip	22
2.4.1. General Introduction	22
2.4.2. Nature of Bond	22
2.4.3. Bond Characteristics	23
2.4.4. A Case for Present Research	29
CHAPTER 3 - GENERAL FINITE ELEMENT ANALYSIS	34
3.1. Introduction	34
3.2. The Displacement Finite Element Method	34
3.3. The Solid Isoparametric Elements	37
3.3.1. The Strain-displacement Relations	37
3.3.2. The Stress Calculation	38
3.3.3. The Element Stiffness Matrix	38
3.3.4. The Load Vectors	38
3.4. The Membrane Isoparametric Elements	39
3.4.1. The Strain-displacement Relations	39
3.4.2. The Stress Calculation	40

	Page
3.5. The Line Elements	41
3.5.1. Two-node Line Elements (Direct Approach)	41
3.5.2. Isoparametric Line Elements	42
3.5.3. Line Element in the Body of the Solid Element	43
3.6. The Three-dimensional Bond Linkage Element	44
CHAPTER 4 - CONSTITUTIVE RELATIONS FOR CONCRETE AND STEEL	53
4.1. Introduction	53
4.2. Literature Review on Compression and Cracking for Concrete	53
4.2.1. The Characteristic Behaviour of Concrete	53
4.2.2. Concrete Cracking Models	58
4.3. Formulation of an Orthotropic Concrete Constitutive Model	60
4.3.1. Incremental Stress-strain Relations	60
4.3.2. Equivalent Uniaxial Strain	63
4.3.3. Equivalent Uniaxial Stress-strain Curve	65
4.3.4. Poisson's Ratio	66
4.3.5. Failure Criteria of Concrete	67
4.3.6. Determination of Four Parameters	69
4.3.7. σ_{ic} Value	70
4.4. Other Concrete Compressive Models	71
4.4.1. Shear and Bulk Moduli Model	71
4.4.2. Concrete Model Based on Endochronic Theory	71
4.5. Concrete Cracking and Crushing Criteria	71
4.5.1. Assumptions	71
4.5.2. Shear on Open and Closed Cracks	73
4.5.3. Concrete Model in Tension and Cracking	74
4.5.3.1. Transformation of Cracked Material Matrix to Global Coordinates	77
4.6. Constitutive Model for Steel	78
4.6.1. Introduction	78
4.6.2. General Elasto-Plastic Constitutive Relations	79

	Page
4.6.3. Hardening Phenomena	83
4.6.4. Elasto-plastic Constitutive Relations for Liner	84
4.6.5. Elasto-plastic Constitutive Relations for Prestressed and Reinforced Steel	86
4.7. Bond and Bond-slip Constitutive Relations	87
4.8. Constitutive Relations using Creep and Thermal Effects	89
CHAPTER 5 - NON-LINEAR SOLUTION TECHNIQUES	109
5.1. Introduction	109
5.2. Non-linear Solution Methods	109
5.3. General Steps for Non-linear Analysis	112
5.3.1. Explanation of Step 4 for Concrete	114
5.3.2. Explanation of Step 4 for Steel	116
5.3.3. Steps for Non-linear Bond-linkage Elements	118
5.4. Steps for Creep and Temperature Analysis	119
5.5. Non-linear Response with Creep	121
5.6. Solution Techniques for Descending Stress-strain Curve	122
5.7. Unloading of a Point in Concrete	123
5.8. Accelerated Newton Raphson Method	124
CHAPTER 6 - DESCRIPTION OF FINITE ELEMENT COMPUTER PROGRAM NSARVE	
6.1. Introduction	132
6.2. Computer Program NSARVE	132
6.3. Description of NSARVE	133
6.3.1. Modules	133
6.3.1.1. Input Data Module	134
6.3.1.2. Initialise Module	134
6.3.1.3. Loads Module	134
6.3.1.4. Stiffness Module	134
6.3.1.5. Solution Module	134
6.3.1.6. Stress and Residuals Module	135
6.3.1.7. Creep Module	135
6.3.1.8. Output Module	135
6.3.2. Description of Subroutines	136

	Page
CHAPTER 7 - EXPERIMENTAL INVESTIGATIONS OF BOND-SLIP SPECIMENS AND BONDED SLAB	161
7.1. Introduction	161
7.2. Material Data from Tests	162
7.3. Details of Test Specimen	163
7.3.1. Bond Slip Test Specimen	163
7.3.2. Details of the Bonded Slab	164
7.4. Brief Details of Test Rigs	165
7.4.1. Bond-slip Test Rig	166
7.4.2. Test Rig of Prestressed Concrete Slab	166
7.5. Testing Procedure and Results of Bond-slip Tests	167
7.5.1. Conclusion	169
7.6. Testing Procedure and Results for the Octagonal Slab	170
CHAPTER 8 - COMPARATIVE STUDY OF RESULTS	196
8.1. Introduction	196
8.2. Validation of Program NSARVE using Simple Problems	197
8.3. Analysis of the Octagonal Prestressed Concrete Slab	197
8.3.1. General Information	197
8.3.2. Finite Element Meshes, Geometry and Material Data	198
8.3.3. Discussions on the Analysis and Results	198
8.4. Analyses of the Prestressed Concrete Reactor Vessel	204
8.4.1. Objective of the Analyses	204
8.4.2. General Introduction of the Vessel	204
8.4.3. Finite Element Meshes and Vessel Data	205
8.4.4. Types of Analyses	207
8.4.5. Discussion on the Analyses and Results	208
8.4.5.1. Normal Operation and Creep Analyses	208
8.4.5.2. Ultimate Load Analyses	210
8.5. Conclusion	217

	Page
CHAPTER 9 - CONCLUSIONS AND RECOMMENDATIONS	292
9.1. Conclusions	292
9.2. Recommendations	294
REFERENCES	296
APPENDIX A	A1
A1.1. Solid Isoparametric Elements	A2
A1.1.1. 8-noded Solid Element	A2
A1.1.2. 20-noded Solid Element	A3
A1.1.3. 32-noded Solid Element	A4
A1.1.4. Derivative Transformation and Jacobian Matrix	A6
A1.1.5. Nodal Forces due to Surface Pressure	A7
A1.1.6. Nodal Loads not directly on Nodes	A8
A1.2. Isoparametric Membrane Elements	A9
A1.2.1. 4-noded Membrane Element	A9
A1.2.2. 8-noded Membrane Element	A9
A1.2.3. 12-noded Membrane Element	A9
A1.2.4. The Strain-displacement Relations	A10
A1.3. Line Elements	A14
A1.3.1. The Stiffness Matrix for 2-noded Line Elements	A14
A1.3.2. Isoparametric Line Elements	A14
A1.3.3. The Strain-displacement Relation	A15
A1.4. Line Elements in the Body of Solid Elements	A17
A1.5. Bond-linkage Stiffness Matrix	A20
A2 Anisotropic Material Matrix	A21
A3 Inclined or Skew Boundary Supports	A23
A4 Stress and Strain Transformation Matrices	A25
A5.1. Shear and Bulk Moduli Approach	A27
A5.1.1. Constitutive Relations	A27
A6.1. Concrete Model based on Endochronic Theory	A30
A6.1.1. Extension of Endochronic Constitutive Relations for Cracking	A34

	Page
A7.1. Creep Strains under Multiaxial Stress	A36
A7.2. Equivalent Load due to Change in Creep Strain	A38
A7.3. Equivalent Load due to Thermal Strain	A39
APPENDIX B	B1
B1 User Manual for NSARVE	B2
B1.1. Program NSARVE	B2
B1.2. Test Examples	B14
B1.3. Typical Data Deck and Output of NSARVE	B18
B2.1. Subroutine Listings	B25

NOTATION

\sim	-	denotes matrix or a vector
B	-	strain-displacement matrix
B_i	-	strain-displacement matrix at node i
C	-	inverse of material matrix
D	-	constitutive matrix
D^*	-	constitutive matrix in crack coordinate system
D_T	-	tangent constitutive matrix in global coordinate system
ϵ_i	-	vector of Cartesian strain components at point i
σ_i	-	vector of Cartesian stress components at point i
ϵ_0	-	initial strain vector
ϵ_c	-	creep strain vector
σ_0	-	initial stress vector
$\Delta \epsilon_i, \Delta \sigma_i$	-	incremental strain/stress vectors
σ^*	-	stress vector in crack directions
ϵ^*	-	strain vector in crack directions
$\Delta \epsilon^*, \Delta \sigma^*$	-	incremental strain/stress vectors in crack directions
$\Delta \epsilon^{\text{th}}$	-	incremental thermal strains
β	-	shear interlocking factor
E_c	-	modulus of elasticity for concrete
ν_c	-	Poisson's ratios for concrete
σ_c	-	concrete cylinder compressive strength
σ_t	-	concrete limiting tensile strength
ρ	-	vector of body forces per unit volume
ϵ_{cu}	-	concrete crushing strain
K^e	-	element stiffness matrix
K	-	global structural stiffness matrix
K_b	-	bond linkage stiffness matrix
L	-	length of the line elements
d	-	diameter of the line element
l, m, n	-	direction cosines relating local to global axes
N_i	-	shape function of node i
N	-	element shape function matrix
ρ_x	-	vector of external element loads
ρ_s	-	vector of surface pressure

\underline{P}	-	global load vector
\underline{T}_ϵ	-	strain transformation matrix
\underline{T}_σ	-	stress transformation matrix
\underline{T}	-	transformation matrix (relating local to global displacements at nodes)
\underline{U}^e	-	element nodal displacement vector
\underline{U}	-	global nodal displacement vector
U_i, V_i, W_i	-	displacements at node i
X, Y, Z	-	global coordinate system
X', Y', Z'	-	local Cartesian coordinate system
X^*, Y^*, Z^*	-	crack coordinate system
ξ, η, ζ	-	local curvilinear coordinates
ds	-	differential surface area
$dvol$	-	differential volume
$\det J$	-	determinant of Jacobian
\underline{J}	-	Jacobian matrix
E_h, E_v, E_ℓ	-	bond slip moduli in horizontal, vertical and lateral directions
$\Delta \underline{\sigma}_b$	-	incremental bond stress vector
$\Delta \underline{s}$	-	incremental slips
$\underline{\sigma}_b$	-	bond stress vector
E_b	-	bond linkage constitutive matrix
t	-	thickness of membrane element
\underline{D}_E	-	elastic material matrix for membrane element
I_1	-	first stress invariant
J_2	-	second invariant of stress deviator tensor
σ_m	-	mean stress
E_1, E_2, E_3	-	moduli of elasticity in three principal directions
ϵ_{iu}	-	uniaxial equivalent strain in ith direction
$\Delta \epsilon_{iu}$	-	incremental uniaxial strain
σ_i	-	principal stresses, $i=1,2,3$
ϵ_i	-	principal strains, $i=1,2,3$
G	-	shear modulus
G'	-	shear modulus for cracked concrete
σ	-	equivalent stress
$\Delta \epsilon_p$	-	plastic strain increment
\underline{D}_E	-	elastic material matrix for steel
\underline{D}_p	-	plastic material matrix for steel
\underline{D}_{ep}	-	elasto-plastic material matrix for steel

CHAPTER 1

General Introduction

In recent years, many complex prestressed concrete structures have been designed and built. The complex nature of the geometric configuration and material behaviour of many of these structures has given rise to many new problems. A prestressed concrete reactor vessel is such a structure, the complex behaviour of which is directly associated with material anisotropy and non-linearity, temperature, creep and shrinkage. Gas increasing pressure, load history and a cracking condition assume important roles in the vessel's short and long-term performance. Where the vessels have been bonded (grouted tendons), the ultimate load carrying capacity is influenced by the complex three-dimensional bond-slip phenomenon. This is the theme of the current research. Prior to the establishment of a case for a bonded vessel, it is essential to discuss this important phenomenon.

In the tension zone within the vessel concrete, bond-slip takes place at the steel-concrete interface prior to cracking. It contributes to further cracking under loads and consequently affects the ultimate load capacity. Bond-slip behaviour is non-linear in nature and is influenced by many factors such as the strength of the concrete, roughness of the steel surface and diameter of the steel. As soon as bond breaks, the steel and concrete separates and wider cracks appear, producing greater slip. During and after the crack formation, prestressing tendons carry most of the load and may deform plastically, thereby affecting the integrity of the vessel. In addition, the effect of temperature and creep also adds additional problems to bond-slip situations.

The bonded vessels under such conditions need to be investigated by sophisticated numerical techniques. In the present research, the finite element method is adopted in order to model the bond strength history of the vessels under increasing loads.

1.1. Bonded and Unbonded Tendons

Bonded and unbonded tendons and their choice for conventional prestressed concrete structures have always been the subject of much controversy. This is more so in the case of prestressed concrete pressure vessels. The proponents of the unbonded tendons suggest that the loss of prestress in tendons due to various sources such as high temperature, shrinkage and creep of concrete cannot be adequately assessed owing to the approximate nature of analyses and material models. On the other hand, unbonded tendons can be inspected and restressed, thus ensuring their load carrying capacity for both short and long-term conditions. The main disadvantage of unbonded tendons lies in the incorrect assessment of the structural reliability of their anchorages. Expensive equipment for inspecting tendons and recording of the losses are additional problems caused by the use of unbonded tendons. These are fully described by Bangash (47).

Vessels with bonded tendons provide reasonably good corrosion protection. In the bonded vessel, the prestress force is transferred from the steel to the concrete through the bond, thus minimising the influence of the structural reliability of the end anchorages. In principle, the grouted tendons in many ways behave like unstressed bonded reinforcement. It is unlikely that a sudden increase in cavity pressures would cause any explosive failure of the vessel. A vessel with bonded tendons has a well-disposed crack pattern. With bonded tendons, the vessel achieves high ductility, if and when a cavity pressure exceeds the prestressing force. The ductility of the vessel is extremely important, since it utilises the full strength capacity of tendons right up to the ultimate conditions. If any well-disposed small cracks exist, this ductile nature will enable the liner to span cracks without yielding. The biggest issue of a leaked liner will be avoided.

From the above brief discussion, the bonded vessel will perform better than the unbonded vessel, provided that correct assessment of the grouted prestressing tendons (analytical, experimental and site monitoring) have been made on reliability of the grouted prestressing tendons.

Little information is available on the behaviour of bonded vessels. It is intended that this investigation will give more understanding of the realistic behaviour of the vessel's short and long-term performance using bonded tendons. The techniques given in this research will encourage many engineers to use bonded tendons in future vessels for advanced gas-cooled reactors, pressurised water reactors, high temperature reactors, fast-breeder reactors, and even for the use of non-nuclear work.

1.2. Scope of the Present Research

The scope of the present research is to analyse bonded and perfectly bonded prestressed concrete reactor vessels. For comparative study, an unbonded vessel is also analysed. The vessel chosen for the analyses is of multicavity type, in which boilers and circulators are housed within the vessel wall and cap thickness.

The main investigation is based on bond between the prestressing tendons and the vessel concrete. An attempt has been made to carry out analytical study on bonded vessels. In order to corroborate results, experimental tests have been performed on an octagonal prestressed concrete slab and pull-out specimens. Using parameters obtained from bond tests, the analyses have been carried out on the slab which represents the top cap of the concrete vessel for an advanced gas-cooled reactor (AGR). Realistic material models with regard to progressive cracking and compression of concrete, steel yielding and bond stress distribution have been developed for analysis, with and without the influence of temperature and creep effects. The following lines cover the programme of this research.

Chapter 2 gives a brief review on the analytical and experimental work of prestressed concrete reactor vessels and end slabs. This Chapter also reviews the subject of bond and local bonded-slip relations for prestressing strands and conventional steel. This is then followed by Chapter 3 which covers the finite elements developed

to model vessel components. Linear equations of these elements are given. Chapter 4 gives non-linear material constitutive relations for concrete (cracking and compressive behaviour), elasto-plastic relations for prestressing tendons and the liner, and a non-linear bond-slip relation for bond linkage elements. Equations for creep and thermal effects have also been given. Non-linear equations are solved using incremental/iterative techniques which are described in Chapter 5.

The above equations are used to develop a computer program which is described in detail in Chapter 6. Flow charts of various segments of the program are also given. This Chapter is supported by a User's Manual given in Appendix B.

Chapter 7 describes the experimental programme carried out during this research. The experimental programme was carried out first to understand the local bond-slip behaviour of prestressing wires, and second to test a bonded prestressed concrete slab representing the top cap of the vessel. Chapter 8 gives the comparative study of the analytical and experimental results.

CHAPTER 2

Literature Review

2.1. Introduction

In this Chapter, an attempt has been made to briefly review the state of the methods of analysis and experimentation of concrete reactor pressure vessels with particular emphasis on bond and bond-slip relations. Wherever possible, bond-slip behaviour of conventional structures has been examined and an analogy is made for the possible bond-slip phenomenon of concrete pressure vessels.

2.2. Step-by-step Review

Several conferences have been held (144, 145a, 145b, 145c, 145d, 145e) on various aspects of the analysis, design and construction of prestressed concrete reactor vessels. A comprehensive review is given by Bangash (21a) concerning the historical development, stress analyses and design of vessels, mostly with unbonded tendons. It is not intended here to repeat this work. However, certain cases relevant to this research have been critically re-examined in order to give a better understanding of the aim of the current research.

2.2.1. Methods of Analyses

Earlier finite element analyses of concrete pressure vessels have been performed assuming axial symmetry in which two-dimensional elements have been used. Rashid (14, 15) carried out linear and non-linear analyses using finite element and predicted deformation, cracking and yielding of steel of the Fort St. Vrain vessel. The analysis performed on this vessel, in which tendons were unbonded, is two-dimensional.

Three-dimensional non-linear analysis of a reactor vessel has been carried out by Sangy et al (22, 23) in which creep effects were

included in the finite element constitutive equations. A failure criterion containing the effect of first and second stress invariants was used. The failure surface in stress space is of cone shape. The non-linear effect of concrete in compression is taken into account by changing the shear moduli which is assumed to be a function of the second stress invariant. The initial stress method was used to solve the finite element equations.

Similarly, a non-linear analysis of a reactor vessel model was performed by Mohraz et al (11) using the lumped parameter method.

Phillips et al (19, 20) carried out a two-dimensional finite element analysis on a model vessel adopted already by Mohraz et al (11), in which a non-linear model of concrete in compression is described by changing the shear moduli and the bulk moduli. An octahedral shear stress law was used as failure criteria once the stress had reached the peak value. This law as appeared there is only applicable to a biaxial state of stress. Cracking was modelled by using tension cut-off.

Argyris et al (10, 10a) analysed prestressed concrete reactor vessels using an elasto-plastic material model. The failure criterion of Mohr-Coulomb was used as yield criterion. A tension cut off model was used in tension.

Bangash (21) analysed vessels using the hypo-elastic concept to model the compression side of the concrete. This concept was first introduced by Truesdell (137) and was later used by Coons and Evans (30) to model non-linear behaviour of plain concrete. Bangash (21a) has carried out ultimate analyses of several unbonded vessels in order to establish a factor of safety for these vessels. To achieve this objective, two types of analyses were performed. The first one was a three-dimensional non-linear finite element analysis in which the hypo-elastic material model was used. The second analysis was based on the limit state concept. Factors of safety from both analyses compared favourably.

Long-term elastic analyses of reactor vessels have been carried out by many other investigators (71, 73, 74, 81, 83, 85, 132a). England et al (74) have used the rate of creep method in which thermal effects were also included. Two-dimensional finite element analyses were performed and the results obtained were fully corroborated. Kawamata et al (81) have used the rate of creep method to analyse a multicavity vessel. Elastic long-term stresses up to 40 years of the vessel's life were predicted in conjunction with their early method of "sliced substructure" (81a). This method is an approximation of the usual three-dimensional finite element method.

Smith et al (83) have carried out reactor vessel analysis using a visco-elastic creep model. The creep compliance function of concrete was expressed as the Dirchlet series with temperature coefficients. A comprehensive experimental work on cylindrical specimens was carried out under multiaxial loading and temperature. Results up to five years were obtained. With these results, a creep compliance function which is fitted to a five term Dirchlet series was obtained. This function was generalised for multiaxial creep strains. Three-dimensional isoparametric finite element analyses, in which the creep model was included, form the basis of his modified program NONSAP. No information is available as to whether the researchers (81, 83, 85) considered any bond-slip phenomenon.

Takeda et al (18) have carried out inelastic analysis of a prestressed concrete multicavity reactor vessel. A 1/20th scale model was selected. The concrete constitutive law in compression was modelled as an elasto-plastic material with Drucker-Prager's failure surface as yield criterion. Concrete in tension was considered to be a linear brittle material. The prestressing steel was also modelled as an elasto-plastic material. The vessel model was then analysed by two and three-dimensional finite elements. This analysis considers both cracking and crushing states of the vessel. Again, no consideration was given for the tendon bond-slip condition.

Connor et al (17) have reported a non-linear numerical procedure for analysing prestressed concrete reactor vessels. Three-dimensional finite element analysis was adopted. The concrete in compression was modelled by a non-linear orthotropic model and for tension, a tension cut-off model was used. Steel (liner and prestressing cables) was treated as elasto-plastic material. Creep and temperature effects were also included. The stress contours and crack patterns are shown for the Fort St. Vrain vessel. Since the tendons are treated as unbonded, no consideration was given to the influence of bond on the load carrying capacity of the vessel.

Gallix et al (17) carried out a two-dimensional non-linear analysis for the multicavity reactor vessels. The vessel concrete was modelled by a non-linear orthotropic stress-strain constitute law and the steel liners and prestressing steel were modelled by an elasto-plastic material using Von Mises yield criterion 1/10th scale Hartlepool vessel and 1/20th scale high temperature gas cooled reactor (HTGCR) were analysed.

A brief description of the comparative results for bonded and unbonded tendons has been given by Bangash (47) for a typical reactor vessel. No detailed analysis is available in this paper.

2.3. Model Techniques and Model Testing

In order to understand the vessel behaviour under overload conditions, several experimental investigations (13, 113, 113a, 113b, 114, 115, 116, 117, 118, 119, 120, 121, 122, 123, 124) have been carried out on scaled models and isolated vessel components in the last decade or so. Some of these are reviewed here. Brading and Hills (113a) presented results of six models, two of which were reinforced slabs. The other four 1/24th scale models had a span to depth ratio of 2.9. The main purposes of the tests were to provide information for the design of the Dungeness 'B' vessels. Only one model was pressurised to failure. Tests on the remainder were discontinued, mainly because of leakage in the liner.

Cambell-Allen et al (13, 113b) have carried out two types of experiment. The first one had seven 263 mm diameter slabs with clear span to depth ratios of 3.67 and 1.835. The hoop prestress, which ranged between 2.35 N/mm^2 and 24.10 N/mm^2 consisted of straight tendons either 5.1 mm or 7.0 mm diameter in unlined ducts. On the second type of experiment, a small number of discs and skirted slabs were loaded to failure. The prestress was applied by external bolts acting against either one or a series of octagonal stiff rings.

Morgan (114) indicated that about twelve models slightly more than 610 mm diameter were tested for checking the design of the Oldbury and Hinkley Point 'B' pressure vessels. No experimental details or results were reported. However, it was stated that shear failure did not take place in any of the models.

Sozen et al (116) at the University of Illinois have carried out 25 tests on skirted prestressed concrete slabs. The span to depth ratios in these investigations covered a range of 1.67 to 5, and the amount of force required to restraint varied between 1.52 N/mm^2 and 2.90 N/mm^2 . It was reported that eight of these slabs failed in shear and the remaining slabs either failed in flexure or the tests were discontinued because of leakage in the pressure system. The reason for the high percentage of liner leakage was given as due to the usage of long length barrel and the lack of hoop forces to prevent the large displacement of the barrel stub.

Langan et al (119) reported a comprehensive description of the design of multicavity pressure vessels used for both the Hartlepool and Heysham nuclear power stations. Elastic analysis of the vessels was carried out using dynamic relaxation. The 1/10th scale model of the Hartlepool model has been successfully tested for serviceability and

ultimate conditions, and the data provided were extremely valuable for three-dimensional analyses. Various graphs were plotted between pressure deflection and pressure strain for cap and wall of the model at the design pressure and at 2.5 times the design pressure. Crack sizes for various internal pressures were given, together with a typical crack pattern at 2.5 times the design pressure.

Meerwald and Schwiers (115) reported a test on a 1/20th scale model of perforated prestressed concrete end slab with a span to depth ratio of 3.1. The applied hoop prestress was about 10.30 N/mm^2 . Failure took place when the central core was forced out at a pressure of 196 N/mm^2 .

Langan and Garas (117) reported tests on more than twenty thick restrained circular slab models in order to study the shear failure mechanism. The variables investigated were the effects of bonded reinforcement, lined and unlined penetrations, span to depth ratio and the level of hoop prestress. The hoop prestress ranged from 2.482 N/mm^2 to 6.206 N/mm^2 which was provided by wire-winding. The vertical prestress varied between 1.345 N/mm^2 and 19.035 N/mm^2 and was provided by the high tensile bars.

Very few models with bonded tendons have been considered. It is necessary to look at conventional structures for more information on various aspects of bond-slip characteristics.

2.4. Bond and Bond-slip

2.4.1. General Introduction

Although a great deal of effort was made a few decades ago to understand the bond characteristics between steel and concrete, the subject is still open to doubt and critical discussion. The questions to various unknown variables affecting bond and bond-slip have not been answered. In concrete reactor vessels subject to multiaxial loading conditions, the accurate investigation of bond and bond-slip with and without the influence of creep and shrinkage is a dilemma. In the last few years, awareness of the importance of bond has increased greatly. This culminated in an international conference on bond in concrete (146) in which subjects ranged from bond between cement paste and aggregate, to that of plain and deformed bars and prestressing strands and concrete. The effect of cyclic, impact and sustained loading, thermal and corrosion have been included. Only simple structures were considered. Complicated structures, such as prestressed concrete reactor vessels, were excluded. Nevertheless, it has become even more important to review the most important research papers on bond relevant to the current research. This review is given below.

2.4.2. Nature of Bond

It is generally considered that bond between steel and concrete is due to a combination of adhesion and friction. Adhesion bond develops first and, after a small slip, it disappears. For relatively larger slips, frictional bond develops between steel and concrete sliding surfaces. The adhesion between steel and concrete is not significant. The bond of plain steel is mainly due to frictional resistance which depends on the roughness of the steel surface and any change in its lateral dimension along the embedded length. The bond between deformed bars and concrete is radically different from that of plain steel bars. It is due to the interlocking of the ribs and surrounding concrete. Adhesion and friction resistance also exists, but the great improvement

of the bond is related to the bearing pressure of the concrete against the lugs. In the case of a plain bar, the failure usually occurs due to slip of the bar and the bar usually pulls out of the concrete. On the other hand, deformed bar failure is almost always associated with longitudinal splitting along the surface nearest the bar.

2.4.3. Bond Characteristics

Bond in pretensioned prestressed concrete is of two types : transfer bond (anchorage) and flexural bond. Transfer bond utilises a part of the available tensile strength of the steel to establish compressive forces in the concrete. Flexural bond results from external force applied on the structure. After cracking, the increase in steel stress above effective prestress causes flexural bond stress between steel and concrete. The two cases are shown in Figures (2.5).

Transfer bond exists near the ends of the member after the load in pretensioned steel (strand) has been transferred. The length over which this transfer is made is known as the prestress-transfer length (or anchorage length), and mainly depends on the amount of prestress and the surface conditions of the steel (strand). Three factors which contribute to bond performance are adhesion, friction and mechanical resistance between the steel and concrete. In the tensile zone, the reduction in tensile strain of the steel is generally not equal to the compressive strain of the concrete at the same point. There is, therefore, a relative movement between the steel and concrete. This indicates that the adhesion does not contribute much to the transfer of prestress. Friction assumes a greater role in prestress transfer. As soon as tension in the strand is released, the strand diameter tends to increase, resulting in radial pressure against the concrete, which in turn, produces high frictional resistance to slip in the transfer zone.

Flexural bond in prestressed concrete is of significant magnitude only if it is loaded up to its cracking stage. When the concrete cracks the bond stress in the immediate vicinity of cracks rises to some

limiting stress and slip occurs over a small portion of strand length adjacent to the cracks. The bond stress near these cracks is then reduced to a low value. With increasing load, the high bond stress generates a wave from the original cracks to the far ends. The bond stress remaining behind this wave is always lower than the maximum value at the peak of the bond stress wave. If the peak of high bond stress wave reaches the prestress transfer length zone, the increase in steel stress resulting from the bond-slip decreases the steel diameter, which reduces the frictional bond resistance in this region. Hence mechanical resistance in a transfer zone becomes important. This resistance is at a minimum for plain smooth wire and maximum in the case of strand.

In order to simulate the above two conditions in prestressed concrete beams, there have been a number of experimental investigations of pull out and beam tension test specimens. Further empirical expressions were obtained from these tests which could be applied to practical structures.

In order to understand the bond characteristics of prestressing strand, Dably (96) carried out a series of tests involving four prestressed concrete beams. Each was reinforced with 11.11 mm (7/16") strands. The anchorage length was determined by measuring the concrete strains at the level of the strand. An anchorage length of 610 mm to 813 mm (24" to 32") was reported and high values for a larger concrete cover under the strand. Base (97) reported an anchorage length of 228.6 mm to 482.6 mm (9" to 19" of 5/16") strand. Ratz (98) conducted 200 tests on concentrically prestressed concrete prisms to study the concrete strength on anchorage length. Bond in this investigation was found to be the direct function of concrete strength for any type of wire and strand. An empirical formula was given in order to calculate the slip within the anchorage zone.

Dinsmore et al (99) performed 42 pull out tests and four prestressed beam tests in order to study the anchorage length required to transfer the prestressing force. Clean strands of 11.11 mm (7/16")

diameter were used. The anchorage length to transfer the prestress force of 950.8 N/mm^2 to 1143.74 N/mm^2 (138 KSI to 166 KSI) range from 228.6 mm to 914.4 mm (9" to 36"). Rehm (100) carried out tests on 16 different types of prestressed steel using concentrically prestressed concrete beams. The general indication of results shows that the increase in concrete strength lead to a decrease in anchorage length. The release of stress, the time effect on anchorage length, was also studied. Kaar et al (101) performed the influence of the concrete strength on the anchorage length of a seven wire strand by testing 36 concrete prisms. Preston (102) reported a comparative study of an anchorage length of clean and rusted 12.7 mm ($\frac{1}{2}$ ") strands. Results indicated that for major cases, the bond characteristics were almost identical. Hulsbos et al (103) studied the load capacity of pretensioned prestressed concrete beams with web reinforcement. They reported anchorage length of 11.11 mm ($\frac{7}{16}$ ") strand for 1067.95 N/mm^2 (155 KSI) stress was 457.2 mm (18").

Over et al (104) investigated the influence of the strand diameter on anchorage length with the aid of six square concrete prisms. The diameters investigated were 63 mm, 9.25 mm and 12.7 mm ($\frac{1}{4}$ ", $\frac{3}{8}$ " and $\frac{1}{2}$ ") and results indicated that anchorage length increased with the increase in strand diameter. Hanson (95) studied the influence of surface roughness on anchorage bond and flexural bond strength in 12 prestressed concrete beams using 11.11 mm and 12.7 mm ($\frac{7}{16}$ " and $\frac{1}{2}$ ") strand. Clean as received, partially rusted and rusted strands were tested. Results show a 30% improvement in the anchorage length when using rusted strand. The flexural bond strength of the beams rusted was high than that for clean strand.

Evans and Robinson (94) tested pretensioned prestressed concrete beams by measuring the strain and slip distribution along the steel wire during loading by means of X-ray photography. Their findings indicate that bond stresses were only detected when cracking commenced, and as the crack opened, the values of bond stresses increased until a slip of 0.1 mm was reached. Thereafter, the bond stresses began to decrease.

Bond stresses found in this investigation are much higher than those normally obtained for wires. They concluded that the tangential friction was the main source of bond in cracked beams and the measured high bond stresses were due to this kind of friction.

Hanson and Kaar (95) carried out tests on rectangular pre-tensioned beams to study the flexural bond of strand. Strain in strands was measured by instrumenting with electrical resistance strain gauges at spacings ranging from 300 mm to 500 mm. The results indicated average flexural bond stresses ranging from 1.05 N/mm^2 to 2.75 N/mm^2 for 12.7 mm strand. Before cracking, the bond stresses were very small. After cracking, the maximum bond stress progressed from the cracks towards the beam ends as the load was increased. The conclusion was drawn that in pretensioned beams, failure in bond mainly depends on the anchorage length, i.e. the distance from the section of maximum steel stress to the beam end.

Stocker and Sozen (105) reported the results of 486 pull out and five beam tests using strands and plain wires with embedment length of 25.0 mm. These tests were performed to provide information on the relationship between bond and slip and to study the effect of the various variables on the bond strength. These are (a) strand diameter, (b) concrete strength, (c) shrinkage, (d) settlement of concrete, (e) confining pressure, (f) concrete cover, (g) time effects. Some of the results from this investigation was reproduced and are shown in Figures 2.1. and 2.2. Figure 2.1. shows a slight trend towards increasing bond stress due to an increase in strand diameter, but a study of all the test data indicated that this trend was not statistically significant. The bond strength was found to increase significantly with the concrete strength (see Figure 2.2.). The unit bond force increased by approximately 10% per 7 N/mm^2 of concrete strength. High bond strengths were also obtained due to dry cured specimens, concrete cover and lateral pressure. The conclusion was drawn that initially bond stress of strand increases at a slip too small to be measured. After having reached a value of approximately 0.0025 mm, the slip increased more

rapidly. Beyond that point, the bond strength continued to increase at a small rate. Some tests on plain wire (the middle wire of the strand) showed that the bond strength of strand was higher than the bond strength of plain wire. Finally, the bond characteristics obtained in the pull out tests were used in calculating the anchorage length of a strand in a pretensioned beam. It was shown that the calculation based on the results of 25 mm embedded length of pull out tests using non-prestressed strand provided a reasonably safe estimate of the anchorage length.

More recently, Edward and Picard (90) reported bond pull out and tension tests on 12.7 mm strand in order to obtain the local bond stress-slip relationship. They used 38.1 mm embedded length with three concrete covers of 12.7 mm, 25.4 mm and 38.1 mm. The results obtained, plotted as bond stress-slip curves showing elasto-plastic type behaviour, are reproduced in Figure 2.4. The results indicated that the average maximum bond strength decreased when the concrete cover was increased. Also, some empirical expressions for crack widths and spacings were given.

Jeager (89) presented a state of the art of corrosion protection of prestressing tendons in prestressed concrete reactor vessels. The advantages and disadvantages of grouted and the non-grouted vessels were also given. Bangash (47) presented in detail certain arguments for and against the use of bonded and unbonded tendons in prestressed concrete reactor vessels. Two-dimensional finite element models were used to calculate bond stresses for bonded reactor vessels. On the basis of this calculation, various tendon types and their sizes for bonded and unbonded tendons were recommended.

Morris Schupack (107, 108, 109) carried out various tests on post-tensioned grouted tendons, mainly used in containment vessels. Grouting tests of a large 54 strand post-tensioning tendon (107) were performed. The tendon was embedded in a concrete beam and it was stressed at 76% of GUTS. After cutting the tendon at 31 days of grouting, the bond transfer length of 3.1 mm to 3.7 mm was found. Mottock et al (110)

carried out a comparative study of prestressed concrete beams with and without bonded tendons. The primary variables were the presence and absence of bond and the amount of bonded reinforcement. The results reported show that the unbonded post-tensioned beams with minimum recommended reinforcement had serviceability characteristics, strength and ductility equal to, or better than, those of comparable bonded post-tensioned tendons.

Naus (112) studied the behaviour of grouted and non-grouted tendons in relation to prestressed concrete reactor vessel application. The various aspects of bond performance were studied experimentally. Flexural tests were performed on beams (dimensions of 3.05 m length, 0.15 m width and 0.31 m depth) prestressed with a 12.7 mm diameter seven wire prestressing strand. Prestressing load (0.5 to 0.7 GUTS) and loading rates of 0.074 KN/second to 74 KN/second were adopted in the tests. The beams were tested in flexure at a loading rate of 0.074 KN/second. The results indicated that the grouted tendon beams have increased cracking and ultimate loads for the same level of prestressing and also improved crack control, i.e. more cracks with smaller widths. On the other hand, rates of loading did not indicate any significant effect on the ultimate load on either tendon system.

Experimental studies of bond between strands and concrete have been carried out by Javor and Lazar (147). Relationships between the compressive strength of concrete and the transfer length of a seven wire strand were obtained. The results obtained indicate that there is a relationship between the strand slip and transfer length and that the stress distribution in the strand over the transfer length is approximately linear.

None of the above experimental tests on bond, except those of Stocker and Sozen (105) and Edward and Picard (90) were carried out for local bond-slip relationships. The local bond-slip relationship of various steel bars (e.g. plain bar, deformed bar, prestressing strand and wire) is very important, since this indicates a local constitutive

relation at the interface of steel and concrete. This relationship has an analogy with the stress-strain relationship of steel. Various difficulties were encountered in obtaining a local bond stress and slip on pull out and tension tests (Fig. 2.6.). A large number of pull out and tension tests were carried out (94, 106a, 90, 91, 106b, 93, 106, 105) differing in the dimensions of the test specimen, measurement of bond stress and slip. A bond pull out test used by Edward and Picard is shown in Figure 2.3. Nilson (92) established the local bond-slip for deformed bars by indirectly calculating strains of steel and concrete. An extensive study of local bond-slip behaviour of plain and deformed reinforcing bar was made by Yannopoulous (91) under static and repeated loading. Bond-slip curves are reproduced in Figure 2.7. for plain bars (16.0 mm diameter).

2.4.4. A Case for Present Research

The above literature review indicates that not many reactor vessel analyses and experiments have been performed for bonded cases. Most of the analyses were performed on unbonded reactor vessels. In order to study the bonded reactor vessels, it is intended in the present research to carry out three-dimensional non-linear finite element analyses in which the effect of bond is included. For comparative purposes, an unbonded reactor vessel is also analysed. The review also indicates that significant work has been done for bond and bond-slip relationships for plain and deformed steel bars. Very little in comparison has been done on bonded prestressing wires and strands. For small or large tendons, it is rare to find any reference work on their bond with concrete. In order to study bond behaviour experimentally and to determine local bond-slip relationships, the following experiments have been carried out :

- (a) Prestressed concrete bonded slab
- (b) Pull out tests on prestressed concrete beams

These are fully described in Chapter 7.

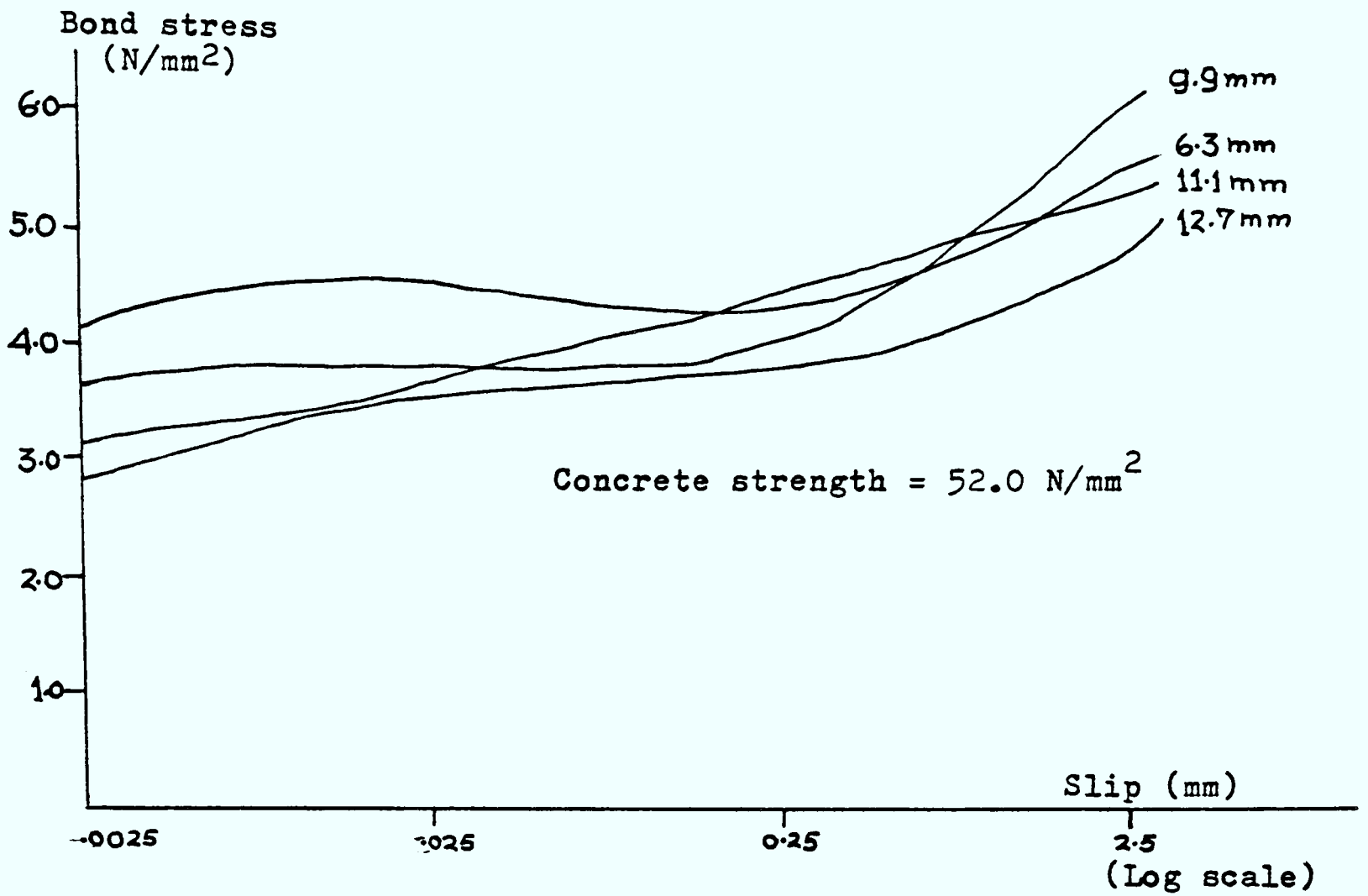


Figure 2.1 Bond-slip Curves for Strands of Different Diameters
(Reference 105 - Stocker and Sozen)

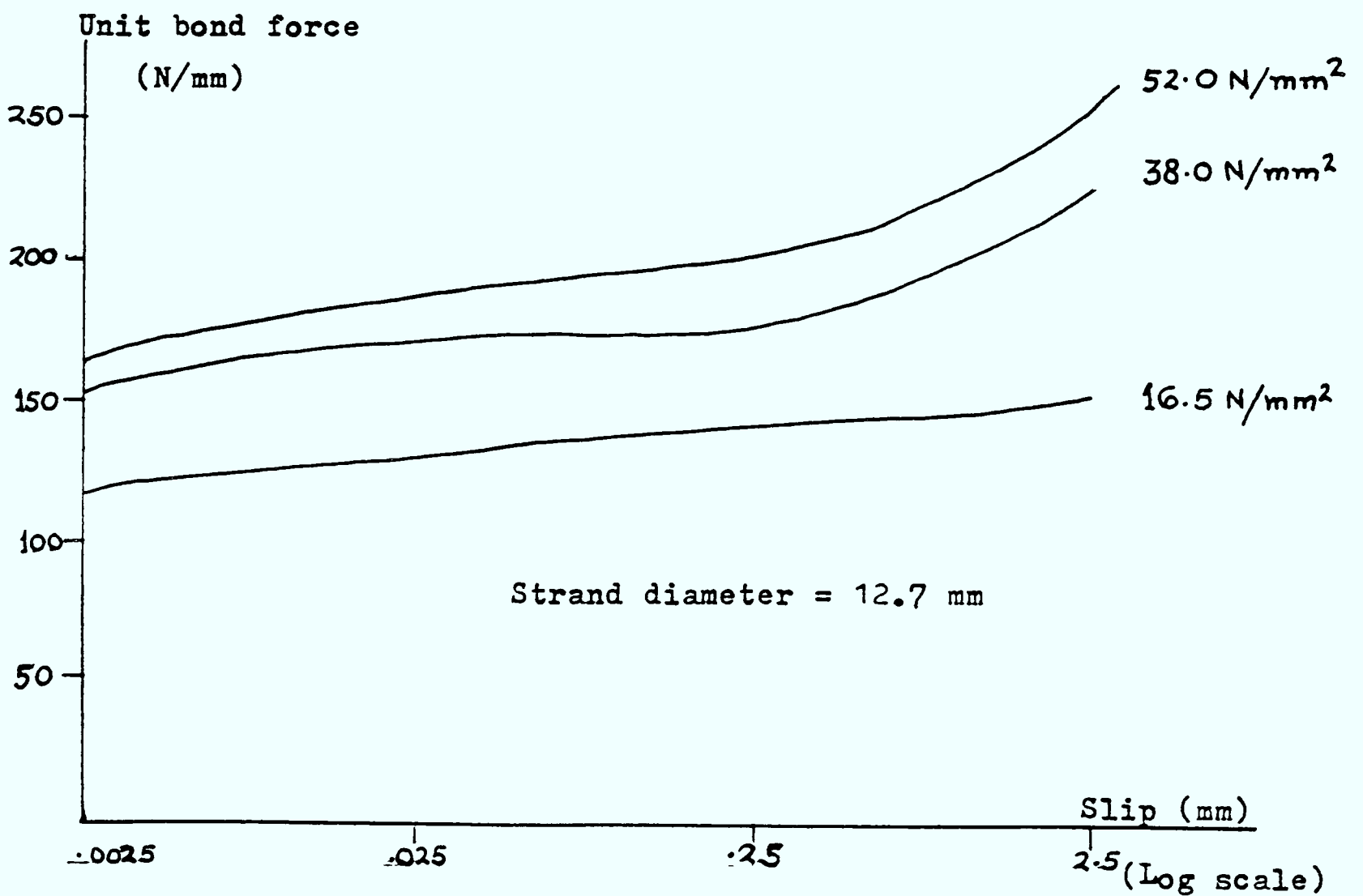


Figure 2.2 Variation of Bond Strength With Concrete Strength
(Reference 105 - Stocker and Sozen)

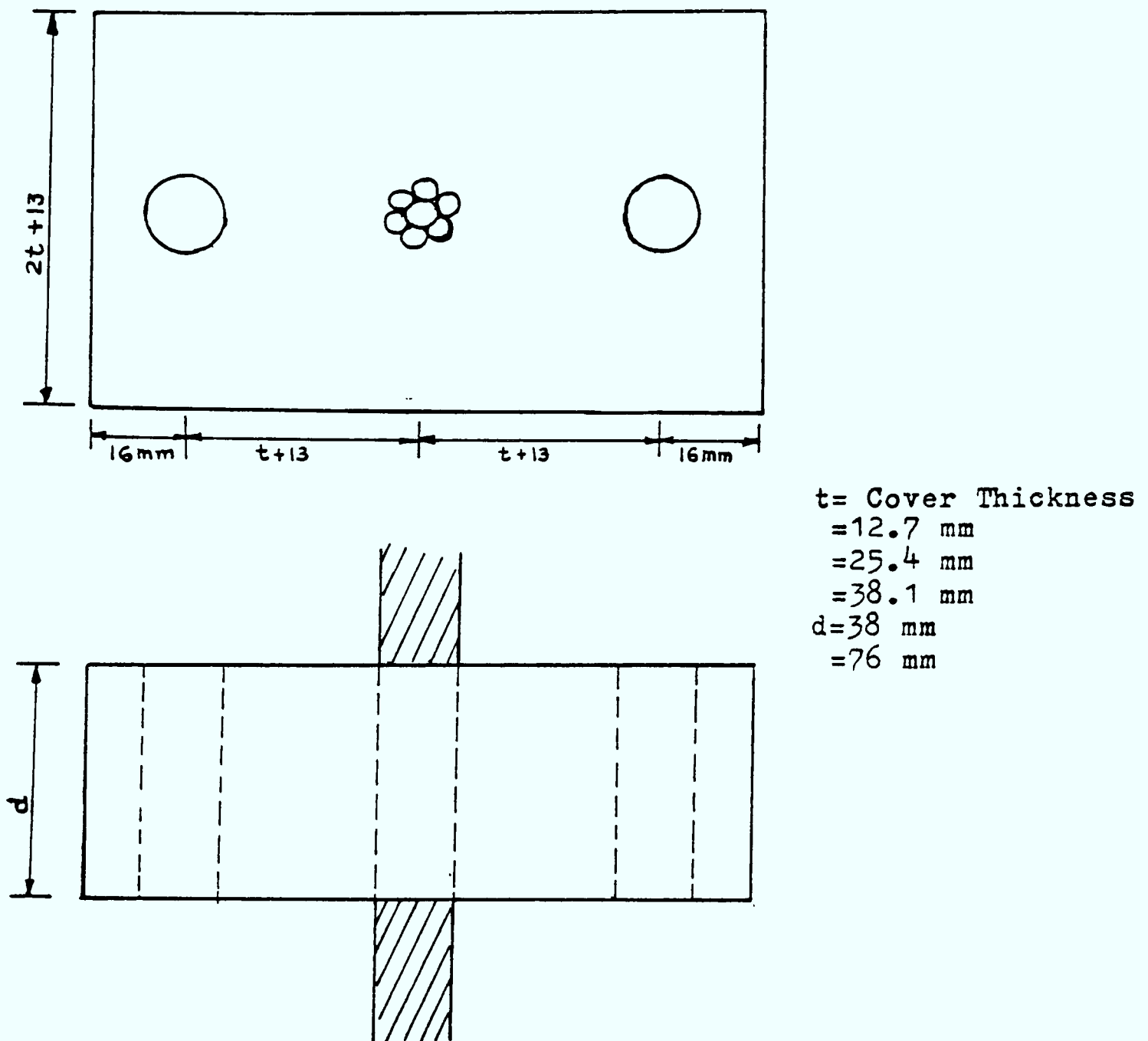


Figure 2.3 Edward and Picard's Bond Specimen (Ref. - 90)

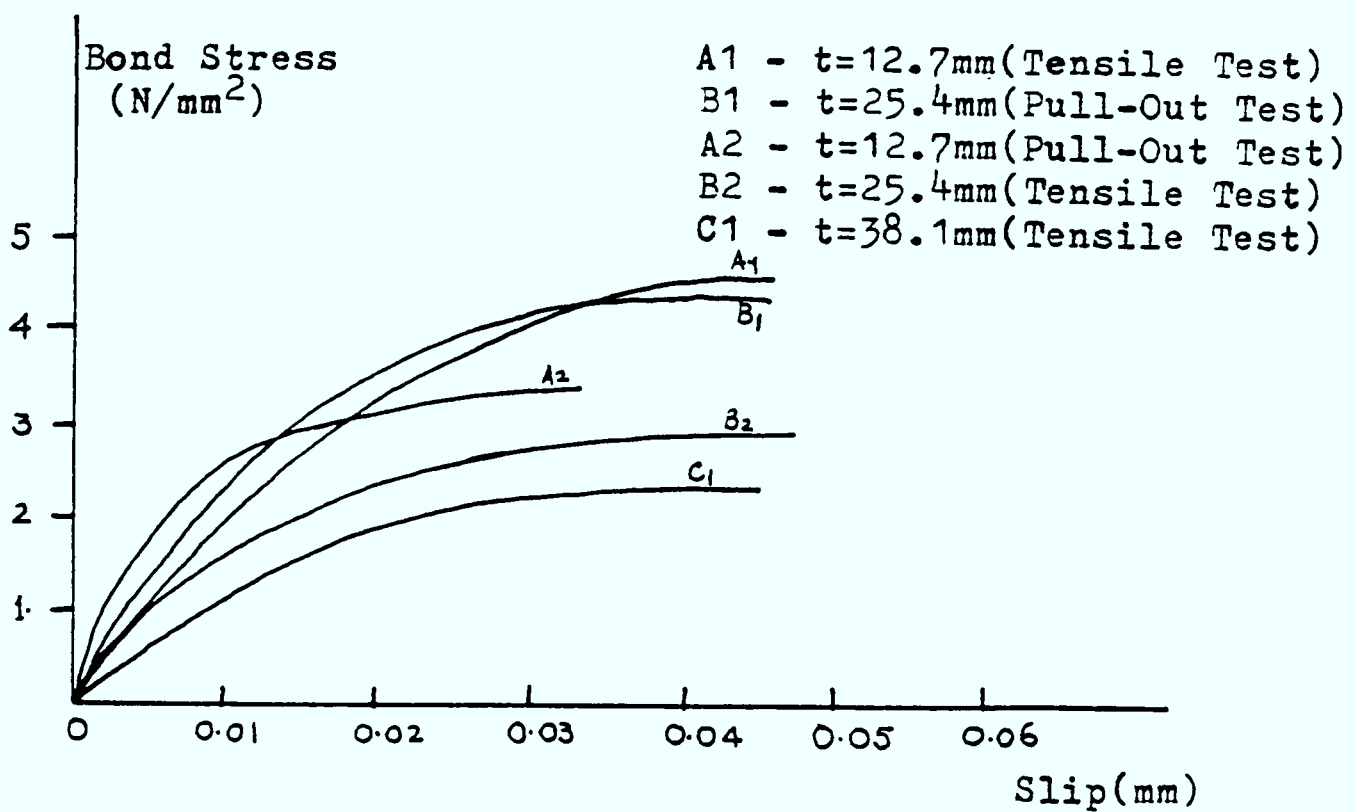


Figure 2.4 Experimental Bond-Slip Curves for 12.7 mm Strand (Ref. - 90)

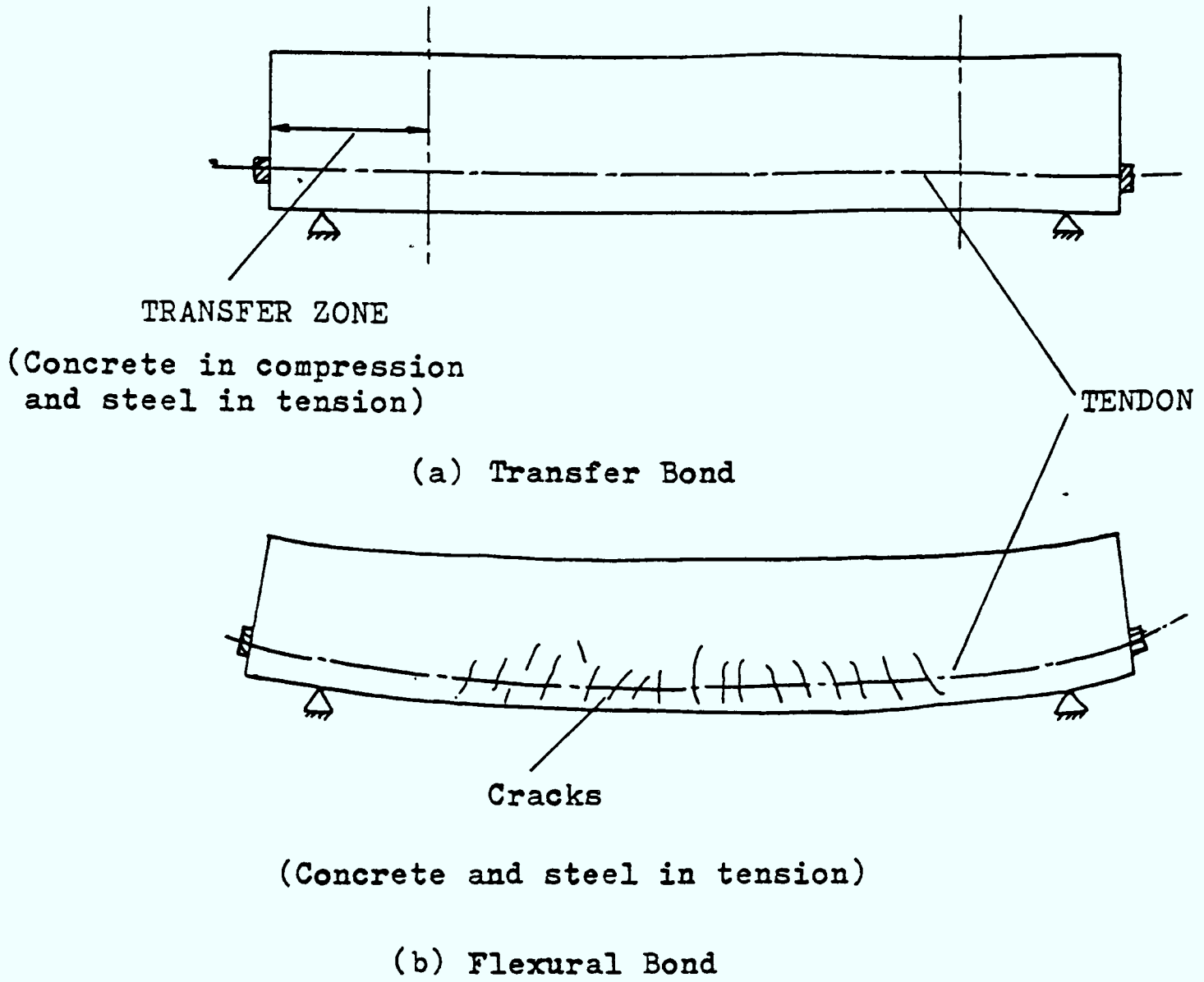


Figure 2.5 Prestressed Concrete Beam

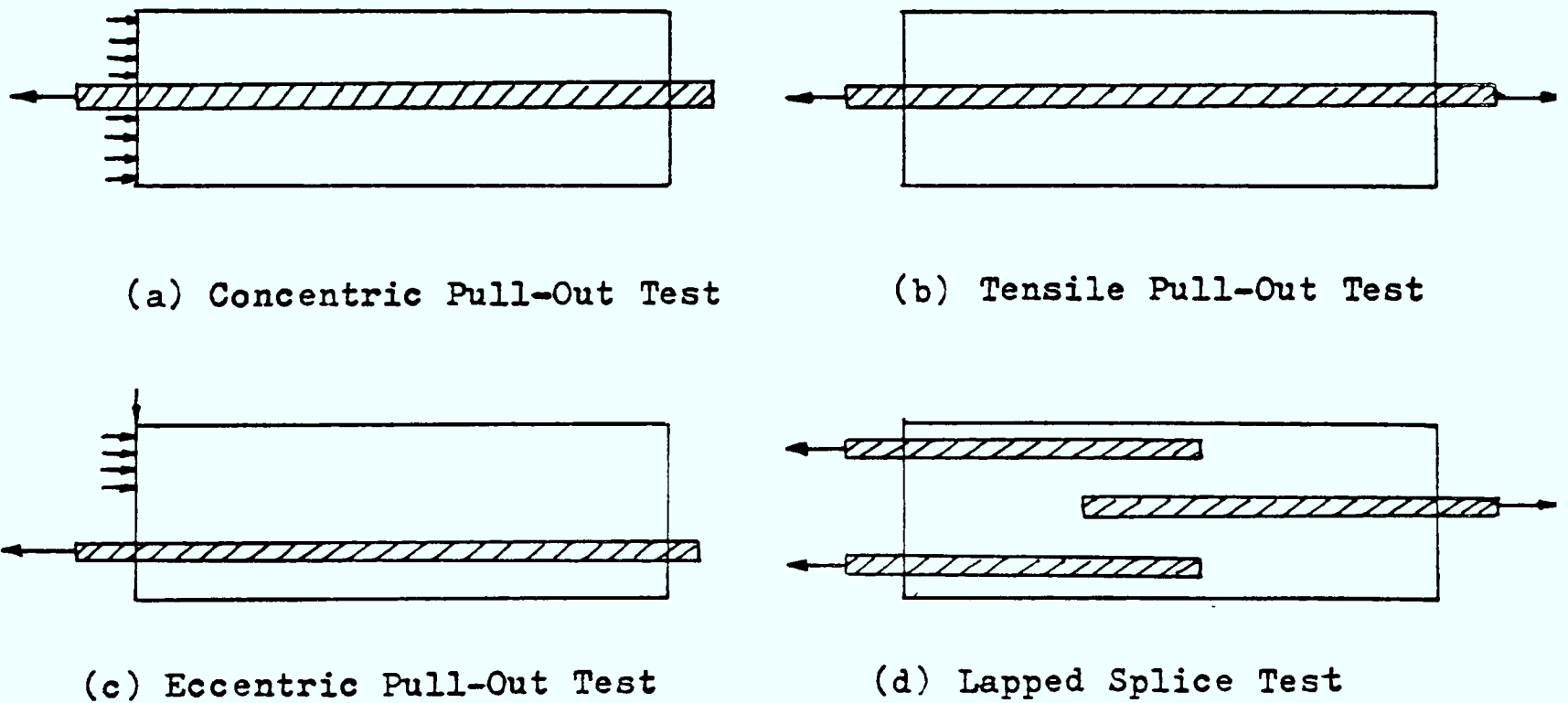


Figure 2.6 Types of Bond Tests

Cover thickness, SL=25mm, BG=35mm
 Back load, LO-No load
 L1=15% of design load of plain bar
 ND-Negative direction of the
 concrete settlements

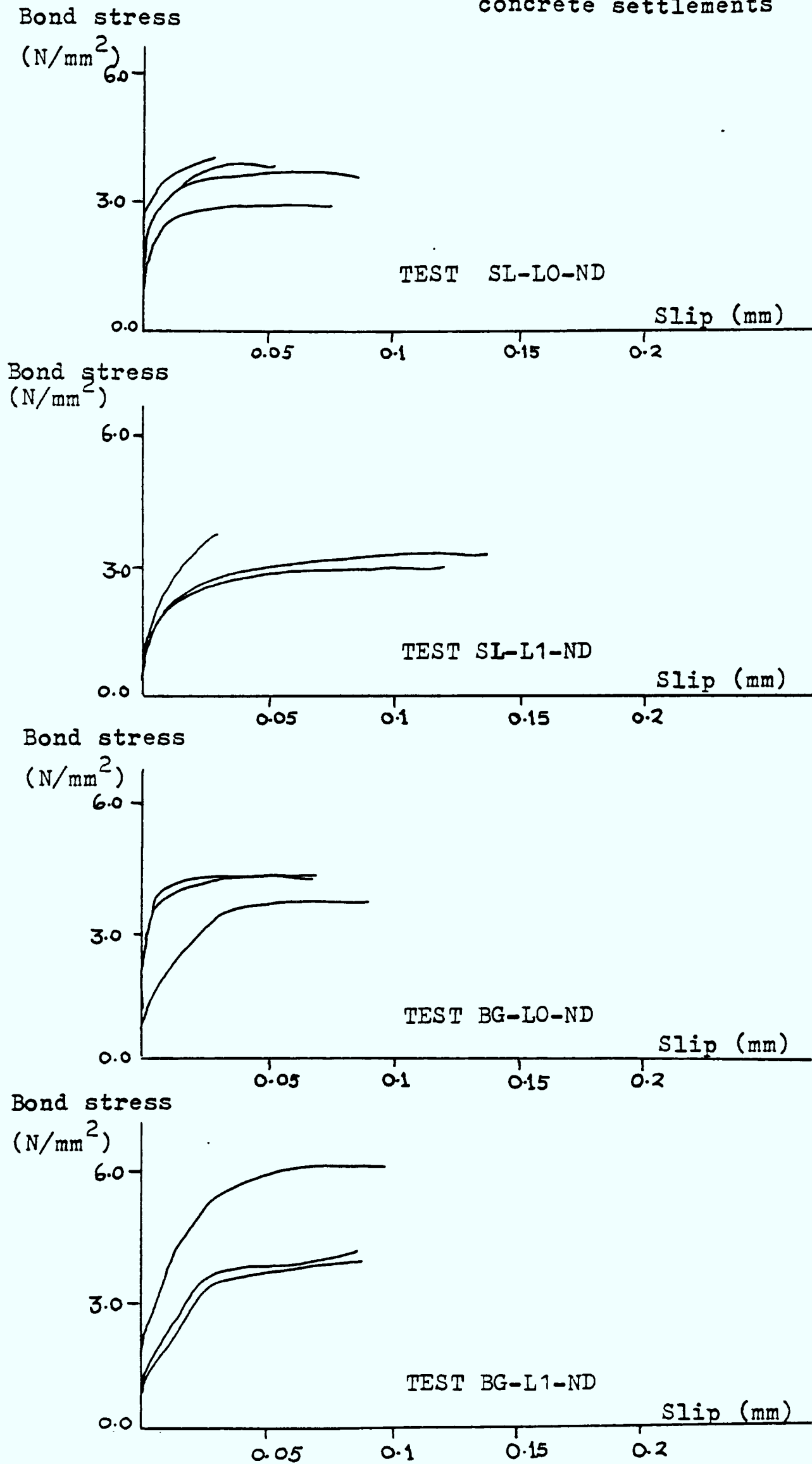


Figure 2.7 Experimental Bond-Slip for 16 mm Dia. Bar(Ref. - 91)

CHAPTER 3

General Finite Element Analysis

3.1. Introduction

This Chapter discusses the general finite element analysis required for the bond strength investigation of prestressed concrete reactor vessels. Three-dimensional isoparametric solid elements were used to model the vessel concrete. Liner and prestressing tendons (bonded reinforcements) were modelled by curved membrane and axial line elements respectively. The interaction between steel and concrete was modelled by specially developed bond-linkage elements. The displacement finite element method was used throughout. As the literature covering the finite element method is vast and comprehensive (1, 2, 3, 4), only the essential features to develop these elements are given. The displacement finite element method is presented first, followed by the expressions for the element stiffness matrices, loads, strains and stresses. Elastic (linear) material constitutive relationships are assumed in this Chapter.

3.2. The Displacement Finite Element Method

The displacement finite element method is adopted. Displacements at nodes are unknown variables. The displacement field within each element can be expressed as :

$$\tilde{u} = \tilde{N} \tilde{u}^e \quad (3.1)$$

$$= \sum_{i=1}^n N_i \tilde{I} \tilde{u}_i \quad (3.1a)$$

where

- \tilde{u}^e - element nodal displacement vector
- \tilde{u}_i - displacements at node i
- \tilde{N} - element shape function matrix
- N_i - shape function of node i

- $\underline{\underline{I}}$ - identity matrix of n x n
 n - number of nodes of an element
 \sim - denotes a matrix or a vector

When the displacements are known at all points within each element, the strain at any point within the element may be written as :

$$\underline{\underline{\xi}} = \sum_{i=1}^n \underline{\underline{B}}_i \underline{\underline{u}}_i = \underline{\underline{B}} \underline{\underline{u}}^e \quad (3.2)$$

$$\underline{\underline{B}} = [\underline{\underline{B}}_1, \underline{\underline{B}}_2, \underline{\underline{B}}_3, \dots, \underline{\underline{B}}_i, \dots, \underline{\underline{B}}_n] \quad (3.3)$$

- where $\underline{\underline{B}}$ - strain-displacement matrix for an element
 $\underline{\underline{B}}_i$ - strain-displacement matrix at node i

In general, the stresses are calculated within the element using the following relationship :

$$\underline{\underline{\sigma}} = \underline{\underline{D}} (\underline{\underline{\xi}} - \underline{\underline{\xi}}_0) + \underline{\underline{\sigma}}_0 \quad (3.4)$$

- where $\underline{\underline{\sigma}}_0$ - initial stresses
 $\underline{\underline{\xi}}_0$ - initial (thermal) strains
 $\underline{\underline{D}}$ - elastic constitutive material matrix

When virtual displacements, $d\underline{\underline{u}}^e$, are applied at the nodes, the sum of work done by the stresses, distributed body and surface forces over the element volume (vol) and surface area(s) is respectively given by :

$$dW = (d\underline{\underline{u}}^e)^T \left(\int_{vol} \underline{\underline{B}}^T \underline{\underline{\sigma}} dvol - \int_s \underline{\underline{N}}^T \underline{\underline{P}}_s ds - \int_{vol} \underline{\underline{N}}^T \underline{\underline{P}}_G dvol \right) \quad (3.5)$$

- where $\underline{\underline{P}}_s$ - surface force per unit surface area
 $\underline{\underline{P}}_G$ - force per unit volume

In order to maintain equilibrium within the element, a system of external nodal forces, $\underline{\underline{P}}_{ex}$, must be applied, and the external work equated to the internal work :

$$(d\underline{u}^e)^T \underline{P}_{ex} = (d\underline{u}^e)^T \left(\int_{vol} \underline{B}^T \underline{\sigma} dvol - \int_S \underline{N}^T \underline{P}_s ds - \int_{vol} \underline{N}^T \underline{P}_b dvol \right) \quad (3.6)$$

Equation (3.6) is valid for any set of virtual displacements, $d\underline{u}^e$, and may be eliminated from both sides of Equation (3.6). Substitute Equations (3.2) and (3.4) to obtain :

$$\underline{P}_{ex} = \left(\int_{vol} \underline{B}^T \underline{D} \underline{B} dvol \right) \underline{u}^e - \int_{vol} \underline{B}^T \underline{D} \underline{\epsilon}_0 dvol + \int_{vol} \underline{B}^T \underline{\sigma}_0 dvol - \int_S \underline{N}^T \underline{P}_s ds - \int_{vol} \underline{N}^T \underline{P}_b dvol \quad (3.7)$$

$$\underline{P}_{ex} = \underline{K}^e \underline{u}^e + \underline{P}_{\epsilon_0}^e + \underline{P}_{\sigma_0}^e + \underline{P}_s^e + \underline{P}_b^e \quad (3.8)$$

Equation (3.8) is the force-displacement relationship with stiffness transformation. In which :

(a) The element stiffness matrix, $\underline{K}^e = \int_{vol} \underline{B}^T \underline{D} \underline{B} dvol \quad (3.8a)$

(b) The element body force, $\underline{P}_b^e = - \int_{vol} \underline{N}^T \underline{P}_b dvol \quad (3.8b)$

(c) The element nodal force due to surface pressure, $\underline{P}_s^e = - \int_S \underline{N}^T \underline{P}_s ds \quad (3.8c)$

(d) The element nodal force due to initial stress, $\underline{P}_{\sigma_0}^e = \int_{vol} \underline{B}^T \underline{\sigma}_0 dvol \quad (3.8d)$

(e) The element nodal force due to initial strain, $\underline{P}_{\epsilon_0}^e = - \int_{vol} \underline{B}^T \underline{D} \underline{\epsilon}_0 dvol \quad (3.8e)$

Equation (3.8) is assembled to form a global stiffness matrix and load vector. The following force-displacement relationship for the entire structure is written as :

$$\underline{P} = \underline{K} \underline{U} \quad (3.9)$$

where \underline{K} - stiffness matrix of the structure
 \underline{P} - generalised force vector for the structure

Equation (3.9) is solved for the unknown nodal displacements, \underline{U} . The strains and stresses at any point within the element are calculated using Equations (3.2) and (3.4) respectively.

3.3. The Solid Isoparametric Elements

The solid isoparametric elements represent concrete of the prestressed concrete reactor vessels and are shown in Figures (3.1a), (3.1b) and (3.1c). The essential features of these solid isoparametric elements in relation to the development of their stiffness matrices and load vectors are briefly given below.

3.3.1. Strain-displacement Relation

The strain displacement relation given earlier in Equation (3.3) is now invoked. For the case of three-dimensional solid elements, the $\underline{\mathbf{B}}$ of node i is given below :

$$\underline{\mathbf{B}}_i = \begin{bmatrix} \frac{\partial N_i}{\partial x} & 0 & 0 \\ 0 & \frac{\partial N_i}{\partial y} & 0 \\ 0 & 0 & \frac{\partial N_i}{\partial z} \\ \frac{\partial N_i}{\partial y} & \frac{\partial N_i}{\partial x} & 0 \\ 0 & \frac{\partial N_i}{\partial z} & \frac{\partial N_i}{\partial y} \\ \frac{\partial N_i}{\partial z} & 0 & \frac{\partial N_i}{\partial x} \end{bmatrix} \quad (3.10)$$

with $\underline{\underline{\xi}} = \sum_{i=1}^n \underline{\mathbf{B}}_i \underline{\underline{u}}_i$; $\underline{\underline{\xi}} = [\epsilon_x, \epsilon_y, \epsilon_z, \gamma_{xy}, \gamma_{yz}, \gamma_{zx}]^T$ (3.10a)

Appendix A1.1.4. gives full details of the coordinate transformations between Cartesian and curvilinear axes. The Jacobian matrix J , and derivatives of Equation (3.10) are obtained in terms of derivatives with respect to curvilinear coordinates. As there are three degrees of freedom at each node, the dimension of $\underline{\mathbf{B}}$ matrices for the 8, 20 and 32 noded elements is (6x24), (6x60) and (6x96) respectively. Although the 32 noded element is not used in this research, nevertheless it is included for future requirements.

3.3.2. The Stress Calculation

The stress at any point within the element is given by Equation (3.4) and is now rewritten as :

$$\underline{\sigma} = \underline{D} (\underline{\xi} - \underline{\xi}_0) + \underline{\sigma}_0 \quad (3.11)$$

in which

$$\underline{\sigma}_{6 \times 1} = [\sigma_x, \sigma_y, \sigma_z, \tau_{xy}, \tau_{yz}, \tau_{zx}]^T ; \quad \underline{\xi}_{6 \times 1} = [\epsilon_{x_0}, \epsilon_{y_0}, \epsilon_{z_0}, 0, 0, 0]^T \quad (3.11a)$$

where $\underline{D}_{6 \times 6}$ - anisotropic material matrix for concrete (see Equation (A2.1))

For isotropic cases, all ν 's and E 's along three principal axes are the same respectively.

3.3.3. The Element Stiffness Matrix

The element stiffness matrix given in Equation (3.8a) is now rewritten as :

$$\underline{K}^e = \int_{vol} \underline{B}^T \underline{D} \underline{B} dvol = \int_{-1}^{+1} \int_{-1}^{+1} \int_{-1}^{+1} \underline{B}^T \underline{D} \underline{B} \det J d\xi d\eta d\zeta \quad (3.12)$$

where \underline{D} , \underline{B} and $\det J$ are defined by Equations (A2.1), (3.10) and (A1.4a) respectively.

3.3.4. The Load Vectors

The various load vectors of Equation (2.8) are now rewritten as :

$$\underline{P}_s^e = - \int_{-1}^{+1} \int_{-1}^{+1} \int_{-1}^{+1} \underline{N}^T \underline{P}_s \det J d\xi d\eta d\zeta \quad (3.13a)$$

$$\underline{P}_s^e = - \int_S \underline{N}^T \underline{P}_s ds \quad (3.13b)$$

$$\underline{P}_{\epsilon_0}^e = - \int_{-1}^{+1} \int_{-1}^{+1} \int_{-1}^{+1} \underline{B}^T \underline{D} \underline{\epsilon}_0 \det J d\xi d\eta d\zeta \quad (3.13c)$$

$$\underline{P}_{\sigma_0}^e = \int_{-1}^{+1} \int_{-1}^{+1} \int_{-1}^{+1} \underline{B}^T \underline{\sigma}_0 \det J d\xi d\eta d\zeta \quad (3.13d)$$

where $\det J$ = determinant of Jacobian

Further details of the calculation of the pressure load vector (Equation (3.13b)) are given in Appendix A1.1.5. The point load vector idea is also extended for the loads which are not acting directly at nodes. These loads are named as patch loads (see Appendix A1.1.6.).

The integrals of Equations (3.12), (3.13a), (3.13b), (3.13c) and (3.13d) are carried out using the Gauss quadrature formula (2).

3.4. The Membrane Isoparametric Elements

The membrane elements are used to model the steel liner in a prestressed concrete reactor vessel and are treated as thin shell elements. The elements are capable of transmitting only in plane actions and the strain in thickness direction is assumed constant (plane stress conditions are enforced). These elements are compatible with the one face of the solid elements modelled for concrete. The element local, global and curvilinear coordinate systems are shown in Figures (3.2a), (3.2b), and (3.2c). Appendix A1.2. gives details of shape functions, their derivatives and B matrix. Details for these elements are given below.

3.4.1. The Strain-displacement Relations

As the element may be in any direction in the three-dimensional space, the strains refer to a local orthogonal Cartesian system (X' , Y' , Z'). The strain components which contribute to the strain

energy are from Equation (A1.10).

$$\begin{aligned}
 \epsilon_{x'} &= \frac{\partial u'}{\partial x'} \\
 \epsilon_{y'} &= \frac{\partial v'}{\partial y'} \\
 \gamma_{x'y'} &= \frac{\partial u'}{\partial y'} + \frac{\partial v'}{\partial x'} \\
 \text{or } \underline{\underline{\epsilon}}' &= \underline{\underline{B}}' \underline{\underline{u}}'
 \end{aligned}
 \tag{3.14}$$

After carrying out the transformation, the following may be written (see Appendix A1.2) :

$$\underline{\underline{\epsilon}}' = \underline{\underline{B}} \underline{\underline{u}} \quad ; \quad \underline{\underline{\epsilon}}'_{3 \times 1} = [\epsilon_{x'}, \epsilon_{y'}, \gamma_{x'y'}]
 \tag{3.14a}$$

The $\underline{\underline{B}}$ matrix in this case is slightly different. Full details are given in Appendix (A1.2). For node i the $\underline{\underline{B}}$ matrix can be rewritten as (Equation (A1.23)).

$$\underline{\underline{B}}_i = \begin{bmatrix} R_{x'x} d\dot{r}_1 & R_{x'y} d\dot{r}_1 & R_{x'z} d\dot{r}_1 \\ R_{y'x} d\dot{r}_2 & R_{y'y} d\dot{r}_2 & R_{y'z} d\dot{r}_2 \\ (R_{x'x} d\dot{r}_2 + R_{y'x} d\dot{r}_1) & (R_{x'y} d\dot{r}_2 + R_{y'y} d\dot{r}_1) & (R_{x'z} d\dot{r}_2 + R_{y'z} d\dot{r}_1) \end{bmatrix}
 \tag{3.15}$$

Further details about the strain-displacement matrix are given in Appendix A1.2.

3.4.2. The Stress Calculation

The local stresses at any point are written as :

$$\underline{\underline{\sigma}}' = \underline{\underline{D}}_M (\underline{\underline{\epsilon}}' - \underline{\underline{\epsilon}}'_0)
 \tag{3.16}$$

$$\text{in which } \underline{\underline{\sigma}}'_{3 \times 1} = [\sigma_{x'}, \sigma_{y'}, \tau_{x'y'}]^T \quad ; \quad \underline{\underline{\epsilon}}'_0_{3 \times 1} = [\epsilon_{x'_0}, \epsilon_{y'_0}, 0]^T
 \tag{3.16a}$$

For the plane stress case, the elastic material matrix is given by :

$$\underline{\underline{D}}_M = \frac{E_s}{1-\nu_s^2} \begin{bmatrix} 1 & \nu_s & 0 \\ \nu_s & 1 & 0 \\ 0 & 0 & \frac{1-\nu_s}{2} \end{bmatrix} \quad (3.17)$$

Where E_s and ν_s are the modulus of elasticity and Poisson's ratio of steel.

3.4.3. The Element Stiffness Matrix

The element stiffness matrix for this element is given by :

$$\underline{\underline{K}}^e = \int_{-1}^{+1} \int_{-1}^{+1} \underline{\underline{B}}^T \underline{\underline{D}}_M \underline{\underline{B}} \det J \, d\xi \, d\eta \quad (3.18)$$

In which $\underline{\underline{D}}_M$ of Equation (3.17) and $\underline{\underline{B}}$ of Equation (3.15) are used. The numerical integration is again adopted for Equation (3.18).

3.5. The Line Elements

The line elements are used to model the vessel prestressing tendons and reinforcements (primary and secondary). The elements are only capable of transmitting axial stress and strain and are classified according to the following categories :

- (a) Two node line element (Direct Approach)
- (b) Two, three and four node elements (Isoparametric Approach)
- (c) Isoparametric line element in the body of solid element (Body Element)

3.5.1. Two Node Line Element (Direct Approach)

This is the simplest element (Figure (3.3a)) in the series of line elements. The element is straight with length L , end nodes 1, 2, cross-sectional area, A , and modulus of elasticity E_s . The following displacement function is taken into consideration :

$$u' = \alpha_0 + \alpha_1 x' \quad (3.19)$$

The stiffness matrix in global system can be written as :

$$\tilde{K}^e = \tilde{T}^T \tilde{K}_L \tilde{T} \quad (3.20)$$

In which \tilde{K}_L is the element stiffness matrix in local system. This may be written as :

$$\tilde{K}_L = \frac{E_s A}{L} \begin{bmatrix} 1 & -1 \\ -1 & 1 \end{bmatrix} \quad (3.20a)$$

And \tilde{T} is the transformation matrix

$$\tilde{T} = \begin{bmatrix} l_1, m_1, n_1 & 0, 0, 0 \\ 0, 0, 0 & l_1, m_1, n_1 \end{bmatrix} \quad (3.20b)$$

where l_1, m_1, n_1 are the direction cosines of element axis with respect to global axes. The explicit form of Equation (3.20) is given in Appendix A1, Equation (A1.25).

The local strain and stress are now written as :

$$\epsilon_{x'} = \frac{1}{L} [l_1 (u_2 - u_1) + m_1 (v_2 - v_1) + n_1 (w_2 - w_1)] \quad (3.21a)$$

$$\sigma_{x'} = E_s (\epsilon_{x'} - \epsilon_{x'_0}) \quad (3.21b)$$

where u_1, v_1, w_1 and u_2, v_2, w_2 are the global nodal displacements of nodes 1 and 2 respectively. E_s is the modulus of elasticity and $\epsilon_{x'_0}$ the initial strain.

3.5.2. Isoparametric Line Elements

The concept used in this case to develop the stiffness matrix is very similar to that for the solid and membrane elements developed in the previous sections. The shape functions, derivatives and the strain-displacement matrices for these elements are given in Appendix A1.3.2.

The element stiffness matrix is then written as (Figures (3.3a), (3.3b) and (3.3c)) :

$$\underline{\underline{K}}^e = \int_{-1}^{+1} \underline{\underline{B}}^T E_s \underline{\underline{B}} A(\xi) L d\xi = \sum_{j=1}^{NG} \underline{\underline{B}}_j^T E_s \underline{\underline{B}}_j L_j W_j A(\xi_j) \quad (3.22)$$

where

$$A(\xi) = \sum_{i=1}^n N_i A_i \quad (3.22a)$$

where A_i - cross-sectional area at node i , n = number of nodes on element
 NG - number of integration points, N_i = shape function at node i

$E_s, \underline{\underline{B}}$ have been defined earlier. Reference is made to Appendix A1.3.2.

The strain and stress are calculated as follows :

$$\underline{\underline{\epsilon}}_{x'} = \underline{\underline{B}} \underline{\underline{u}}^e \quad (3.23)$$

$$\underline{\underline{\sigma}}_{x'} = E_s \underline{\underline{\epsilon}}_{x'}. \quad (3.24)$$

where $\underline{\underline{u}}^e$ is the global nodal displacement vector for the element.

3.5.3. Line Element in the Body of the Solid Element (refer to Figure (3.4))

The main use of this element is in modelling the reinforcement inside the concrete. The solid element, together with this element represents a composite element. An assumption made in deriving the $\underline{\underline{B}}$ matrix (Appendix A3.3) is that the steel has to lie in the directions of local curvilinear axis (ξ, η, ζ) of the parent solid element. The stiffness matrix of this element may be written as :

$$\underline{\underline{K}}^e = \int_{-1}^{+1} \underline{\underline{B}}^T E_s \underline{\underline{B}} A(\xi) \det J d\xi \quad (3.25)$$

where $\underline{\mathfrak{B}}$ is defined by Equations (A1.36) and (A1.37) and $\det J$ is defined by the determinant of Jacobian matrix.

3.6. The Three-dimensional Bond-linkage Element

The three-dimensional bond linkage element, the Ahmlink element, has been developed to model the interface relationship between steel and concrete. This element connects the line and the solid elements together and has two nodes as is shown in Figure (3.5). This element was first developed in a two-dimensional form by Scordelis (8) and was later used by others (9, 44). In this work, the element is extended to three dimensions. Physically, the element does not exist, but its mechanical action is represented by three orthogonal springs connected in the horizontal, vertical and lateral directions to steel and concrete elements. The horizontal spring represents the bond stiffness and acts as bond between the steel and concrete. The other two springs represent the vertical and the lateral adhesion between the steel and concrete. The procedure for the derivation of stiffness matrix and computation of stresses is given below :

Let X, Y, Z and X', Y', Z' , be the global and the local coordinate systems (Figure (3.5)) respectively. The direction cosines of the local axes (X', Y', Z') with respect to global axes (X, Y, Z) are (l, m, n) , $(p, q, 0)$ and (r, s, t) . Let P, Q be the line element nodes. The direction cosines in terms of nodal coordinates may be written as follows :

$$\begin{aligned}
 l &= \frac{X_Q - X_P}{L} & ; & & m &= \frac{Y_Q - Y_P}{L} & ; & & n &= \frac{Z_Q - Z_P}{L} \\
 p &= \frac{-m}{\sqrt{1-n^2}} & ; & & q &= \frac{l}{\sqrt{1-n^2}} \\
 r &= \frac{-ln}{\sqrt{1-n^2}} & ; & & s &= \frac{-mn}{\sqrt{1-n^2}} & ; & & t &= \sqrt{1-n^2}
 \end{aligned}
 \tag{3.26}$$

in which
$$L = \sqrt{(X_Q - X_P)^2 + (Y_Q - Y_P)^2 + (Z_Q - Z_P)^2} \tag{3.27}$$

In the case of $l=m=0$ and $n=1$, the direction cosines take the following values :

$$p=0; q=1; t=0; r=-1; s=0 \quad (3.28)$$

With this definition for the direction cosines, the local X' is always tangential to line element with the other two directions being orthogonal to it.

Let $\Delta S_h, \Delta S_v$ and ΔS_ℓ be the incremental slips in the horizontal, lateral and vertical directions of the steel element. The incremental relationship between the slip and the nodal displacements can then be written as :

$$\begin{Bmatrix} \Delta S_h \\ \Delta S_v \\ \Delta S_\ell \end{Bmatrix} = \begin{bmatrix} -l & -m & -n & l & m & n \\ -p & -q & 0 & p & q & 0 \\ -r & -s & -t & r & s & t \end{bmatrix} \begin{Bmatrix} \Delta U_i \\ \Delta V_i \\ \Delta W_i \\ \Delta U_j \\ \Delta V_j \\ \Delta W_j \end{Bmatrix} \quad (3.29)$$

or

$$\Delta \underline{S}^e = \underline{T} \Delta \underline{U}^e \quad (3.29a)$$

where \underline{T} is the transformation matrix, $\Delta \underline{U}^e$ are the global element displacements.

The local incremental bond stress and bond-slip may be written as :

$$\begin{Bmatrix} \Delta \sigma_h \\ \Delta \sigma_v \\ \Delta \sigma_\ell \end{Bmatrix} = \begin{bmatrix} E_h & 0 & 0 \\ 0 & E_v & 0 \\ 0 & 0 & E_\ell \end{bmatrix} \begin{Bmatrix} \Delta S_h \\ \Delta S_v \\ \Delta S_\ell \end{Bmatrix} \quad (3.30)$$

or

$$\Delta \underline{\sigma}^e = \underline{E}_b \Delta \underline{S}^e \quad (3.30a)$$

where E_h, E_v and E_ℓ are the bond-slip moduli in the three directions.

These can be obtained by using an idealised bond-slip curve. These curves are shown in Chapter 2 and elsewhere in this thesis.

Here $E_h = \frac{\Delta \beta}{\Delta S}$

where $\Delta\beta, \Delta s$ are the incremental bond stress and slip from a specified bond-slip curve.

Assuming bond stresses as average stresses along the length of the steel with length L , the incremental nodal force and the stress relation may be written in the following form :

$$\Delta \underline{P}^e = \pi d L \underline{T}^T \Delta \underline{\sigma}_b^e \quad (3.31)$$

where $\Delta \underline{\sigma}_b^e = [\Delta \sigma_h, \Delta \sigma_v, \Delta \sigma_z]^T$
 $\Delta \underline{P}^e = [\Delta P_u^i, \Delta P_v^i, \Delta P_w^i, \Delta P_u^j, \Delta P_v^j, \Delta P_w^j]^T$
 d - diameter of steel embedded in concrete
 $\pi d L$ - surface area over which the linkage element is connected with the steel

Now the relationship between the incremental nodal forces and the incremental displacements by substituting Equation (3.29) and (3.30) in Equation (3.31) :

$$\Delta \underline{P}^e = \pi d L \underline{T}^T \underline{E}_b \underline{T} \Delta \underline{U}^e \quad (3.32)$$

$$\Delta \underline{P}^e = \underline{K}_b^e \Delta \underline{U}^e \quad (3.32a)$$

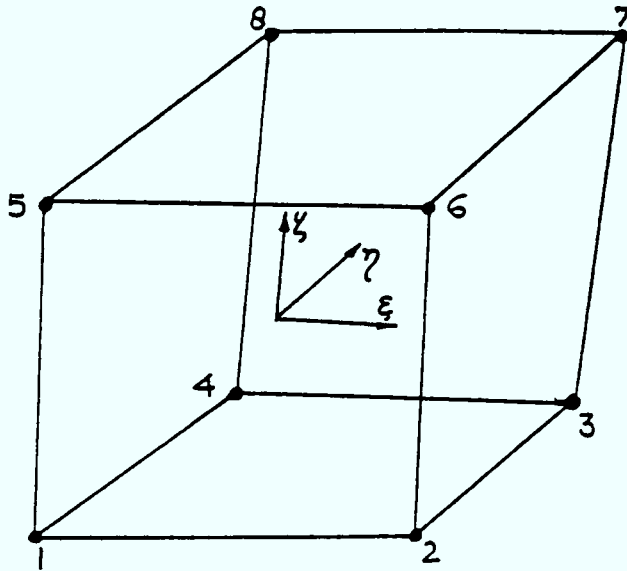
where $\underline{K}_b = \pi d L \underline{T}^T \underline{E}_b \underline{T} \quad (3.32b)$

\underline{K}_b - bond-linkage stiffness matrix
 \underline{K}_b - 6×6

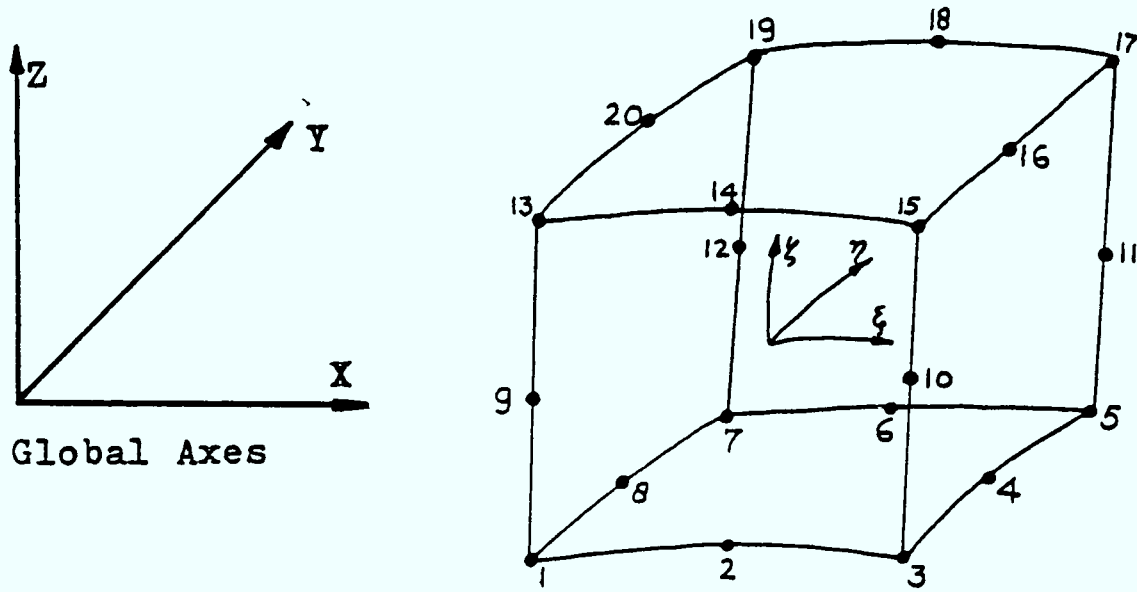
The explicit form of \underline{K}_b is given in Appendix (A1.5).

The stresses in terms of nodal displacements can be calculated by substituting Equation (3.29a) in Equation (3.30a) as follows :

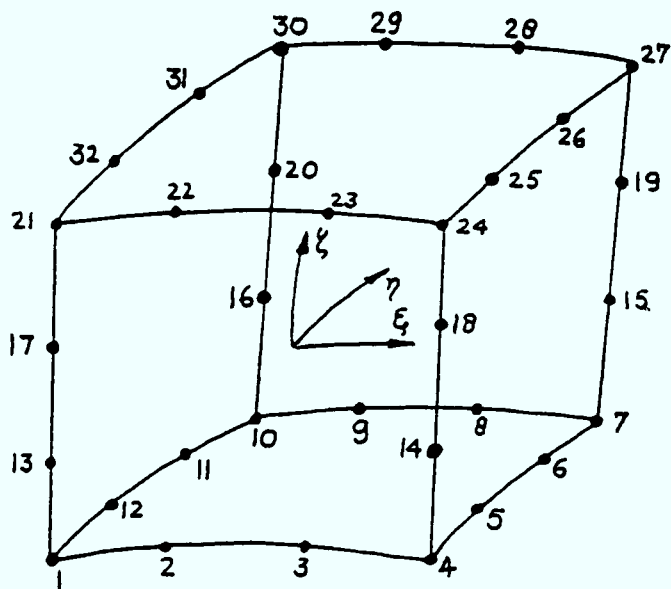
$$\Delta \underline{\sigma}_b^e = \underline{E}_b \underline{T} \Delta \underline{U}^e \quad (3.33)$$



(a) 8 Noded Solid Element



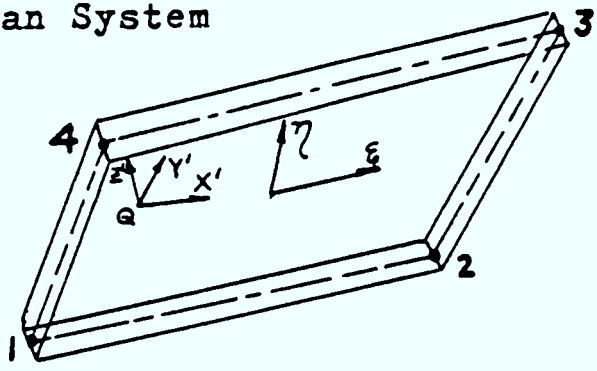
(b) 20 Noded Solid Element



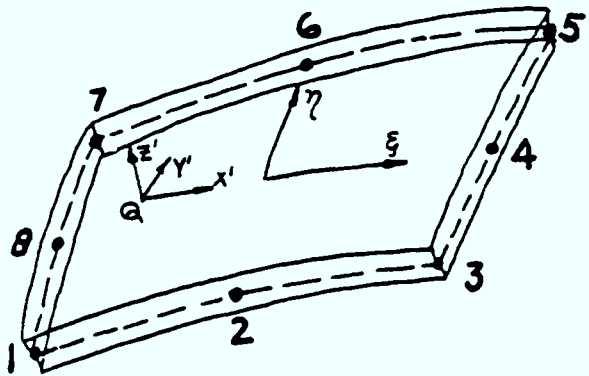
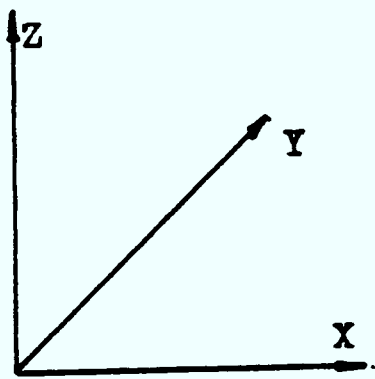
(c) 32 Noded Solid Element

Figure 3.1 Isoparametric Solid Elements

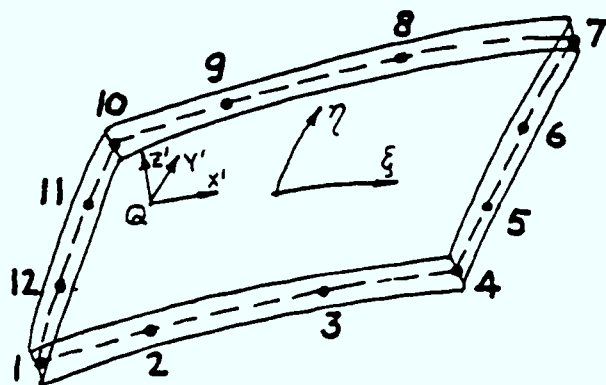
XYZ - Global Cartesian System
 X'Y'Z' - Local Cartesian System



(a) 4 Noded Membrane Element

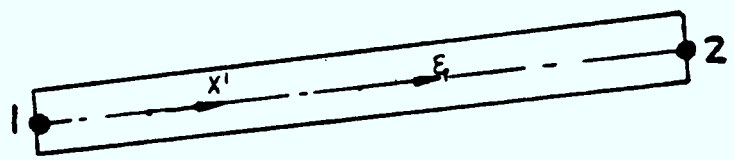
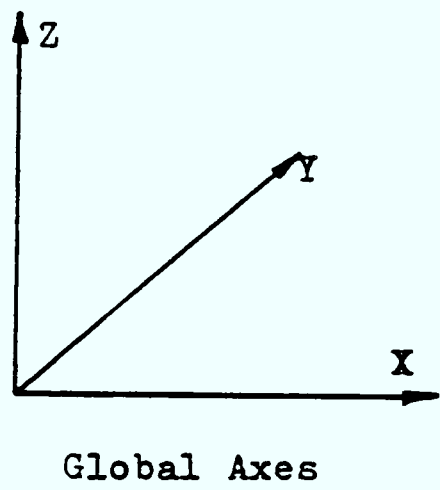


(b) 8 Noded Membrane Element

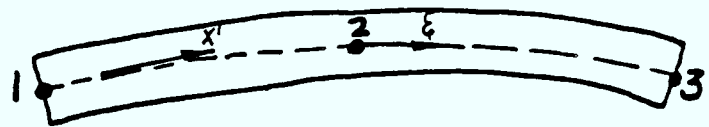


(c) 12 Noded Membrane Element

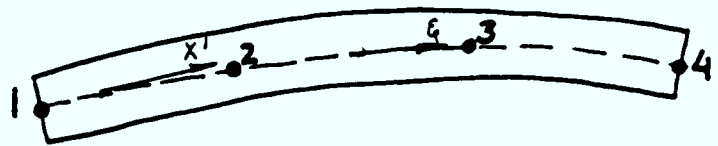
Figure 3.2 Isoparametric Membrane Elements



(a) 2 Noded Line Element



(b) 3 Node Line Element



(c) 4 Noded Line Element

Figure 3.3 Isoparametric Line Elements

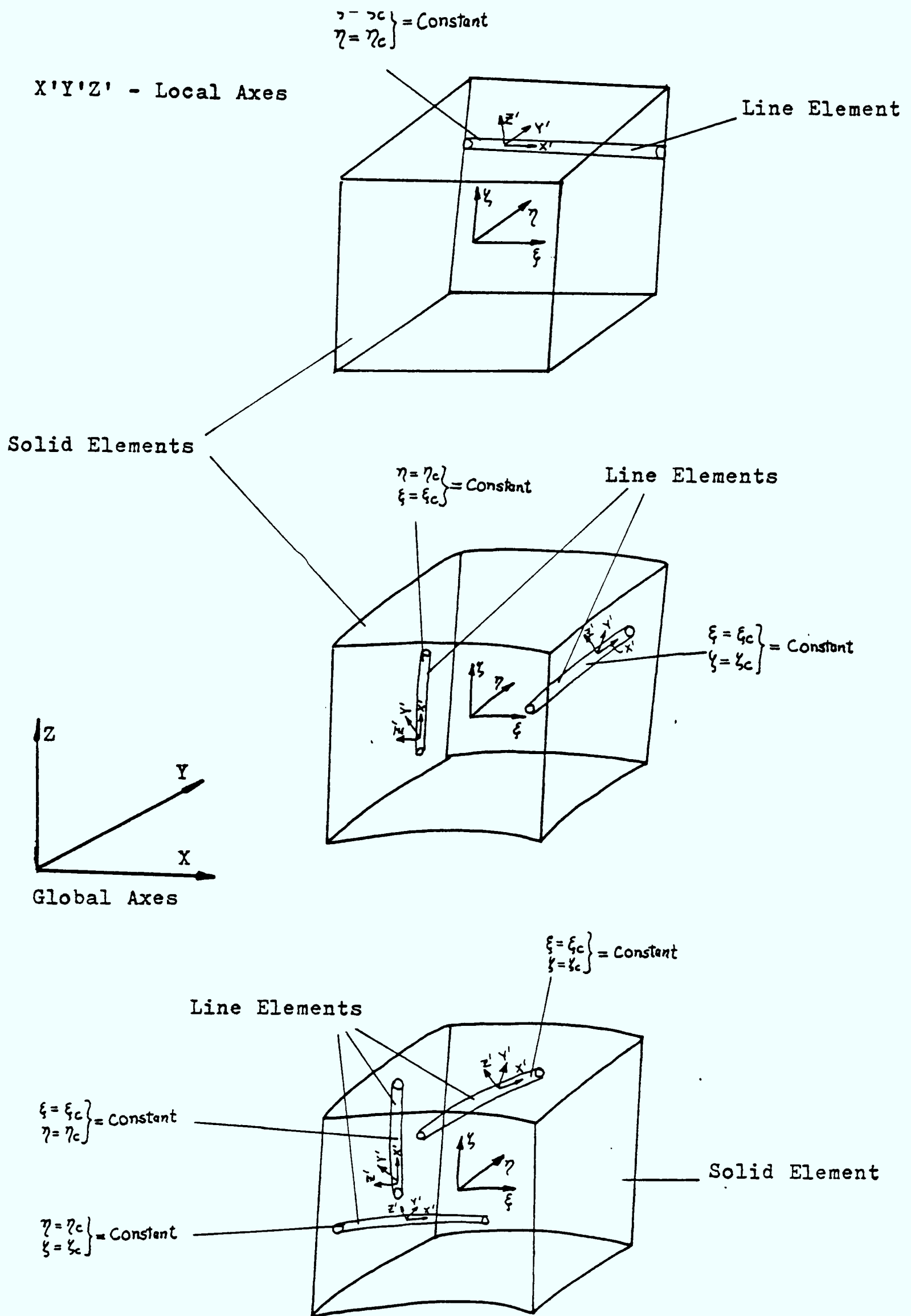
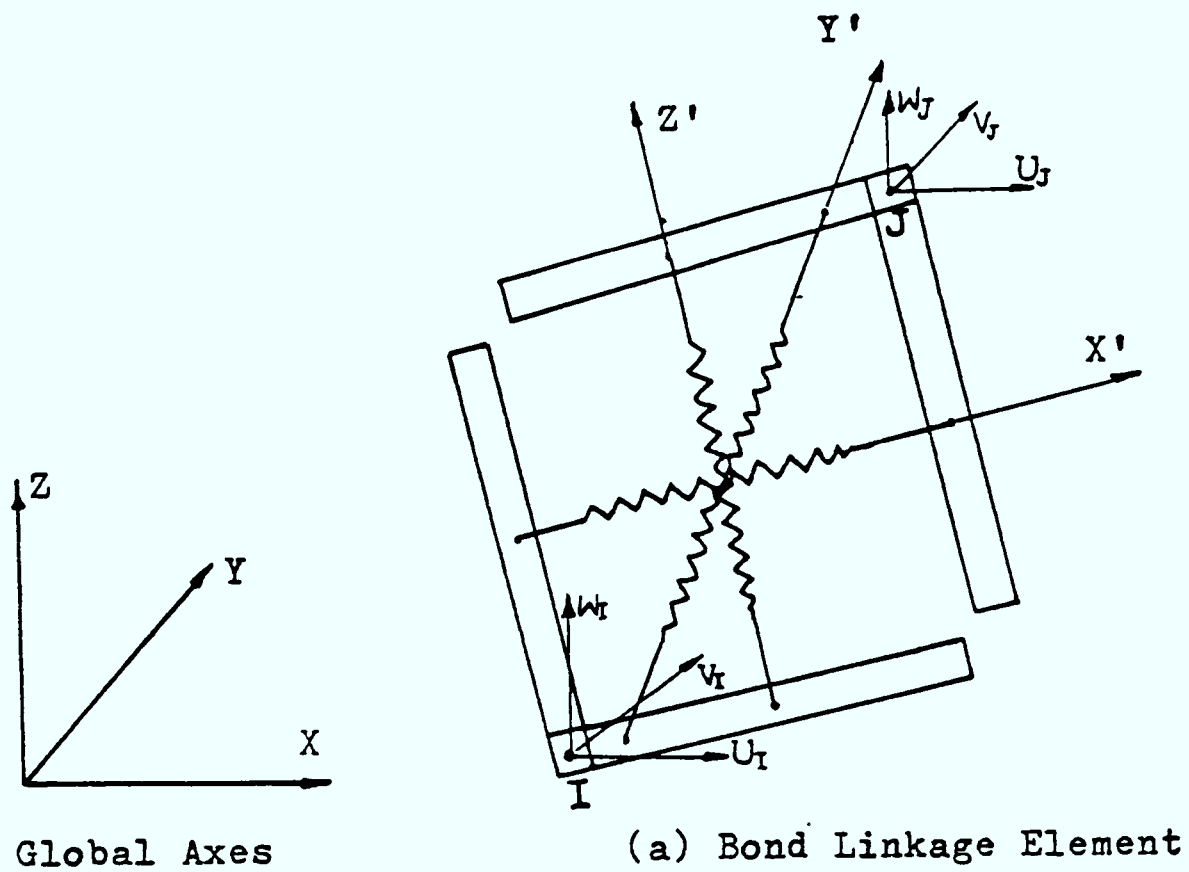


Figure 3.4 Line Elements in the Body of Solid Element



X'Y'Z' - Local Axes

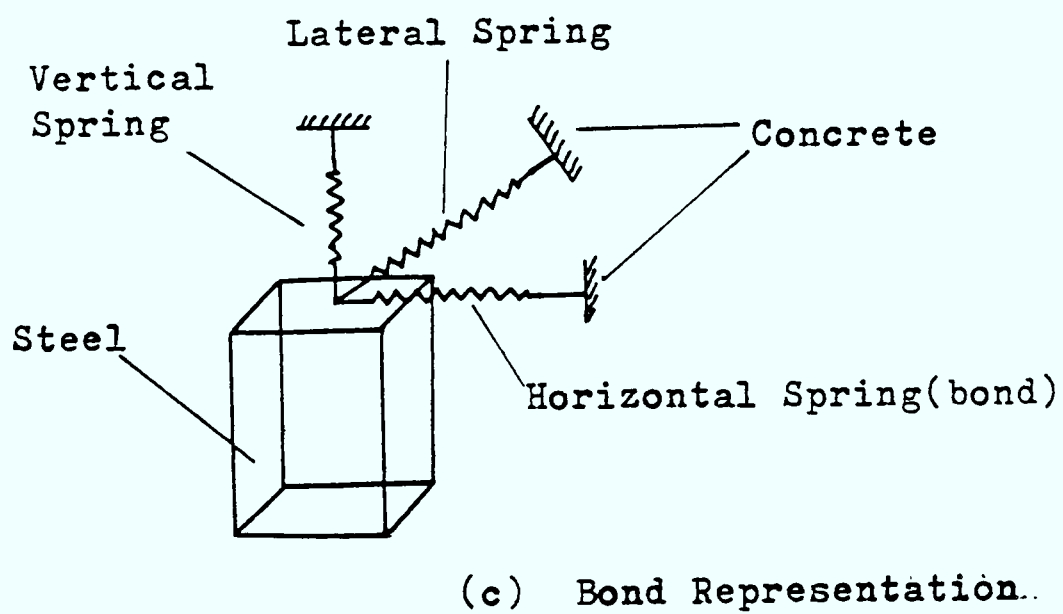
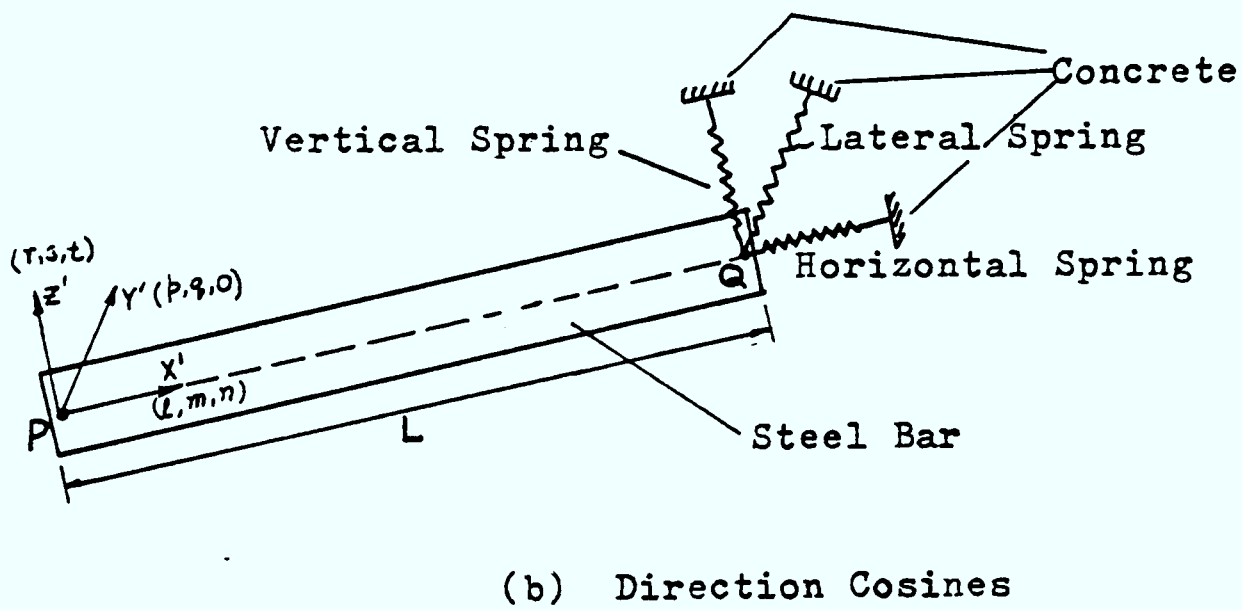
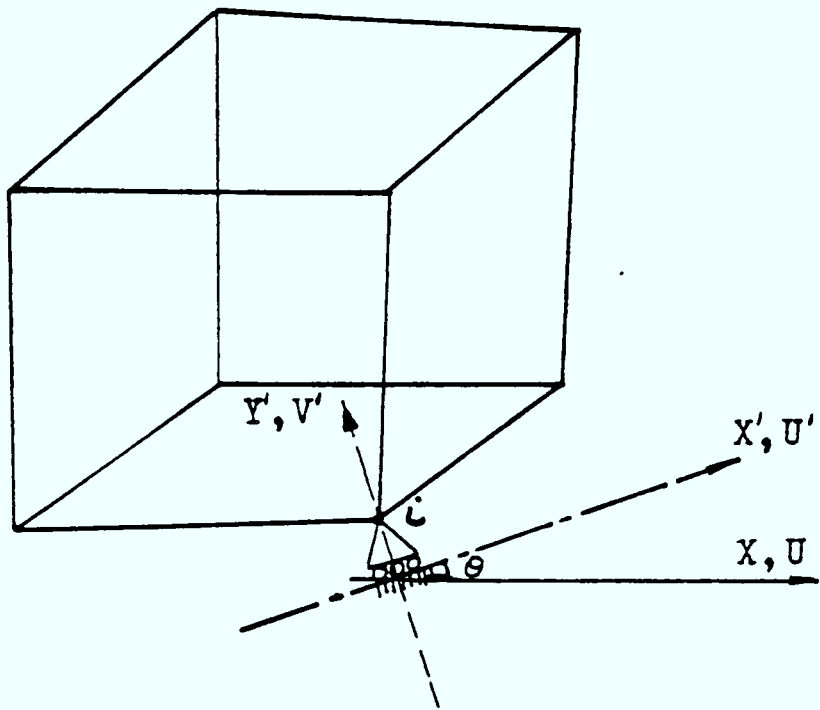
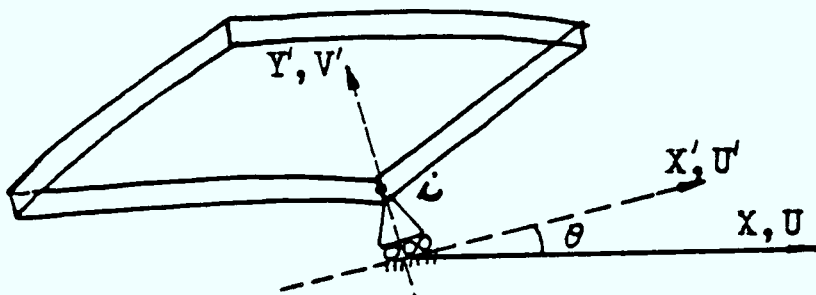


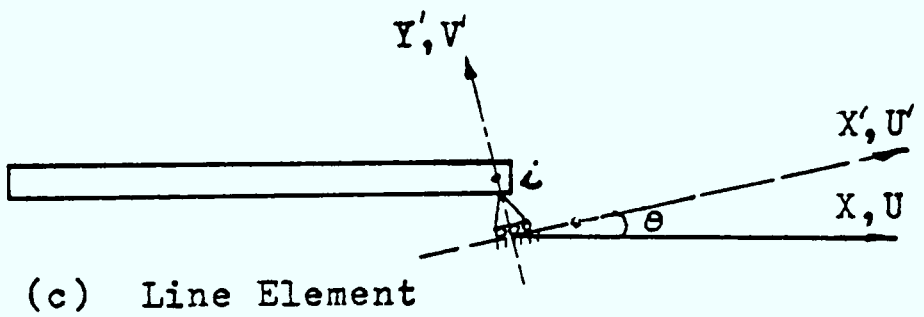
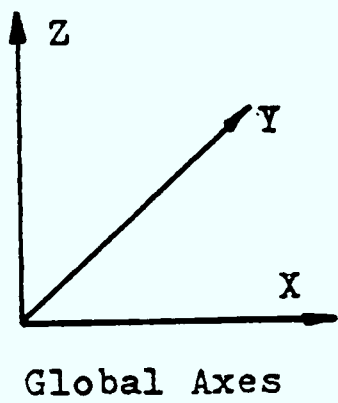
Figure 3.5 Three Dimensional Bond Linkage Element



(a) Solid Element



(b) Membrane Element



$X'Y'Z'$ - Local Coordinate System at Node i
 θ - Angle Between X and X' Axis

Figure 3.6 Inclined (Skew) Boundary Supports

CHAPTER 4

Constitutive Relations for Concrete and Steel

4.1. Introduction

During the past two decades, considerable research and development effort has been devoted to the analytical modelling of concrete structures. Different techniques have been developed in order to model linear and non-linear behaviour of concrete and steel. Despite all this effort, no one method has come out as yet to solve the complex nature of the multi-axial behaviour of concrete under compression, cracking in tension and related phenomena such as aggregate interlock, dowel action of steel (reinforcements and prestressed tendons), bond-slip between steel and concrete, temperature and creep. In this Chapter, an attempt has been made to present a unified approach by bringing together all these areas. In order to achieve this objective, this Chapter gives the non-linear constitutive relations of concrete (compression and tension cracking), elasto-plastic constitutive relations of steel (liner and prestressing tendons) and non-linear bond-slip relations at the steel-concrete interface. These relations are further extended by the inclusion of thermal and creep effects.

4.2. Literature Review on Compression and Cracking of Concrete

4.2.1. The Characteristic Behaviour of Concrete

The characteristic stages of reinforced concrete behaviour can be illustrated by a typical load-displacement relationship as shown in Figure 4.1a. This highly non-linear relationship is roughly divided into three intervals : the "uncracked elastic stage", "crack propagation" and the "plastic" stage. The non-linear response is caused by two major material effects, i.e. "cracking" of concrete and "plasticity" of steel and the compression of concrete. Moreover, time-independent non-linearities arise from the non-linear behaviour of the individual

constituents of reinforced concrete, for example, bond-slip between steel and concrete, aggregate interlock of a cracked concrete and dowel action of reinforcing steel. The time-dependent effects, such as creep, shrinkage and temperature change, also contribute to the non-linear response.

In all these areas, multi-dimensional stress-strain relations have been developed which adequately describe the basic characteristics of concrete materials subjected to monotonic and cyclic loading. These constitutive equations are the most fundamental relations required for any analysis of reinforced or prestressed concrete structures. Several approaches for defining the complicated stress-strain behaviour of concrete under various stress states can be divided into four main groups :

1. Representation of given stress-strain curves by using curve fitting methods, interpolation or mathematical functions.
2. Linear and non-linear elasticity theories.
3. Perfect and work hardening plasticity theory.
4. The endochronic theory of plasticity.

Looking at the mathematical representation of concrete in compression, the three models, namely hypoelastic (9, 31, 30, 40, 41, 42, 44), plastic flow (10, 24, 27, 28, 38, 39, 51, 52, 111) and endochronic (63, 64) are widely accepted.

The hypoelastic models have been used in various forms. The earlier forms of hypoelastic models to represent the non-linear behaviour of concrete were based on the non-linear elasticity (9, 31, 44). In these models, the material constitutive matrix depends on the current state of stress, the increment of stress during loading calculated generally as :

$$\int d\sigma_i = \underline{D}(\sigma_{i-1}) d\xi_i \quad (4.1a)$$

In numerical applications, the incremental relations of Equation (4.1a) are combined with an equilibrium equation as :

$$\underline{\underline{D}} \underline{\underline{d}}\epsilon_i = \underline{\underline{d}}\sigma_i(\epsilon_i) \quad (4.1b)$$

where ϵ_i is the point on the non-linear stress-strain curve
 $\underline{\underline{D}}$ = material matrix at stress level σ_{i-1}

Initially the concrete is assumed isotropic. However, due to the dependence of material moduli (E and ν) on different stress components, a stress induced anisotropy occurs. Many researchers later on took interest in the anisotropy of concrete. A hypoelastic model of degree one is proposed by Coon and Evans (30) in which concrete moduli depends only on two stress invariants. Strains in this model are implied to be infinite at maximum stress. A similar concept of hypoelastic model is used by Bangash (21, 22) where non-linear behaviour of concrete was adequately modelled using orthotropic approach. Similar orthotropic models (17, 40, 41, 42) have been developed in which concrete moduli are calculated from a non-linear uniaxial stress-strain curve (34) in individual principal stress directions. The effect of biaxial or triaxial stress ratios on the concrete moduli has been taken into consideration.

Non-linear incremental elastic models are proposed by Phillips et al (19, 20) in which the bulk modulus (K) is assumed constant and the tangential shear modulus (G) is assumed to be a function of the octahedral shear stress only. A similar approach has been adopted by Cedolin et al (29) who considers the bulk and shear moduli to depend on all the stress invariants. The proposed model is applicable to triaxial compressive states only.

Another triaxial model of non-linear type was proposed by Saugy et al (22, 23) in which the bulk modulus was considered as constant while the shear modulus was assumed to vary as logarithmic function of the second stress invariant. This model has been used for three-dimensional

analyses of prestressed concrete reactor vessels. This model is fully corroborated with experimental results.

Ottosen (36) uses a non-linear elasticity model in which secant values of modulus of elasticity (E_s) and Poisson's ratio (ν_s) are changed according to non-linearity index. The non-linearity index is determined by triaxial failure criterion proposed also by Ottosen (35). The model includes the effect of all three stress invariants, concrete dilatation near failure and the tensile state of stress. The failure criterion (35) contains all three stress invariants and it corresponds to a smooth convex failure surface with curved meridians, open in negative direction of hydrostatic stress axis. The trace in the deviatoric plane changes from nearly triangular to more circular shape with increasing hydrostatic pressure. This failure criterion for concrete is known as "four parameter model".

In many other investigations the non-linear compressive behaviour of concrete is represented by the flow theory of plasticity (10, 10a, 38, 39; 51, 52, 24, 27, 28, 18, 111). In these models the main effort has been to develop suitable yield criteria, flow rules and hardening and softening rules to get a good approximation of non-linear behaviour of concrete. Argyris et al (10, 10a) have used Mohr Coulomb and Drucker Prager yield criteria. William et al (24) have used a more refined concrete yield surface (five parameter model) in conjunction with the flow theory of plasticity. Chen et al (27, 28) in their elasto-plastic models, investigated the post-yield behaviour of concrete by including the hardening rules of plasticity. In all the elasto-plastic models of concrete the objection is that the flow rule of plasticity is not applicable to concrete.

Another concrete compressive model is proposed by Bazant and Bhatt (63) and is called the endochronic theory inelastic model. The theory of the model is very similar to plasticity model except that it does not have yield surface. The theory was first proposed for steel by Valanis (65). Important characteristics of concrete, such as dilation,

softening and realistic failure stresses are simulated, and the model can be applied to general state of stress. All the inelastic concrete parameters were determined with only concrete compressive strength and are applicable to a particular type of concrete. A critical appraisal is given (66) of this model in which doubts have been expressed regarding the model's stability.

Baker (150, 151) suggested concrete failure criteria which was based on the fact that concrete has heterogeneous system and the principal causes of cracking and failure are due to the differential stiffness between the aggregate, matrix and their interface, the bond interaction and the weakness in tension of the mortar matrix. He modelled the failure surface by using a tetrahedron (Figure 4.1b) in which the Poisson thrust ring, plastic flow and cracking effects are represented by the relative stiffness of the rods, which, in turn, depend on the changing behaviour of load. He developed expressions assuming that crack forms in the mortar pocket then eventually extends around the stone interfaces. It is an impressive contribution to improving the situation in which the Poisson's ratio, ν , and the Young's modulus, E , change rapidly as the failure approaches. The following two equations were proposed by Baker (150):

$$\frac{\sigma_1 + \sigma_2}{\sigma_c} = 1 + 4.5 \frac{\sigma_3}{\sigma_c} \quad \text{for } \sigma_1 > \sigma_2 = \sigma_3 \quad (4.2a)$$

$$\frac{\sigma_1 + \sigma_2}{\sigma_c} = 2.2 + 10 \frac{\sigma_3}{\sigma_c} \quad \text{for } \sigma_1 = \sigma_2 > \sigma_3 \quad (4.2b)$$

where σ_1 , σ_2 , σ_3 are the principal stresses and σ_c is the uniaxial compressive strength of concrete.

A test case in the above equations proves what Vile (152) has established. It is interesting to note from the above that the triaxial compressive quadrant of stress space can be achieved by rewriting Equation (4.2a) and (4.2b) in the following form :

$$\sigma_1 = \sigma_2 + 3.5 \sigma_3 \quad (4.2c)$$

$$\sigma_1 = 1.1\sigma_2 + 5 \sigma_3 \quad (4.2d)$$

When Equations (4.2c) and (4.2d) are plotted in stress space, as shown in Figures (4.1c) and (4.1d), the failure envelope agrees both in shape and magnitude as suggested by Hannant and Frederick (153). In the case of high triaxial compression, when $(\sigma_1 + \sigma_2 + \sigma_3) > 16\sigma_c$ the constants in Baker's equations need to be adjusted.

The above experimental equations are flexible enough to accommodate all the experimental parameters of researchers mentioned earlier. Any new experiments to be carried out must be such to warrant the necessary accurate parameters required by Baker's equations. In this regard, efforts have been made by Chinn and Zimmermann (141) and Acroyd (154) and Newmann (138).

4.2.2. Concrete Cracking Models

In the finite element analysis of concrete structures, three different approaches have been employed for crack modelling :

- (a) Smearred cracking model.
- (b) Discrete cracking model.
- (c) Fracture mechanics model.

The selection of any of the three models depends upon the purpose of the analysis. In the smeared cracking model, the cracked concrete is assumed to remain in continuum, i.e. the cracks are smeared out in a continuum fashion. Here, an assumption is made that after first cracking, concrete becomes orthotropic or transversely orthotropic and one of the material axes has oriented along the direction of cracking. In this approach, shear strength reserves due to concrete aggregate interlocking can be accounted for by retaining a positive shear modulus. Here the crack is not discrete, but the model considers an infinite number of parallel fissures across the finite element.

An alternative to the above model is the introduction of "discrete cracks" (8). This is done by disconnecting the displacement at nodal points for adjoining elements. Here the difficulty is that the location and orientation of the cracks are not known in advance. Hence geometrical restrictions imposed by the preselected finite element mesh can hardly be avoided. To some extent, this can be rectified by redefining the element nodes. Such techniques are complex and time-consuming. For problems involving a few dominant cracks such as the diagonal tension crack in reinforced concrete beams, the discrete model offers a more realistic representation, i.e. this crack represents a strain discontinuity. The success of fracture mechanics theory is based on the fact that concrete is a notch-sensitive material and the cracking criterion based on tensile strength can be handled without being unconservative. Bazant and Cedolin (148) have produced some results. At present this area is being very actively studied by several researchers (148, 149).

The cracking of concrete in tension has been studied by various investigators. The first such study using finite elements was made by Ngo and Scordelis (8). They treated both steel and concrete as linear elastic materials while incorporating linear elastic bond-linkage elements. Here cracks are predefined and are represented by separation of nodal points. Nilson (9) extended this work by introducing non-linear material behaviour. With crack propagation and hence continually redefinition of structural topology made this approach unpopular. Franklin (44) tried to overcome this problem by predefined the expected total length of a shear crack which he observed in various experiments of reinforced concrete beams. Two sides of a crack were initially held rigidly together by very stiff linkage elements. By varying the stiffness value of the linkage elements, the crack propagation was simulated without redefining the nodal points.

Cervarka (39) studied two-dimensional crack problems using iterative methods. The initial stress method (51) applicable to elasto-plastic problems is extended to cracking of reinforced concrete by Valliappan and Doolan (134). Schnobrich (135) suggested periodically updating the stiffness matrix. Cracking was considered as changing the material

properties of concrete. This way of introducing crack allows some shear capacity to be retained in the cracked concrete. This allowance for shear corresponds to taking into account the concept of aggregate interlock across the crack surface. Suidan and Schnobrich (38) used the same general approach for three dimensional case. They keep small values of shear stiffness across the open cracks.

Lin and Scordelis (136) analyse reinforced concrete shells. Triangular layered elements are adopted in which steel is represented as smeared layer. A concept of "tension stiffening" is introduced in which open cracks have a decreasing (rather than zero) tensile strength after cracking. Using this concept, the effect of bond between steel and concrete is incorporated in their cracking analysis.

Based on the above mentioned study, three constitutive models selected for concrete in compression are :

1. Orthotropic model.
2. Shear and bulk moduli model.
3. Endochronic theory model.*

*The endochronic theory model has been included later on in the computer program. It has been a part of the validation procedure, tested on simply supported beams only.

4.3. Formulation of an Orthotropic Concrete Constitutive Model

4.3.1. Incremental Stress-strain Relations

Here an attempt has been made to give a three-dimensional non-linear stress-strain relationship developed for concrete using hypo-elastic orthotropic approach, which incorporates the equivalent uniaxial

strain concept of Darwin and Pecknold (40, 41), the non-linear representation of Saenz (34), and the ultimate surface of Ottosen (35) in such a way as to represent the actual concrete behaviour. The concrete constitutive relations are then written in an incremental form in which material parameters are obtained from uniaxial stress-equivalent uniaxial strain relations.

The incremental stress-strain relations for general three-dimensional orthotropic material can be written as :

$$\begin{aligned}
 d\varepsilon_1 &= \frac{d\sigma_1}{E_1} - \nu_{12} \frac{d\sigma_2}{E_2} - \nu_{13} \frac{d\sigma_3}{E_3} \\
 d\varepsilon_2 &= -\nu_{21} \frac{d\sigma_1}{E_1} + \frac{d\sigma_2}{E_2} - \nu_{23} \frac{d\sigma_3}{E_3} \\
 d\varepsilon_3 &= -\nu_{31} \frac{d\sigma_1}{E_1} - \nu_{32} \frac{d\sigma_2}{E_2} + \frac{d\sigma_3}{E_3} \\
 d\gamma_{12} &= \frac{\tau_{12}}{G_{12}} \\
 d\gamma_{23} &= \frac{\tau_{23}}{G_{23}} \\
 d\gamma_{31} &= \frac{\tau_{31}}{G_{31}}
 \end{aligned} \tag{4.3}$$

or in matrix form

$$\begin{Bmatrix} d\varepsilon_1 \\ d\varepsilon_2 \\ d\varepsilon_3 \\ d\gamma_{12} \\ d\gamma_{23} \\ d\gamma_{31} \end{Bmatrix} = \begin{bmatrix} 1/E_1 & -\nu_{12}/E_2 & -\nu_{13}/E_3 & 0 & 0 & 0 \\ -\nu_{21}/E_1 & 1/E_2 & -\nu_{23}/E_3 & 0 & 0 & 0 \\ -\nu_{31}/E_1 & -\nu_{32}/E_2 & 1/E_3 & 0 & 0 & 0 \\ 0 & 0 & 0 & 1/G_{12} & 0 & 0 \\ 0 & 0 & 0 & 0 & 1/G_{23} & 0 \\ 0 & 0 & 0 & 0 & 0 & 1/G_{31} \end{bmatrix} \begin{Bmatrix} d\sigma_1 \\ d\sigma_2 \\ d\sigma_3 \\ d\tau_{12} \\ d\tau_{23} \\ d\tau_{31} \end{Bmatrix} \tag{4.3a}$$

where E_1, E_2, E_3 and ν_{12}, ν_{21} and ν_{31} are moduli and Poisson's ratios. Due to symmetry, the following relations are defined :

$$\begin{aligned}
 \nu_{12} E_1 &= \nu_{21} E_2 \\
 \nu_{23} E_2 &= \nu_{32} E_3 \\
 \nu_{13} E_1 &= \nu_{31} E_3
 \end{aligned} \tag{4.4}$$

Also define equivalent Poisson's ratios :

$$\begin{aligned}\bar{\nu}_1^2 &= \nu_{12}\nu_{21} \\ \bar{\nu}_2^2 &= \nu_{23}\nu_{32} \\ \bar{\nu}_3^2 &= \nu_{31}\nu_{13}\end{aligned}\tag{4.5}$$

Using Equations (4.4), Equation (4.3a) is written as

$$\begin{Bmatrix} d\varepsilon_1 \\ d\varepsilon_2 \\ d\varepsilon_3 \\ d\gamma_{12} \\ d\gamma_{23} \\ d\gamma_{31} \end{Bmatrix} = \begin{bmatrix} 1/E_1 & -\nu_{12}/\sqrt{E_1E_2} & -\nu_{13}/\sqrt{E_1E_3} & 0 & 0 & 0 \\ & 1/E_2 & -\nu_{23}/\sqrt{E_2E_3} & 0 & 0 & 0 \\ & & 1/E_3 & 0 & 0 & 0 \\ & & & 1/G_{12} & 0 & 0 \\ \text{SYM.} & & & & 1/G_{23} & 0 \\ & & & & & 1/G_{31} \end{bmatrix} \begin{Bmatrix} d\sigma_1 \\ d\sigma_2 \\ d\sigma_3 \\ d\tau_{12} \\ d\tau_{23} \\ d\tau_{31} \end{Bmatrix}$$

which, upon inversion and using relations of Equation (4.5), becomes :

$$\begin{Bmatrix} d\sigma_1 \\ d\sigma_2 \\ d\sigma_3 \\ d\tau_{12} \\ d\tau_{23} \\ d\tau_{31} \end{Bmatrix} = \frac{1}{\bar{\nu}} \begin{bmatrix} E_1(1-\bar{\nu}_2^2) & \sqrt{E_2E_3}(\bar{\nu}_2\bar{\nu}_3+\bar{\nu}_1) & \sqrt{E_1E_3}(\bar{\nu}_1\bar{\nu}_2+\bar{\nu}_3) & 0 & 0 & 0 \\ & E_2(1-\bar{\nu}_3^2) & \sqrt{E_2E_3}(\bar{\nu}_2+\bar{\nu}_1\nu_3) & 0 & 0 & 0 \\ & & E_3(1-\bar{\nu}_1^2) & 0 & 0 & 0 \\ & & & G_{12}\bar{\nu} & 0 & 0 \\ \text{SYM.} & & & & G_{23}\bar{\nu} & 0 \\ & & & & & G_{13}\bar{\nu} \end{bmatrix} \begin{Bmatrix} d\varepsilon_1 \\ d\varepsilon_2 \\ d\varepsilon_3 \\ d\gamma_{12} \\ d\gamma_{23} \\ d\gamma_{31} \end{Bmatrix}$$

or

$$d\tilde{\sigma} = \underline{D}_T d\tilde{\varepsilon}\tag{4.6}$$

where
$$\bar{\nu} = 1 - \bar{\nu}_1^2 - \bar{\nu}_2^2 - \bar{\nu}_3^2 - 2\bar{\nu}_1\bar{\nu}_2\bar{\nu}_3\tag{4.7}$$

\underline{D}_T is the tangent material matrix

In the above orthotropic material matrix \underline{D}_T , it is required to determine three shear moduli defined above. At present, no experimental results are available to determine shear moduli under triaxial state of stress. It is assumed that no particular direction is favoured with

regard to shear moduli and they remain invariant upon the rotation of material axes. If \underline{D}_T is transformed to a new set of axes 1', 2', and 3' and the constraint is imposed that the shear moduli remain invariant, the following values of shear moduli are obtained :

$$\begin{aligned}
 G_{12} &= \frac{1}{4\nu} \left\{ E_1 + E_2 - 2\bar{\nu}_1 \sqrt{E_1 E_2} - (\sqrt{E_1} \bar{\nu}_2 + \sqrt{E_2} \bar{\nu}_3)^2 \right\} \\
 G_{23} &= \frac{1}{4\nu} \left\{ E_2 + E_3 - 2\bar{\nu}_2 \sqrt{E_2 E_3} - (\sqrt{E_2} \bar{\nu}_3 + \sqrt{E_3} \bar{\nu}_1)^2 \right\} \\
 G_{13} &= \frac{1}{4\nu} \left\{ E_3 + E_1 - 2\bar{\nu}_3 \sqrt{E_1 E_3} - (\sqrt{E_1} \bar{\nu}_2 + \sqrt{E_3} \bar{\nu}_1)^2 \right\}
 \end{aligned} \tag{4.8}$$

Equation (4.6) is the main incremental constitutive relation in which six independent material parameters, E_1 , E_2 , E_3 , $\bar{\nu}_1$, $\bar{\nu}_2$, and $\bar{\nu}_3$ are the function of current state of stress. These are determined from the uniaxial stress-equivalent uniaxial strain relations. The concept of equivalent uniaxial strain follows.

4.3.2. Equivalent Uniaxial Strain

According to this concept (41), the degradation of stiffness and strength of plain concrete is described during load-history and also the actual triaxial stress-strain curves can be duplicated from uniaxial curves. In this way the variation of incremental moduli with respect to the variation of stress is determined using the uniaxial stress-strain curves. In a uniaxial case, the strain is always a function of stress in the direction of load. For the triaxial case, the strain in one direction is not only a function of stress in that direction, but also it is affected by the stresses in two orthogonal directions due to Poisson's effect (See Equation (4.3a)). The concept of uniaxial strain provides a method to separate the Poisson effect from the cumulative strain. The definition of equivalent uniaxial strain is written using Equation (4.3) by ignoring the Poisson effect, i.e.

$$\underline{d\varepsilon_{iu}} = \underline{d\sigma_i / E_i} \quad , \quad i=1,2,3 \tag{4.9}$$

In matrix form, it is written as :

$$\begin{Bmatrix} d\varepsilon_{1u} \\ d\varepsilon_{2u} \\ d\varepsilon_{3u} \end{Bmatrix} = \begin{bmatrix} 1/E_1 & 0 & 0 \\ 0 & 1/E_2 & 0 \\ 0 & 0 & 1/E_3 \end{bmatrix} \begin{Bmatrix} d\sigma_1 \\ d\sigma_2 \\ d\sigma_3 \end{Bmatrix} \quad (4.9a)$$

and the total equivalent uniaxial strains for the load path are written by integrating Equation (4.9) along the load path as :

$$\varepsilon_{iu} = \int \frac{d\sigma_i}{E_i}$$

or

$$\varepsilon_{iu} = \sum_{\substack{\text{all} \\ \text{load increments}}} \frac{\Delta\sigma_i}{E_i} \quad (4.10)$$

in which $\Delta\sigma_i$ = change in stress in the i th direction

E_i = tangent modulus in the i th direction

It should be mentioned here that the concept of introducing $d\varepsilon_{iu}$ and ε_{iu} is purely fictitious (except in the uniaxial test) and they have significance as a measure on which to base the variation of material parameters. These also do not transform in the same manner as stresses and strains of Equation (4.3). The stresses in Equation (4.3) are defined in material principal axes of orthotropy. If these are assumed to follow the current principal axes of total stress, it indicates immediately that $d\varepsilon_{iu}$ must be defined with respect to the current principal axes of orthotropy. This last statement implies a similarity between equivalent strain parameters in elasto-plastic analyses ($d\bar{\varepsilon}_p$) and equivalent uniaxial strains (42). Since ε_{iu} are not transformable, they are assumed to be defined only in the current principal stress directions.

The general constitutive relationship using this concept can now be written as :

$$d\bar{\sigma} = F(d\bar{\varepsilon}, \int d\bar{\sigma}) \quad (4.11)$$

in which the stress increment is a function of the strain increment during the current iteration and the state of stress accumulated to date. The above relationship is path-dependent, and has a strong resemblance with the hypo-elastic law proposed by Truesdell (137).

4.3.3. Equivalent Uniaxial Stress-strain Curve (Figure 4.2)

The concept of equivalent uniaxial strain is utilised now to define equivalent uniaxial stress-strain curves for plain concrete. In order to calculate parameters for tangent material matrix developed in Equations (4.6) and (4.7), it is necessary to write Saenz's relation (34) in terms of equivalent uniaxial strain given by Elwi and Murray (42) :

$$\sigma_i = \frac{E_0 \epsilon_{iu}}{1 + \left(\frac{E_0}{E_s} + R - 2\right) \left(\frac{\epsilon_{iu}}{\epsilon_{ic}}\right) - (2R - 1) \left(\frac{\epsilon_{iu}}{\epsilon_{ic}}\right)^2 + R \left(\frac{\epsilon_{iu}}{\epsilon_{ic}}\right)^3} \quad (4.12)$$

where E_0 = initial modulus of elasticity

$$E_{sec} = \frac{\sigma_{ic}}{\epsilon_{ic}} = \text{secant modulus at maximum stress} \quad (4.12a)$$

ϵ_{iu} = uniaxial strain in the i th direction

σ_{ic} = maximum stress associated with direction i

which depends on the current principal stress ratios

$$\begin{aligned} \epsilon_{ic} &= \text{maximum strain associated with } \sigma_{ic} \\ &= 3.47 \sigma_{ic}^{1/4} (31.5 - 3.47 \sigma_{ic}^{1/4}) \times 10^{-5} \end{aligned} \quad (4.12b)$$

σ_{if} = stress at failure of descending branch of the curve

$$= 0.85 \sigma_{ic} \quad (4.12c)$$

ϵ_{if} = failure strain

$$R = \frac{E_0}{E_{sec}} \left\{ \frac{R_\sigma - 1}{R_\epsilon - 1} \right\} - \frac{1}{R_\epsilon} \quad (4.12d)$$

$$R_\sigma = \frac{\sigma_{ic}}{\sigma_{if}}$$

$$R_\epsilon = \frac{\epsilon_{ic}}{\epsilon_{if}}$$

The tangent elastic moduli are obtained by differentiating Equation (4.12) with respect to equivalent uniaxial strains as :

$$E_i = \frac{d\sigma_i}{d\epsilon_{iu}}, \quad i = 1, 2, 3 \quad (4.13)$$

$$E_i = \frac{E_o \{1 + (2R-1) \epsilon_R^2 - 2R \epsilon_R^3\}}{\left\{1 + \left(\frac{E_o}{E_{sec}} + R - 2\right) \epsilon_R - (2R-1) \epsilon_R^2 + R \epsilon_R^3\right\}^2} \quad (4.14)$$

where
$$\epsilon_R = \frac{\epsilon_{iu}}{\epsilon_{ic}} \quad (4.14a)$$

Therefore the material moduli of Equations (4.14) are in general a function of accumulated equivalent uniaxial strains and current state of stress. Equations (4.12) and (4.14) are applied to the whole stress-strain curve including the descending portion of the curve (see Figure (4.2)). If the ascending part of the uniaxial stress-strain curve is required, it can readily be obtained by setting $R=0$ in Equations (4.12) and (4.14).

4.3.4. Poisson's Ratios

The incremental moduli can now be determined from Equation (4.14) provided the parameters described above are known for a particular ratio of the total stresses. Nevertheless, the incremental stress-strain relation cannot be achieved without evaluating Poisson's ratios. Poisson's ratio is determined from uniaxial compression data of the Kupfer et al tests (25) as a function of strain by a least square fit of a cubic polynomial. This results in the expression given by Elwi and Murray (42) :

$$\nu = \nu_o \left\{ 1 + 1.3763 \left(\frac{\epsilon_{iu}}{\epsilon_{ic}}\right) - 5.36 \left(\frac{\epsilon_{iu}}{\epsilon_{ic}}\right)^2 + 8.586 \left(\frac{\epsilon_{iu}}{\epsilon_{ic}}\right)^3 \right\} \quad (4.15)$$

or
$$\nu_i = f \left(\frac{\epsilon_{iu}}{\epsilon_u}\right) \quad (4.15a)$$

Three independent Poisson's ratios are postulated as :

$$\bar{\nu}_1^2 = \nu_1 \nu_2 \quad , \quad \bar{\nu}_2^2 = \nu_2 \nu_3 \quad , \quad \bar{\nu}_3^2 = \nu_3 \nu_1 \quad (4.15b)$$

with $i = 1, 2, 3$

where ν_o = initial value of the Poisson's ratio

ϵ_u = ϵ_{ic} for uniaxial test

ϵ_{iu} = strain in the direction of uniaxial loading

It should be noted from Equation (4.7) that $\bar{\nu}$ may become negative for $\bar{\nu}_i$ greater than 0.5 which is not acceptable. Therefore a restriction on Equation (4.15) is imposed which is this when $\nu_i \geq 0.5$, the $\bar{\nu}_i$ should be set to 0.5. This limit physically means that there is a zero incremental volume change as is the case in incompressible material. Kostovos and Newmann (138) noted that the point at which this limit is reached corresponds to the onset of unstable microcrack propagation. This causes concrete to dilate upon approaching the ultimate strength.

4.3.5. Failure Criteria of Concrete

The strength of concrete under multiaxial stress is a function of the state of stress and cannot be predicted by limitations of simple tensile, compressive and shearing stresses independently of each other. The strength of concrete can be adequately evaluated by considering the interaction of the various components of the state of stress.

4.3.5.1. Stress and Strain Invariants

A failure criterion of materials based on the state of stress is an invariant function of the state of stress. One method of representing such a function is to use the principal stresses, i.e.

$$f(\sigma_1, \sigma_2, \sigma_3) = 0 \quad (4.16)$$

to show the general functional form of the failure criterion. Under multiaxial state of stress, this approach to establishing a failure function is difficult to pursue. This difficulty is due to supplying information on the basis of both a geometrical and a physical explanation of failure. It is therefore important to rewrite Equation (4.16) using three particular principal invariants which are more susceptible to geometrical and physical interpretations and which are independent of the properties of the materials. The Equation (4.16) is written as :

$$f(I_1, J_2, J_3) = 0 \quad (4.16a)$$

Various versions of Equation (4.16a) have been adopted and verified. The analytical versions of the failure envelope based on Equation (4.16a) have been adopted by Sangy et al (22, 23), Willam and Warnke (29) and Ottosen (35).

A failure criterion proposed by Ottosen (35) known as the "four parameter failure criterion" has been adopted. This failure surface contains all three stress invariants and has the following characteristics :

- (a) The surface is smooth and convex with curved meridians.
- (b) It is open in the negative direction of the hydrostatic axis.
- (c) Trace in deviatoric plane changes from an almost triangular to circular shape with increasing hydrostatic pressure.
- (d) The surface is in good agreement with experimental results over a wide range of stress state including those where tensile stresses occur.

Figures (4.3) and (4.4) show the surface in principal stress coordinate system in which the compressive meridian, ρ_c ($\theta=60^\circ$, $\sigma_1=\sigma_2>\sigma_3$) and the tensile meridian, ρ_t ($\theta=0^\circ$, $\sigma_1=\sigma_2<\sigma_3$) are defined. The meridians are curved, smooth and convex and ρ increases with increasing hydrostatic pressure.

An analytical failure surface containing all the above characteristics is defined in the following form by Ottosen (35) :

$$f(I_1, J_2, J) = a \frac{J_2}{\sigma_c^2} + \lambda \frac{\sqrt{J_2}}{\sigma_c} + b \frac{I_1}{\sigma_c} - 1 = 0 \quad (4.17)$$

where $I_1 = \sigma_x + \sigma_y + \sigma_z =$ first invariant of stress tensor (4.17a)

$$J_2 = \text{second invariant of stress deviator tensor} \\ = \frac{1}{2}(s_x^2 + s_y^2 + s_z^2) + \tau_{xy}^2 + \tau_{yz}^2 + \tau_{zx}^2 \quad (4.17b)$$

$$J = \cos 3\theta = 1.5 \sqrt{3} \frac{J_3}{\sqrt{J_2}} \quad (4.17c)$$

$$\begin{aligned} J_3 &= \text{third invariant of stress deviator tensor} \\ &= S_x S_y S_z + 2 \tau_{xy} \tau_{yz} \tau_{zx} - S_x \tau_{yz}^2 - S_y \tau_{xz}^2 - S_z \tau_{xy}^2 \end{aligned} \quad (4.17d)$$

$$\begin{aligned} S_x &= \sigma_x - I_1/3 \\ S_y &= \sigma_y - I_1/3 \\ S_z &= \sigma_z - I_1/3 \end{aligned} \quad (4.17e)$$

$$\lambda = \lambda(\cos 3\theta) > 0 ; a \text{ and } b \text{ are constant}$$

$$\lambda = K_1 \cos\left(\frac{1}{3} \cos^{-1}(K_2 \cos 3\theta)\right) \text{ for } \cos 3\theta > 0 \quad (4.17f)$$

$$\lambda = K_1 \cos\left(\frac{\pi}{3} - \frac{1}{3} \cos^{-1}(-K_2 \cos 3\theta)\right) \text{ for } \cos 3\theta \leq 0$$

K_1, K_2, a and b are material parameters to be determined

σ_c = uniaxial compressive cylinder strength for concrete

σ_t = uniaxial tensile strength for concrete

Equation (4.17) defines the failure at a point if $f \geq 0$ and $f < 0$ which also corresponds to a point inside the failure surface. A failure will not occur at a point under compressive hydrostatic pressure, i.e. three equal compressive stresses will never fail the material.

4.3.6. Determination of Four Parameters (a, b, K_1, K_2)

The four material parameters are determined with the biaxial test results of Kupfer et al (25) and triaxial results of Balmer (140) and Richert et al (139). The following three failure states were represented :

1. Uniaxial compressive strength, σ_c .
2. Biaxial compressive strength, $\sigma_1 = \sigma_2 = -1.16\sigma_c$, $\sigma_3 = 0$
(test results of Kupfer et al (25)).

3. Uniaxial tensile strength, $\sigma_t = k \sigma_c$

Hereafter the method of least squares is adopted to obtain the best fit of the compressive meridian for $\xi/\sigma_c \gg -5.0$ to test the results of Balmer (140) and Richart et al (139). Figure (4.5) shows the process where compressive meridian passes through a point (where $\xi/\sigma_c, \rho/\sigma_c = (-5, -4)$). With this procedure, the values of material parameters are determined as given in Table (4.1 and (4.2. From these Tables, it is clear that the material parameters show considerable dependence on $k = \sigma_t/\sigma_c$ but the failure stresses in compressive regime are only slightly affected.

4.3.7. σ_{ic} Value

It remains now to assess σ_{ic} ($i = 1, 2, 3$) the peak stress for the calculation of tangent moduli (Equation (4.12)) for various principal stress ratios. Under uniaxial conditions, σ_{ic} is equal to the compressive cylinder strength (σ_c). However, under multiaxial stress conditions, the compressive strength of concrete increases. To obtain σ_{ic} in three directions for principal stress ratio, a surface in stress space is used. First of all, current principal stresses are established (let these be $\sigma_{p1}, \sigma_{p2}, \sigma_{p3}$ where $\sigma_{p1} > \sigma_{p2} > \sigma_{p3}$). It is then assumed that σ_{p1} and σ_{p2} are held constant while the third principal stress is changed such that it reaches to the failure surface. This establishes that the ultimate stress is σ_{3c} . Similarly, σ_{1c} and σ_{2c} are calculated by increasing their values while the other two stresses remain constant. This means that the principal stresses are substituted in failure surface (Equation (4.17)) and then one of the stresses (more compressive) is increased while the other two remain constant until Equation (4.17) is satisfied.

4.4. Other Concrete Compressive Models

4.4.1. Shear and Bulk Moduli Model*

Constitutive relations for this model are given in Appendix A5. Most of this work is due to Sangy et al (22, 23).

4.4.2. Concrete Model Based on Endochronic Theory*

This type of model was initially developed for steel by Valanis (65) and has subsequently been modified by Bazant and Bhat (63) and is given in Appendix A6. Here constitutive equations are arranged in modified form by Ahmad to suite the three dimensional finite element analysis proposed in this research.

*Both these models have been included in the program NSARVE described elsewhere in this research.

4.5. Concrete Cracking and Crushing Criteria

4.5.1. Assumptions

The cracking criterion is based on the concept of changing the material properties and allowing the effect of cracking by redistributing the stresses to the surrounding material. Maximum principal stress and strain criteria are used to define the cracks. When a principal stress (strain) in any direction exceeds a prescribed value (allowable limiting tensile strength, σ_t or tensile strain, ϵ_{cr}), a "crack" forms perpendicular to the principal stress (strain) direction. Thus, for cracking :

$$\sigma_i \geq \sigma_t \quad (4.18)$$

or

$$\epsilon_i \geq \epsilon_{cr} \quad (4.19)$$

where $i = 1, 2, 3$

The model developed herein is applicable to general three-dimensional problems. On further loading, it is possible that new cracks will form at some angle to the first crack. It is assumed that further cracks are only allowed in orthogonal directions to the first crack.

Concrete in tension up to the point of cracking is linearly elastic material. However, the material becomes orthotropic as soon as it cracks. When a crack first occurs, it is assumed that direct tensile stresses can not be supported in the direction normal to the crack. Moreover, the material matrix in this direction is reduced to a small value (or zero) and also it is assumed that there is no interaction between this and other directions. The material parallel to the crack is still capable of carrying stresses which are given by the new material constitutive relationship.

The crack initiation (onset of cracking) is always defined using the maximum principal stress criterion. This is because for cyclic loading the crack may initiate upon unloading from compressive state in which a tensile stress at compressive strain may be reached as shown in Figure (4.6b). A crack is assumed to close when the strain normal to the crack is compressive and also it is less than the strain at which the crack was opened. Figures (4.6a) and (4.6b) show a uniaxial crack initiation, closing and reopening criteria for both cases where first load in tension and compression is applied. In both cases loading starts at point A. Crack is assumed to open at point B where stress suddenly drops to zero. Towards the CD direction, the crack remains open. Upon reverse loading at point E (at strain where zero stress was last reached) the crack closes. By further cyclic loading at points F and G the crack will be assumed to reopen and close. In reality, the strain values when the crack closes will be influenced by the relative movements parallel to the crack. This effect is not included in this study.

4.5.2. Shear on Open and Closed Cracks

The surfaces of a typical cleavage crack in general will be rough and irregular. Due to the parallel differential movement of an open crack, it is possible that opposite faces will have aggregate interlock restraining this movement. For a widely opened crack, the opposite faces will completely separate and there is no interlocking effect. The most important effect of interlocking is that the shear stress along the crack will not be zero. Due to the lack of experimental information, the interlocking is taken into account by assuming that the shear stress along the crack is a linear function of shear strain, such that :

$$\tau^* = G' \gamma^* \quad (4.20)$$

where $G' = \beta G$ (4.20a)

G = shear modulus of uncracked concrete

β = shear retention factor having values

τ^* = shear stress along the crack

γ^* = shear strain along the crack

For an open crack, $\beta = 0.5$ was used in numerical calculations. For a closed crack, it is assumed that full shear stress develops along the crack, i.e.

$$\tau^* = \beta G \gamma^* \quad (4.20b)$$

where $\beta = 1.0$

For other ranges, Bangash (21) gives the value of β between 0.5 to 0.87.

4.5.3. Concrete Model in Tension and Cracking

The constitutive relationships of uncracked concrete for the three-dimensional case is written as :

$$\Delta \underline{\sigma} = \underline{D}_T \Delta \underline{\epsilon} \quad (4.21)$$

where \underline{D}_T is the tangent material matrix and can be written as :

$$\underline{D}_T = \begin{bmatrix} D_{11} & D_{12} & D_{13} & 0 & 0 & 0 \\ D_{21} & D_{22} & D_{23} & 0 & 0 & 0 \\ D_{31} & D_{32} & D_{33} & 0 & 0 & 0 \\ 0 & 0 & 0 & D_{44} & 0 & 0 \\ 0 & 0 & 0 & 0 & D_{55} & 0 \\ 0 & 0 & 0 & 0 & 0 & D_{66} \end{bmatrix} \quad (4.21a)$$

in which D_{11} to D_{66} are given by the values of Equation (4.6).

As soon as crack occurs, orthotropic conditions are introduced and the incremental constitutive relations are written in the cracked material directions. The total normal stress across the crack is reduced to zero and also the shear terms are introduced to account for any aggregate interlocking. Write the following in the crack coordinate system :

$$\Delta \sigma_x^* = D_{11} \Delta \epsilon_x^* + D_{12} \Delta \epsilon_y^* + D_{13} \Delta \epsilon_z^* \quad (4.22a)$$

$$\Delta \sigma_y^* = D_{21} \Delta \epsilon_x^* + D_{22} \Delta \epsilon_y^* + D_{23} \Delta \epsilon_z^* \quad (4.22b)$$

$$\Delta \sigma_z^* = D_{31} \Delta \epsilon_x^* + D_{32} \Delta \epsilon_y^* + D_{33} \Delta \epsilon_z^* \quad (4.22c)$$

$$\Delta \tau_{xy}^* = D_{44} \gamma_{xy}^* \quad (4.22d)$$

$$\Delta \tau_{yz}^* = D_{55} \gamma_{yz}^* \quad (4.22e)$$

$$\Delta \tau_{zx}^* = D_{66} \gamma_{zx}^* \quad (4.22f)$$

The asterisk (*) refers to crack directions (see Figure (4.8b)).

Upon cracking in direction '1', the concrete offers no resistance in this direction, i.e.

$$\Delta \sigma_x^* = 0 \quad (4.23a)$$

From Equations (4.22a) and (4.23a) :

$$\Delta \epsilon_x^* = - \frac{D_{12}}{D_{11}} \Delta \epsilon_y^* - \frac{D_{13}}{D_{11}} \Delta \epsilon_z^* \quad (4.23b)$$

Substitute Equation (4.23b) into Equations (4.22b) and (4.22c), and the following expressions are obtained :

$$\Delta \sigma_y^* = \left(D_{22} - \frac{D_{12}D_{21}}{D_{11}} \right) \Delta \epsilon_y^* + \left(D_{23} - \frac{D_{21}D_{13}}{D_{11}} \right) \Delta \epsilon_z^* \quad (4.23c)$$

$$\Delta \sigma_z^* = \left(D_{32} - \frac{D_{31}D_{12}}{D_{11}} \right) \Delta \epsilon_y^* + \left(D_{33} - \frac{D_{31}D_{13}}{D_{11}} \right) \Delta \epsilon_z^* \quad (4.23d)$$

Shear in the plane of crack due to interlocking effect can be written as :

$$\Delta \tau_{xy}^* = \beta D_{44} \gamma_{xy}^* \quad (4.23e)$$

$$\Delta \tau_{zx}^* = \beta D_{66} \gamma_{zx}^* \quad (4.23f)$$

and
$$\Delta \tau_{yz}^* = D_{55} \gamma_{yz}^* \quad (4.23g)$$

Equations (4.23a) to (4.23g) can be written in matrix form for concrete cracked in direction '1' as :

$$\underline{\Delta \sigma}^* = \underline{D}_T^* \underline{\Delta \epsilon}^* \quad (4.24)$$

If the concrete cracks in two directions (say in directions '1' and '2'), then from Equations (4.22a) and (4.22b) :

$$\Delta \sigma_x^* = 0 = D_{11} \Delta \epsilon_x^* + D_{12} \Delta \epsilon_y^* + D_{13} \Delta \epsilon_z^* \quad (4.25a)$$

$$\Delta \sigma_y^* = 0 = D_{21} \Delta \epsilon_x^* + D_{22} \Delta \epsilon_y^* + D_{23} \Delta \epsilon_z^* \quad (4.25b)$$

Solve for $\Delta \varepsilon_x^*$ and $\Delta \varepsilon_y^*$ from Equations (4.25a) and (4.25b) :

$$\Delta \varepsilon_y^* = \left(\frac{D_{23} D_{11} - D_{21} D_{31}}{D_{21} D_{12} - D_{11} D_{22}} \right) \Delta \varepsilon_z^*$$

$$\Delta \varepsilon_x^* = \left(\frac{D_{13} D_{22} - D_{12} D_{23}}{D_{21} D_{12} - D_{11} D_{22}} \right) \Delta \varepsilon_z^*$$

Substituting $\Delta \varepsilon_x^*$ and $\Delta \varepsilon_y^*$ in Equation (4.22c), the expression for $\Delta \sigma_z^*$ is obtained as :

$$\Delta \sigma_z^* = \left\{ D_{33} - D_{31} \left(\frac{D_{13} D_{22} - D_{12} D_{23}}{D_{11} D_{22} - D_{21} D_{12}} \right) - D_{32} \left(\frac{D_{11} D_{23} - D_{21} D_{31}}{D_{11} D_{22} - D_{21} D_{12}} \right) \right\} \Delta \varepsilon_z^*$$

Shear stresses are then given by :

$$\Delta \tau_{xy}^* = \beta D_{44} \gamma_{xy}^* \quad (4.25d)$$

$$\Delta \tau_{yz}^* = \beta D_{55} \gamma_{yz}^* \quad (4.25e)$$

$$\Delta \tau_{zx}^* = \beta D_{66} \gamma_{zx}^* \quad (4.25f)$$

Similarly, for two open cracks in '2' and '3' directions, and '3' and '1' directions :

2-3 direction

$$\Delta \sigma_y^* = 0 \quad , \quad \Delta \sigma_z^* = 0 \quad (4.26a)$$

$$\Delta \sigma_x^* = \left\{ D_{11} - D_{12} \left(\frac{D_{12} D_{33} - D_{23} D_{31}}{D_{33} D_{22} - D_{32} D_{23}} \right) - D_{13} \left(\frac{D_{31} D_{22} - D_{32} D_{21}}{D_{33} D_{22} - D_{32} D_{23}} \right) \right\} \Delta \varepsilon_x^* \quad (4.26b)$$

3-1 direction

$$\Delta \sigma_x^* = 0 \quad , \quad \Delta \sigma_z^* = 0 \quad (4.27a)$$

$$\Delta \sigma_y^* = \left\{ D_{22} - D_{21} \left(\frac{D_{12} D_{33} - D_{32} D_{13}}{D_{11} D_{33} - D_{31} D_{13}} \right) - D_{23} \left(\frac{D_{11} D_{32} - D_{31} D_{12}}{D_{11} D_{33} - D_{31} D_{13}} \right) \right\} \Delta \varepsilon_y^* \quad (4.27b)$$

Shear stresses for both cases are given by Equations (4.25d) to (4.25f).

For all three directions cracked, the material matrix becomes null and concrete at this point carries no stress. Hence $\underline{D}_T^* = [\underline{0}]$ should be adopted in Equation (4.24).

Figures (4.7a), (4.7b) and (4.7c) show these types of crack for the three-dimensional concrete for which the constitutive relations are defined above. Figures (4.8a) and (4.8b) show the state of stress before and after cracking. Equation (4.24) with $\underline{D}_T^* = [\underline{0}]$ also applies if concrete crushes in compression.

4.5.3.1. Transformation of Cracked Material Matrix to Global Coordinates

As \underline{D}_T^* refers to a local (crack) coordinate system (Figure (4.8b)), it is necessary to transform it back into the global coordinate system for the calculation of stiffness matrix. This is performed as follows :

First of all, the strain and stress vectors between the two coordinate systems are related using the following relationship :

$$\Delta \underline{\underline{\varepsilon}}^* = \underline{\underline{T}}_\varepsilon \Delta \underline{\underline{\varepsilon}} \quad (4.28)$$

and

$$\Delta \underline{\underline{\sigma}}^* = \underline{\underline{T}}_\sigma \Delta \underline{\underline{\sigma}} \quad (4.29)$$

where $\underline{\underline{T}}_\varepsilon$ and $\underline{\underline{T}}_\sigma$ are 6x6 strain and stress transformation matrices and are given in Appendix A4 (Equations A4.3 and A4.4). From Equations (4.28) and (4.29), the following equations are obtained :

$$\Delta \underline{\underline{\varepsilon}} = \underline{\underline{T}}_\varepsilon^{-1} \Delta \underline{\underline{\varepsilon}}^* \quad (4.28a)$$

and

$$\Delta \underline{\underline{\sigma}} = \underline{\underline{T}}_\sigma^{-1} \Delta \underline{\underline{\sigma}}^* \quad (4.29a)$$

By observing the special relationship between $\underline{\underline{T}}_\varepsilon$ and $\underline{\underline{T}}_\sigma$, it can be easily shown that :

$$\underline{\underline{T}}_\varepsilon^{-1} = \underline{\underline{T}}_\sigma^T \quad (4.30)$$

and

$$\underline{\underline{T}}_\sigma^{-1} = \underline{\underline{T}}_\varepsilon^T \quad (4.30a)$$

Therefore, the values of $\underline{\Delta \varepsilon}$ and $\underline{\Delta \sigma}$ become

$$\underline{\Delta \varepsilon} = \underline{T}_{\sigma}^T \underline{\Delta \varepsilon}^* \quad (4.31)$$

$$\underline{\Delta \sigma} = \underline{T}_{\varepsilon}^T \underline{\Delta \sigma}^* \quad (4.32)$$

If it is argued that the energy computed in the two coordinate systems must be independent of the coordinate system, then :

$$\delta U^o = \underline{\Delta \varepsilon}^T \underline{\Delta \sigma} = \underline{\Delta \varepsilon}^{*T} \underline{\Delta \sigma}^* \quad (4.33)$$

Substituting Equations (4.21), (4.24) and (4.28) in the above expression, the following relationship is obtained :

$$\underline{\Delta \varepsilon}^T \underline{D}_T \underline{\Delta \varepsilon} = \underline{\Delta \varepsilon}^{*T} \underline{D}_T^* \underline{\Delta \varepsilon}^* \quad (4.33a)$$

$$= \underline{\Delta \varepsilon}^T (\underline{T}_{\varepsilon}^T \underline{D}_T^* \underline{T}_{\varepsilon}) \underline{\Delta \varepsilon} \quad (4.33b)$$

Hence

$$\underline{D}_T = \underline{T}_{\varepsilon}^T \underline{D}_T^* \underline{T}_{\varepsilon} \quad (4.34)$$

Frequent transformations are required in finite element stress and strain calculations related to two systems. Equations (4.28), (4.29), (4.31), (4.32) and (4.34) will always be called upon in the computer program discussed elsewhere to solve constitutive equations for cracking.

4.6. Constitutive Model for Steel

4.6.1. Introduction

Steel liner, prestressing tendons and reinforcements of prestressed concrete vessels are modelled as elasto-plastic materials. The theory describing their material behaviour is based on the incremental theory of plasticity (51, 52, 53, 54, 55, 56, 62). In this section, a brief discussion is presented firstly on the elasto-plastic constitutive relations of steel for general three-dimensional cases, and secondly, these equations are specialised for steel liner (plane stress case) and prestressed tendons (uniaxial case).

4.6.2. General Elasto-Plastic Constitutive Relations

There are three main items used in formulating the elasto-plastic constitutive relations for steel, and these are :

- (a) A yield function
- (b) A flow rule
- (c) Post-yield surfaces (strain hardening)

During the loading, before elasto-plastic constitutive relations are applied, it is necessary that the yield function must be satisfied, i.e. the stress state must be on yield surface using :

$$F(\underline{\sigma}, K) = \bar{\sigma} - K \quad (4.35)$$

where K depends on the plastic deformation and is characteristic of strain hardening.

$$\underline{\sigma} = [\sigma_x, \sigma_y, \sigma_z, \tau_{xy}, \tau_{yz}, \tau_{zx}]^T$$

$$\bar{\sigma} - \text{equivalent stress} \quad (4.36)$$

For Von Mises yield criterion :

$$\bar{\sigma} = (3 J_2)^{1/2} \quad (4.36a)$$

$$\text{where } J_2 = \frac{1}{2} (S_x^2 + S_y^2 + S_z^2) + \tau_{xy}^2 + \tau_{yz}^2 + \tau_{zx}^2 \quad (4.36b)$$

and

$$S_x = \sigma_x - \sigma_m \quad (4.36c)$$

$$S_y = \sigma_y - \sigma_m$$

$$S_z = \sigma_z - \sigma_m$$

$$\sigma_m = (\sigma_x + \sigma_y + \sigma_z) / 3 = \text{mean stress} \quad (4.36d)$$

For a small increment of load, the incremental constitutive relation may be written as :

$$\Delta \underline{\sigma} = \underline{D}_T \Delta \underline{\epsilon} \quad (4.38)$$

For elastic material, $\underline{D}_T = \underline{D}_E$, where \underline{D}_E is the elastic material matrix defined earlier. $\underline{\Delta \varepsilon} = [\Delta \varepsilon_x, \Delta \varepsilon_y, \Delta \varepsilon_z, \Delta \gamma_{xy}, \Delta \gamma_{yz}, \Delta \gamma_{zx}]^T$ is the total mechanical strain increment.

This strain increment is decomposed into elastic and plastic components as :

$$\underline{\Delta \varepsilon} = \underline{\Delta \varepsilon}_E + \underline{\Delta \varepsilon}_P \quad (4.39)$$

The elastic strain increment may be written as (Hook's law) :

$$\underline{\Delta \varepsilon}_E = \underline{D}_E^{-1} \underline{\Delta \sigma} \quad (4.39a)$$

From Equations (4.39) and (4.39a) :

$$\underline{\Delta \varepsilon} = \underline{D}_E^{-1} \underline{\Delta \sigma} + \underline{\Delta \varepsilon}_P \quad (4.40)$$

or

$$\underline{\Delta \sigma} = \underline{D}_E (\underline{\Delta \varepsilon} - \underline{\Delta \varepsilon}_P) \quad (4.40a)$$

which may be written as :

$$\underline{\Delta \sigma} = \underline{\Delta \sigma}_E - \underline{\Delta \sigma}_P \quad (4.40b)$$

with elastic stress increment as :

$$\underline{\Delta \sigma}_E = \underline{D}_E \underline{\Delta \varepsilon} \quad (4.40c)$$

and plastic stress increment as :

$$\underline{\Delta \sigma}_P = \underline{D}_E \underline{\Delta \varepsilon}_P \quad (4.40d)$$

If Equation (4.40d) is written as :

$$\underline{\Delta \sigma}_P = \underline{D}_P \underline{\Delta \varepsilon} \quad (4.41)$$

where \underline{D}_P - plastic material matrix

Then from Equations (4.40a), (4.40b) and (4.41)

$$\Delta \underline{\sigma} = (\underline{D}_E - \underline{D}_P) \Delta \underline{\epsilon} = \underline{D}_{EP} \Delta \underline{\epsilon} \quad (4.42)$$

$$= \underline{D}_T \Delta \underline{\epsilon} \quad (4.42a)$$

where $\underline{D}_T = (\underline{D}_E - \underline{D}_P)$ is the tangent material matrix or the elasto-plastic matrix.

Therefore the material constitutive relations in elastic and elasto-plastic ranges are fully defined by Equations (4.38) and (4.42a) respectively.

Next, the plastic strain increment (Equation 4.40d) and the plastic material matrix, \underline{D}_P (Equation 4.41) are determined in order to define the stress increment in the plastic region.

Assuming that the plastic strain increment is always normal to the plastic potential, $Q(\underline{\epsilon}, \kappa)$ which is similar to yield function given in Equation (4.35), then :

$$Q(\underline{\epsilon}, \kappa) = 0 \quad (4.43)$$

The plastic strain increment is given by (flow rule) :

$$\Delta \underline{\epsilon}_P = \lambda \frac{\partial Q}{\partial \underline{\epsilon}} = \lambda \underline{b} \quad (4.44)$$

where λ - proportionality constant and greater than zero

$$\underline{b} = \frac{\partial Q}{\partial \underline{\epsilon}} \quad (4.44a)$$

If $F = Q$, the plastic strain increment is normal to the yield surface.
For example :

$$\Delta \underline{\epsilon}_P = \lambda \frac{\partial F}{\partial \underline{\epsilon}} = \lambda \underline{a} \quad (4.44b)$$

$$\underline{a} = \frac{\partial F}{\partial \underline{\epsilon}} \quad (4.44c)$$

Later on, special cases are given simply replacing \underline{b} of Equation (4.44) by \underline{a} of Equation (4.44a).

The consistency equation for plastic deformation $dF = 0$ is given by :

$$dF = \frac{\partial F}{\partial \underline{\sigma}} d\underline{\sigma} + \frac{\partial F}{\partial \underline{k}} d\underline{k} \quad (4.45)$$

Define
$$A = - \frac{1}{\lambda} \frac{\partial F}{\partial \underline{k}} d\underline{k} \quad (4.45a)$$

then
$$\frac{\partial F}{\partial \underline{\sigma}} \Delta \underline{\sigma} - \lambda A \quad (4.45b)$$

or
$$\underline{a}^T \Delta \underline{\sigma} - \lambda A \quad (4.45c)$$

Premultiply Equation (4.40) by $\underline{a}^T \underline{D}_E$ substituting $\Delta \underline{\varepsilon}_p$ from Equation (4.44), one obtains the following equation :

$$\underline{a}^T \underline{D}_E \Delta \underline{\varepsilon} = \underline{a}^T \Delta \underline{\sigma} + \underline{a}^T \underline{D}_E \underline{b} \lambda \quad (4.45e)$$

From Equations (4.45c) and (4.45e), an expression for λ is obtained as :

$$\lambda = \frac{\underline{a}^T \underline{D}_E \Delta \underline{\varepsilon}}{[A + \underline{a}^T \underline{D}_E \underline{b}]} \quad (4.46)$$

From Equations (4.44) and (4.46), the plastic strain increment is obtained :

$$\Delta \underline{\varepsilon}_p = \frac{\underline{b} \underline{a}^T \underline{D}_E \Delta \underline{\varepsilon}}{[A + \underline{a}^T \underline{D}_E \underline{b}]} \quad (4.47)$$

From Equations (4.40d), (4.41) and (4.47) :

$$\underline{D}_p = \frac{\underline{D}_E \underline{b} \underline{a}^T \underline{D}_E}{[A + \underline{a}^T \underline{D}_E \underline{b}]} \quad (4.48)$$

And finally, the tangent material matrix of Equation (4.42) can be written as :

$$\underline{D}_T = \underline{D}_{EP} = \left(\underline{D}_E - \frac{\underline{D}_E \underline{b} \underline{a}^T \underline{D}_E}{[A + \underline{a}^T \underline{D}_E \underline{b}]} \right) \quad (4.49)$$

Since the associated flow rule is adopted in this study, \underline{b} in Equations (4.46) to (4.49) should be replaced by \underline{a} . By making $A = 0$, the rigid plastic conditions are achieved.

4.6.3. Hardening Phenomena

The hardening phenomena in metals can be modelled in many ways. There are three types of hardening models used in metal plasticity. The first model which is known as isotropic work hardening was proposed by Hill (55) and Hodge (57). In this case, it is assumed that during plastic flow the yield surface expands uniformly without changing its shape and origin. The special case in this category is the ideal plastic where surface remains constant during the plastic flow. The second hardening model was proposed by Prager (58) and it was later proposed in different form by Ziegler (59) and is known as kinematic hardening. According to this model it is assumed that during plastic flow, the yield surface translated in stress space (π - plane) and there is no expansion of yield surface. This type of hardening model is useful in cyclic loading, where Bauschinger's effect is represented. The model proposed by Hodge (61), known as Combined Hardening, gave a better approximation to the actual material behaviour. This model assumes that during plastic flow the yield surface translates according to kinematic hardening and at the same time expands according to isotropic hardening. Haisler (62) gives more details on this model.

Since this study is not concerned with the cyclic loading, the isotropic hardening model is used. The ideal plasticity can be derived from the isotropic strain hardening model. The main thing which represents the hardening phenomena in the constitutive equation is the parameter A . For ideal plasticity, A is set to zero. For isotropic strain hardening material, it can be shown (52) that :

$$A = H \quad (4.50)$$

where $H = \frac{\partial \bar{\sigma}}{\partial \bar{\epsilon}_p} \quad \text{:: strain hardening parameter} \quad (4.50a)$

which is the slope of the equivalent stress versus equivalent plastic

strain curve. If uniaxial stress strain curve is available, then H can be calculated in the following manner :

$$E_t = \frac{d\sigma}{d\varepsilon} \quad (4.50b)$$

where E_t = tangent modulus

Let E be the elastic modulus at zero stress. Then :

$$\frac{1}{E_t} = \frac{d\varepsilon}{d\sigma} = \frac{d\varepsilon_E}{d\sigma} + \frac{d\varepsilon_P}{d\sigma} = \frac{1}{E} + \frac{1}{H} \quad (4.50c)$$

$$H = \frac{E E_t}{E - E_t} \quad (4.50d)$$

Therefore, if the initial modulus and the stress-strain curve of the material is known, the strain hardening parameter, H, can be calculated. On the other hand, if it is a bi-linear stress strain curve, then E_t is simply a post-yield modulus.

4.6.4. Elasto-plastic Constitutive Relations for Liner

The vessel liner is treated as two-dimensional material under plane stress condition. The elastic constitutive relations are defined in Chapter 3 (Equation (3.16)). This can be written in incremental form as :

$$\begin{bmatrix} \Delta\sigma_x \\ \Delta\sigma_y \\ \Delta\tau_{xy} \end{bmatrix} = \frac{E_s}{1-\nu_s^2} \begin{bmatrix} 1 & \nu_s & 0 \\ \nu_s & 1 & 0 \\ 0 & 0 & \frac{1-\nu_s}{2} \end{bmatrix} \begin{bmatrix} \Delta\varepsilon_x \\ \Delta\varepsilon_y \\ \Delta\gamma_{xy} \end{bmatrix} \quad (4.51)$$

or

$$\Delta\sigma = \underline{D}_E \Delta\varepsilon$$

where $\Delta\sigma = [\Delta\sigma_x, \Delta\sigma_y, \Delta\tau_{xy}]^T$; $\Delta\varepsilon = [\Delta\varepsilon_x, \Delta\varepsilon_y, \Delta\gamma_{xy}]^T$ (4.51a)

and $\underline{D}_E = \frac{E_s}{1-\nu_s^2} \begin{bmatrix} 1 & \nu_s & 0 \\ \nu_s & 1 & 0 \\ 0 & 0 & \frac{1-\nu_s}{2} \end{bmatrix}$ (4.51b)

Now the equations of the previous section are specialised as follows :

4.6.4.1. Von Mises Yield Criterion

Equations (4.35) and (4.36) are rewritten in modified form as :

$$F = \bar{\sigma} - \sigma_y = 0 \quad (4.52)$$

where
$$\bar{\sigma} = \sqrt{\frac{3}{2}} (S_x^2 + S_y^2 + S_z^2 + 2\tau_{xy}^2)^{1/2} \quad (4.52a)$$

$$\begin{aligned} S_x &= (2\sigma_x - \sigma_y) / 3 \\ S_y &= (2\sigma_y - \sigma_x) / 3 \\ S_z &= -(\sigma_x + \sigma_y) / 3 \end{aligned} \quad (4.52b)$$

where σ_y = uniaxial yield stress of the liner

In Equation (4.49) b is replaced by a

where
$$a = \frac{\partial F}{\partial \underline{\sigma}} = \begin{Bmatrix} \frac{\partial F}{\partial \sigma_x} \\ \frac{\partial F}{\partial \sigma_y} \\ \frac{\partial F}{\partial \tau_{xy}} \end{Bmatrix} = \frac{3}{2\bar{\sigma}} \begin{Bmatrix} S_x \\ S_y \\ 2\tau_{xy} \end{Bmatrix} \quad (4.53)$$

Therefore, Equation (4.38) may be written as :

$$\begin{aligned} \Delta \underline{\sigma} &= \underline{D}_E \Delta \underline{\xi} & - \text{if } \bar{\sigma} < \sigma_y \\ \Delta \underline{\sigma} &= \underline{D}_{EP} \Delta \underline{\xi} & - \text{if } \bar{\sigma} \geq \sigma_y \end{aligned} \quad (4.54)$$

The post-yield stress calculation is performed in two ways. The first is the ideal plasticity case where H in Equation (4.49) is set to zero.

The second is the strain hardening case where H in Equation (4.50) is calculated from bi-linear stress-strain curve as shown in Figure (4.9).

The strain hardening parameter, H, in terms of initial and post yield moduli is given by Equation (4.50d).

4.6.5. Elasto-plastic Constitutive Relations for Prestressed and Reinforced Steel

Prestressed tendons and reinforcements are assumed to transmit only axial stress and strain. Therefore, their material behaviour is described by a uniaxial stress-strain curve (Figure (4.9)). From Chapter 3 (Equation (3.24)), the incremental stress-strain relation is given by :

$$\Delta \underline{\sigma}_{|x|} = \underline{D}_E \Delta \underline{\epsilon}_{|x|} \quad (4.55)$$

where

$$\begin{aligned} \Delta \underline{\sigma} &= \Delta \sigma_x \\ \Delta \underline{\epsilon} &= \Delta \epsilon_x \end{aligned} \quad (4.56)$$

$\underline{D}_E = E_s$ - initial modulus of tendon or reinforcement

4.6.5.1. Von Mises Yield Criterion

For this case, Equations (4.35) and (4.36) are modified :

$$F = \bar{\sigma} - \sigma_y \quad (4.57)$$

where

$$\bar{\sigma} = \sigma_x \quad (4.57a)$$

σ_y = uniaxial yield stress of tendon or reinforcement

Equation (4.49) for associated flow rule and isotropic strain hardening can be modified to include :

$$A = H \quad , \quad \underline{a} = \frac{\partial F}{\partial \sigma_x} = 1 \quad (4.57b)$$

By substituting \underline{a} and \underline{D}_E from the above, Equation (4.49) assumes the following simplified form :

$$\underline{D}_{EP} = \frac{E_s H}{(H + E_s)} \quad (4.58)$$

The stress increment becomes :

$$\begin{aligned} \Delta\sigma_x &= \underline{D}_E \Delta\varepsilon_x & \text{if } \bar{\sigma} < \sigma_Y \\ \Delta\sigma_x &= \underline{D}_{EP} \Delta\varepsilon_x & \text{if } \bar{\sigma} \geq \sigma_Y \end{aligned} \quad (4.59)$$

For strain hardening, Equation (4.50) is invoked.

4.7. Bond and Bond-slip Constitutive Relations

The mechanism of bond and bond-slip is given in detail in Chapter 2 (section 2.4.). In this section, the local bond and bond-slip constitutive relations governing the interface behaviour are given. The stress transfer by bond between steel and concrete is difficult to model realistically because of the several variables affecting the bond problem. The bond spring stiffness (Chapter 3, Equation (3.30)) along the length of the steel is determined as :

$$E_h = \frac{d\sigma_b}{ds} = \frac{\Delta\sigma_b}{\Delta s} \quad (4.60)$$

where E_h = slope of the local bond slip curve at any point on the curve (tangent modulus)

$d\sigma_b$ = incremental local bond stress

ds = incremental local slip

In order to model various types of interface characteristics, an experimental bond-slip curve idealised as shown in Figure (4.10a) is used. The non-linear curve is idealised by a series of bond stress and slip points joined linearly. The slope (E_h) at point i of the bond slip curve is given as :

$$E_{hi} = \frac{\sigma_{bi+1} - \sigma_{bi}}{s_{i+1} - s_i} = \frac{\Delta\sigma_{bi}}{\Delta s_i} \quad (4.61)$$

and the other two spring coefficients in vertical and lateral directions of the steel are taken as :

$$E_{vi} = \alpha E_{hi} \quad (4.62)$$

$$E_{li} = \alpha E_{hi}$$

where α is a multiplication factor which was taken between 10^2 to 10^6 . This means that the vertical and lateral springs are rigidly connected between steel and concrete. Once the incremental moduli E_{hi} , E_{vi} and E_{li} are known, the incremental bond stresses are calculated using the constitutive relations of Chapter 3 (Equation (3.30)) as :

$$\begin{Bmatrix} \Delta\sigma_{bc} \\ \Delta\sigma_{vi} \\ \Delta\sigma_{li} \end{Bmatrix} = \begin{bmatrix} E_{hi} & 0 & 0 \\ 0 & E_{vi} & 0 \\ 0 & 0 & E_{li} \end{bmatrix} \begin{Bmatrix} \Delta S_{hi} \\ \Delta S_{vi} \\ \Delta S_{li} \end{Bmatrix} \quad (4.63)$$

or

$$\Delta\sigma_{bc}^e = E_{bc} \Delta S_{hi}^e \quad (4.63a)$$

The element nodal force vector given by Equation (3.31) can be rewritten as :

$$\Delta P_i^e = \pi d L \underline{T}^T \Delta\sigma_{bc}^e \quad (4.64)$$

and the element stiffness matrix (Equation (3.32b)) :

$$\underline{K}_b = \pi d L \underline{T}^T E_{bc} \underline{T} \quad (4.65)$$

where \underline{T} is the transformation matrix given in Equation (3.29).

The constitutive relations (4.63) are valid between points O and A (Figure (4.10a)); thereafter the bond stress increment becomes zero (region AB), i.e. the slip occurs at constant bond stress. The bond is assumed to fail at point B (Figure (4.10a)) when maximum allowed slip has been reached. At this point, the total bond stress is released. This creates a non-equilibrium state which is corrected by performing equilibrium iterations (e.g. by the initial stress method).

Now a scheme is suggested to calculate a correct bond stress from a specified bond-slip curve (see Figure (4.10b)). Let S_r be the total slip reached at any point in the calculation. This slip lies between the points $i-1$ and i on the specified curve. Bond stresses are

calculated which are compatible with the total slip (S_r) by linear interpolation as :

$$\sigma_{br} = \sigma_{bi-1} + \theta (S_r - S_{i-1}) \quad (4.66)$$

where θ = slope of the specified curve at point $i-1$

$$= \left(\frac{\sigma_{bi} - \sigma_{bi-1}}{S_i - S_{i-1}} \right) \quad (4.67)$$

Let the total bond stress calculated using constitutive equation (4.63) be σ_{bi} . The difference ($\sigma_{bi} - \sigma_{br}$) is treated as initial stress and is corrected by performing equilibrium iterations.

4.8. Constitutive Relations using Creep and Thermal Effects

Concrete exhibits time-dependent strains due to creep and shrinkage which profoundly affect the behaviour of concrete as a structural material. The literature covering concrete creep is comprehensive (67, 68, 69, 70, 71, 72, 73, 74, 75, 76, 77, 78, 79, 84, 126, 127, 128, 129, 130). It is not intended to review this literature in greater depth. However, a brief discussion on the results obtained by various researchers (70, 72, 76, 77, 126, 127, 128, 129, 130) is given.

Creep in concrete represents the dimensional change in the material under the influence of sustained mechanical loading. Quite small loads will cause the concrete to deform. The phenomenon of creep occurs at elevated and at ambient temperatures. The rate of creep is increased at elevated temperatures. Various experimental tests (126, 127, 128) have been conducted to identify the effect of temperature on concrete creep. England and Ross (126) presented results of sealed and unsealed cylinders up to the temperature of 140°C and a testing duration of 60 days. The results on sealed cylinders show that the creep at 80°C and 140°C was about 3.5 and 4.2 times the value at 20°C. Nasser and Neville (127) reported their observations from experimental tests at temperatures ranging from 21.1°C to 96.1°C with stress/strength ratios from 0.35 to 0.7. The concrete was cured at 41.34 N/mm² (6000 psi) and tested after

24 hours of casting. They found that the pronounced maximum for the creep rate at a temperature of about 71°C. This creep rate was based on creep measurements made during a period from 21 to 91 days after loading. Hannant (128) conducted creep tests on sealed 104.775 mm (4 1/8") by 305 mm (12") cylinders of an approximately 62 N/mm² (9000 psi) limestone aggregate after curing them 5 months in water and an additional month in a sealed and saturated condition. Results showed a nearly linear increase of specific creep with a range of 27°C to 77°C for loading periods of two years. The creep at 77°C was approximately 4 to 4.8 times that at 27°C. Up to stresses of 12.78 N/mm² (2000 psi) creep remained proportional to stress. Poisson's ratios of creep determined on sealed specimens were similar in magnitude to its elastic value.

In order to understand the influence of creep, a typical deformation Vs time curve is shown in Figure (4.11). A concrete specimen loaded under uniaxial compression gives an immediate elastic deformation. If this load is sustained, additional deformation due to creep occurs. The rate of the deformation decreases with time (Figure (4.11)). If this load is removed, there is an immediate recovery of deformation and following this, a recovery of creep deformation (delayed recovery) rate occurs, which rapidly decreases with time as shown in Figure (4.11)). At the end of this, a residual deformation is left which is greater than the initial elastic deformation. Figure (4.12) shows time-dependent strain curve for ambient and elevated temperatures between time t_1 and t_2 . The creep recovery strain occurs immediately after the instantaneous elastic strain which is extensive at first, but reduces after a short period of time. The creep recovery is essentially independent of temperature (127).

At a low level of stress, a concept of specific creep is introduced. Specific creep or creep strain per unit of stress is a useful indicator of creep effects. It is also sometimes useful to normalise creep strain data with respect to stress and temperature. This quantity is known as specific thermal creep.

Various methods of creep analysis have been used over the last fifty years. Among those available, they may be classified into two main categories.

- (a) Direct methods.
- (b) Iterative or step-by-step methods.

The direct methods allow the calculation of creep effects in a single time step. The effective modulus (130) and steady state (70) methods are examples of this category. Other direct methods, in refined form, have been presented by England (72, 76).

In the iterative methods, the period of time (over which creep is sought) is divided into a number of steps and separate calculations are carried out for each step. An assumption is made that stress is constant during each time step while strain is being calculated. The accuracy and stability of the solution depends on the length of the time step chosen and successive calculations depend on those in previous time steps. The iterative type of methods of creep solution are :

- ✓ 1. Method of superposition (129).
- ✓ 2. Rate of creep (130)
- ✓ 3. Strain hardening.
- ✓ 4. Rate of flow method (77)

The constitutive relation for concrete under uniaxial stress is established based on the rate of flow method. The total time-dependent strain in concrete may be written as :

$$\begin{aligned} \epsilon(t) &= \epsilon_e(t) + \epsilon_f(t) + \epsilon_d(t) \quad \checkmark \\ &= \frac{\sigma(t)}{E(t)} + \int_0^t \frac{\partial \sigma(\tau)}{\partial \tau} J_f(t-\tau) d\tau + \int_0^t \frac{\partial \sigma(\tau)}{\partial \tau} J_d(t-\tau) d\tau \quad (4.68) \end{aligned}$$

where $\epsilon(t)$ = total strain ; $\epsilon_f(t)$ = irreversible or flow component of creep strain

where $\epsilon_e(t)$ = elastic strain ; $\epsilon_d(t)$ = reversible or delayed
elastic component of creep strain
 $J_f(t)$ = specific flow (flow strain per unit of stress)
 $J_d(t)$ = delayed elastic strain per unit of stress
 t = age of concrete
 τ = time under load

Components of strain are shown in Figure (4.13). Creep compliance for concrete may be written as (E is assumed constant with time t) :

$$J(t, \tau) = \frac{1}{E} + J_f(t - \tau) + J_d(t - \tau) \quad (4.69)$$

A parameter is introduced at this stage known as pseudo time, t' , which itself is specific flow component and this may be used in place of actual time, t , together with the representation of a non-ageing visco-elastic material. The pseudo time concept transforms the age-dependent creep relationship in real time to the simpler non-ageing Maxwell law in pseudo time. The time transformation eases the analytical or numerical computation which leads to a solution without changing the basic creep equation. Now, with this transformation, J_f (69) may be written as :

$$J_f(t' - \tau') = t' - \tau' \quad (4.70)$$

and also the delayed elastic strain :

$$J_d(t' - \tau') = J_{d\alpha} (1 - e^{-\beta(t' - \tau')}) \quad (4.71)$$

If we represent the constitutive model in the pseudo time axis by a Maxwell fluid unit (model 1 in Figure (4.14)) and connect it in series with a Kelvin solid unit (model 2 in Figure (4.14)) to make it what is known as Burger's model (Figure (4.14)), in this model the dashpot and the Kelvin unit correspond to flow and delayed elastic components respectively. Equation (4.69) may then be written as :

$$J(t' - \tau') = \frac{1}{E} + (t' - \tau') + J_{d\alpha} (1 - e^{-\beta(t' - \tau')}) \quad (4.72)$$

Appendix A7 gives formulations for creep strains under multiaxial stress and kinematically equivalent loads due to changes in creep and thermal strains.

Table 4.1. Four Material Parameters ($k = \sigma_t / \sigma_c$)

k	a	b	k_1	k_2
0.08	1.8076	4.0962	14.4863	0.9914
0.10	1.2759	3.1962	11.7365	0.9801
0.12	0.9218	2.5969	9.9110	0.9647

Table 4.2. Values of Function ($k = \sigma_t / \sigma_c$)

k	λ_t	λ_c	λ_c / λ_t
0.08	14.4725	7.7834	0.5378
0.1	11.7109	6.5315	0.5577
0.12	9.8720	5.6979	0.5772

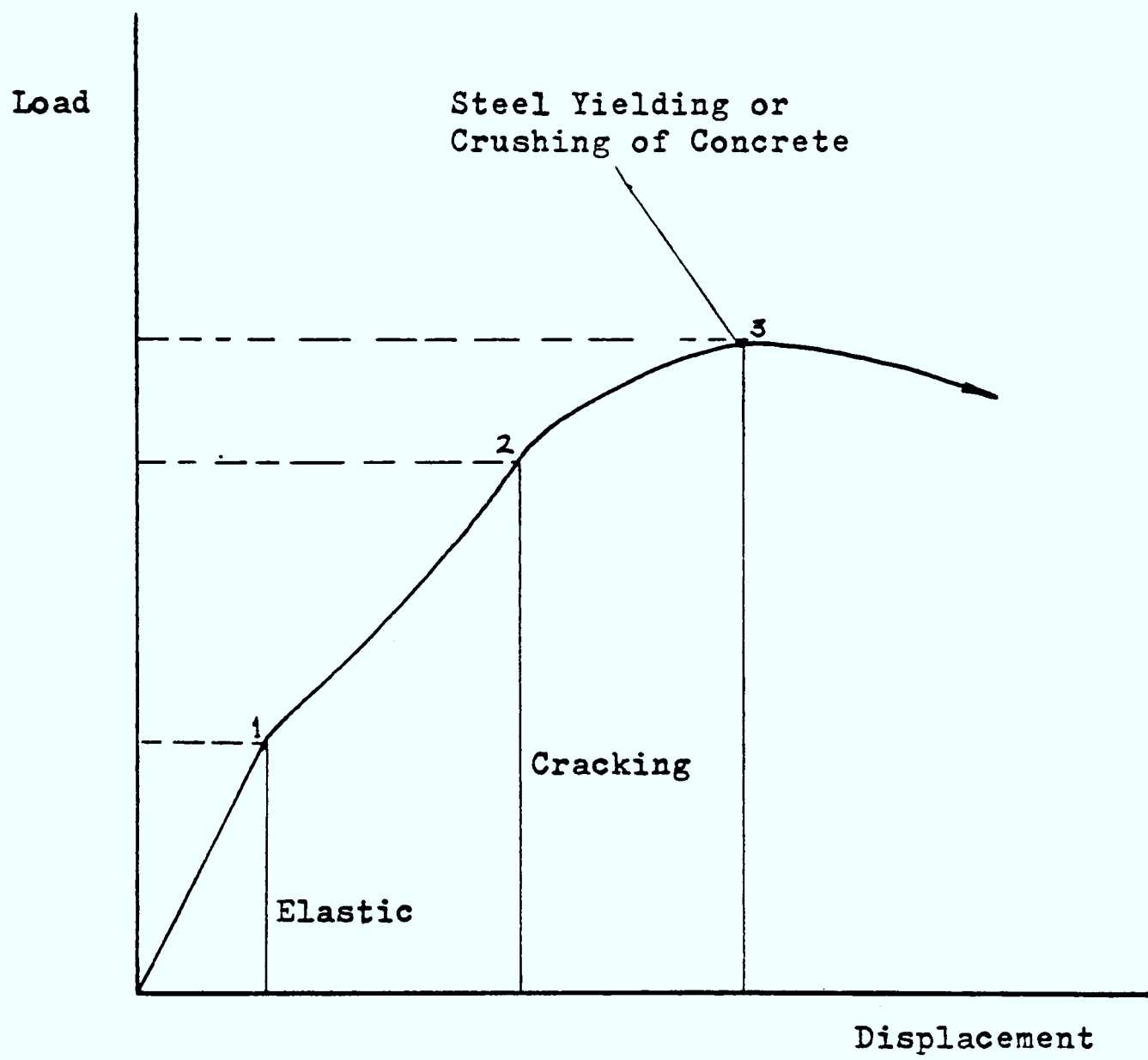


Figure 4.1a Load - Displacement Diagram for Reinforced Concrete

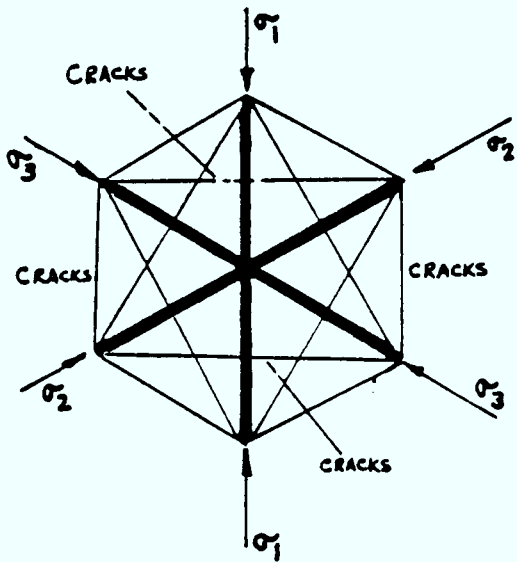


Figure 4.1b Tetrahedral Model (Baker - 150)

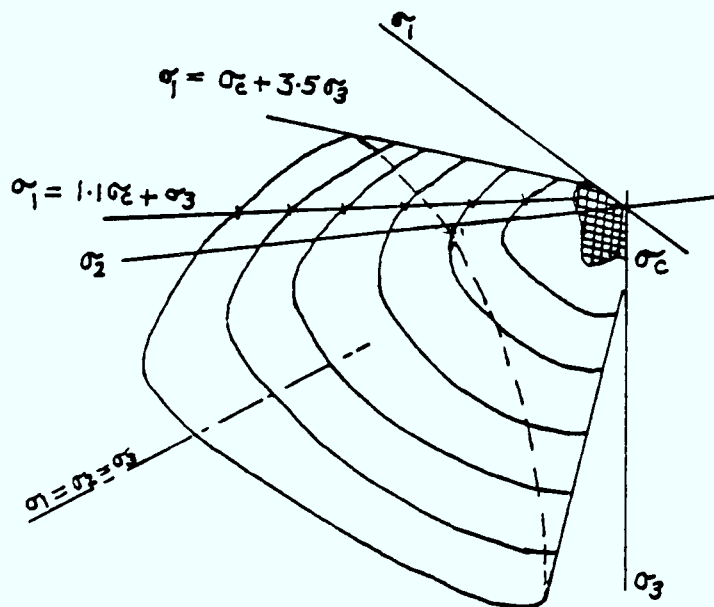


Figure 4.1c Failure Surface in Compression Quadrant of Stress Space

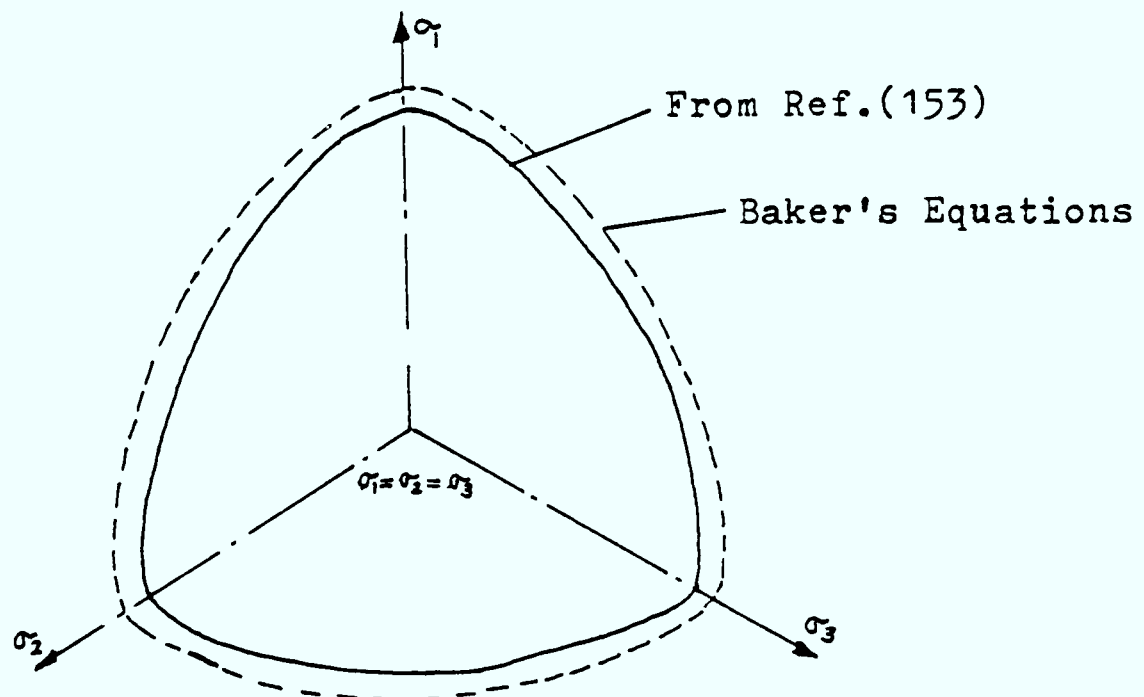
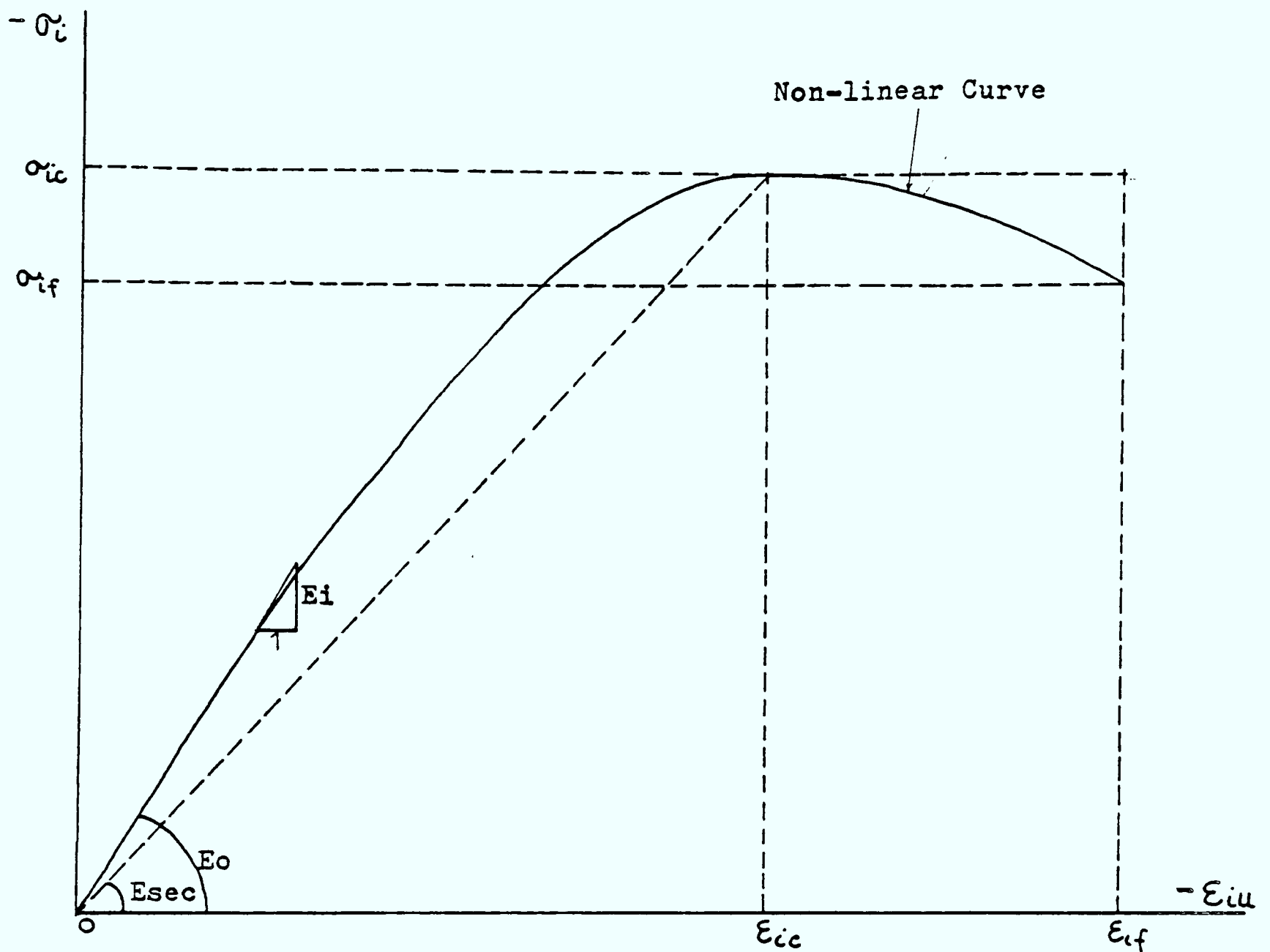


Figure 4.1d Failure Surface on Deviatoric Plane



$$\sigma_i = \frac{E_o \epsilon_{iu}}{[1 + (\frac{E_o}{E_{sec}} + R - 2)\epsilon_R - (2R - 1)\epsilon_R^2 + R\epsilon_R^3]}$$

$$E_i = \frac{d\sigma_i}{d\epsilon_{iu}} = \frac{E_o [1 + (2R - 1)\epsilon_R^2 - 2R\epsilon_R^3]}{[1 + (\frac{E_o}{E_{sec}} + R - 2)\epsilon_R - (2R - 1)\epsilon_R^2 + R\epsilon_R^3]^2}$$

$$\epsilon_R = \frac{\epsilon_{iu}}{\epsilon_{ic}} \quad ; \quad \sigma_{if} = 0.85 \sigma_{ic}$$

$$E_{sec} = \frac{\sigma_{ic}}{\epsilon_{ic}} = \text{Secant modulus at ultimate stress}$$

E_o = Initial modulus

ϵ_{if} = Concrete failure strain

σ_{ic} = Maximum stress

ϵ_{ic} = Maximum strain at σ_{ic}

$$= 3.47 \sigma_{ic}^{1/4} (31.5 - 3.47 \sigma_{ic}^{1/4}) \times 10^{-5}$$

Figure 4.2 Typical Compressive Stress-Uniaxial Equivalent Strain Curve

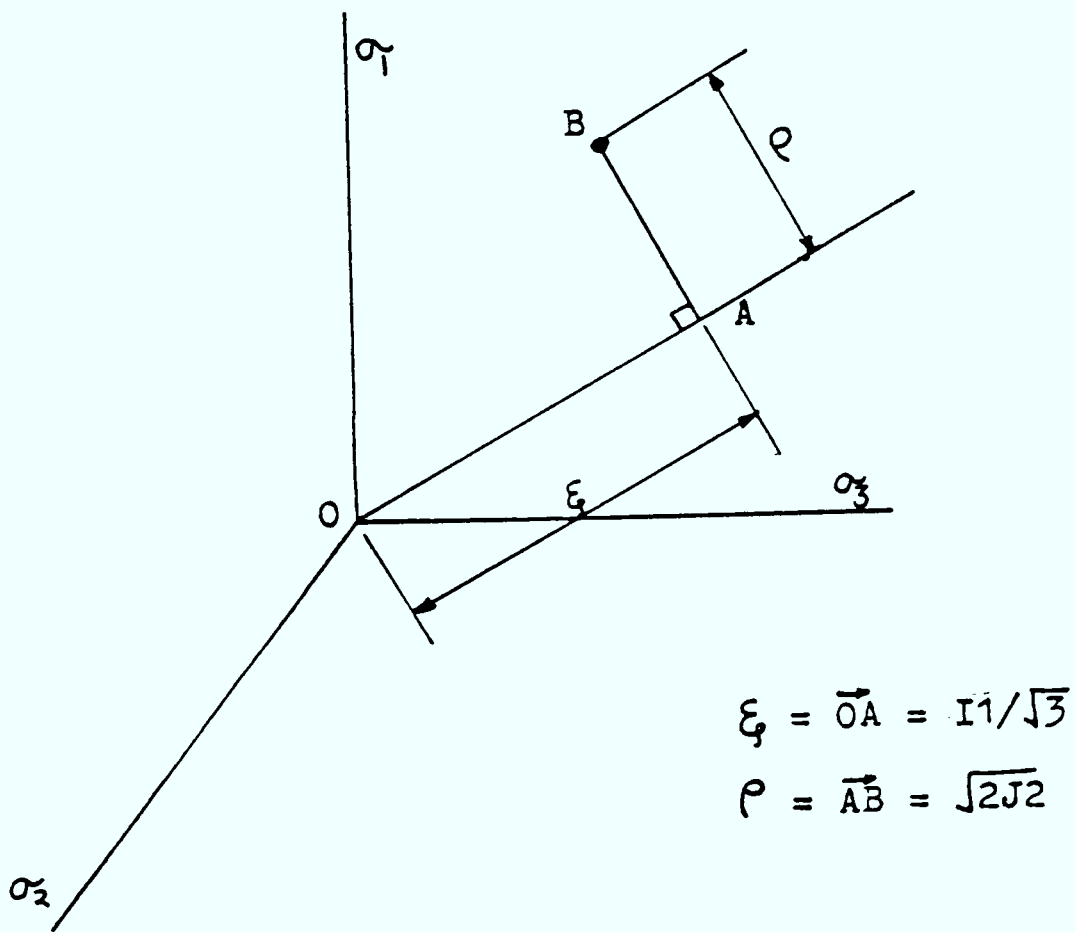


Figure 4.3 Haig-Westergaard Coordinate System

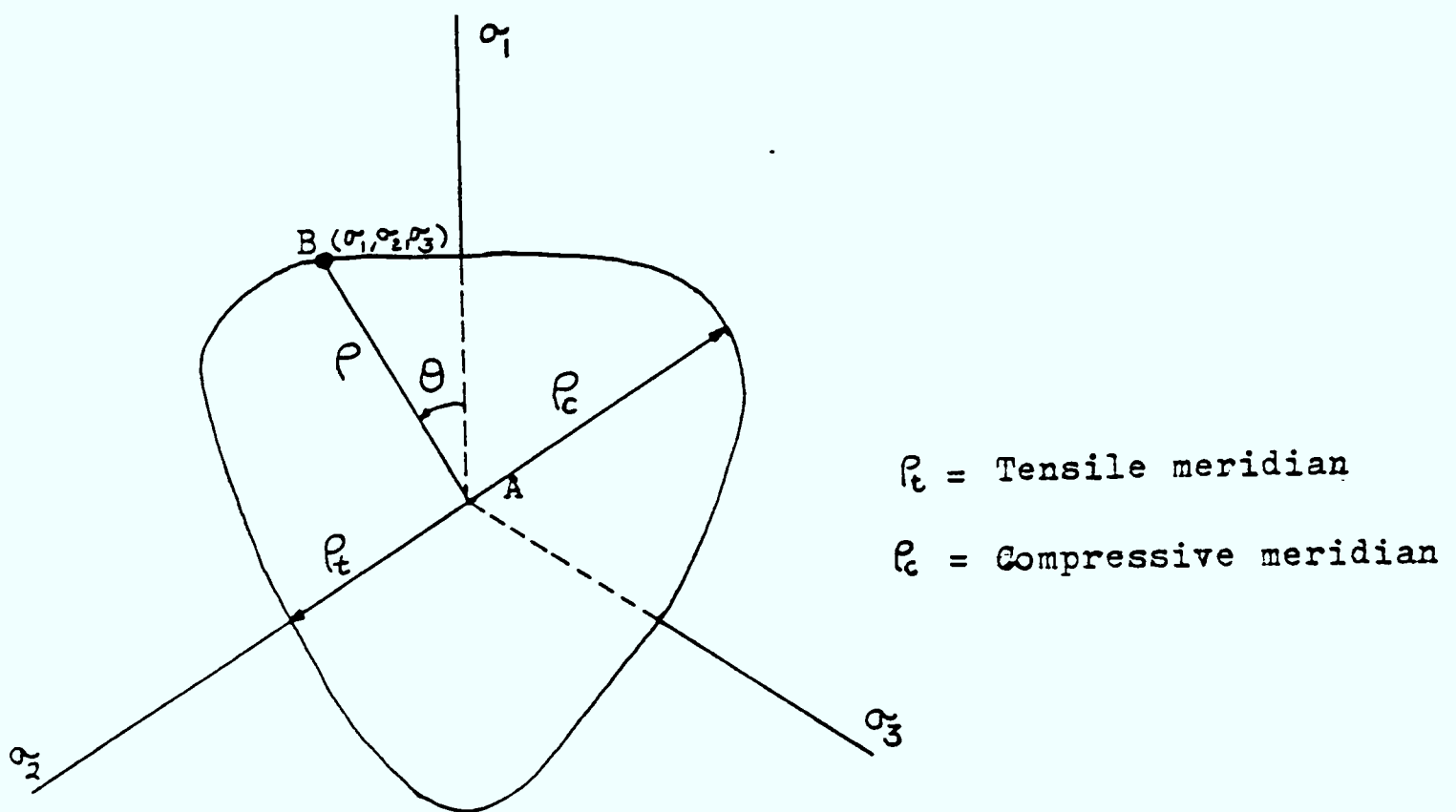
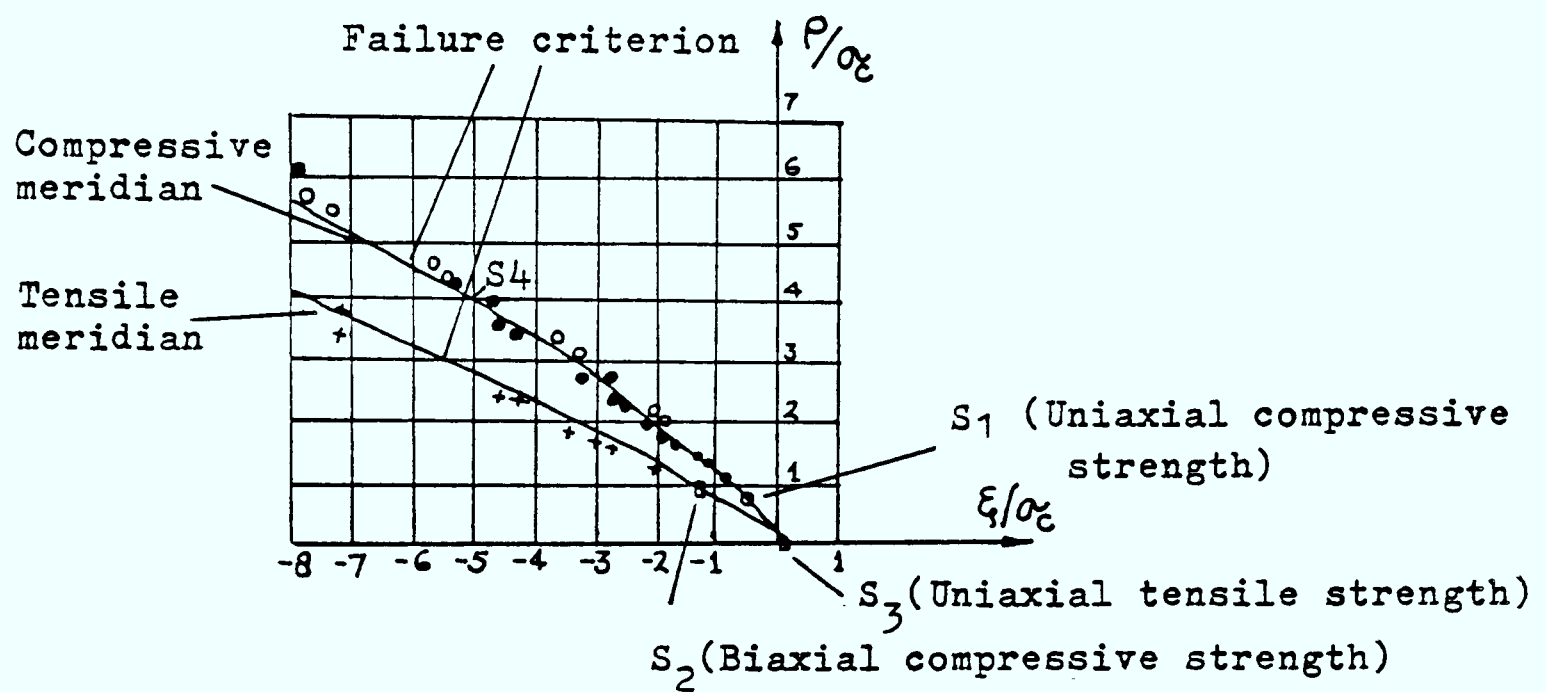
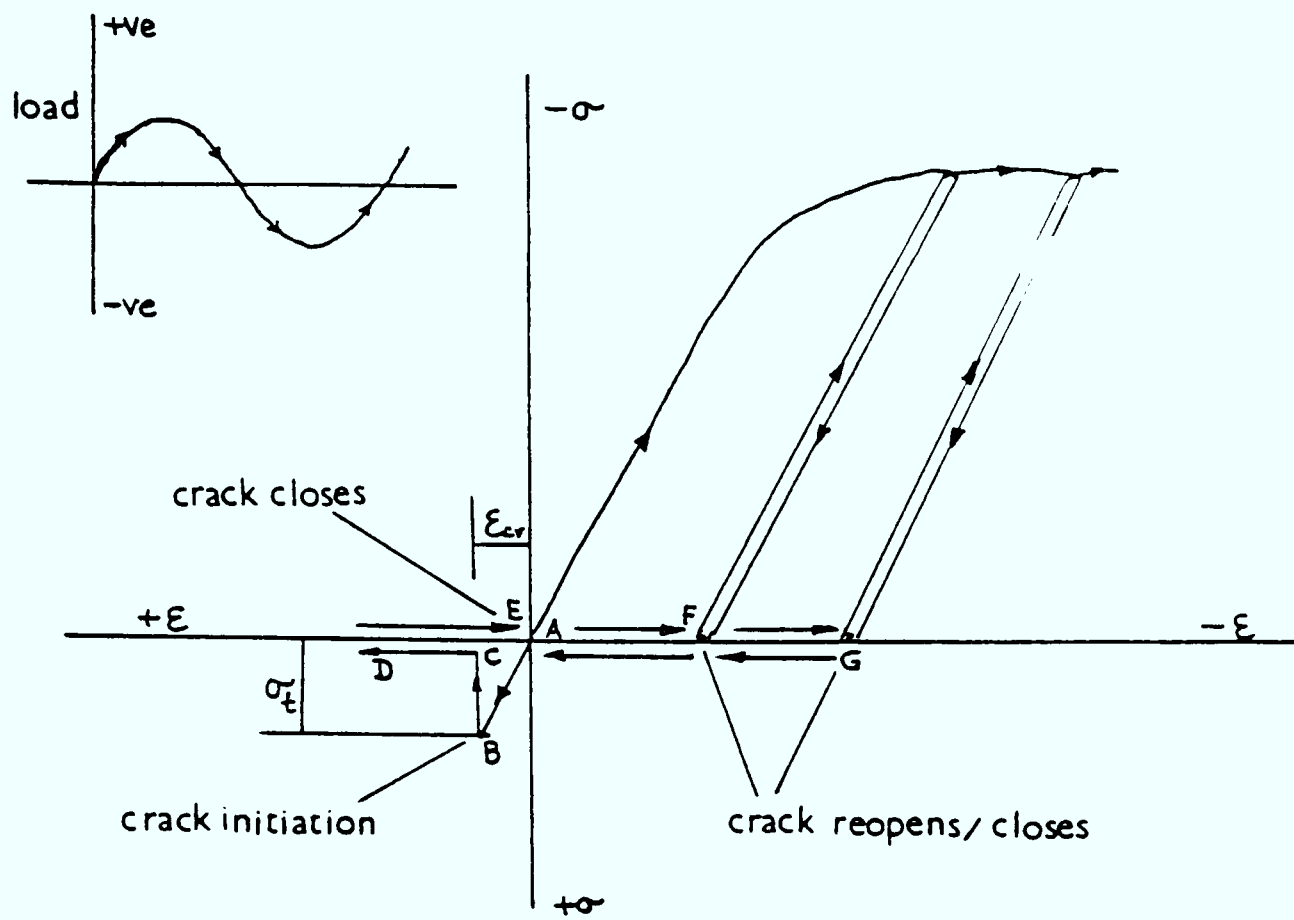


Figure 4.4 Failure Surface in Deviatoric Plane

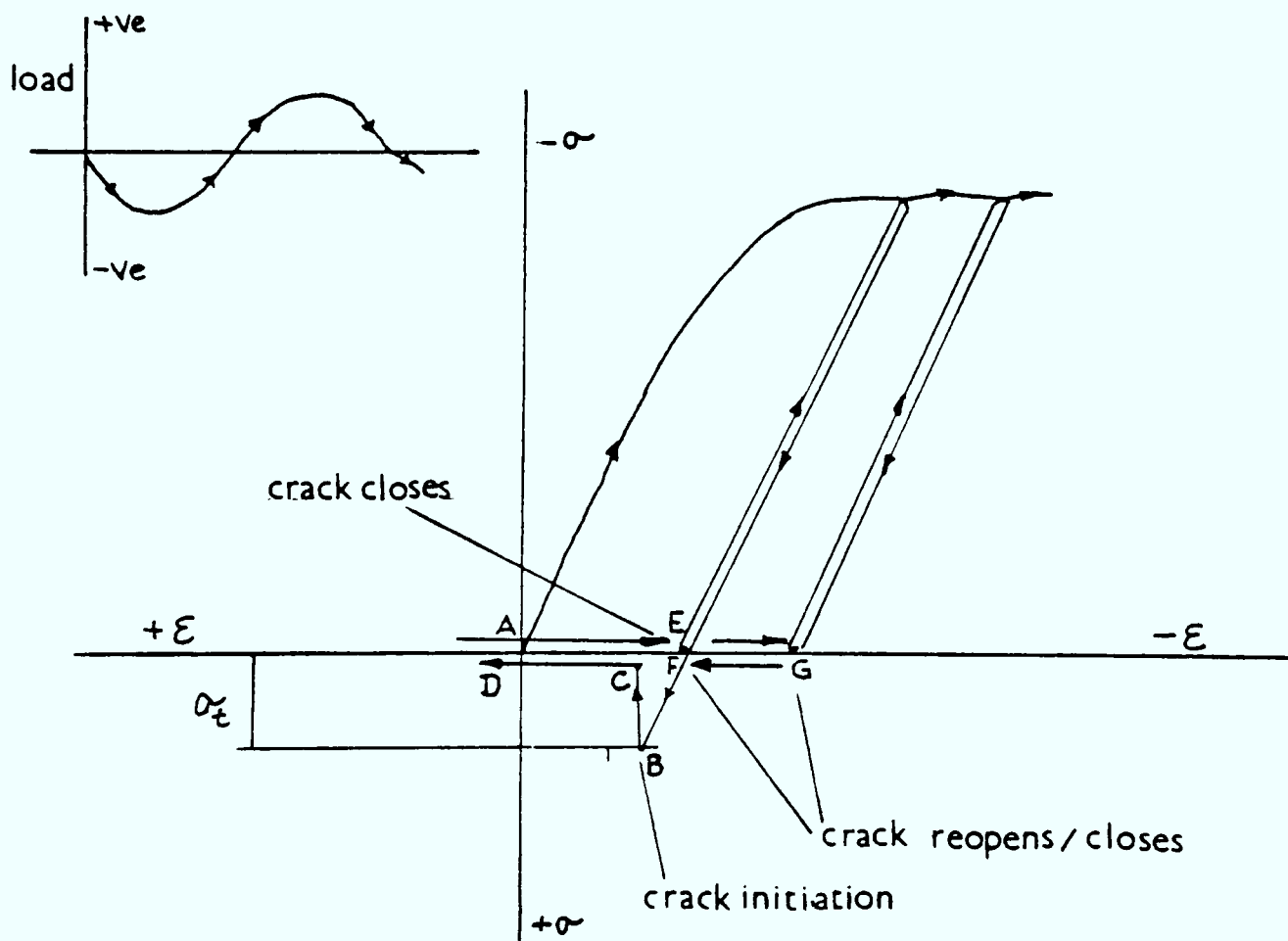


Test results - Balmer(140) - o (compressive)
 Richart et al (139) - ● (compressive)
 + (Tensile)
 Kupfer et al (25) - □ (Tensile)

Figure 4.5 Determination of Material Parameters
 (S_1, S_2, S_3, S_4 - Failure Stresses)



(a) First load in tension



(b) First load in compression

Figure 4.6 Crack Initiation, Closing and Reopening Criteria

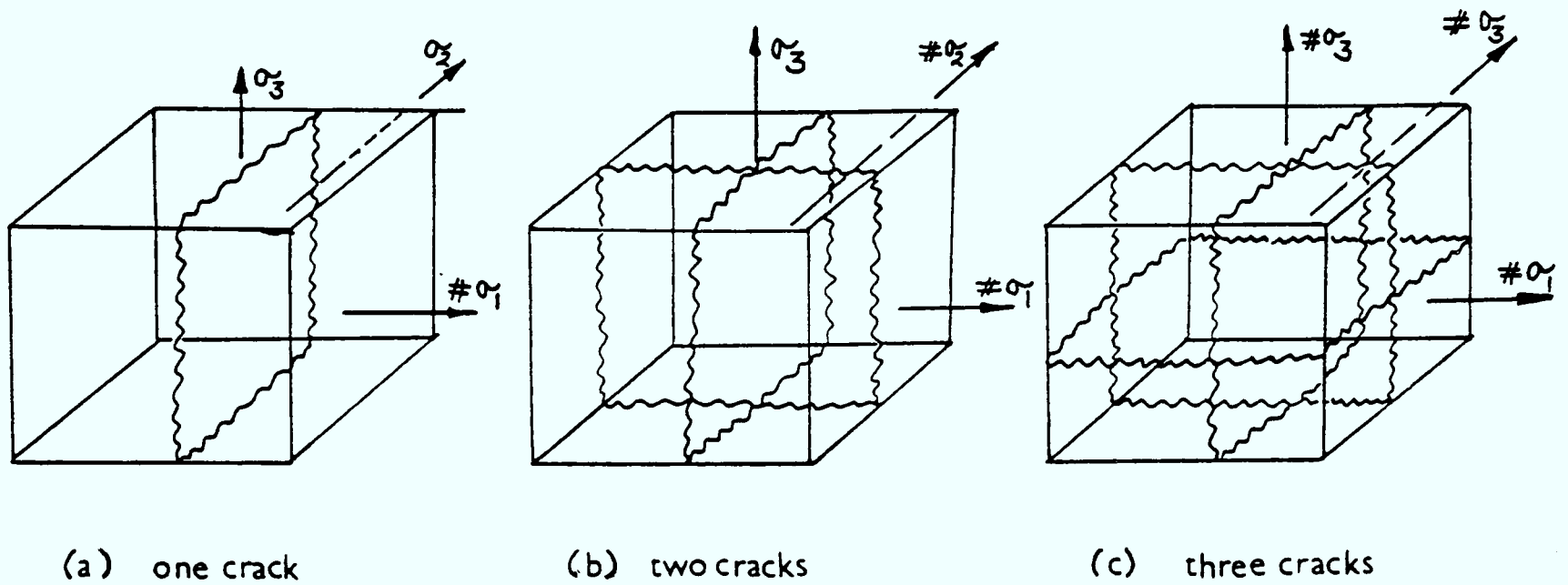


Figure 4.7 Types of Cracks for Three Dimensional Case

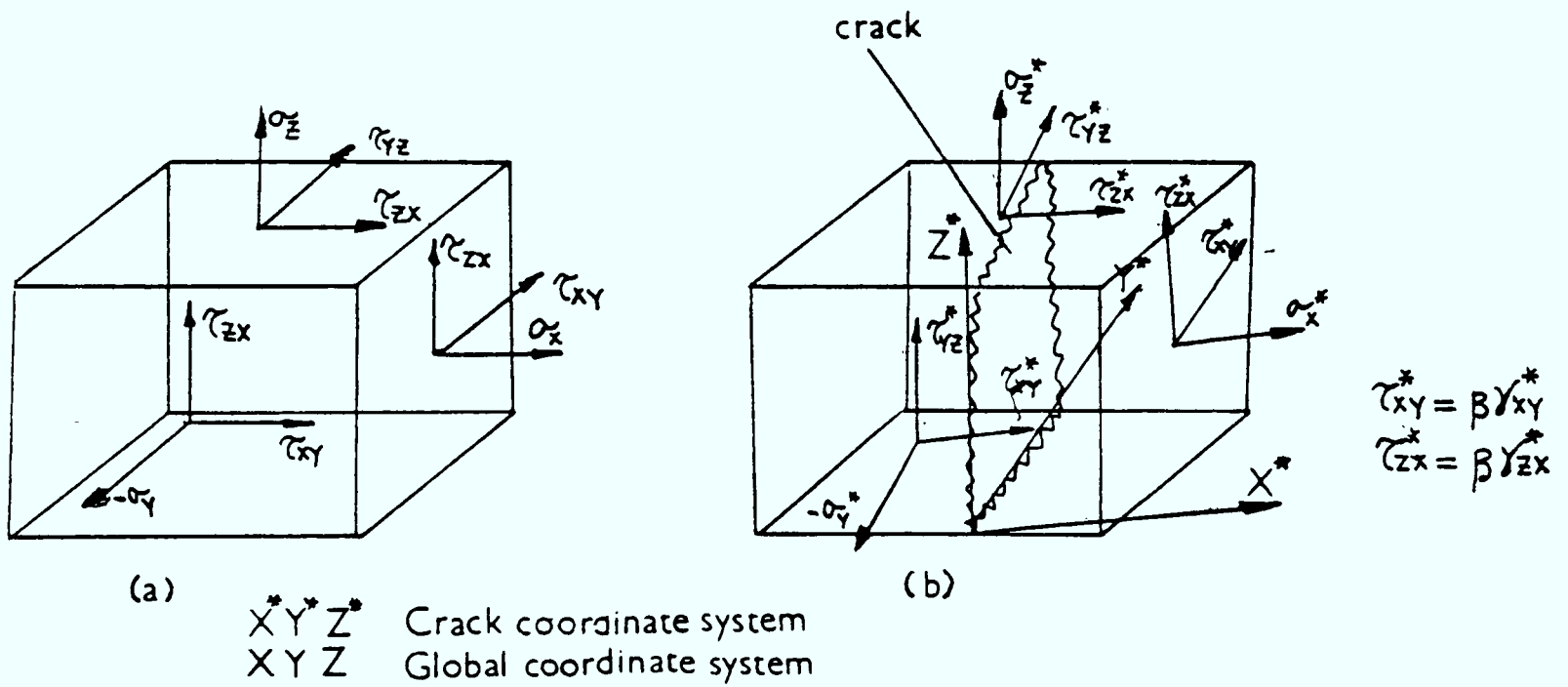


Figure 4.8a State of Stress Before Cracking

Figure 4.8b State of Stress After Cracking

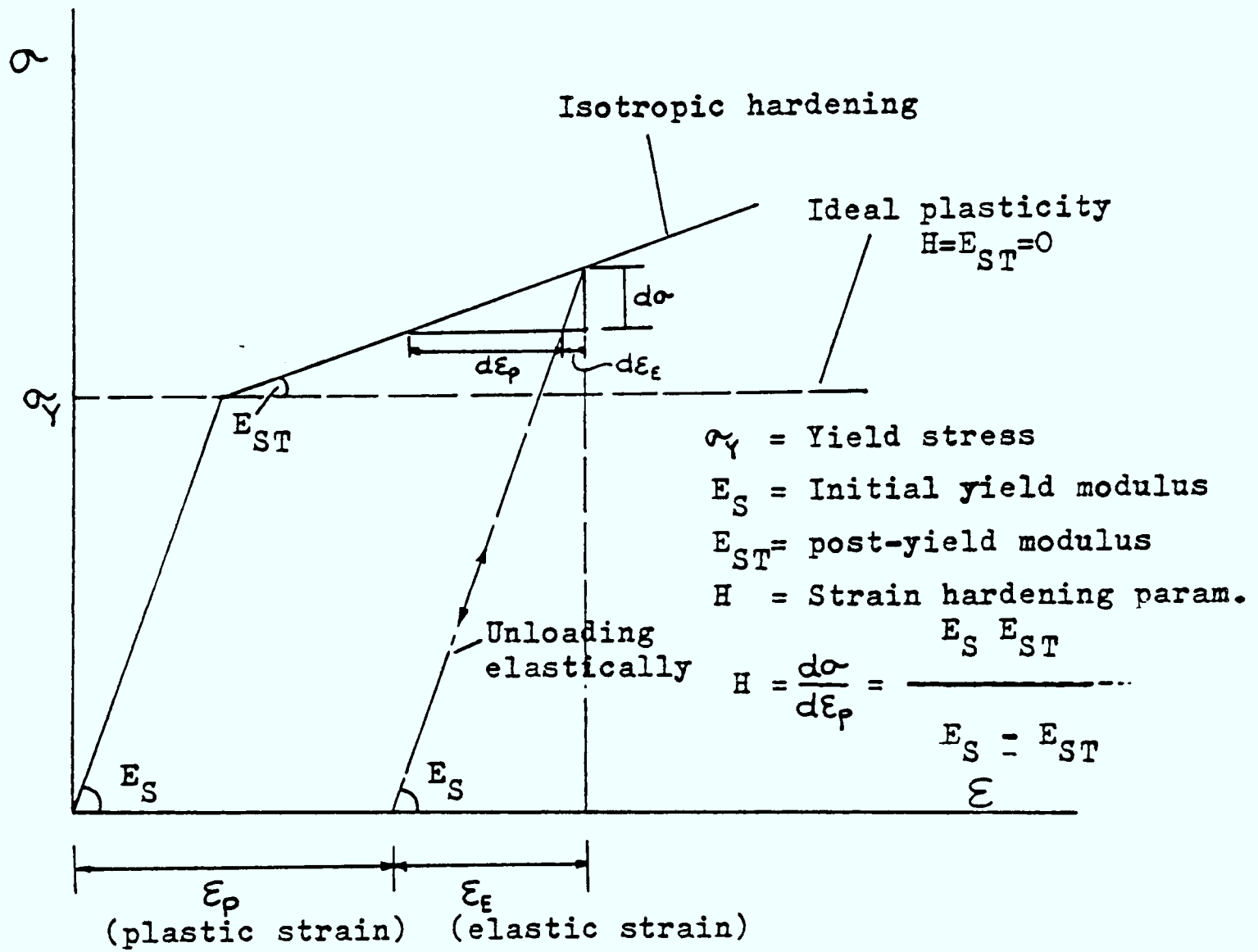


Figure 4.9 Uniaxial Stress - Strain Curve for Steel

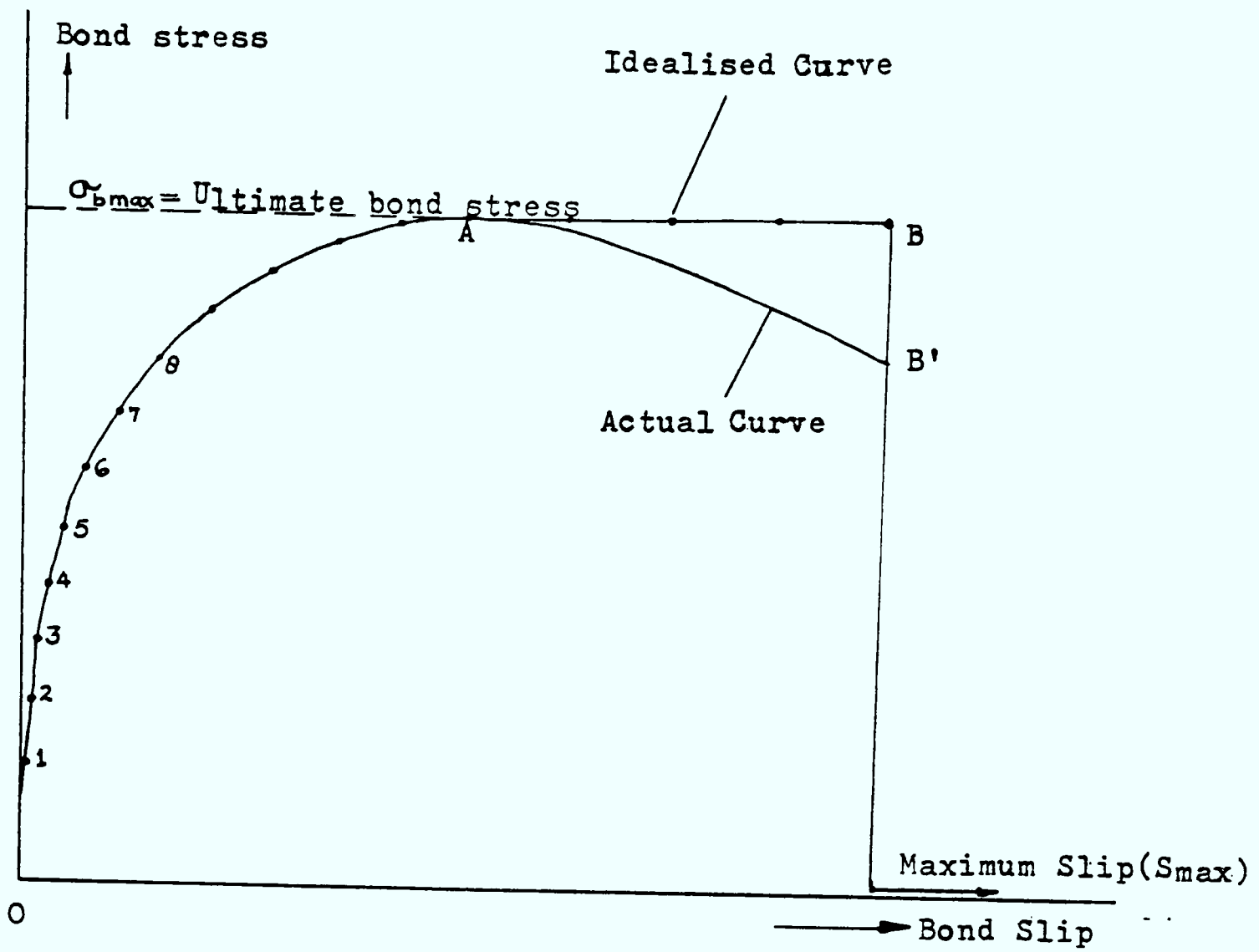


Figure 4.10a A Typical Idealised Bond-Slip Curve

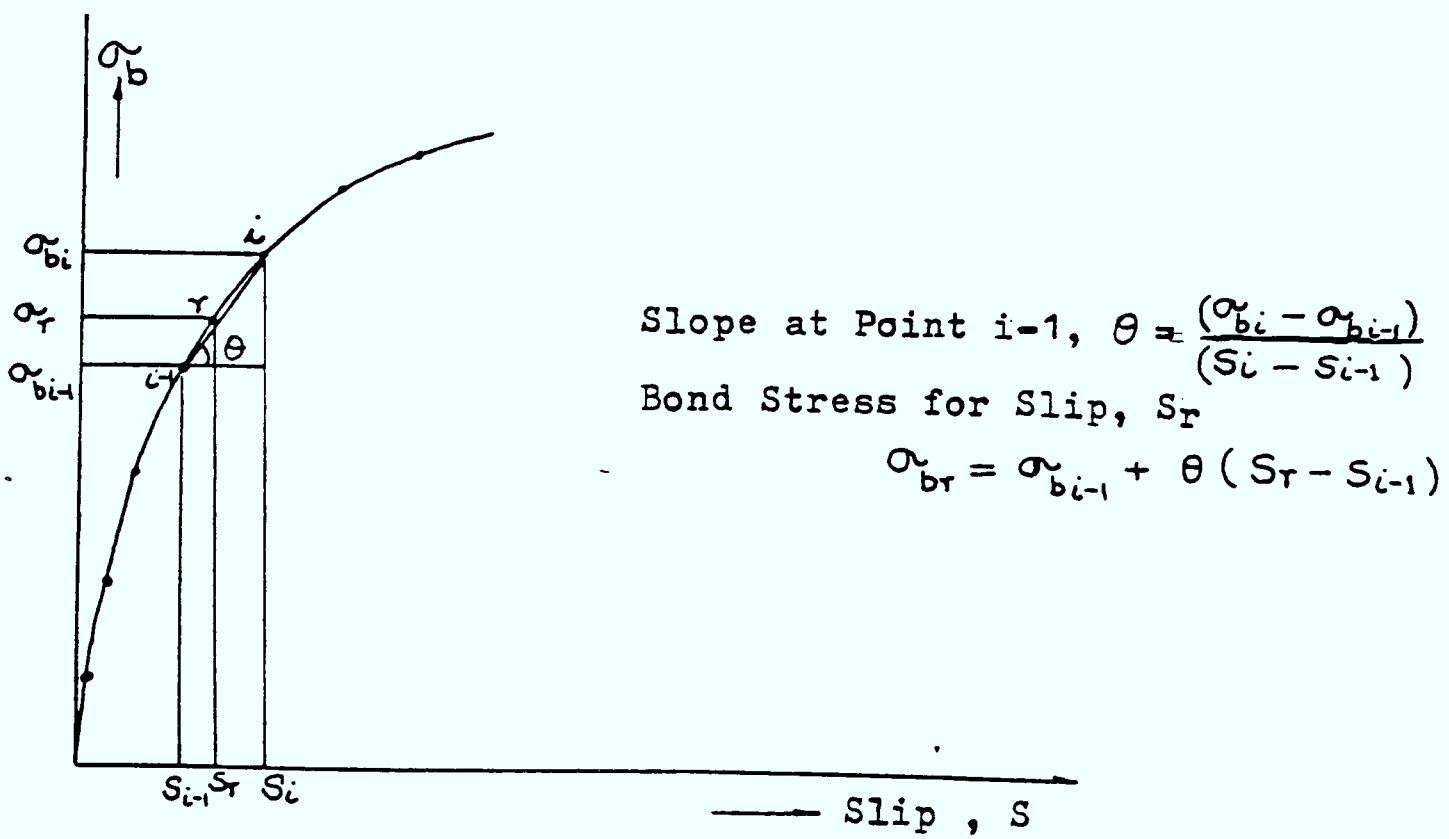


Figure 4.10b Linear Interpolation of Non-linear Bond-slip Curve

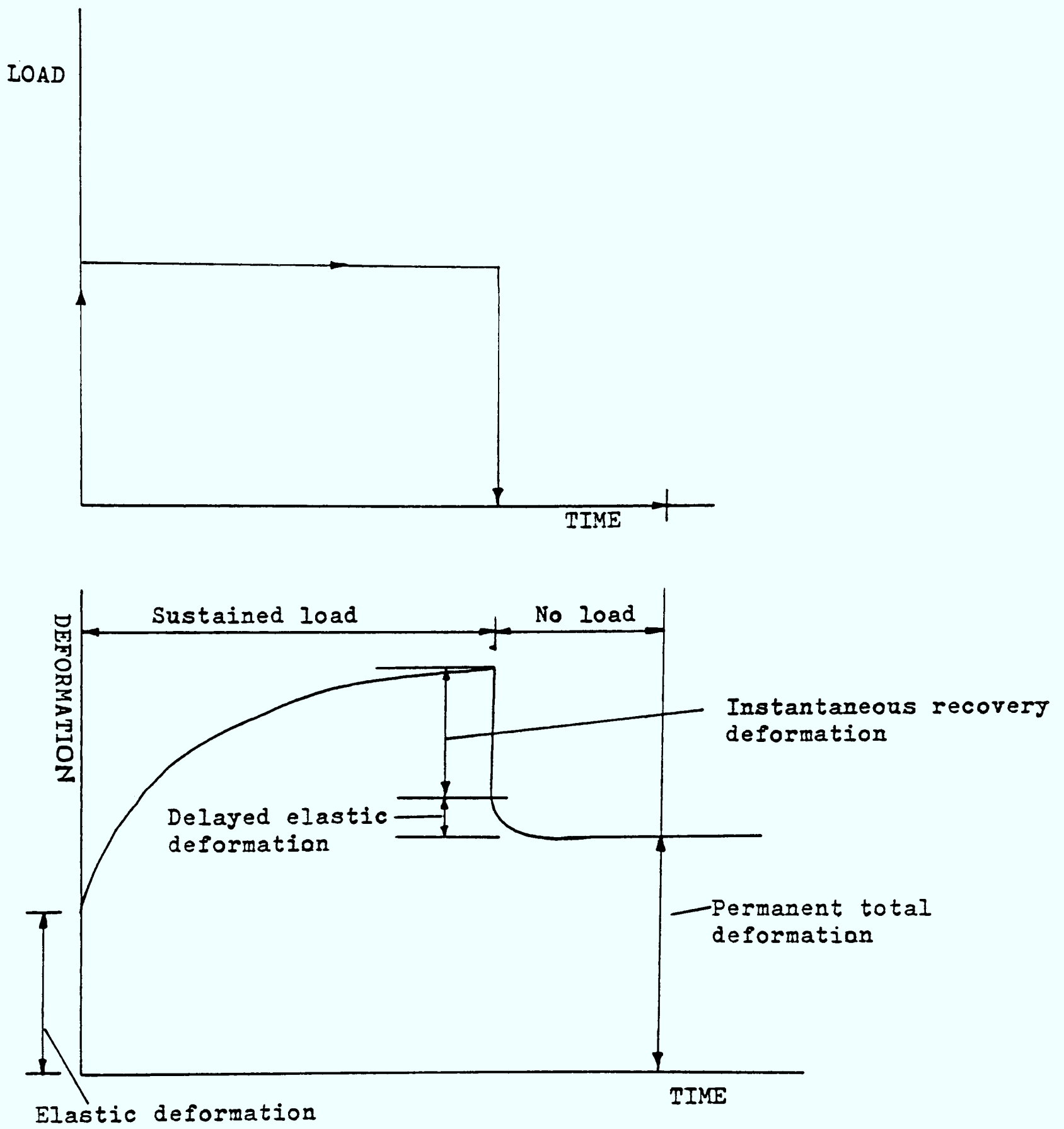
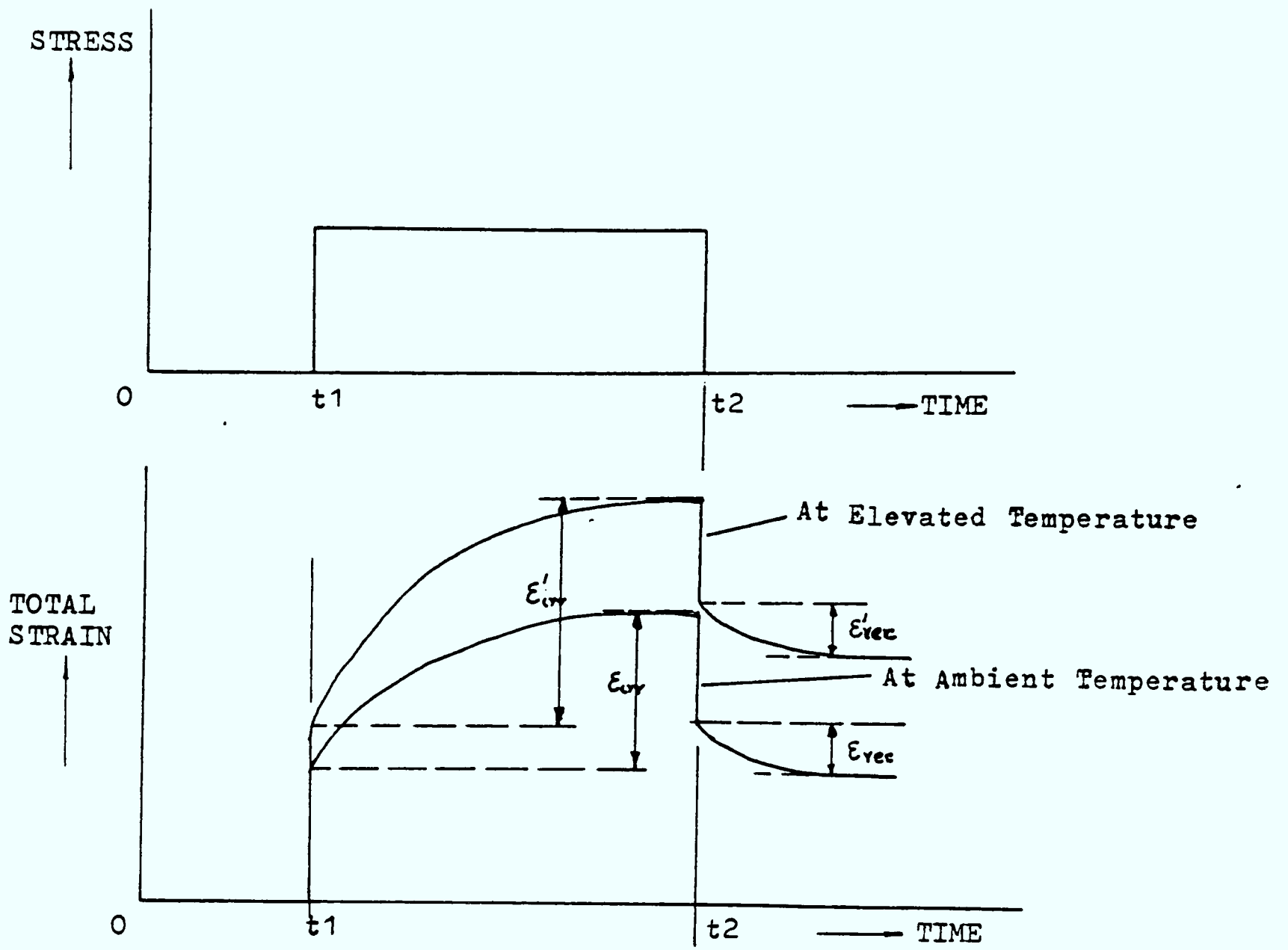


Figure 4.11 Typical Deformation Vs Time Curves for Concrete Under Constant Load



ϵ_{rec} - Recoverable Creep Strain

ϵ_{irr} - Irrecoverable Creep Strain

Figure.4.12 Time - Dependent Strains in Concrete

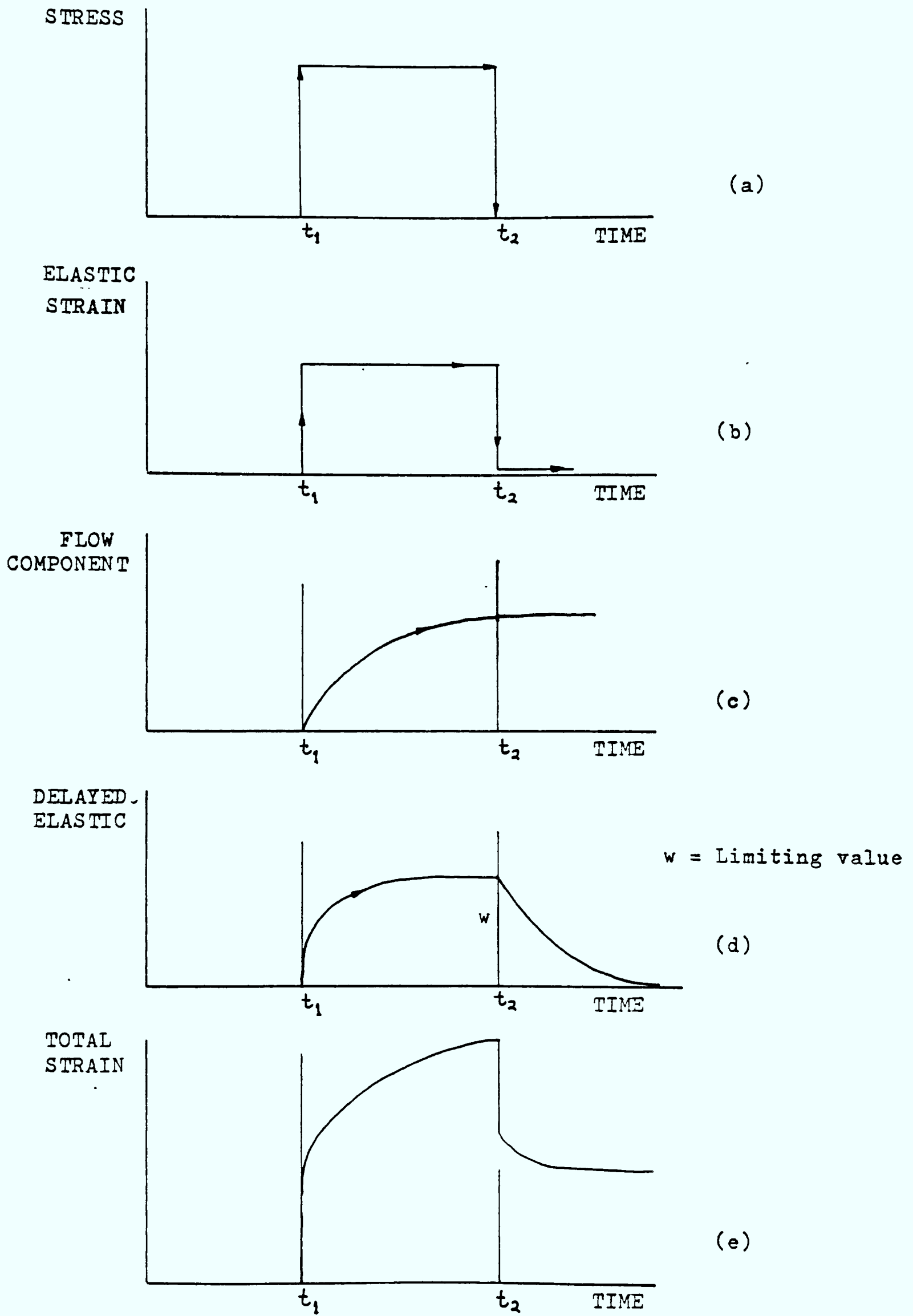
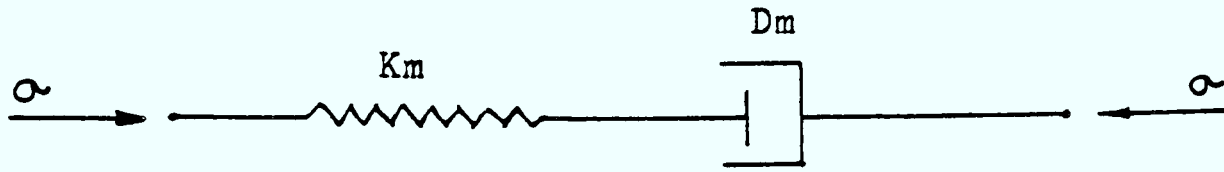
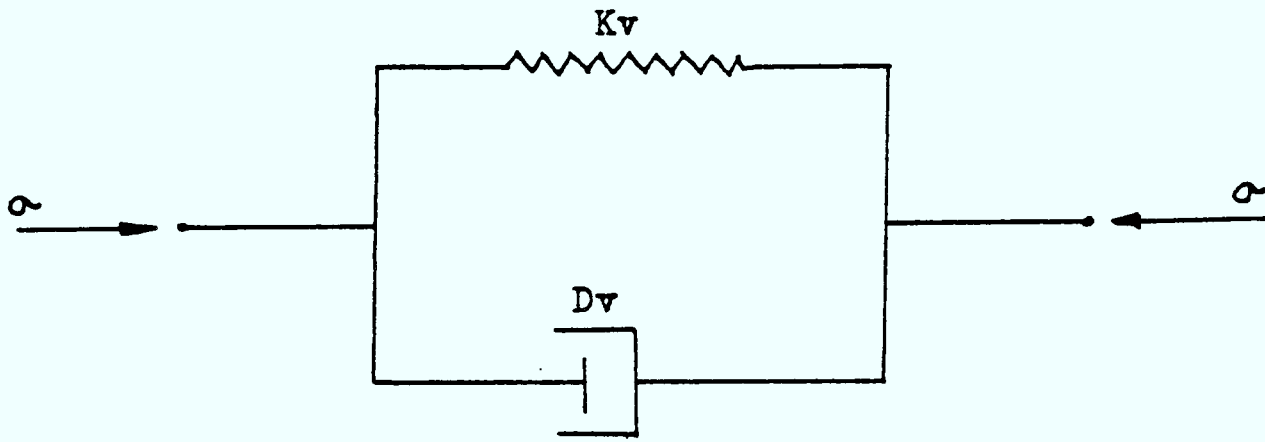


Figure 4.13 Components of Strain in Concrete

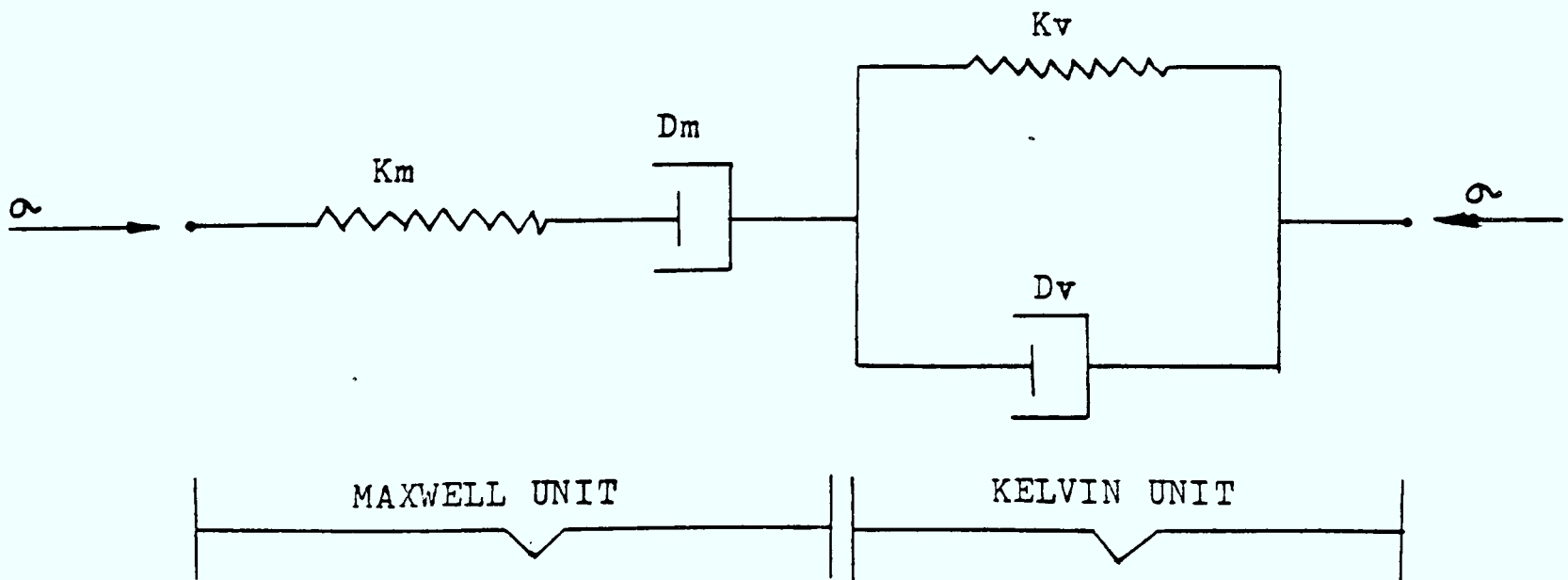
Figure 4.14 Visco-Elastic Models for Concrete Creep



(a) Model 1 - The Maxwell Model of Creep Strain
(Flow Component)



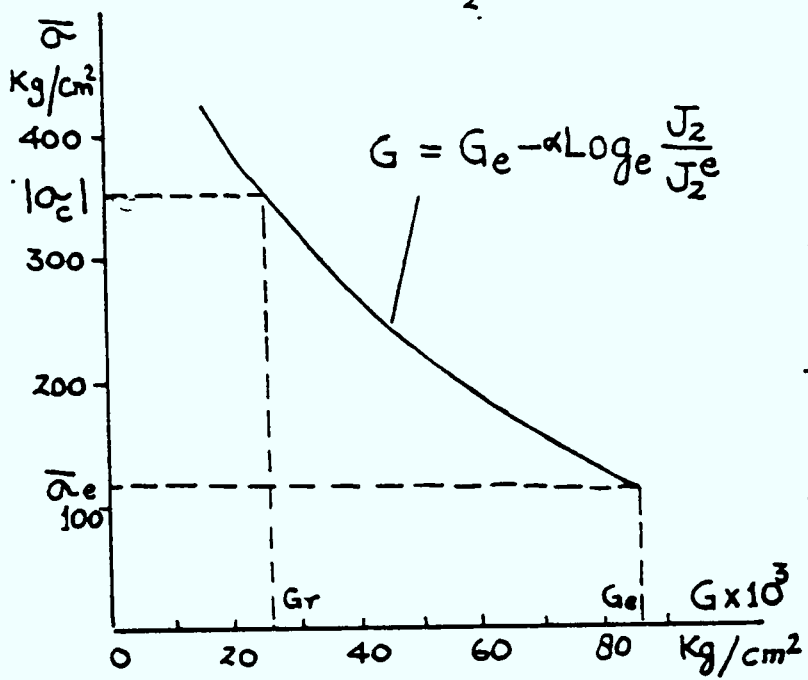
(b) Model 2 - The Kelvin Model of Creep Strain
(Delayed Elastic Component)



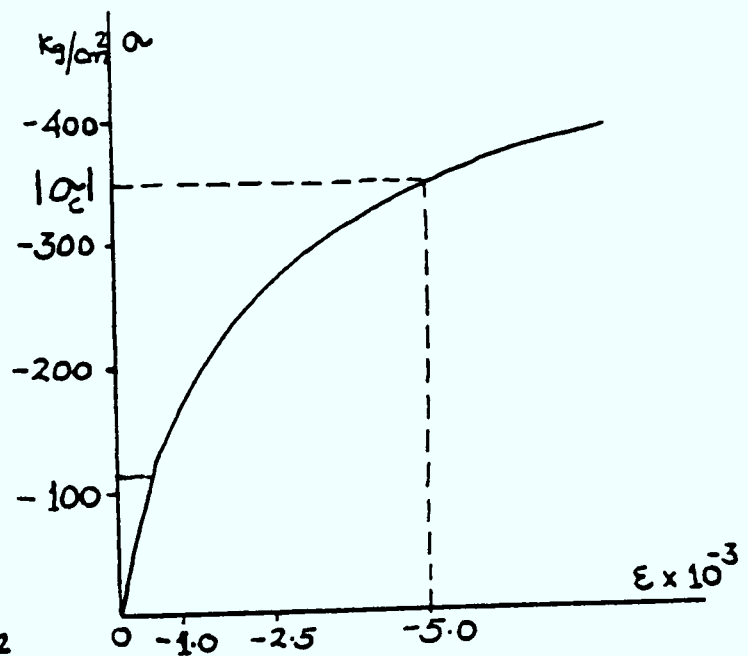
(c) Model 3 - The Burger Model of Creep Behaviour

$$\bar{\sigma} = \sqrt{\frac{3}{2}} J_2$$

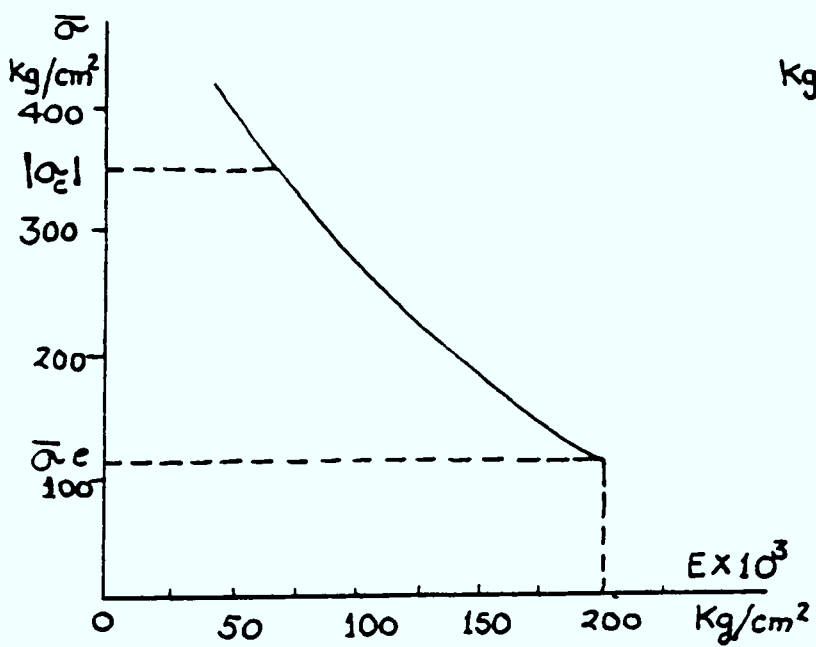
$$\bar{\sigma}_e = \sqrt{\frac{3}{2}} J_2^e$$



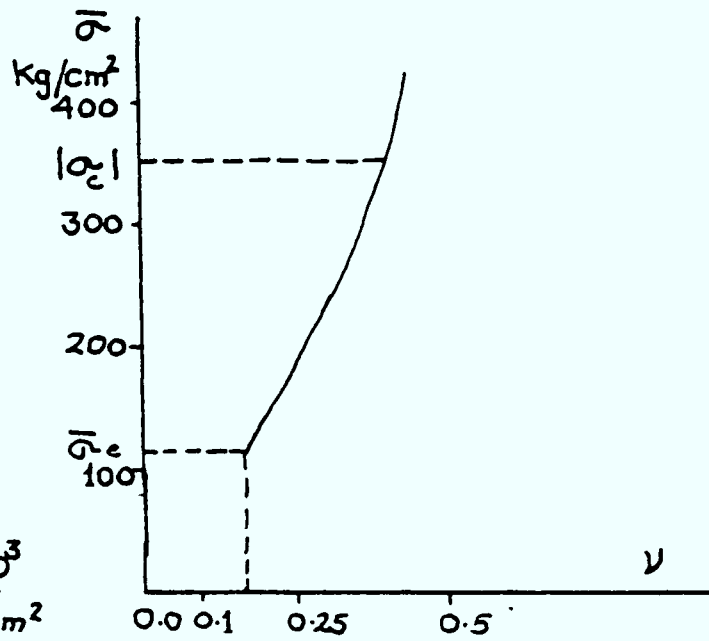
(a) Variation of G with J_2



(b) Uniaxial Stress-Strain Curve



(c) Variation of E with J_2



(d) Variation of ν with J_2

Figure 4.15 Non-linear Stress-Strain Relationships of Concrete in Compression (From References 22,23)

CHAPTER 5

Non-linear Solution Techniques

5.1. Introduction

This Chapter discusses the solution techniques for general non-linear problems. The non-linear solution techniques have been applied successfully to both geometric and material non-linear problems. The non-linearity which stems from the material constitutive relations for concrete, steel and bond-slip, is considered. A detailed description of the relations defining these effects is given in Chapter 4. General steps for the solution of non-linear problems are presented first, and these are followed by solution procedures for temperature and creep effects and loading and unloading schemes for steel and concrete.

5.2. Non-linear Solution Methods

The application of the finite element to non-linear problems is well established (1, 2). The non-linear solution methods have been successfully applied to both geometric and material non-linear problems (1, 2, 51, 52, 53). In this research, strains are assumed small and therefore the strain-displacement relations are linear. A non-linear solution is obtained by piecewise successive linear solutions until the material constitutive laws and the conditions of equilibrium (also compatibility) are satisfied within a specified tolerance. Therefore, using this solution technique, the basic linear finite element formulations of Chapter 3 are still applicable.

The solution process is incremental and therefore path-dependent. At any stage of loading, the externally applied loads are compared with the internal nodal loads due to total stress. The difference between the two is taken as a set of residual loads that can be interpreted as a measure of any lack of equilibrium. To maintain equilibrium, the

residual loads are then applied to the structure and the problem is solved again. This process is repeated until the residuals are sufficiently small.

Now rewrite equilibrium Equation (3.6) from Chapter 3 in this form :

$$\underline{R} = \int_{vol} \underline{B}^T \underline{\sigma} dvol - \underline{P}_{ext} \quad (5.1)$$

where \underline{P}_{ext} - total externally applied loads from all the sources
 \underline{R} - residual loads

$\underline{\sigma}$ are the total actual stresses to date and may be expressed in a general form as :

$$f(\underline{\sigma}, \underline{\epsilon}) = 0 \quad (5.2)$$

For non-linear problems, the residuals, $\underline{R} \neq 0$, so consider the variation of \underline{R} due to the changes of displacements, \underline{u} , using Equation (5.1) :

$$dR = \int_{vol} \underline{B}^T d\underline{\sigma} dvol + \int_{vol} d\underline{B}^T \underline{\sigma} dvol - d\underline{P}_{ext} \quad (5.3)$$

Since \underline{B} and \underline{P}_{ext} are independent of displacements, \underline{u} , their variation is therefore zero, so :

$$dR = \int_{vol} \underline{B}^T d\underline{\sigma} dvol \quad (5.3a)$$

If the incremental stress is evaluated using the material constitutive law from a given incremental strain as :

$$d\underline{\sigma} = \underline{D}_T d\underline{\epsilon} \quad (5.4)$$

where \underline{D}_T may be the incremental, tangent or initial material matrix. Then from Equation (5.3a) :

$$d\underline{R} = \left(\int_{vol} \underline{B}^T \underline{D}_T \underline{B} dvol \right) d\underline{u} \quad (5.5)$$

where $d\underline{\xi} = \underline{B} d\underline{u}$ (from Chapter 3)

Thus :

$$d\underline{R} = \underline{K}_T d\underline{u} \quad (5.6)$$

where

$$\underline{K}_T = \int_{Vol} \underline{B}^T \underline{D}_T \underline{B} dvol \quad (5.7)$$

Equation (5.6) is the basic ingredient for a solution technique. This is known as the pure Newton-Raphson method. By starting from a trial solution \underline{u}_i which produces non-zero residuals, \underline{R}_i , using Equation (5.1). An incremental displacement field may be obtained using Equation (5.6) as :

$$\Delta \underline{u}_{i+1} = \underline{K}_{T_i}^{-1} \underline{R}_i \quad (5.8)$$

where \underline{K}_{T_i} is the tangent stiffness matrix evaluated at displacement \underline{u}_i . This process continues until \underline{R}_i (residuals) become sufficiently small. The general form of the Newton-Raphson process is the variable stiffness method given by Equation (5.8) and it is illustrated in Figure (5.1a) for the one-dimensional case. There are many variants of Equation (5.8), the first being one where a constant stiffness matrix, \underline{K}_0 , replaces \underline{K}_T , is known as the Modified Newton-Raphson method, or the initial stress method (51) (see Figure (5.1b)). In this case, Equation (5.8) may be written as :

$$\Delta \underline{u}_{i+1} = \underline{K}_0^{-1} \underline{R}_i \quad (5.9)$$

Equation (5.8) (tangent stiffness method) suffers from an economic disadvantage because the entire stiffness matrix is reformulated for each iteration. Equation (5.9) (initial stress method), on the other hand, although economic, often shows a slow rate of convergence, especially when the structure behaves in a very non-linear manner. Therefore, a combination of both techniques in which the stiffness matrix is updated every so often is considered as an attractive compromise. Two such alternatives were included in this work. In the first case, the stiffness

matrix is updated at the beginning of each load increment and then kept constant. In the second, the stiffness matrix is updated at every second iteration of each load increment. This is known as KT2 option. Various examples were analysed using these methods, but for the main reactor vessel analysis, because of the prohibitive cost involved in reformulating the stiffness matrix, the initial stiffness method was used. Two types of convergence criteria were used. They were the residuals and the displacements convergence. The Euclidian norms were tested as :

$$(a) \quad \left(\frac{\|\underline{R}\|}{\|\underline{P}_{ext}\|} \right) \leq Tol \quad (5.10)$$

$$(b) \quad \left(\frac{\|\underline{\Delta u}\|}{\|\underline{u}\|} \right) \leq Tol \quad (5.11)$$

where $\|\underline{R}\| = \sqrt{\underline{R}_i^T \underline{R}_i}$ is the Euclidian norm of the residuals, $\|\underline{P}_{ext}\| = \sqrt{\underline{P}_{ext}^T \underline{P}_{ext}}$ is the Euclidian norm of the externally applied load, $\|\underline{\Delta u}\| = \sqrt{\underline{\Delta u}_i^T \underline{\Delta u}_i}$ is the Euclidian norm of the incremental displacements, $\|\underline{u}\| = \sqrt{\underline{u}_i^T \underline{u}_i}$ is the Euclidian norm of the total displacements and the tolerance limit was usually taken between 0.03 and 0.001 for the various problems analysed.

5.3. General Steps for Non-linear Analysis

A brief outline is presented for the application of non-linear methods to concrete structures. The non-linearities considered are that of concrete, steel and bond-slip described in Chapter 4. The detailed discussion and flow charts of the individual material non-linearities is given in separate sections.

1. Apply a load increment, $\underline{\Delta P}_n$, where n is the load increment. Accumulate total load $\underline{P}_n = \underline{P}_{n-1} + \underline{\Delta P}_n$ and $\underline{R} = \underline{\Delta P}_n$ where \underline{R} is the residual load vector.

2. Solve $\Delta \underline{u}_i = \underline{K}^{-1} \underline{R}$, where i is the iteration number and \underline{K} is the stiffness matrix of the structure. Here, various solution options may be used (see the section on non-linear methods of solution), e.g. $\underline{K} = \underline{K}_0$ - initial stress method, $\underline{K} = \underline{K}_T$ - pure Newton-Raphson method, or \underline{K} may be updated at the beginning of each load increment only, etc. Accumulate total displacements :

$$\underline{u}_i = \underline{u}_{i-1} + \Delta \underline{u}_i$$

3. For each element type calculate strain increments :

$$\Delta \underline{\epsilon}_i = \underline{B} \Delta \underline{u}_i$$

and strains

$$\underline{\epsilon}_i = \underline{\epsilon}_{i-1} + \Delta \underline{\epsilon}_i$$

If initial strains, such as creep and thermal strains, are present, then :

$$\Delta \underline{\epsilon} = \Delta \underline{\epsilon}_i - \Delta \underline{\epsilon}^{th} - \Delta \underline{\epsilon}^c$$

4. For each element type, the stress increments are calculated using the current non-linear constitutive matrices. For concrete, the cracking and compressive criteria are considered; for steel, elasto-plastic relations are considered and non-linear bond-slip relations at steel-concrete are considered. They may all be expressed in the general form :

$$\Delta \underline{\sigma}_i = f(\underline{\sigma}) \Delta \underline{\epsilon}$$

Accumulate stresses :

$$\underline{\sigma}_i = \underline{\sigma}_{i-1} + \Delta \underline{\sigma}_i$$

5. The total stresses are converted into equivalent internal loads as :
- $$\int_{vol} \underline{B}^T \underline{\sigma}_i dvol$$

and the residual load vector is calculated by :

$$\underline{R} = \underline{P}_n - \int_{vol} \underline{B}^T \underline{\sigma}_i dvol$$

6. Check for convergence. If convergence is not achieved, go to step 2. and repeat all the steps for the next iteration. If convergence is achieved, then go to step 1. and repeat the process with the next load increment.

5.3.1. Explanation of Step 4 for Concrete

For each element and its integration points the following are calculated :

- (a) Firstly an estimate of stress is calculated as :

$$\underline{\sigma}_i' = \underline{\sigma}_{i-1} + \Delta \underline{\sigma}_i'$$

where $\Delta \underline{\sigma}_i' = \underline{D}_T \Delta \underline{\varepsilon}$ and in which \underline{D}_T is the current tangent material matrix for concrete. This is calculated on the basis of current material state, i.e. according to the crack indicator and loading and unloading state.

- (b) Calculate :

- If no cracks are already present at this point, principal stresses and strains :

$$\sigma_j = f(\sigma_i'), \quad j = 1, 2, 3$$

$$\varepsilon_j = f(\varepsilon_i), \quad j = 1, 2, 3$$

- If cracks are already present at this point, transform stresses and strains as :

$$\Delta \underline{\varepsilon}^* = \underline{T}_\varepsilon \Delta \underline{\varepsilon} \quad ; \quad \underline{\varepsilon}_i^* = \underline{T}_\varepsilon \underline{\varepsilon}_i$$

$$\underline{\sigma}_{i-1}^* = \underline{T}_\sigma \underline{\sigma}_{i-1} \quad ; \quad \underline{\sigma}_i^{*'} = \underline{T}_\sigma \underline{\sigma}_i'$$

- (c) With either the current principal stresses (σ_j , $j = 1, 2, 3$) or the transformed current stresses, $\underline{\sigma}_i^{*'}$, check for concrete cracking. Also, check for crack closing or reopening by :

$$\underline{\varepsilon}_i^* > 0 \quad - \quad \text{crack open}$$

$$\underline{\varepsilon}_i^* \leq 0 \quad - \quad \text{crack closed}$$

Update the crack indicator according to the current crack state. Check for loading or unloading state at this point and update the unloading indicator. For loading and unloading, the total equivalent strain criteria is used (i.e. $\bar{\epsilon}_i = \sqrt{\frac{2}{3} \epsilon_{ij} \epsilon_{ij}}$). If the equivalent strain $\bar{\epsilon}_i$ is less than its value from the last load increment, then unloading at this point is defined (see Figure (5.2)).

- (d) According to the current material state (which includes cracks, loading and unloading state, and concrete compression criterion, there are three options available (see section 4.3.); form the material matrix and calculate :

$$\left. \begin{array}{l} \Delta \underline{\sigma}_i = \underline{D}_T \Delta \underline{\epsilon} \\ \underline{\sigma}_i = \underline{\sigma}_{i-1} + \Delta \underline{\sigma}_i \end{array} \right\} \text{ - if no crack}$$

or

$$\left. \begin{array}{l} \Delta \underline{\sigma}_i^* = \underline{D}_T^* \Delta \underline{\epsilon}^* \\ \underline{\sigma}_i^* = \underline{\sigma}_{i-1}^* + \Delta \underline{\sigma}_i^* \end{array} \right\} \text{ - if there are cracks}$$

- (e) Release stresses normal to the open cracks and transform back the stresses into global directions if already in crack directions :

$$\underline{\sigma}_i = \underline{T}_\epsilon^T \underline{\sigma}_i^*$$

- (f) Check that the stress state is within the failure surface (see concrete failure criteria defined in section 4.3.5.)

5.3.2. Explanation of Step 4 for Steel

- ISP - stress point indicator
 = 0 - elastic point
 = 1 - plastic point
 = 2 - unloading from plastic state
 σ_Y - uniaxial yield stress

- (a) Firstly, the stress increment is calculated using the elastic material matrix as $\Delta \underline{\sigma}_i' = \underline{D}_E^s \Delta \underline{\epsilon}$; where \underline{D}_E^s is the elastic material matrix for steel liner or reinforcements or tendons. (These are defined in Chapter 3).

First estimate of total stress :

$$\underline{\sigma}_i' = \underline{\sigma}_{i-1} + \Delta \underline{\sigma}_i'$$

- (b) Calculate :

$$\bar{\sigma}_i = f(\underline{\sigma}_i') \quad ; \quad \bar{\sigma}_{i-1} = f(\underline{\sigma}_{i-1}) \quad - \text{ Von Mises yield criterion}$$

- (c) If plastic point (i.e. ISP = 1), go to step (e).

- (d) - If $\bar{\sigma}_i \geq \sigma_Y$ - point plastic (ISP = 1), transition from elastic to plastic, calculate factor, fac :

$$\text{fac} = \frac{(\sigma_Y - \bar{\sigma}_{i-1})}{\bar{\sigma}_i - \sigma_{i-1}} \quad (\text{see Figure (5.3a)})$$

stress at yield surface, $\underline{\sigma}_i^Y = \underline{\sigma}_{i-1} + \text{fac} * \Delta \underline{\sigma}_i'$

calculate elasto-plastic stress increment

$$\Delta \underline{\sigma}_i = \underline{D}_{ep}^s(\underline{\sigma}_i^Y) * (1 - \text{fac}) \Delta \underline{\epsilon}$$

total stress, $\underline{\sigma}_i = \underline{\sigma}_i^Y + \Delta \underline{\sigma}_i$

set ISP = 1; go to (g)

- If $\bar{\sigma}_i < \sigma_Y$ - elastic point, $\underline{\sigma}_i = \underline{\sigma}_i'$; go to step (h).

- (e) Plastic point in the previous iteration, check for unloading, i.e. $\bar{\sigma} \geq \sigma_y$; go to step (f). (See Figure (5.5) also).

Unloading at this point, set $ISP = 2$, total stress $\underline{\sigma}_i = \underline{\sigma}_{i-1} + \Delta \underline{\sigma}_i'$ and set $\sigma_y = \bar{\sigma}_{i-1}$; go to step (h).

- (f) Loading at this point, $\Delta \underline{\sigma}_i = \underline{D}_{ep}^s(\underline{\sigma}_{i-1}) \Delta \underline{\epsilon}$
total stress $\underline{\sigma}_i = \underline{\sigma}_{i-1} + \Delta \underline{\sigma}_i$

- (g) Stress calculated using the elasto-plastic material matrix usually drifts from the yield surface as shown in Figure (5.3b). The following correction is suggested which is based on the equivalent stress-strain curve. Correct stress from the equivalent stress-strain curve :

$$\bar{\sigma}_{corr} = \bar{\sigma}_{i-1} + H \Delta \bar{\epsilon}_p$$

where $\Delta \bar{\epsilon}_p = \sqrt{\frac{2}{3} \Delta \epsilon_{ij}^p \Delta \epsilon_{ij}^p} = \frac{2}{3} \underline{a}^T \underline{a} \lambda$ - equivalent plastic strain increment

H is the strain hardening parameter. For one-dimensional case, such as reinforcements, $\Delta \bar{\epsilon}_p = \lambda$.

Equivalent stress calculated from the current stress state :

$$\bar{\sigma}_i = f(\underline{\sigma}_i)$$

$$\text{factor} = \frac{\bar{\sigma}_{corr}}{\bar{\sigma}_i}$$

Therefore the correct stress state which is on the yield surface :

$$\underline{\sigma}_i = \text{factor} * \underline{\sigma}_i$$

- (h) End.

5.3.4. Steps for Non-linear Bond-linkage Elements (Step 4)

- (a) Calculate incremental slip from the nodal displacements (Equation (3.29)) :

$$\Delta \underline{S}_i = \underline{T} \Delta \underline{U}_i$$

where \underline{T} is the transformation matrix and $\Delta \underline{U}_i$ are the element nodal displacements.

Total slip at iteration i :

$$\underline{S}_i = \underline{S}_{i-1} + \Delta \underline{S}_i$$

- (b) Calculate the incremental stress based on the bond stress at iteration $i-1$:

$$\Delta \underline{\sigma}_{b_i} = \underline{E}_b(\underline{\sigma}_{b_{i-1}}) \Delta \underline{S}_i$$

Total stress :

$$\underline{\sigma}_{b_i} = \underline{\sigma}_{b_{i-1}} + \Delta \underline{\sigma}_{b_i}$$

- (c) Check the state of the bond, i.e. whether bond is broken or not and calculate stress accordingly.

- If $|\underline{S}_i| > S_{\max}$, set flag $I_{\text{flag}} = 1$, i.e. bond is broken. At this point, the bond stress is instantaneously dropped to zero, i.e. $\underline{\sigma}_{b_i} = 0.0$, where S_{\max} is the maximum slip allowed.
- If $|\underline{S}_i| < S_{\max}$, calculate the bond stress which is compatible with the slip, \underline{S}_i . This is obtained by linear interpolation of a non-linear bond-slip curve. The curve is simulated by multi-linear lines. Figure (4.10b) gives the scheme for the linear interpolation. Let $\underline{\sigma}_b^r$ be the bond stress compatible with the slip, \underline{S}_i . The difference

between $\underline{\sigma}_{bi}$ and $\underline{\sigma}_b^r$ is treated as initial stress and this may be converted into nodal loads, i.e.

$$\Delta \underline{\sigma}_D = \underline{\sigma}_{bi} - \underline{\sigma}_b^r$$

The correct stress, $\underline{\sigma}_{bi} = \underline{\sigma}_{bi} - \Delta \underline{\sigma}_D$

- (d) Total internal equivalent loads and residuals are calculated as :

$$\underline{P}_{int} = \pi d L \underline{T}^T \underline{\sigma}_{bi}$$

$$\underline{R} = \underline{P}_{ext} - \underline{P}_{int}$$

5.4. Steps for Creep and Temperature Analysis

The following steps are performed to include the effects of creep and temperature in the constitutive relations discussed earlier.

1. At time $t = 0$, carry out elastic (linear analysis). If thermal loads are considered calculate the kinematically equivalent load as Equation (A7.13) :

$$\Delta \underline{P}^{th} = \int_{Vol} \underline{B}^T \underline{D} \underline{\Delta \varepsilon}^{th} dvol$$

Calculate stresses, strains, etc.

2. Specify a small time increment, Δt , during which the stresses are assumed to remain constant. The creep strain increment for concrete is calculated using Equation (A7.3) as :

$$\underline{\Delta \varepsilon}^c = f(\underline{\sigma}, \Delta t, t, T)$$

3. Convert creep strain increment into kinematically equivalent load using Equation (A7.12) as :

$$\underline{\Delta P}^c = \int_{Vol} \underline{B}^T \underline{D} \underline{\Delta \varepsilon}^c dvol$$

where \underline{D} - elastic material matrix

4. Assuming ΔP^c as external load, the incremental nodal displacement may be obtained as :

$$\Delta \underline{U} = \underline{K}^{-1} \Delta \underline{P}^c$$

where \underline{K} - stiffness matrix of the structure.

Total displacement :

$$\underline{U}_{t+\Delta t} = \underline{U}_t + \Delta \underline{U}$$

5. Calculate the total incremental strain as :

$$\Delta \underline{\epsilon} = \underline{B} \Delta \underline{U}$$

Total strain :

$$\underline{\epsilon}_{t+\Delta t} = \underline{\epsilon}_t + \Delta \underline{\epsilon}$$

6. Calculate the stress increment as :

$$\Delta \underline{\sigma} = \underline{D} (\Delta \underline{\epsilon} - \Delta \underline{\epsilon}^c - \Delta \underline{\epsilon}^{th})$$

-if temperature load was applied in Step 1.

$$\Delta \underline{\sigma} = \underline{D} (\Delta \underline{\epsilon} - \Delta \underline{\epsilon}^c)$$

-if no temperature was applied in Step 1.

Total stress at the end of current Δt :

$$\underline{\sigma}_{t+\Delta t} = \underline{\sigma}_t + \Delta \underline{\sigma}$$

7. This solution process is conditionally stable. The stability requirement (80) is that the stress increment, $\Delta \underline{\sigma}$, must be small compared to the previous stress, $\underline{\sigma}_t$. If this condition is not satisfied, the same process from Step 2 should be repeated taking smaller Δt , otherwise go to Step 2 for the next time increment and repeat this process until the final time step is reached.

8. If creep analysis of more than one load increment is to be calculated, then go to Step 1 and apply the next load increment and repeat the Steps from 2 to 7 for time increments.

It should be noted that during initial or transient states of creep, the stresses change very rapidly and it is essential to choose exceptionally small time increments in this region. However, as the solution approaches a steady state condition (i.e. $\dot{\underline{\sigma}} \rightarrow 0$) it is possible to increase the time step without violating any assumptions.

5.5. Non-linear Response with Creep

The steps required to carry out creep analysis with non-linear material response are very similar to those for linear material behaviour. The difference is that at the end of each time step the equilibrium is restored. The creep strains cause incompatibility which is corrected by applying a kinematically equivalent load due to creep strain to the structure.

1. Apply load and time increments separately. (For example, the load increment is applied first, then the time increments are followed).
2. Using the stresses that exist in the structure at the end of the previous load increment, calculate the change in creep strain (Equation (A7.3) :

$$\Delta \underline{\underline{\epsilon}}^c = f(\underline{\underline{\sigma}}, \Delta t, t, T)$$

Convert $\Delta \underline{\underline{\epsilon}}^c$ into kinematically equivalent load vector using Equation (A7.12) :

$$\Delta \underline{\underline{P}}^c = \int_{Vol} \underline{\underline{B}}^T \underline{\underline{D}}_T \Delta \underline{\underline{\epsilon}}^c dvol$$

where $\underline{\underline{D}}_T$ is the tangent material matrix based on the current state of stress.

3. Solve incremental nodal displacement :

$$\Delta \underline{u}_i = \underline{K}^{-1} \Delta \underline{P}^c$$

Accumulate :

$$\underline{u}_i = \underline{u}_{i-1} + \Delta \underline{u}_i$$

4. Strain increment :

$$\Delta \underline{\epsilon}_i = \underline{B} \Delta \underline{u}_i$$

Total strain :

$$\underline{\epsilon}_i = \underline{\epsilon}_{i-1} + \Delta \underline{\epsilon}_i$$

5. Calculate the stresses due to additional non-linearities found (due to higher compression or cracking described in Chapter 4) :

$$\Delta \underline{\sigma}_i = \underline{D}_T (\Delta \underline{\epsilon}_i - \Delta \underline{\epsilon}^c)$$

and

$$\underline{\sigma}_i = \underline{\sigma}_{i-1} + \Delta \underline{\sigma}_i$$

6. Iterations for time or load increment are performed to restore equilibrium. If convergence is achieved, then go to Step 1 and apply new load or time increment. This process is repeated until the total load for time is reached.

5.6. Solution Technique for Descending Stress-strain Curve

Figure (5.4) shows the downward sloping portion of the stress-strain curve. The tangent modulus of elasticity for this portion of the loading curve is negative. However, using a negative value of E in the constitutive matrix may lead to non-positive definite stiffness matrix. In order to circumvent this problem, the tangent modulus on the downward portion of the stress-strain curve is set to zero for the purposes of numerical solution (Figure (5.4)) and the stress is corrected to the proper value at the end of each iteration.

5.7. Unloading of a Point in Concrete

Unloading of concrete in compression is treated differently than for tension. For compression, the unloading of a point is calculated based on the maximum equivalent strain ever reached in the analysis. If the equivalent strain $(\sqrt{\frac{2}{3} \epsilon_{ij} \epsilon_{ij}})$ of a point is less than the equivalent strain in the previous load increment, the point is considered to be unloading during this load increment. The unloading is treated as elastic as shown in Figure (5.2). The equivalent strains of all points from where unloading started need to be stored. For example, the unloading in the figure starts at point 2 and follows the linear line 20' and the equivalent strain of point 2 is stored. Reloading of this point will follow the unloading line 0'2 until the equivalent strain of point 2 is reached. After that, the non-linear curve is followed. For example, upon reloading at point 1 (see Figure (5.2)) the curve 123 is followed. In this case, part of the strain increment is treated as linear and the rest as non-linear. The linear and non-linear strains are calculated as follows (Figure (5.2)).

Fraction of linear (elastic) strain increment, $FRAC = (\bar{\epsilon}_2 - \bar{\epsilon}_1) / (\bar{\epsilon}_3 - \bar{\epsilon}_1)$

where $\bar{\epsilon}_1$, $\bar{\epsilon}_2$, $\bar{\epsilon}_3$ are the equivalent strains at point 1, 2 and 3 respectively

$$\bar{\epsilon}_1 = \sqrt{\frac{2}{3} \epsilon_1^T \epsilon_1} \quad ; \quad \bar{\epsilon}_2 = \sqrt{\frac{2}{3} \epsilon_2^T \epsilon_2} \quad ; \quad \bar{\epsilon}_3 = \sqrt{\frac{2}{3} \epsilon_3^T \epsilon_3} \quad (5.12)$$

Linear (elastic) part of the strain increment :

$$\Delta \epsilon_L = FRAC * \Delta \epsilon \quad (5.13)$$

Non-linear part of the strain increment :

$$\Delta \epsilon_{NL} = (1 - FRAC) * \Delta \epsilon \quad (5.14)$$

$$\text{where } \Delta \epsilon = \Delta \epsilon_L + \Delta \epsilon_{NL} = \text{total strain increment} \quad (5.15)$$

Unloading of a point in tension is treated as elastic provided the point is uncracked. For a cracked point, the strain across the crack is checked to see if it is positive in which case the crack is assumed to be open and the material matrix of this point is adjusted. If the strain across the crack is negative, then this point can develop compressive stress in that direction and the material matrix in compression is calculated. On further loading, this point may develop tensile strain and the crack will be assumed to be open if the strain across the crack becomes positive. A full scheme of crack closing/opening is shown in Figures (4.6a) and (4.6b).

5.8. Accelerated Newton-Raphson Method

Various accelerating techniques for improving the convergence in certain non-linear problems have been used (86, 134). In these, the previous displacement and residual load vector histories are examined and those from which a more accurate displacement increment is calculated. In this work, the Accelerated Newton-Raphson Method (86) is used. The method was successfully applied to some examples analysed. The method is fully explained by Crisfield in reference (86) and therefore a brief review is presented in the following.

The essence of the method is to predict an accurate incremental displacement field at the end of each iteration so that the solution converges faster. Firstly, we write the steps for the modified Newton-Raphson method.

For a load increment, $\Delta \underline{P}$, the incremental displacement is calculated as :

$$\Delta \underline{u}_0 = \underline{K}^{-1} \Delta \underline{P} \quad (5.16)$$

and

$$\underline{u}_1 = \underline{u}_0 + \Delta \underline{u}_0 \quad (5.17)$$

where \underline{u}_0 is the displacement vector at the end of the previous increment and \underline{K} may be the tangent or initial stiffness, as the case may be.

For subsequent iterations, the Newton-Raphson method gives :

$$\underline{\Delta u}_i^* = \underline{K}^{-1} \underline{R}_i \quad (5.18)$$

$$\underline{u}_{i+1} = \underline{u}_i + \underline{\Delta u}_i^* \quad (5.19)$$

where \underline{R}_i - residual load vector
 i - iteration i

With the Accelerated Newton-Raphson method, Equation (5.19) is written as :

$$\underline{u}_{i+1} = \underline{u}_i + \underline{\Delta u}_i \quad (5.20)$$

where $\underline{\Delta u}_i$ is the updated incremental displacement field which is calculated as follows :

$$\underline{\Delta u}_i = e_i \underline{\Delta u}_{i-1} + \underline{\Delta u}_i^* h_i \quad (5.21)$$

where $e_i = h_i (1 - \frac{c_i}{b_i}) - 1$; $h_i = - a_i / b_i$ (5.22)

$$a_i = \underline{\Delta u}_{i-1}^T \underline{R}_{i-1}$$

$$b_i = \underline{\Delta u}_{i-1}^T (\underline{R}_i - \underline{R}_{i-1}) \quad (5.23)$$

$$c_i = \underline{\Delta u}_i^{*T} (\underline{R}_i - \underline{R}_{i-1})$$

where \underline{R}_{i-1} , \underline{u}_{i-1} are the residuals and displacement increments from the previous iteration. Therefore, the Accelerated Newton-Raphson method may be implemented easily in an existing Newton-Raphson computer program by simply storing two extra vectors, \underline{R}_{i-1} and $\underline{\Delta u}_{i-1}$. When applying the accelerated procedure to non-linear problems, returning to the standard modified Newton-Raphson method is sensible in certain unusual circumstances. In the event that this is considered desirable, two checks are made :

1. If the angle between the accelerated and standard iterative direction is too large :

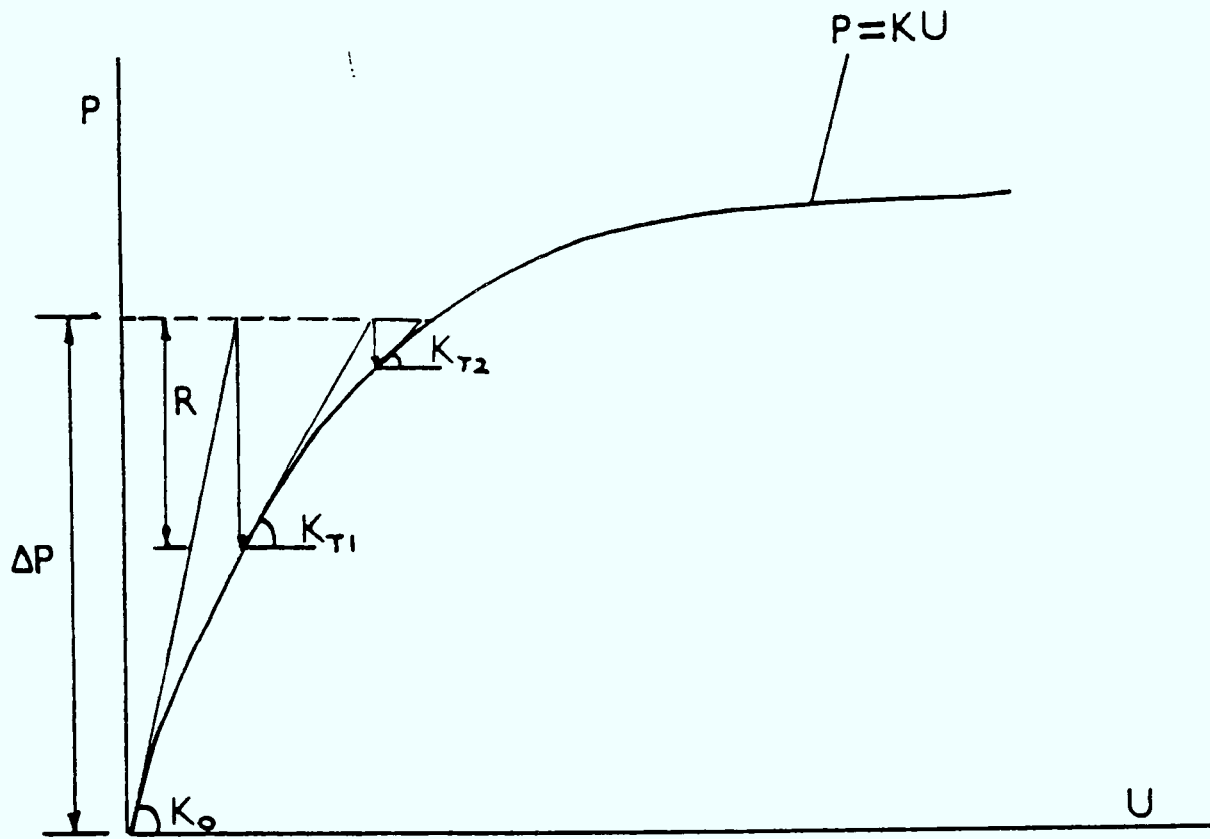
$$\theta = \frac{(\underline{\Delta u}_i^{*T} \underline{\Delta u}_i)}{\|\underline{\Delta u}_i^*\| \|\underline{\Delta u}_i\|} < 1/4 \quad ; \quad \|\underline{\Delta u}_i^*\| = \sqrt{\underline{\Delta u}_i^{*T} \underline{\Delta u}_i^*}$$

$$\|\underline{\Delta u}_i\| = \sqrt{\underline{\Delta u}_i^T \underline{\Delta u}_i}$$
(5.24)

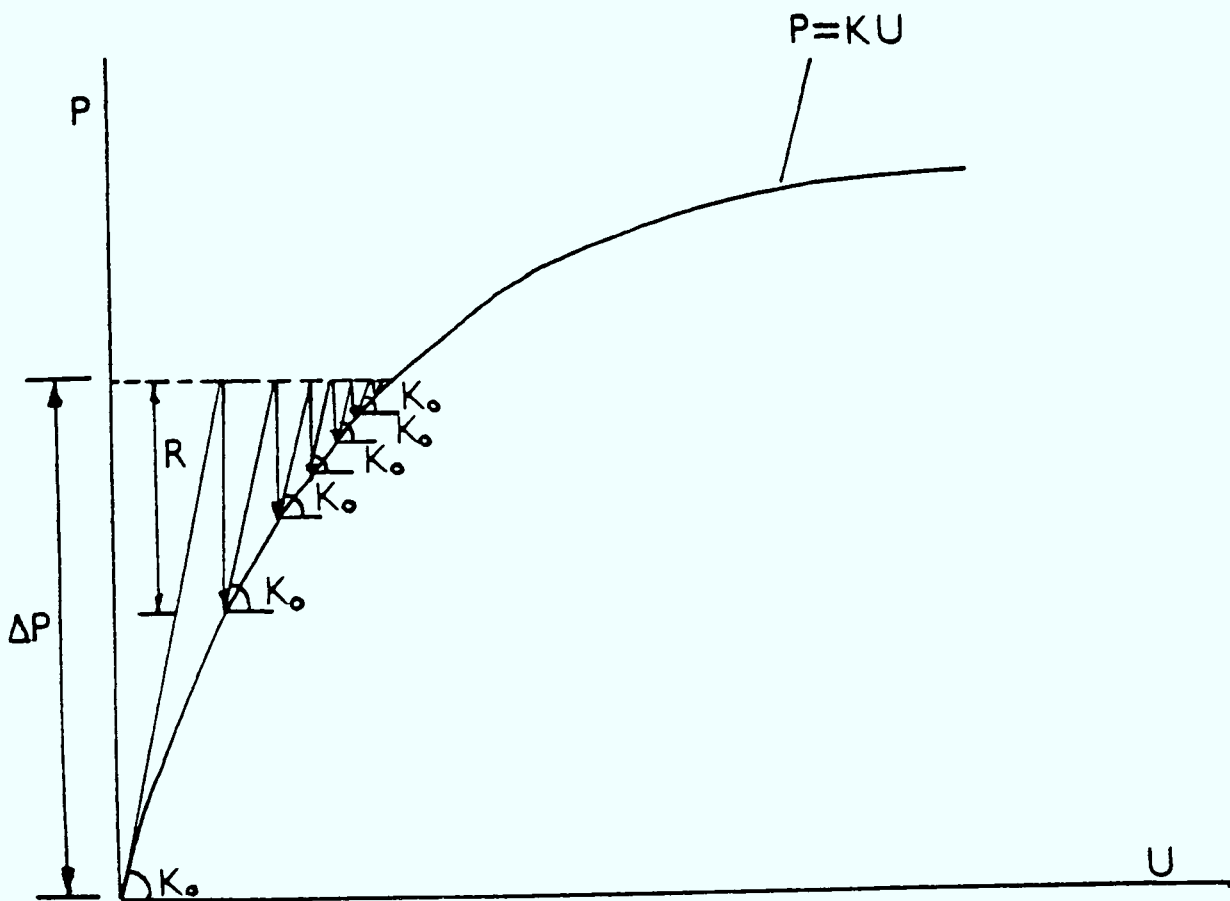
2. If the contribution of the previous iterative displacement (due to e_i) is too large, i.e.

$$|e_i| > 2 \tag{5.25}$$

If any of the above two conditions are satisfied, the original Newton-Raphson method is used. For such cases, set $e_i = 0$ and $h = 1.0$ in Equation (5.21).



(a) Newton - Raphson Method (Tangent Stiffness Method)



(b) Initial Stress Method (Constant Stiffness Method)

Figure 5.1 Load - Displacement Diagrams

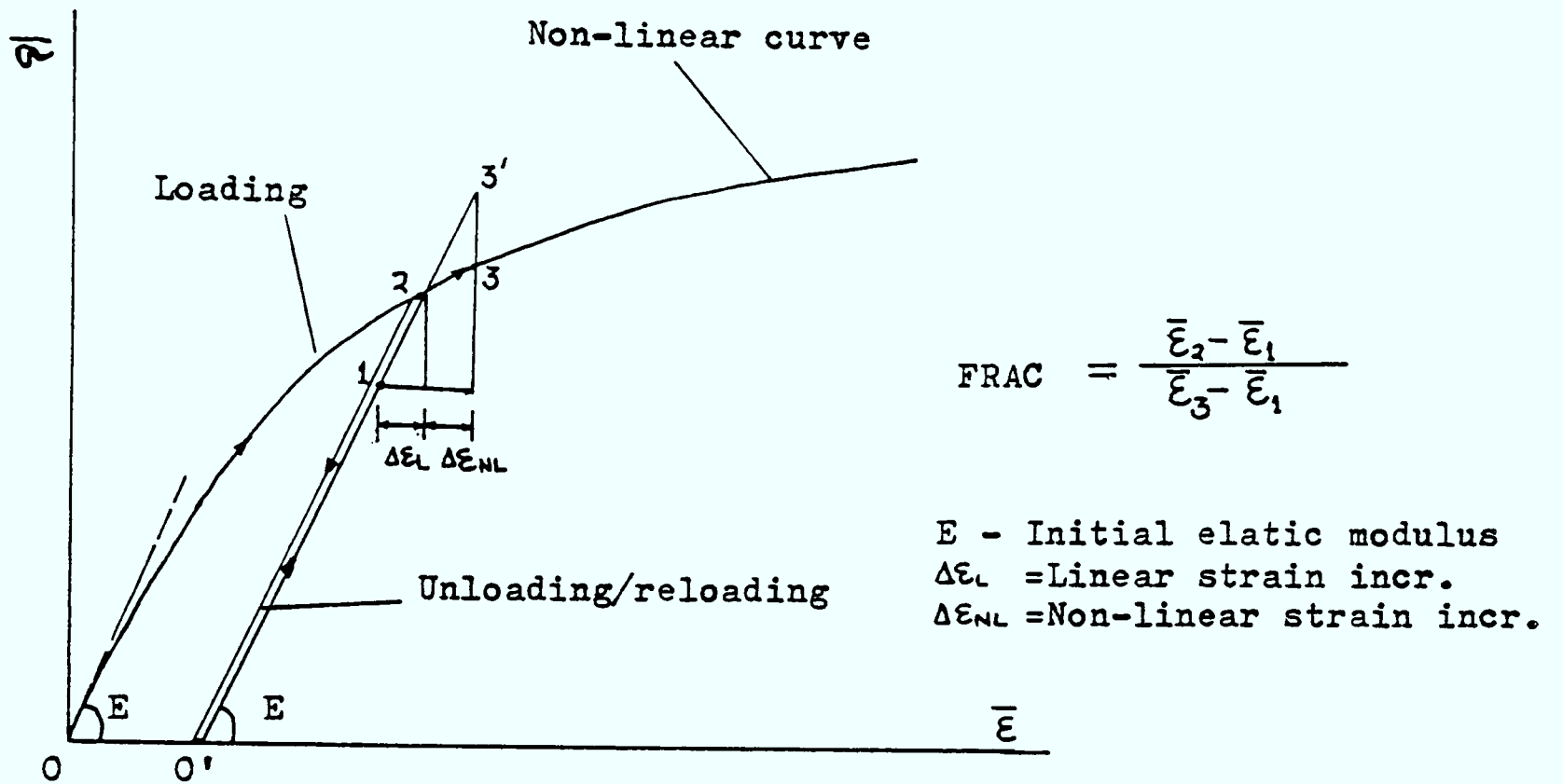


Figure 5.2 Equivalent Stress/Strain Curve for Concrete
(Loading Unloading Scheme)

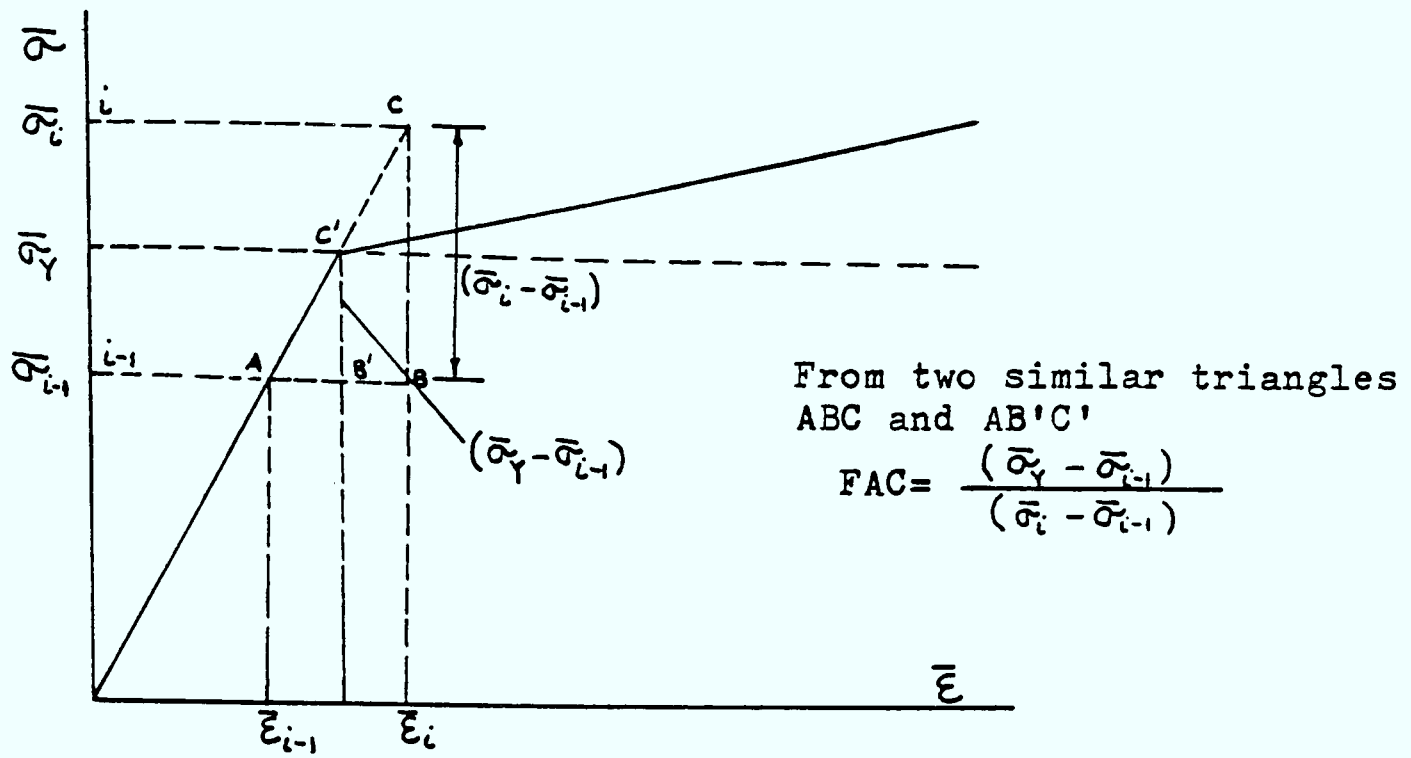


Figure 5.3a Equivalent Stress - Strain Curve for Steel

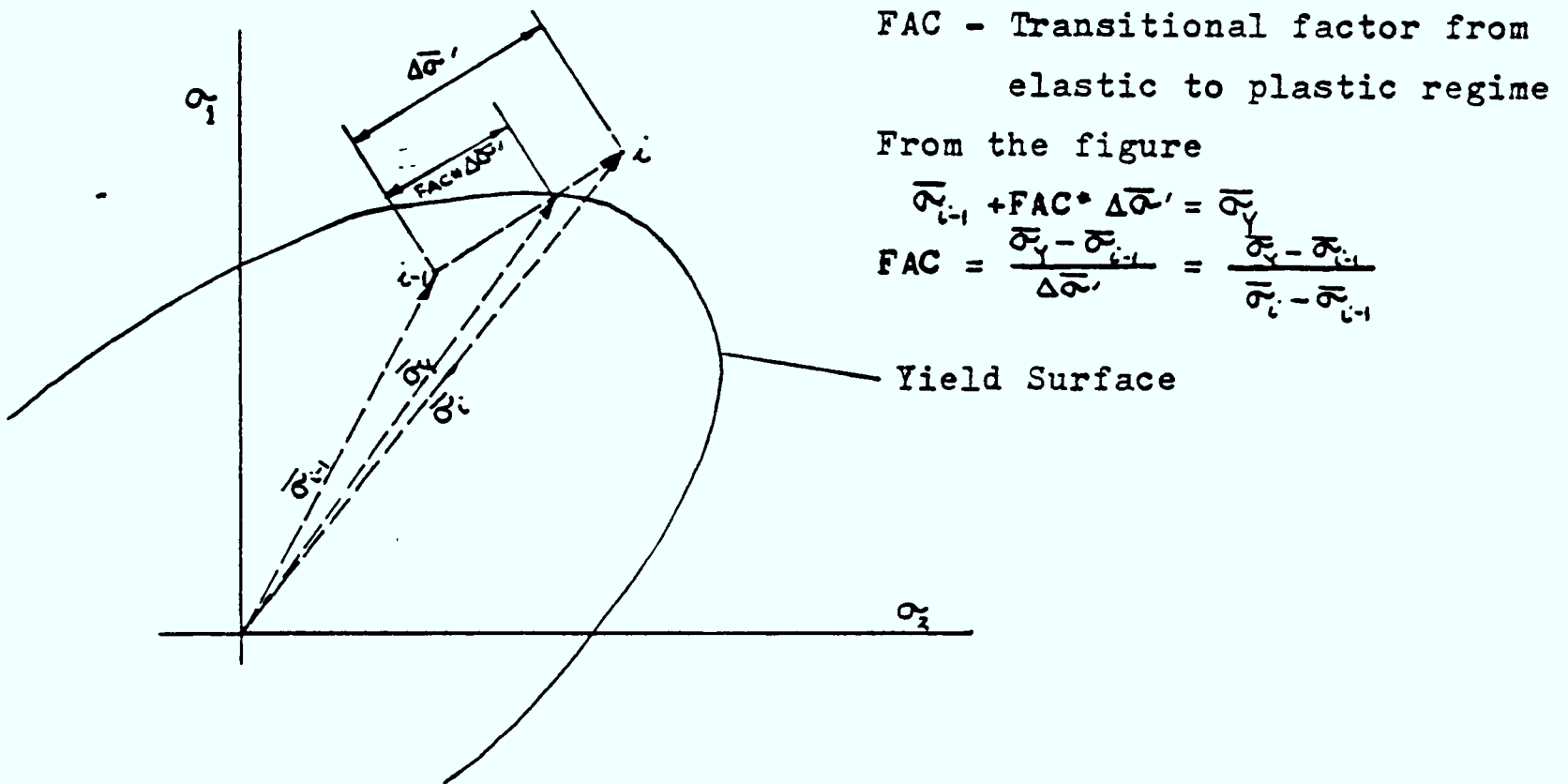


Figure 5.3b Yield Surface in Principal Stress Axes

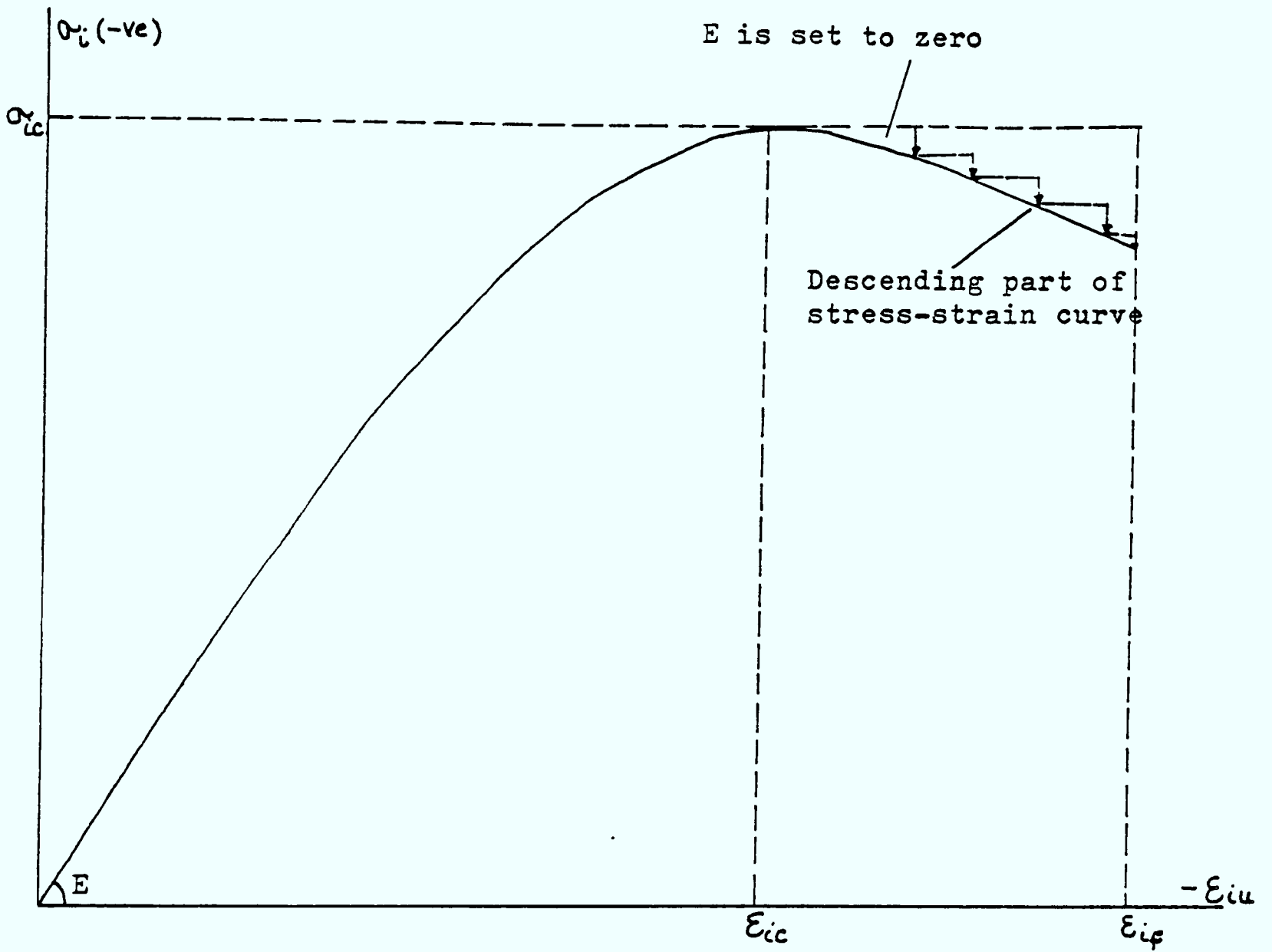
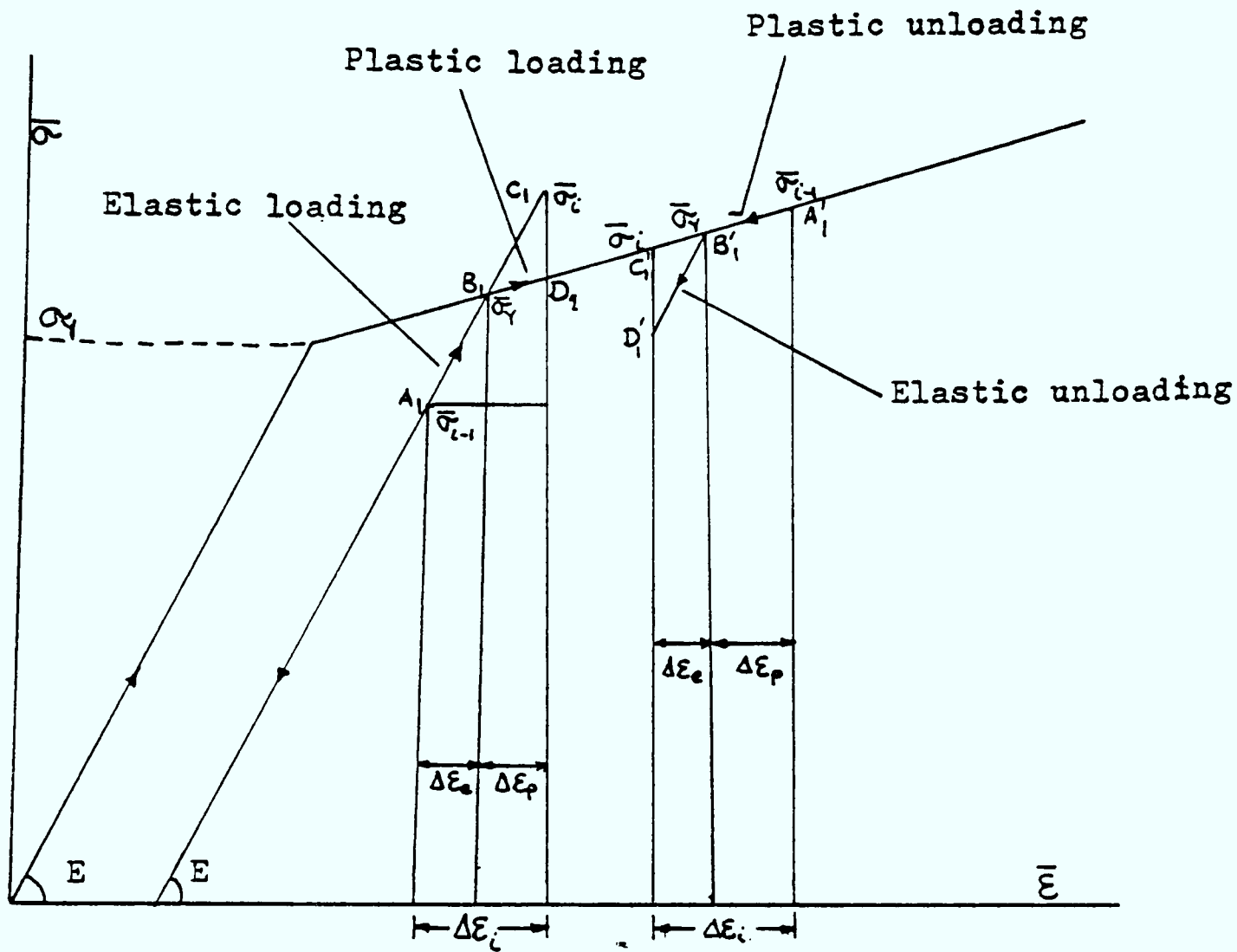


Figure 5.4 Solution Technique for Downward Part of the Stress - Strain Curve



E - Modulus of elasticity for steel
 σ_y - Initial yield stress
 FAC - Transitional factor

$$= \frac{\sigma_y - \sigma_{i-1}}{\sigma_i - \sigma_{i-1}}$$

Figure 5.5 Loading/Unloading Scheme for Steel Used in the Program

CHAPTER 6

Description of Finite Element Computer Program NSARVE

6.1. Introduction

This Chapter gives the main features of the computer program NSARVE developed for this research. The program is written to deal with the non-linear response of reinforced and prestressed concrete structures in general, and prestressed concrete reactor vessels in particular. The theoretical models as developed in Chapters 3 and 4, are fully implemented. Individual modules and subroutines, their functions and capabilities, are fully described. A complete flowchart supported by Appendix B is included to acquaint the user with the salient features of the program.

6.2. Computer Program NSARVE

The computer program NSARVE is developed to carry out two and three-dimensional analyses of prestressed concrete reactor vessels. It is based on the displacement-type finite element formulation. The reactor vessel components are modelled by three-dimensional isoparametric solid concrete elements, rectangular steel liner elements are one-dimensional steel bar elements. The bond at the interface of steel and concrete is modelled by non-linear bond-linkage elements. Under increasing loads, the behaviour of reactor vessels is predicted in terms of displacements, strains, stresses, etc., plasticity and cracks. Temperature and visco-elastic creep models are included for short and long-term behaviour of vessels.

Loads and times are applied in increments. Equilibrium iterations are performed for each load and time increment. Results are printed at the end of each load and time increment. The program has the flexibility to suppress the output of any load increment. Any node on the structure can be suppressed in any three global X, Y, Z, directions and also in

a skew direction on the X-Y plane, i.e. in a direction θ from global X-axis. The program uses incore and out of core assembly and equation solution techniques. Hence very large problems can be analysed. For large problems, the stiffness matrix and load vectors are stored in auxiliary storage devices such as tapes or discs. Seven disc files are used for NSARVE. The first five disc files are used for the solution of out of core equations and the other two files are used to store element stresses, strains, stress indicators etc. Where an incore solution is used, the first five discs are ignored. At the end of a successful analysis, all the auxiliary files are closed and deleted.

The program was written in the FORTRAN IV language and has been run on a DEC-KL10 and a PRIME-750 computer. The User's Manual given in Appendix B gives sample examples which are analysed on these two machines.

6.3. Description of NSARVE

The sequence of the main program NSARVE is given by the flowchart in Figure 6.1. The sequence of operations and functions of various modules and subroutines is given below.

6.3.1. Modules

The program is divided into eight modules, each of which has a distinct operational function. Each module is called by the main program which controls of the flow of operations. The main program is called NSARVE (Non-linear Stress Analysis of Reactor Vessel). Each module is composed of one or more subroutines. One subroutine may be called in different modules. The modules are :

- | | | |
|----------------|----------------|--------------------------|
| (a) INPUT DATA | (b) INITIALISE | (c) LOADS |
| (d) STIFFNESS | (e) SOLUTION | (f) STRESS AND RESIDUALS |
| (g) CREEP | (h) OUTPUT | |

6.3.1.1. INPUT DATA Module

This module handles all input data to the finite element program. The module reads in all the controlling parameters, geometry, element topology, material and geometric properties, etc. This is the first module called by NSARVE. INPUT DATA module is used only once.

6.3.1.2. INITIALISE Module

This module initialises all the necessary arrays and controlling parameters. Some of the arrays are initialised to zero, while others are initialised to a specified value. This module is called only once by NSARVE.

6.3.1.3. LOADS Module

This module reads in the incremental or total external loads. Various load types are included and they are : pressure loads, point loads, patch loads, self-weight and temperature loads. This module is called once for each load increment. The incremental loads are accumulated as well. Flexibility exists for the inclusion of other types of loads including seismic, impact and blast loads.

6.3.1.4. STIFFNESS Module

This module organises the stiffness calculations of various element types (isoparametric solid elements, membrane elements, line elements and bond-linkage elements, etc.) and assembles the global stiffness matrix. The global stiffness matrix is decomposed (triangularised) using the Gaussian elimination method.

6.3.1.5. SOLUTION Module

This module mainly solves for the nodal displacements. The incremental load or residual load vector is resolved and back substitution is performed.

6.3.1.6. STRESS AND RESIDUALS Module

This module carries out the calculation of strains, stresses and "residuals" for various element types. The stress increments are calculated using the non-linear constitutive relations (see Chapter 4) including those of cracking of concrete, yielding of steel and non-linear bond-slip response at steel-concrete interfaces. Equilibrating internal loads are calculated by integrating total stresses. "Residuals" are calculated by subtracting external and internal loads. The module is divided into three submodules, each of which carries out the non-linear stress and "Residuals" calculations for concrete, steel and bond at the steel-concrete interface. Flowcharts of submodules are given in Figures 6.2., 6.3. and 6.4.

6.3.1.7. CREEP Module

This module controls the creep analysis of each time increment. If a creep analysis is not requested, then this module is ignored and bypassed. This module has two functions : (1) it calculates the incremental creep strains for each concrete element using the visco-elastic creep model (see Chapter 4), and (2) it calculates the kinematically equivalent loads due to the incremental creep strains and assembles them into a global load vector.

6.3.1.8. OUTPUT Module

This module is called at the end of each load and time increment. This module prints out displacements at nodes, strains, stresses, principal stresses (direction cosines) and stress indicators at integration points of each element. It is controlled by a parameter from the INPUT module.

6.3.2. Description of Subroutines

A brief description of the main functions of each subroutine is given below.

INPUT

This routine reads in all the input data except the load data. The main items read in are the controlling parameters, nodal coordinates, element connectivity, material and geometric properties, nodal fixities, nodal temperatures, etc. The number of equations and the semi-bandwidth are also calculated for the stiffness matrix. All the read items are echoed and checked for obvious errors.

INITL

INITL initialises all the necessary arrays and variables used in the program. The arrays and variables are initialised to zero or to a specified value.

EQVINT

EQVINT updates the equivalent stresses or the equivalent strains at the end of each load increment. These equivalent quantities are used during the stress recovery of steel or concrete materials to establish loading or unloading. This routine calls two functions : SIGEFF and ZMISE.

PRNRES

This routine prints out the global residual load vector upon request.

LOAD1P

Subroutine LOAD (see later) is called by LOAD1P. This routine calculates the total load applied and stores it in an array. During the analysis, this load is factored using the set of pseudo times specified. This routine also calls ROTATE.

LODINC

LODINC is called for each load increment and calls subroutines LOAD and ROTATE. The total external load is also accumulated.

LOAD

The function of this routine is to read in the controlling parameters concerning loads and to identify the type of loading used in the analysis. According to controlling parameters, the routine further reads in necessary loading details and kinematically equivalent nodal loads are calculated. The types of loading available are :

- (a) Surface pressure (uniform or variable)
- (b) Point loads
- (c) Patch loads (loads not directly on nodes)
- (d) Gravity loads
- (e) Thermal loads

The routines called by LOAD are ISOP2, IFACE, DEMAT, STFLIN, TMINTP, ISOP3, ASSLOD and LINEL.

IFACE

This routine sets up face numbers for solid elements. For more details of face numbering scheme, refer to the User's Manual given in Appendix B.

ASSLOD

This routine assembles the element load vectors into the global load vector.

RESID

Calculates the internal element load vector and also assembles it into the global load vector :

i.e.
$$\tilde{p}^e = \int_{vol} \tilde{B}^T \tilde{\sigma} dvol$$

and
$$\tilde{P} = \sum p^e$$

The routine ISOP2 is called by this routine.

RZERO and RZERO

Routines to set real and integer arrays to zero respectively.

MVECT

This routine multiplies an array of dimension nxm with a vector of dimension mx1, i.e. $C = A * V$

MPRODT

This routine multiplies two rectangular matrices, A and B (dimensions lxm and mxn respectively) to produce a resulting matrix C.

ROTATE

This subroutine transforms the global load vectors into local load vectors for inclined boundary supports (skew boundary conditions). The displacement vectors are also transformed before stresses are calculated.

INCLNE

This routine transforms the element stiffness matrix of those nodes which have inclined boundary supports.

GAUSS

GAUSS sets up the Gauss point positions and corresponding weighting coefficients. The number of Gauss points available are 1,2,3,4, and 14. Any combination of these can be used, depending upon the user's requirements. The defaults are 2x2x2 for solid elements, 2x2 for membrane elements and 3 points for axial line elements.

STIF and STIFF

These two routines calculate element stiffness matrices for each of the element types used in the analysis. The first routine calculates the stiffness matrix with the assembly being performed at the same time. The second routine calculates the element stiffness matrix and puts it

to a temporary backing file. This is recovered at the time of assembly in the assembly routine (this routine is suitable for very large problems). These routines call the following routines : ELSTIF, MBNSTF, LINEL and LINKEL.

ELSTIF

Calculates the element stiffness matrix for the solid elements. The contribution of the line element in the body of the solid element is also included in the stiffness matrix. The stiffness matrix is transformed to the local inclined directions if inclined supports are present. The following routines are called by this routine : STFLIN, ISOP2, DVARB, INCLNE and BOUNDC.

MBNSTF

Calculates the element stiffness matrix for the membrane elements. The stiffness matrix for the inclined supports is also transformed into the local axis system. The following routines are called by this routine : ISOP3, MEMDAT, INCLNE and BOUNDC.

LINEL

In this routine the element stiffness matrix, the internal element load vector and the thermal load vector are calculated for the AXIAL LINE elements. The routines called are ZESBAR, INCLNE, TMINTP and BOUNDC.

STFLIN

The element stiffness matrix, the load vector and the thermal load vector are calculated for the line element in the body of the solid element. The routines called by this routine are ZESBAR, ISOP2, ASSLOD and TMINTP.

LINKEL

The element stiffness matrix and the element (internal) load vector for the 2 node linkage element are calculated. The element stiffness matrix is transformed if the element node has inclined boundary supports. This routine calls INCLNE and BOUNDC.

STFDEC

This routine sets up solution controls and calls incore or out of core assembly and decomposition routines. The Gaussian elimination method is used to decompose the stiffness matrix. The routines called are FORMEQ, DECOMP, ASSEMB and LEQSOL.

FORMEQ

The element stiffness matrices are assembled into the global stiffness matrix. Incore or out of core assembly may be used upon request by the user. The minimum storage for the stiffness matrix (declared as a dimension) is $2 \times \text{NHBD} \times \text{NHBD}$ for it to remain incore, where NHBD is the semi-bandwidth of the stiffness matrix. The routine called by this routine is STIF.

ASSEMB

This routine performs the same task as FORMEQ but the whole operation is performed out of core with no restriction on the size of the stiffness matrix. The stiffness matrix is divided into blocks and they are put to the backing file once full. Subroutine STIFF is called by this routine.

DECOMP

This routine decomposes the stiffness matrix assembled by FORMEQ in triangular form using Gaussian elimination.

LEQSOL

The stiffness matrix assembled in the routine ASSEMB is decomposed (Gaussian elimination). The load vector is also resolved and back-substitution is performed. All these operations are carried out using the out of core scheme.

RESOLV

This routine resolves the load vector and performs the back-substitution using the decomposed stiffness matrix produced by the routine DECOMP.

SOLVE

This routine calls RESOLV and LEQSOL.

TOSTRS

This routine calls the appropriate stress routines. The stress, strain and residual load vectors are calculated by the routine called by TOSTRS. These routines are ROTATE, MEMBST, LINEST, BONSTR, PRNRES and SOLDST.

SOLDST

Stresses, strains (total and incremental), creep strain, thermal strain and the equilibrating forces are calculated for the solid elements. The stress calculation at each Gauss point is performed using the appropriate constitutive matrix (cracking and high compression). The routines called by this routine are STRESS, TMINTP, ISOP2, CREEP, NONSTR and ASSLOD.

STRESS

This subroutine calculates the incremental strain and stress for each element type. The following routines are called : DVARB, DMEMB, TMINTP, ZESBAR, BONDST and ISOP2.

TMINTP

This subroutine checks the temperature distribution for the solid, membrane and axial line elements. If temperatures are found for the element type which are not allowed, then that temperature is overwritten by this routine. For example, temperature type constant, linear and quadratic are allowed for the linear, quadratic and cubic elements respectively. This ensures that the thermal strain is of the same order as the mechanical strains produced by the temperature load.

ISOP2

Shape functions, derivatives of the shape functions, determinant of the Jacobian and the strain-displacement matrix are calculated for the solid and line element in the body of the solid element.

ISOP3

Shape functions, derivatives of the shape functions, determinant of the Jacobian and the strain-displacement matrix are calculated for the membrane elements.

OUTPUT

OUTPUT prints out the displacements and external loads for all nodes. Stresses, strains and element indicators are also printed for each element type.

NONSTR

NONSTR calculates the stress increments according to the current state of stress and the state of the material (concrete compression and cracking). Loading and unloading at the current point is checked and the current stress state updated. The routines called by this routine are CRACK, DMATL, ENDOST, PRINCL and TRANSF.

MEMBST

Stresses and equilibrating forces are calculated for the membrane elements. The incremental theory of plasticity with isotropic hardening is used. The following routines are called : ISOP3, TMINTP, STRESS, ASSLOD and PLASTM.

LINEST

Stress and stress increments are calculated for the axial line and line element inside the solid element using the incremental plasticity theory. The routines called are STFLIN, LINEL, STRESS and STELST.

CRACK

This is the main crack routine which examines the state of stress and strain at a point and sets up the current crack indicator. The crack initiation, possibility of crack closures and reopening of the closed cracks are also considered. The routines performing these tasks are GETNCK, GETNCR, CRACLS, CRKOPN and CRINT.

GETNCK and GETNCR

The crack at a point is represented by a single number or by three numbers in three principal directions. GETNCK gets three numbers for a given number and GETNCR does the reverse.

CRINT

This routine initiates crack(s) at a point. The maximum principal stress criteria is used to initiate crack(s) normal to the principal stress under consideration. CRKIN is called by this routine.

CRACLS

Checks the existing crack closure and updates the crack indicator accordingly.

CRKOPN

Checks the reopening of closed crack(s). The principal strain criteria is used and the crack updated accordingly.

CRKIN

Checks that any of the principal stresses exceed a specified limiting tensile stress. The crack flag is set up accordingly.

BONSTR

This routine calls the routines BONDST and STRESS.

BONDST

BONDST calculates the incremental bond stress and slip. The current stress and slip are also accumulated. Finally, the equilibrating forces are calculated.

CONVER

The Euclidian norms of the total external loads, total displacements, residual loads and incremental displacements are calculated. Also the following ratios :

$$\begin{aligned}
\|R\| &= \sqrt{\underline{R}^T \underline{R}} \\
\|P\| &= \sqrt{\underline{P}^T \underline{P}} \\
\|\Delta \underline{u}\| &= \sqrt{\Delta \underline{u}^T \Delta \underline{u}} \\
\|\underline{u}\| &= \sqrt{\underline{u}^T \underline{u}} \\
f_R &= \|R\| / \|P\| \\
f_u &= \|\Delta \underline{u}\| / \|\underline{u}\|
\end{aligned}$$

where

- \underline{R} - residual load vector
- \underline{P} - total external load
- $\Delta \underline{u}$ - increment displacement
- \underline{u} - total displacement
- T - transpose

are calculated. These are checked against a specified tolerance by the main program.

CCREEP

This routine was written to convert the creep strains into kinematically equivalent nodal loads. The routines CREEP and ROTATE are called by this routine.

CREEP

The element incremental creep strain is calculated in this routine. The following routines are called : ISOP2, RESID, DEMAT and RESID.

DVARB

DVARB sets up the material matrix for the solid elements. The constitutive matrix is calculated according to the material state. The cracked matrix is transformed to the global system. Adjustment is also made for higher concrete compression. The routines called by DVARB are DMATL, DDMAT, TRANSF and PRINCL.

DMATL

DMATL sets up the material matrix according to the type of concrete compression criteria used. The endochronic theory, the uniaxial equivalent strain concepts and the shear-bulk modulus approach are the compression criteria available. The routines called are COMPRN, DTBRK, DZIMER and GETNCK.

DZIMER

Sets up the concrete constitutive matrix based on the bulk-shear modulus approach. The shear modulus is assumed to be a function of the second invariant of stress.

BOUNDC

Boundary conditions at the element stiffness level are imposed. The strategy adopted is to zero out the row and column associated with the degrees of freedom under consideration and to set the diagonal term to one.

INTPOL

Interpolates the modulus of elasticity for concrete at higher temperature using linear interpolation.

PLASTM

The elasto-plastic stress increment and the current stress are calculated for the membrane elements. The stress at the end of the iteration is brought back to the yield surface. The routines called are SUBINST, MEMDAT and ZMISE.

SBINST

This routine calculates the stress increment of a plastic point using the sub-incremental method. The routines called are MEMDAT and ZMISE.

STELST

Elastic or elasto-plastic stress increment and the total stress are calculated by this routine for the line elements. This routine calls the function ZESBAR.

TRANSF

TRANSF sets up the transformation matrices for stress and strain transformations between local (crack) and global axes. The cracked material matrix is also transformed into the global coordinate system.

DDMAT

Sets up the material matrices in the local (crack) directions for the Gauss points where cracks have developed.

DMAT

Three-dimensional elastic material matrix is set up by this routine.

PRINCL

This subroutine calculates the principal stresses and strains and the direction cosines.

ZMISE

This function calculates the equivalent stress (Von Mises) for the plane stress condition.

ZECJ2

Calculates the equivalent strain for the three-dimensional solid elements.

ZESBAR

Returns elastic or an elasto-plastic modulus for the uniaxial line elements.

DMEMB

The elastic material matrix is set up for plane stress membrane elements.

MEMDAT

The elastic or elasto-plastic material matrix is set up for plane stress membrane elements. The routine called by this routine is DMEMB.

SECANT

This subroutine sets up the orthotropic material matrix for the solid elements. Three moduli in three principal directions and corresponding Poisson's ratio are used.

COMPRN

The moduli of elasticity for concrete in three principal directions are calculated using the uniaxial strains and the ratios of principal stresses. The routines called by this routine are CONSTV and SECANT.

CONSTV

This routine calculates the ultimate stress and strain for given principal stress ratios.

OTTENS

This routine uses Equation (4.16) to calculate the ultimate stress using Ottosen failure surface (35).

CONWEL

This routine calculates the ultimate stress using Argyris William failure surface.

MEMTRF

Local membrane stresses are transformed to global stresses.

ACCNEW

This subroutine calculates the modified displacement increment using the current and old displacement increments and the residual load vector. This is called the accelerated Newton Raphson procedure.

CONCRI

This routine calculates the concrete failure surface according to Equation (4.16).

The following are routines based on the endochronic theory :

ENDOST

Calculates the stress increment using the endochronic theory. The routines called by this routine are PARAM and ENDITR.

PARAM

Sets up concrete parameters used in the endochronic theory formulation.

ZPARAM

This subroutine calculates the intrinsic time function and the inelastic dilatency parameter (λ). The function ZECJ2 is also called.

UPDIST

Calculates the inelastic stress increment if cracks are present.

ENDCHN

This routine calculates the inelastic stress increment and constitutive matrix using the endochronic theory. The following routines are called by this routine : ZPARAM, DTBRK, GETNCK, UPDIST and DDMAT.

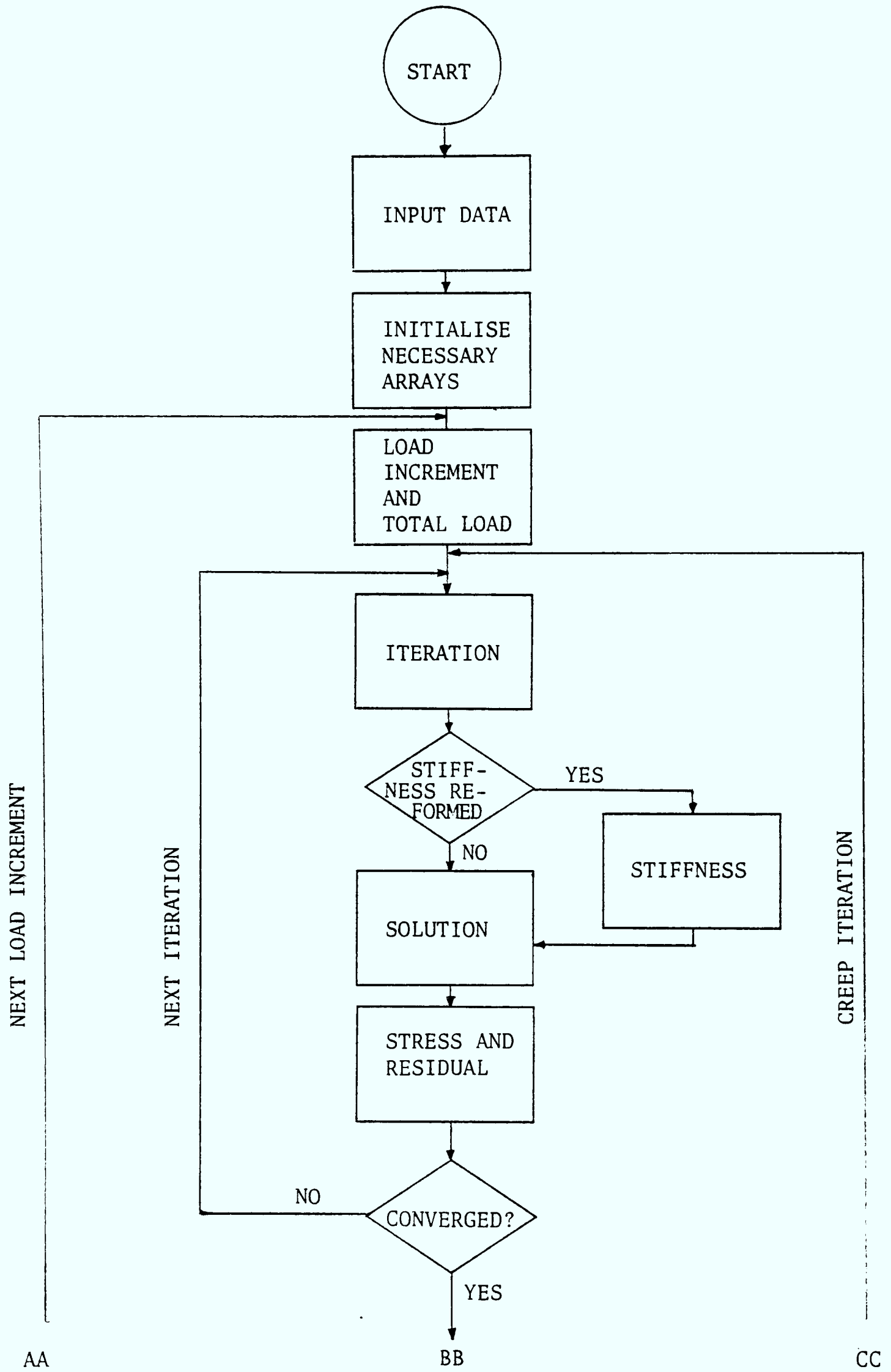
DTBRK

Sets up the constitutive matrix based on the endochronic theory.

ENDITR

Calculates the incremental stress for the loading and unloading points based on the endochronic theory. The routines ENDCHN and DTBRK are also called.

FIGURE 6.1. Flow Chart of the Non-linear Program NSARVE



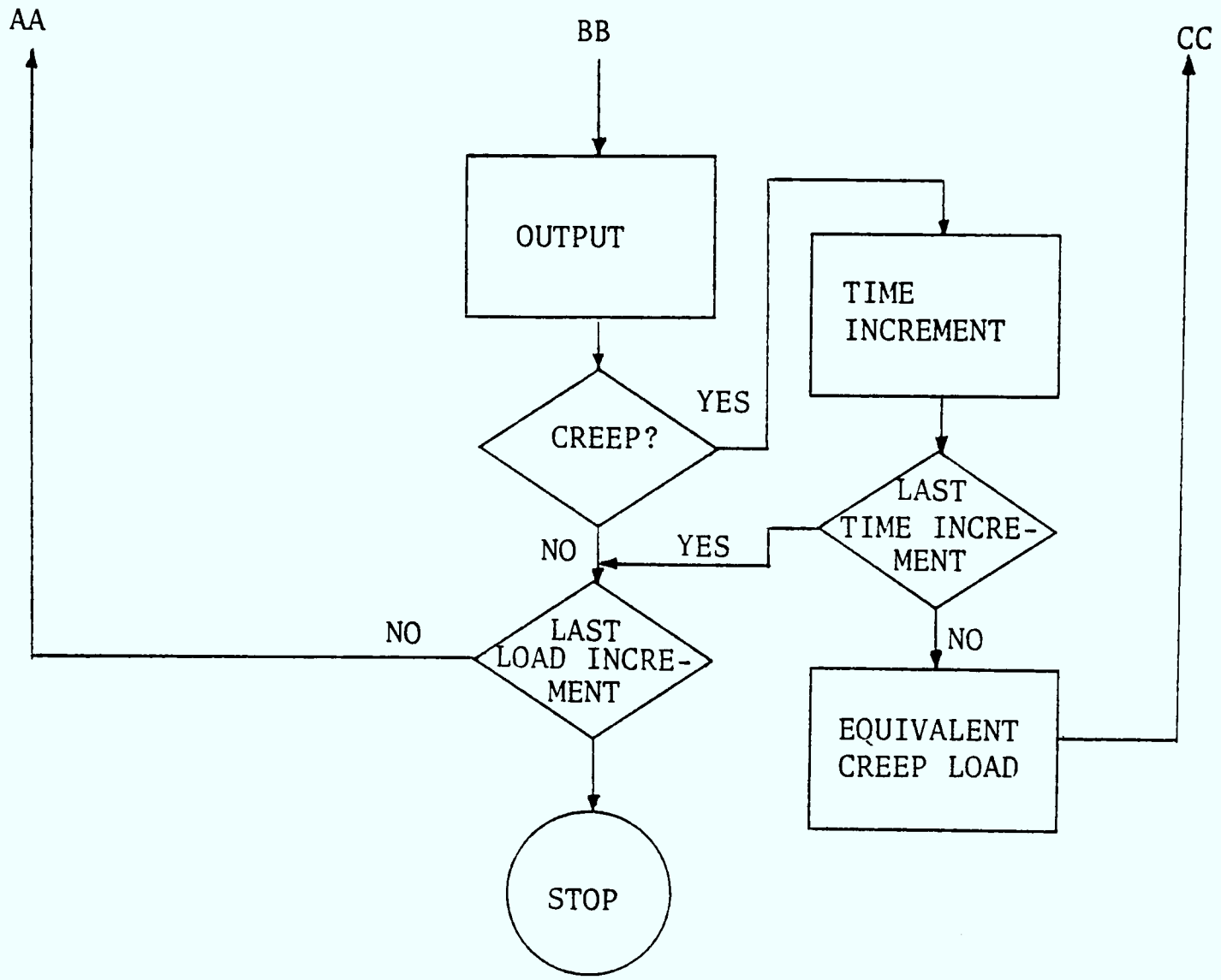
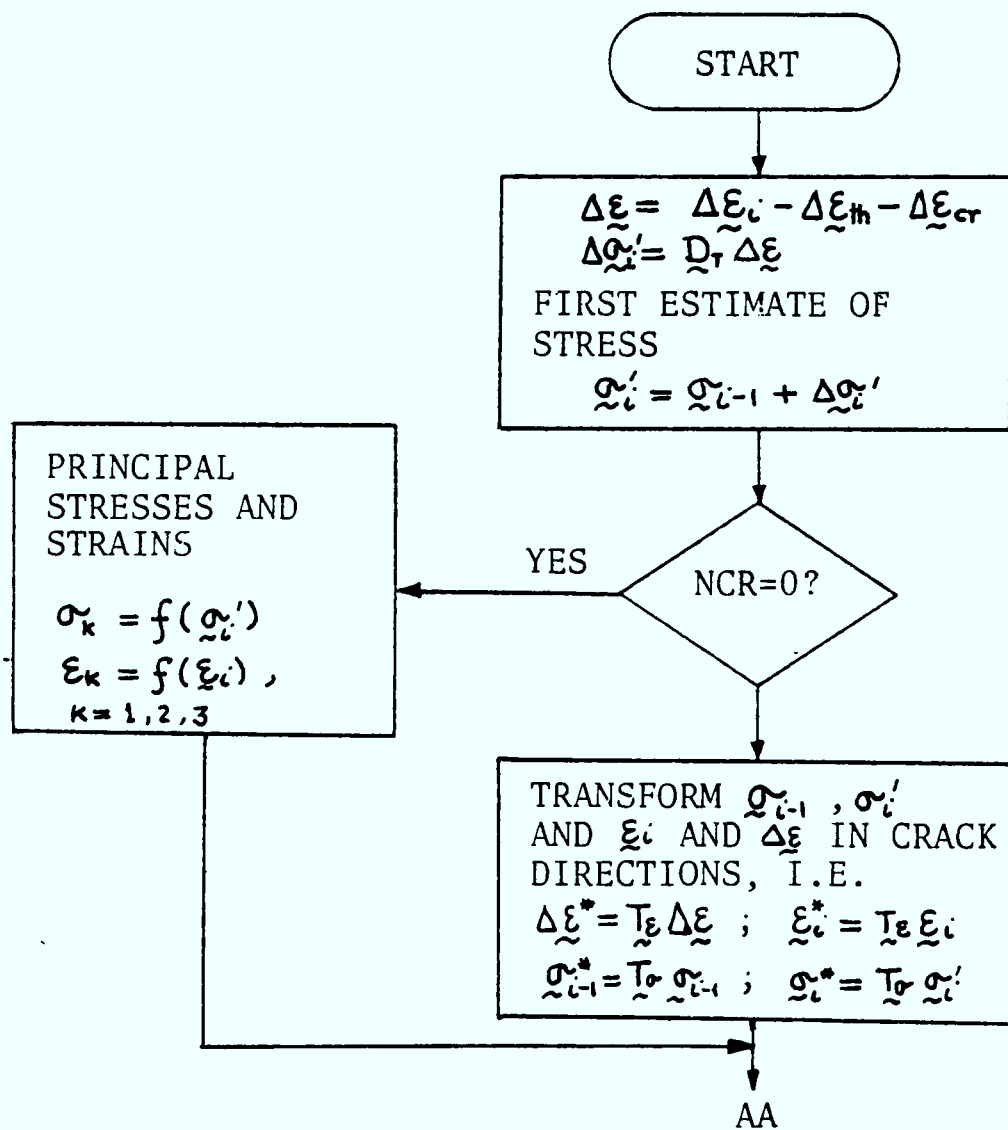


FIGURE 6.2. Flow Chart of STRESS and RESIDUAL for Concrete

- i - ith iteration
- *
- NCR - crack indicator
- $\Delta \underline{\sigma}_i$ - stress increment
- $\underline{\sigma}_{i-1}$ - stress at the beginning of the ith iteration
- $\underline{\sigma}_i$ - global stress at the end of this iteration
- $\Delta \underline{\epsilon}_i$ - strain increment (total)
- $\Delta \underline{\epsilon}_{th}$ - thermal strain increment
- $\Delta \underline{\epsilon}_{cr}$ - creep strain increment
- $\underline{\epsilon}_i$ - total strain
- \underline{T}_σ - stress transformation matrix
- \underline{T}_ϵ - strain transformation matrix
- $\underline{D}_T, \underline{D}^*$ - concrete material matrices
- \underline{R} - residual load vector
- \underline{P}_{ex} - total external load



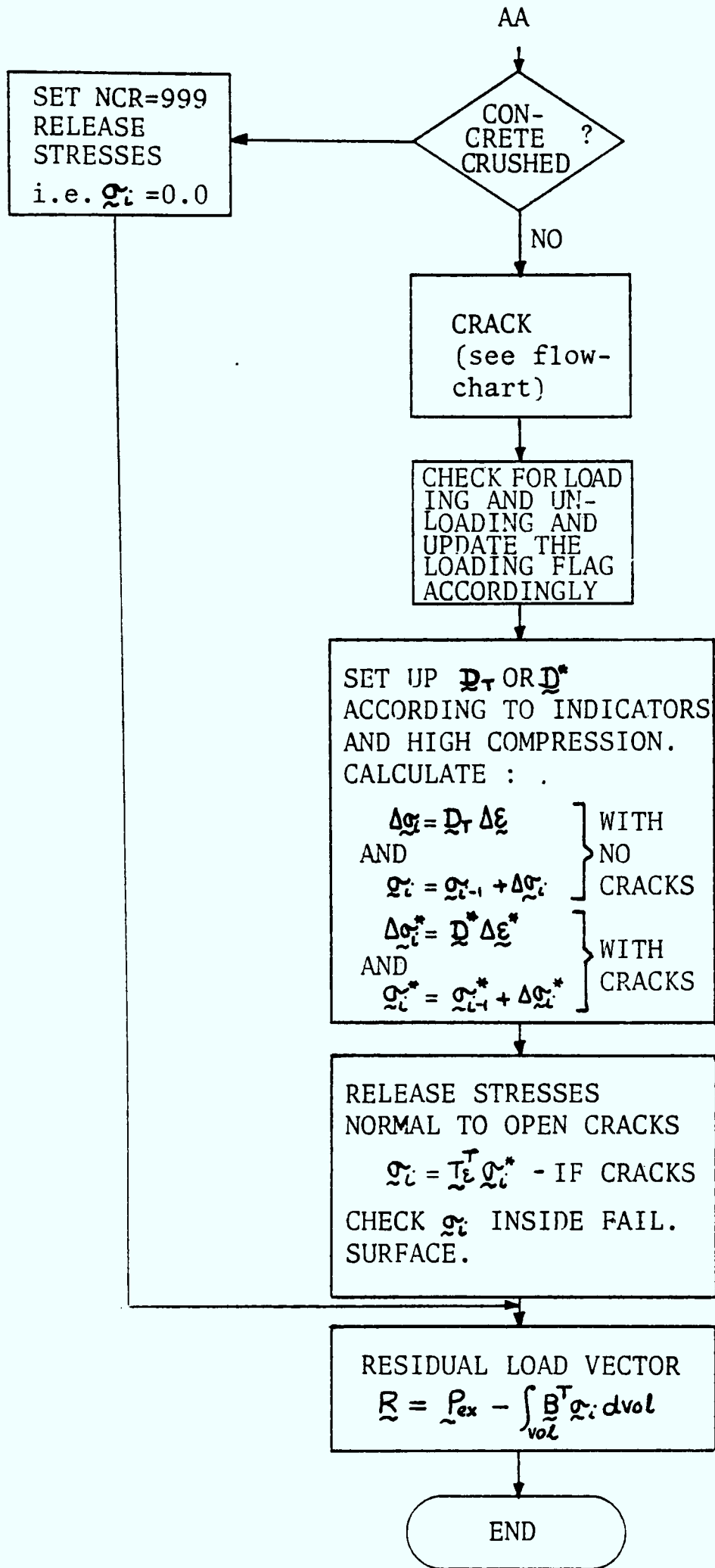


FIGURE 6.2a Flow Chart of CRACK

Crack indicators - NCK(1), NCK(2), NCK(3)

NCK(1) - crack normal to the principal stress '1'

NCK(2) - crack normal to the principal stress '2'

NCK(3) - crack normal to the principal stress '3'

NCK(1)=0
NCK(2)=0
NCK(3)=0 } - no cracks

NCK(1)=1
NCK(2)=1
NCK(3)=1 } - cracks open

NCK(1)=2
NCK(2)=2
NCK(3)=2 } - cracks closed

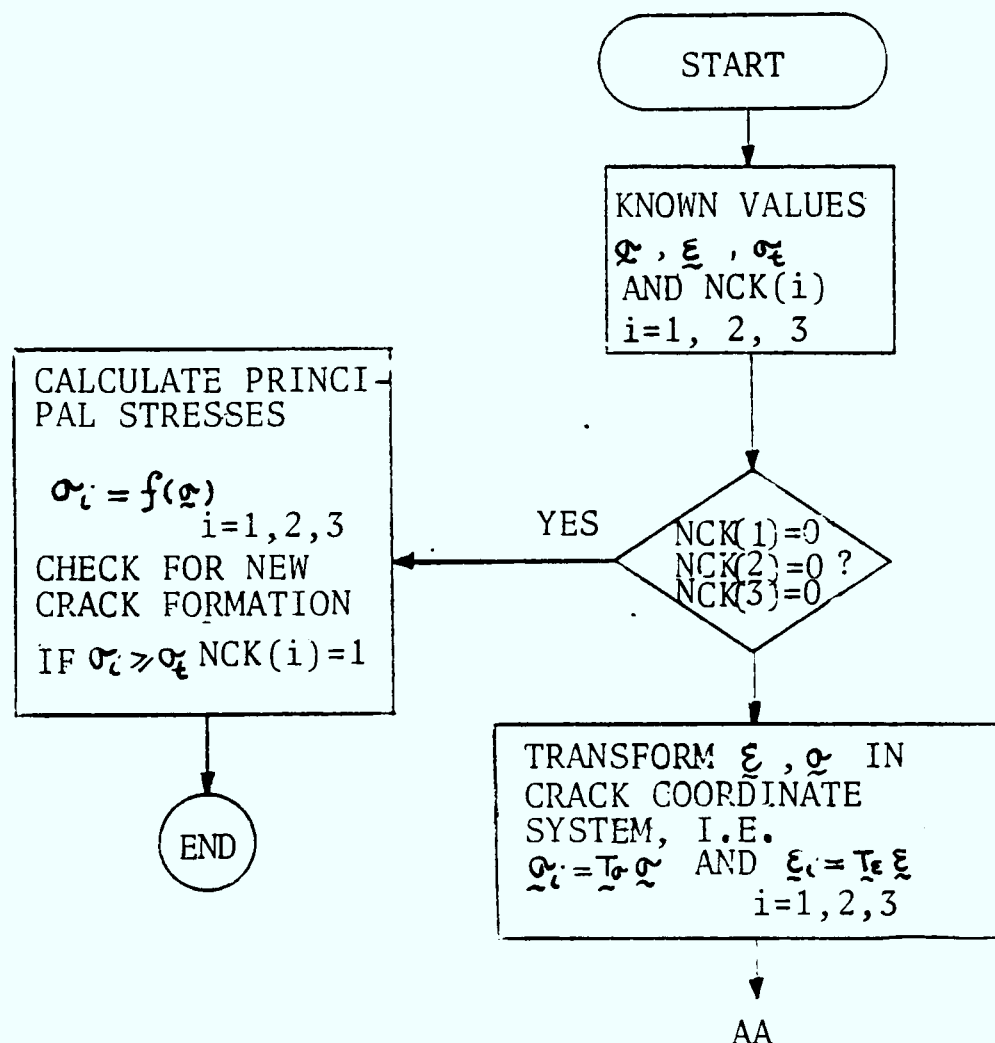
$\sigma, \underline{\epsilon}$ - stress/strain state at integration point

ϵ_i - principal strains

σ_i - principal stresses; i=1, 2, 3

σ_c - limiting tensile strength of concrete

T_ϵ, T_σ - transformation matrix



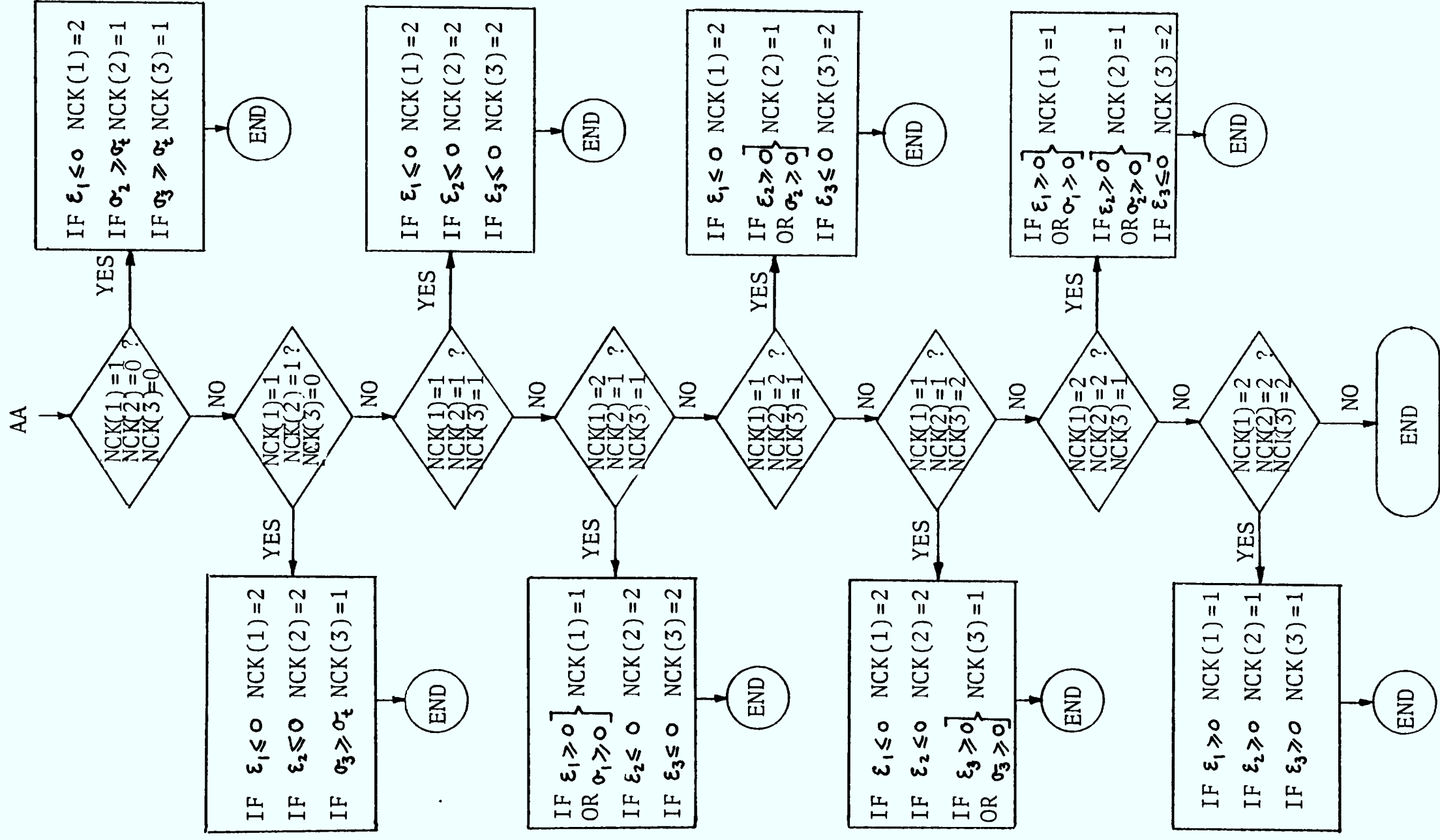
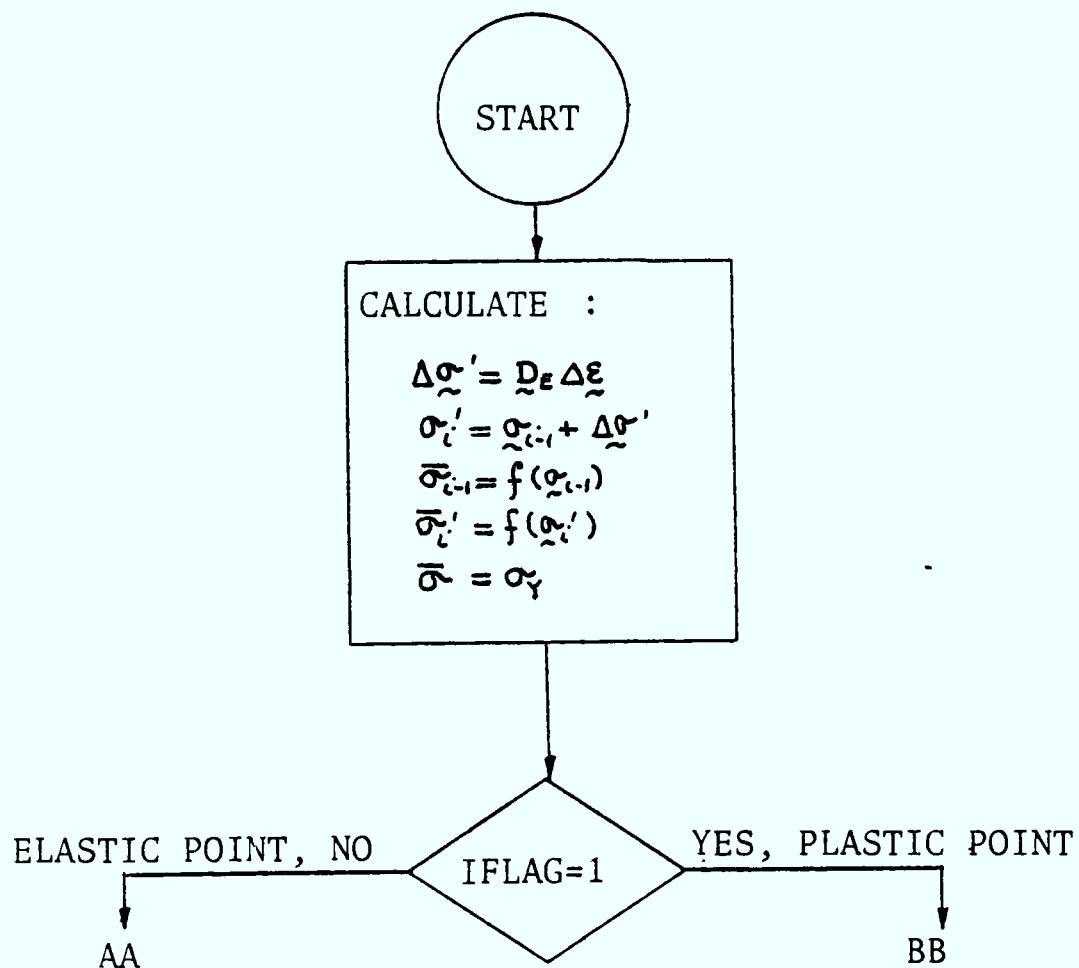
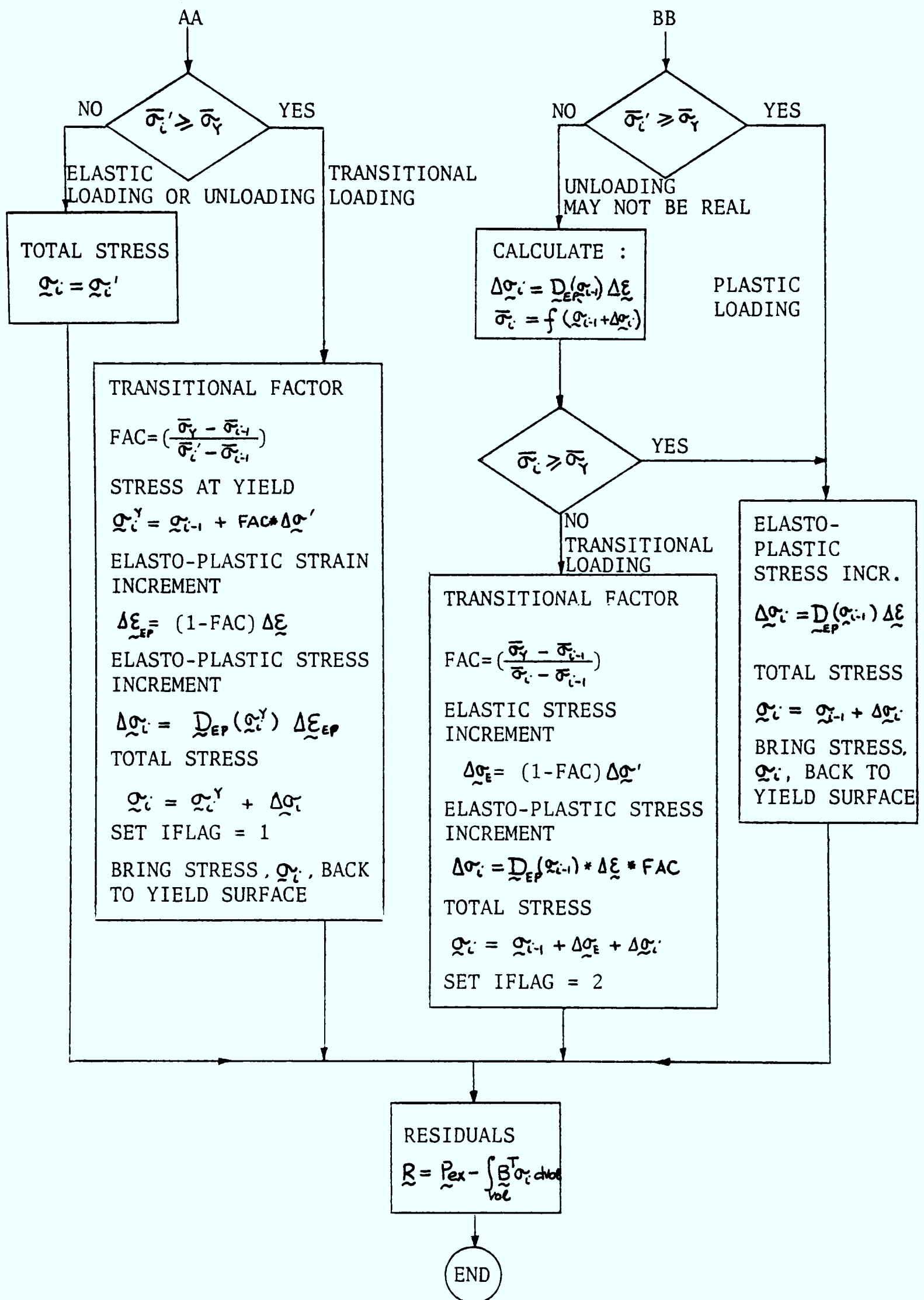


FIGURE 6.3. Flow Chart of STRESS and RESIDUAL for Steel

- \bar{P}_{ex} - total external load
 $\Delta \bar{\epsilon}$ = $(\Delta \bar{\epsilon}_i - \Delta \bar{\epsilon}_{th})$ - strain increment
 $\Delta \bar{\epsilon}_{th}$ - thermal strain increment
 $\bar{\epsilon}_{i-1}$ - strain at iteration i-1
 $\bar{\epsilon}_i$ - strain at iteration i
 $\bar{\sigma}_{i-1}$ - stress at iteration i-1
 $\bar{\sigma}_i$ - stress at iteration i
 $\Delta \bar{\sigma}_i$ - stress increment
 IFLAG - stress point indicator
 =0 - elastic point
 =1 - plastic point
 =2 - unloading from plastic state
 σ_y - uniaxial yield stress
 $\bar{\sigma}_y$ - equivalent stress
 $\bar{\sigma} = f(\bar{\sigma})$ - Von Mises yield function
 \bar{D}_E - elastic material matrix
 \bar{D}_{EP} - elasto-plastic material matrix

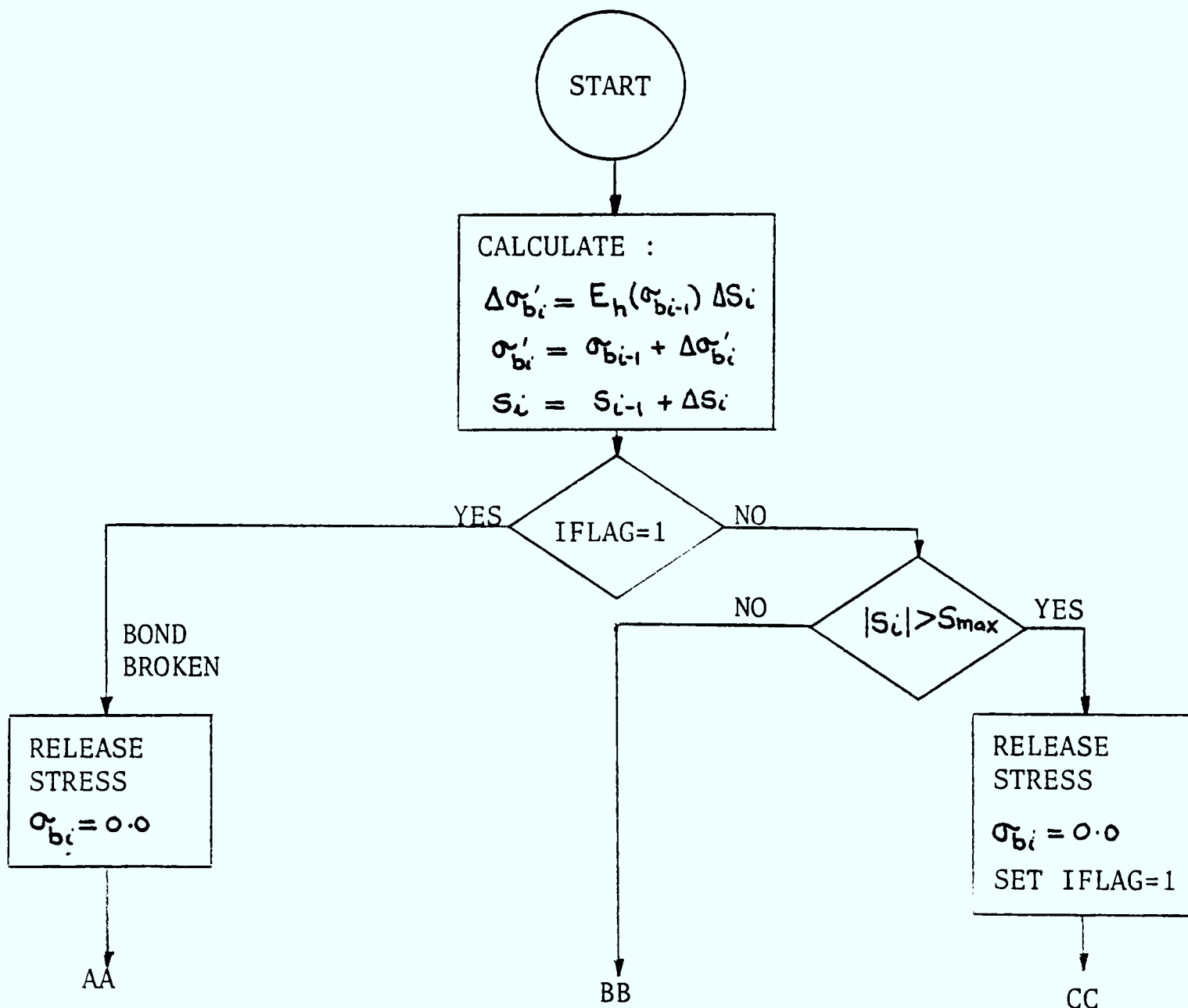




At the end of each load increment, yield stress is updated for plastic points only, i.e. If IFLAG=1,

FIGURE 6.4. Flow Chart of Stress and Residual for Bond

- ΔS_i - incremental slip at iteration i
- $\Delta \sigma_{bi}$ - incremental bond-stress at iteration i
- S_{i-1} - total slip at iteration i-1
- S_i - total slip at iteration i
- σ_{bi-1} - total bond stress at iteration i-1
- σ_{bi} - total bond stress at iteration i
- S_{max} - maximum value of slip
- σ_{bmax} - maximum value of bond stress
- σ_b^c - bond stress from non-linear bond-slip curve using linear interpolation
- IFLAG - bond stress indicator
 - =0 - bond not broken
 - =1 - bond broken
- E_h - slope of local bond-slip curve



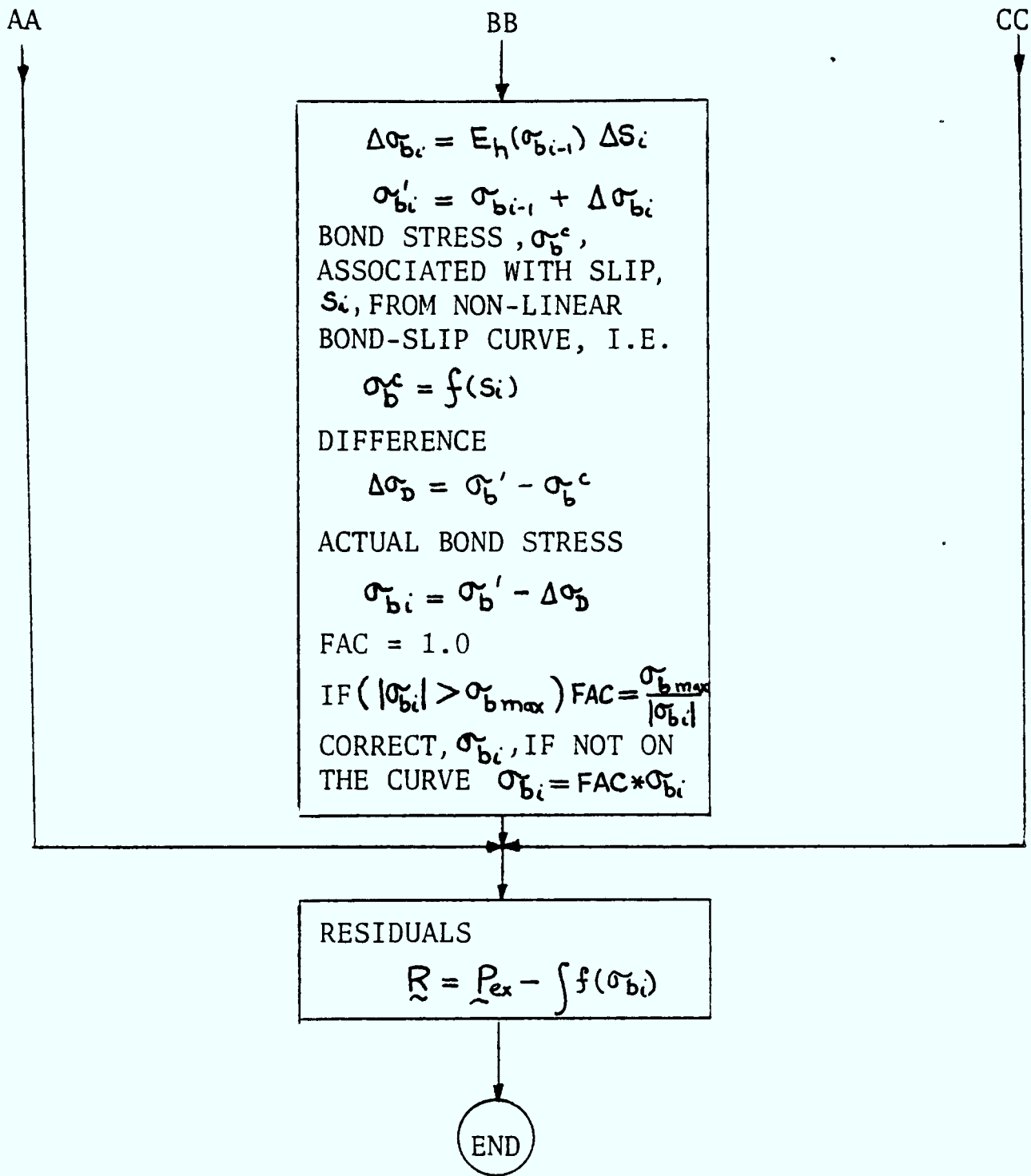
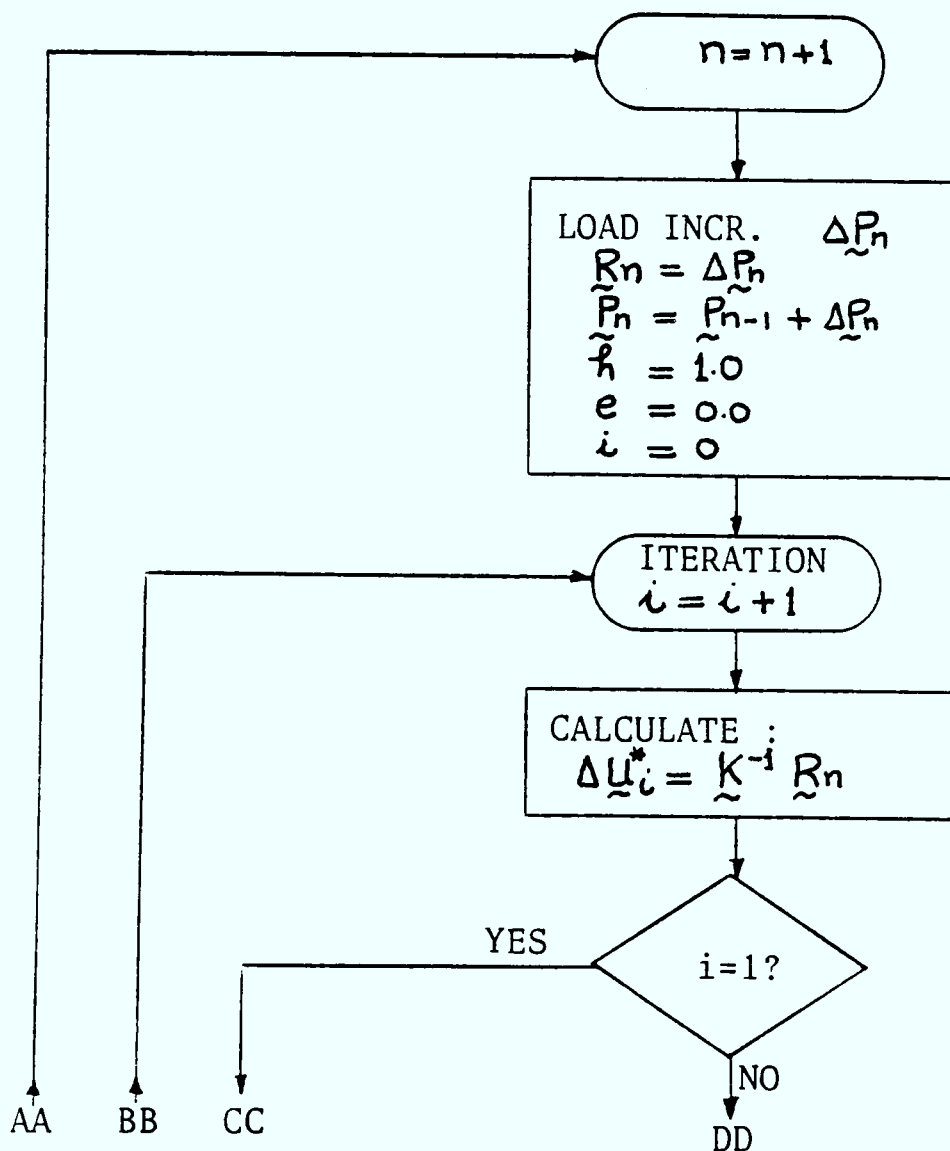
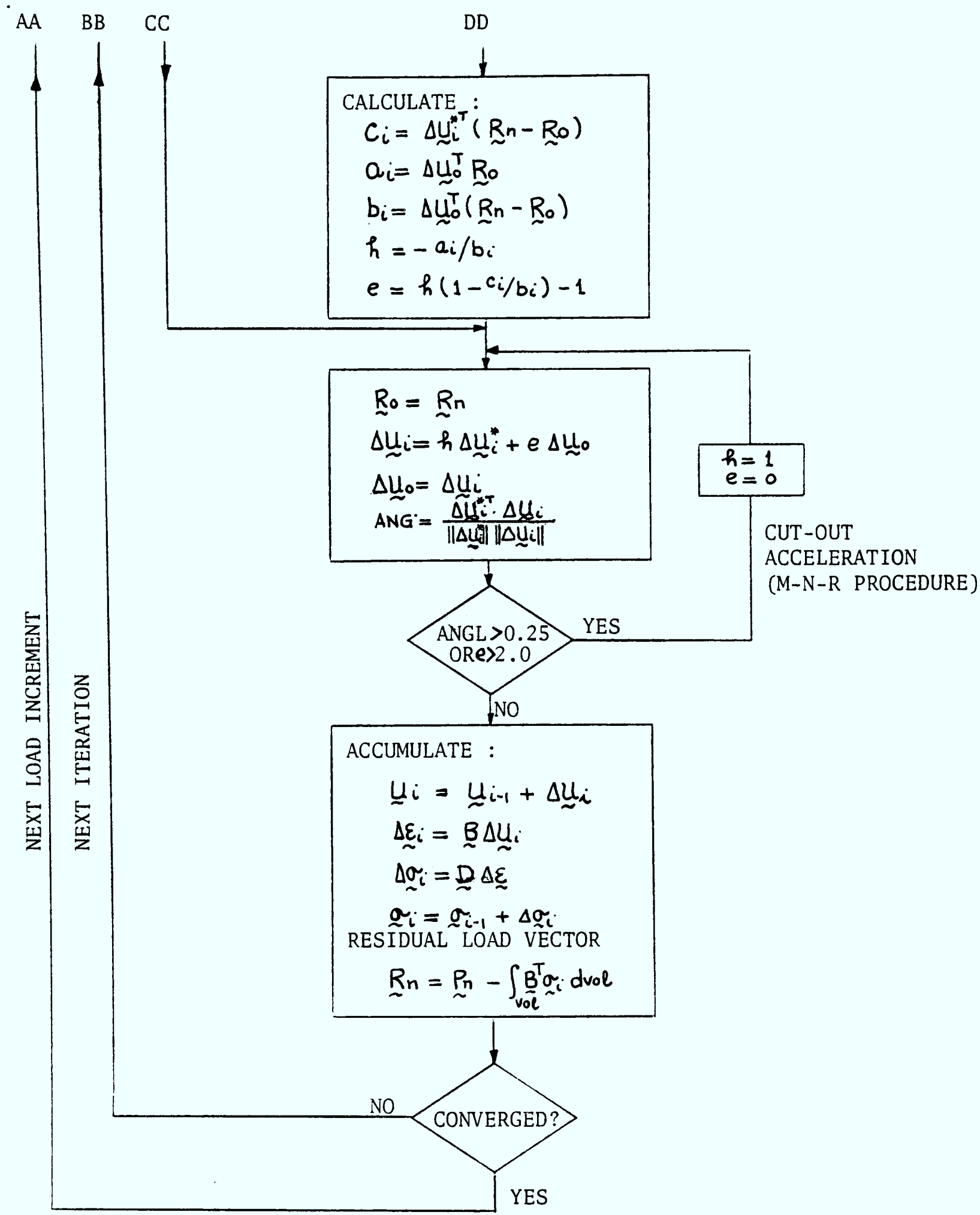


FIGURE 6.5. Accelerated Newton-Raphson Procedure

- n - nth load increment
- i - ith iteration
- $\Delta \underline{u}_o$ - old incremental displacement
- $\Delta \underline{u}_i^*$ - incremental displacement due to applied load or residual
- $\Delta \underline{u}_i$ - current incremental displacement
- \underline{R}_o - old residual load vector
- \underline{R}_n - new residual load vector
- \underline{B} - strain-displacement matrix
- \underline{D} - constitutive matrix
- $\Delta \underline{\epsilon}_i$ - strain increment
- $\Delta \underline{\sigma}_i$ - stress increment
- $\underline{\sigma}_i$ - current state of stress
- $\|\Delta \underline{u}_i^*\| = \sqrt{\Delta \underline{u}_i^{*T} \Delta \underline{u}_i^*}$
- $\|\Delta \underline{u}_i\| = \sqrt{\Delta \underline{u}_i^T \Delta \underline{u}_i}$





CHAPTER 7

Experimental Investigations of Bond-Slip Specimens and Bonded Slab

7.1. Introduction

A limited number of isolated scale model tests (13, 113a, 114, 115, 116, 119) have been performed on post-tensioned slabs using unbonded tendons. These tests assess the behaviour of such slabs under elastic, inelastic and cracking conditions. A valuable experimental data on unbonded slabs is now available. However, there is a lack of experimental data on the non-linear and cracking conditions of slabs using bonded tendons.

In this Chapter, a test has been carried out on a scaled model of an octagonal slab, post-tensioned with 5 mm and 7 mm high tensile steel wires in the two orthogonal directions. In certain areas, mild steel bars of 12 mm diameter have also been provided. This slab together with prestressing wires and conventional reinforcements have been designed using the Yield Line Analysis. Loads in various increments have been applied on this slab and the results have been processed using data logger. In addition pull-out tests have been carried out on bonded prestressed concrete specimens in order to obtain local bond-slip data. These are several beams in which the same 5 mm and 7 mm prestressing wires have been used.

Results from both these experiments are presented in this Chapter. It is intended to use these results in the constitutive relationships for Ahmlink element given earlier.

7.2. Material Data from Tests

For bond test specimens and octagonal slab, the concrete mix was designed. The mix properties by weight were :

Water	0.46
Cement	1.0
Sand	1.6
Coarse aggregate	2.32

The grout mix was designed from cement, water and admixture (cabaco expanding agent). The water/cement ratio for this mix was 0.45 by weight. The expanding agent was added according to the supplier's instructions in order to control shrinkage. This grout mixture was used for both the bond specimens and the octagonal slab.

The concrete properties using this mix were determined by testing concrete cubes and cylinders. Three cubes of 150 mm were tested in compression. Six cylinders of 150 mm x 300 mm diameter were chosen for testing, three under compression and three for splitting conditions. The modulus of elasticity and Poisson's ratio were measured on cylinder tests. The average material properties determined from these tests at 28 days are as follows :

Uniaxial concrete cube crushing strength,	$\sigma_{cu} = 45.0 \text{ N/mm}^2$
Uniaxial concrete compressive cylinder strength,	$\sigma_c = 39.76 \text{ N/mm}^2$
Uniaxial concrete tensile strength,	$\sigma_t = 3.93 \text{ N/mm}^2$
Modulus of elasticity ,	$E_c = 27.5 \times 10^3 \text{ N/mm}^2$
Poisson's ratio ,	$\nu_c = 0.17$

Steel used in these tests were of two types : (a) plain mild steel bars (12 mm diameter), and (b) high tensile steel wires (5 and 7 mm diameter). The following material properties were obtained :

Modulus of elasticity for steel,	$E_s = 200,000 \text{ N/mm}^2$
Yield stress for mild steel bars,	$\sigma_{y1} = 297 \text{ N/mm}^2$
Yield stress for high tensile steel wires,	$\sigma_{y2} = 1,340 \text{ N/mm}^2$

7.3. Details of Test Specimen

Details of the local bond strength and bonded post-tensioned slab specimens are given below :

7.3.1. Bond-Slip Test Specimen

The test specimen chosen was based on 'flexural only case'. A rectangular beam (cross-section 152 mm x 152 mm) of one metre length was chosen (Figure (7.1.)) with two rectangular holes on each side of a 38 mm bonded length (L_b). A circular duct running along the beam through the centre of the cross-section was cast void for later insertion of the prestressing wire. This duct in the central part of the specimen between rectangular holes was grouted using the cement grout after post-tensioning.

Two strain gauges (gauge factor 2.5) were mounted onto the wire 50 mm apart from the centre of the wires prior to the insertion of the wires in the ducts. The strains on these wires were recorded from the Peekel strain indicator (photograph 7.1.). Four high precision displacement transducers were placed at both ends of the bonded length (with two at each end). The slip of the wires was measured using these transducers with a measuring accuracy of 10^{-5} mm (photograph 7.2.). The slip was directly recorded from the transducer measuring unit (photograph 7.1.).

The load was applied with a prestressing hydraulic jack and the accuracy of the load increment was recorded using a load cell. A complete general view of the bond test specimen is shown in Figure (7.1.).

To study the influence of various parameters on the bond between the prestressing wire and the grout, two main parameters were investigated; the magnitude of the prestress force and the wire diameter. Wires of diameters 5 and 7 mm were prestressed to 65% and 75% of the guaranteed ultimate tensile strength (GUTS). Ten beam specimens were

tested. Table 7.1. shows the prestressing loads and wire diameters for these beams.

7.3.2. Details of the Bonded Slab

A scaled model of a prestressed concrete slab (Figure (7.2.)) representing the top cap of a typical prestressed concrete reactor vessel was tested. The object of the test was (a) to study the physical behaviour of a prestressed concrete slab with bonded tendons under increasing load up to the point of failure, thereby providing load displacement relationships, distribution of cracking and the failure mechanism, and (b) to compare these results with those obtained from the analytical model developed in Chapters 4 and 8.

Yield Line Theory was used to size up initially the octagonal bonded slab. Table 7.3 shows the yield line analysis and results obtain major cracks only along the two centre lines of the slab. A sufficient amount of ordinary reinforcement was provided in certain areas in order to help the initiation of these cracks.

The octagonal prestressed concrete slab representing the top cap of a vessel was prestressed with 5 mm and 7 mm diameter wires in two orthogonal directions. A conventional reinforcement of 12 mm diameter mild steel bars were provided as shown in Figure (7.2.). Four 7 mm diameter wires were placed along the centre line BB, two on either side of the centre line at distances 115 mm (C_1) and 350 mm (C_2) respectively. These wires are shown with broken lines were at height of 36.5 mm from the bottom surface of the slab. Eight 5 mm diameter wires were placed along the centre line AA, four on either side of the centre line at distances 115 mm and 350 mm and at heights of 18 mm and 55 mm from the bottom surface of the slab. Eight 12 mm diameter bars spaced at 65 mm were provided in one quadrant of the slab. A total of 32 bars were provided in the slab as shown in Figure (7.2.).

Photographs were taken at various stages of the construction of this slab. Photograph 7.3. shows a formwork of an octagonal shape with mild steel reinforcing bars. Special hooks were provided for lifting the slab from the mould after it was cast and cured. Photograph 7.4. shows the next stage of this construction in which temporary steel rods were provided (marked C) in the formwork which were removed later on in order to leave holes for the post-tensioning wires. The same photograph shows a steel frame used to hold straight steel rods (marked A). Strain gauges placed on reinforcements are also shown. After the slab was cast, the temporary rods from both sides were taken out. These were replaced by 5 mm and 7 mm diameter prestressing wires on which strain gauges were placed to measure the steel strain.

The prestress force was provided by stressing 8 number of 5 mm diameter and 4 number of 7 mm diameter wires in two orthogonal directions. A uniform prestress force was applied by stressing in sequence in both directions using CCL prestressing system. Each wire was stressed up to 75% of GUTS. Photograph 7.5. shows the slab after it has been prestressed. The prestressing wires were then grouted using a cement grout. The grout was injected under high pressure. The slab was then lifted and placed on to the rigid and roller supports. The rigid supports were placed diagonally opposite to the roller supports (Photograph 7.6.). The slab was transversely loaded with an approximately uniformly distributed load. This required a typical rigid steel frame (Photograph 7.6.) through which this load is applied. The dial gauges were placed on one-quarter part of the top surface of the slab to measure the transverse deflection. Rosette strain gauges were also placed on the top surface of the slab.

7.4. Brief Details of Test Rigs

The details of test rigs for both experiments are briefly given below.

7.4.1. Bond-Slip Test Rig (Figure (7.1.))

The complete test set-up of the bond-slip experiment is shown in Photograph 7.1. To accurately measure the applied loading, a load cell was used between hydraulic jack and a steel plate. The load was directly recorded with the load cell measuring unit. Four linear displacement transducers, two on each side of the bonded length, were clamped with a 1.5 mm thick steel sleeve, which was glued to the beam surface. Two rigid brackets were clamped to prestressing wire and the transducers were in contact with these brackets (Photograph 7.2.). Therefore any movement of the prestressing wire was recorded by the transducers.

7.4.2. Test Rig of Prestressed Concrete Slab (Figure (7.3.))

The slab was loaded with the loading rig producing four load points on the main steel frame and 12 load points on the slab. The loading rig is shown in Photograph 7.6. Four deep steel I sections were welded together at 90° to make a main rigid steel frame. This frame was supported by two strong steel beams running across the slab, which were supported by the columns. Each rigid frame was connected to a hydraulic jack. Hydraulic jacks were connected to a common hydraulic pump. Each hydraulic ram was lowered onto a three-legged spreader frame, with the load being transferred between each leg and the slab with a steel plate. This steel plate has a rubber pad underneath it to distribute the load. The steel plates and rubber pads were spread over a diameter of approximately 1780 mm. 100 KN load cells were used on each hydraulic jack for accurate measurement of load. The load was applied from the common hydraulic pump whereby each hydraulic jack applied a load on one-quarter of the slab. Figure (7.3a) shows the schematic details of the loading rig where points A, B, C and D are the positions of the hydraulic jacks. Figure (7.3b) shows the details of the three-legged frame representing the position A of the hydraulic jack. The schematic view is also shown in Figure (7.3c). The relationship between uniformly distributed load and the total load is given by :

$$p = P/A \quad 0.40185 \times 10^{-6} P$$

where

p = uniform pressure, N/mm^2

P = total loads from all hydraulic jacks (Newton)

The vertical deflections were measured on the top surface of the slab with dial gauges which were capable of measuring with an accuracy of 2×10^{-3} mm. The dial gauges were placed only on one-quarter of the slab due to symmetry and these were clamped with rigid steel beam which was running across the slab. The locations of 24 dial gauges are shown in Figure (7.4.). Strain gauges were embedded onto prestressing wires and reinforcements. The locations of strain gauges on these steel wires are shown in Figure (7.5.). The surface strains of concrete were measured using rosette strain gauges (see Figure (7.4a)). The strain gauges and the rosette strain gauges were connected to a data logger (compulog) as shown in Photograph 7.6. For each load increment, the strains were recorded by compulog and these were also printed on the teletype. The positions of dial gauges and strain gauges in Figures (7.4.) and (7.5.) were chosen such that they matched with the finite element mesh, the details of which are provided in Chapter 8.

7.5. Testing Procedure and Results of Bond-Slip Tests

The load in bond tests was applied at one end of the wire by using the prestressing hydraulic jack and it was measured with a load cell (see Photograph 7.1.). The load was applied in increments of 0.25 KN. For each load increment, the readings were taken. The steel strains were recorded with the Peckel strain indicator and the slips were recorded with the transducer measuring unit. The load was stopped when change in bond stress became nearly zero. The bond stresses, σ_b , were calculated from measured steel strains using the expression :

$$\sigma_b = \frac{\Delta P}{\pi d L_b} = \left(\frac{E_s A_s}{\pi d L_b} \right) \Delta \epsilon_s \quad (7.2.)$$

where ΔP = change in steel force over the bonded length, L_b
 $\Delta \epsilon_s = \epsilon_L - \epsilon_f$ = change in steel strain over the bonded length
 ϵ_L = steel strain at the loaded end
 ϵ_f = steel strain at the free end
 A_s = steel cross-sectional area
 E_s = modulus of elasticity for steel
 L_b = bond (embedded) length
 d = diameter of steel
 $\pi d L_b$ = embedded surface area of steel

The slip was obtained by taking an average value of the transducer readings.

The experimental bond-stress slip results obtained are plotted in Figures (7.6.) to (7.9.). It can be seen from these figures that at the early stages of loading the bond stress increased with a very small slip. With the increase in load, the rate of slip also increased. In all cases, the curves show that up to a maximum bond stress, there is a non-linear relationship with slip, and when slip increases beyond a certain value, the bond stress is almost constant and is equal to its maximum value. This occurs at a slip varying from 0.019 mm to 0.065 mm in different curves. Slip values of 0.01 mm to 0.06 mm were reported by Yannopolous (91) in his experiments of plain bars. The slope of the curves decreases with increasing slip, having a maximum value at zero slip and approximately zero at maximum bond stress. The initial slope (slip modulus, E_b) of the bond-slip curves (Figures (7.6.) to (7.9.)) are not much different. The average value of initial slip modulus is $501.40 \text{ N/mm}^2/\text{mm}$. Results of all tests are summarised in Table 7.2.

Results shown in Figure (7.6.) are for beams 1, 2, 3 of 5 mm diameter wires which were stressed up to 75% GUTS. There is a scatter of results for the beams tested under the same conditions. This is because of the complicated nature of the steel-concrete interface factors such as local shrinkage, settlement of the grout which give rise to

variation in the bond strength. An average maximum bond stress in this series of tests is approximately 1.64 N/mm^2 at an average slip of 0.048 mm when bond stress stops increasing.

In the second series of three tests (beams 4, 5 and 6) in which 7 mm diameter prestressing wire with a prestress of 75% GUTS are shown in Figure (7.8.). The bond-slip curves again become non-linear at the final stages with an average maximum bond stress of 1.80 N/mm^2 and an average slip of 0.057 mm. The bond stress at this point stopped increasing its value. The maximum value of bond stress is slightly higher than that in the previous case of beams 1, 2 and 3. These results indicate that 7 mm diameter wire gave slightly higher bond stress in comparison with 5 mm diameter wire.

Figure (7.9.) shows the results for beams 7 and 8 in which 7 mm diameter wire was also used with a prestress of 65% GUTS. In this case as shown in Figure (7.9.) a relatively large scatter of results are obtained for maximum bond stress. An average value of maximum bond stress is found to be 2.05 N/mm^2 at an average slip of 0.025 mm when bond stress stops increasing. In this case curves indicate less non-linearity and maximum bond stress is relatively larger than that for beams 3, 4 and 5. The maximum slip at which the bond stress stops increasing is less here than for beams 3, 4 and 5. Figure (7.7.) shows the results for beams 9 and 10 in which 5 mm diameter with prestress of 65% GUTS is used. The average maximum bond stress is found to be 2.21 N/mm^2 . The slip at which this maximum bond stress was obtained is 0.0205 mm. Comparing these results with those of beams 1, 2 and 3 it can be seen that the maximum bond stress is larger with a smaller slip.

7.5.1. Conclusion

From the above results it may be concluded that the maximum bond stress decreases with the increase of prestressing force in the wire and at a lower slip value. The effect on maximum bond stress due to the variation of steel wire diameters is negligible. For any definite conclusions on large tendons, much more testing with variations of prestress and tendon diameter need to be performed. There are so many

local factors at the steel-concrete interface which need to be investigated, especially for commercial prestressing tendons, if ever bonded. The tests carried out for bond-slip and average maximum bond stress are enough for the present research to be used in the constitutive relationship of Ahmlink linkage element.

7.6. Testing Procedure and Results for the Octagonal Slab

The load was applied in small increments using a hydraulic pump which had four hydraulic jacks as stated in section 7.4.2. connected to it. At each load increment, the readings of the dial gauges and the strain gauges were recorded. In the early stages of the loading larger load increments of 20 KN (0.032 N/mm^2) were applied. At the later stages of loading, smaller load increments of 8 KN (0.01286 N/mm^2) were applied. The bottom part of the slab was painted with whitewash in order to observe the cracks. The part of the slab which was vulnerable to cracking was divided into small 50mm square divisions in order to accurately estimate the positions and propagation of cracks. The slab was examined for cracks at each load increment. As cracks appeared, they were marked with a dark pencil so that they were visible in the mirror placed underneath the slab. A camera was mounted at the corner of the slab to take photographs of the cracks reflected in the mirror.

The total load up to the point of failure of the slab was applied in 53 increments. The results obtained are plotted in the form of load-displacement curves. The experimental load-displacement curve at the centre of the slab for the entire load history is shown in Figure (7.10). The deflected shapes of the slab along two centre lines (i.e. AA and BB) for various loads are shown in Figures (7.11) and (7.12). Photographs of cracks at the bottom surface of the slab were taken at various stages of loading. Photographs 7.7. to 7.9. show crack patterns of the slab at 428 KN (0.17199 N/mm^2) and at failure. The marked cracks at the bottom surface of the slab are shown in Figures (7.13) to (7.17).

The numbers marked on these cracks indicate the load in KN at which these cracks have occurred.

The slab behaved elastically (linear) up to a load of 160 KN (0.0643 N/mm^2). This initial linear behaviour mainly depends on the amount of prestress provided in the slab and the type of boundary supports. The early non-linearity of load-deflection curve (Figure (7.10)) is caused by the flexural cracks at the bottom surface of the slab. The initiation of first such cracks occurred at a load of 180 KN (0.007233 N/mm^2) as shown in Figure (7.13). As the load increased further up to 200 KN (0.0804 N/mm^2) the existing cracks are extended with the addition of some new cracks. The cracks marked at this load are shown in Figure (7.14) and are related to the load-displacement diagram (Figure (7.10)) where a slight deviation in the load-displacement curve has occurred which is due to the loss of stiffness as a result of cracking. This loss is contributed possibly by the reduced load of grouted tendon, ineffective grout and the variable boundary conditions imposed on the slab.

With the further load increments, the existing cracks are enlarged and are joined by the newly developed cracks in the region. Figure (7.15) shows the crack pattern up to the total load of 248 KN (0.09966 N/mm^2). By studying the results shown in this Figure and comparing them with those of Figure (7.13), it becomes clear that the yield lines are beginning to form in the direction of free edges of the slab. At this stage, a large part of the slab has already cracked and the stiffness is lost. The vulnerable load in stages are 200 to 250 KN. This might explain the sudden small depression on the load-displacement curve shown between the load of 200 KN (0.0804 N/mm^2) and 248 KN (0.09966 N/mm^2) as shown in Figure (7.10). This deviation of the load deflection curve is marked as AB in Figure (7.10). At this stage of loading, the displacement of the slab started increasing at a faster rate than before.

As the load increased further, more cracks developed forming additional yield lines. At a load of 280 KN (0.1125 N/mm^2) the crack pattern assumes the form as shown in Figure (7.16). It can be seen from the figure that most of the slab has cracked at this stage and yield lines have formed in the direction of the free edges. As a result of the formation of these cracks, a further degradation in the stiffness of the slab has occurred as shown in Figure (7.10). In this region of loading (marked C in BC region, see Figure (7.10)) large deflections of the slab were observed visually and most of the cracks were clearly visible. With the further increase in load in the region CD in Figure (7.10) the deflection of the slab has occurred due to the rotation of the slab about the yield lines section. As a result, due to large existing cracks additional strains occurred both prestressing and conventional steel. As a result, the rotation of the slab about the yield line occurs and the concrete compressive zone (at the top surface of the slab) is being gradually reduced (point D in Figure (7.10)) and prestressing wires have started yielding. This can also be seen in Figures (7.11) and (7.12) showing as well the deflection profiles along the two centre lines of the slab with increasing loads.

Figure (7.17) shows the crack pattern of the slab just before failure. The figure only indicates the position and the distribution of cracking at the surface of the slab, but it does not show the depth and width of cracks. This can, however, be seen in the photograph taken at failure (Photographs 7.8. and 7.9.). The slab finally failed at the load of 544 KN (0.2186 N/mm^2) where deflections large and beyond the limit of the available deflection measuring gauges.

Table 7.1. Parameters of Bond-Slip Specimen

Beam No.	Diameters (mm)	Amount of Pre-stress (% GUTS)
1	5	75
2	5	75
3	5	75
4	7	75
5	7	75
6	7	75
7	7	65
8	7	65
9	5	65
10	5	65

Table 7.2. Results of Bond Tests

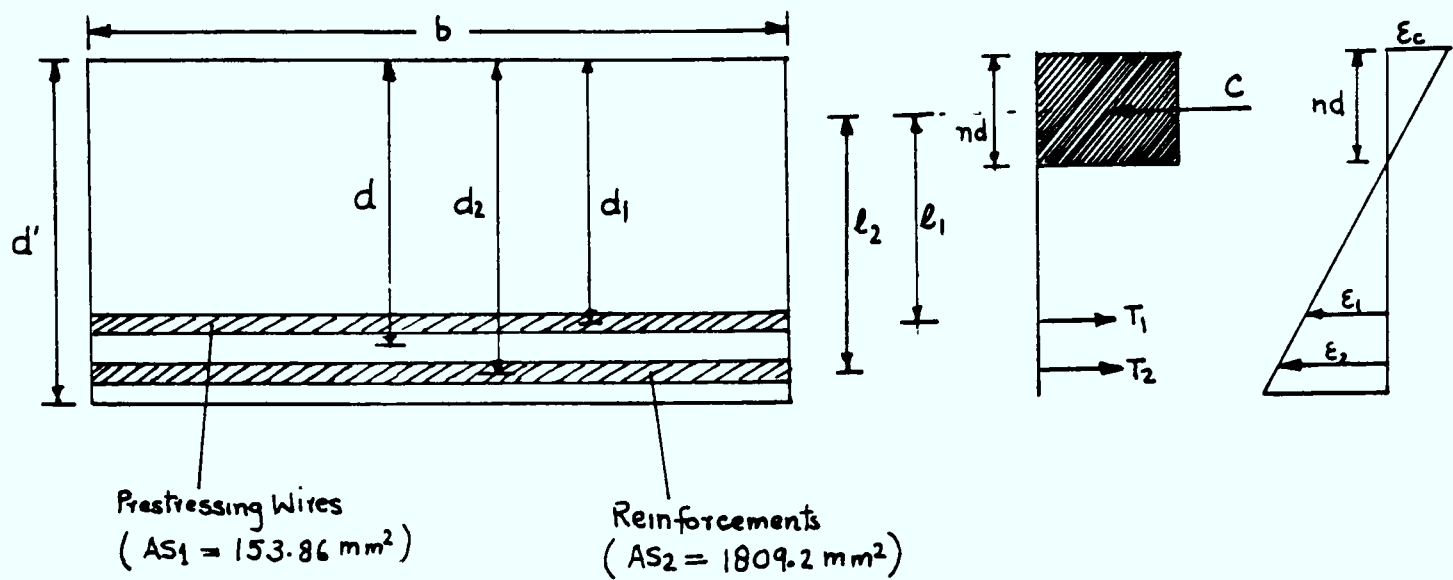
Beam No.	Dia. (mm)	Prestress force (% GUTS)	σ_{bmax} (N/mm ²)	Average σ_{bmax} (N/mm ²)	Slip (mm)	Average slip (mm)	E_h (N/mm ² /mm)	Average E_h (N/mm ² /mm)
1	5	75	1.6]	1.64	0.044]	0.048	380]	473.3
2		75	1.64]		0.052]		540]	
3		75	1.68]		0.05]		500]	
9	5	65	2.2]	2.21	0.019]	0.0205	509]	526.0
10		65	2.22]		0.022]		543]	
4	7	75	1.84]	1.8	0.055]	0.057	510]	523.3
5		75	1.81]		0.065]		520]	
6		75	1.75]		0.052]		540]	
7		65	2.1]		0.026]		466]	
8		65	2.0]		2.05		0.024]	

σ_{bmax} = ultimate (maximum) bond stress

E_h = initial slope or slip modulus

Average value of E_h = 501.4 N/mm²/mm

Table 7.3. Yield Line Analysis



Numerical values :

$$\begin{aligned} \sigma_{cu} &= 45 \text{ N/mm}^2 & d' &= 109 \text{ mm} \\ d_1 &= 72.5 \text{ mm} & d_2 &= 79 \text{ mm} \\ d &= 75.75 \text{ mm} & b &= 1990 \text{ mm} \\ \varepsilon_c &= 0.003 \end{aligned}$$

- nd - depth of neutral axis
- C - compressive force in stress block
- T_1 - tensile force in prestressing steel
- ε_1 - strain in prestressing steel
- ε_2 - strain in reinforcements
- T_2 - tensile force in reinforcements

The value of n is calculated by balancing compressive force in concrete and tensile force in steel, as

$$C = \sum T = T_1 + T_2 \quad (1)$$

$$C = \alpha \sigma_{cu} b n d, \quad \alpha = 0.4$$

$$C = 2.7133 \times 10^6 n$$

From the geometry of the above figure

$$\varepsilon_1 = \left(\frac{d_1}{nd} - 1\right) \varepsilon_c + \left(\frac{45.3}{200 \times 38.46}\right) \text{ -- prestrain in the wire}$$

$$\varepsilon_2 = \left(\frac{d_2}{nd} - 1\right) \varepsilon_c$$

$$\text{for } n = 0.3$$

$$C = 0.814 \times 10^6$$

$$\varepsilon_1 = 0.01245$$

$$\varepsilon_2 = 0.00743$$

From stress strain curves of reinforcements and prestressing wires

$$\sigma_1 = 1568 \text{ N/mm}^2, \quad \sigma_2 = 317 \text{ N/mm}^2$$

$$\text{Therefore } T_1 = \sigma_1 AS_1, \quad T_2 = \sigma_2 AS_2$$

$$T_1 + T_2 = 0.814 \times 10^6$$

So for $n = 0.3$ Equation (1) is satisfied.

$$nd = 22.72 \text{ mm}$$

$$l_1 = 64.13 \text{ mm}, \quad l_2 = 67.64 \text{ mm}$$

Total moment along yield line

$$\begin{aligned} M_{y1} &= \sigma_1 AS_1 l_1 + \sigma_2 AS_2 l_2 \\ &= 54.27 \times 10^6 \text{ N-mm} \end{aligned} \quad (2)$$

The external moment is calculated due to external loads as shown in the figure overleaf

$$M_{ex} = \frac{W}{2} Y_o - \frac{W}{2} Y_c,$$

$$= 161.6 W \text{ N-mm}$$

W = total load

$$Y_o = 701.3 \text{ mm}, \quad Y_c = 378 \text{ mm}$$

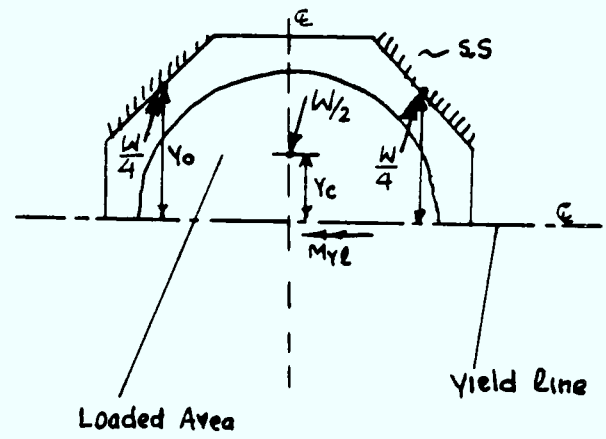
$$(3)$$

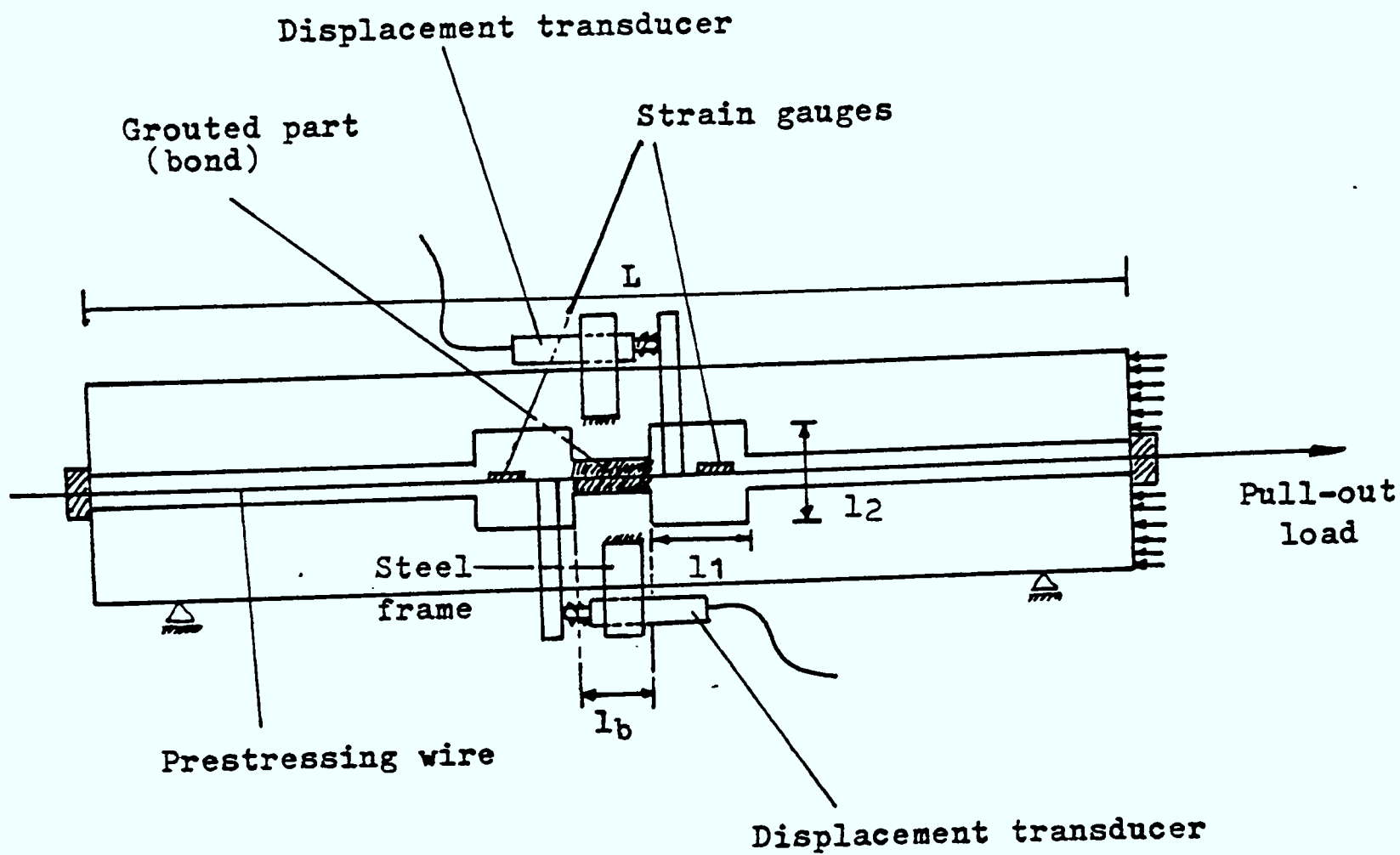
Equate (2) and (3)

$$161.6 W = 54.27 \times 10^6$$

$$W = 336 \text{ KN}$$

Total load = 336 KN





DIMENSIONS:

$L = 1000.0$ mm

$l_b = 38.0$ mm

$l_1 = 76.0$ mm

$l_2 = 38.0$ mm

Figure 7.1 Details of Prestressed Concrete Pull-Out Specimen

Dimensions :
 $a=820$ mm
 $b=1990$ mm
 $c=940$ mm
 $c_1=115$ mm
 $c_2=350$ mm
 $t=109$ mm
 $t_1=18$ mm
 $t_2=22$ mm
 $t_3=37$ mm
 $t_4=55$ mm

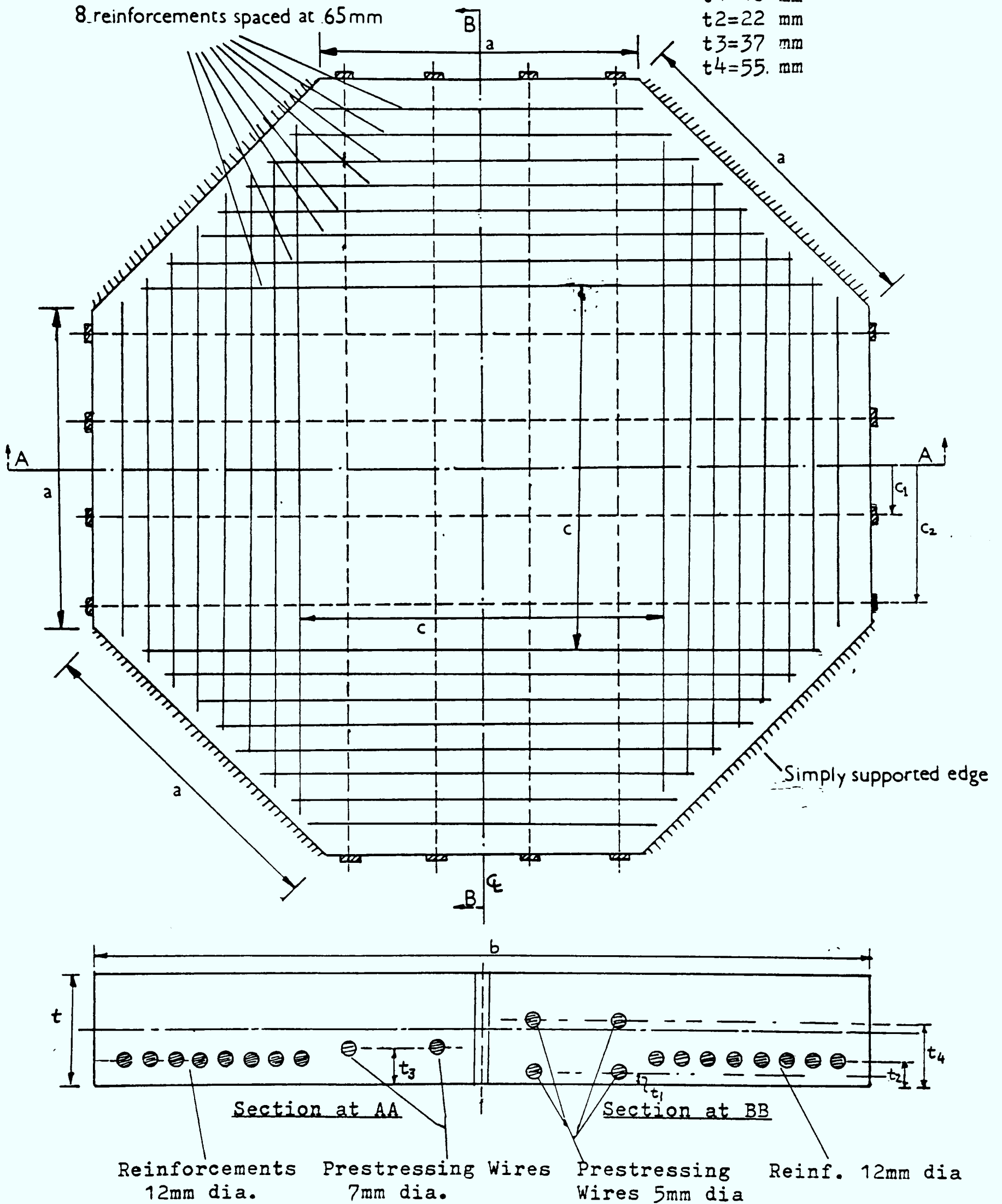


Figure 7.2 Details of Prestressed Concrete Slab

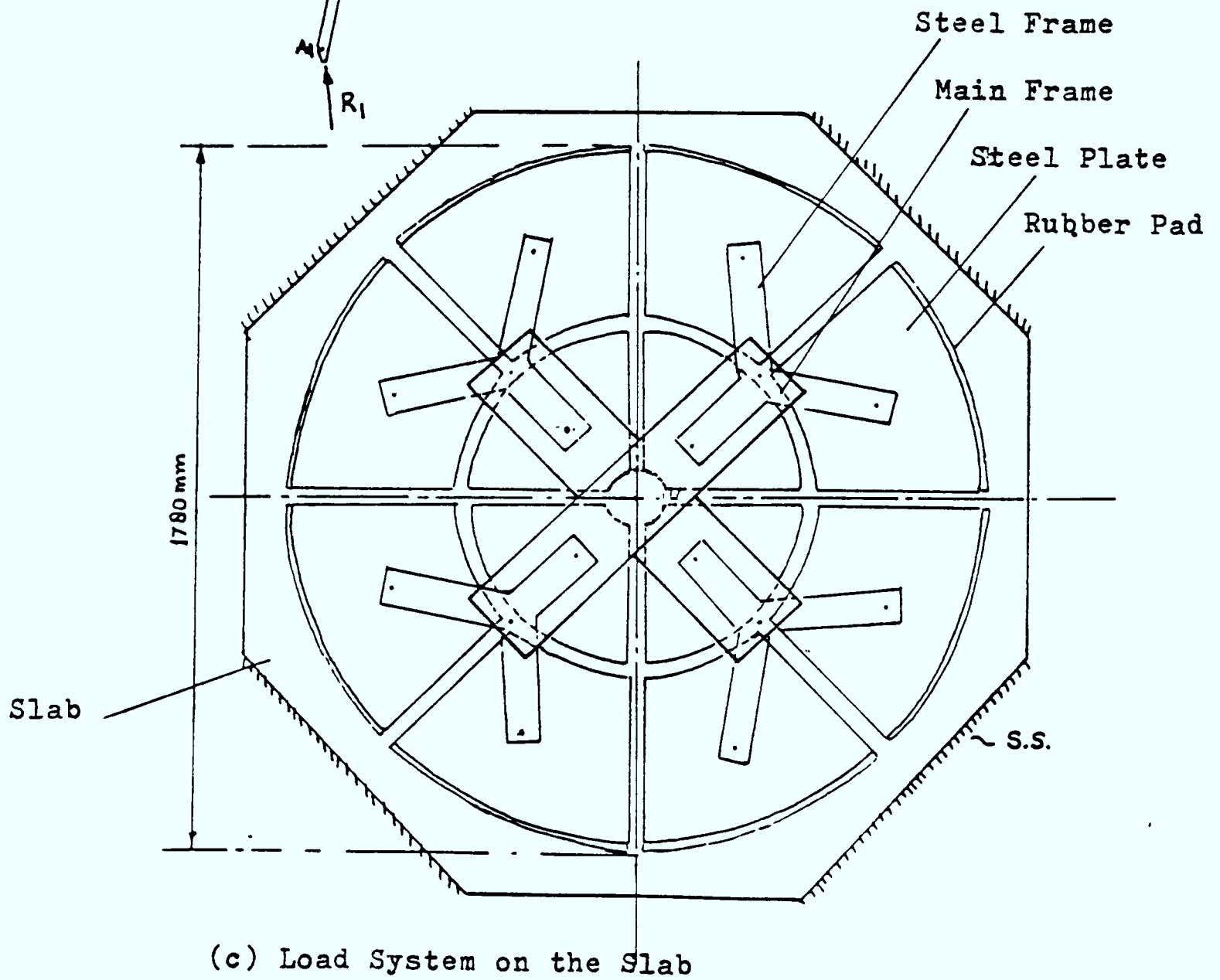
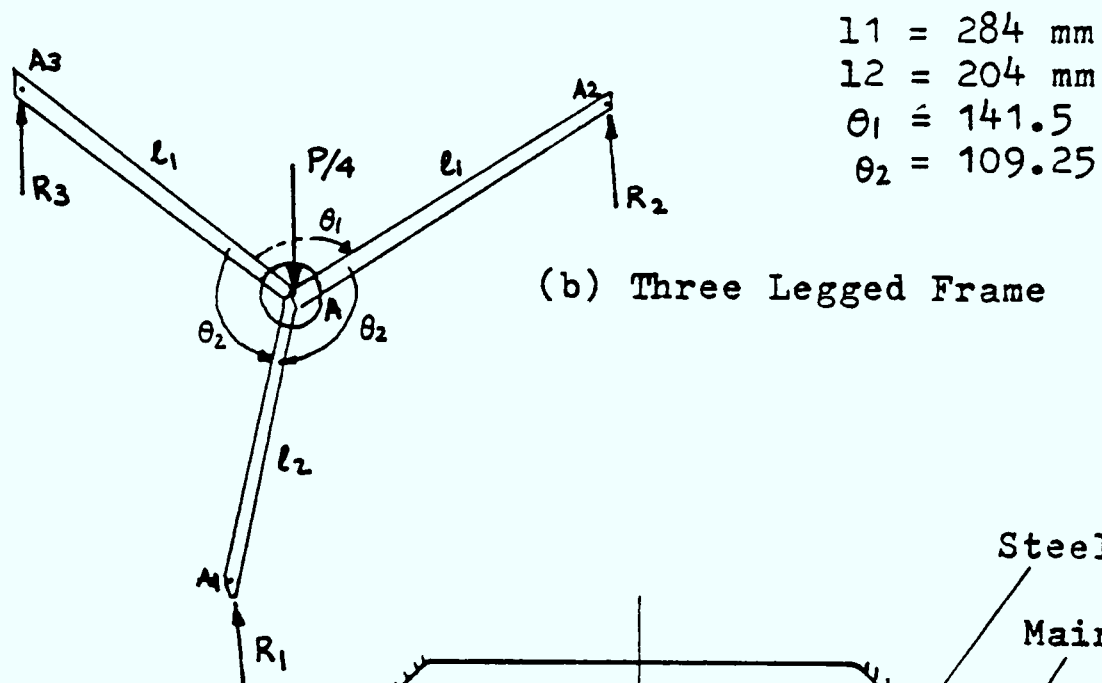
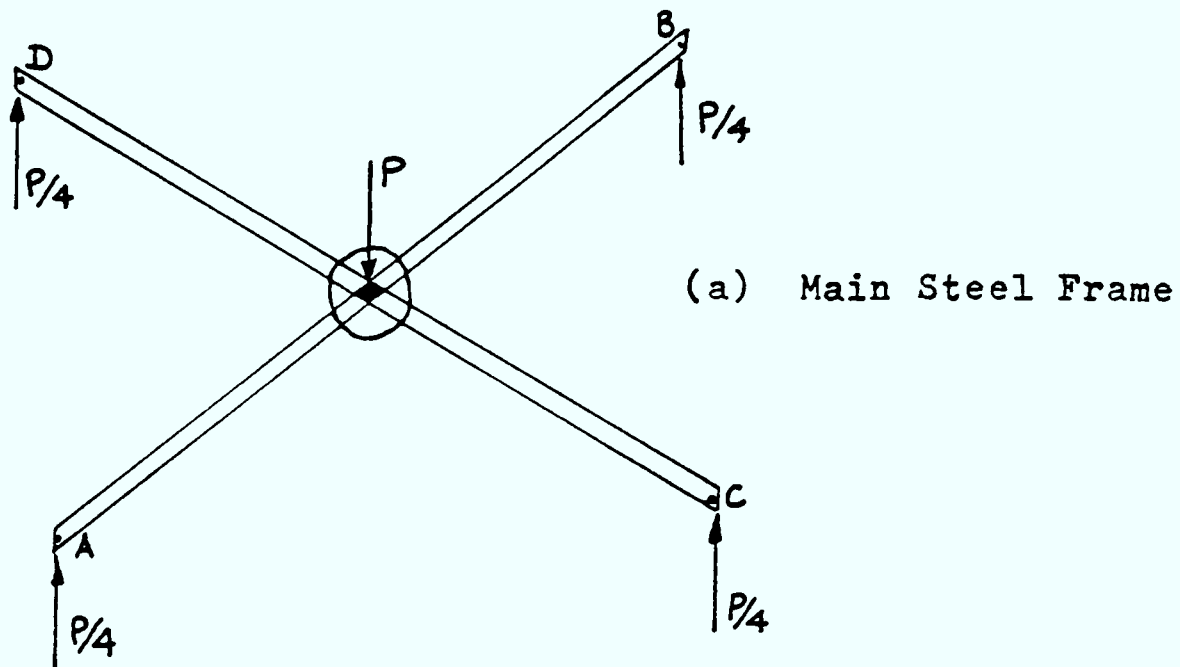


Figure 7.3 Load System of the Rig

○ - Dial Gauge

All Dimensions in mm

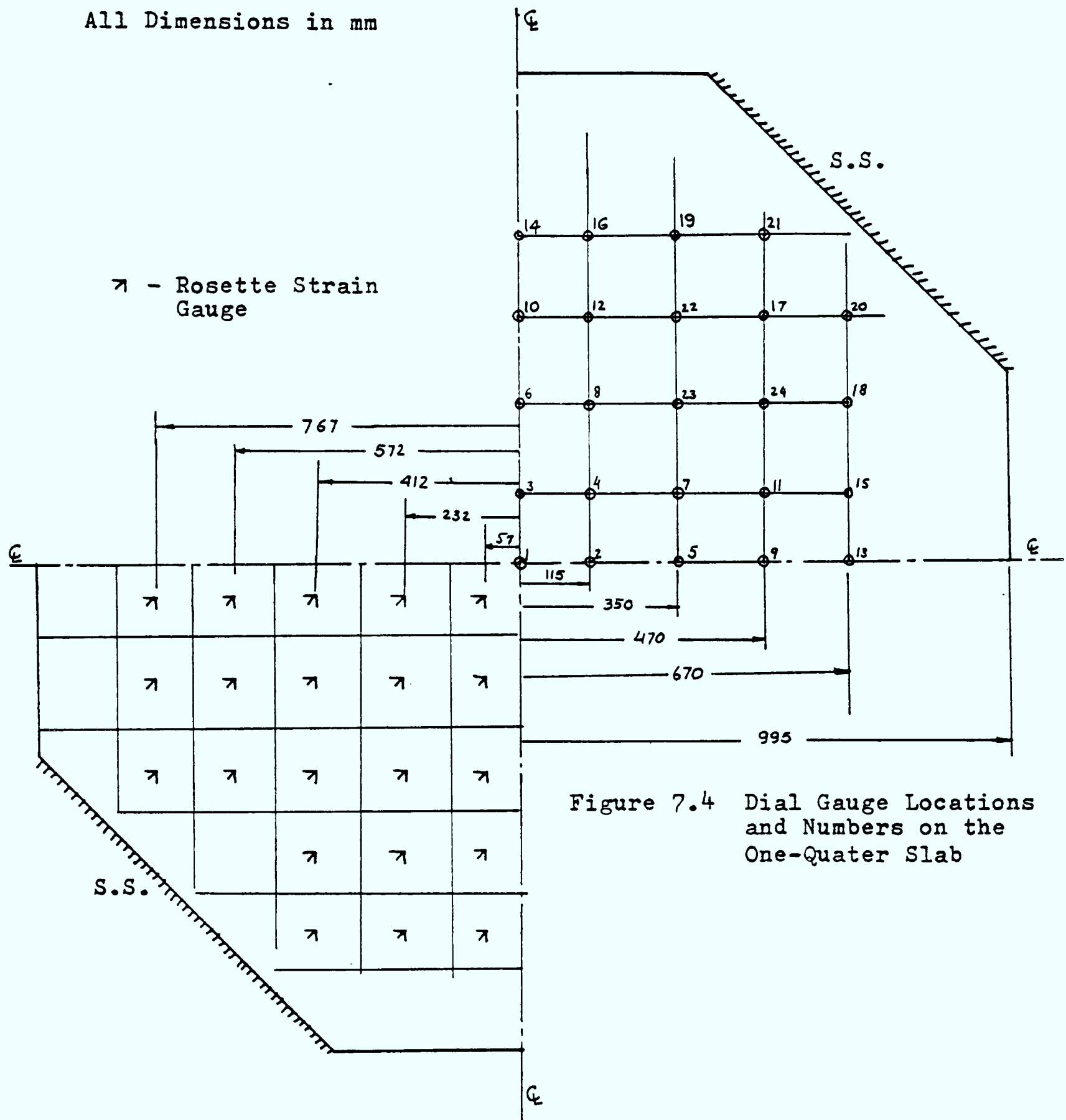


Figure 7.4a Rosette Strain Gauge Locations on the One-Quarter Slab

All Dimensions in mm

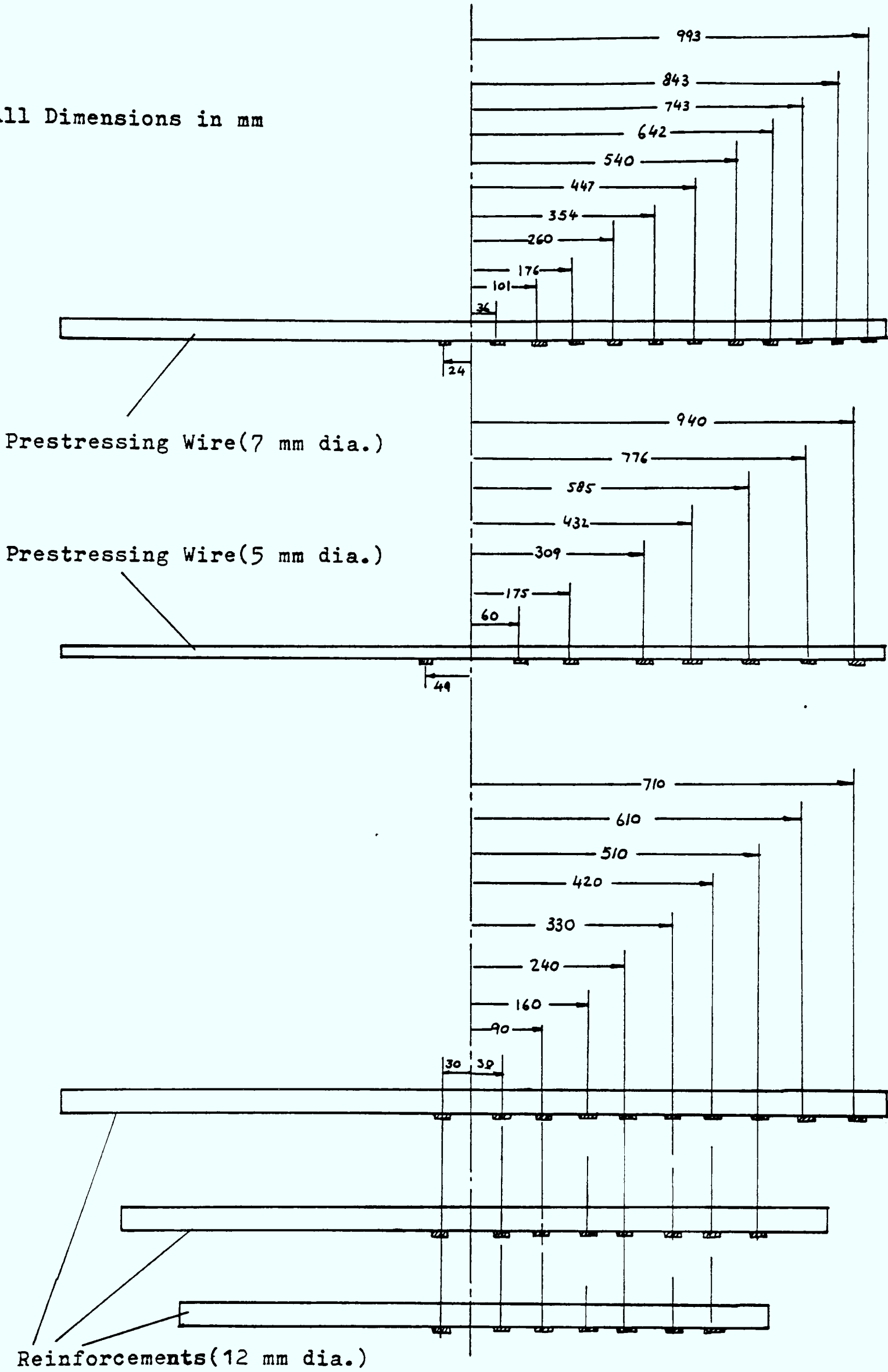


Figure 7.5 Strain Gauge Positions on Prestressing Wires and Reinforcements

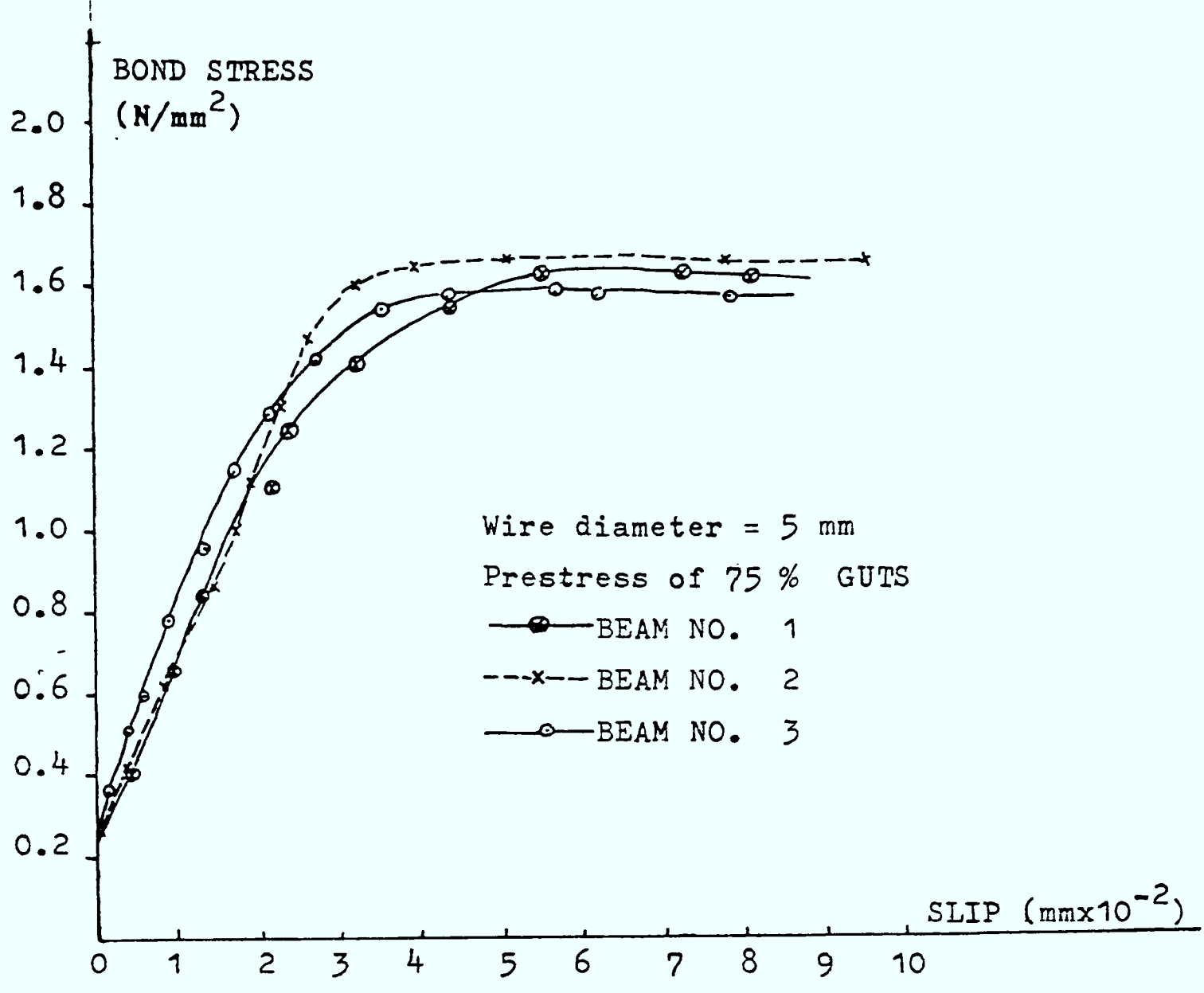


Figure 7.6 Experimental Bond Stress-Slip Curve of 5 mm Diameter Prestressing Wire

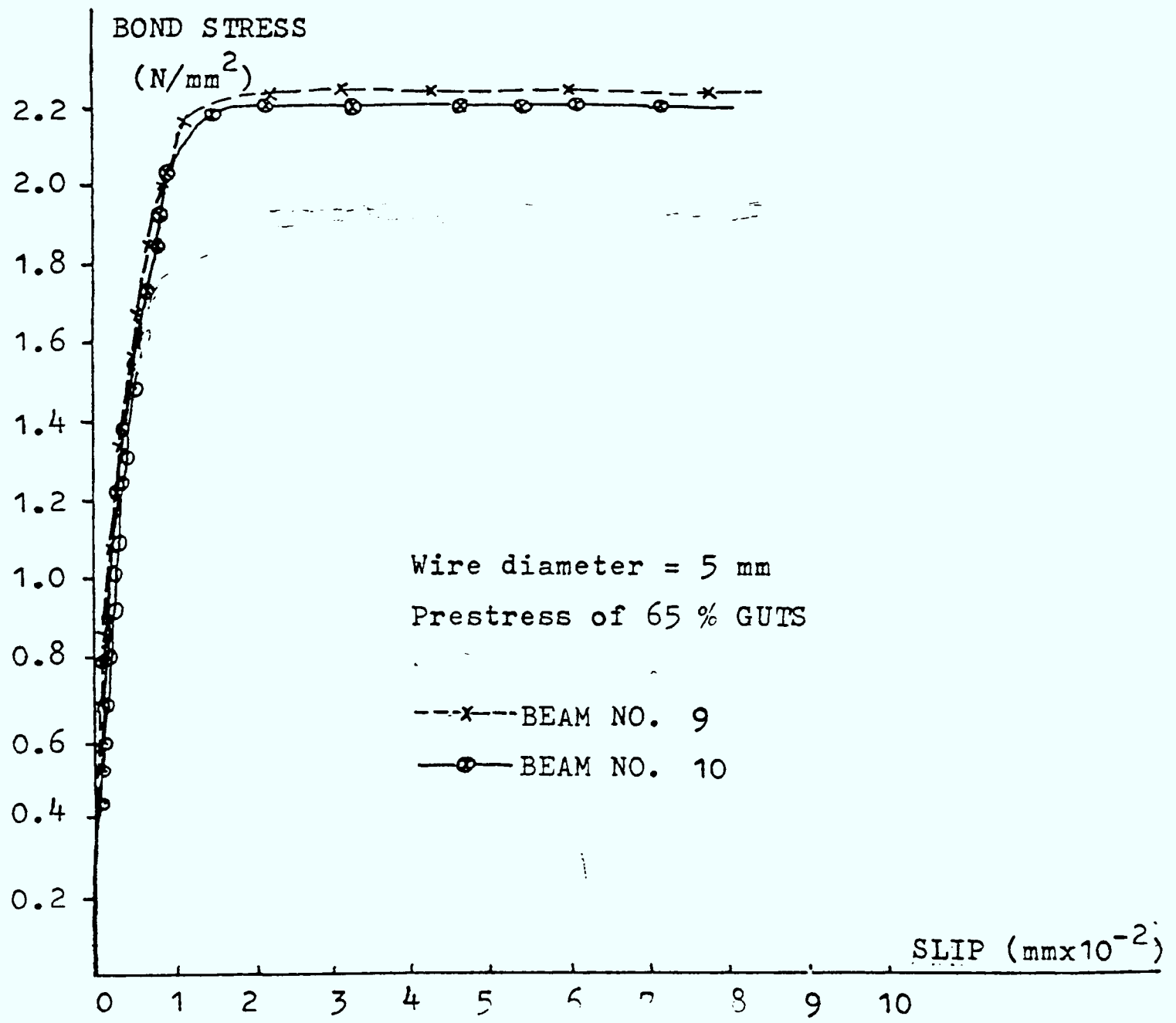


Figure 7.7 Experimental Bond Stress-Slip Curve of 5 mm Diameter Prestressing Wire

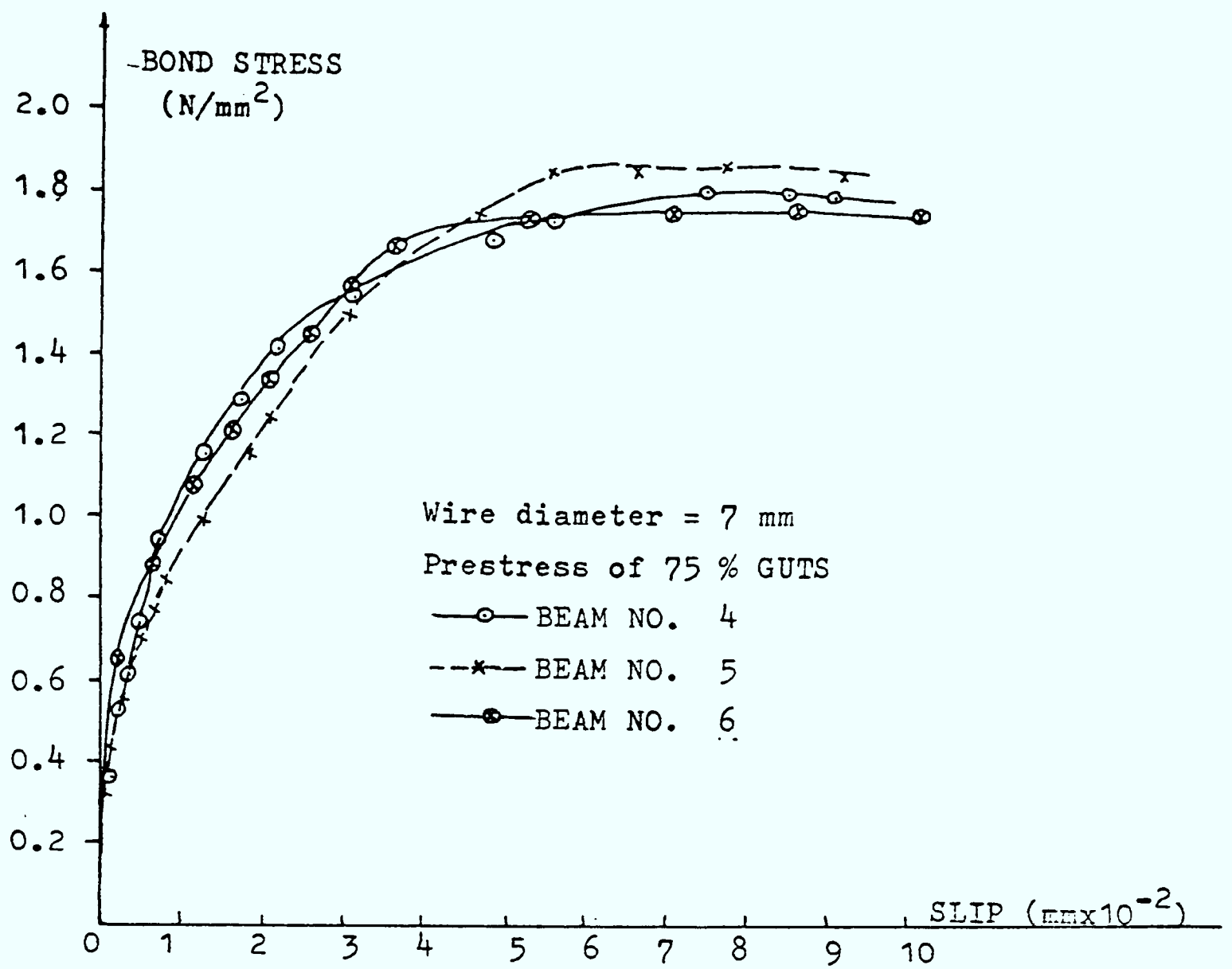


Figure 7.8 Experimental Bond Stress-Slip Curve of 7 mm Diameter Prestressing Wire

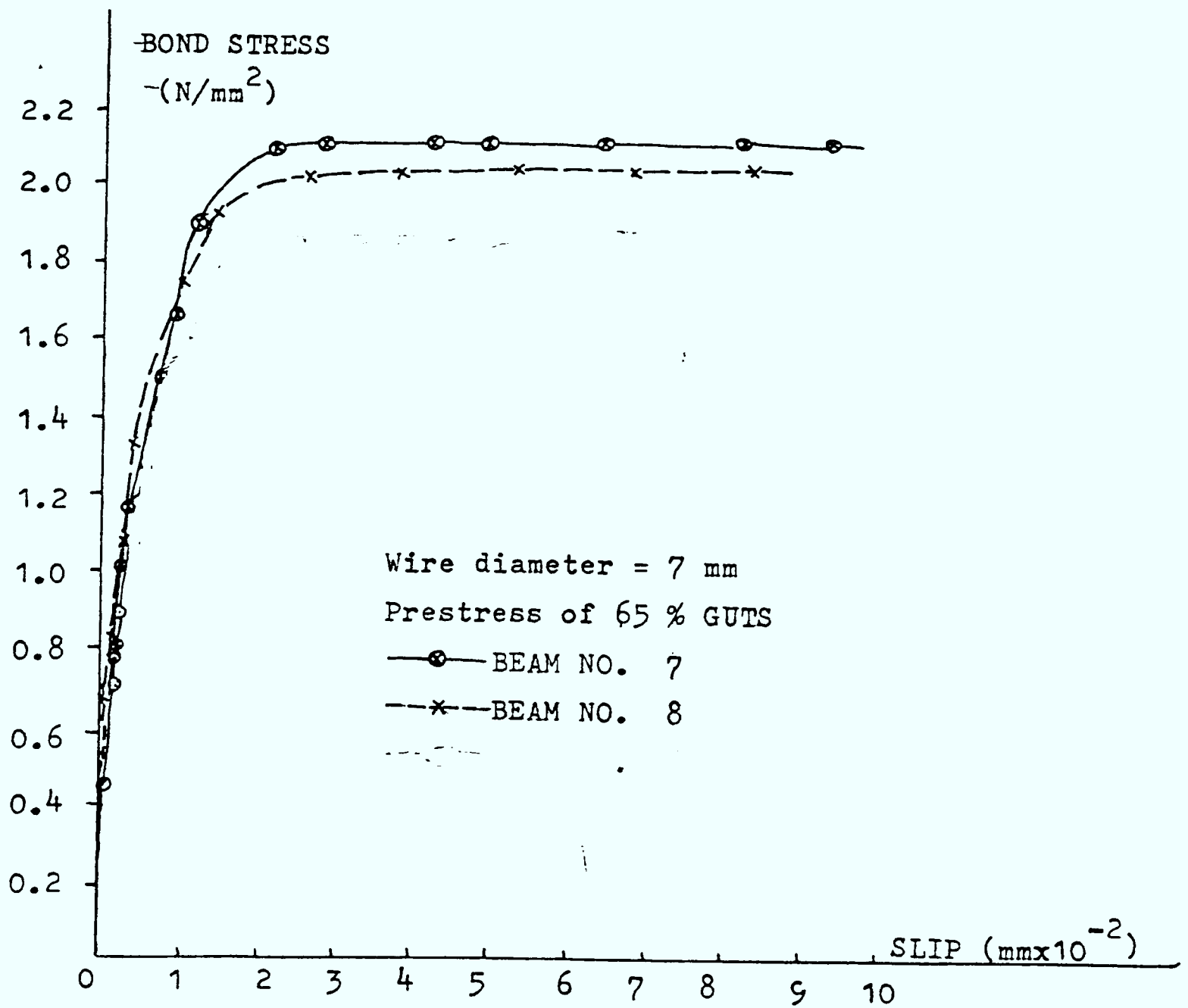


Figure 7.9 Experimental Bond Stress-Slip Curve of 7 mm Diameter Prestressing Wire

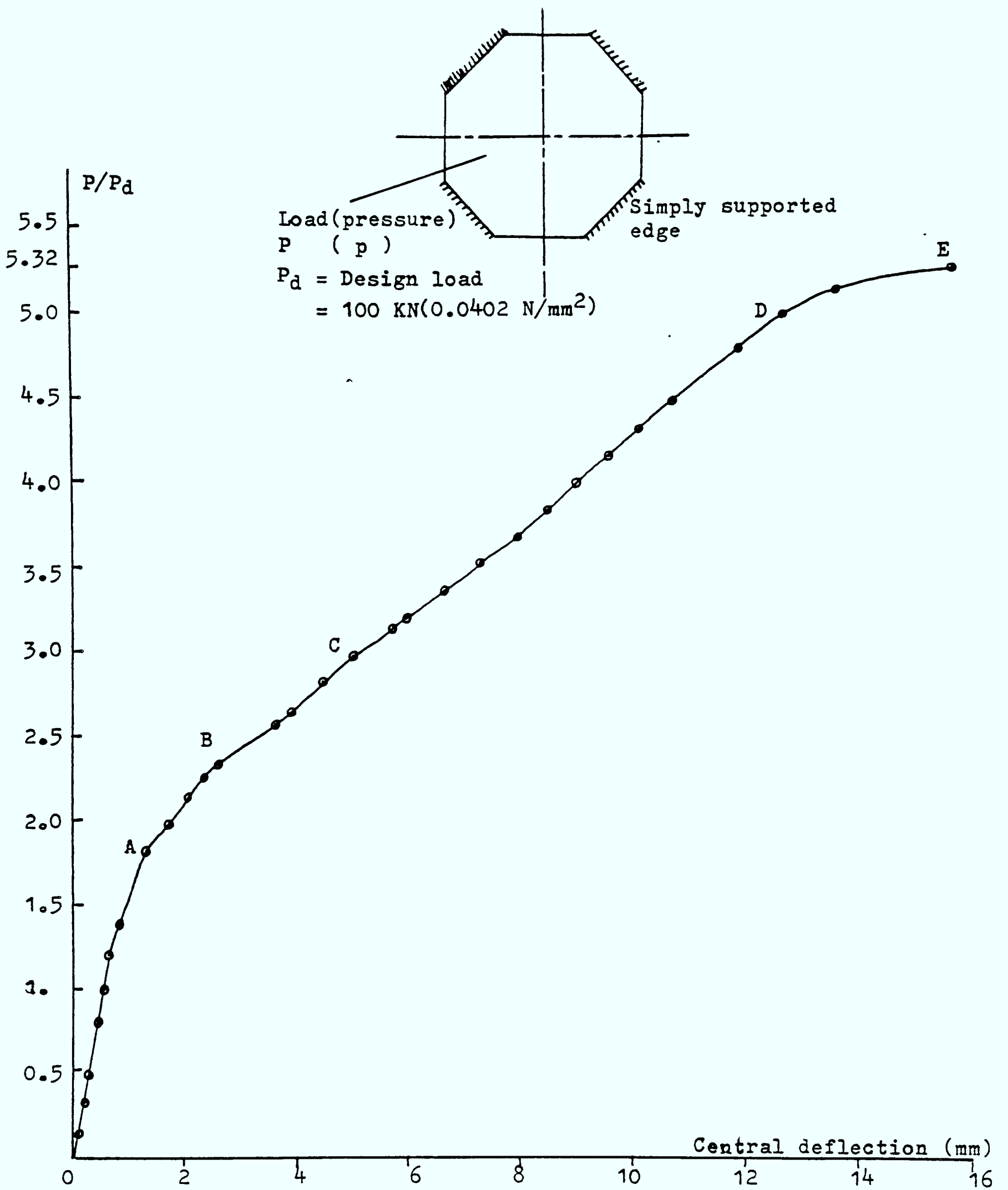


Figure 7.10 Experimental Load-Displacement Curve of the Octagonal Prestressed Concrete Slab

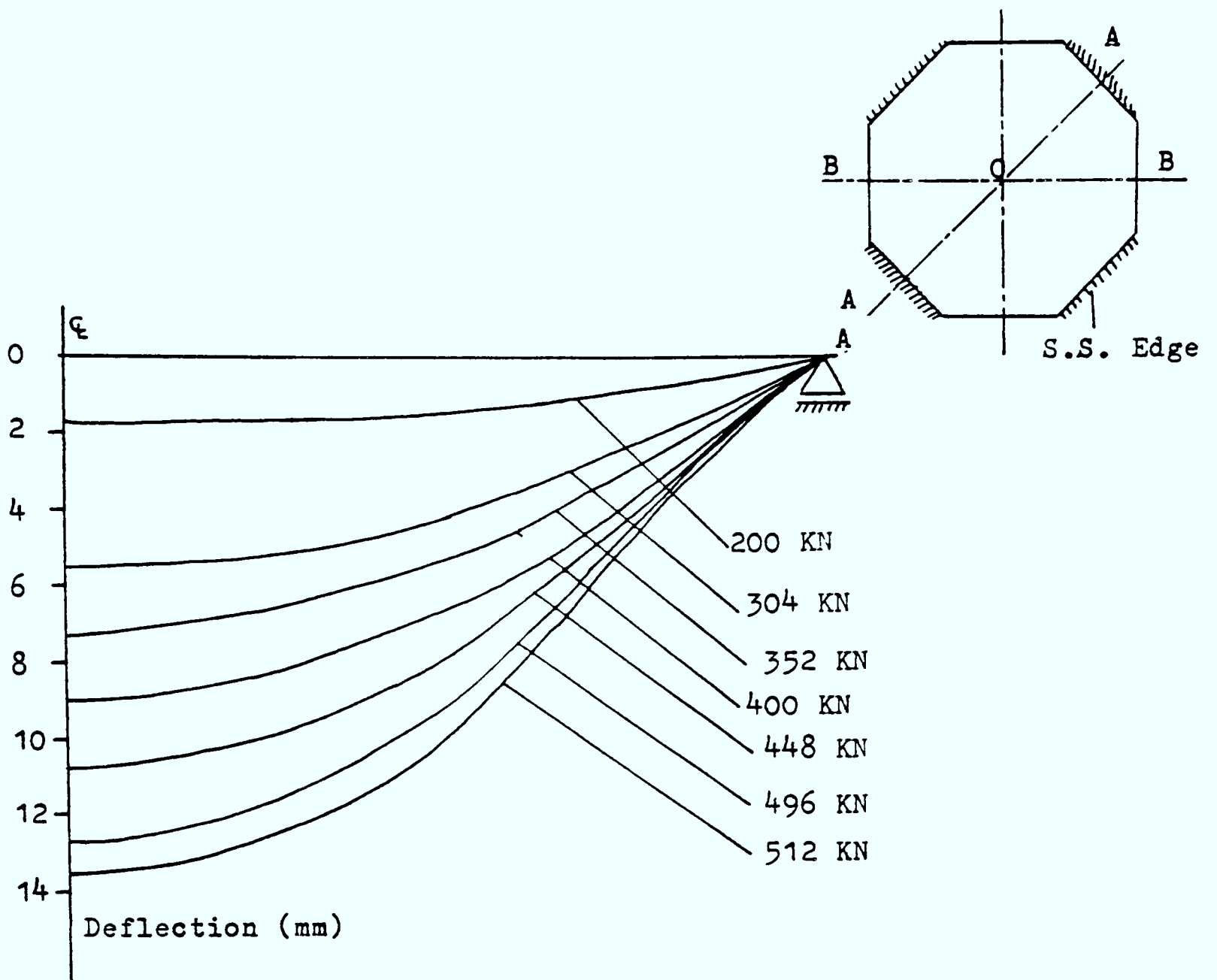


Figure 7.11 Experimental Deflected Shapes Along AA

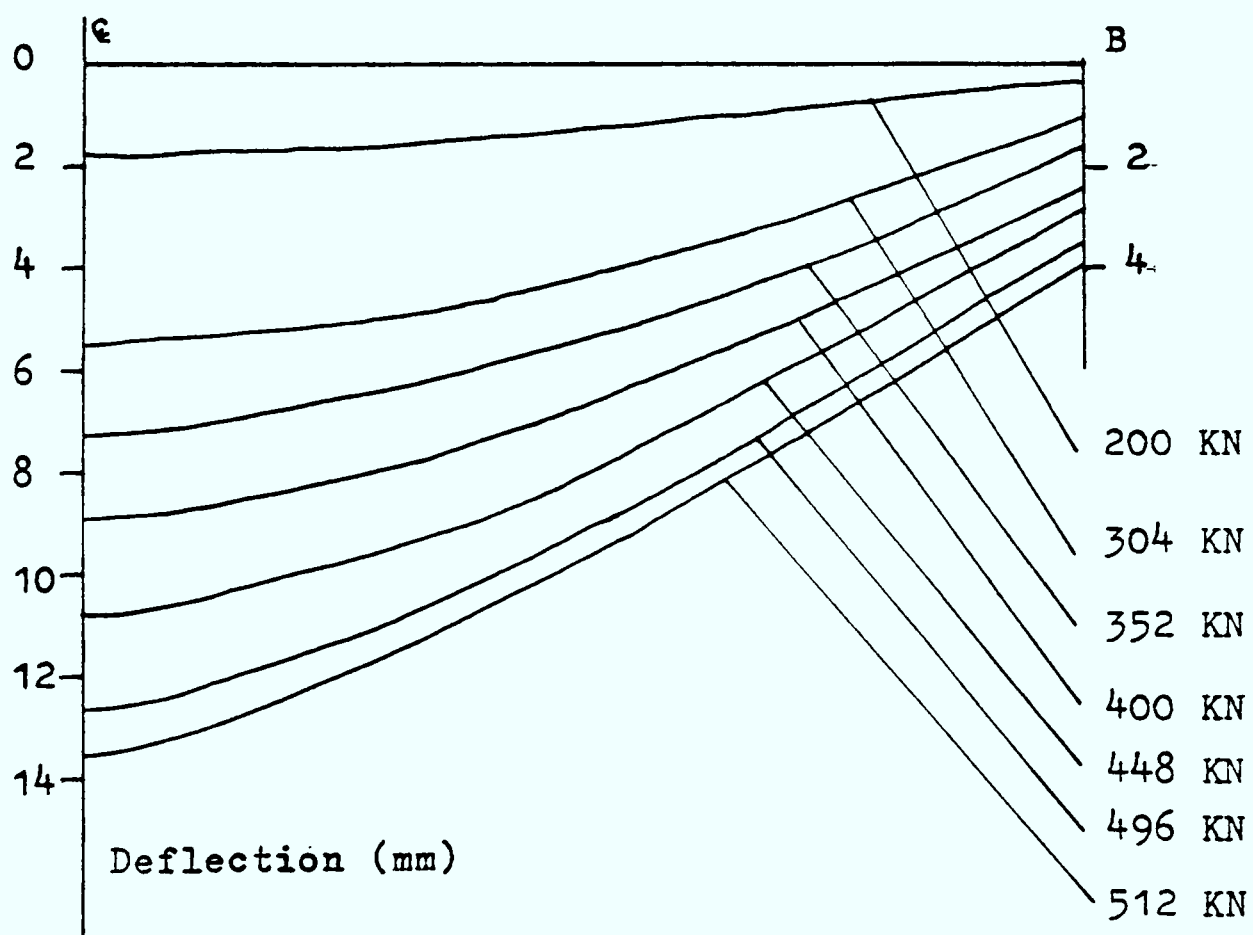


Figure 7.12 Experimental Deflected Shapes Along BB

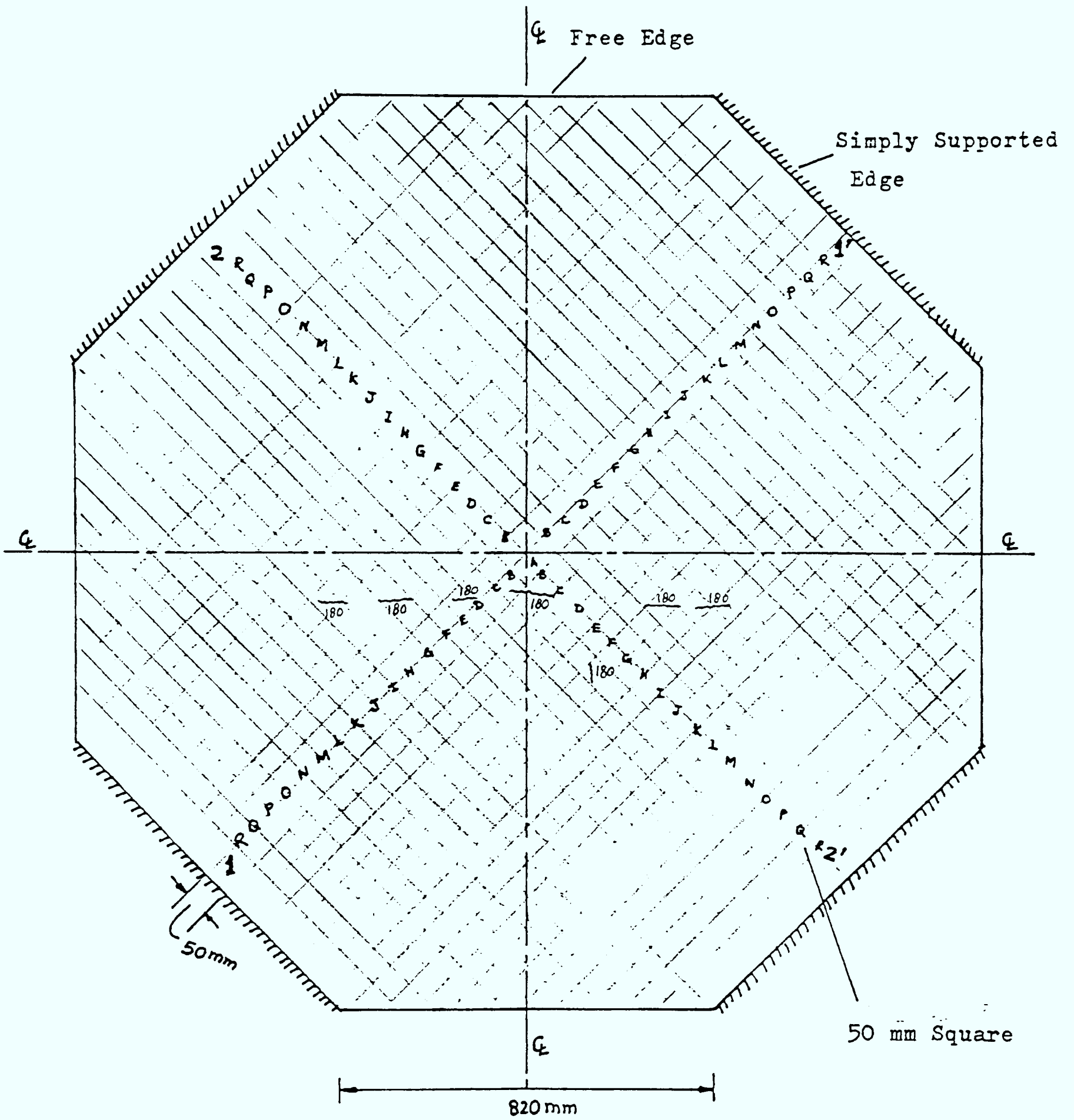


Figure 7.13 Experimental Cracks at the Bottom Surface of the Slab
 (Upto the Total Load of 180KN(0.0723 N/mm²))

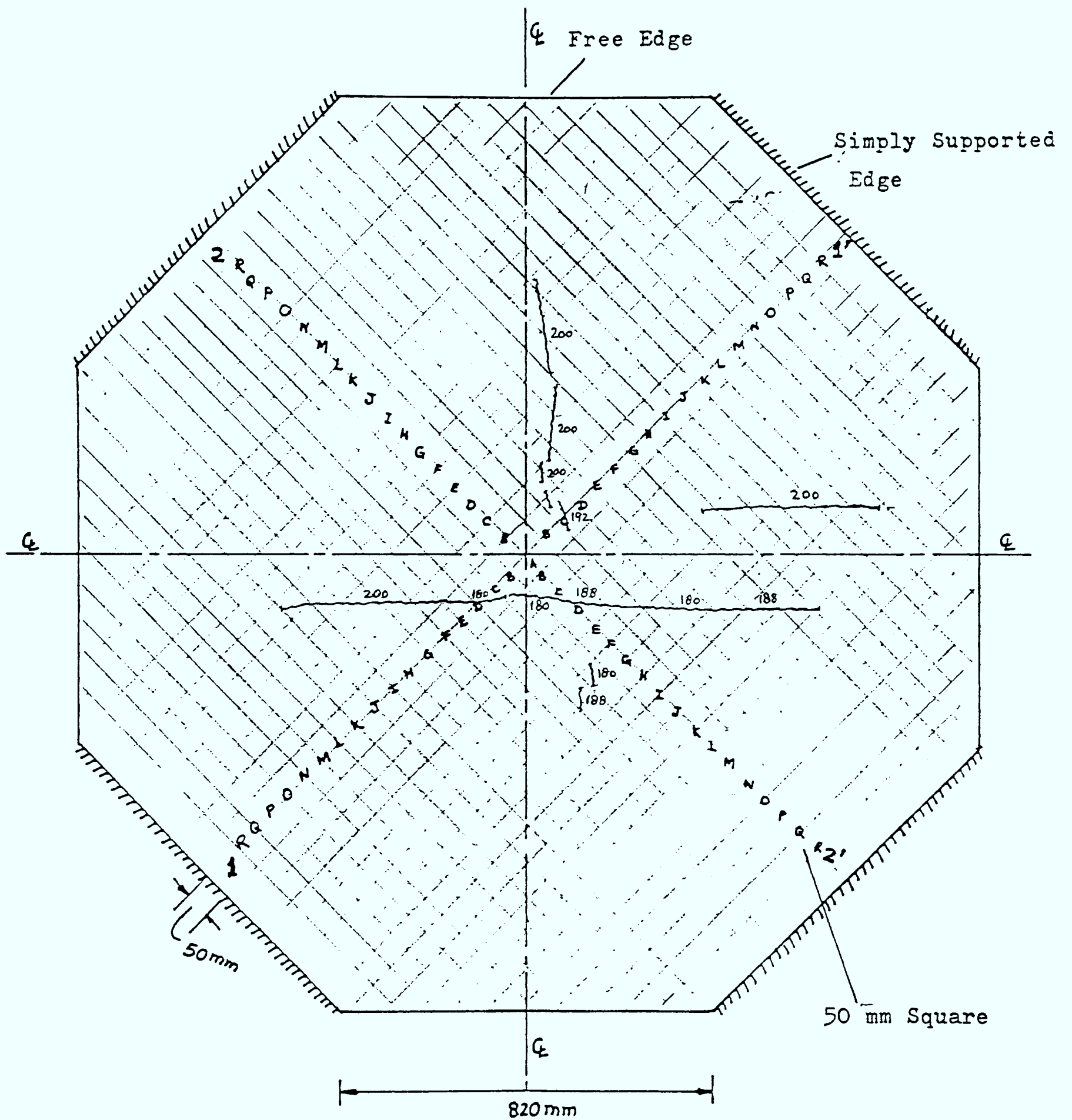


Figure 7.14 Experimental Cracks at the Bottom Surface of the Slab
 (Upto the Total Load of 200KN(0.0803 N/mm²))

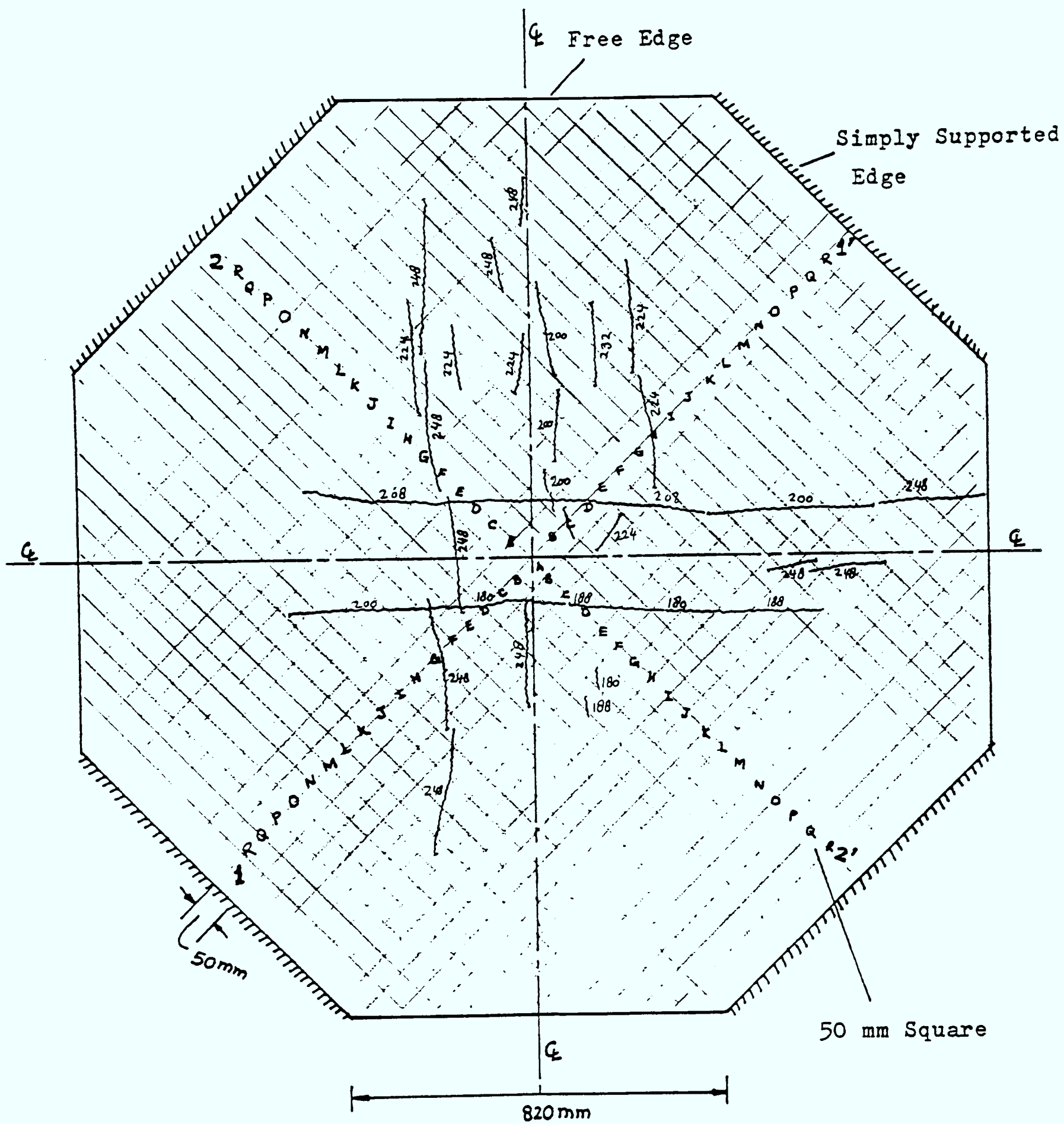


Figure 7.15 Experimental Cracks at the Bottom Surface of the Slab (Upto the Total Load of 248KN(0.0996 N/mm^2))

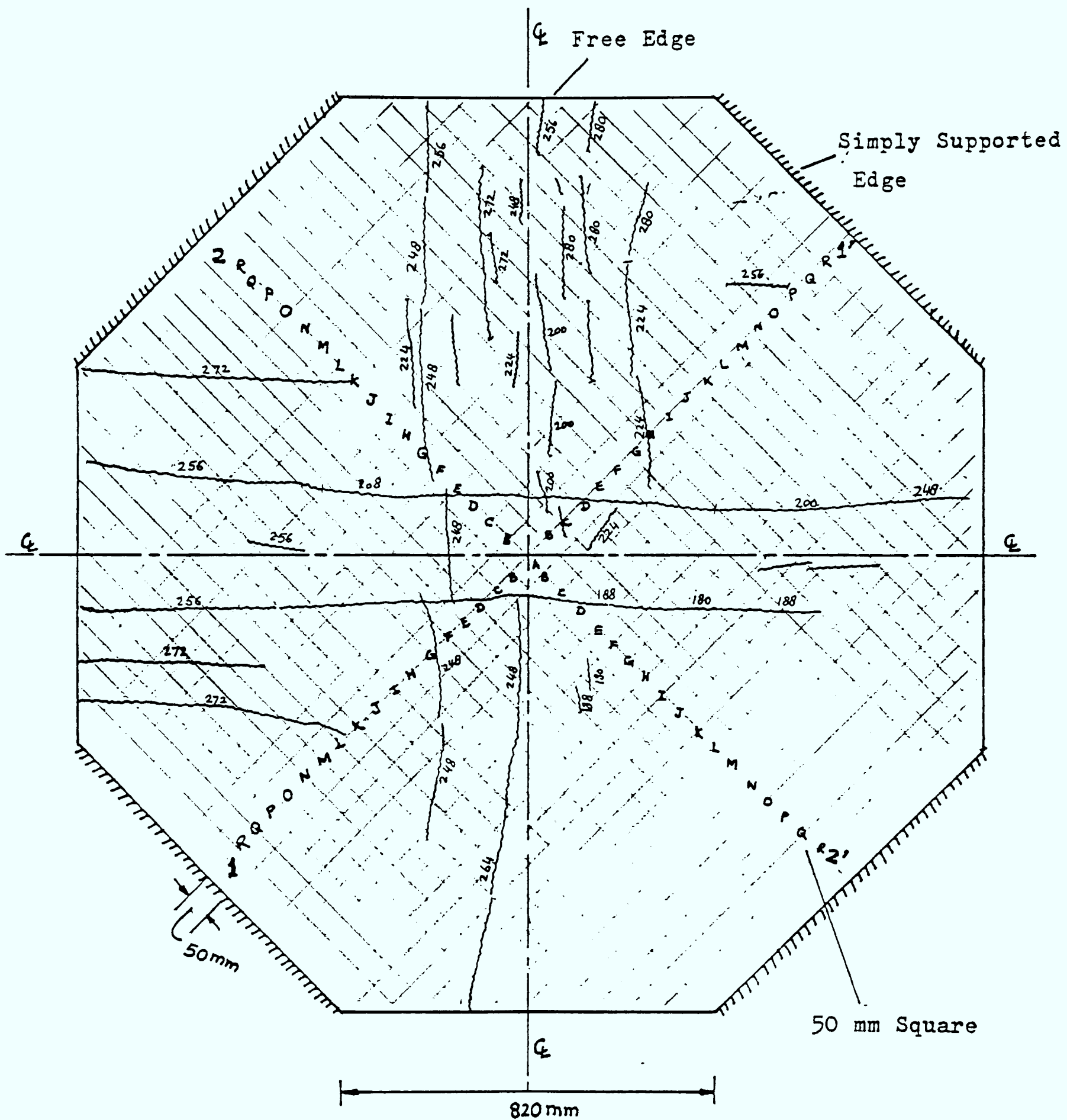


Figure 7.16 Experimental Cracks at the Bottom Surface of the Slab
 (Upto the Total Load of 280KN (0.1125 N/mm^2))

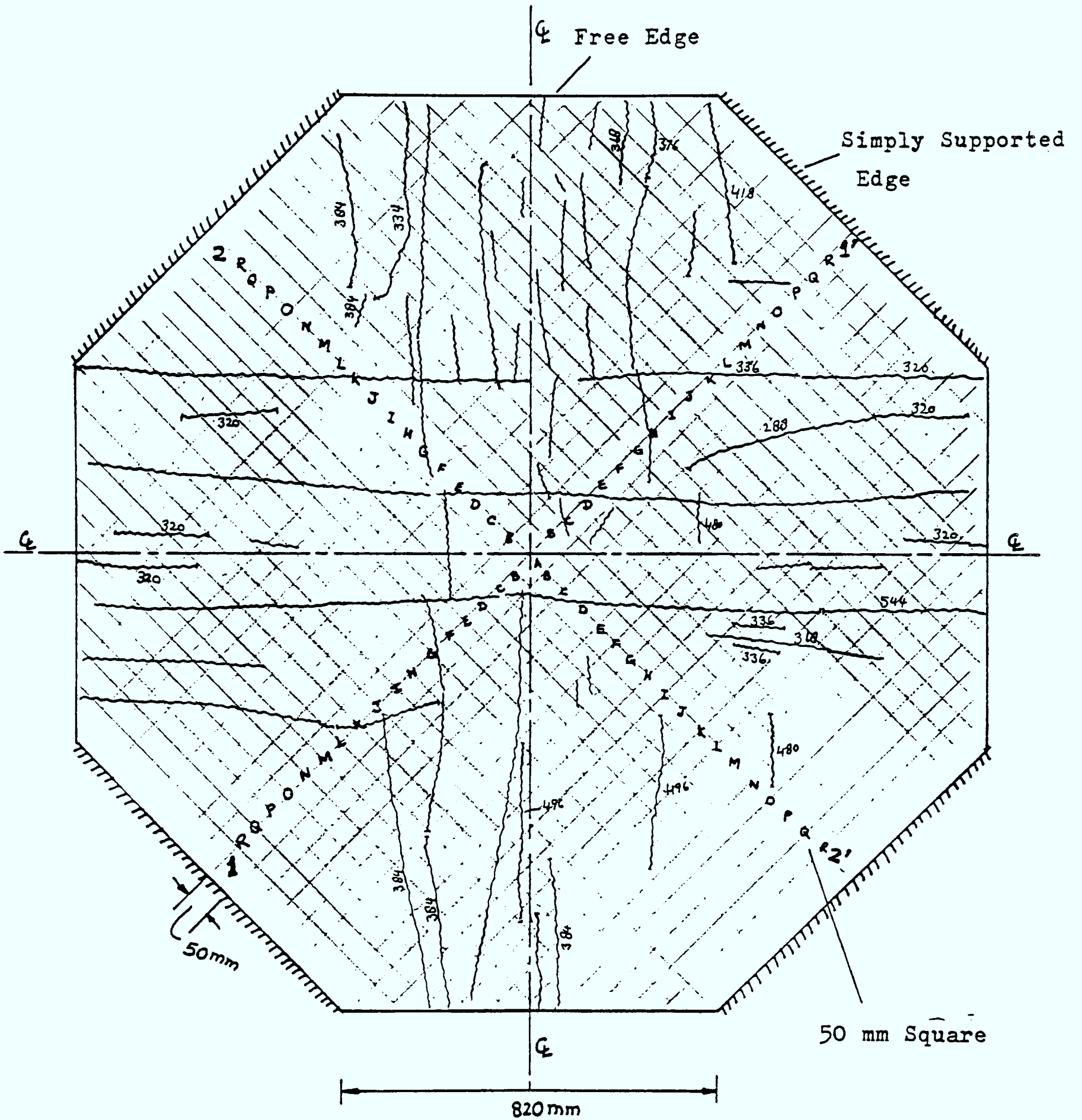


Figure 7.17 Experimental Cracks at the Bottom Surface of the Slab just Before Failure

CHAPTER 8

Comparative Study of Results

8.1. Introduction

In this Chapter, the numerical analysis of various problems is carried out using the proposed analytical model. Two main problems are considered. The first problem is the prestressed concrete octagonal slab (see Chapter 7). The slab given in Chapter 7 is of an octagonal shape and is post-tensioned with prestressing wires. The prestressing wires are bonded. Two types of analyses of bonded slab are performed. In the first, the bond between the steel and concrete is considered by a specially developed linkage element, whereby slip between the steel and concrete is allowed. The second analysis assumes a perfect bond (i.e. no slip between the steel and concrete). Both these analyses on the slab are 8 noded solid and 2 noded axial line elements. The analytical results from both these analyses have been compared with those from the experimental results.

Greater confidence is obtained by validating the analytical tool on this slab. This work is then taken further and is applied to various cases of prestressed concrete reactor vessels.

The vessel under consideration is stressed vertically by means of longitudinal tendons and circumferentially by means of wire/strand winding. These tendons may or may not be bonded. Three cases of vessel analysis are performed, namely unbonded, bonded and perfectly bonded. For bonded vessel, the bond between the tendon and concrete is represented by linkage elements. For perfectly bonded vessel, a rigid bond between the tendon and concrete is assumed. For unbonded vessel, there is no bond between the tendon and concrete and the load is transferred through anchorages. In all cases the vessel is modelled by 20 noded solid, 8 noded membrane and 3 noded line axial elements to

represent vessel concrete, liner and prestressing tendons respectively. The vessel for above three cases is analysed under both normal operation (up to 40 years of vessel creep) and with gas increasing pressure up to the point of failure. Deformed shapes, load-displacement diagrams, crack patterns and safety margins have been obtained for all the above mentioned cases.

8.2. Validation of Program NSARVE using Simple Problems

The validity of the finite element computer program NSARVE has been tested on a number of problems. The main purpose is to demonstrate the accuracy of the theoretical model and to test various facilities provided within the program NSARVE. Linear, materially non-linear, thermal and creep analyses are tested using different formulations, elements and material models available in the program. The numerical results obtained are compared with analytical and published data. The representative test examples are briefly given in Appendix B1.2.

8.3. Analysis of the Octagonal Prestressed Concrete Slab

8.3.1. General Information

Details of the experimental results for this slab are given in Chapter 7. Figure (7.2.) gives the main dimensions of the slab together with the positions and locations of prestressing wires and ordinary reinforcements. The wires are stressed up to 75% of the guaranteed ultimate tensile strength (GUTS) and are grouted. The slab is now treated as bonded and is simply supported on four edges as shown in Figure (8.8.). The slab has been analysed using three-dimensional finite element program NSARVE given in Chapter 6. The analytical results have been given for the following three cases :

- Case I Bonded Prestressed Concrete Slab - the interface behaviour between the steel and concrete is modelled using Linkage (Ahmlink) Element
- Case II Perfectly Bonded Prestressed Concrete Slab - the steel element is placed on one side of the solid element and a perfect (rigid) bond is assumed between the two
- Case III Unbonded Prestressed Concrete Slab - the steel elements are not included in the analysis but their prestress forces are included in the analysis of slab

All loads due to prestressing are treated as uniform pressures on four opposite edges of the slab. The pressure, after taking into consideration various prestressing losses, is 1.89 N/mm^2 . The applied load on the top surface of the slab is also treated as uniform pressure. A total load at failure from the experiment is 544 KN (0.2186 N/mm^2).

8.3.2. Finite Element Meshes, Geometry and Material Data

Due to symmetry, only one-quarter of the slab is analysed (Figure (8.8a)). This slab is restrained from moving in Y direction along AB (i.e. $v = 0$) and in X direction along AC (i.e. $u = 0$). The centre point A is restrained in both the X and Y directions (i.e. $u = 0$, $v = 0$). The edge DE is supported in the Z direction (i.e. $w = 0$). Figure (8.8a) shows these boundary conditions. The finite element mesh of one-quarter of the slab with element dimensions is shown in Figure (8.8b). The choice of this mesh is made so that the prestressing wires and reinforcements are to lie on the sides of the solid elements. The nodes of solid elements and line elements are connected either by Ahmlink elements for bonded slab or by rigidly interconnected for perfectly bonded slab. Where a large amount of ordinary reinforcement is closely spaced in the slab, they are modelled as line elements in the body of the solid elements. Such elements are shown as broken lines in Figure (8.8b). Two solid elements are chosen through the thickness of the slab. The line elements are placed at an effective depth of 72.5 mm

(Figure 8.8b). The details of finite element meshes for three different cases are given below :

Case I : Bonded Slab

The slab concrete is modelled using 8 noded isoparametric solid elements, the reinforcements and prestressing wires are modelled using 2 noded axial line elements and the bond between the steel and concrete is modelled using 2 noded Ahmlink elements. Figure (8.9.) shows the finite element mesh for this case only. The mesh comprises 60 solid isoparametric elements, 48 line elements, 28 Ahmlink elements and 40 body axial line elements (these are shown as broken lines in Figure (8.9.)). The nodes for steel and concrete are represented by different numbers, although they occupy the same points in space. The Ahmlink elements (joining steel and concrete) are located at nodal points along the steel-concrete interfaces. Figure (8.9.) shows the Ahmlink elements connected to solid elements. Here, solid element nodes 26, 29, 47 and 50 are connected to the line element nodes 130, 131, 137 and 138 through the Ahmlink elements. Node numbers 26 and 130, 29 and 131, 47 and 137 and 50 and 138 have the same coordinates in space. There are a total 150 nodes and 450 degrees of freedom for this case.

Case II : Perfectly Bonded Slab

Finite element mesh for this case is shown in Figure (8.10). The mesh is similar to the bonded slab case except that Ahmlink elements are replaced by traditional line elements rigidly placed on solid elements. It is assumed to have a perfect bond between the solid element and the line element. The steel line elements are assumed to lie along the sides of solid element sharing the same nodes (Figure (8.10)). The finite element mesh for this case comprises 60 isoparametric solid elements, 48 line elements and 40 body axial line elements. There are total 126 nodes and 378 degrees of freedom.

Case III : Unbonded Slab

In this case the line elements representing prestressing steel are not included in this analysis since they are unbonded. The finite element mesh (Figure 8.10) in this case is identical to the case of perfectly bonded slab except that here the line elements representing prestressing wires are excluded. The finite element mesh comprises 60 isoparametric solid elements representing concrete, 24 axial line elements and 40 body axial line elements representing ordinary reinforcements. There are total 126 nodes and 378 degrees of freedom.

Table 8.1. gives the details of geometric and material property data for the slab. The stiffness properties of bond-linkage elements (see Chapter 3, Equations (3.30) and (3.32b)) are obtained from the experimental tests described in Chapter 7. A local bond stress-slip curve for 7 mm of wire (Figure (8.11)) is a mean curve obtained from the statistics of the experimental curves. Fifteen points are taken on the bond slip curve and they are assumed to be joined by linear lines. The bond stress-slip relations for these 15 points are taken as an input for the program NSARVE. The program has the flexibility to take other types of bond-slip curves. The instructions to prepare data deck for program NSARVE are given in Appendix B1.

8.3.3. Discussions on the Analyses and Results

As mentioned earlier that the slab has been analysed for three different cases, namely bonded, perfectly bonded and unbonded cases. The total load (pressure) on the slab has been applied in 11 increments. The first load increment is due to prestress applied on the edges of the slab. The second increment and onwards are due to the transverse pressure applied on the top surface of the slab. These pressures are given below :

prestress (N/mm^2) : 1.89
pressures (N/mm^2) : 0.0603, 0.0804, 0.1005, 0.1206, 0.1407, 0.1608,
0.1809, 0.201, 0.2074, 0.2138

For each load increment, iterations are performed to correct the equilibrium. A maximum of 12 iterations per increment are allowed and iterations are generally terminated when the Euclidian norm of the residual loads becomes less than the specified tolerance ($\text{Tol} = 3 \times 10^{-2}$). The constant stiffness option (Initial Stress Method) is employed for all cases. The orthotropic concrete model in compression and tension cut-off model for cracking of concrete and elasto-plastic model with strain hardening for steel (Chapter 4) have been adopted throughout.

The results obtained from these analyses are plotted in the form of load-displacement curves, crack patterns and deflected shapes as shown in Figures (8.12) to (8.18). Cracking of concrete has a particularly strong influence on the behaviour of the slab. Figure (8.12) shows the load-central deflection history of the slab. The experimental curve is also shown for comparison. It is seen that the predicted results for three cases compare favourably with the experimental results. These curves show that they are in very good agreement in the early stage of loading (between 180 kN (0.0723 N/mm^2) to 280 kN (0.112 N/mm^2)). At this stage most of the cracking takes place. There is a slight disagreement between the computed load-deflection curve and the experimental curve between the load range of 300 kN (0.1205 N/mm^2) to 450 kN (0.18 N/mm^2). This is due to the facts described in Chapter 7. The ultimate load computed from the analysis is less than the experimental failure load. The difference between the two is roughly 2.2%. These variations are due to assumptions built into the analysis and probability of variations of material data and boundary conditions. In the analysis very large displacements are predicted at load level of 544 kN indicating the collapse of the slab. The computed crack distribution of the slab for various load levels are plotted in Figures (8.17) and (8.18) for bonded and fully bonded slab cases respectively. Comparing these two cases, there seems to be close

relationship in certain areas. These crack patterns have also been compared with experimentally obtained crack patterns as shown in Figures (7.13), (7.16) and (7.17). At a load of 200 KN (0.0803 N/mm^2) the cracks have formed along the two centre lines of the slab which compares favourably well with the experimental cracks. At load of 280 KN a large part of the slab is cracked and between 280 KN and 336 KN practically the whole bottom surface of the slab is cracked as can be seen in Figures (8.17) and (7.16) and (7.17). The comparison between the computed and the experimental crack patterns is reasonably good. The analytical results only show the position and the direction of cracking which is based on the principal directions of the stress state. Nevertheless, they do not show the sizes of cracks.

The crack patterns of the slab from the analysis may be related to the load-displacement curve of Figure (8.12). Initially the slab is linear (elastic) up to the load of 150 KN (0.602 N/mm^2) when the first set of cracks developed at a load level of 200 KN (0.0803 N/mm^2) the curve has deviated slightly from its linear path. At load of 280 KN (0.1125 N/mm^2), as a result of more cracking, the curve deviates further due to the loss of stiffness. When load reached at 336 KN (0.135 N/mm^2) a large part of the slab has cracked already in two directions indicating further loss of stiffness which is clear from Figure (8.12). Thereafter, the curve is almost linear (between 336 KN to 450 KN) indicating the widening of the existing cracks up to the point when yielding of steel starts. After that, the slab has failed due to excessive cracking producing large deflections.

By making the comparison of load-deflection curve (Figure (8.12)) for the above mentioned three cases, namely bonded, perfectly bonded and unbonded cases, it is clear that the results are almost identical in the early stage of loading. As soon as sufficient cracks are developed in the slab, the results from perfectly bonded analysis are rather higher than the bonded and unbonded analyses. This would be expected, since in the perfectly bonded analyses the steel and the concrete is assumed to be rigidly connected, which allows no slip between the steel and the concrete

The difference in the ultimate strength of the two cases is about 1.4%. In addition, the third case of unbonded slab has also been analysed for comparison. The computed ultimate load is reasonably close to the other two analyses, but the computed displacements at the ultimate load are much too large. This reason is explained earlier. Figures (8.13) and (8.14) illustrate the deflected shapes along the two centre lines of the slab. The computed and the experimental deflected shapes are in close agreement. Figure (8.15) shows the maximum steel stress (reinforcement and prestressing tendon) as a function of applied load as computed from the analysis.

7 A re-analysis has been carried out for the above two cases I and II. The bonded slab in case I is analysed this time with smaller load increments. The total number of 18 increments has been adopted using the initial stress method and equilibrium iterations. A further sophistication in results has been achieved and the results are in good agreement with those from the experiment. With smaller increments within the total range of the same load, large deflections, as expected, have been computed. Although the ultimate load of the analysis is taken to be the same as the experimental load, but the deflections in comparison are much too large. It is seen that there is a depression in the load-deflection curve for load level of 250 KN to 350 KN. With the small load increments the results do show the depression in the nearby region which could not be observed by using large load increments. In case II, the slab has been analysed using incremental approach with no iterations. In this case, the stiffness matrix is updated according to the Newton Raphson method. The results of this incremental method are shown in Figure (8.12). It can be seen from the figure that the ultimate load for this analysis is highly overestimated, while the deflections at ultimate load are much too small. The ultimate strength of the slab for this case has been overestimated by 11%. The reason is gathered from the fact that because of no iterations, the released stresses as a result of this cracking are not redistributed to the surrounding material. This assumed case is normally adopted for approximate analysis and gives much higher results.

8.4. Analyses of the Prestressed Concrete Reactor Vessel

8.4.1. Objective of the Analyses

The purpose of the present analyses is to predict the structural response of the prestressed concrete reactor vessel (Figure 8.19) under increasing gas pressure up to the point of failure at various stages of its life. The influence of creep on the normal operational condition up to 40 years of vessel life is also investigated. The vessel is analysed for three cases, namely bonded, perfectly bonded and unbonded. Analyses will be expected to predict short and long-term stress distribution, load-displacement curves, crack patterns and safety margins for such vessels. It is intended to examine and compare these results and to assess the structural integrity of both bonded and unbonded vessels.

8.4.2. General Introduction of the Vessel

A High Temperature Gas-Cooled Reactor (HTGCR) Vessel is chosen for the analysis as shown in Figure (8.19). The Prestressed Concrete Reactor Vessel (PCRVR) is a multicavity thick-walled cylindrical concrete structure with an external diameter of 24.5 m and overall height of 32.31 m. The main pressure cavity (core cavity) is 11.21 m in diameter and 21.946 m high and contains the reactor core and its shielding. The wall contains eight equally spaced vertical cavities for the boilers (steam generators) of 3.048 m diameter. They are linked by radial gas ducts to the top and bottom of the main cavity. All cavities are lined with a 19.0 mm thick continuous steel liner. The PCRVR is prestressed by two post-tensioning systems. The prestress force in the circumferential direction is provided by the wire/strand winding system. The BBRV system was used for the vertical prestressing of the PCRVR. Each vertical tendon has a guaranteed ultimate tensile strength of 9.75 mN. These tendons may be grouted (bonded) or left ungrouted (unbonded) for the reasons discussed elsewhere.

8.4.3. Finite Element Meshes and Vessel Data

Due to symmetry only 1/16th part ($22\frac{1}{2}^\circ$ wedge) of the vessel is analysed. Only the top half of the vessel is considered for the analysis. Boundary conditions as shown in Figure (8.24) are applied in order to maintain three-dimensional symmetry. The vessel is restrained from moving in Y direction along AB and in Y' direction along CD. Inclined or skew boundary conditions are applied along CD which are also fully discussed in Appendix A. At the mid-height of the vessel along EF, the vessel is restrained from moving in Z direction. Finite element meshes of $22\frac{1}{2}^\circ$ wedge of the vessel are described below.

I Bonded Vessel with Ahmlink Element

The vessel concrete is modelled using 20 noded isoparametric solid elements and the steel liner is modelled using 8 noded isoparametric membrane elements. The prestressing tendons are modelled using 3 noded line elements. The line elements are also used as body line elements within the solid elements. The bond-slip behaviour at the steel and concrete interface is represented by using Ahmlink elements. Figure (8.20) shows the finite element mesh for this case. The mesh is generated using the FEMGEN preprocessor. The instructions to prepare finite element meshes are given in the FEMGEN User Manual (155). A detailed finite mesh of the same vessel with element and node numbers at various levels is given in Figure (8.21). The mesh comprises 62 solid isoparametric elements, 32 membrane elements, 72 line elements, 36 line elements in the body of the solid elements and 156 Ahmlink elements. There are a total of 632 nodes and 1896 degrees of freedom for this case.

II Unbonded and Perfectly Bonded Vessel

Figure (8.22) shows the three-dimensional finite element mesh of the unbonded and perfectly bonded vessels. For perfectly bonded vessels, the prestressing tendons are assumed to lie along the sides

of the solid elements sharing the same nodes or they are modelled inside the solid elements. Both cases represent a perfect bond between the vessel concrete and the tendons. A detailed finite element mesh element, together with node numbers at various levels is given in Figure (8.23). The mesh comprises 62 solid elements representing vessel concrete, 32 membrane elements representing the steel liner, 72 line elements and 36 body axial line elements, representing the tendons. The total number of nodes and degrees of freedom are 472 and 1428 respectively.

The finite element mesh for the unbonded vessel is the same as for perfectly bonded vessels, except the vessel tendons at various mesh levels are not taken into consideration.

Full details of geometric and material data of this vessel are given in Table 8.2. The stiffness properties of bond-linkage elements (Chapter 3, Equations (3.30) and (3.32)) are obtained from the experimental bond-slip curves of 12.5 mm strand. The local bond stress-slip curves for 12.5 mm ($\frac{1}{2}$ ") strand are due to Edward and Picard (90) and are given in Chapter 2 (Figure (2.4.))

Very little difference has been found in the stress strain behaviour of strands used in the Dungeness B model tests (156) and the tendons adopted in the vessel for the Dungeness B station (the same tendons are used for the vessel under consideration). Hence bond-slip curves for strands obtained from these results are thus assumed to be identical to Dungeness B vessel tendons if bonded.

An average local bond stress-slip curve with 23 points joined by straight lines as shown in Figure (8.25) are used in the analysis. These points are input to the program NSARVE and are given in Table 8.2. However, the computer program is flexible enough to include any other bond-slip data.

The solid elements are integrated using 3x2x3 integration rule, the membrane elements by 2x2 integration rule and the line elements by 4 point integration rule. Figure (7.27c) shows the main dimensions of the finite element mesh and the Gauss point locations.

The loading conditions in the PCRV are idealised as follows.

- (a) Normal operational condition - this includes prestress forces, internal gas pressure at the design level and the design operational temperatures. The details of prestress forces, internal gas pressure and the temperature distribution in the vessel are given in Figures (8.25) and (8.27a) and (8.27b). The prestress forces given in the figures at present do not deduct losses due to various conditions. The details for losses are given in Table 8.2. The pressures in the radial ducts and the boiler cavity are assumed equal to the main cavity pressure (5.68 N/mm^2).
- (b) Ultimate loading condition - the pressure in all cavities (main cavity, duct, boiler) is increased gradually until the failure conditions of the vessel are met under normal temperatures.

8.4.4. Types of Analyses

Three main types of analyses are performed for bonded and unbonded vessels. The first one is for unbonded vessels. In this case it is assumed that vertical tendons only contribute to the prestress force in the vertical direction and the tendon forces are transferred through the anchorages. The traditional method of analysing bonded vessels is to assume a perfect bond between the tendons and the vessel concrete. This means that the displacements and strains of both tendons and the concrete are assumed to be the same. In practice, however, when substantial cracking has occurred, this assumption ignores the differential movement between the tendon and

the concrete. To account for this effect, the bonded vessel is analysed using a specially developed linkage element known as the Ahmlink element after the name of the author. This gives a realistic representation of the bonded vessel behaviour.

The bonded vessel is also analysed assuming a perfect bond between the tendons and the vessel concrete. In order to assess the strength history, the vessels are analysed for the following cases.

- I Linear analyses under normal operational conditions and creep analyses for 40 years of bonded, unbonded and perfectly bonded vessels. This covers the reactor operational conditions.
- II Ultimate load analysis of unbonded vessel
- III Ultimate load analysis of perfectly bonded vessel
- IV Bonded reactor vessel analysis using Ahmlink element
 - (a) Ultimate load analysis for short-term prestress losses (1-5 years)
 - (b) Ultimate load analysis after 10 years prestress losses
 - (c) Ultimate load analysis after 20 years prestress losses
 - (d) Ultimate load analysis after 30 years prestress losses

For cases (a) to (d) long-term material properties for steel and concrete are used.

8.4.5. Discussion of the Analyses and Results

8.4.5.1. Normal Operational and Creep Analyses

All three vessel cases are analysed first for normal operational conditions and then with 40 years of creep. This is usually the service life of the vessel. Creep analysis is performed with 'rate of flow' method, and the Burger visco-elastic creep model (see Chapter 4).

The total creep time of 40 years is applied in small time increments during which incremental creep strain under the sustained stress and temperature is evaluated. This is followed by the calculation of redistribution of stresses through a cycle of elastic analysis. In the beginning of the analysis the stresses do change rapidly, therefore a careful selection of time increments is required. The following time increments are chosen :

7., 36., 66., 76., 80., 100., 365., 400., 695., 825., 1000., 1650., 2000., 3650., 3650., days

The obtained results are plotted in the form of stress and deformation histories. The results obtained for three vessel types are almost identical, the reasons for this being that the effect of bond in the elastic range of loading is almost negligible. The results of the normal operational analysis are first examined. The vessel is in compression at most places, except at the outside wall near the equator where vertical tensile stresses were found. These values are small and are unable to cause any cracking (see Figure (8.30c)). The deformations of the vessels for normal operation and creep analysis are shown in Figures (8.28), (8.28a) and (8.28b). A vessel deformations of these vessel cases when compared show very little difference. Figure (8.29) shows the principal stress distribution just at the beginning of the normal operation, while Figure (8.29a) shows those under normal operation after 40 years of creep. Since the PCRV has a non-uniform temperature distribution (i.e. temperature gradients through the wall and the cap), the stresses change with time and redistribution takes place due to temperature-dependent creep in the early stage of creep analysis. Owing to creep, the tensile stresses were converted into compressive stresses at the outer surface near the mid-height of the vessel.

The analysis in general predicts a significant stress reduction and redistribution due to concrete creep. A maximum compressive hoop stress of 22.0 N/mm^2 is calculated under normal operational conditions

at the inner side of the main cavity at mid-height of the PCRV. This value is reduced to 15.73 N/mm^2 after 40 years of creep, a reduction of stress by 30%. Similarly, the tensile stress at the outer surface of the wall at mid-height is reduced from 1.7 N/mm^2 to a compressive stress of 8.6 N/mm^2 .

Figure (8.30) shows the variation of circumferential stresses with time. A steady state condition is reached after 10 years of creep. Figures (8.30a) and (8.30c) show the variation of circumferential stress in the wall of the vessel, while Figure (8.30b) shows the variation of circumferential stress in the top cap of the vessel. The figures indicate a substantial stress redistribution due to creep.

8.4.5.2. Ultimate Load Analyses

For the ultimate loading conditions, in addition to the normal operational loads of the vessel, the pressure in all cavities of the vessel is increased monotonically until failure occurs. The internal pressure to the point of failure of vessel is applied in 15 increments. The first increment is the normal operational condition loads (prestressing forces, internal pressure at the design level and temperature loads) and the rest of the increments are carefully chosen as a fraction of the design pressure. This decision is taken so as not to cause any excessive non-linearity within the load increments. Analyses are performed at the following pressures (N/mm^2) :

5.68, 7.384, 9.08, 10.792, 11.928, 13.064, 14.2, 15.336, 16.188, 17.04, 17.892, 18.744, 19.312, 19.88, 20.448

The constant stiffness method (initial stress method) is used for all cases analysed in this section. An average of 10 iterations per increment are required for the convergence of the solution. Iterations within each load increment are terminated when a norm of residuals has reached a specified tolerance of 3×10^{-2} .

The ultimate load analyses are performed for the following two conditions :

- TYPE I Ultimate analyses of bonded, perfectly bonded and unbonded vessels in which short-term prestress losses were considered
- TYPE II Ultimate analyses of bonded vessel for long-term prestress losses due to creep, relaxation and shrinkage, etc.

The analyses also take into account the changing material properties with time and have been performed for 10 years, 20 years and 30 years in terms of prestress losses and material properties. Details are given in Table 8.2.

The obtained results of these analyses are plotted in the forms of pressure-deflection curves for the entire loading history, deflected shapes and crack patterns of the vessel.

TYPE I CASE I+CASE II+CASE III AND IV(a)

Figures (8.31) to (8.38c) show a history of pressure-deflection, deflected shapes and crack patterns of bonded, perfectly bonded and unbonded vessels. The pressure-deflection histories are plotted for the centre of the top cap and at the outside of the mid-height wall. As a result of increased internal cavity pressure and the boiler pressure, the PCRV's displaced upward in the vertical direction (cap) and outward in the radial direction. This results in some bending in the wall and the top cap as shown in Figures (8.33), (8.34) and (8.35). The cracks formed at the outside surface of the wall are due to the vertical extension and bending of the wall causing horizontal cracks (due to the vertical stress). The radial cracks are formed at the top surface of the end slab and in the wall near the inner surface. These are formed due to the radial expansion causing circumferential tensile stresses. Inclined cracks have also formed in the radial/circumferential direction near to the junction of the cap and wall. Cracks and failure in compression are marked at the integration points.

The study of the load-deflection history can be made in relation to cracks developed, since this is the major source of non-linearity in the vessel. Figure (8.32) shows the load-displacement curves of the wall for three vessel types analysed. It can be seen that the curves of the three vessel types are identical up to the load factor of 2.5 (14.2 N/mm^2). The reason for this can be explained by examining the crack patterns of these three types shown in Figures (8.36b), (8.37b) and (8.38b). From these figures it is seen that the crack patterns developed in three vessel types are identical. When the pressure is increased further up to the load factor of 3.0 (17.04 N/mm^2) the three curves start deviating. The results of the bonded vessel with Ahmlinks and perfectly bonded vessels are higher than the unbonded results. Cracks at this stage of loading in the three vessels are shown in Figures (8.36c), (8.37c) and (8.38c). By comparing these figures, it may be seen that the crack patterns of bonded and perfectly bonded vessels are still identical, except in a few places where the extent of cracking in the bonded vessel is more. However, for the unbonded vessel, the analysis seems to indicate much more cracking especially between the boiler and the outside wall, where most of the section has cracked in two directions. This causes more radial displacement of the wall. The extent of damage of these vessels at this load level is excessive and the vessel has substantially cracked at this load level. Examination of the top cap indicates that still very little cracking has occurred. This can also be assessed from Figure (8.31) where the pressure deflection curves of the top cap of the three vessel types are plotted. The pressure deflection curves up to the load factor of 2.5 are almost linear. A slight non-linearity is observed between load factors 2.5 to 3.0. This non-linearity may be due to crack formation at the junction of the cap and wall.

When pressure is increased further to a load level of 3.3 (18.74 N/mm^2), excessive deflections occur for the unbonded vessel, especially in the caps of the vessel. The solution for this vessel could not converge after 12 iterations. The analysis was stopped at this load level. This is now considered to be failure load of the unbonded vessel. Crack patterns, deflected shapes and the load-

deflections of the wall and the cap at this load level are shown in Figures (8.38d), (8.31), (8.32) and (8.35). Due to crushing of the concrete at the inner surface of the cap (see Figure (8.38d)) and extensive cracking at the upper part of the cap, this has caused a local instability in the numerical model (the stiffness matrix of the system) thereby resulting in excessive deformation of the cap (Figure (8.35)). Nevertheless, changes in the shape of the vessel with increasing internal pressure shown in Figure (8.35) can easily explain the progressive failure of the vessel. On the other hand, the computed crack patterns of the vessel (Figures (8.38a) to (8.38d)) provide a useful guide in interpreting the internal failure process of the vessel.

When the pressure is increased to a load factor of 3.5 (19.88 N/mm^2), a further crack development takes place for bonded and perfectly bonded vessels. The crack patterns for this load level are shown in Figures (8.36d) and (8.37d). At this stage, the whole vessel is cracked and the most damage the bonded vessel has received (Figure (8.36d)) is in the cap of the vessel where failure in compression (due to crushing) and triaxially cracked concrete have resulted. This may have caused the unstable state of the system in the numerical model resulting in excessive deformation of the cap as shown in Figure (8.33). The obtained solution for the bonded vessel did not converge in 12 iterations and therefore the analysis was stopped at this load level. This load-displacement curve of the bonded vessel (Figure (8.31)) indicates an abrupt change of slope between load factors 3.0 and 3.3, with a further increase in the load and excessive deflection of the centre of the slab. Comparing the crack patterns of bonded and perfectly bonded vessels (Figures (8.38d) and (8.37d)) generally the wall of each vessel has very identical cracks. However, a marked difference in these can be seen in the cap. The cap of the bonded vessel has crushed and cracked, while the cap of the perfectly bonded vessel did not damage to that extent. This is seen in Figure (8.34) where deformed shapes of perfectly bonded vessel are plotted.

A further pressure was increased to a load factor of 3.6 (20.448 N/mm²) where this vessel also failed due to the excessive deformation of the wall. The solution did not converge in 12 iterations and therefore the analysis was stopped at this load level. Deformed shapes of perfectly bonded vessel for various pressures are shown in Figure (8.34).

TYPE II CASES IVa, b, and c

In this category, the bonded vessel was studied using long-term effects on loading and material properties. The object is to investigate the influence of the effect of loading (mainly as a result of prestress losses) and concrete material properties on the structural integrity of the vessel. This means that the bonded vessel is to be overloaded at suitable intervals of its service life. The periods for these analyses were chosen as 1-5 years, 10 years, 20 years and 30 years. The prestress losses and material properties for these periods are given in Table 8.2. The vessel for 1-5 years has already been analysed, as discussed in TYPE I. The other three cases are analysed in this section. The results obtained for the four above analyses are compared with one another in order to assess the effect of the long-term loading on the behaviour of the bonded vessel. The predicted results are expected to give some insight into the failure of bonded vessel with increasing internal pressure for both long and short-term conditions. The analyses compare the following :

- load-deflection histories at the centre of the top cap and at mid-height wall
- deformed shapes of the vessel with increasing internal pressure
- damage of the vessel due to cracks and compression failure
- safety margin

Figures (8.39) to (8.46b) show results for the above cases. The pressure deflection histories are plotted for two points on the vessel, one at the centre of the top cap and the other at the mid-height wall. Curves for all above four cases are shown in Figures (8.39) and (8.40). As a result of increased pressure, the PCRV displaces upward in the vertical direction (cap) and outward in the radial direction (wall). as

shown in Figures (8.41), (8.42) and (8.43). This results in the formation of cracks in the wall and the cap as shown in Figures (8.44) to (8.46b). The integration points are marked where the status of the integration point indicates cracking or crushing.

Figures (8.39) and (8.40) show the comparison of pressure deflection curves for the above four cases for both the wall and the cap. It can be seen that the curves for the cap are similar and identical up to load factor of 2.5 and thereafter the curves start deviating, although the margin of deviation for these curves is negligible. On the other hand, the load-displacement curves for the wall (Figure (8.39)), shows a marked difference in curves for various cases starting from the origin to the point of failure. The reason for this difference is due to the fact that when overload analysis started giving different deformations in the wall due to different prestress losses in the radial direction. The curves seem to suggest that the load carrying capacity of the wall for 1-5 years old vessel is more than the 30 years old vessel, i.e. the older the vessel, the more flexible is the wall.

The picture on the top cap side is totally different from the wall. (Figure (8.40)). In this case, more flexibility in the 1-5 year old vessel is observed than an old vessel with 30 years life.

The study of load-displacement history and deformed shapes with increasing internal pressure can be made in relation to the formation of cracks for various cases. In all cases, the cracking has occurred in the horizontal direction (due to vertical stress) in between the boiler and the outer wall near the equator of the vessel (Figure (8.36)). When pressure is increased to a load factor of 2.3 (13.064 N/mm^2) cracks in two directions (radial and horizontal) are formed as shown in Figures (8.44), (8.45), and (8.46). These are the cracks calculated for 10, 20 and 30 years old vessel respectively. It is seen from these figures that much more cracking has occurred between the boiler and the inner wall of the vessel for the 30 year old vessel than for the 10 year old vessel. This is reflected in the pressure-deflection

curves of the wall (Figure (8.39)), as discussed earlier. It is interesting to note that very little cracking has occurred in the top cap of all vessel types at this level of loading. This is reflected in the pressure-displacement curves of the top cap (Figure (8.40)).

When pressure is further increased at load factor of 3.0 (17.04 N/mm^2) the resulting crack patterns for the four cases are shown in Figures (8.36c), (8.44a), (8.45a) and (8.46a). At this load level practically the whole wall for section AA has cracked (section through the boiler) while there are still very few cracks in the top cap. Radial cracks at the outer surface of the top cap have developed indicating a slight non-linearity in the pressure-deflection curve (Figure (8.40)). Deformed shapes at load level 3.3 (18.744 N/mm^2) are shown in Figures (8.33), (8.41), (8.42) and (8.43). By comparing these figures it seems to suggest that the larger deformations of the wall are observed for older vessels and the reverse is true for the top cap.

When the pressure is slowly increased to load factor 3.5 (19.88 N/mm^2) a further damage to the vessels is done in the form of more extensive cracking and compression failure. Solution at this load level did not converge in all cases and therefore the analysis is stopped. The extensive cracking and crushing of the vessels at this failure load level is shown in Figures (8.36d), (8.44b), (8.45b) and (8.46b). It is clear from these figures that the damage of the vessel at 30 years load is much more in the wall of the vessel than in the top cap. This gives results opposite to those of the vessel when loaded at an earlier age. The damage of these vessels is reflected in the pressure-displacement curves (Figures (8.39) and (8.40)). Figures (8.33), (8.41) to (8.43) deformed shapes of these vessel at failure which definitely indicates that an 1-5 year old vessel is likely to fail with the excessive deformation of the cap while the 30 year old vessel is likely to fail with the excessive deformation of the wall. The numerical model at this load level has become unstable due to triaxially cracked and crushed points resulting in a sudden loss of stiffness. It is for this reason that a few inconsistencies in the deformed shapes can be seen. Nevertheless, the deformed shapes of the vessel are a useful guide as a failure indicator of the vessel.

8.5. Conclusion

The application of the non-linear model has been illustrated on various problems starting from simple beams to a complex pre-stressed concrete reactor vessel. Results obtained on a bonded pre-stressed concrete slab are in close agreement with those from the experiment. Predicted results of bonded (with Ahmlink elements) and perfectly bonded slabs do not differ substantially. The predicted ultimate load from the perfectly bonded analysis is 1.4% higher than the bonded analysis. Various cases of vessel analysis assuming bonded and unbonded tendons show that the load carrying capacity of bonded vessel is always higher than a similar unbonded vessel. Creep analyses of bonded and unbonded vessels at normal operation show a considerable redistribution of stresses due to non-uniform temperature distribution through the wall and the cap. Ultimate analyses of the bonded vessel at various stages of its life indicate that the overall performance of 1-5 year old vessel is better than a 30 year old vessel.

Table 8.1. Geometric and Material Data for Slab

<u>Concrete</u>	
E_c	= 27500.0 N/mm ²
ν_c	= 0.17
σ_c	= 39.0 N/mm ²
σ_t	= 3.9 N/mm ²
ϵ_{cu}	= 0.0035
β , shear retention factor for cracked concrete	= 0.5
Integration rule for all solid elements	= 2x2x2
<u>Steel</u>	
Prestressing wires :	
diameter	= 7.0 mm
E_s	= 200,000 N/mm ²
H	= strain hardening parameter = 20000.0 N/mm ²
σ_{y1}	= 1340.0 N/mm ²
Reinforcements :	
diameter	= 12.0 mm
E_s	= 200,000 N/mm ²
H	= 20000.0 N/mm ²
σ_{y2}	= 297 N/mm ²
Tolerance for convergence, Tol = 3.0×10^{-2}	
Pressure due to prestress = 1.89 N/mm ²	
Total pressure due to vertical load = 0.2186 N/mm ² (544 KN)	
at failure	

Data for bond linkage (Ahmlink) element (see Figure (8.11))

The following data is adopted for Ahmlink element in the form of multi-linear curve. Total 15 points are taken on the curve and their values are given overleaf :

Curve points	Bond stress (N/mm ²)	Slip (mm)
1	0.0	0.0
2	0.5	0.001
3	0.8	0.0025
4	0.9	0.003
5	1.0	0.004
6	1.2	0.005
7	1.3	0.006
8	1.4	0.007
9	1.5	0.008
10	1.6	0.01
11	1.7	0.013
12	1.75	0.015
13	1.8	0.018
14	1.84	0.025
15	1.86	0.05

Time summary of slab analyses on PRIME 750

	CPU
(a) Perfectly bonded slab (11 load increments)	65 minutes
(b) Bonded slab (11 load increments)	77 minutes
(c) Unbonded slab (11 load increments)	63 minutes
(d) Bonded slab (18 load increments)	108 minutes
(e) Bonded slab (Newton Raphson method - no iterations, 30 load increments)	138 minutes

Table 8.2. HTGCR Vessel Data

<u>Geometry</u>	
Internal height, H	= 21946.0 mm
Internal diameter, d	= 11125.0 mm
Wall thickness, tw	= 6630.0 mm
Top and bottom cap thickness, D	= 5182.0 mm
Boiler diameter	= 3048 mm
Connecting duct diameter	= 1118.0 mm
<u>Material</u>	
σ_c , concrete cylinder strength	= 39.0 N/mm ²
σ_t , tensile strength	= 4.69 N/mm ²
E_c , initial modulus (short-term)	= 41400 N/mm ²
E_c , for standpipe region	= 0.75 E_c
E_{cu} , concrete ultimate strain	= 0.0035
ν_c	= 0.17
β , shear retention factor for cracked concrete	= 0.5
α_c , coefficient of thermal expansion for concrete	= 9.4×10^{-6} /degrees centigrade
<u>Liner</u>	
Liner thickness, t_l	= 19.0 mm
E_s , elastic modulus	= 200,000 N/mm ²
ν_s , Poisson's ratio	= 0.3
σ_y , uniaxial yield stress	= 365.0 N/mm ²
α_T , coefficient of thermal expansion for steel	= 5.5×10^{-6} /degrees centigrade
H, strain hardening parameter	= 0.1 E_s

Prestressing Tendons

Es, elastic modulus = 200,000 N/mm²

σ_y , uniaxial yield stress = 734.15 N/mm²

Diameter of prestressing strand = 127.0 mm

Guaranteed ultimate tensile strength (GUTS) of each prestressing tendon, F_{ult} = 9750.0 KN

Transfer load = $0.75 F_{ult}$ = 7312.5 KN

Prestress force due to circumferential

wire winding (see Figure (8.26)) p1 = 18.589 N/mm²

p2 = 12.39 N/mm²

p3 = 10.395 N/mm²

Pressure in all cavities (design pressure)

(main cavity, boilers and connecting ducts)

= 5.68 N/mm²

Temperature at the core liner surface = 60°C

Temperature at the outside = 25°C

Temperature gradient = 35°C

For details of temperature distribution in the vessel see Figure (8.27a) and (8.27b).

Details of Bond-linkage Elements

The following bond-slip curve was adopted for linkage elements. The bond-slip curve is for prestressing strand and is taken from Edward and Picard's (90) experimental tests (see Chapter 2 for more details).

Curve Points	Bond Stress (N/mm ²)	Slip (mm)
1	0.0	0.0
2	0.4593	0.001334
3	0.8038	0.0024667
4	1.1483	0.003334
5	1.378	0.0046667
6	1.7225	0.006
7	2.2967	0.008866
8	2.6412	0.01133
9	3.1005	0.014
10	3.6172	0.018
11	3.7895	0.02
12	4.0192	0.022
13	4.2488	0.025
14	4.3636	0.02733
15	4.4785	0.0303
16	4.4785	0.0333
17	4.4785	0.0366
18	4.4785	0.04
19	4.4785	0.0433
20	4.4785	0.0466
21	4.4785	0.05
22	4.4785	0.053
23	4.4785	0.075

Prestress Forces and Losses (see Figure (8.26))

Short-term losses (1-5 years) :

- (a) Vertical tendons - 7.26% on the top of the transfer load
(i.e. 0.75 GUTS)
- (b) Circumferential wire winding (pressure) - 10% on the
values shown in Figure (8.26).

Losses at 10 years :

- (a) Vertical tendons - 12% on the top of the transfer load
- (b) Circumferential wire winding - 15% on the values shown in Figure (8.26)

Losses at 20 years :

- (a) Vertical tendons - 17% on the top of the transfer load
- (b) Wire winding - 23.3% on the values shown in Figure (8.26)

All the steel and concrete material properties should also be reduced by 5%.

Losses at 30 years of vessel life :

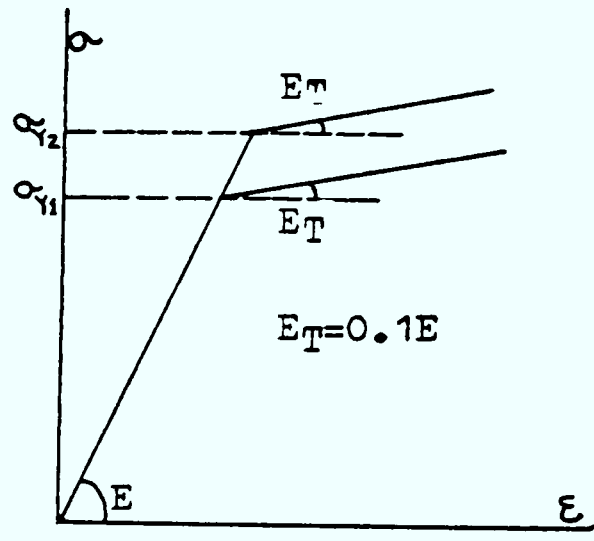
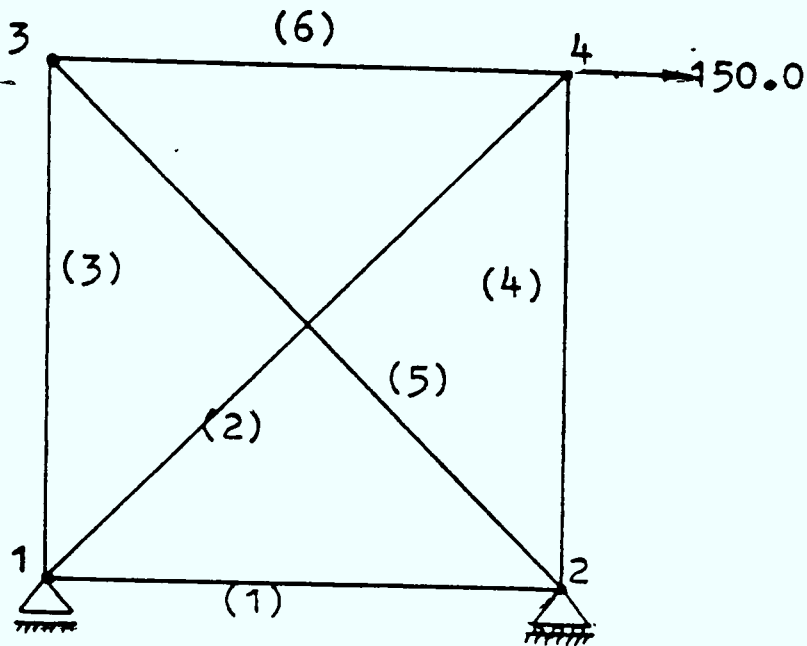
- (a) Vertical tendons - 20% on the top of the transfer load
- (b) Wire winding - 30% on the values shown in Figure (8.26)

All the steel and concrete material properties should also be reduced by 5%.

Time Summary of Vessel Analysis on Prime 750

	CPU
Bonded vessel analysis	292 minutes
Perfectly bonded vessel analysis	286 minutes
Unbonded vessel analysis	276 minutes

An average analysis time per vessel : 284 minutes (4 hrs 40 mins)



(a) Finite Element Mesh

(b) Uniaxial Stress-Strain Curve

$E=2500.0$

$\alpha_2=30.$ (for elements 2&5)

$\alpha_1=25.$ (for elements 1,3,4&6)

$H= 277.78 =$ Strain hardening parameter

$$\frac{E_T E}{E - E_T}$$

Diameters of elements 2 & 5

1.8975

Diameters of elements 1,3,4 & 6

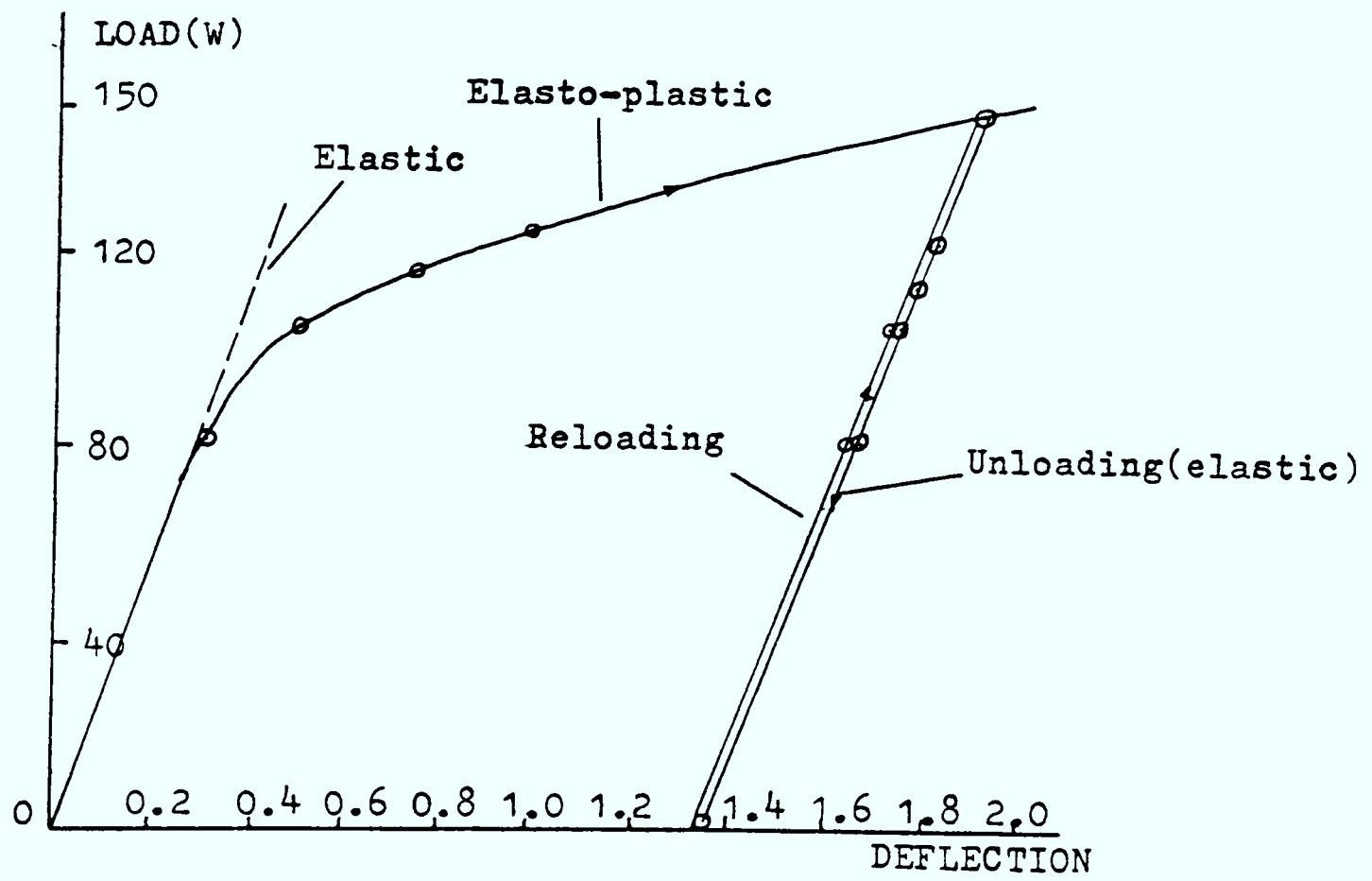
1.5957

$Tol = 3 \times 10^{-2}$

Total load, $W=150.$

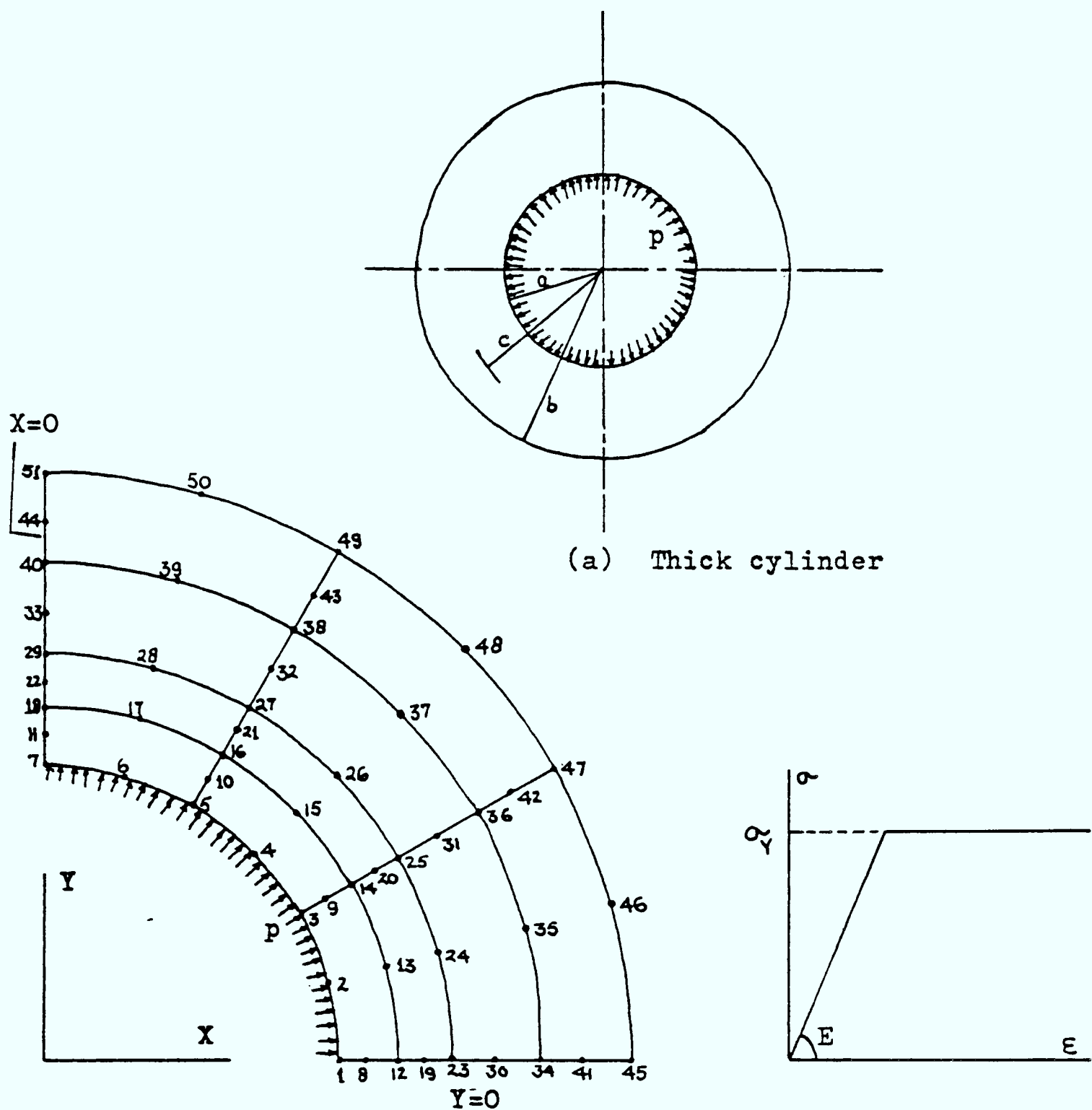
Load increments

0.54, 0.7, 0.77, 0.83, 1.0



(c) Load-Deflection Curve at Node 4

Figure 8.1 Elasto-Plastic Analysis of Square Braced Frame



Details

$E = 2600.$

$\nu = 0.3$

$\alpha_y = 5.196$

$a = 1.0$

$b = 2.0$

$t = 1.0$

Integration - 3x3

Pressure, $p=3.74529$

Load increments

$0.63p, 0.7p, 0.8p, 0.9p, 1.0p$

Tol = 10^{-2}

Figure 8.2 Elasto-Plastic Analysis of Thick Cylinder Under Internal Pressure

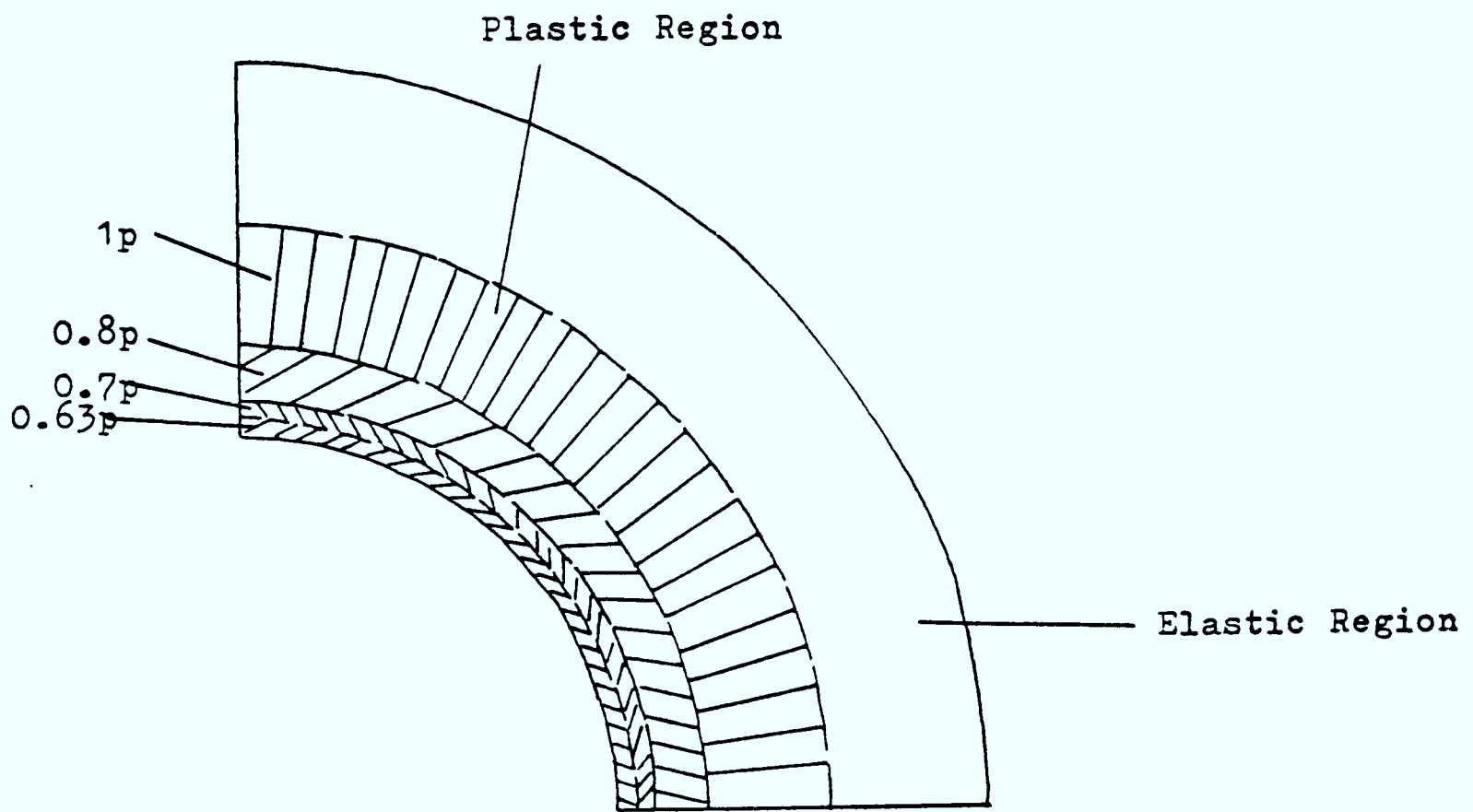


Figure 8.3b Spread of Plasticity in the Cylinder

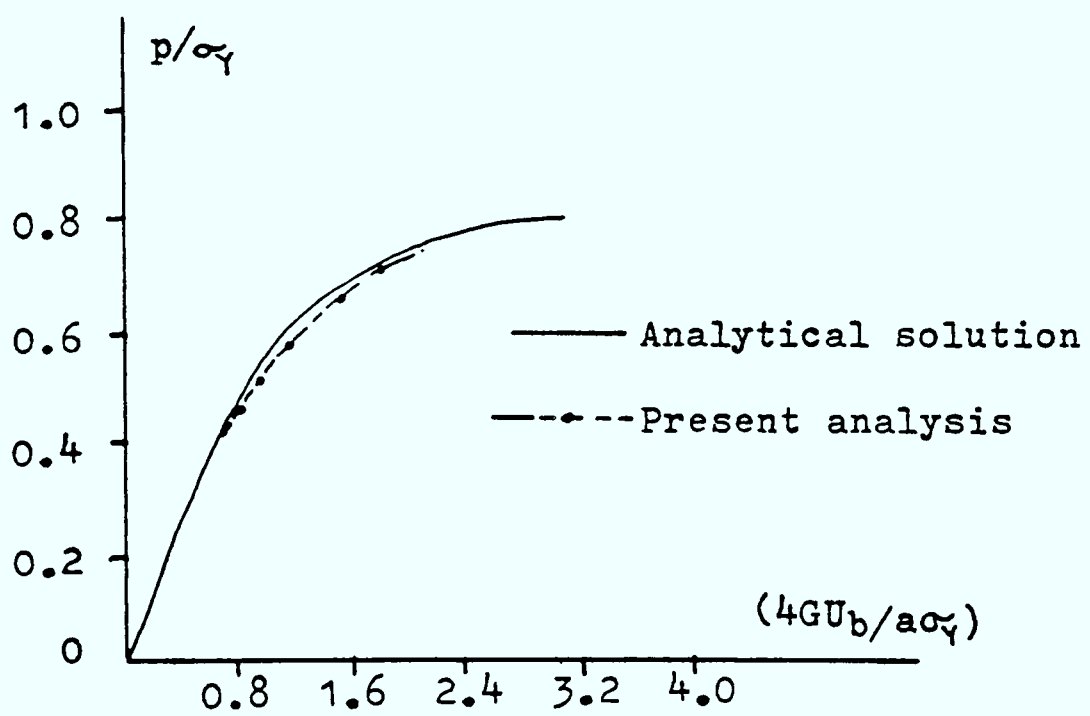
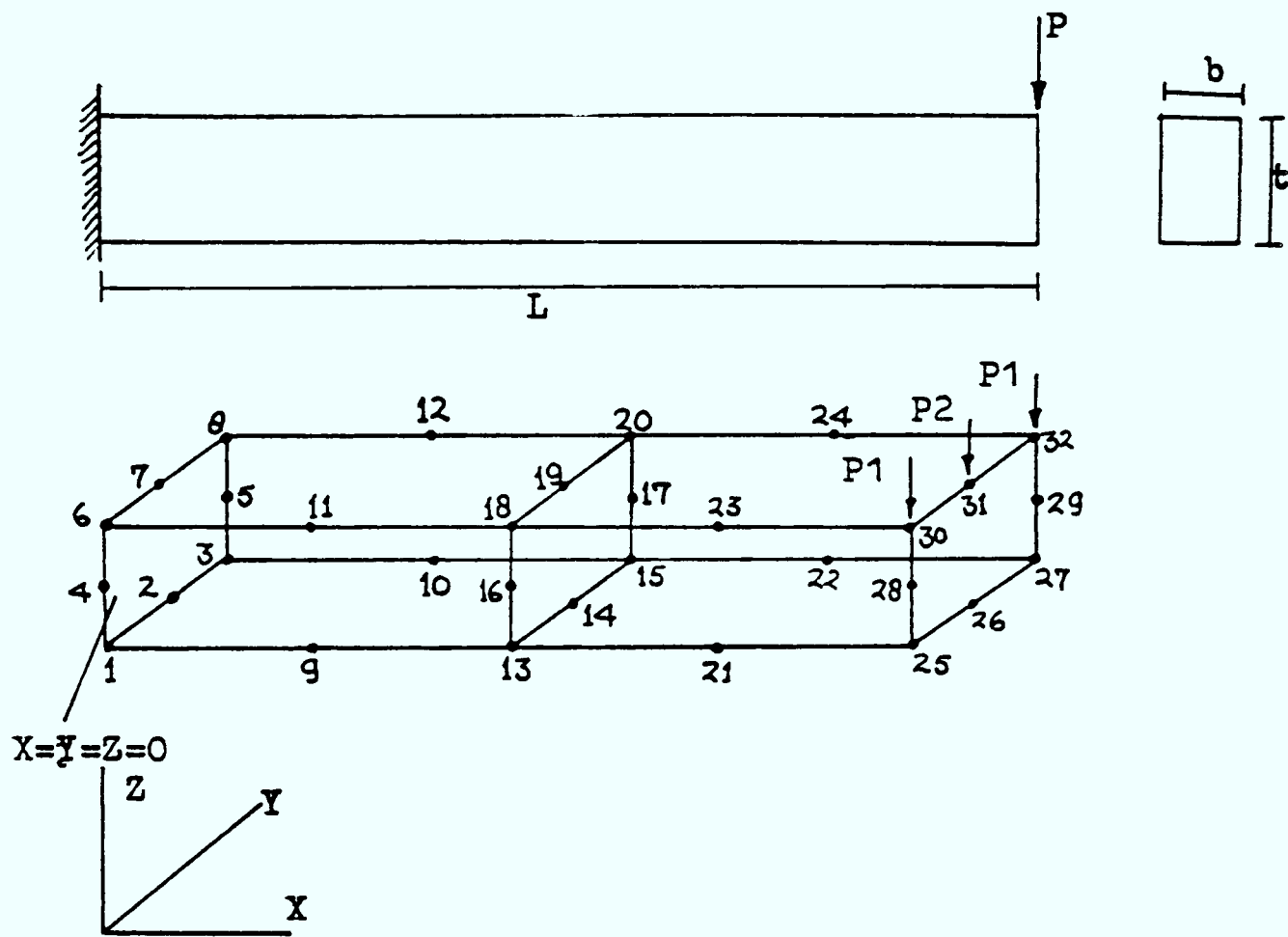


Figure 8.3b Normalised Pressure-Displacement Curve



Finite Element Mesh

Material and geometric details

 $E = 30000.0 \text{ N/mm}^2$

$\nu = 0.3$

$L = 20.0 \text{ mm}$

$b = 3.0 \text{ mm}$

$t = 5.0 \text{ mm}$

$P = 1.0 \text{ Newton}$

$P1 = 0.166667 \text{ N}$

$P2 = 0.666667 \text{ N}$

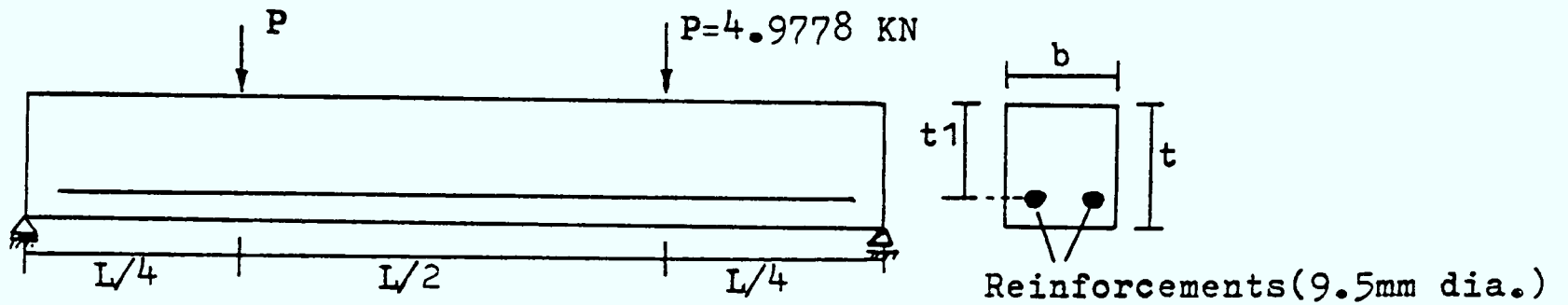
Integration (1) $3 \times 3 \times 3$ (2) $2 \times 2 \times 3$

Analytical tip deflection, $w = \frac{PL^3}{3EI} = 0.002844 \text{ mm}$

Computed tip deflection, $w = 0.002849 \text{ mm}$ - $2 \times 2 \times 3$

$w = 0.002831 \text{ mm}$ - $3 \times 3 \times 3$

Figure 8.4 Elastic Analysis of Cantilever Beam



(a) Reinforced Concrete Beam

Maximum mid-span deflection

7.874 mm (Experimental)

6.731 mm (Analysis)

Concrete

$$E_c = 23219.3 \text{ N/mm}^2$$

$$\nu_c = 0.167$$

$$\sigma_c = 24.115 \text{ N/mm}^2$$

$$\sigma_t = 2.4115 \text{ N/mm}^2$$

$$E_{cu} = 0.0035$$

Steel

$$E = 199810. \text{ N/mm}^2$$

$$\sigma_y = 413.4 \text{ N/mm}^2$$

$$H = 0.0$$

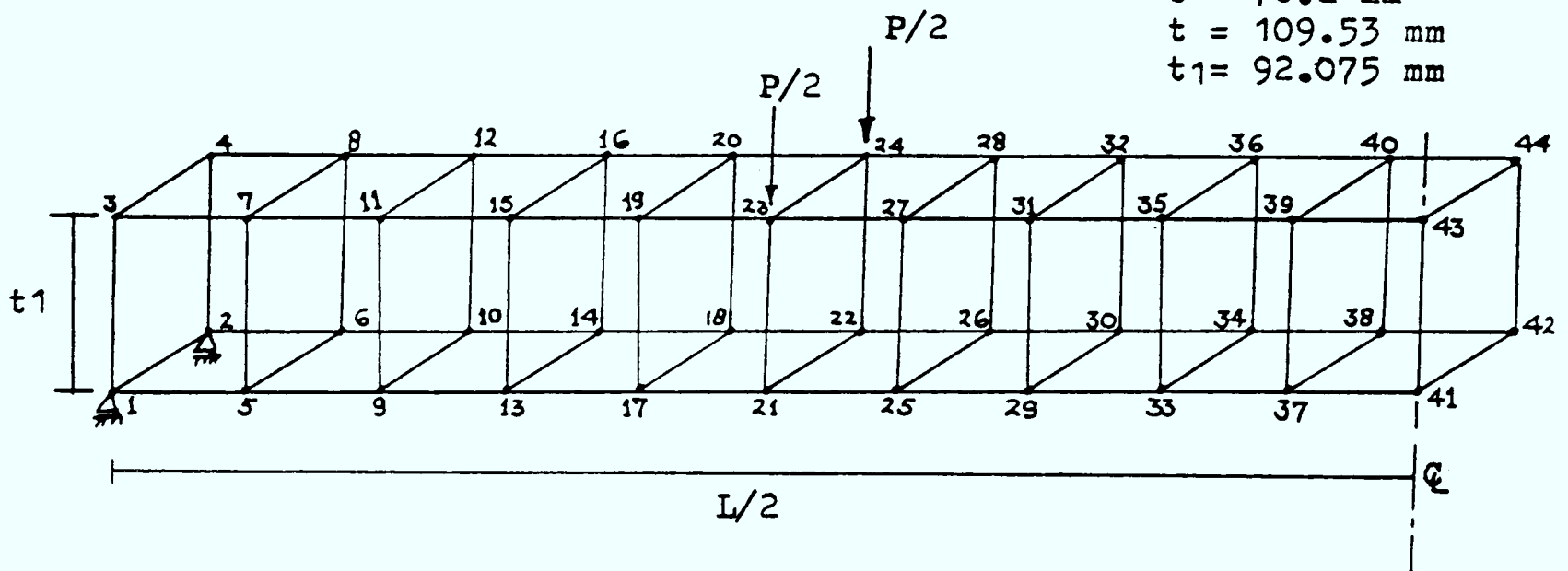
Geometry

$$L = 1828.8 \text{ mm}$$

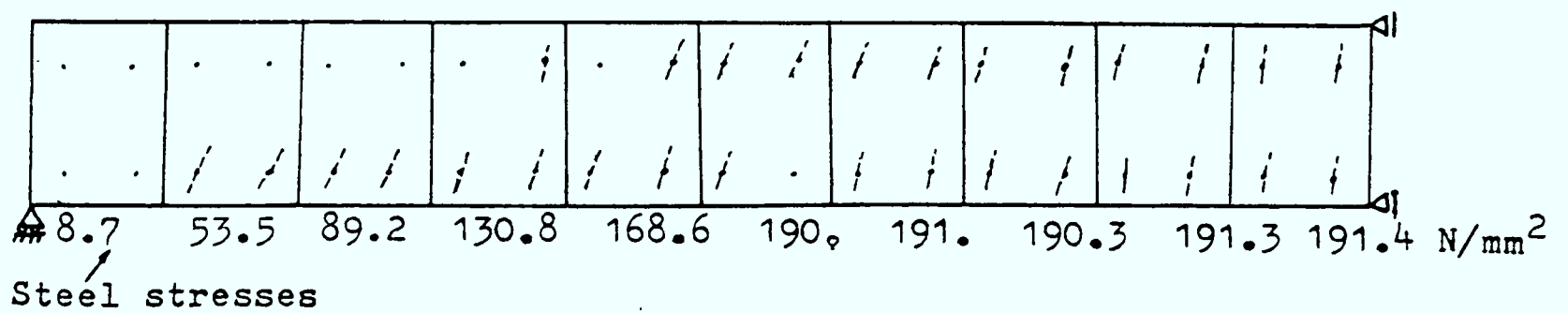
$$b = 76.2 \text{ mm}$$

$$t = 109.53 \text{ mm}$$

$$t_1 = 92.075 \text{ mm}$$



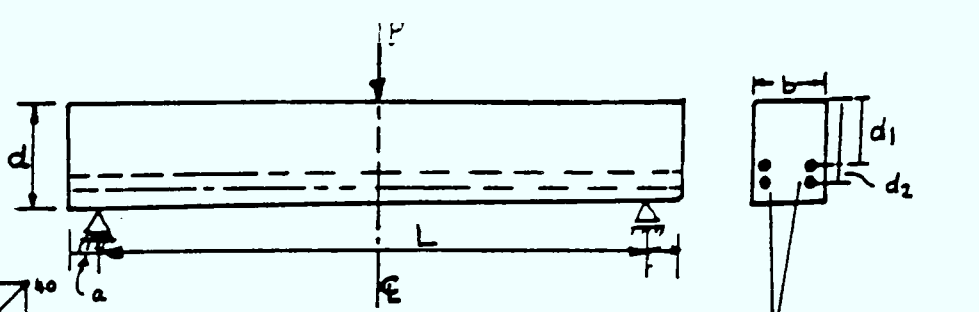
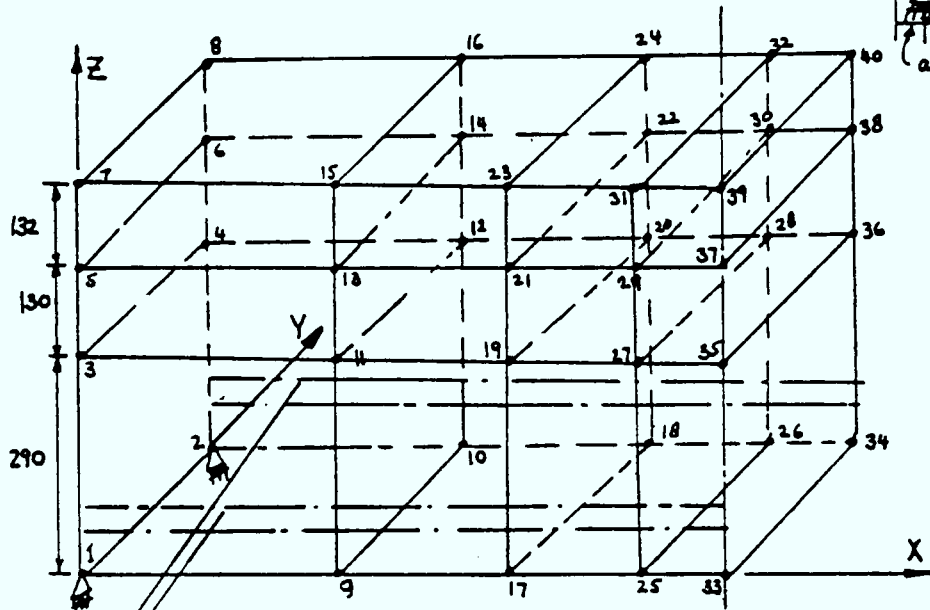
(b) Finite Element Mesh



(c) Computed Crack Pattern

Figure 8.5 Analysis of Simply Supported Reinforced Concrete Beam

All Dimensions in mm



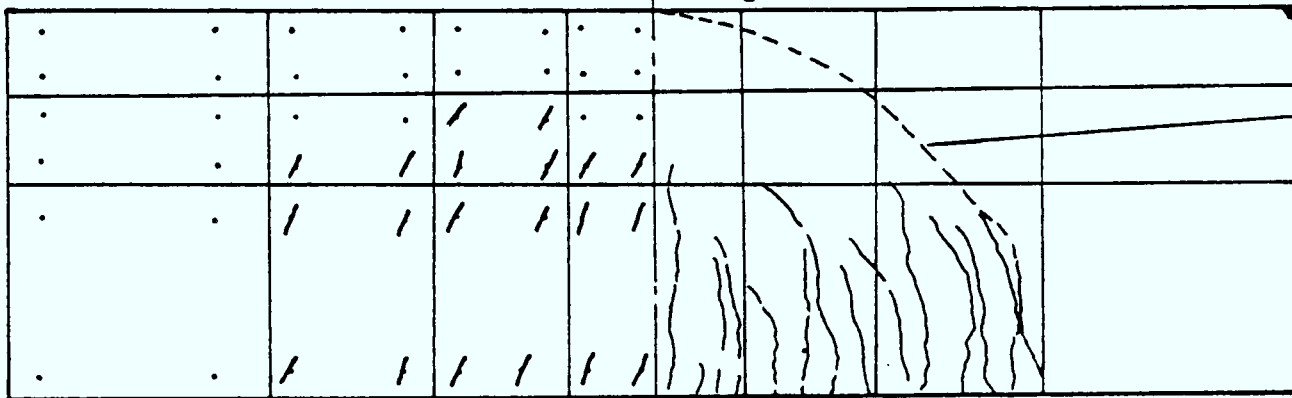
$d=552.5$, $L=3657.6$
 $d_1=425.5$, $d_2=489$
 $b = 228.6$, $a=228.6$
 $E_c=21300$ N/mm² $\nu_c=0.18$
 $\sigma_c = 24.6$ N/mm² $\sigma_t = 3.198$ N/mm²
 $E_s = 191435$ N/mm²
 $H = 17708$ N/mm²
 Diameter = 28.58

Reinforcement No. 9. (dia = 28.5mm)

Finite Element Mesh

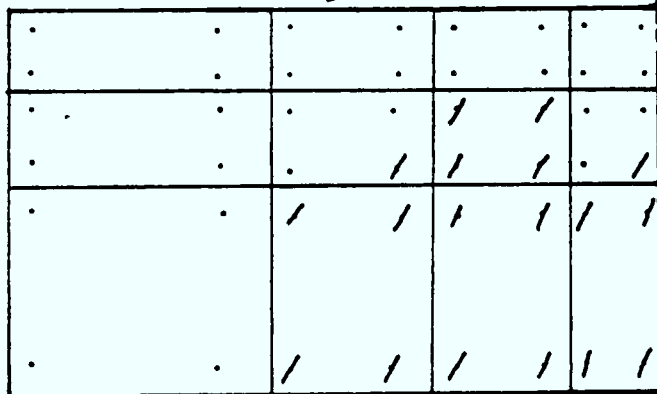
Reinforcements At 245.2KN

Experimental Crack Pattern at 249.2KN



Experimental Failure

At 215.2KN



Computed Crack Patterns

Figure 8.6 Simply Supported Reinforced Concrete Beam(Ref. 43)

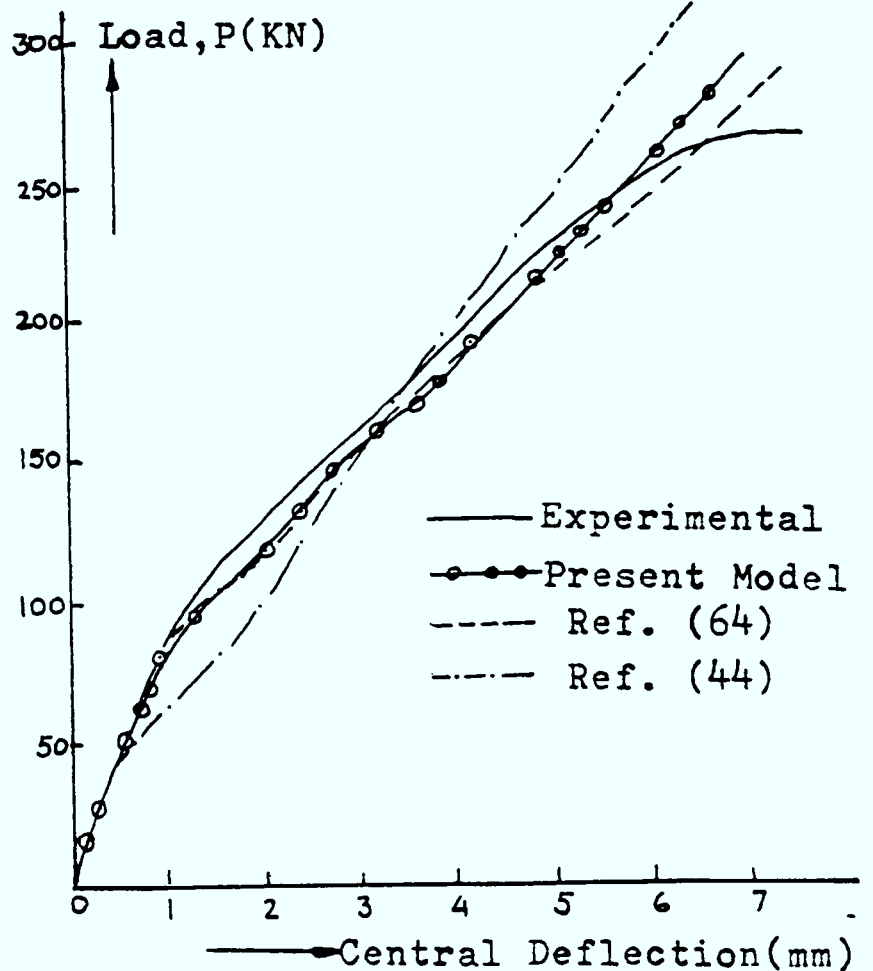


Figure 8.7 Load-Deflection Curve

All Dimensions
in mm

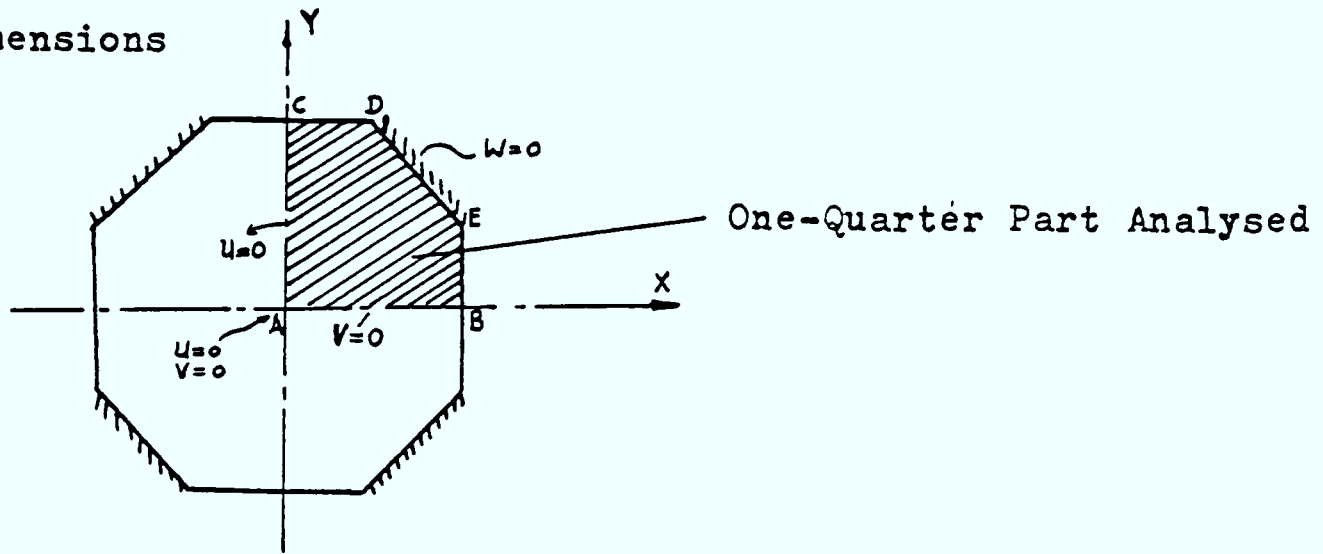
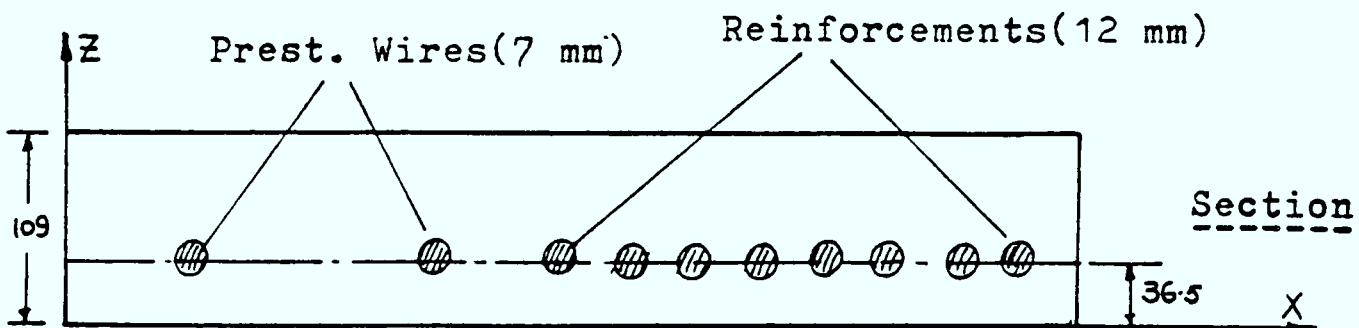
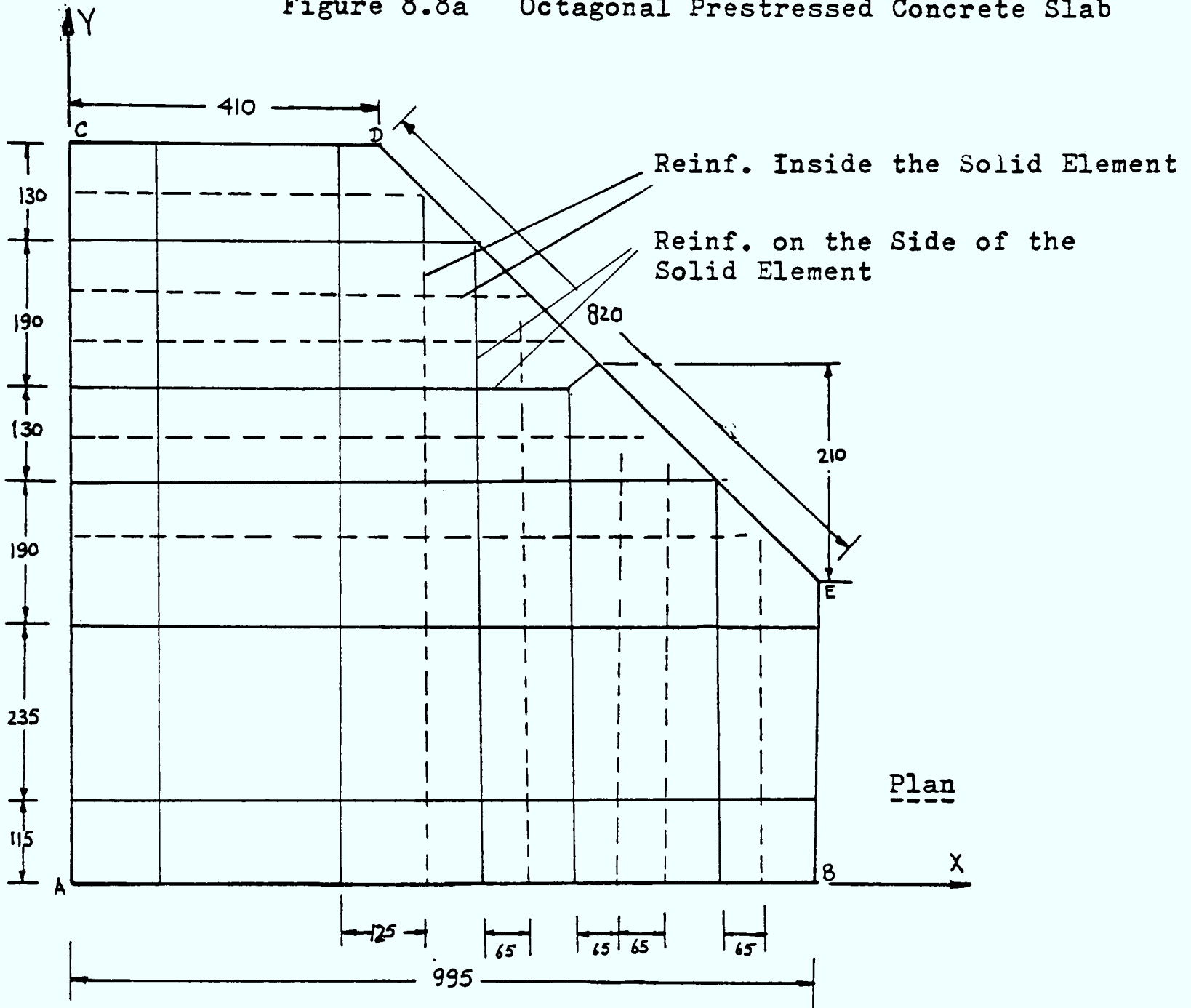


Figure 8.8a Octagonal Prestressed Concrete Slab



Reference is made to Figure 7.2

Figure 8.8b Main Dimensions of Finite Element Mesh of the Slab

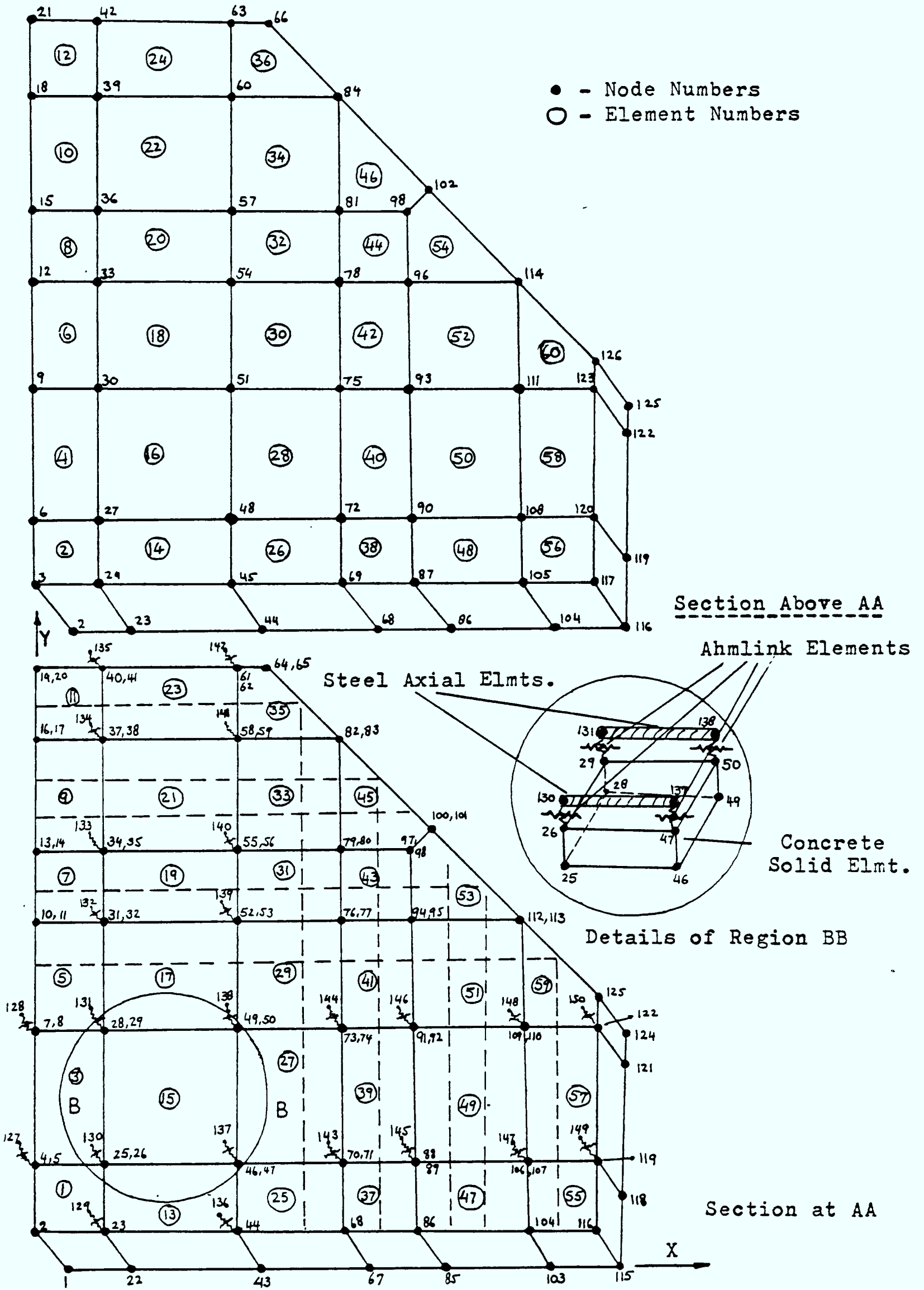
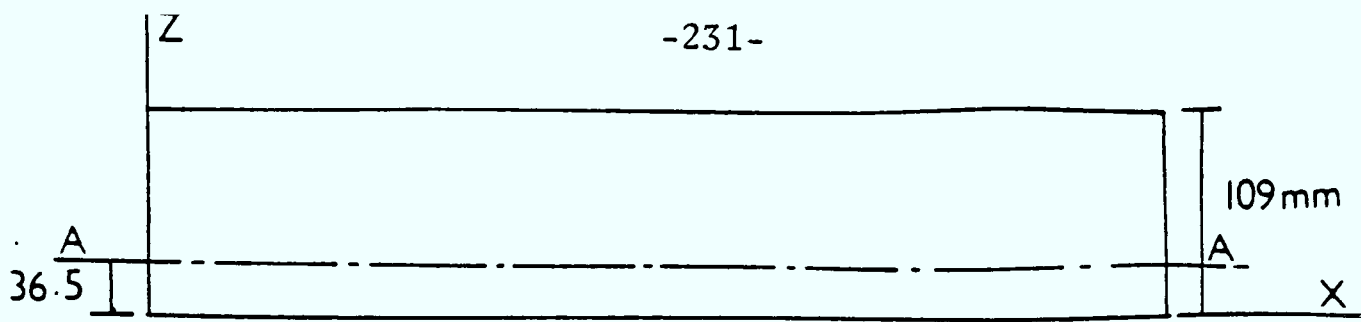
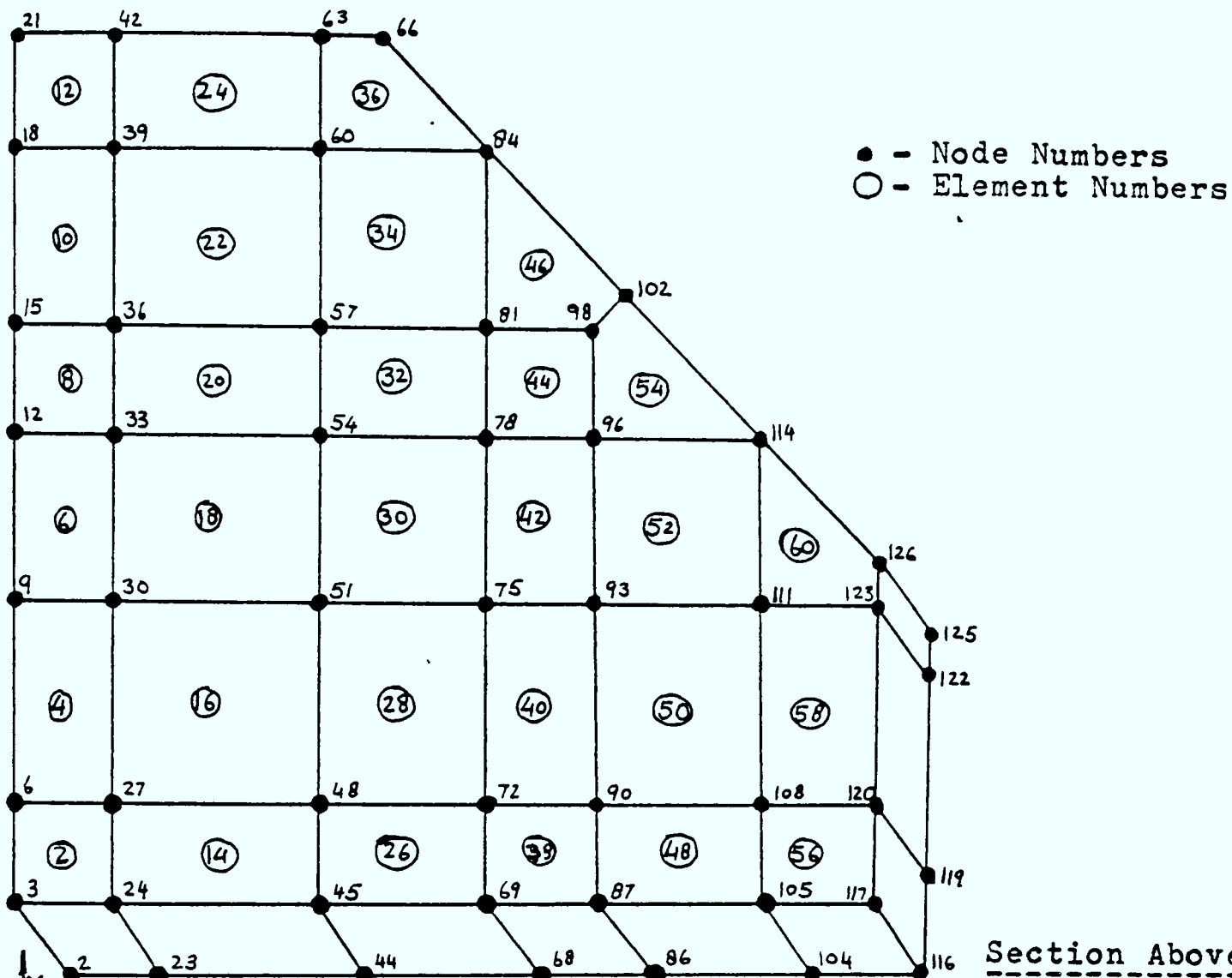
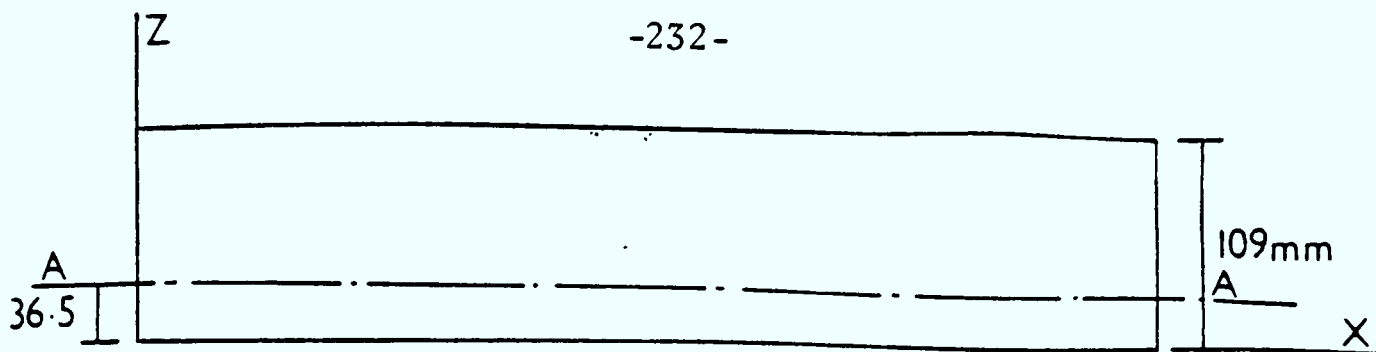
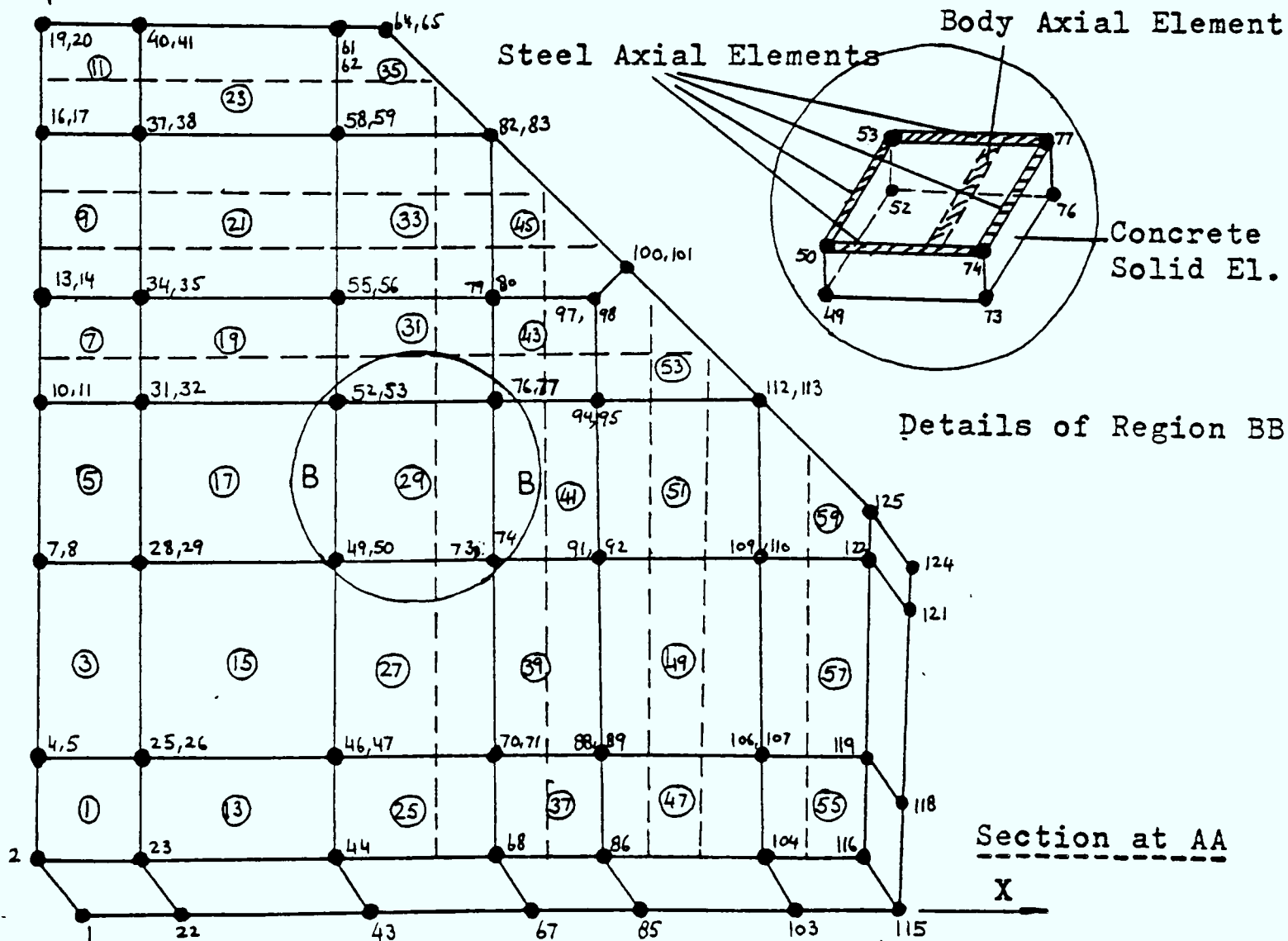


Figure 8.9 Finite Element Mesh of Bonded Slab



Section Above AA



Section at AA

Figure 8.10 Finite Element Mesh of Perfectly Bonded Slab

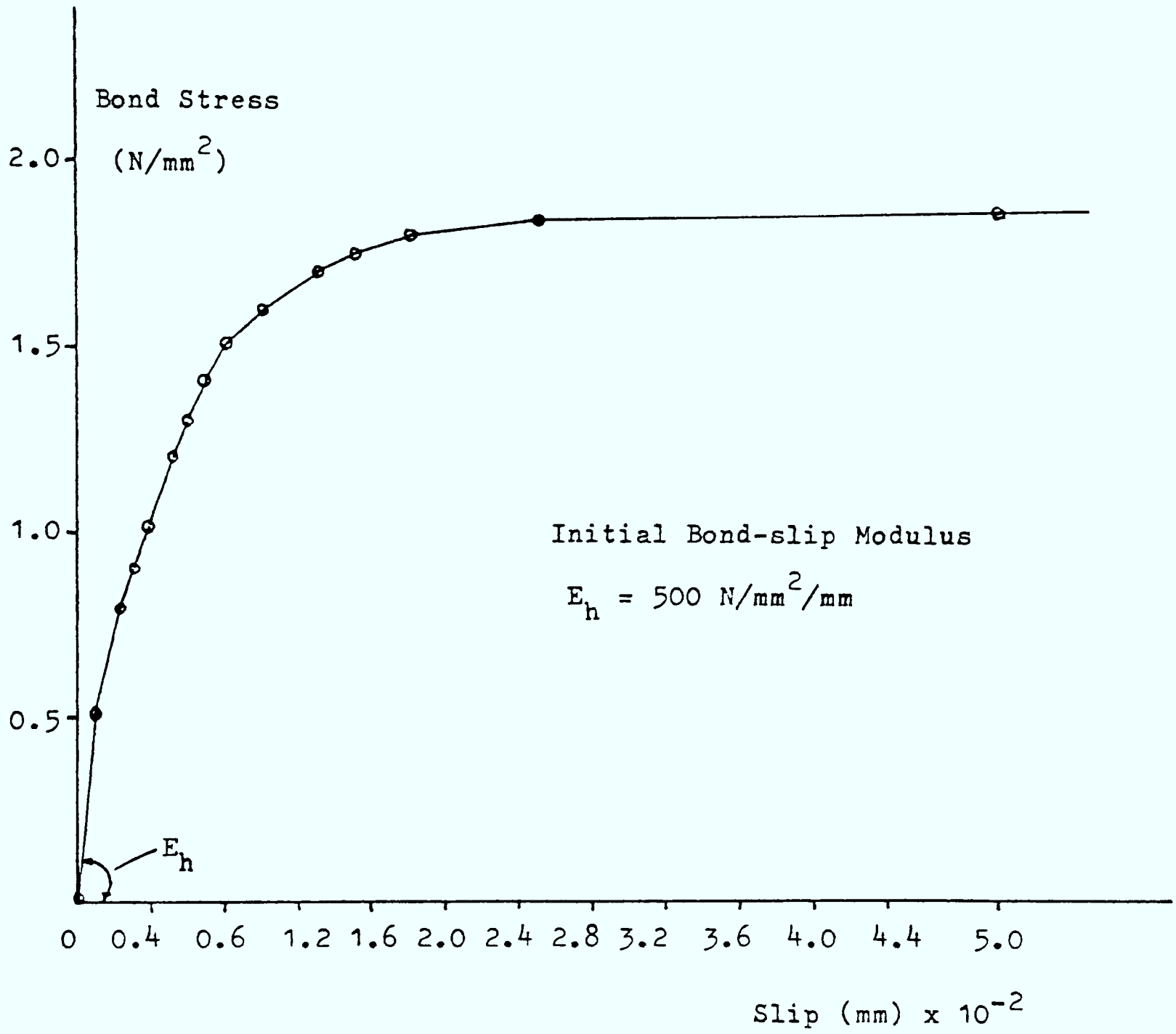


Figure 8.11 Bond Stress-Slip Curve Used in the Finite Element Analysis of Prestressed Concrete Slab

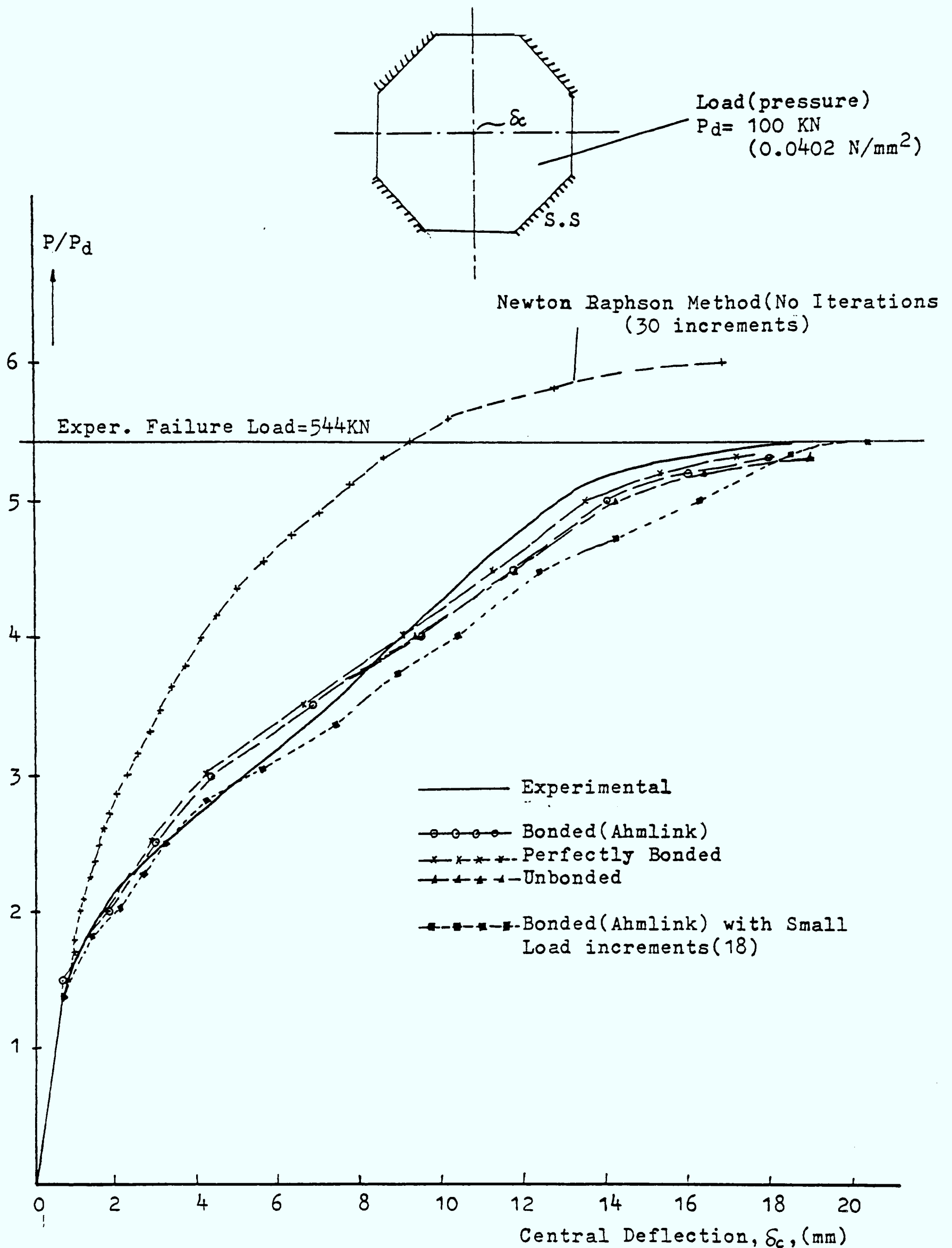


Figure 8.12 Load - Displacement Curves of Prestressed Concrete Slab

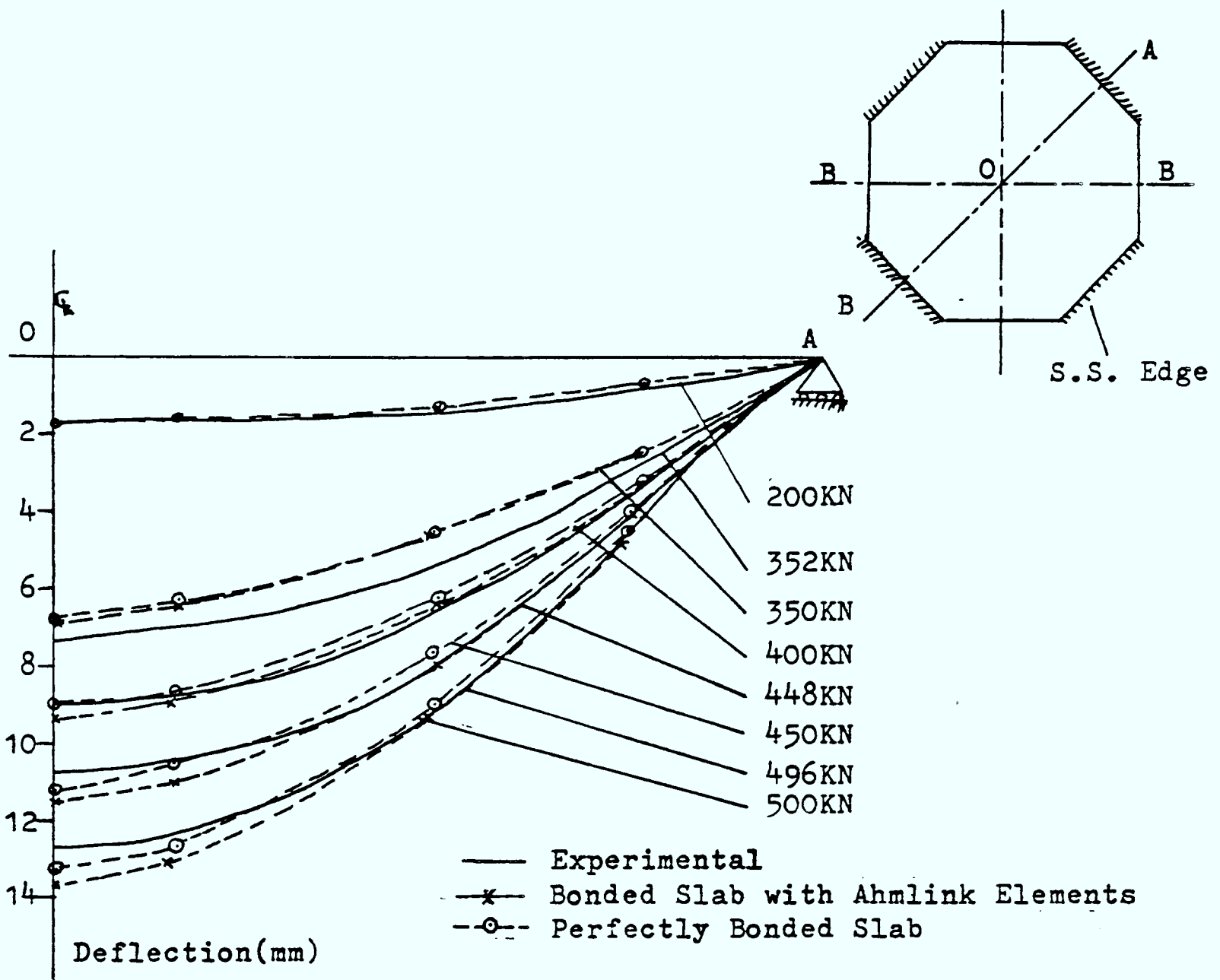


Figure 8.13 Deflected Shapes at Various Loads Along AA

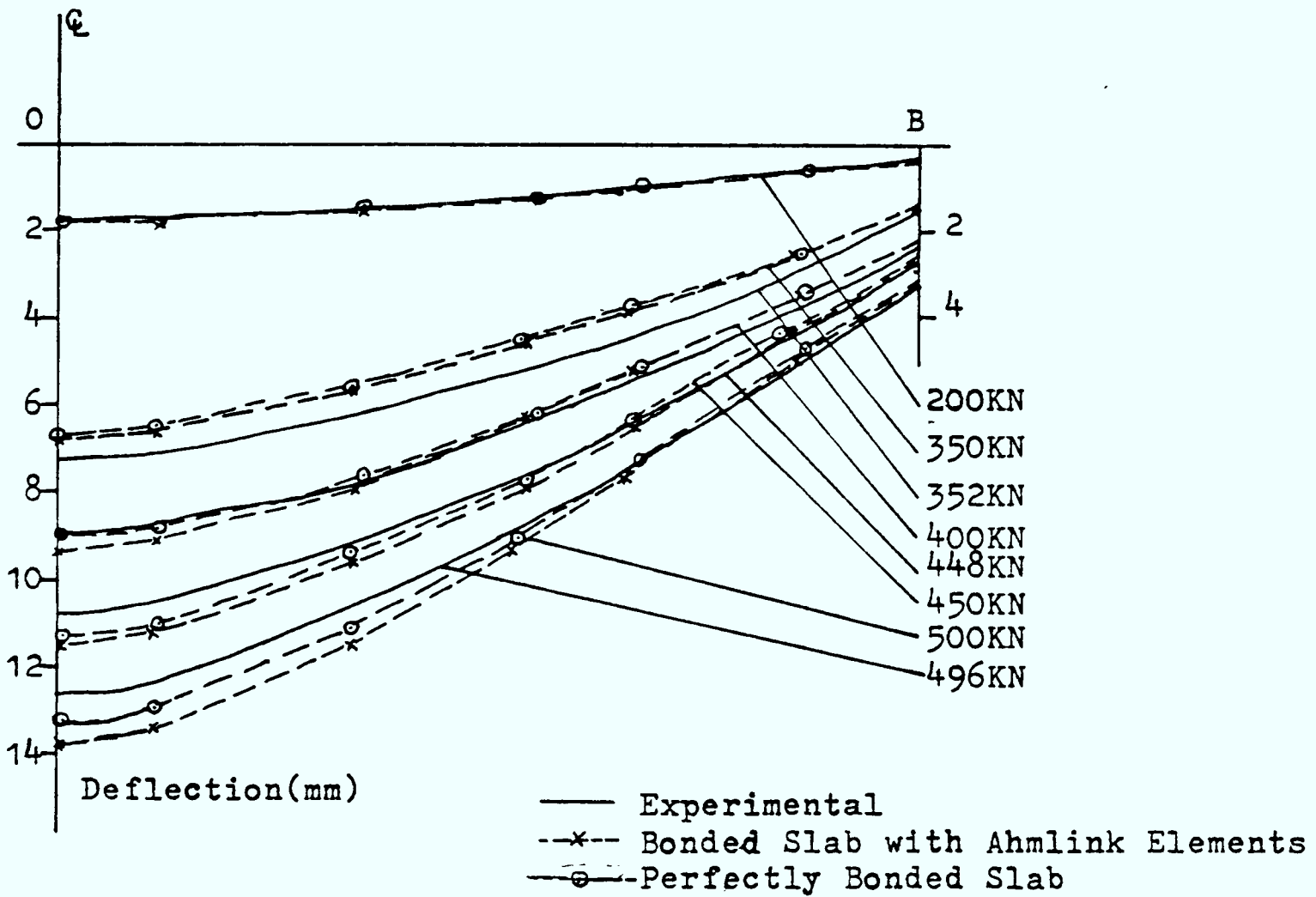


Figure 8.14 Deflected Shapes at Various Loads Along BB

$$P_d = 100\text{KN}(0.0402 \text{ N/mm}^2)$$

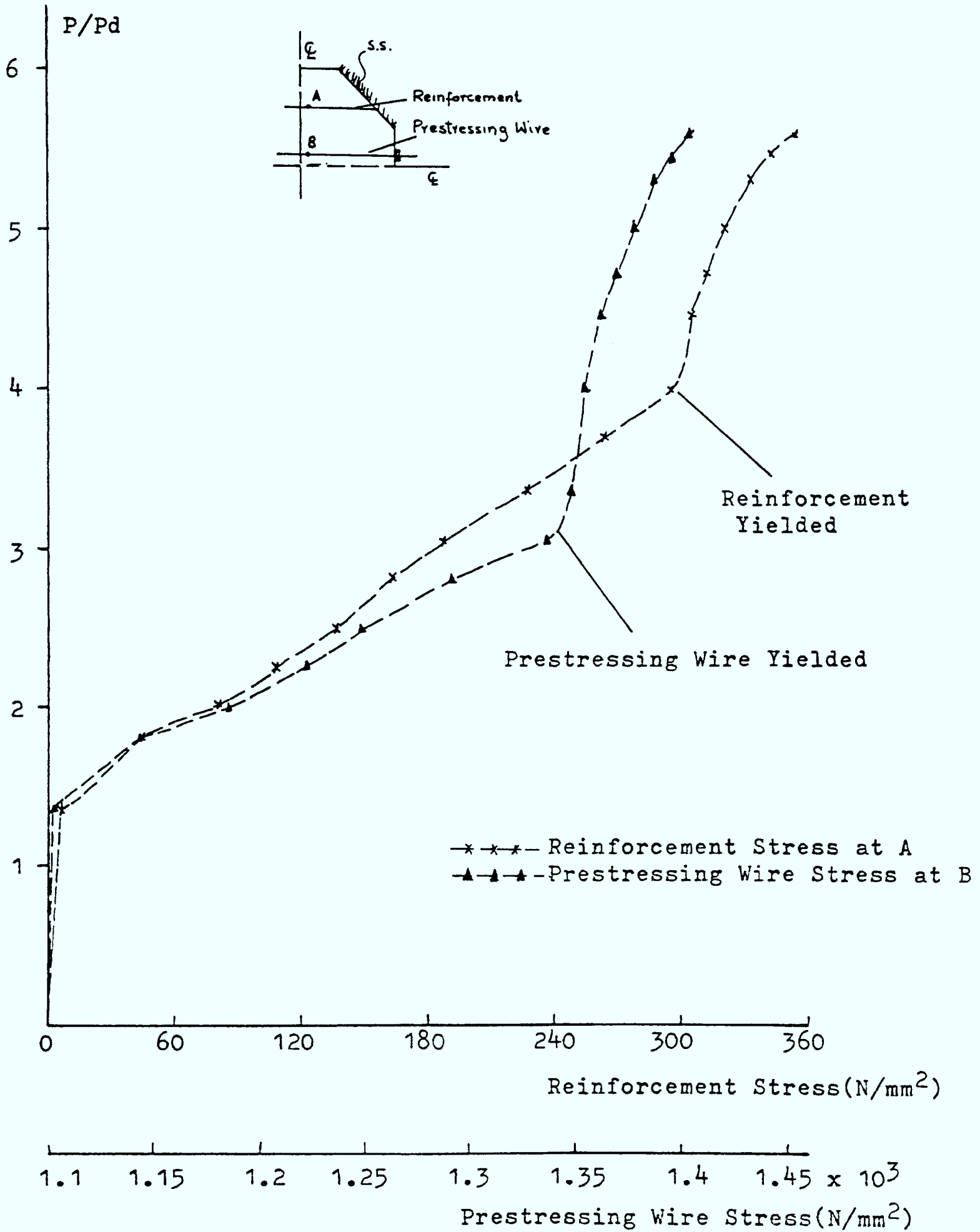
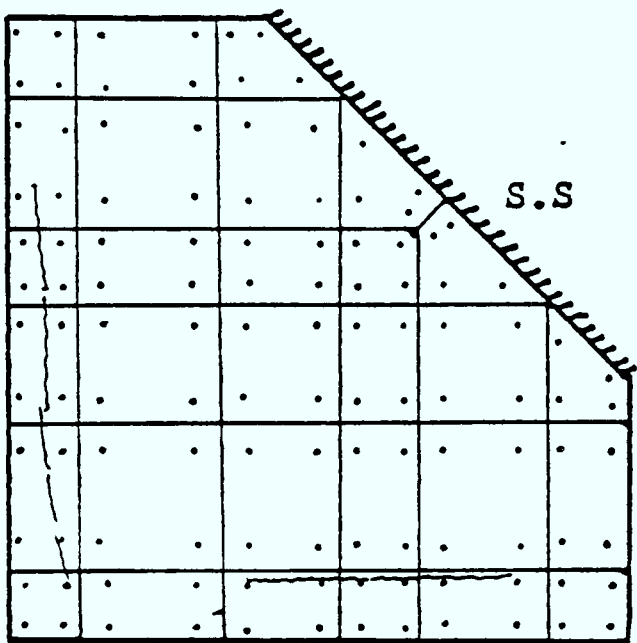
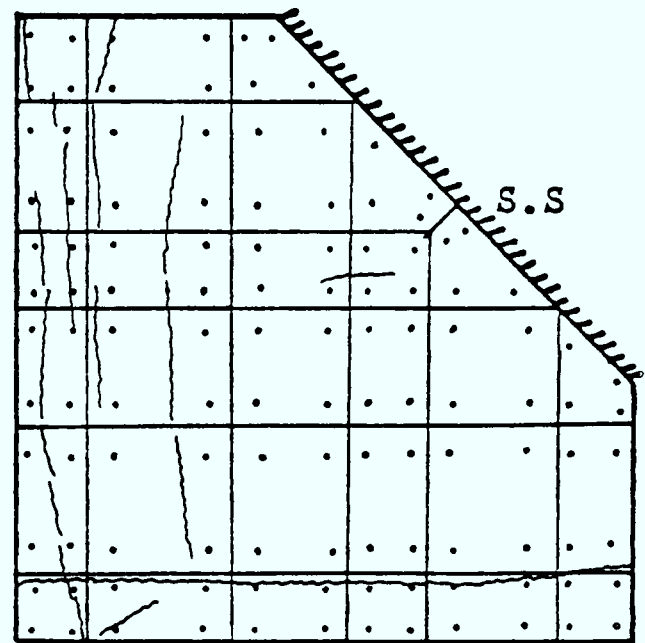


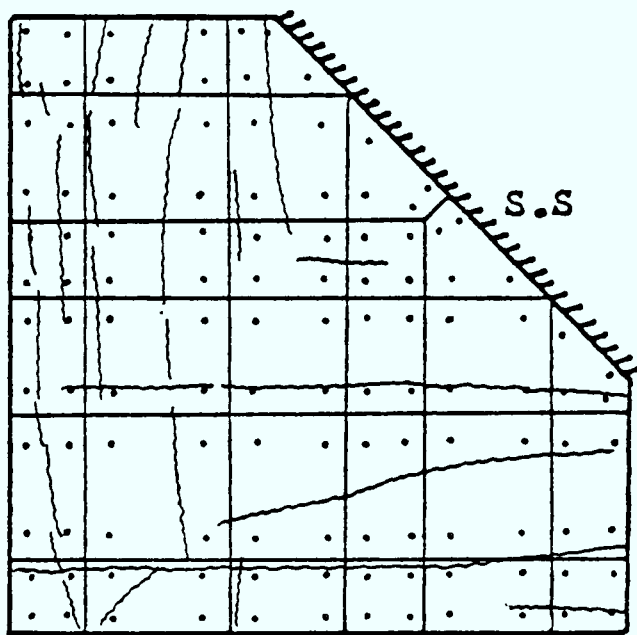
Figure 8.15 Variation of Steel Stress With Load in the Prestressed Concrete Slab



Load 200KN(0.0803 N/mm²)



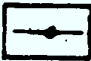



Load 280KN(0.1125 N/mm²)

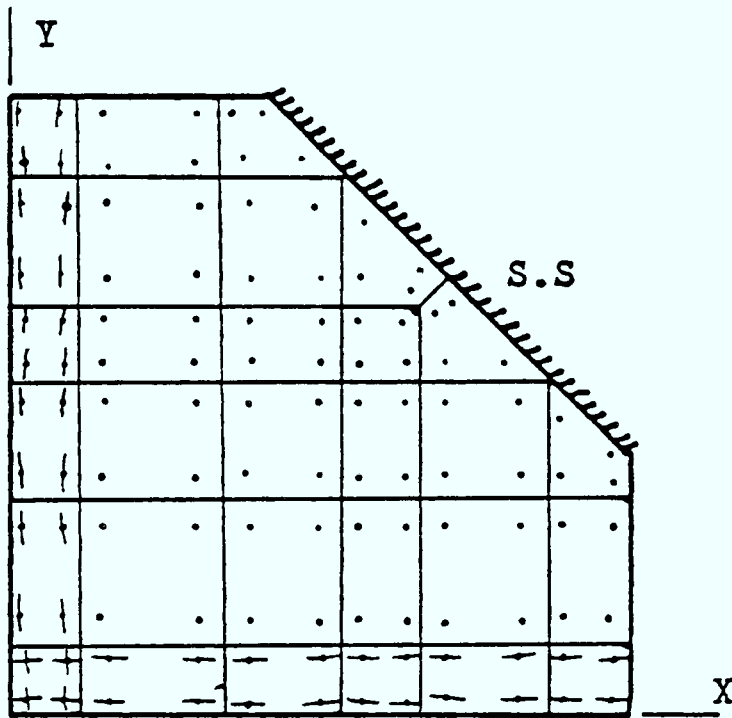
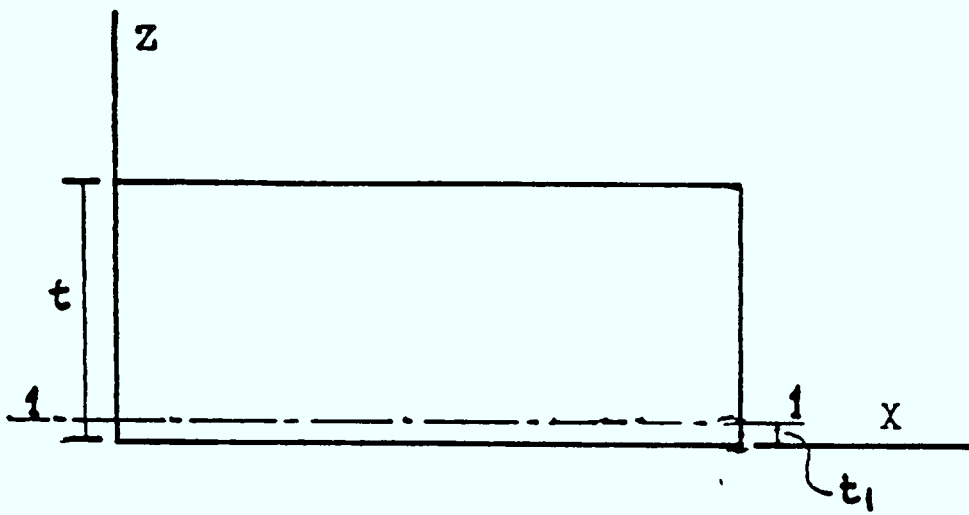


Load at Failure

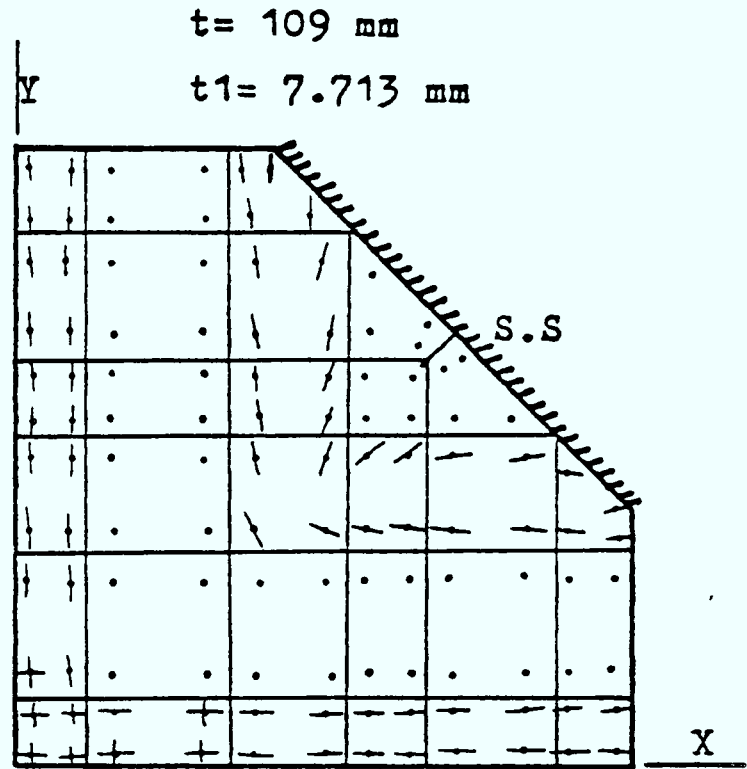
Figure 8.16 Experimental Cracks at the Bottom Surface of the Slab

SYMBOLS

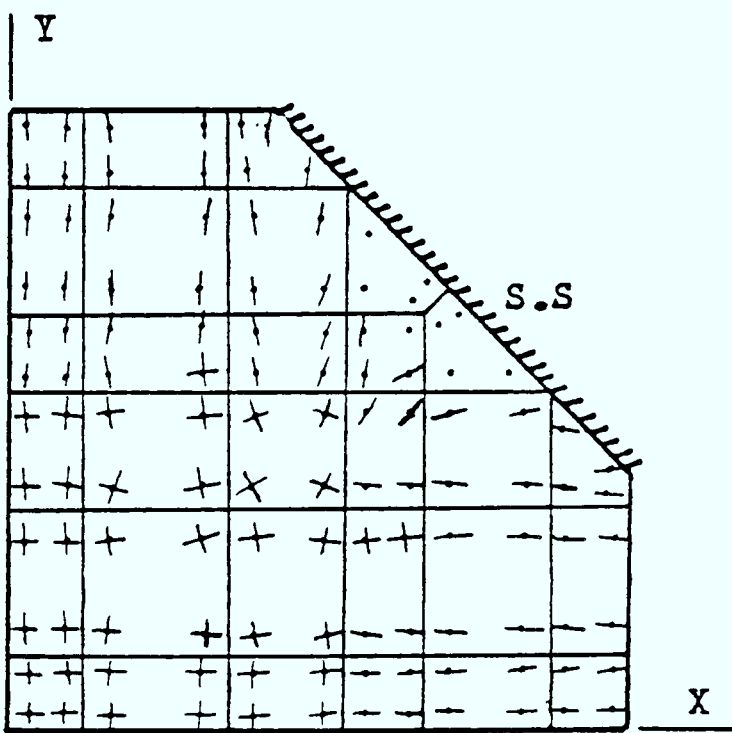
-  One Crack $\perp \sigma_1$
-  Two Cracks $\perp \sigma_1, \sigma_2$
-  Three Cracks $\perp \sigma_1, \sigma_2, \sigma_3$
-  Uncracked Gauss Point



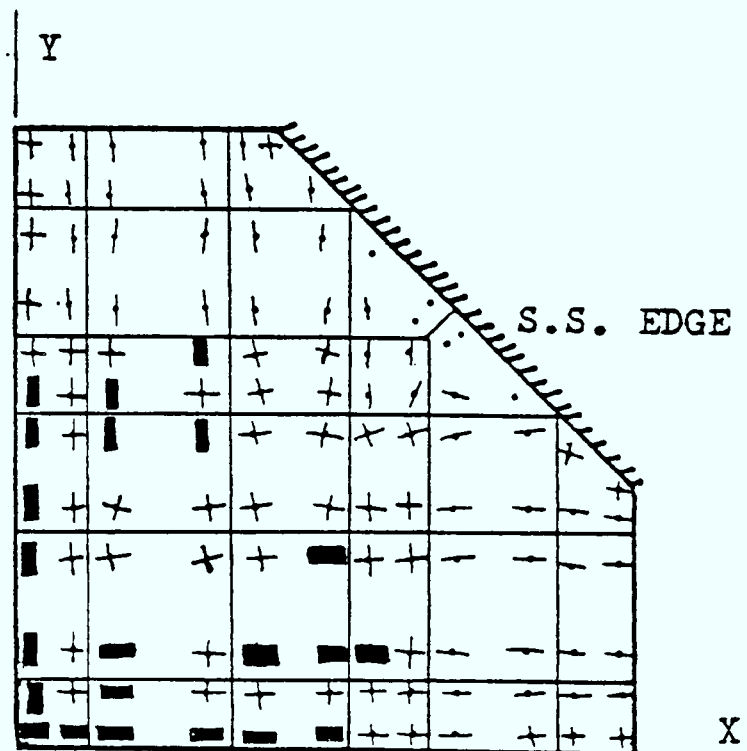
Load 200kN (0.0803 N/mm²)



Load 280kN (0.1125 N/mm²)



Load 336kN (0.135 N/mm²)




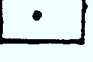


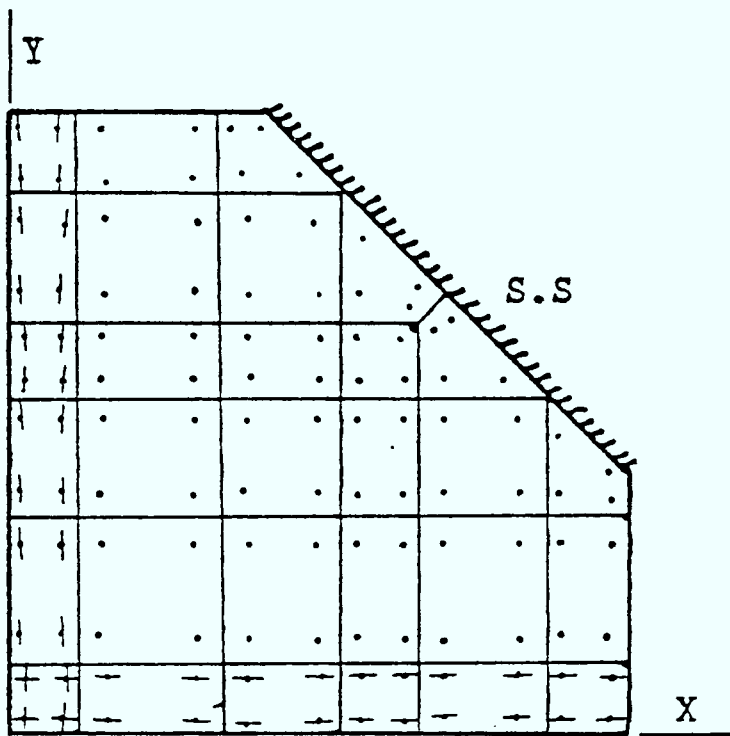
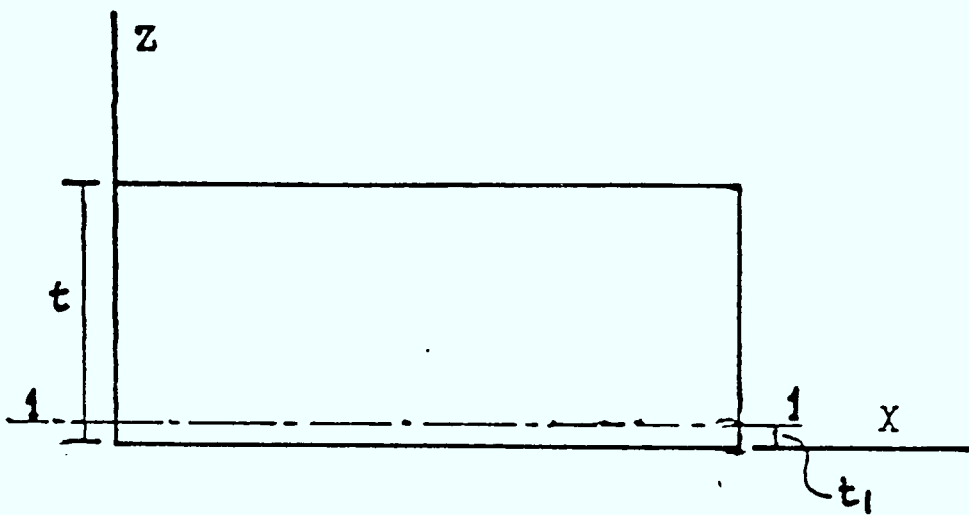
Load 400kN (0.1606 N/mm²)

Slab Type - Bonded

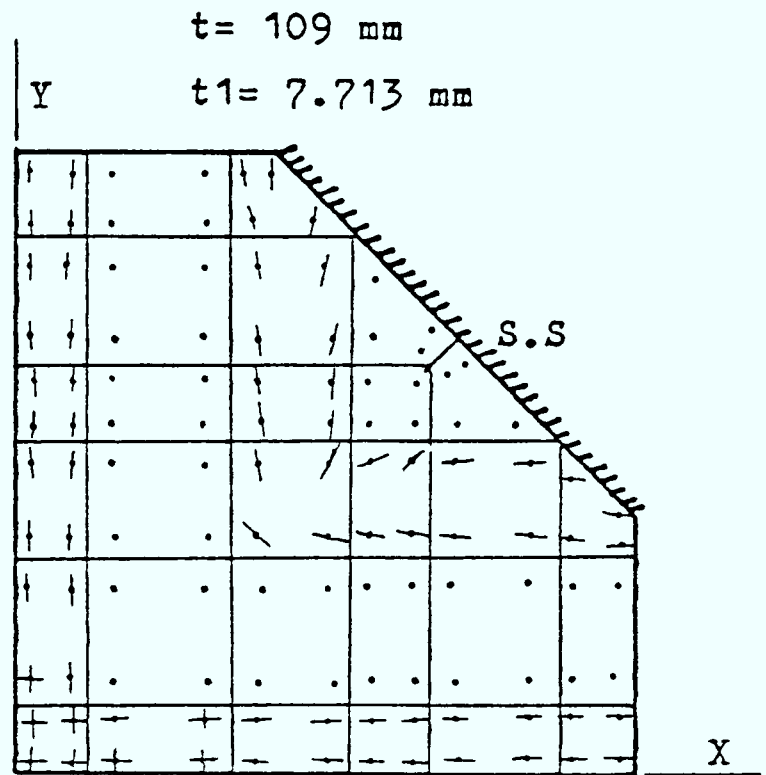
Figure 8.17 Crack Patterns of the Slab at 1-1

SYMBOLS

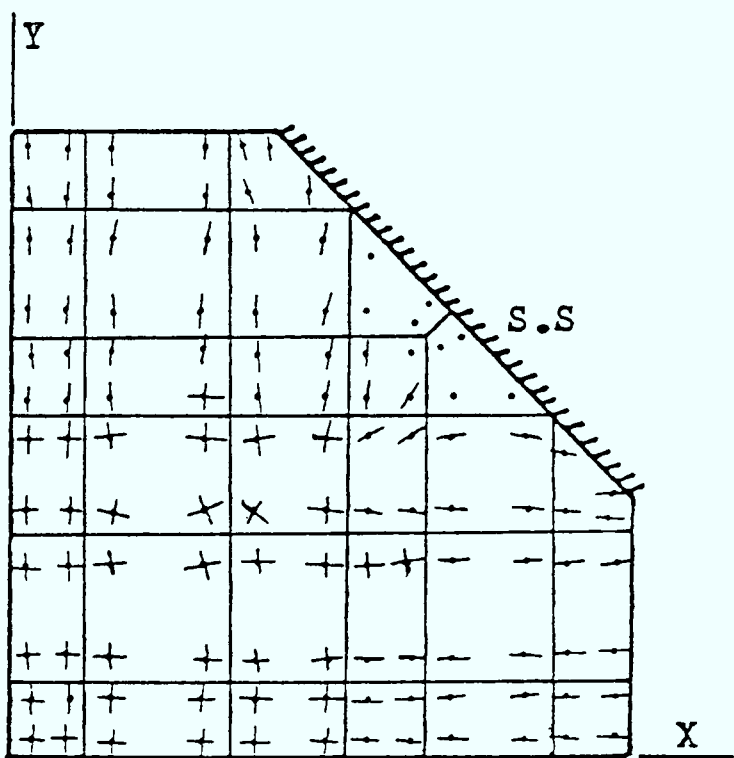
-  One Crack $\perp \sigma_1$
-  Two Cracks $\perp \sigma_1, \sigma_2$
-  Three Cracks $\perp \sigma_1, \sigma_2, \sigma_3$
-  Uncracked Gauss Point



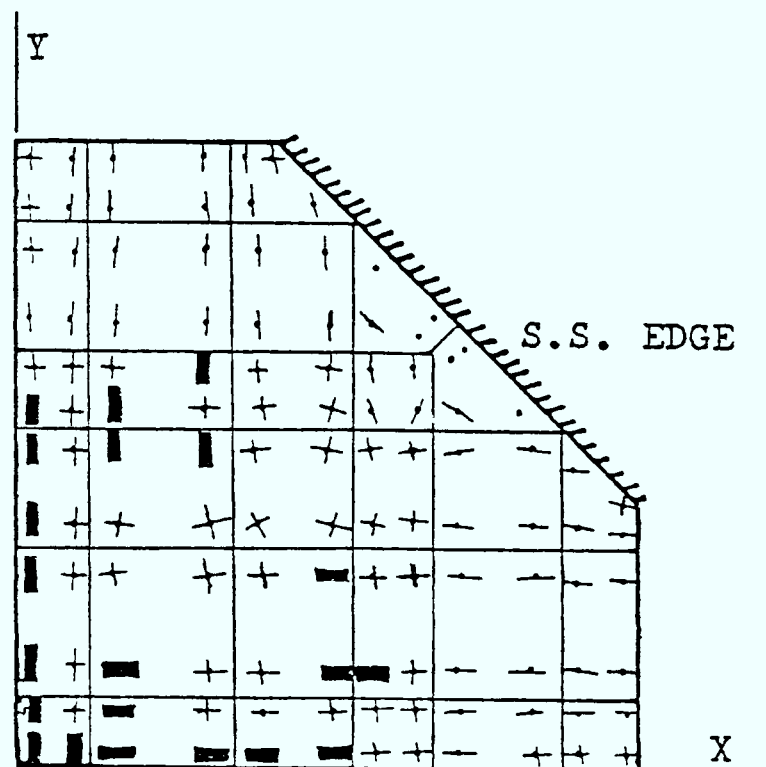
Load 200KN(0.0803 N/mm²)



Load 280KN(0.1125 N/mm²)



Load 336KN(0.135 N/mm²)



Load 400KN(0.1606 N/mm²)

Slab Type - Perfectly Bonded

Figure 8.18 Crack Patterns of the Slab at 1-1

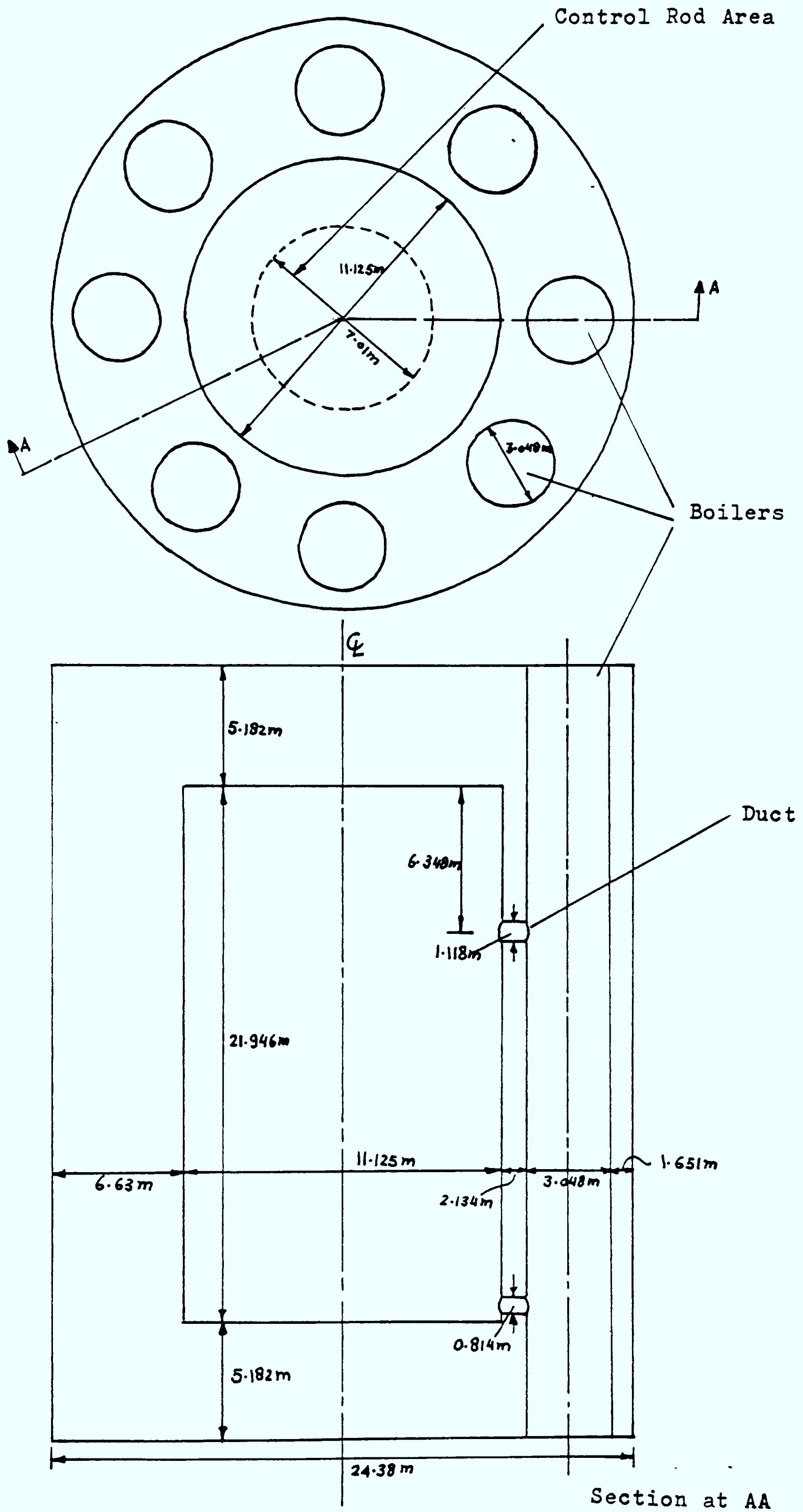


Figure 8.19 Prestressed Concrete Reactor Vessel (HTGCR)

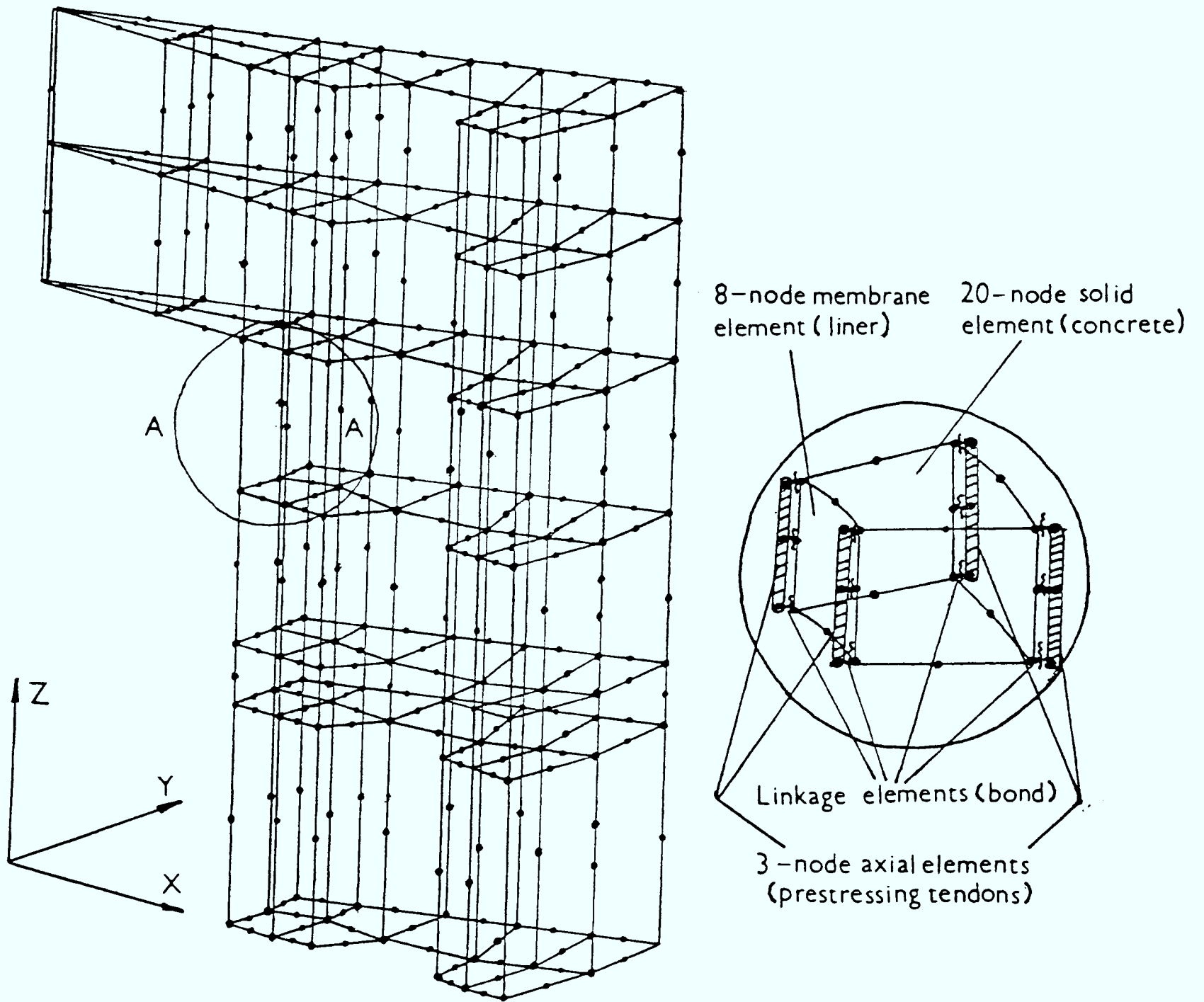
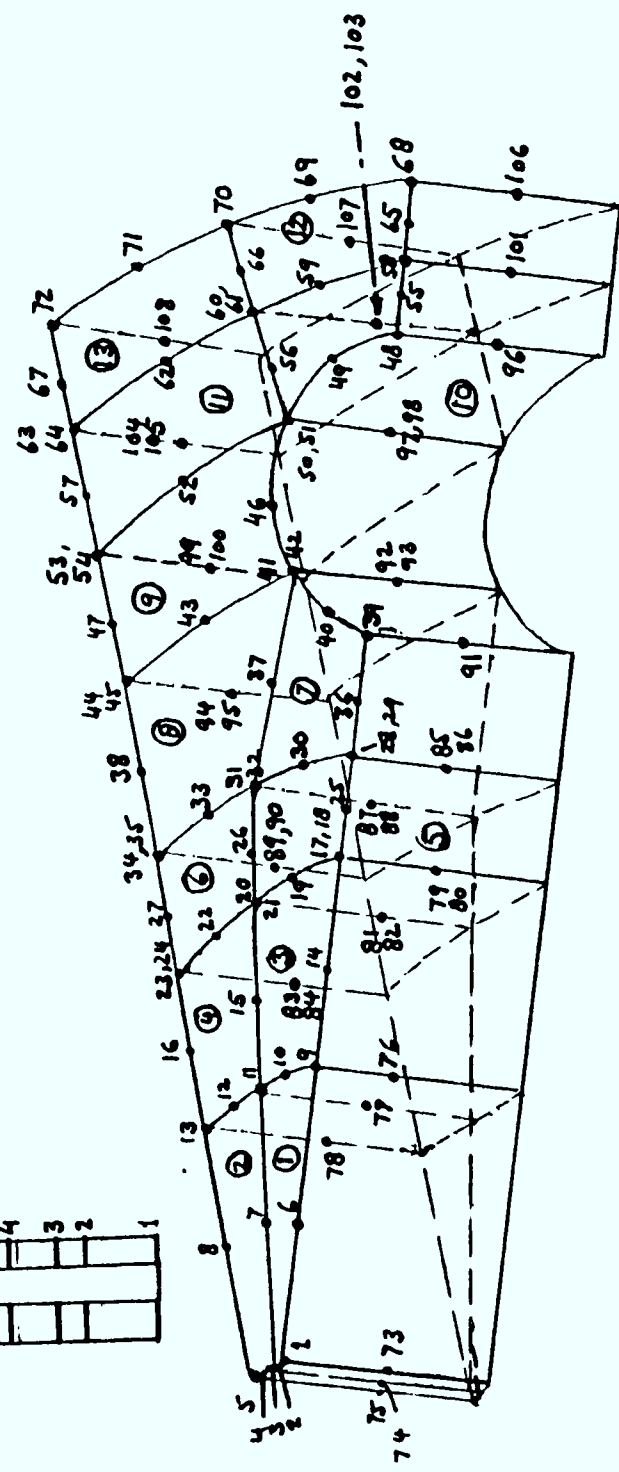
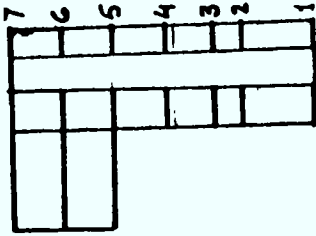
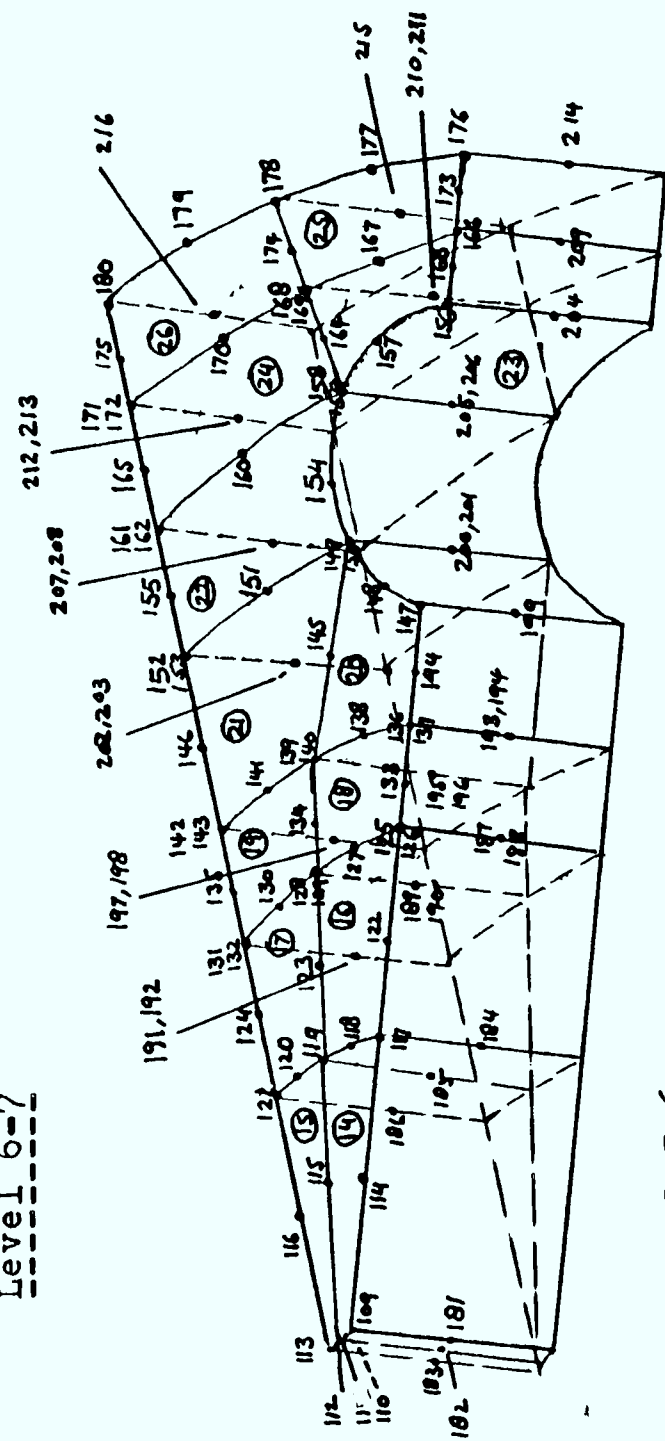


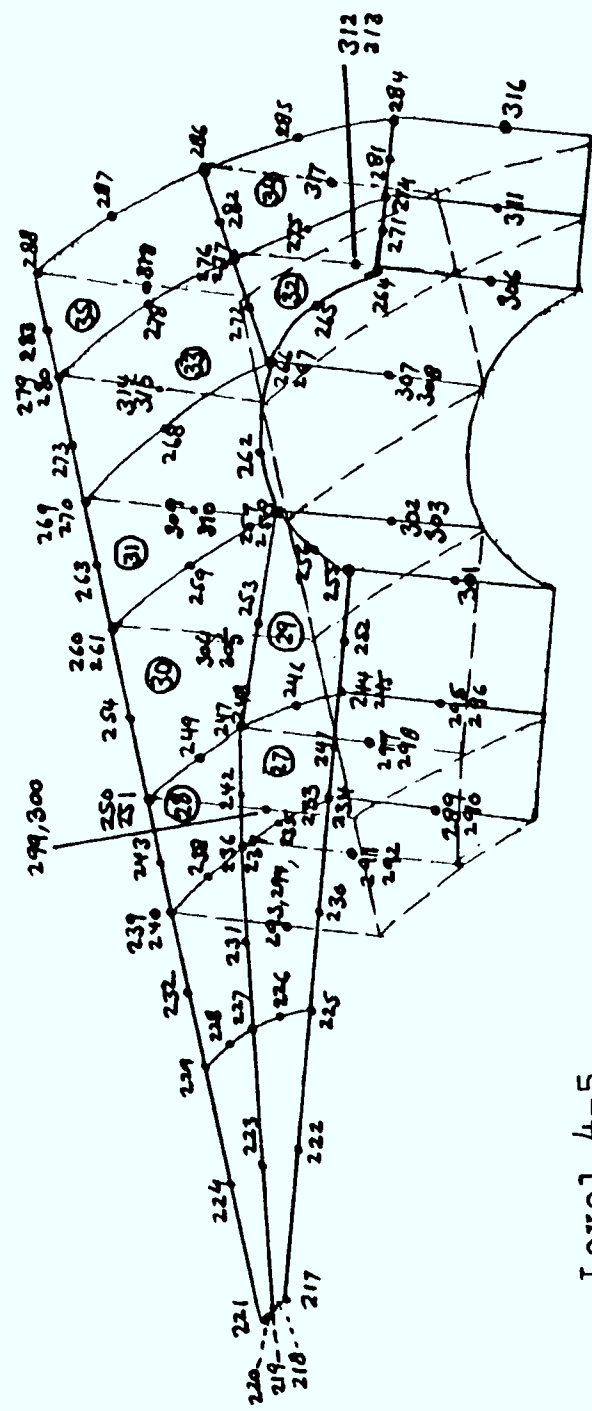
Figure 8.20 Finite Element Mesh of Bonded Reactor Vessel



Level 6-7



Level 5-6

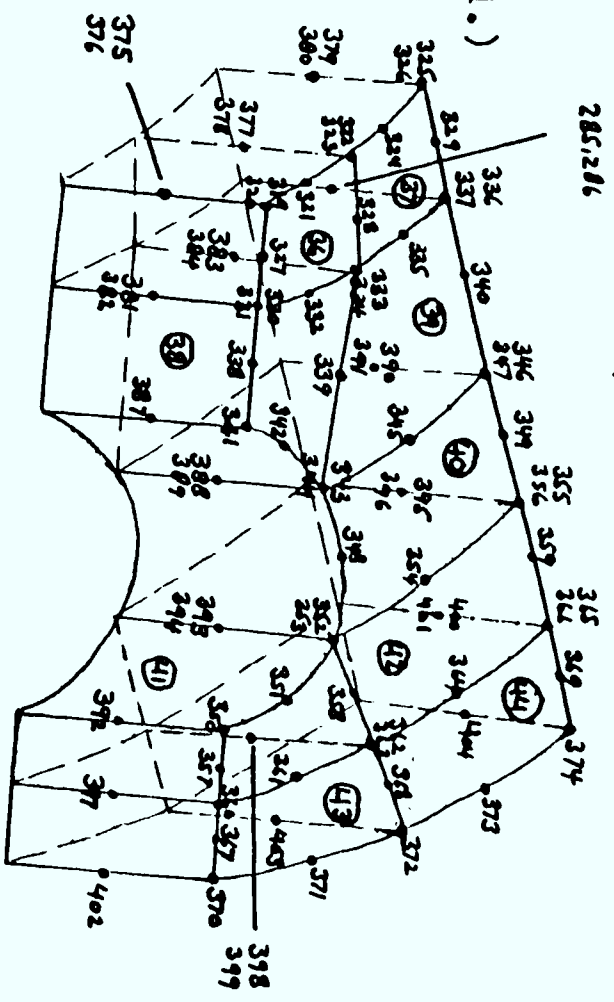


Level 4-5

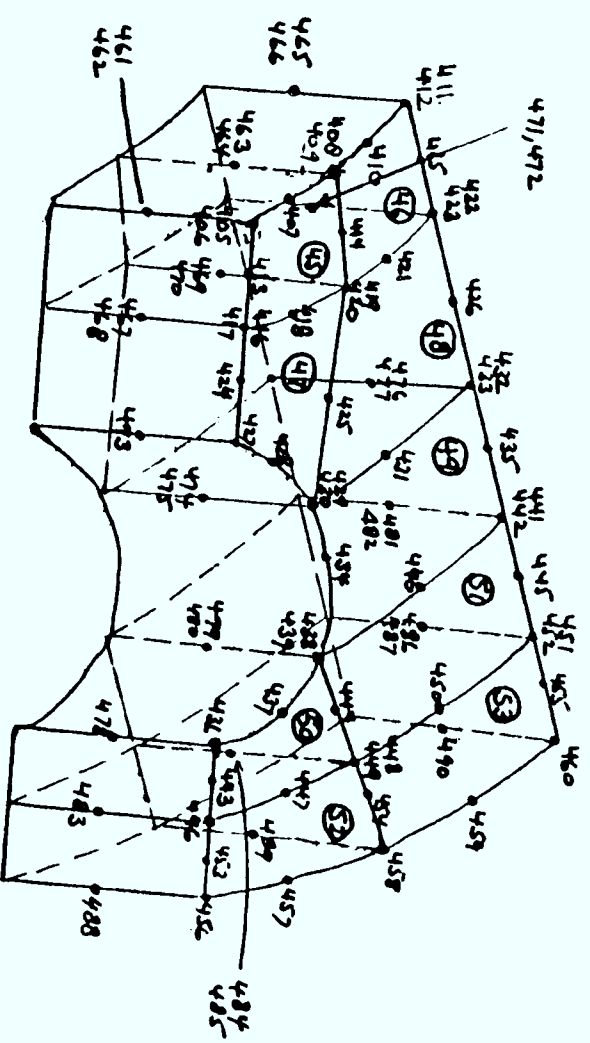
• - Node Number
 O - Element Number

Figure 8.21 Detailed Finite Element Mesh for Bonded Reactor Vessel

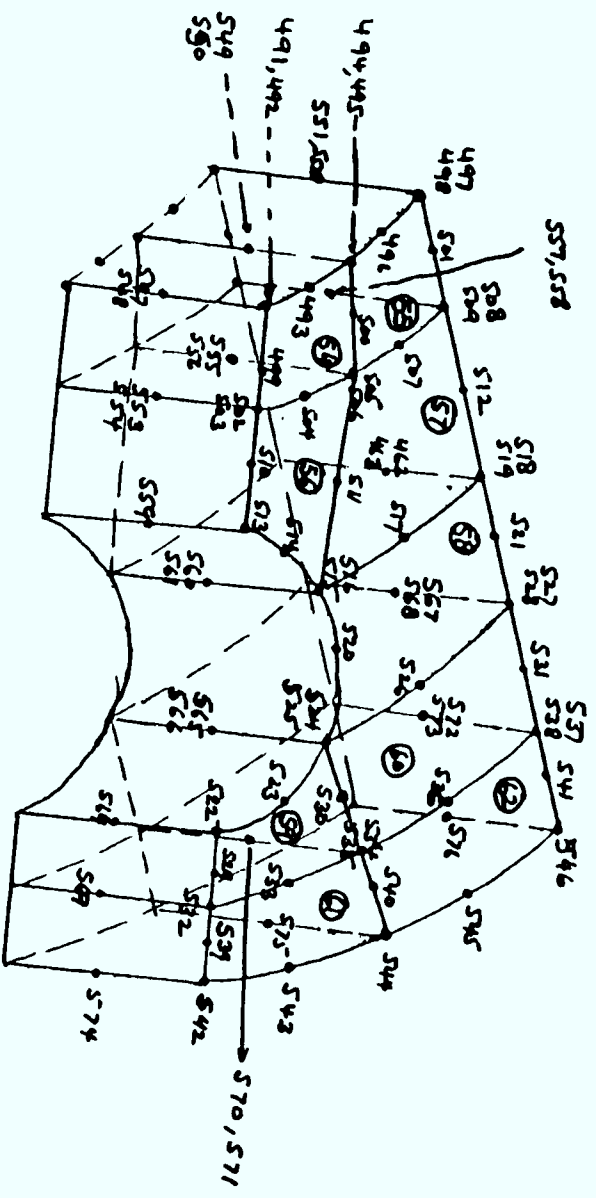
Figure 8.21 (Contd.)



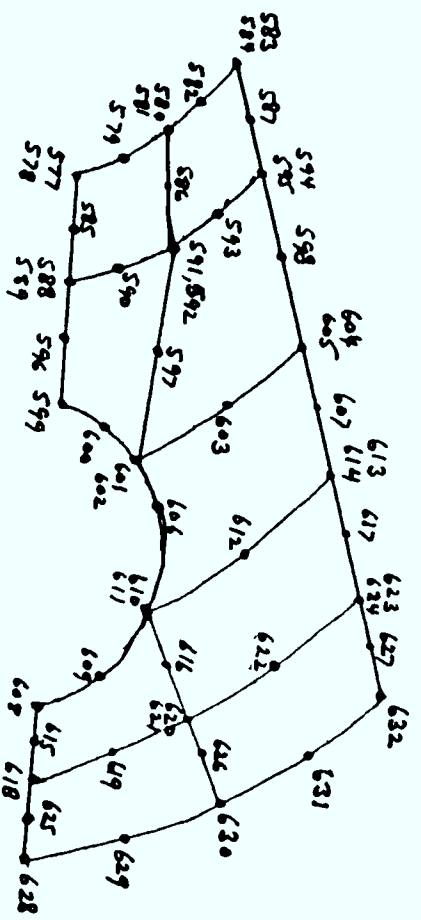
Level 3-4



Level 2-3



Level 1-2



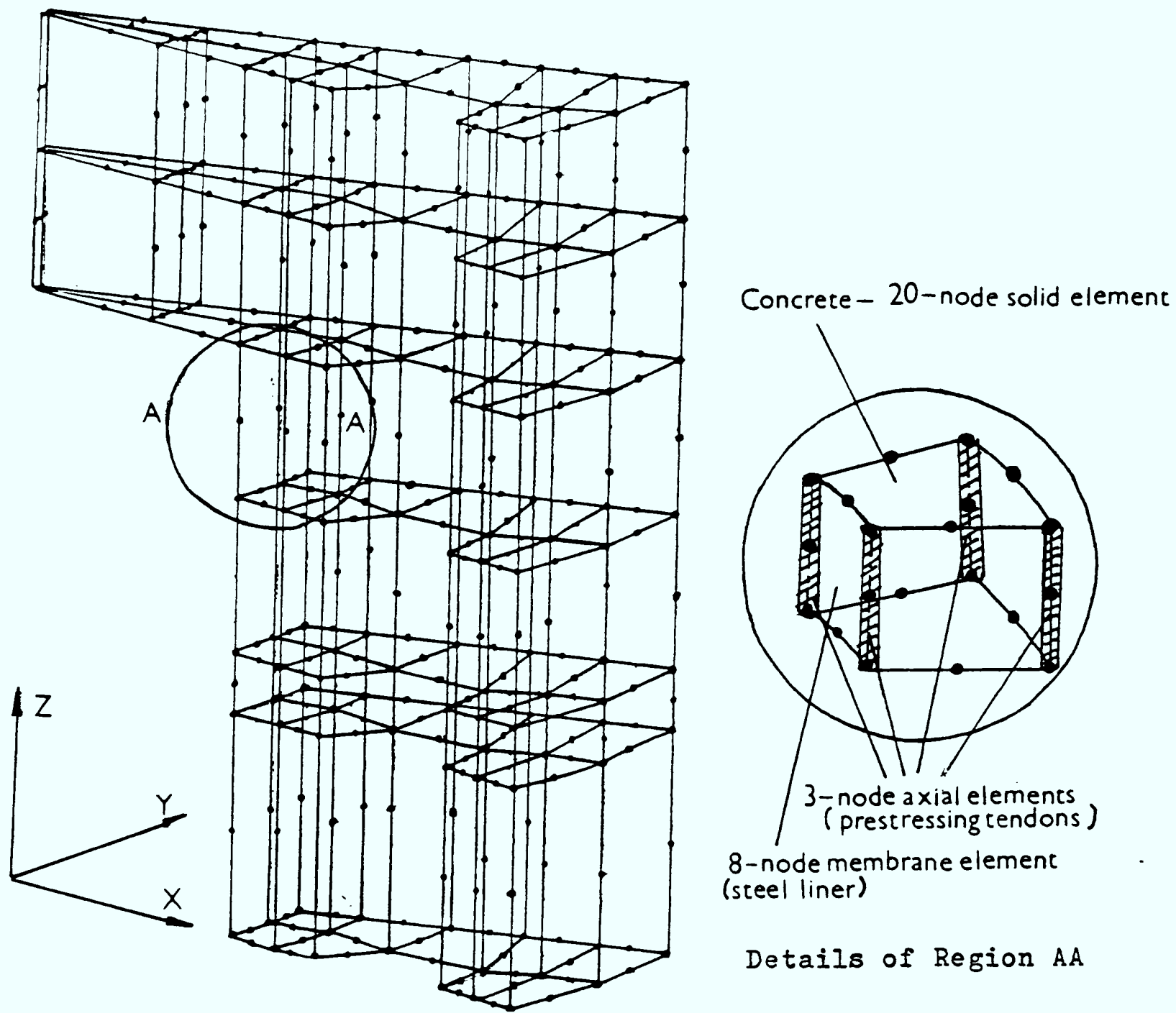
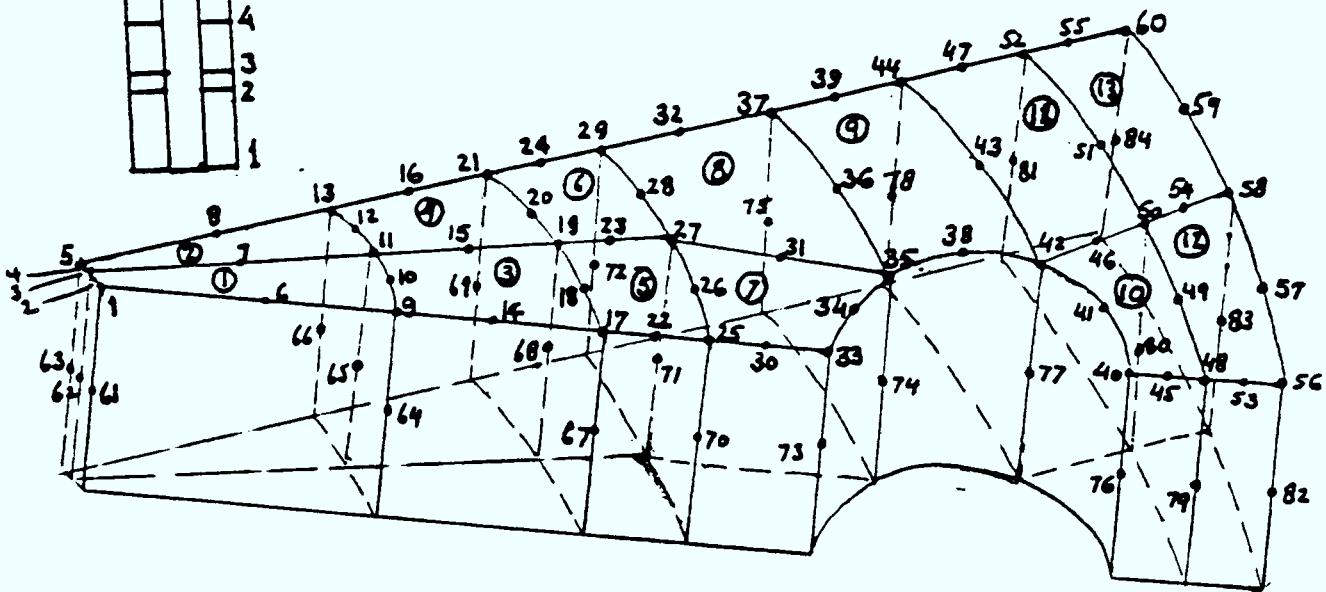
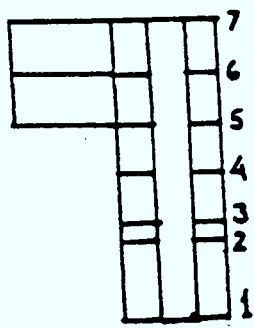
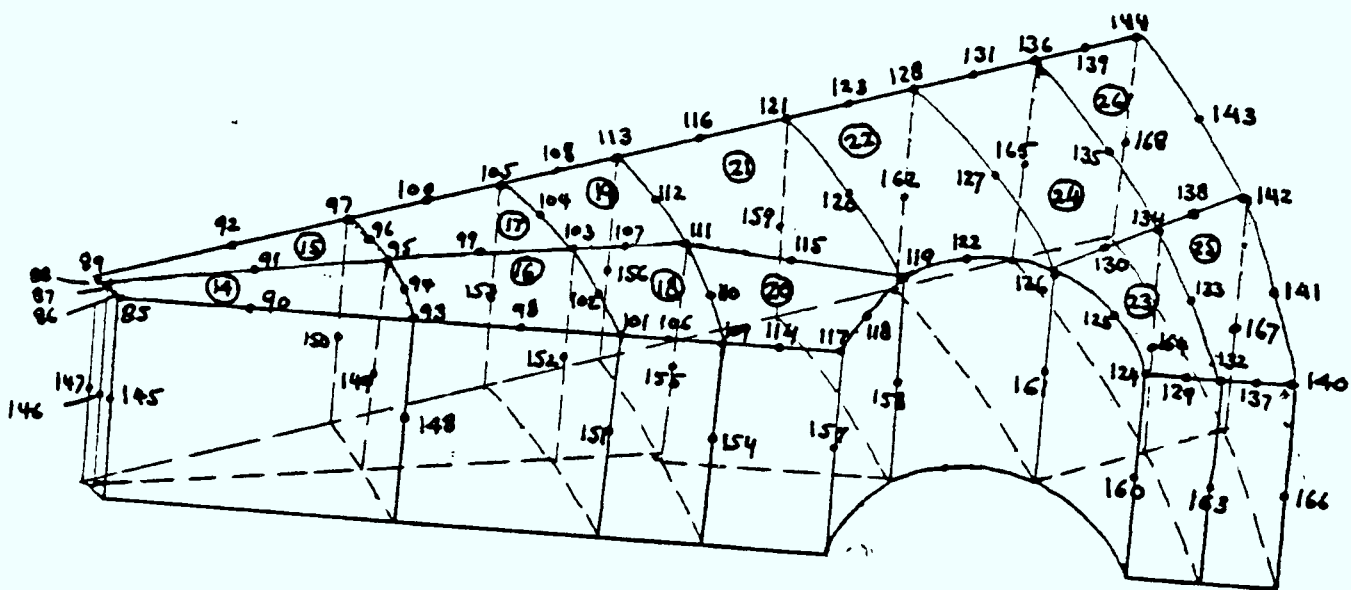


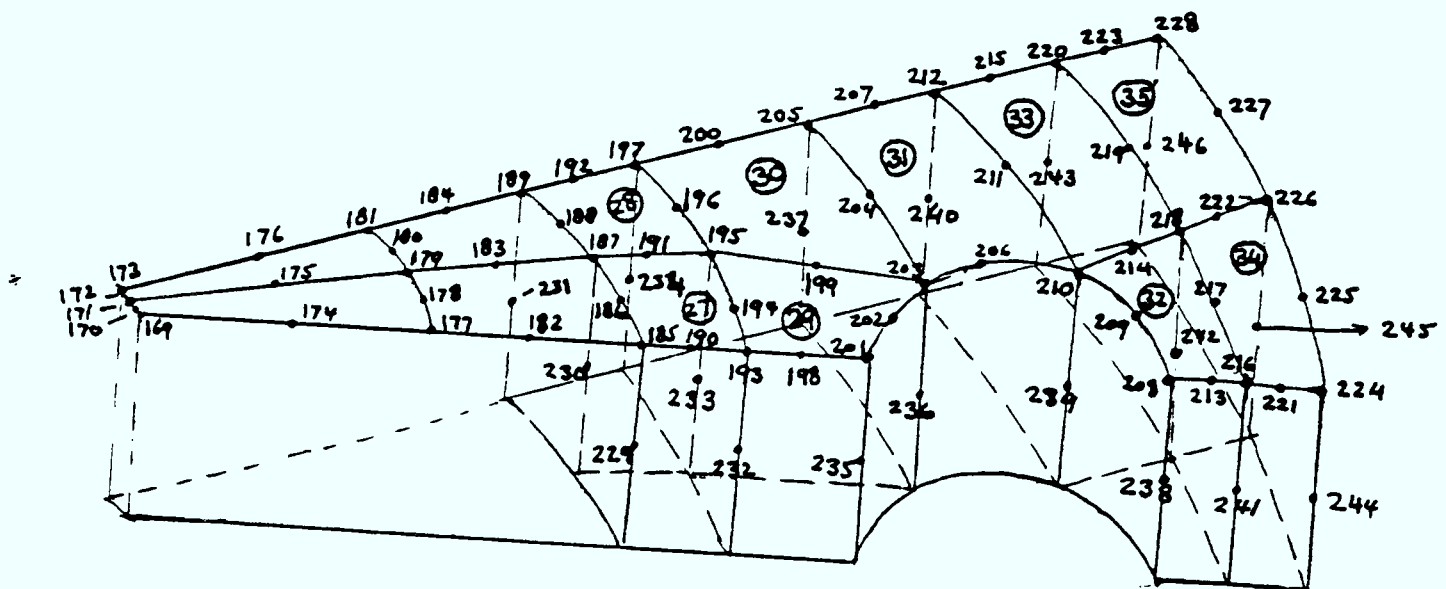
Figure 8.22 Finite Element of Perfectly Bonded Reactor Vessel



Level 6-7



Level 5-6



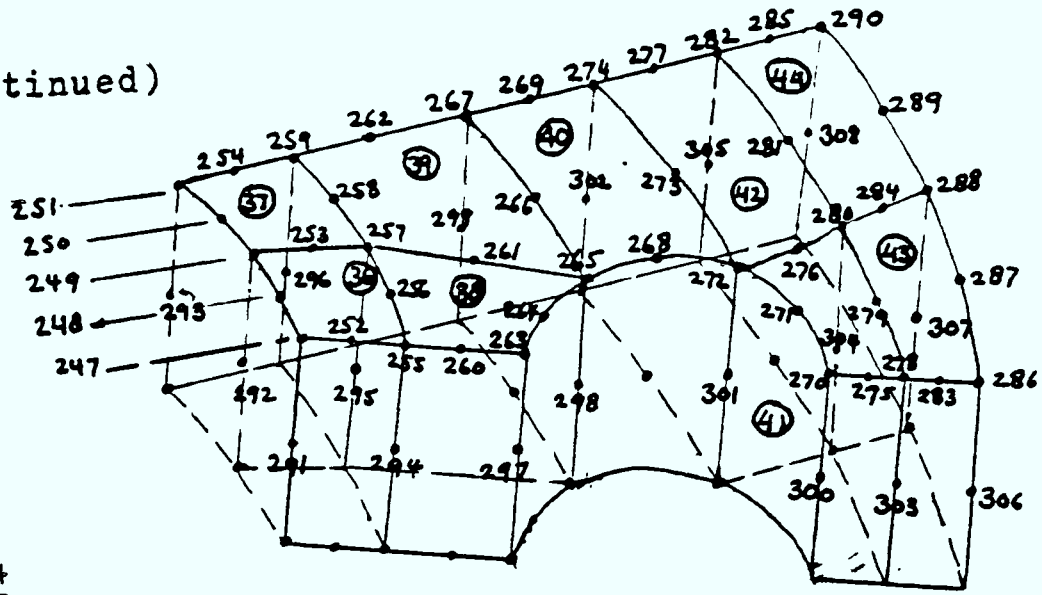
Level 4-5

• - Node Number

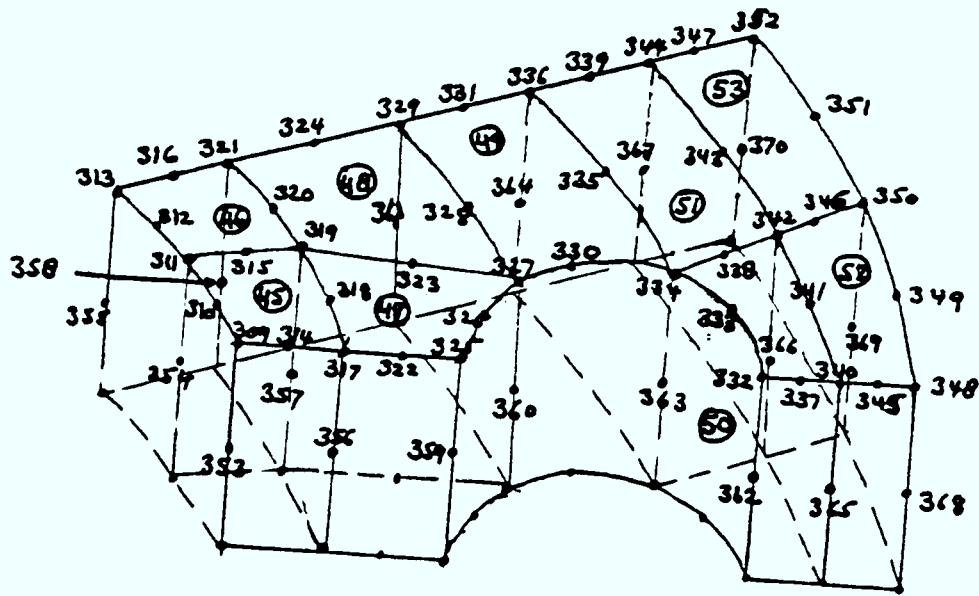
○ - Element Number

Figure 8.23 Detailed Finite Element Mesh for Perfectly Bonded Reactor Vessel

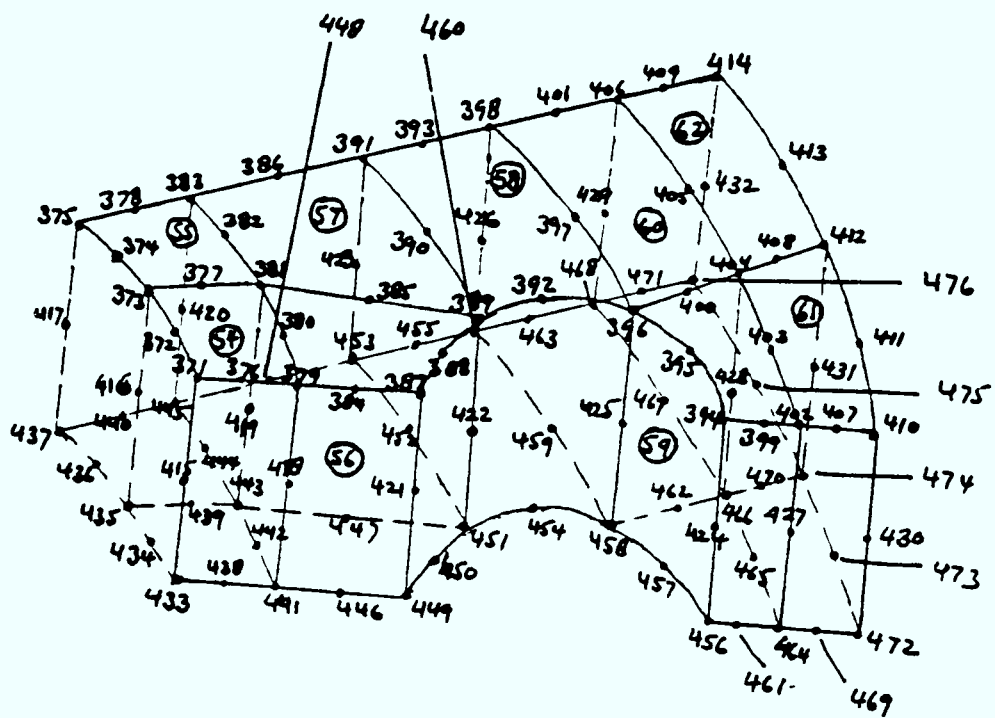
Figure 8.23 (Continued)



Level 3-4



Level 2-3



Level 1-2

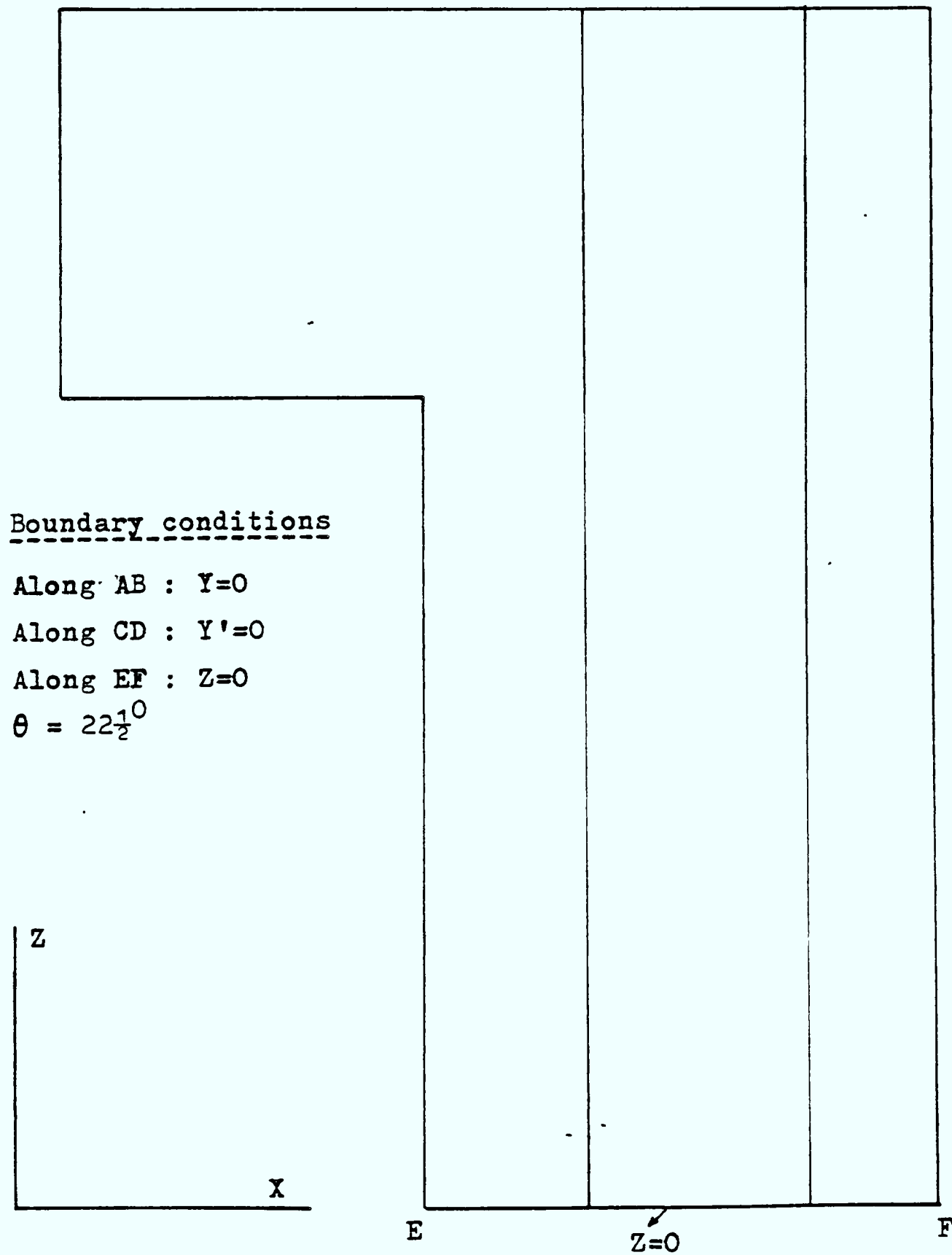
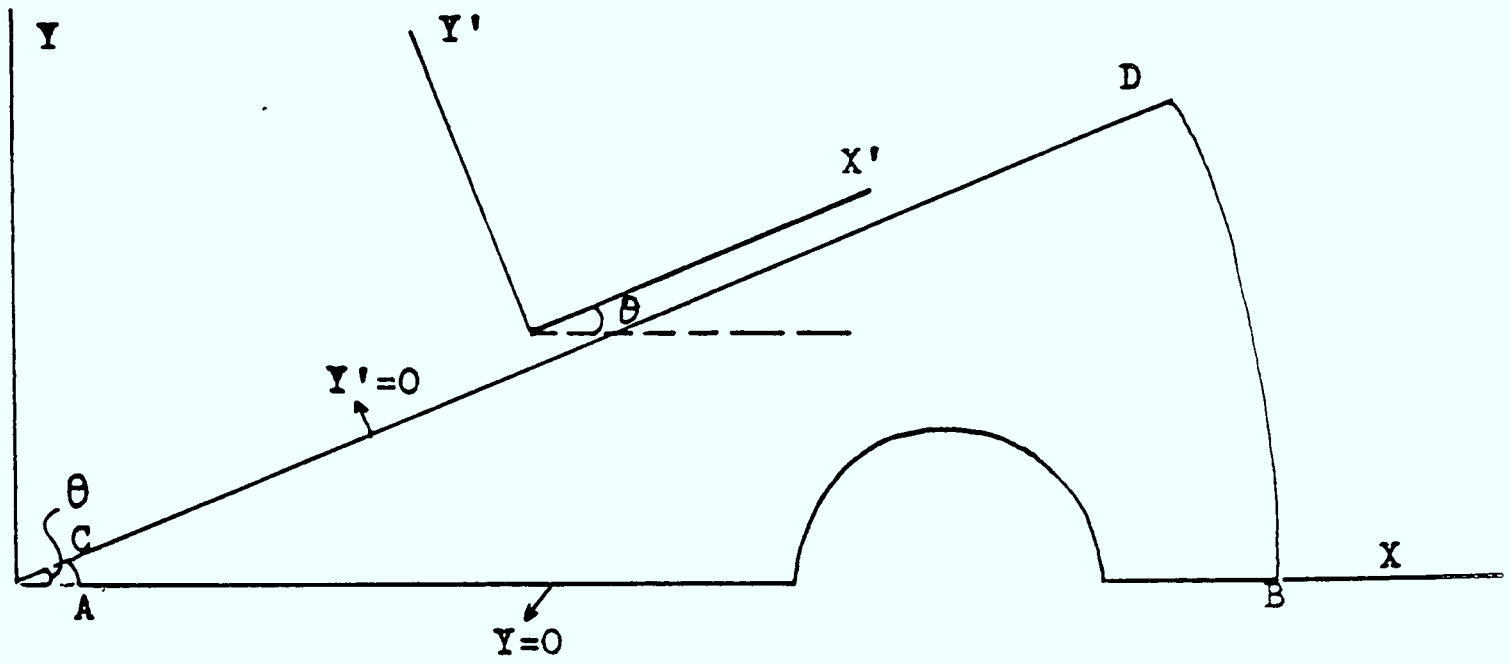


Figure 8.24 Boundary Conditions Applied on the Vessel
-247 -

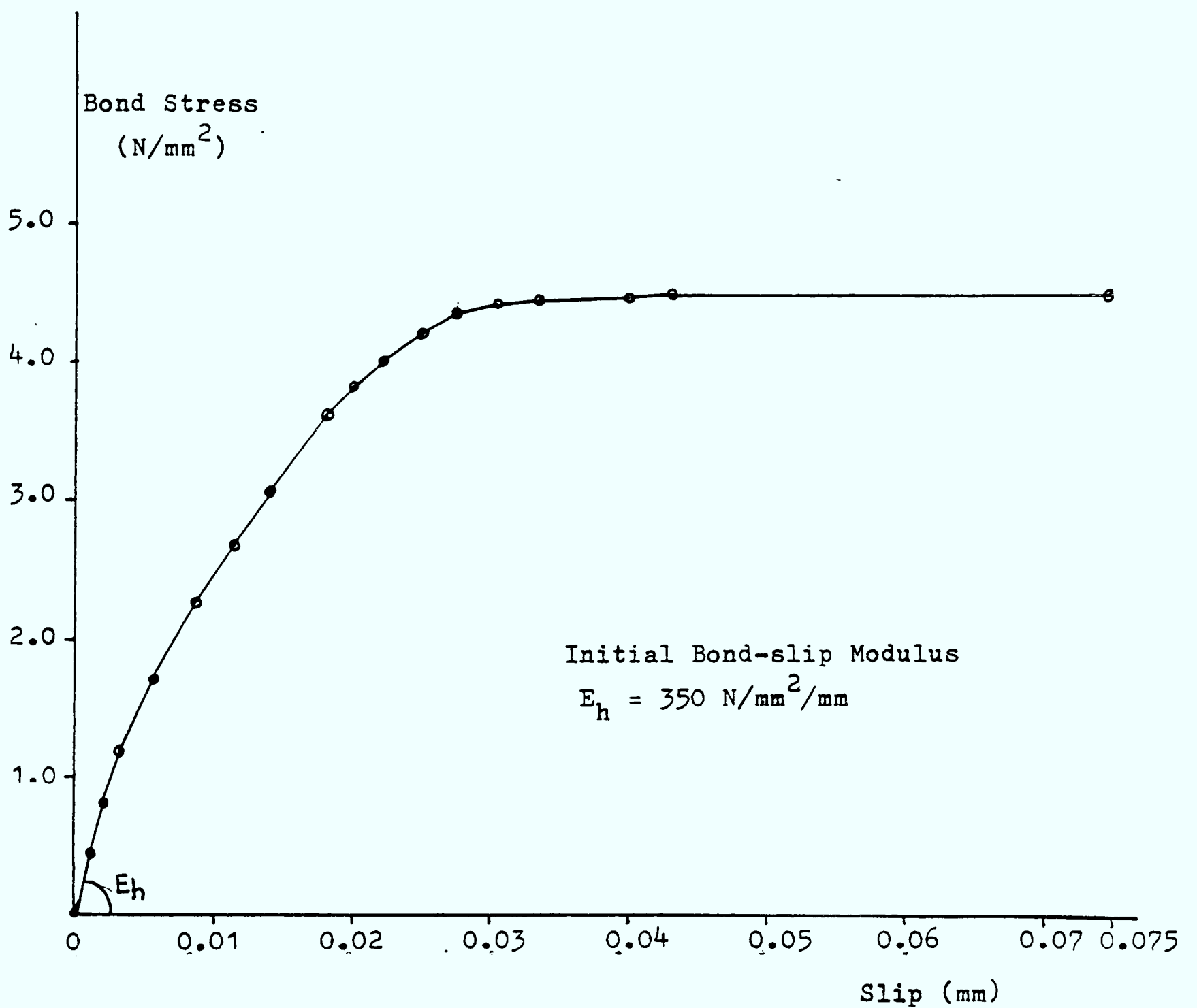


Figure 8.25 Bond Stress- Slip Curve used in the Finite Element Analysis of Prestressed Concrete Reactor Vessel(From Edward and Picard - Ref 90)

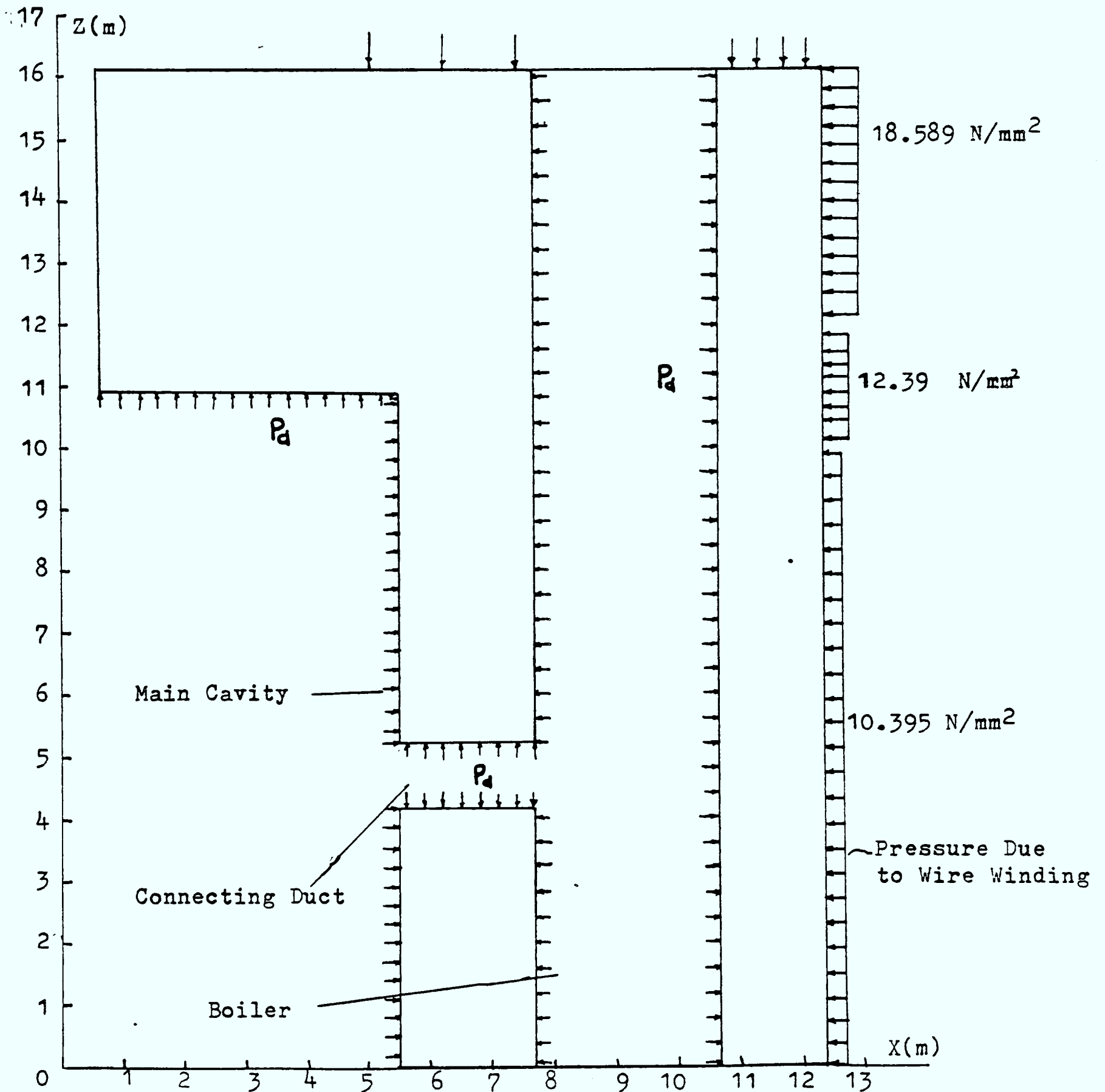
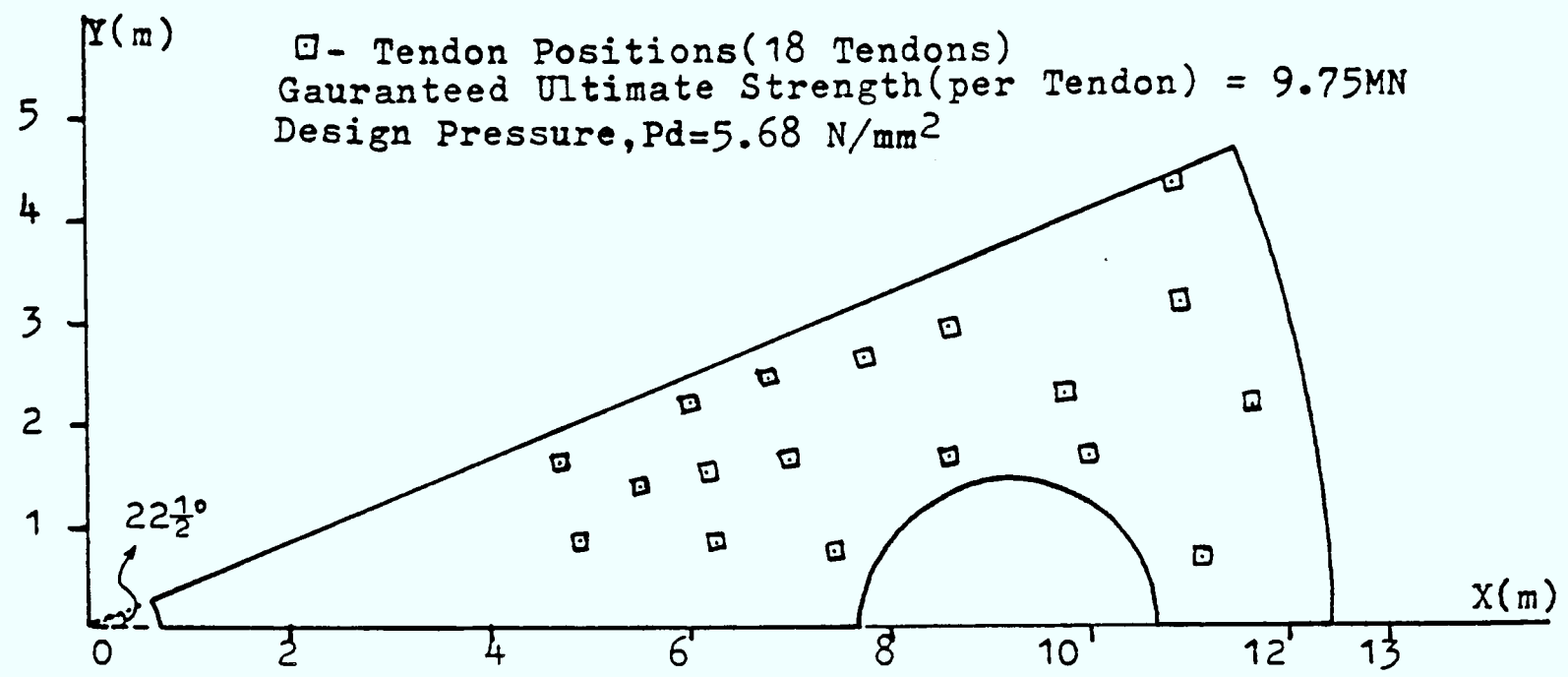


Figure 8.26 Load Distribution on the HTGCR Vessel

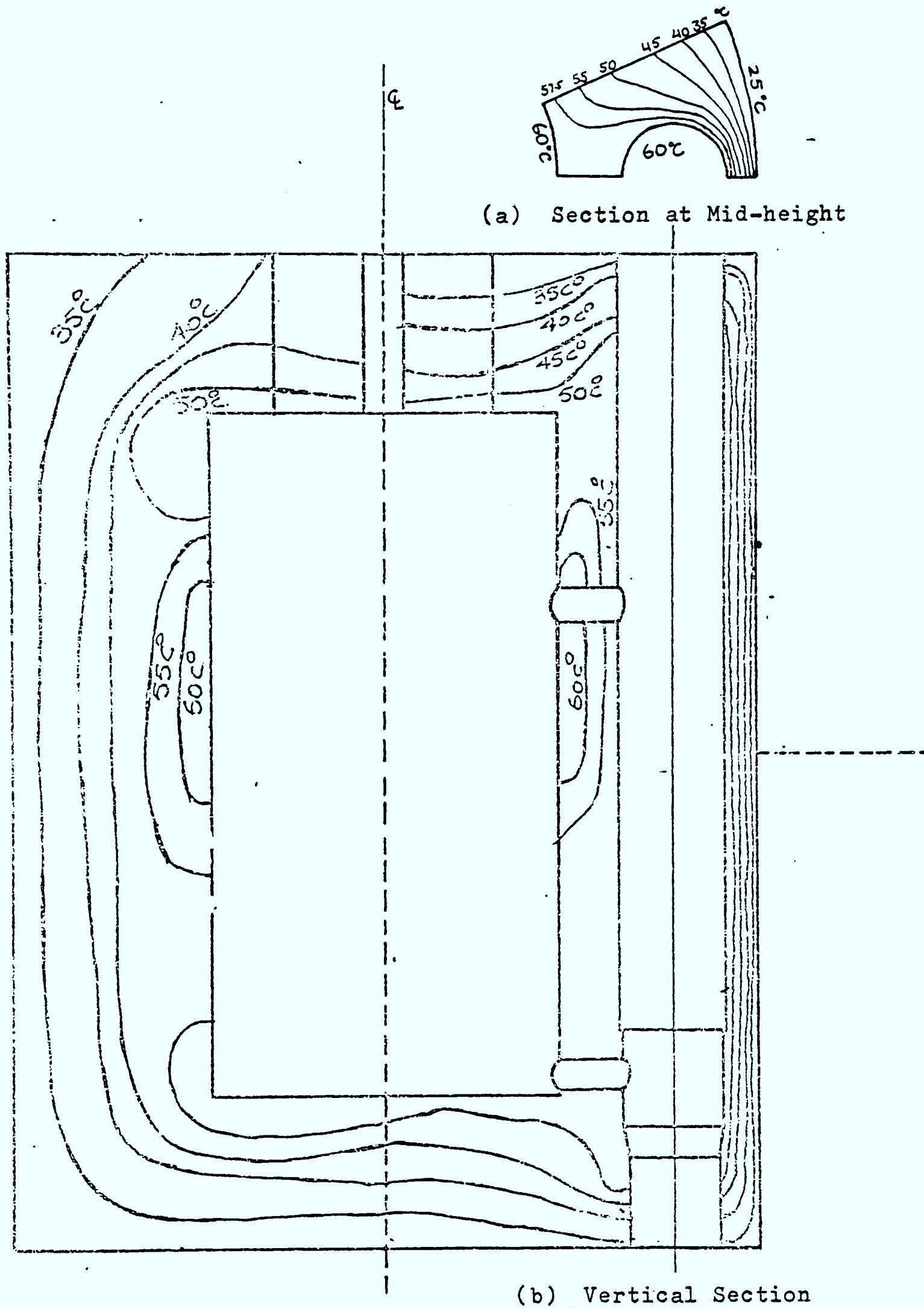


Figure 8.27 Temperature Distribution for HTGCR Vessel



Vessel Scale

ALL DIMENSIONS IN METRES

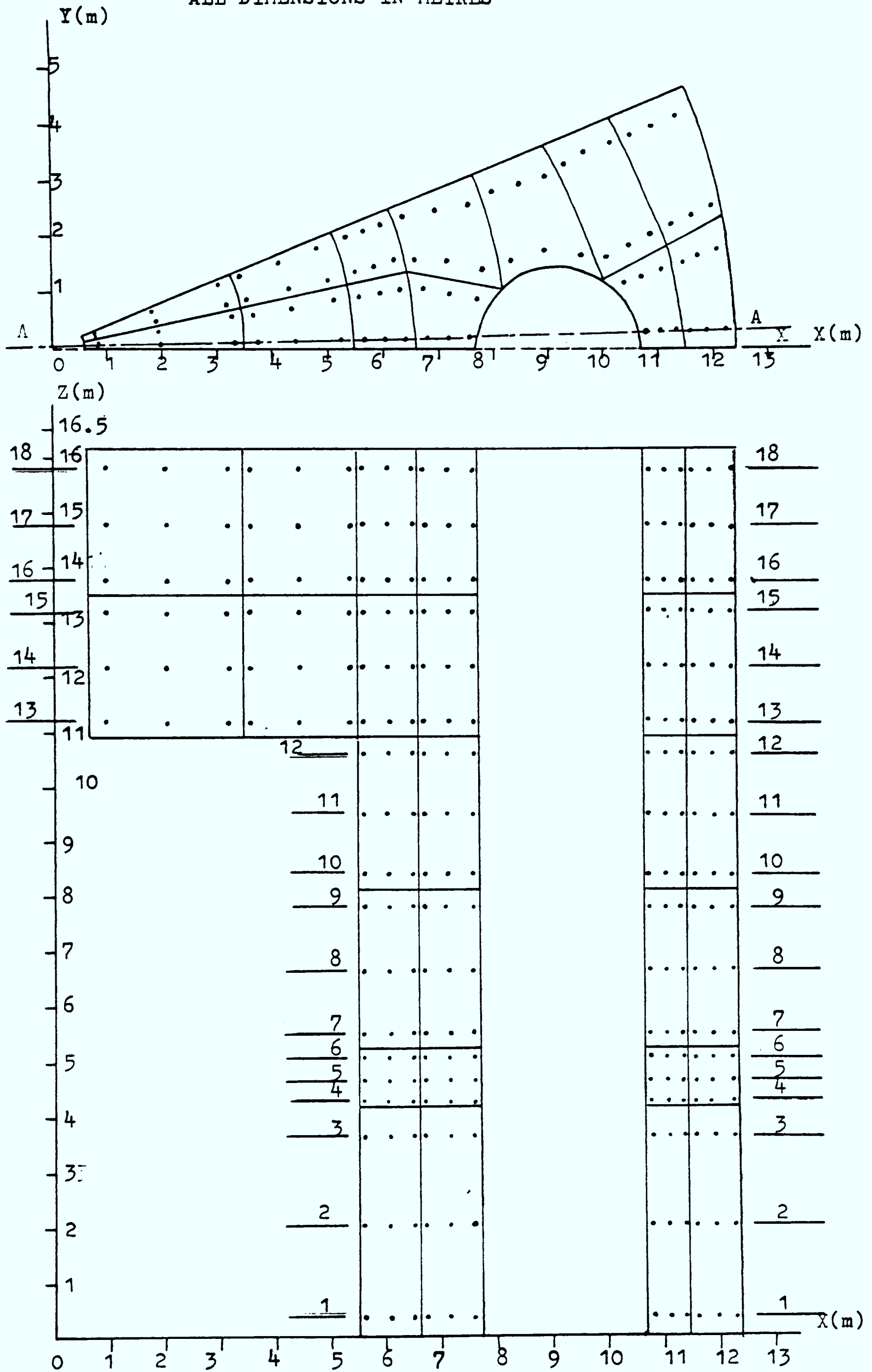
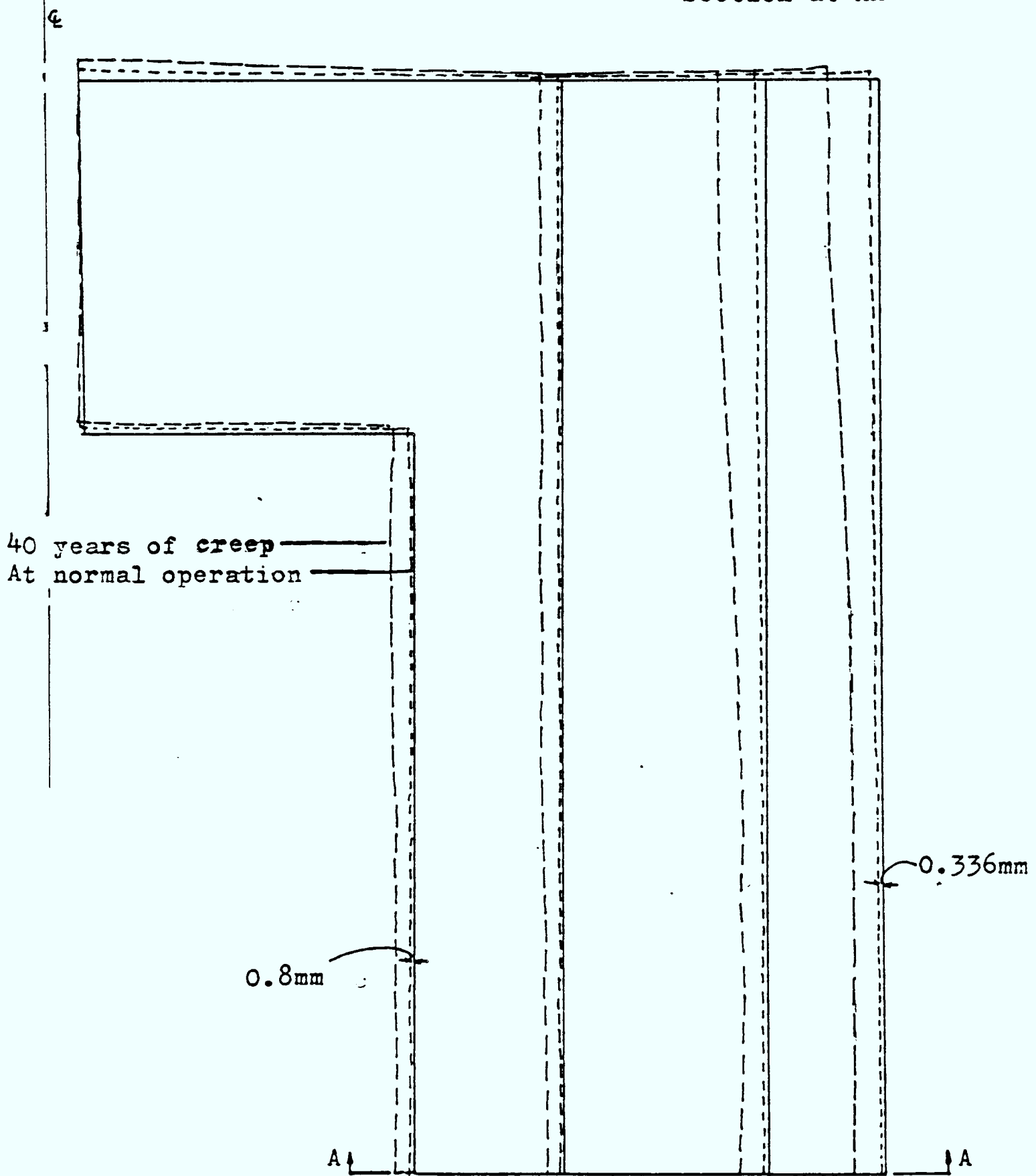
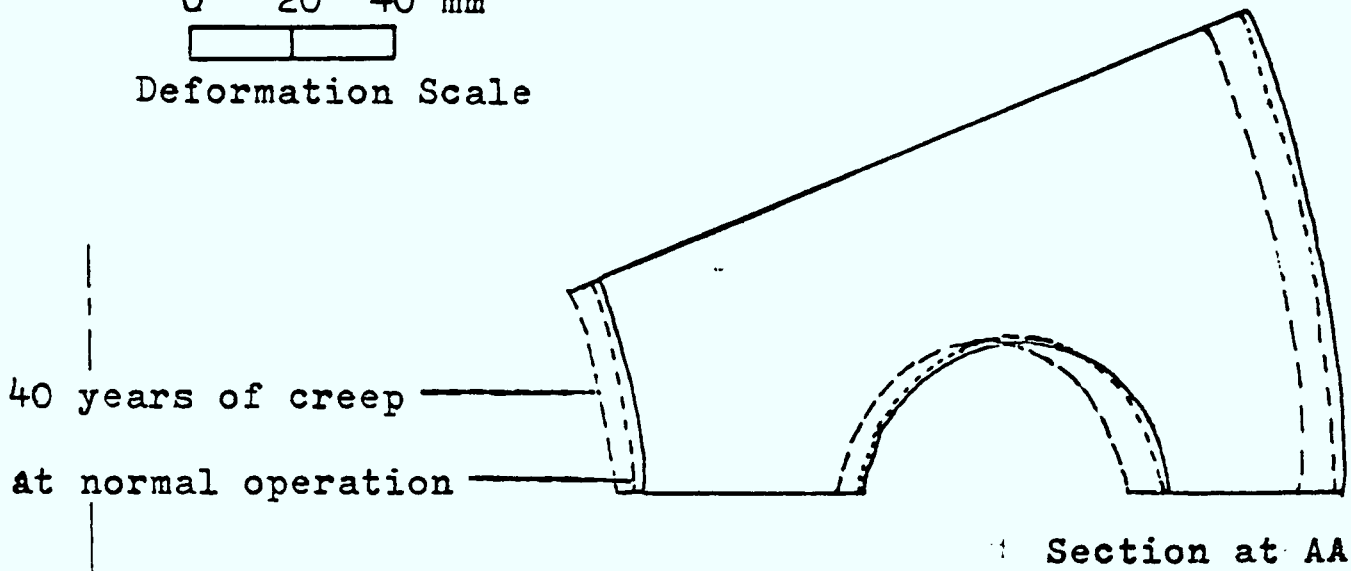
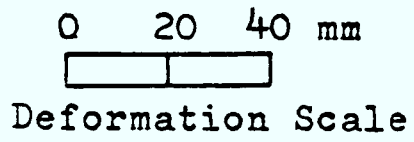
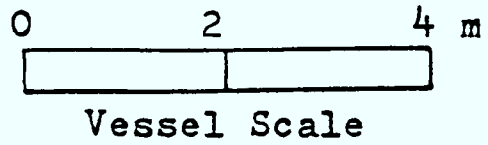
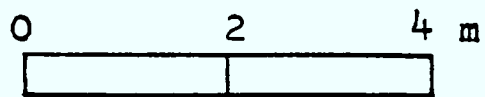


Figure 8.27c Gauss Point Locations in the Reactor Vessel

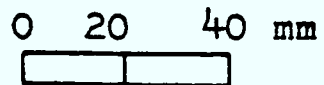


Vessel Type - Bonded (with Ahmlink Element)

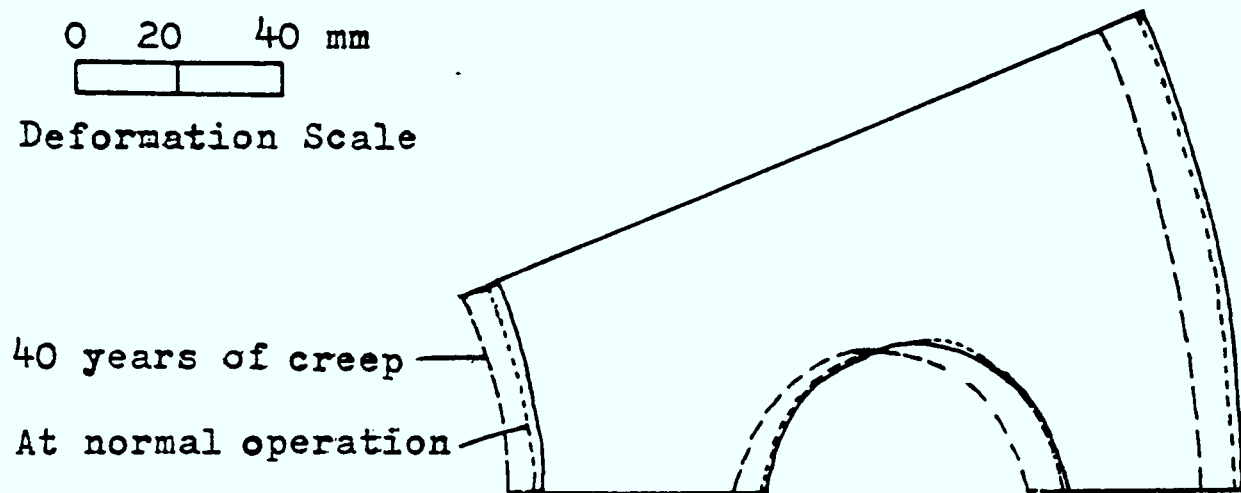
Figure 8.28 Deformations Under Normal Operation and 40 Years of Creep



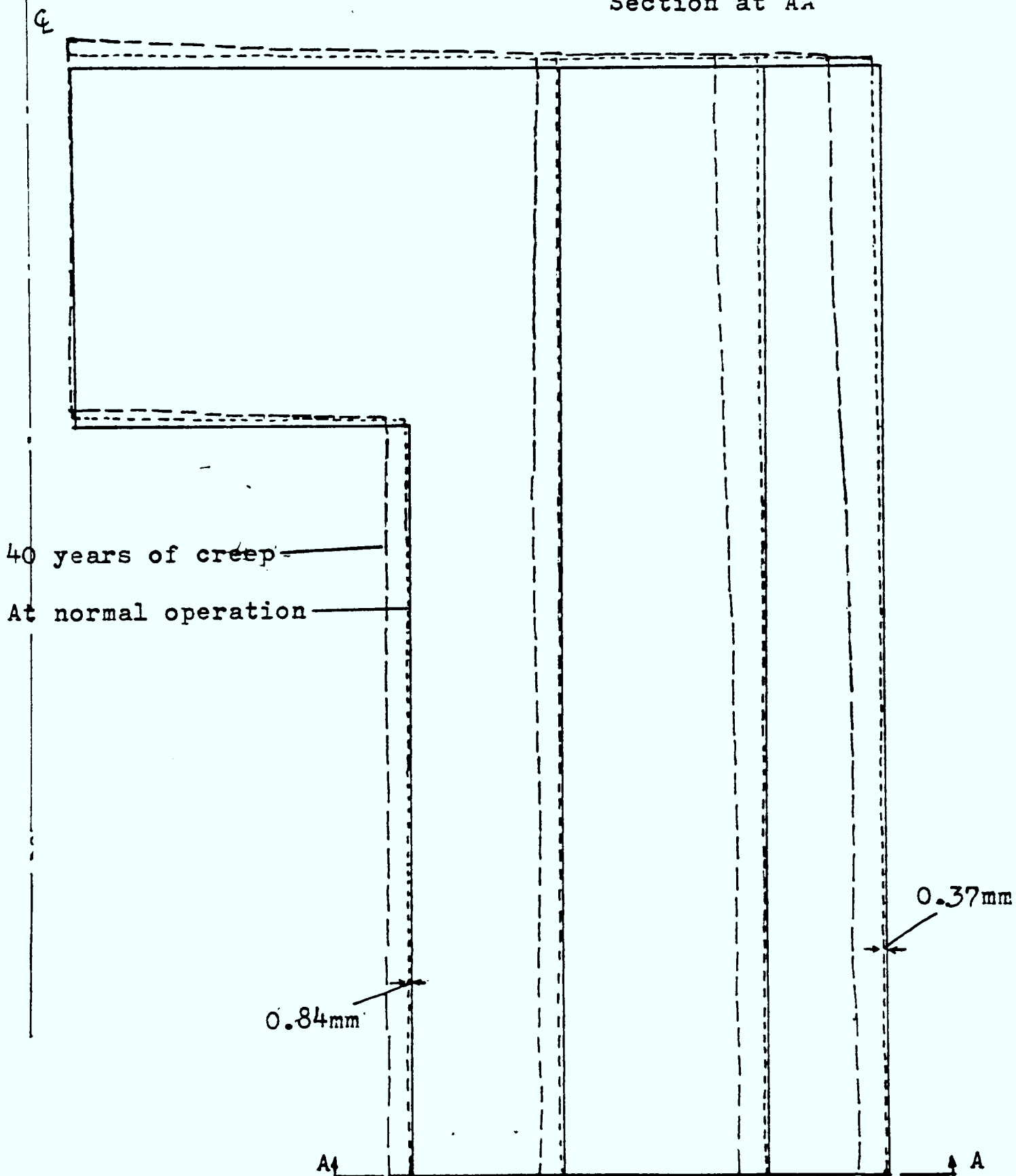
Vessel Scale



Deformation Scale



Section at A₁



Vessel Type - Perfectly Bonded

Figure 8.28a Deformations Under Normal Operation and 40 Years of Creep

0 2 4 m

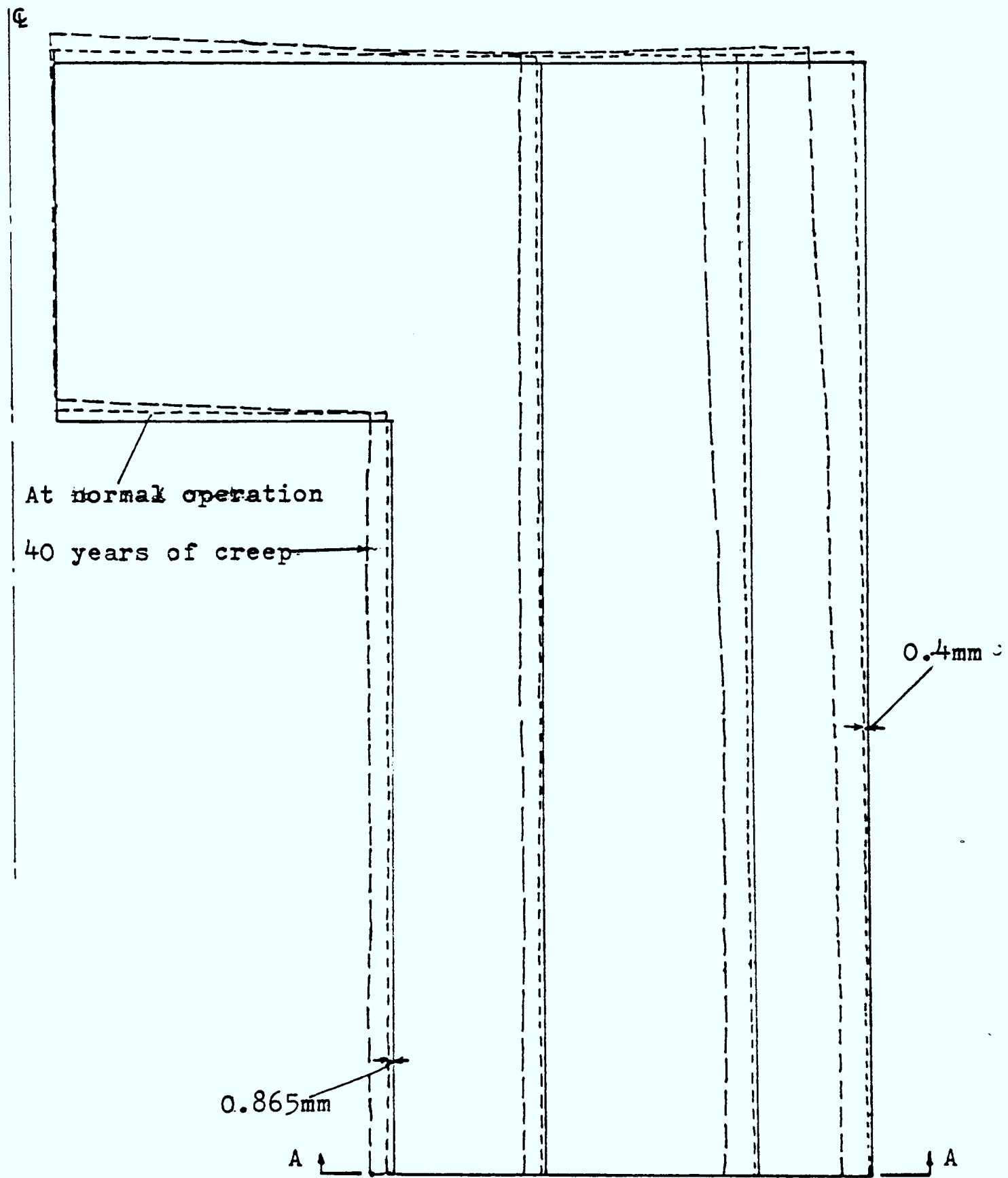
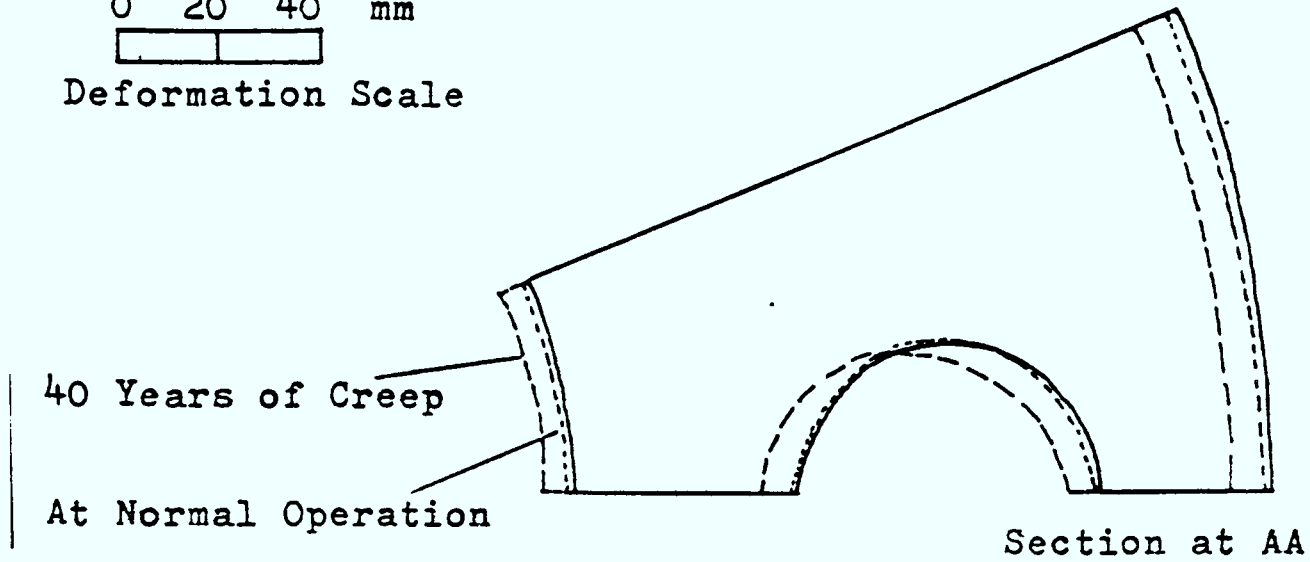


Vessel Scale

0 20 40 mm



Deformation Scale



Vessel Type - Unbonded

Figure 8.28b Deformations Under Normal Operation and 40 Years of Creep

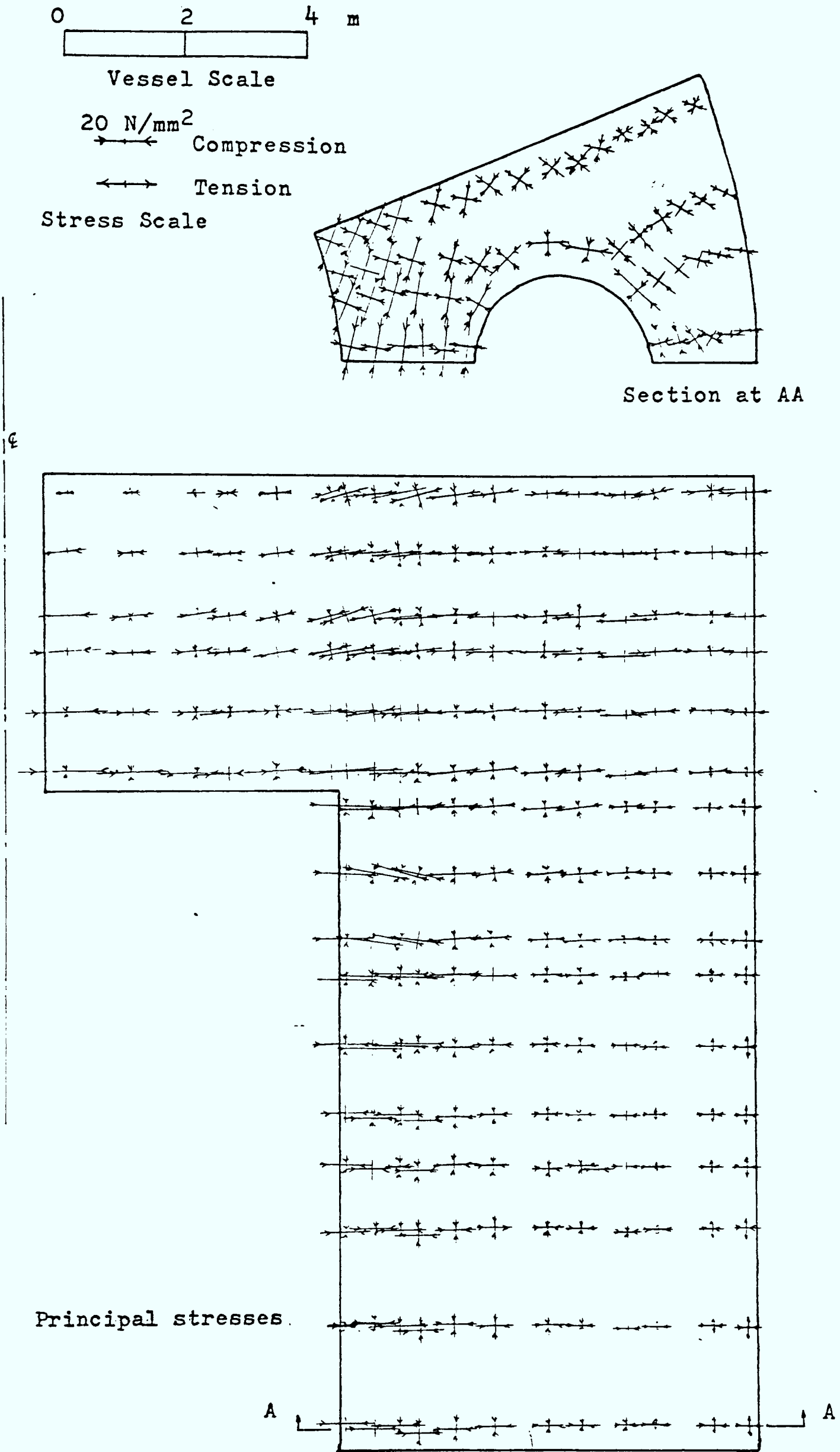
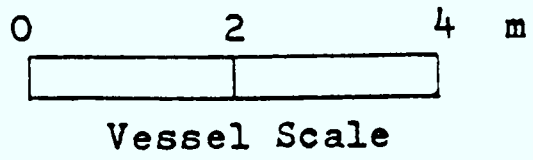
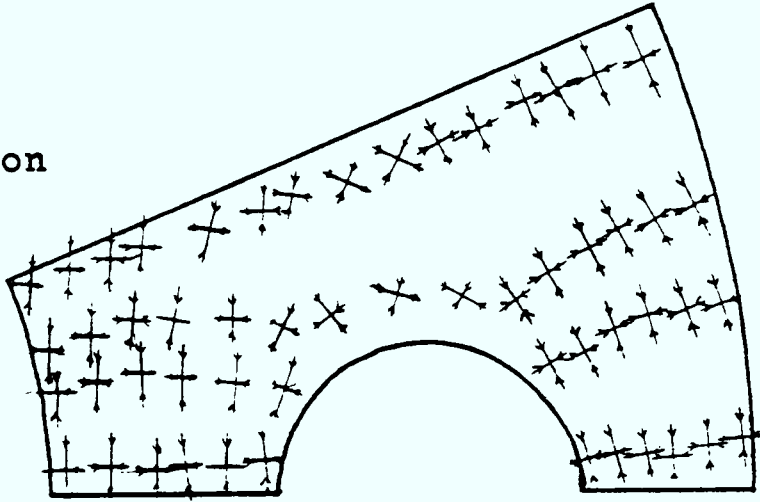


Figure 8.29 Stress Distribution in the Vessel at Normal Operation

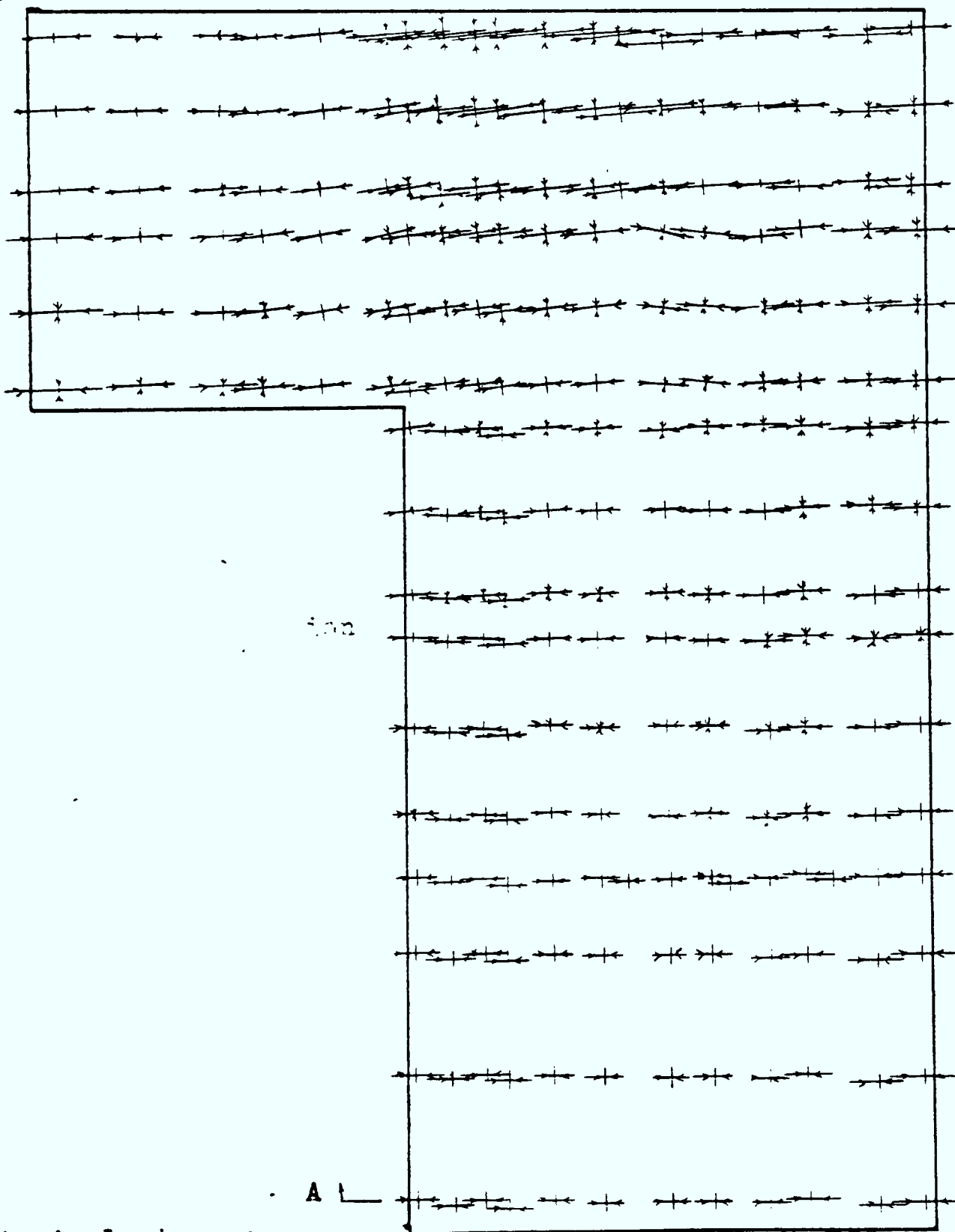


20-N/mm²
 ←→ Compression
 ←→ Tension
 Stress Scale



Scale at AA

Q



Principal stresses

Figure 8.29a Stress Distribution in the Vessel Under Normal Operation After 40 Years of Creep

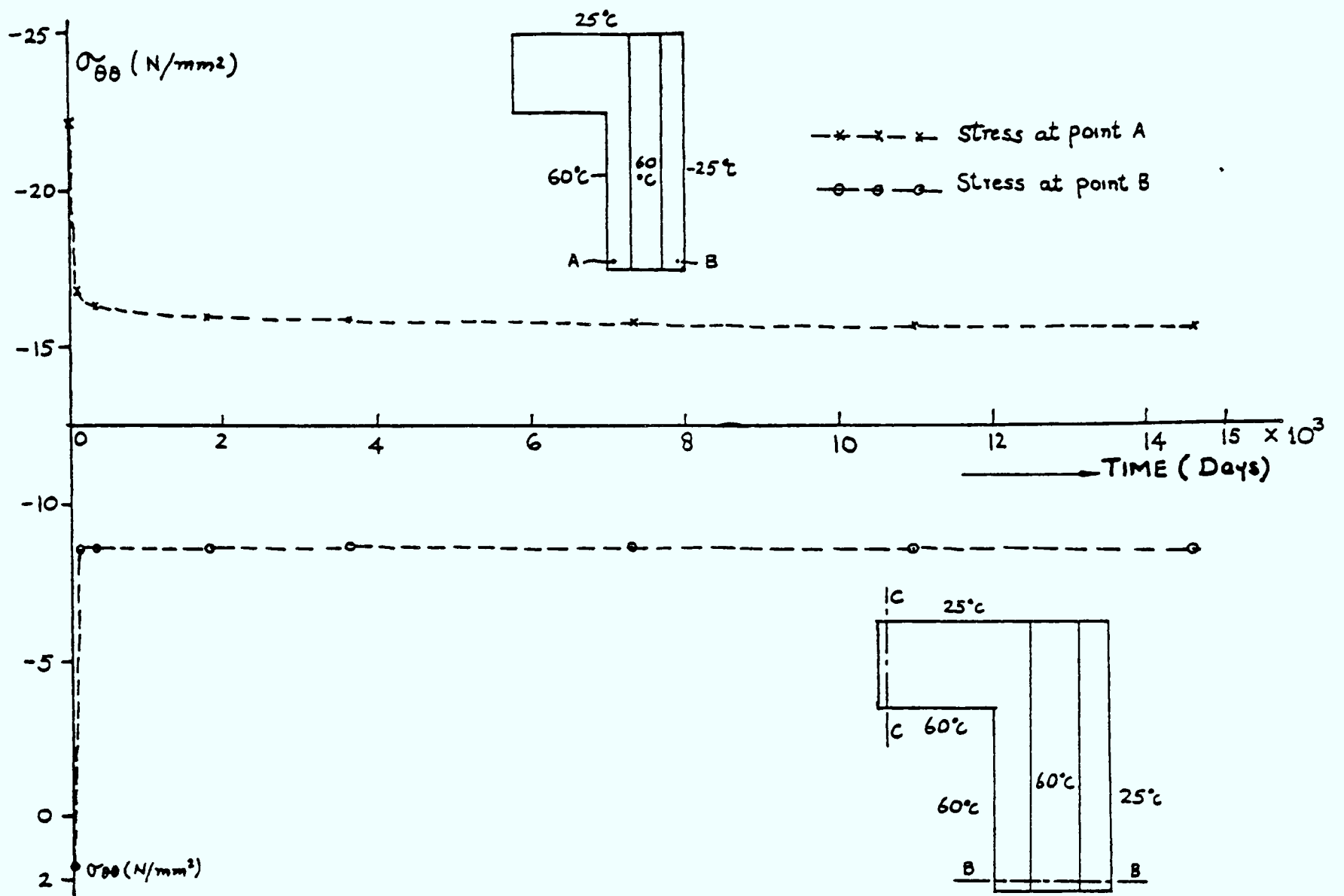


Fig. 8.30 Variation of Hoop Stresses With Time

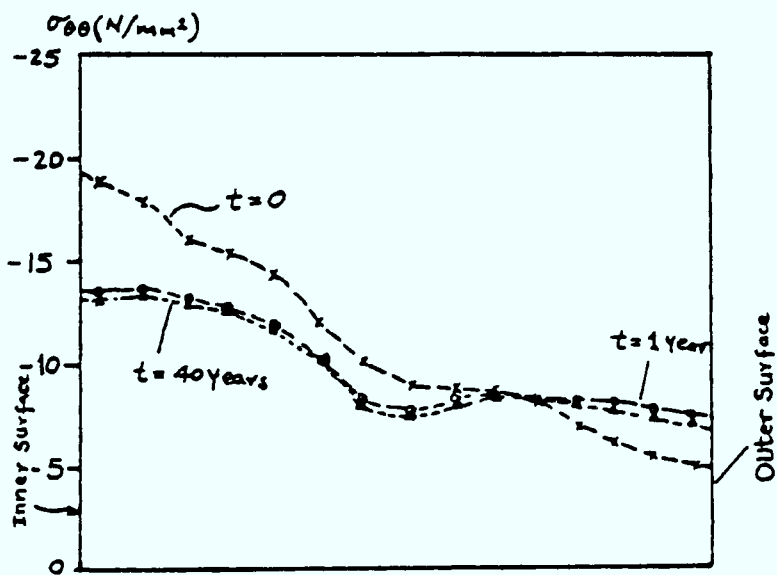


Fig. 8.30a Hoop Stress in the Wall, Section AA

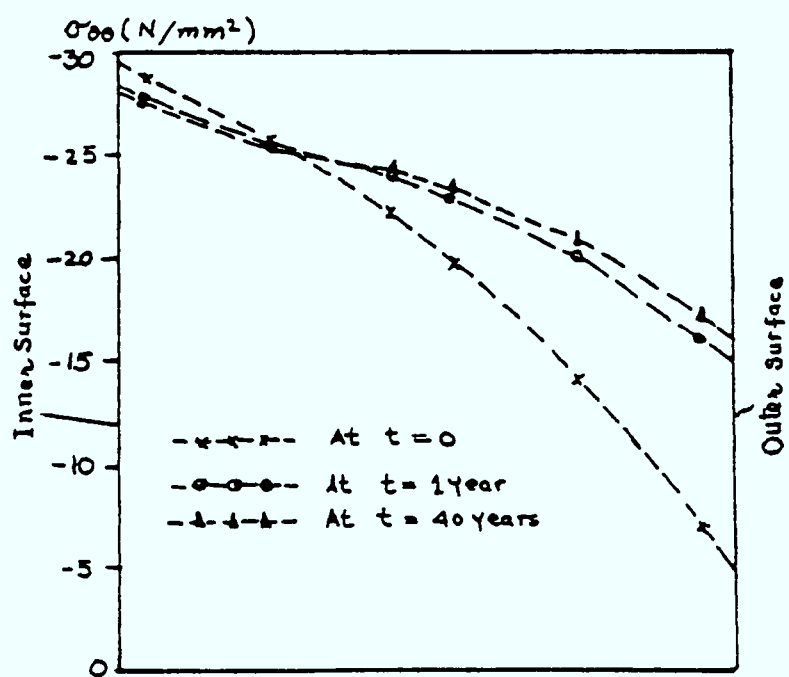


Fig. 8.30b Hoop Stress in the Top Cap, Section CC

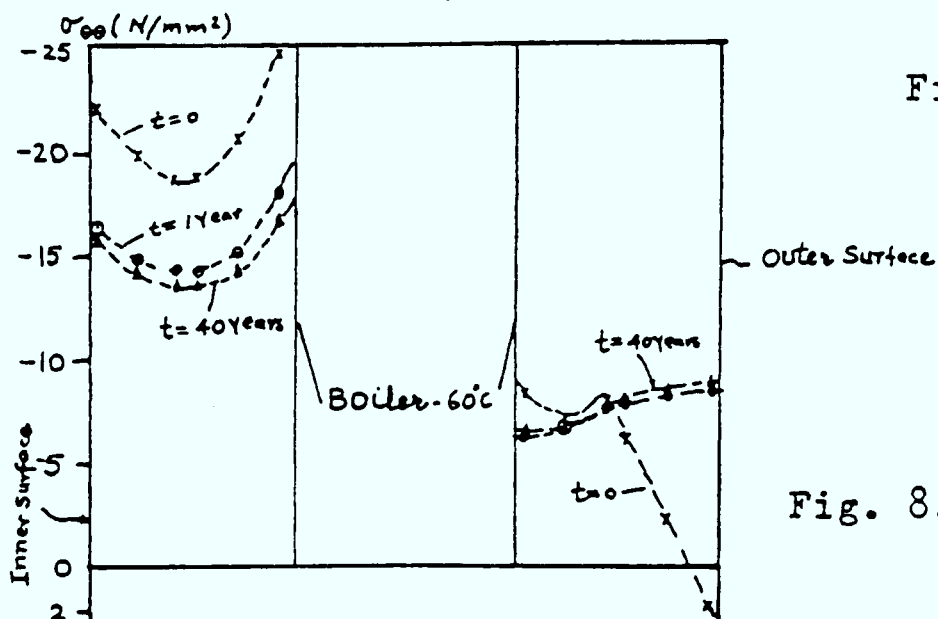


Fig. 8.30c Hoop Stress in the Wall, Section BB

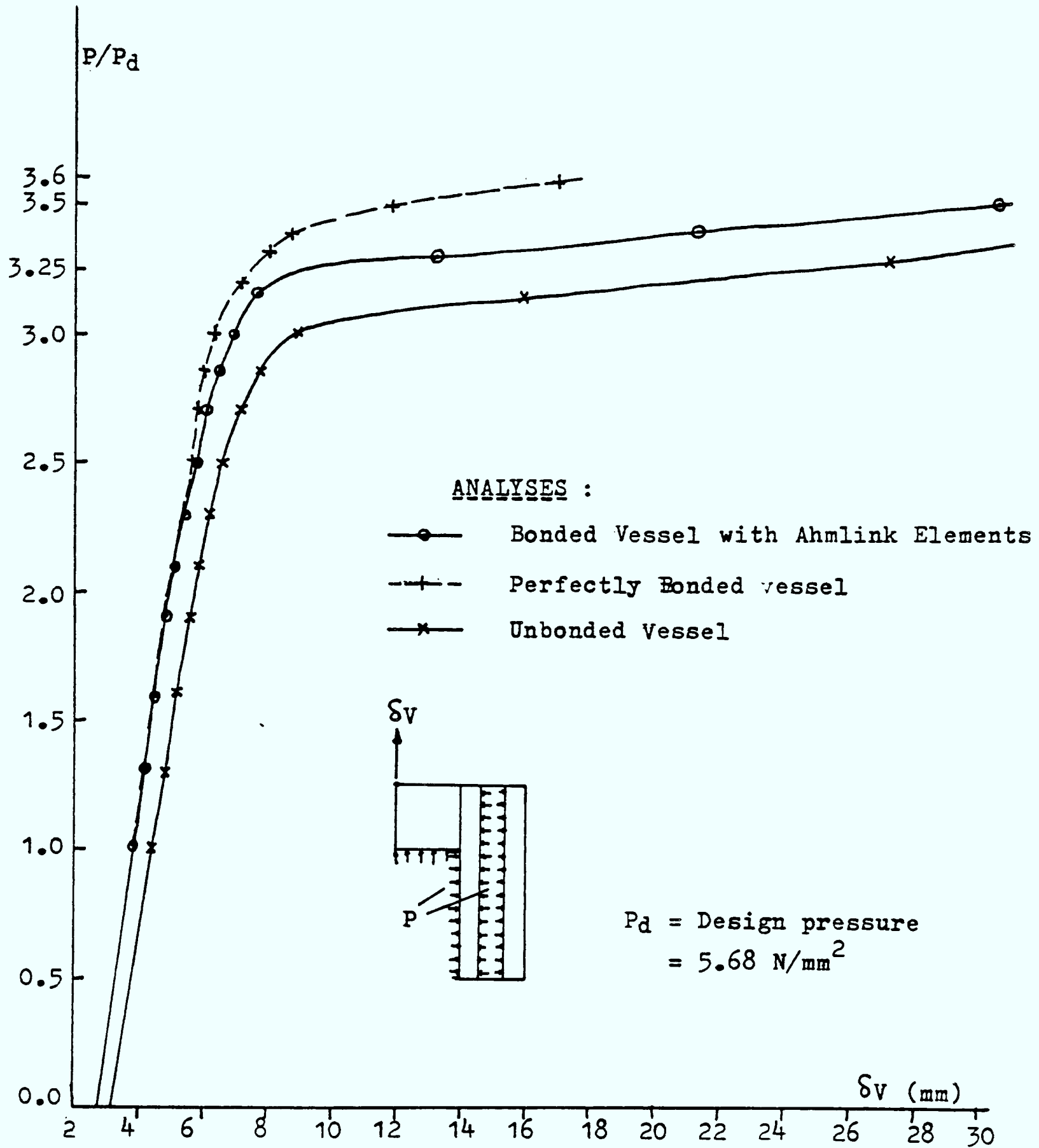


Figure 8.31 Pressure Displacement Curves for Prestressed Concrete Reactor Vessel

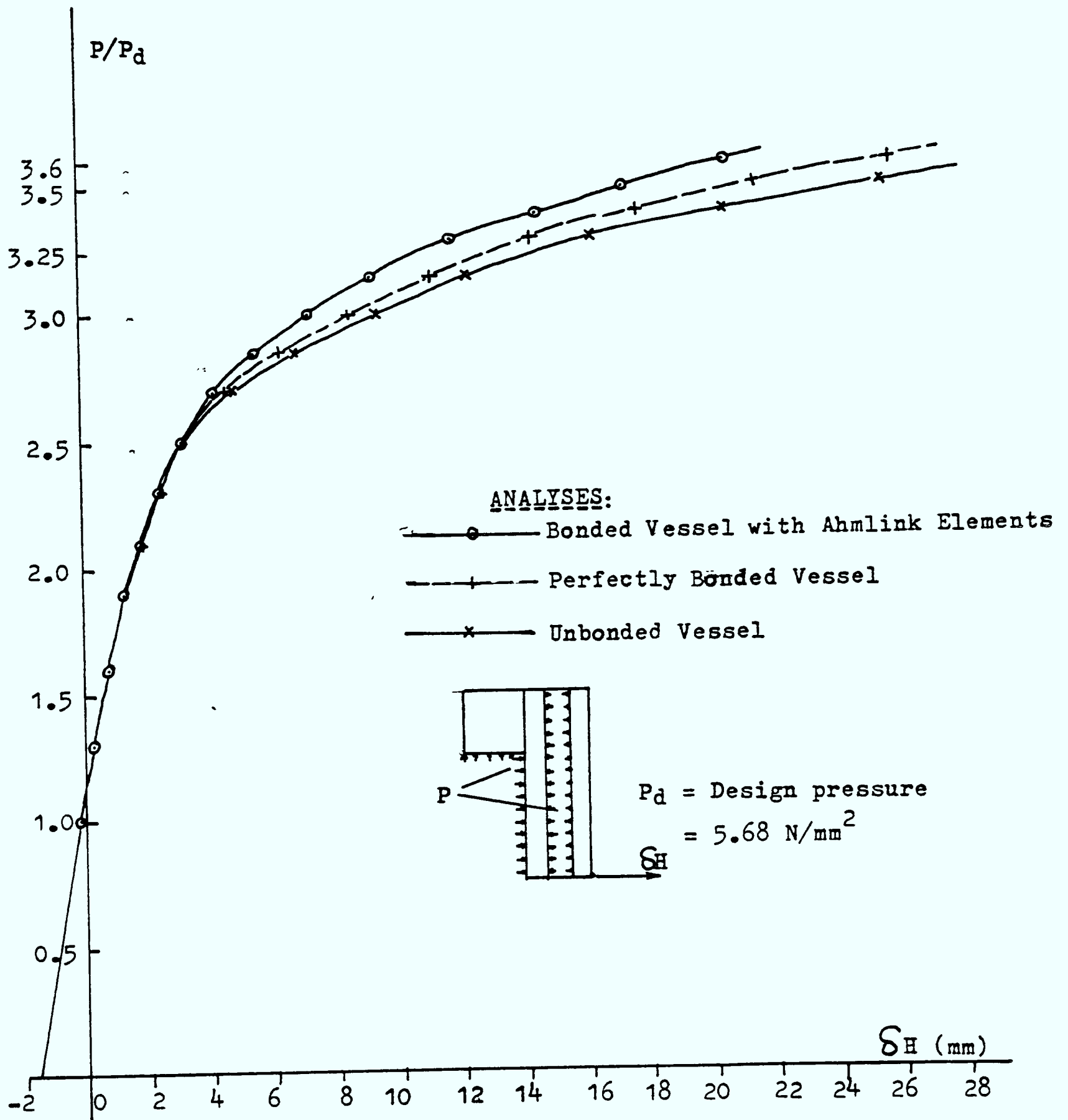
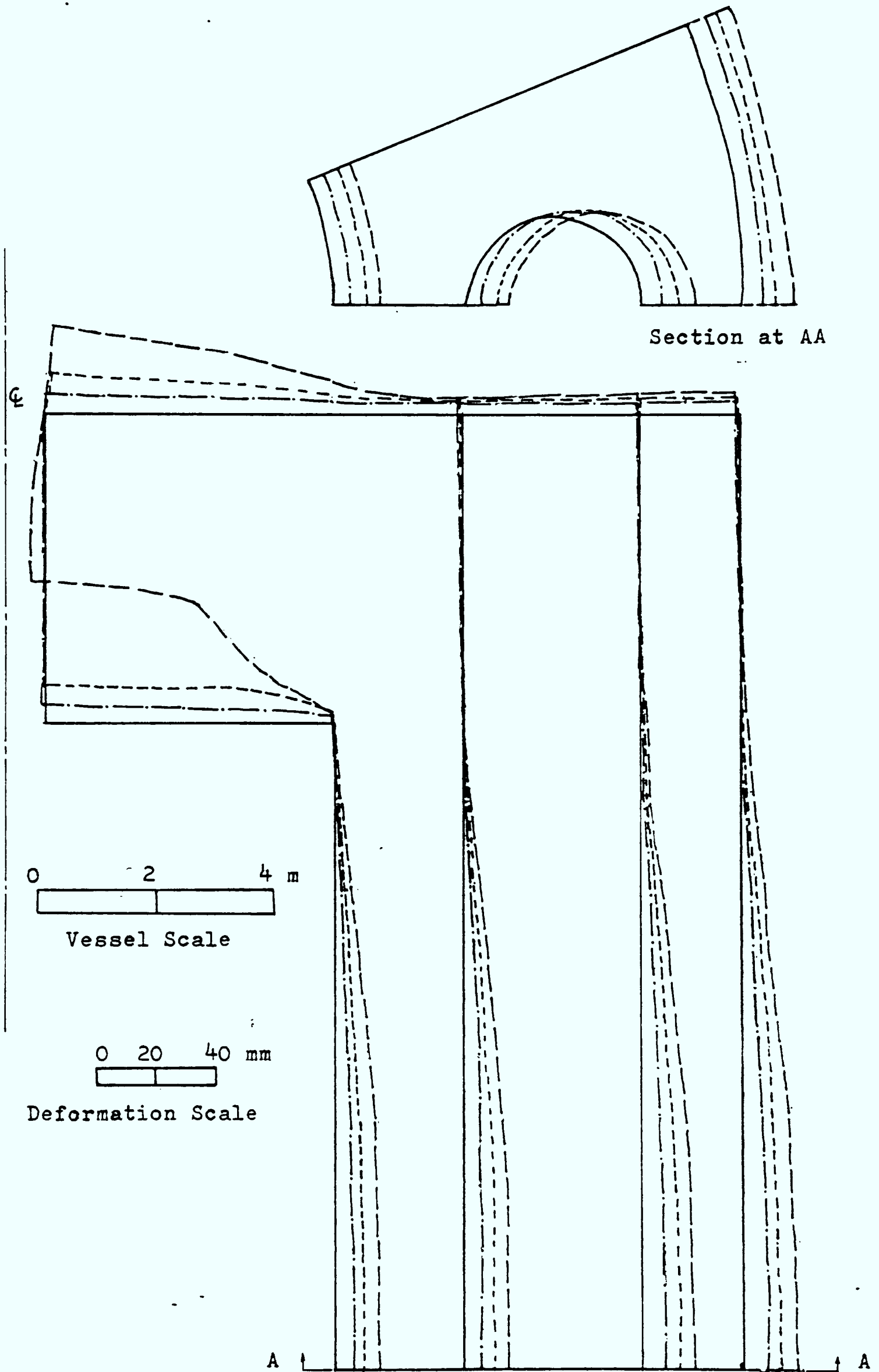


Figure 8.32 Pressure Displacement Curves for Prestressed Concrete Reactor Vessel

- Deformed shape at 3.0
- - - Deformed shape at 3.3
- Deformed shape at 3.5



Vessel Type - Bonded Vessel with Ahmlink Element

Figure 8.33 Deformed Shapes at Various Pressures

- Deformed shape at 3.0
- Deformed shape at 3.3
- Deformed shape at 3.5
- Deformed shape at 3.6

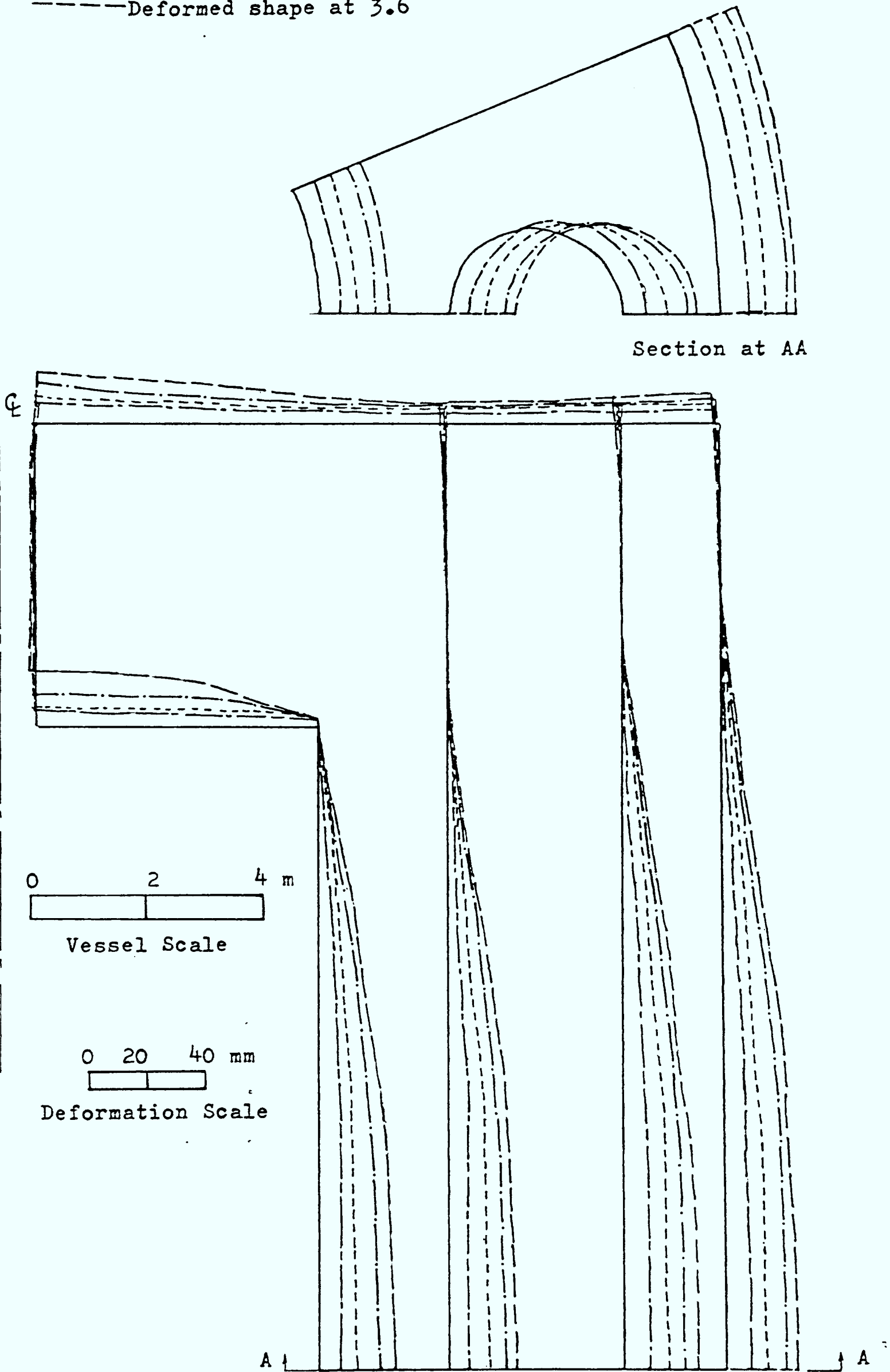
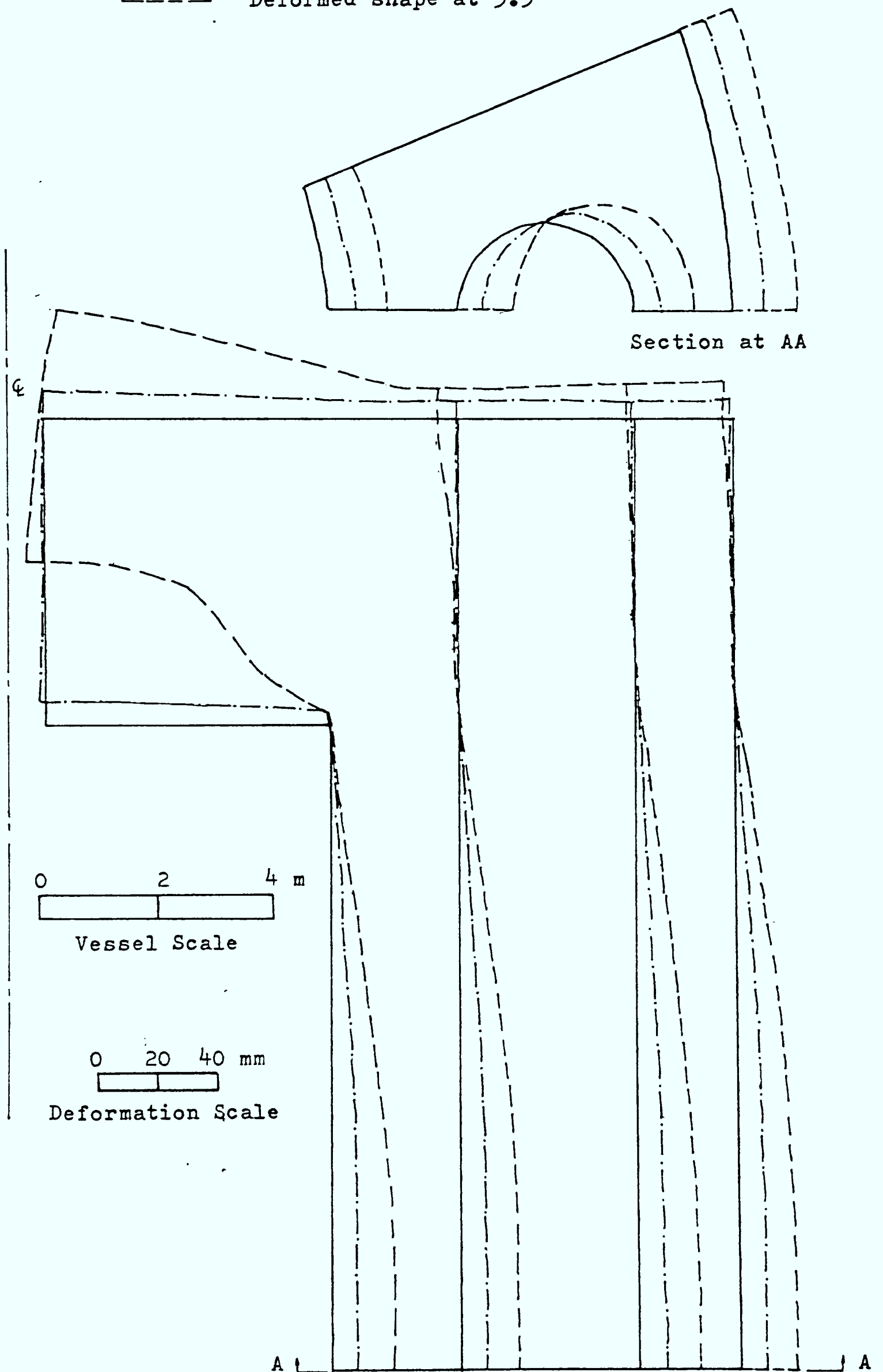


Figure 8.34 Deformed Shapes at Various Pressures

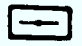

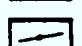
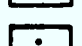
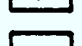

— · — · — Deformed shape at 3.0
- - - - - Deformed shape at 3.3



Vessel Type - Unbonded

Figure 8.35 Deformed Shapes at Various Pressures

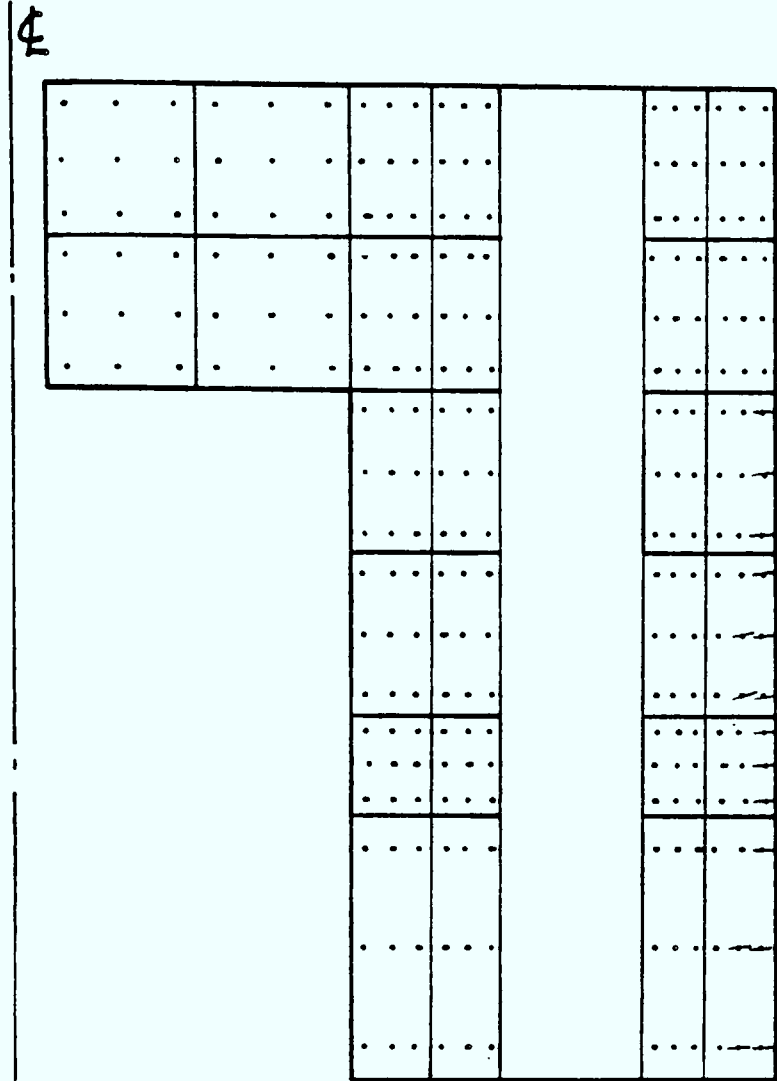
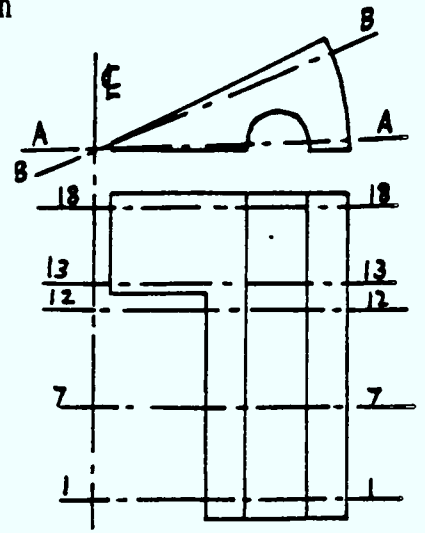
Symbols

-  Horizontal Crack
-  Radial Crack
-  Inclined Crack
-  Uncracked Gauss Point
- 
- 

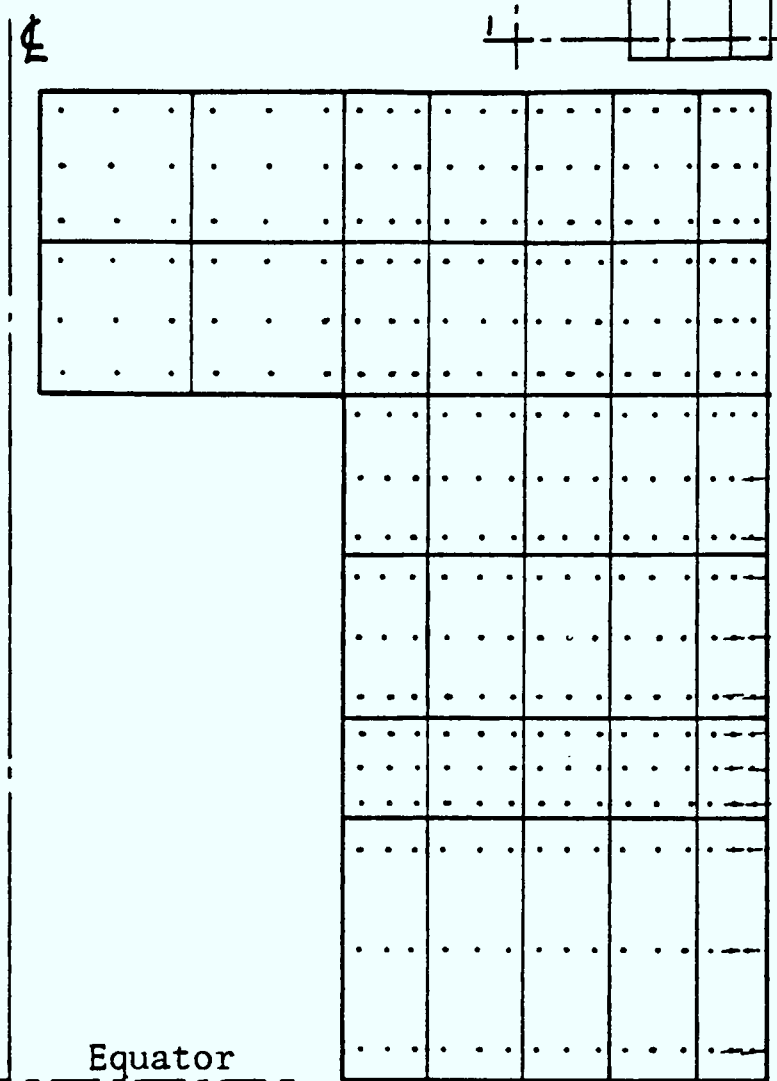
0 2 4 6 m



Vessel Scale

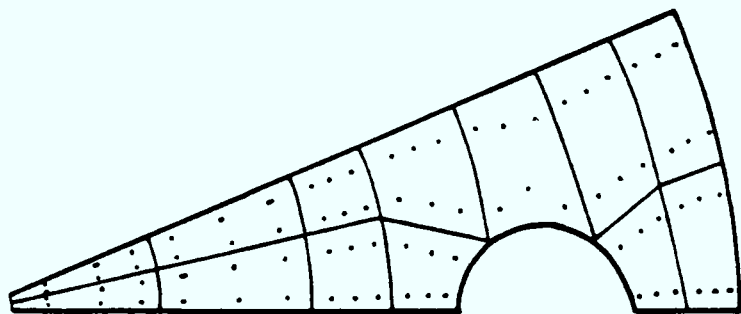


Section at AA



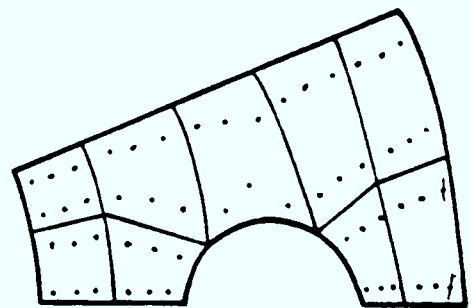
Equator

Section at BB

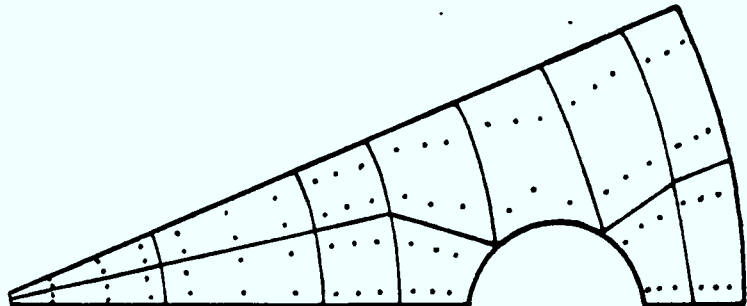


Level 18-18

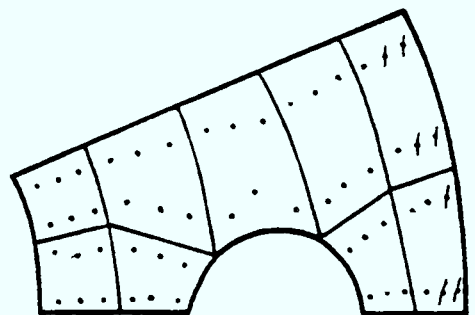
Level 12-12



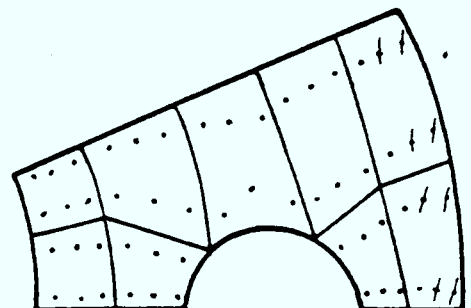
Level 7-7



Level 13-13



Level 1-1

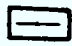

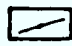





Vessel Type - Bonded

Pressure = 9.088 N/mm²

Figure 8.36 Crack Pattern of the Vessel at Load Factor 1.6

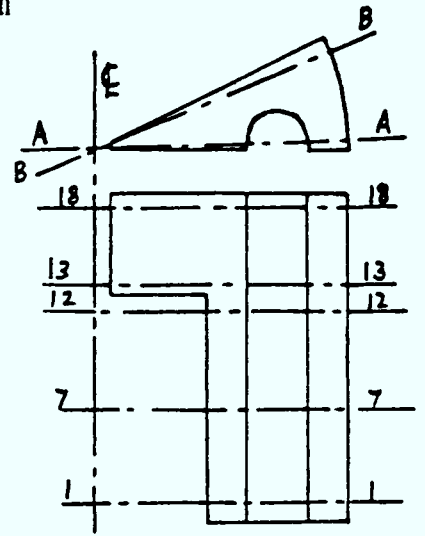
Symbols

-  Horizontal Crack
-  Radial Crack
-  Inclined Crack
-  Radial and Horizontal Cracks
-  Uncracked Gauss Point
- 

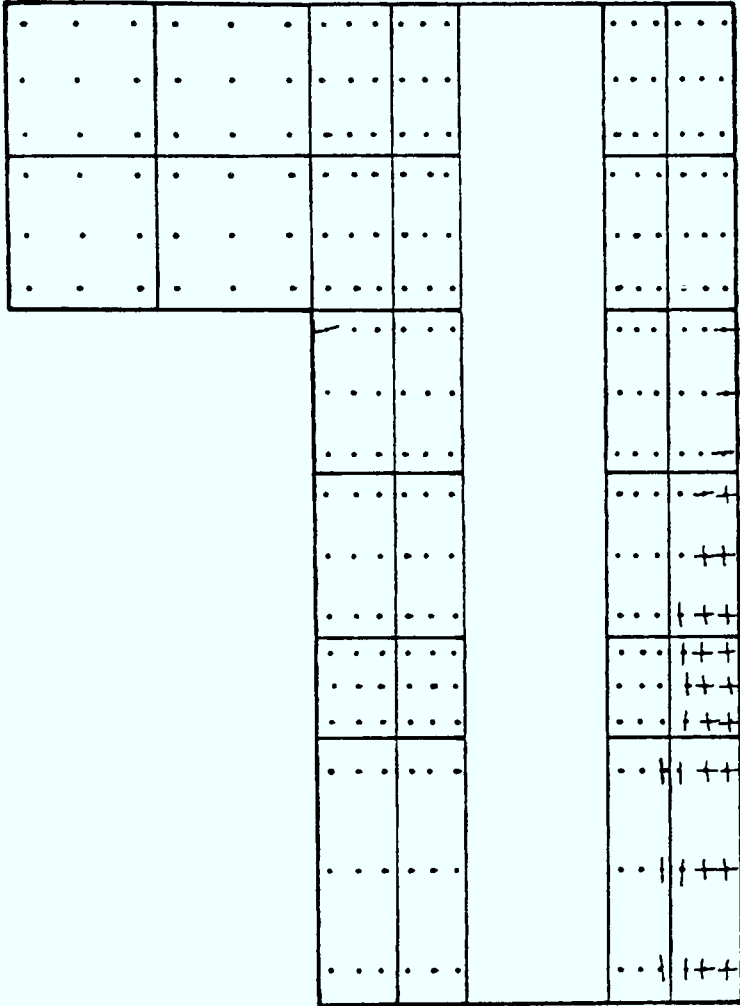
0 2 4 6 m



Vessel Scale

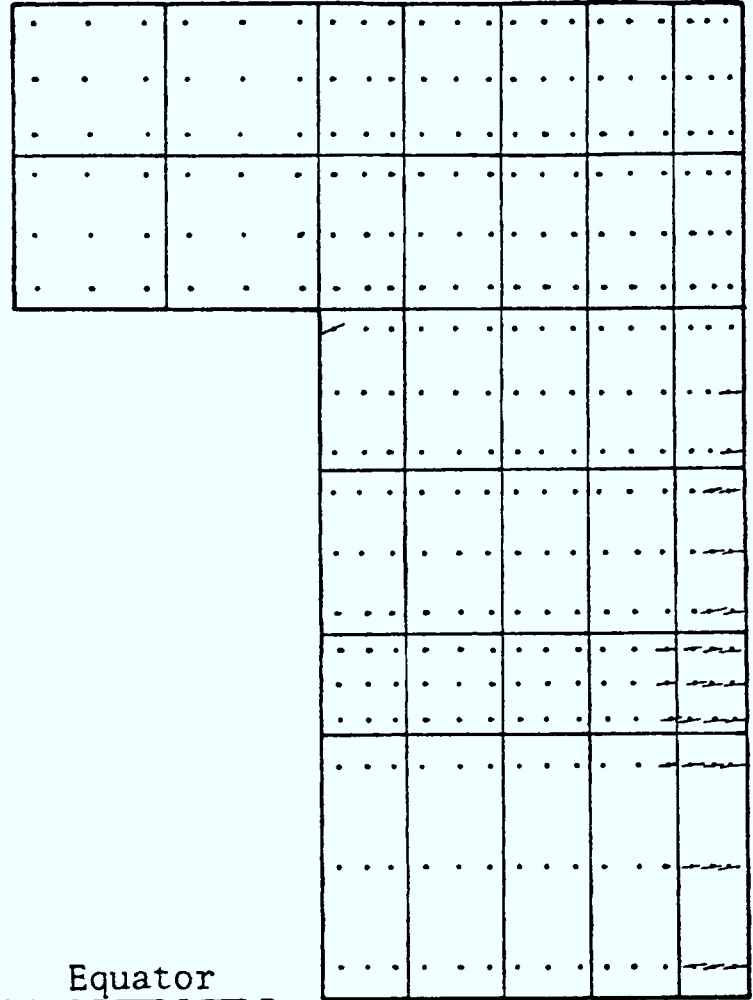


⊕



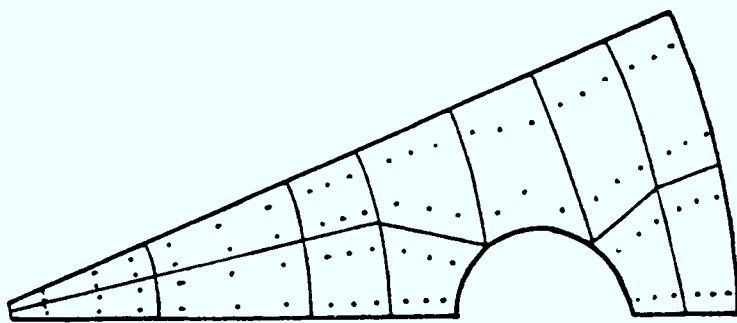
Section at AA

⊕



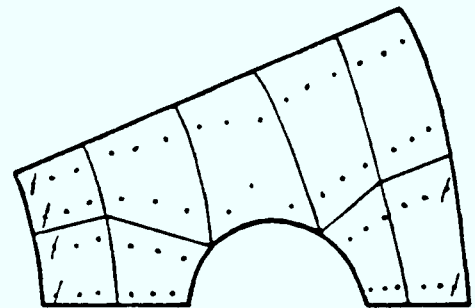
Section at BB

Equator

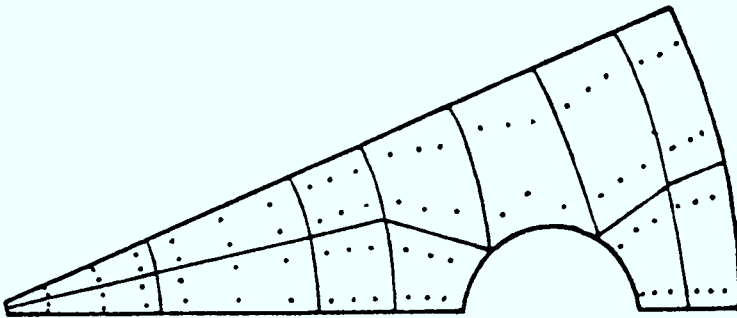
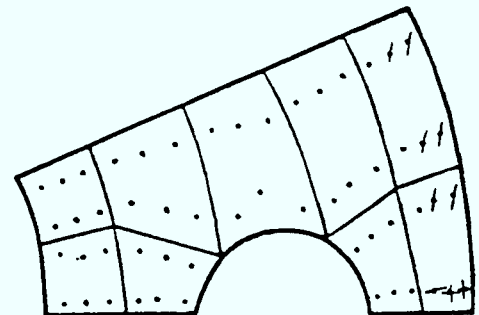


Level 18-18

Level 12-12

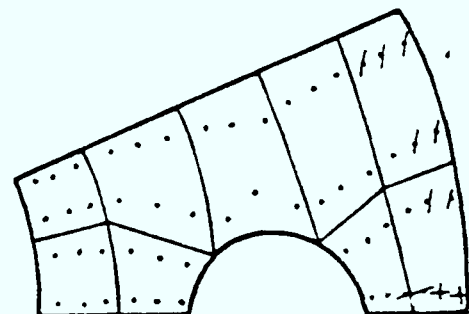


Level 7-7



Level 13-13

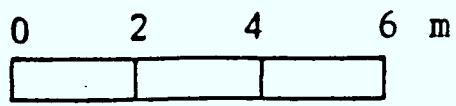
Level 1-1



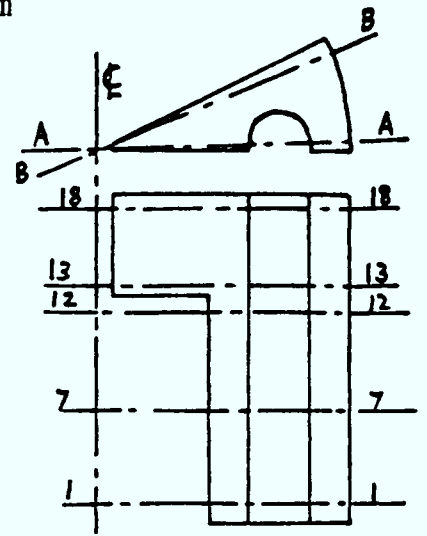
Vessel Type - Bonded

Pressure = 11.928 N/mm²

Figure 8.36a Crack Pattern of the Vessel at Load Factor 2.1

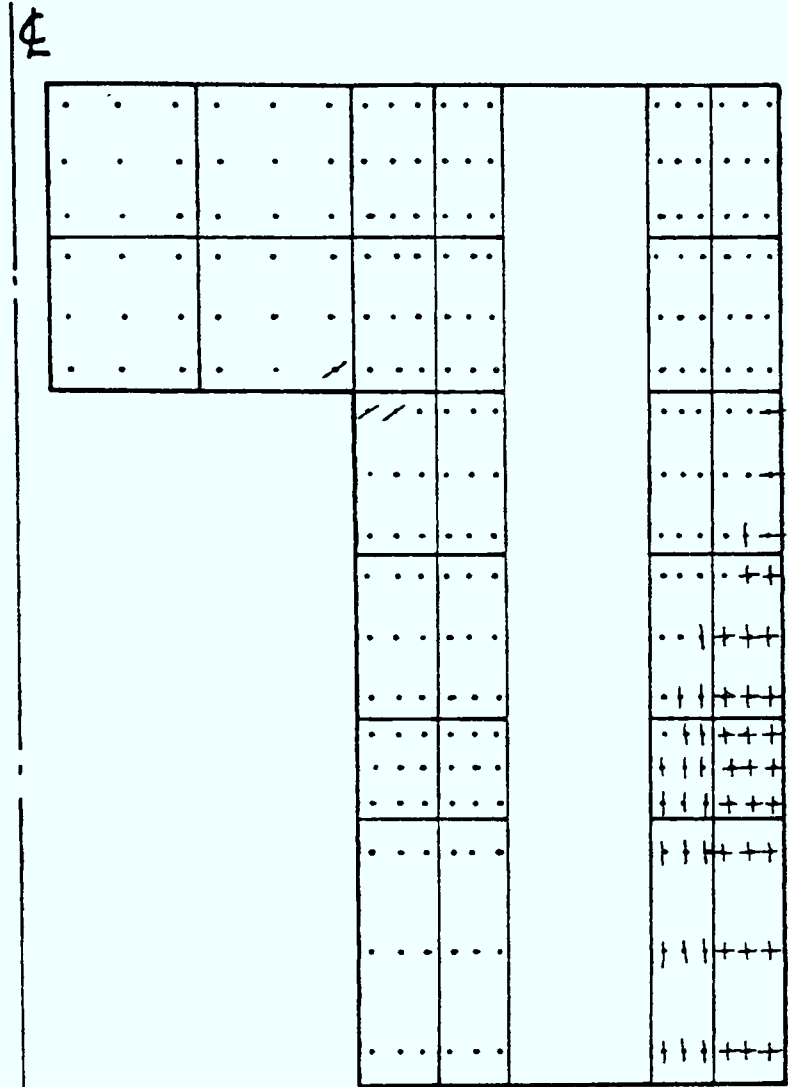


Vessel Scale

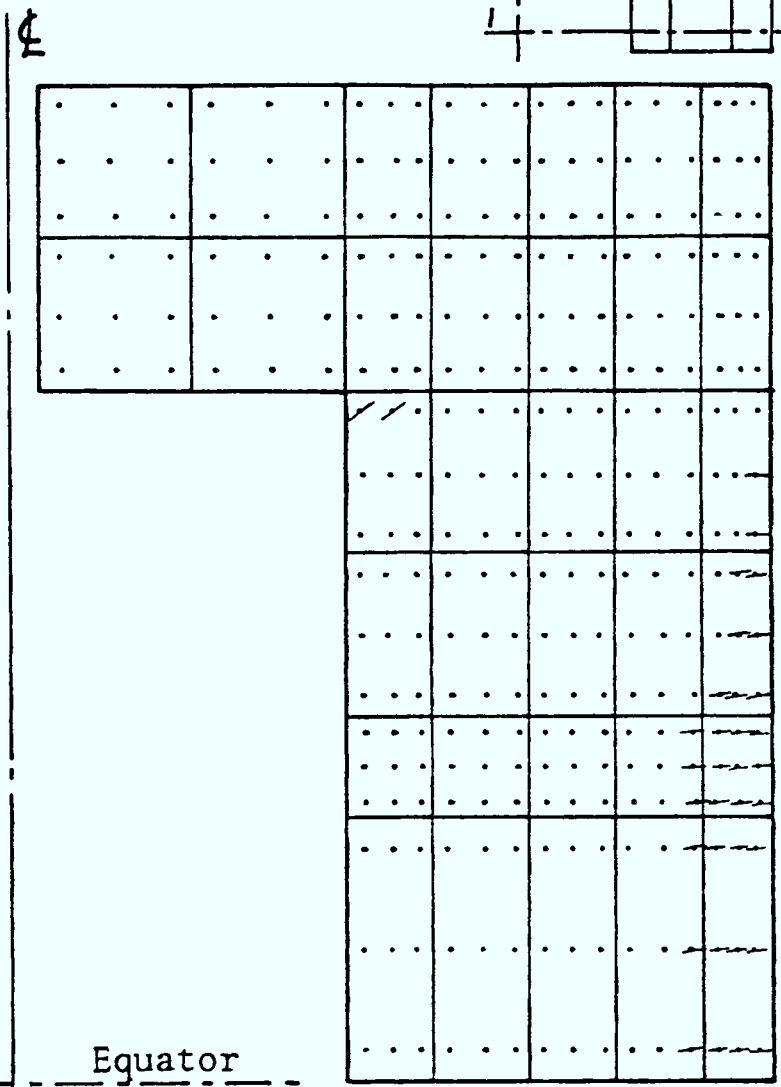


Symbols

- Horizontal Crack
- Radial Crack
- Inclined Crack
- Radial and Horizontal Cracks
- Uncracked Gauss Point
-

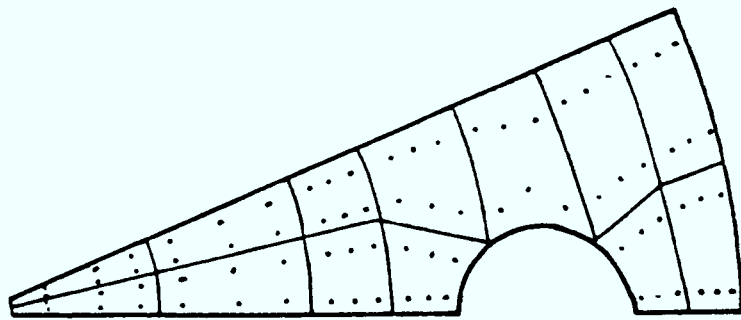


Section at AA

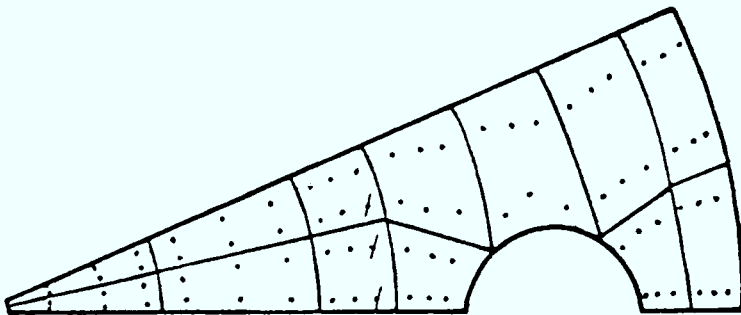


Equator

Section at BB

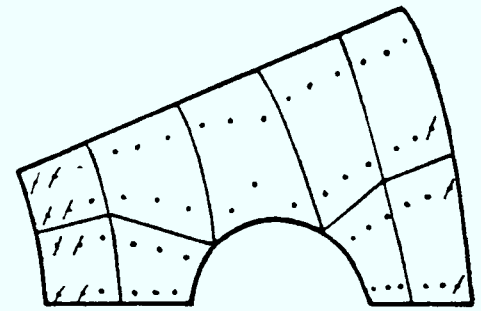


Level 18-18

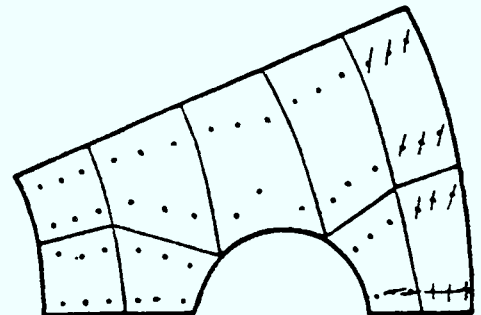


Level 13-13

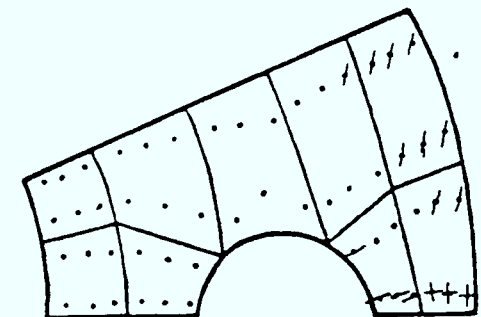
Level 12-12



Level 7-7



Level 1-1



Vessel Type - Bonded

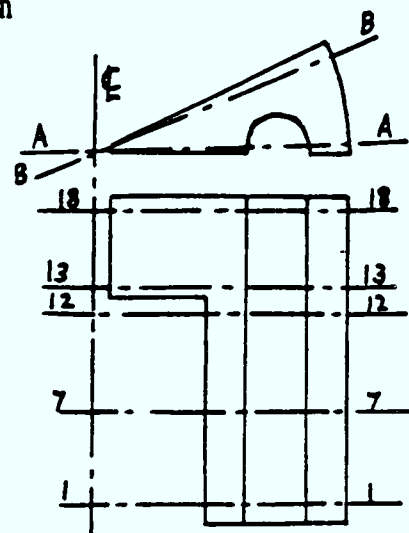
Pressure = 14.2 N/mm²

Figure 8.36b Crack Pattern of the Vessel at Load Factor 2.5

0 2 4 6 m

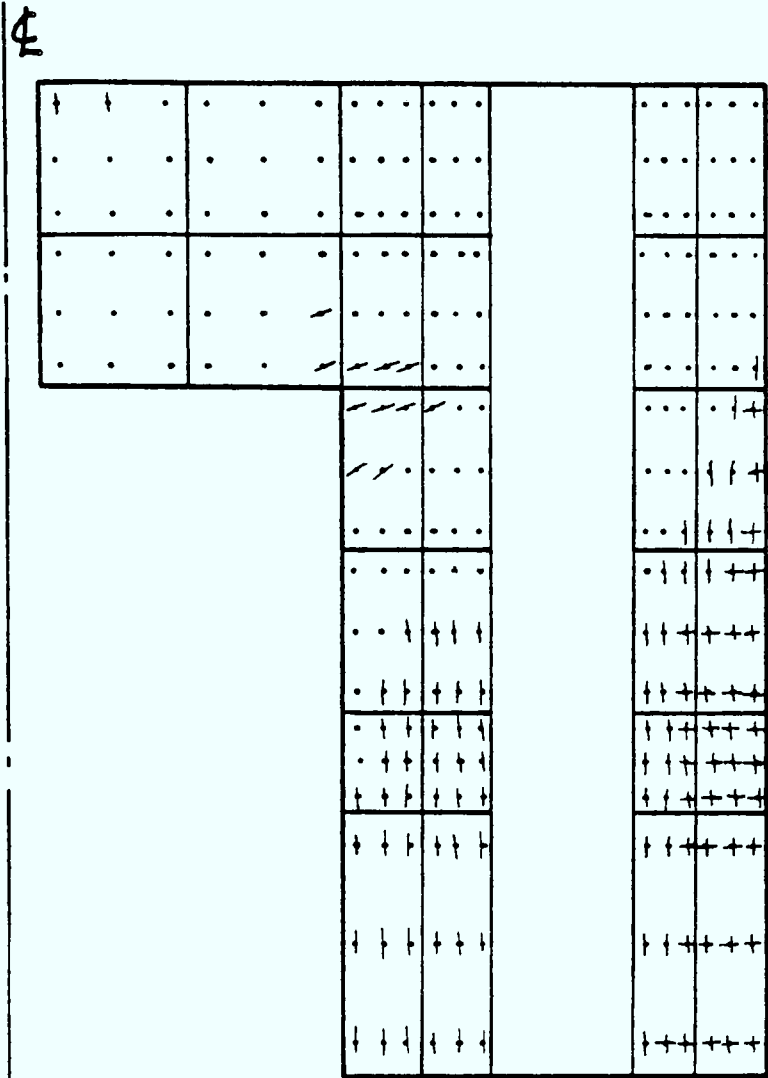


Vessel Scale

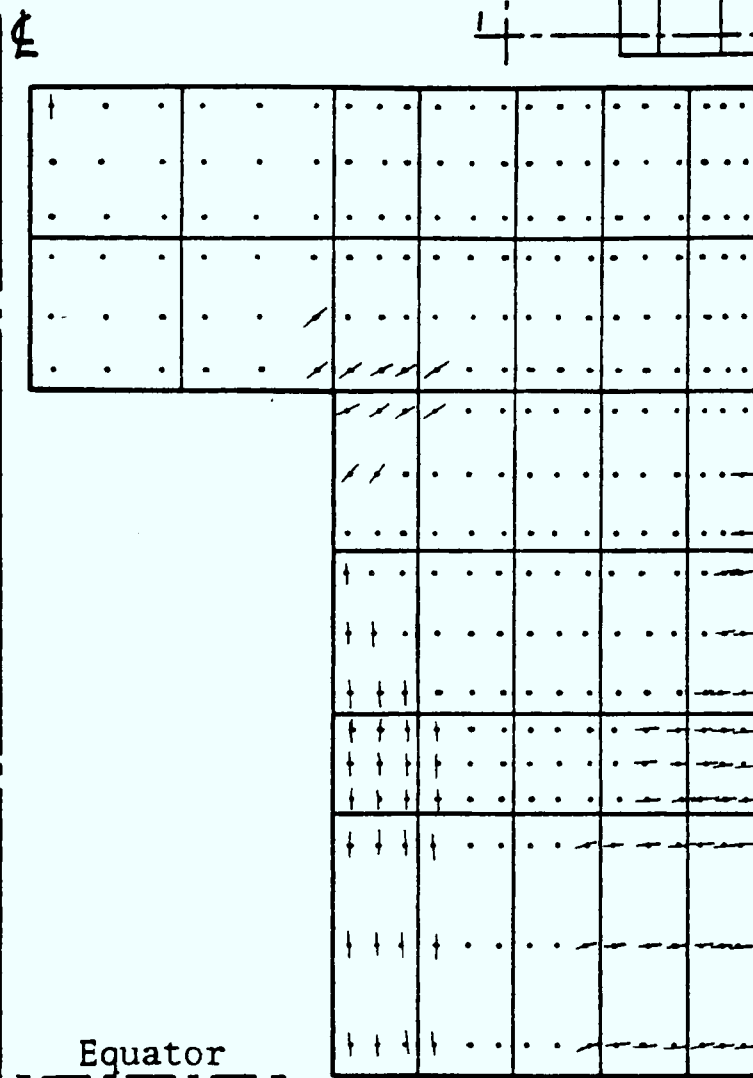


Symbols

- Horizontal Crack
- Radial Crack
- Inclined Crack
- Radial and Horizontal Cracks
- Uncracked Gauss Point
-

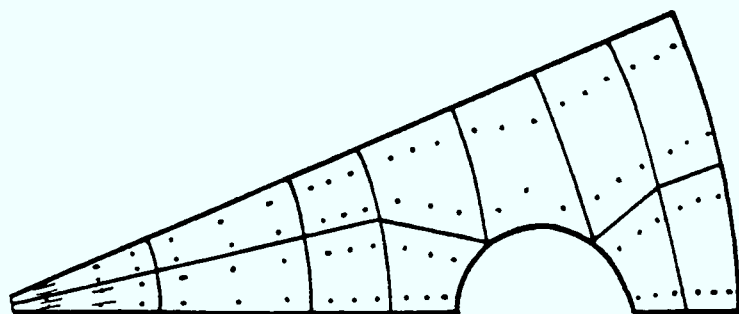


Section at AA



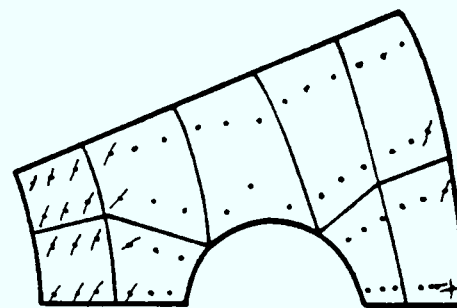
Equator

Section at BB

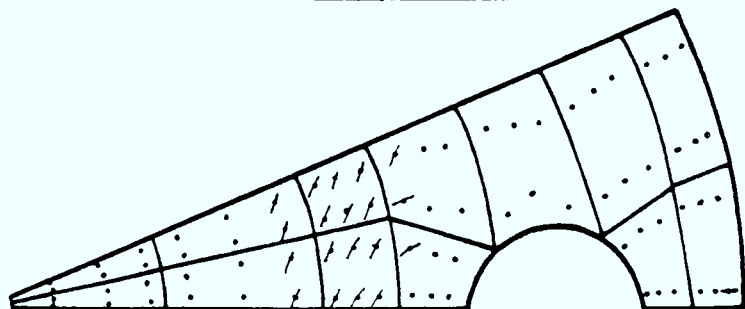


Level 18-18

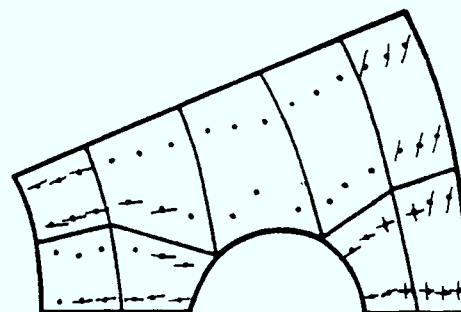
Level 12-12



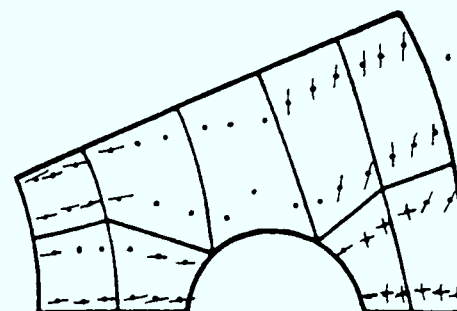
Level 7-7



Level 13-13



Level 1-1

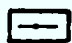
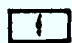






Vessel Type - Bonded

Pressure = 17.04 N/mm²

Figure 8.36c Crack Pattern of the Vessel at Load Factor 3.0

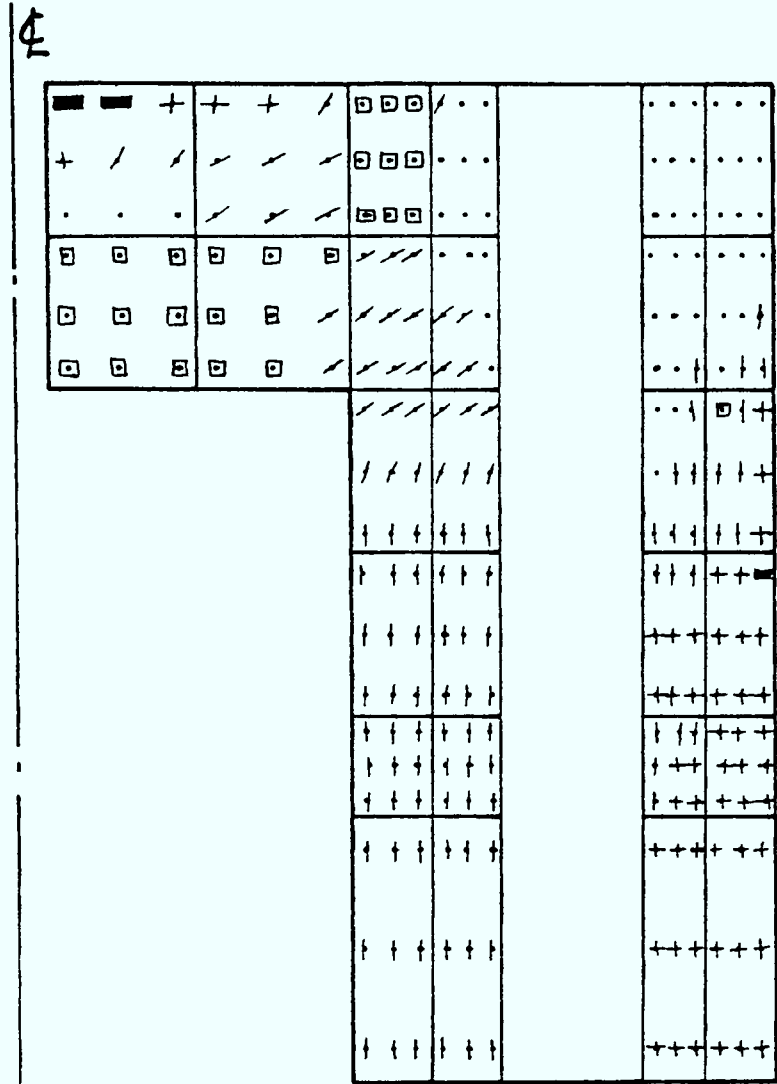
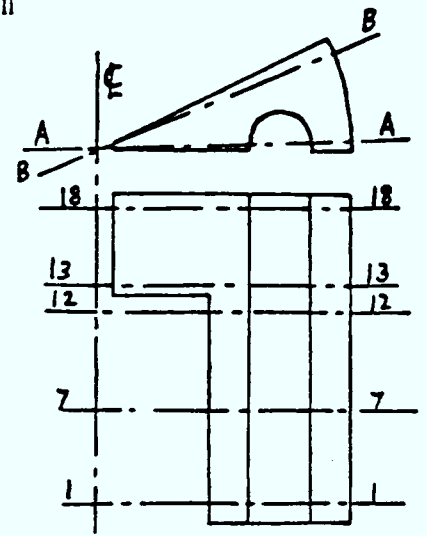
Symbols

-  Horizontal Crack
-  Radial Crack
-  Inclined Crack
-  Radial and Horizontal Cracks
-  Three Cracks
-  Compression Failure (crushing)

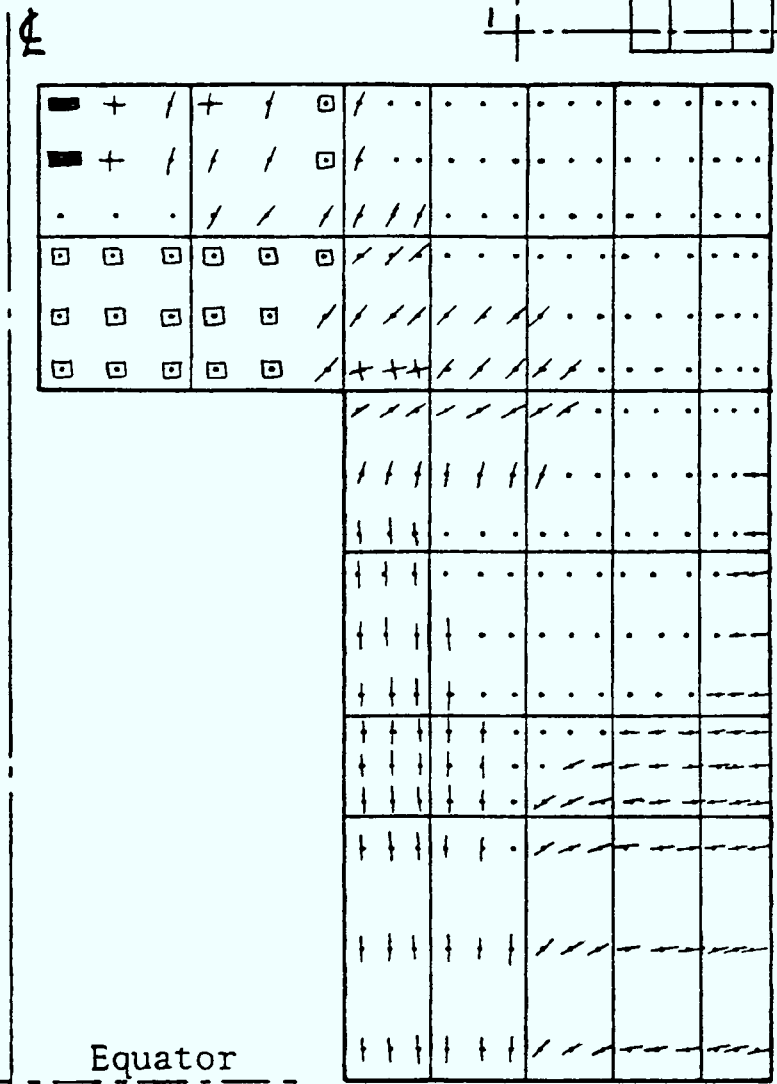
0 2 4 6 m



Vessel Scale

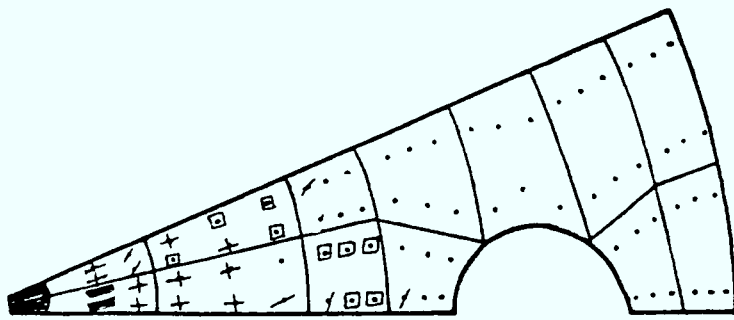


Section at AA



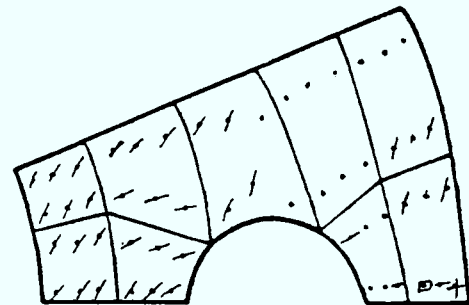
Equator

Section at BB

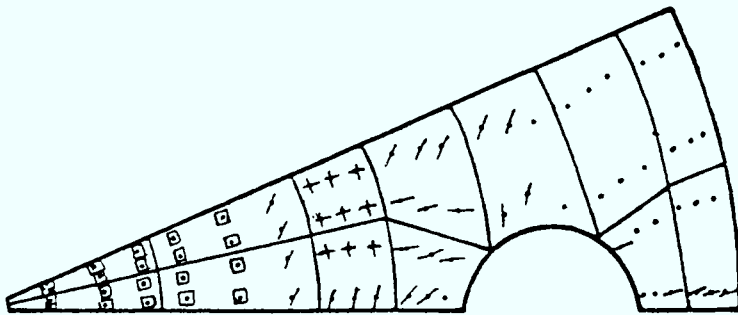


Level 18-18

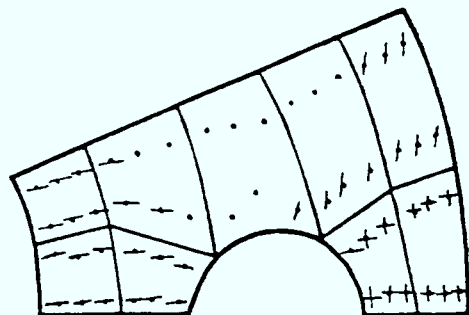
Level 12-12



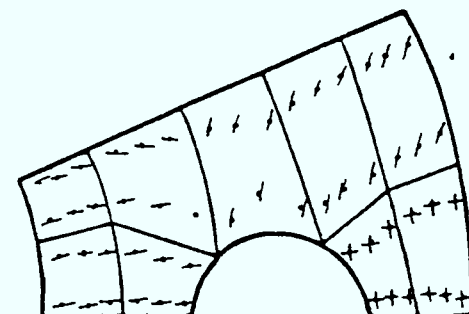
Level 7-7



Level 13-13



Level 1-1



Vessel Type - Bonded

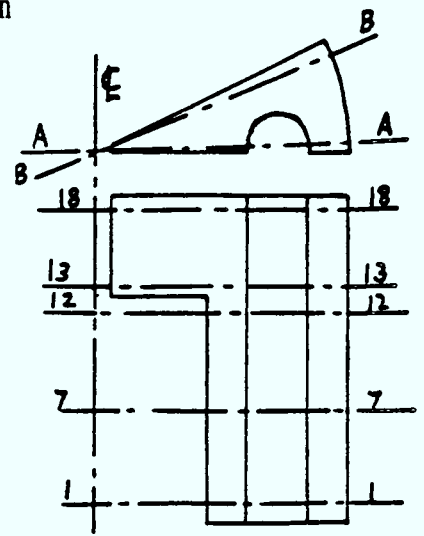
Pressure = 19.88 N/mm²

Figure 8.36d Crack Pattern of the Vessel at Load Factor 3.5

0 2 4 6 m

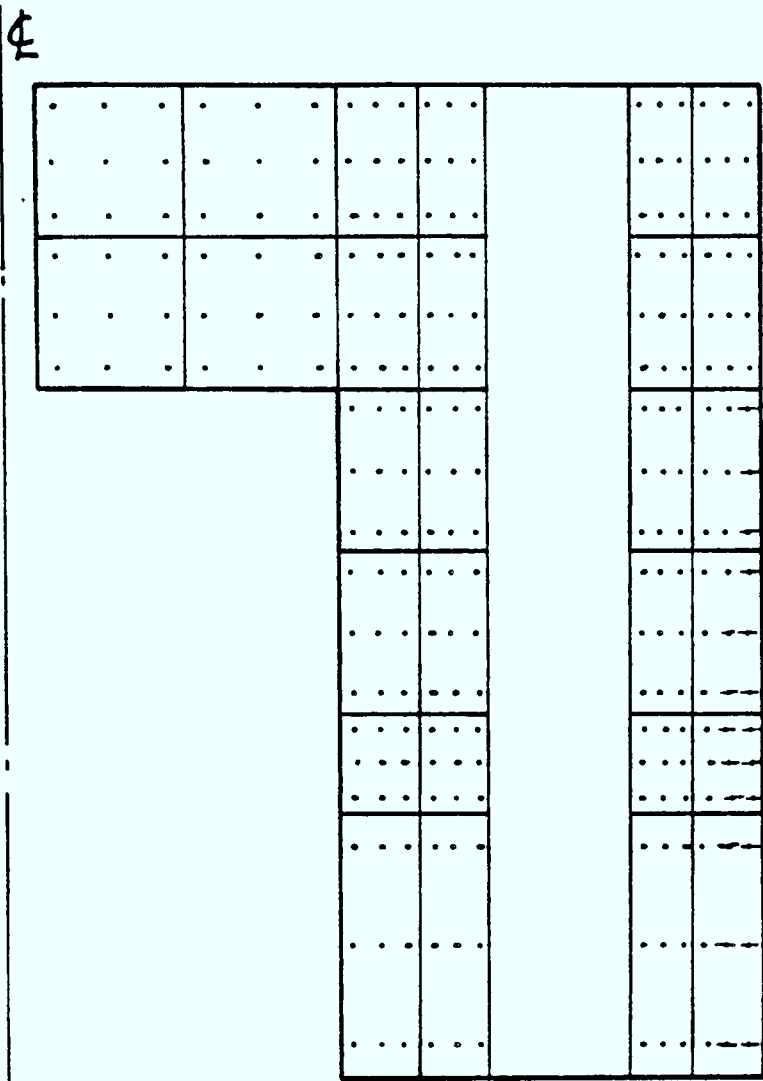


Vessel Scale

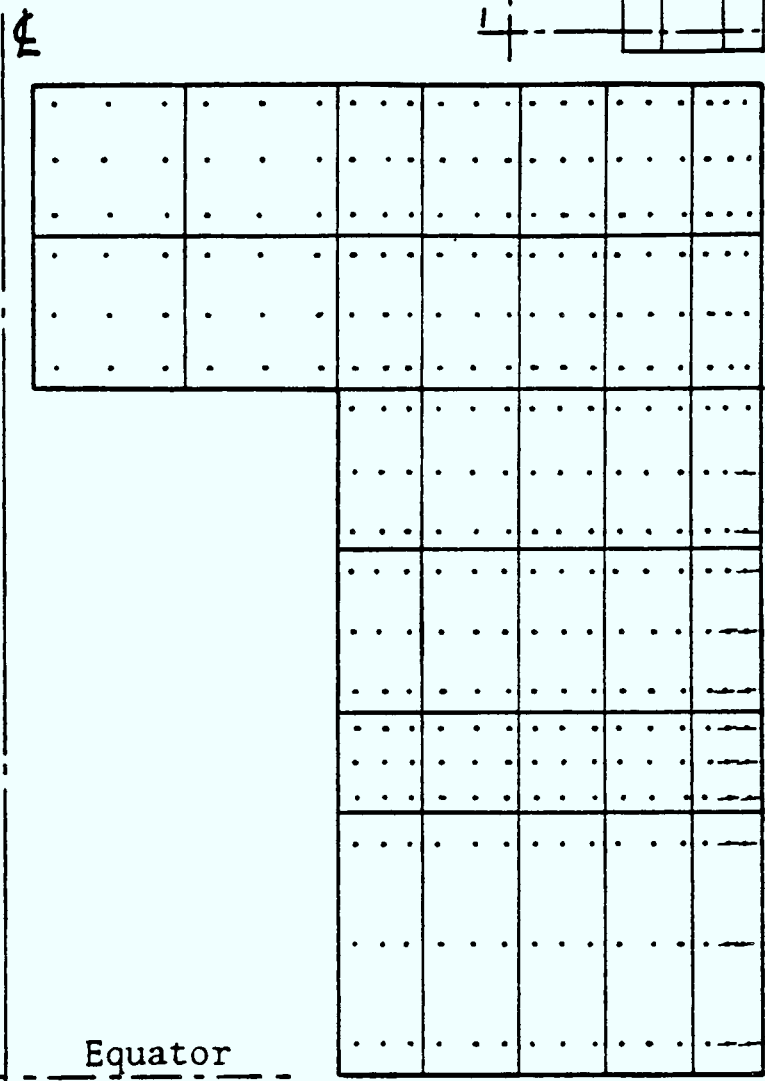


Symbols

- Horizontal Crack
- Radial Crack
- Inclined Crack
- Radial and Horizontal Cracks
- Uncracked Gauss Point
-

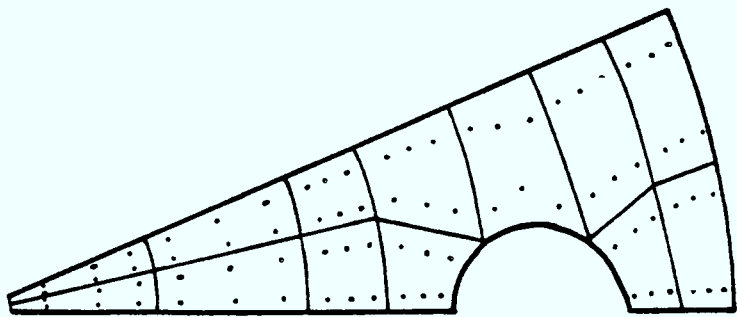


Section at AA



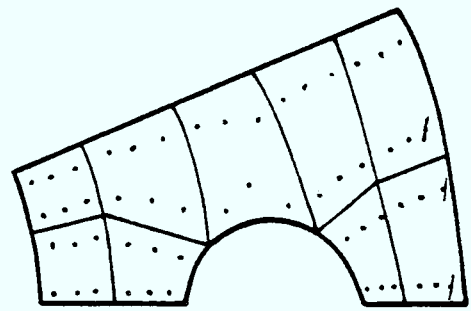
Equator

Section at BB

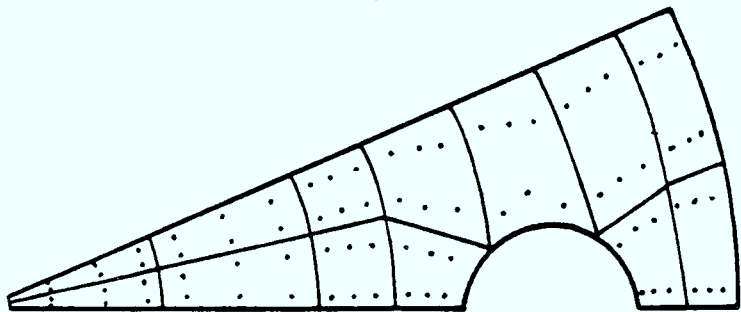
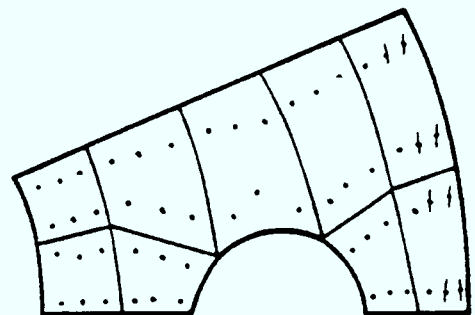


Level 18-18

Level 12-12

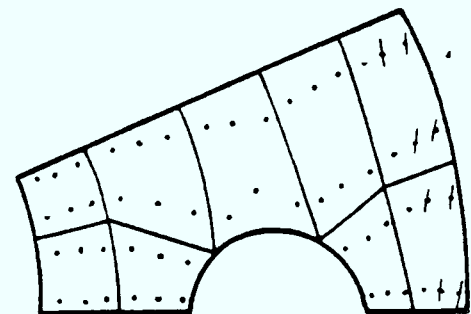


Level 7-7



Level 13-13

Level 1-1









Vessel Type - Perfectly Bonded

Pressure = 9.088 N/mm²

Figure 8.37 Crack Pattern of the Vessel at Load Factor 1.6

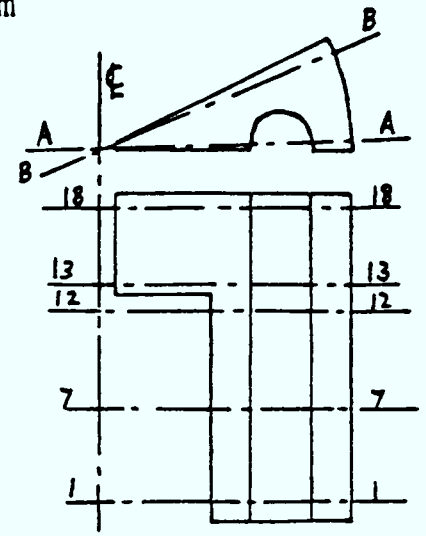
Symbols

-  Horizontal Crack
-  Radial Crack
-  Inclined Crack
-  Radial and Horizontal Cracks
-  Uncracked Gauss Point
- 

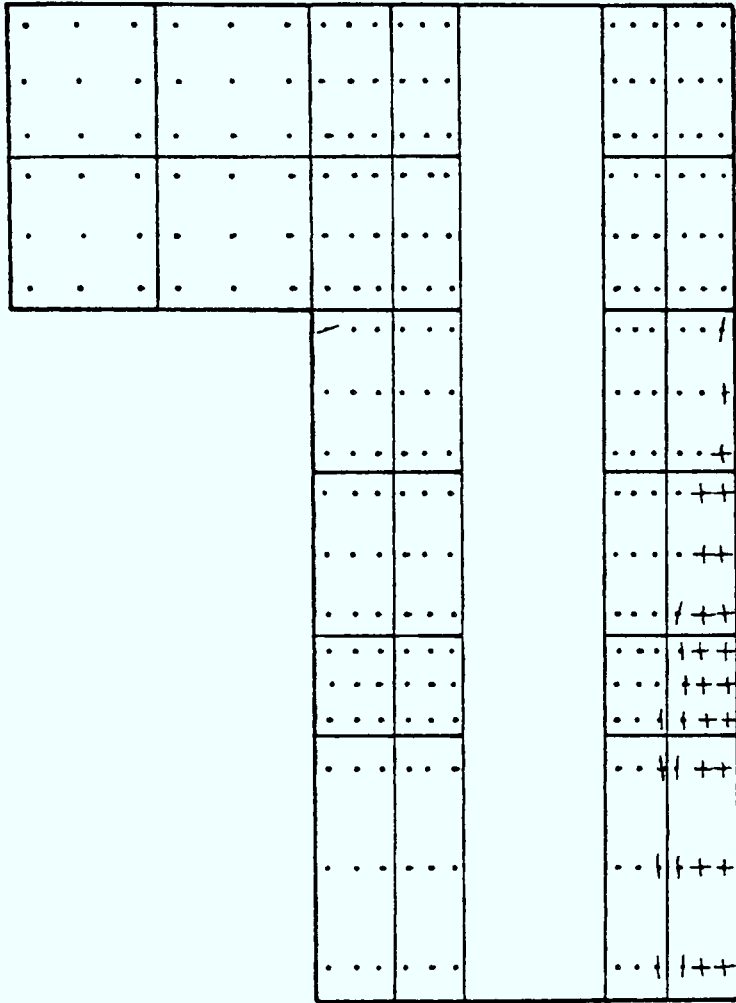
0 2 4 6 m



Vessel Scale

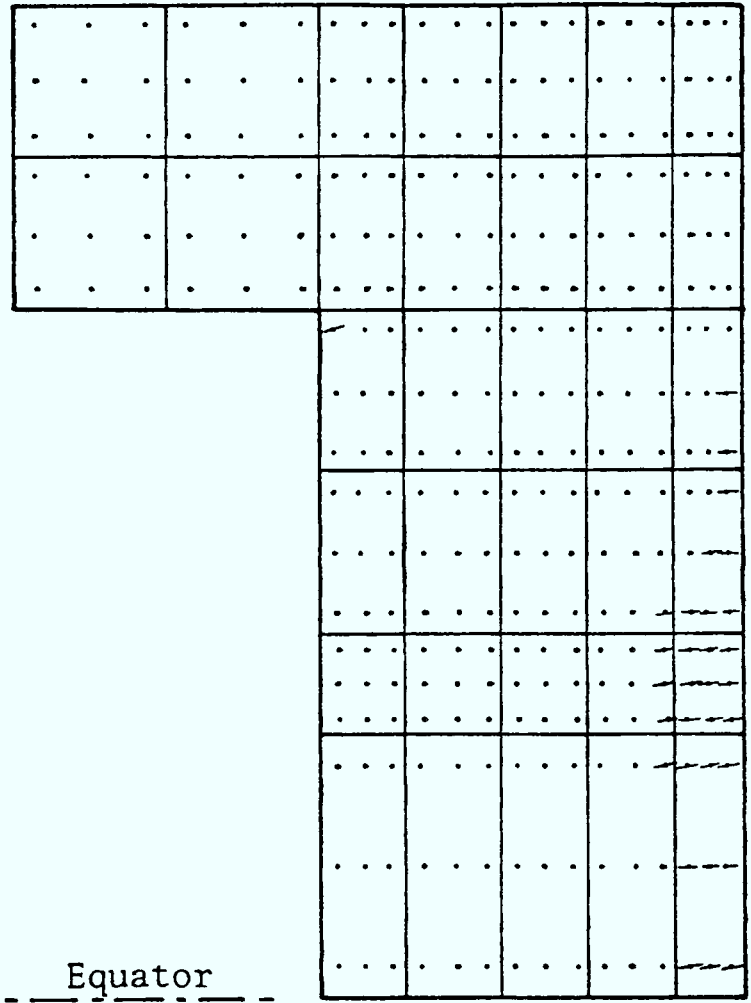


⊕



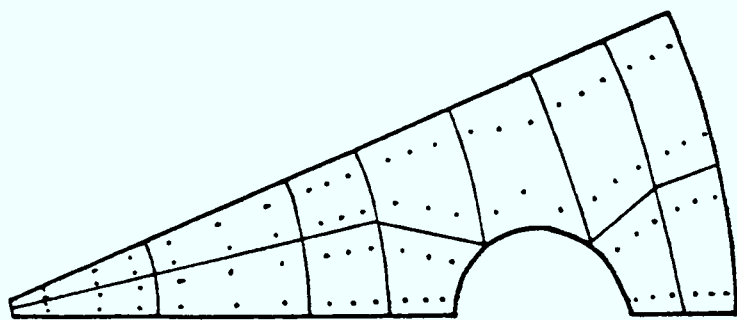
Section at AA

⊕

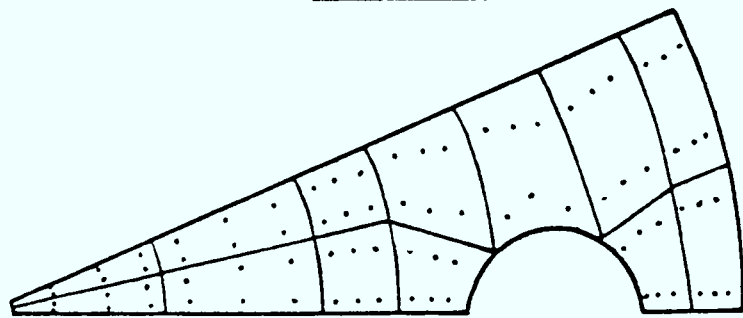


Section at BB

Equator

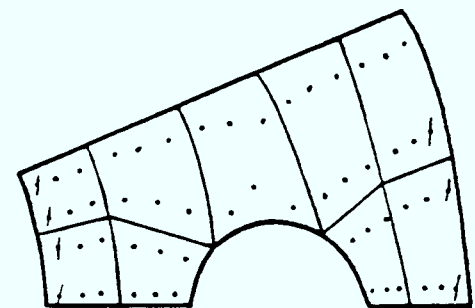


Level 18-18

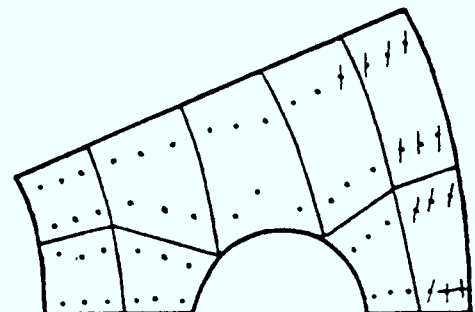


Level 13-13

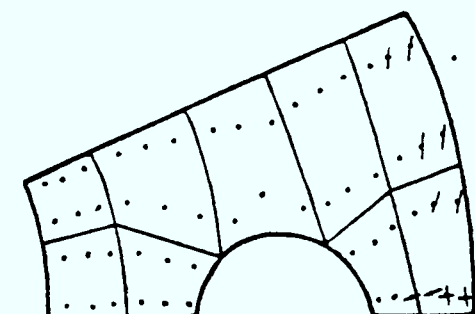
Level 12-12



Level 7-7



Level 1-1









Vessel Type - Perfectly Bonded

Pressure = 11.928 N/mm²

Figure 8.37a Crack Pattern of the Vessel at Load Factor 2.1

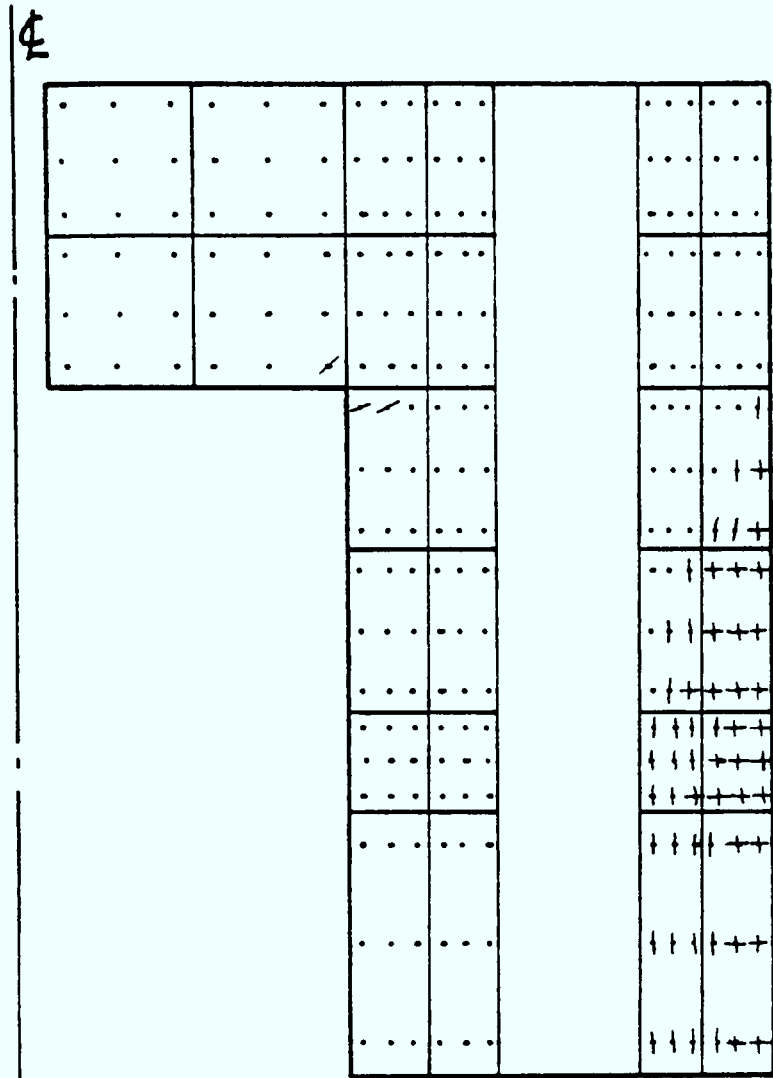
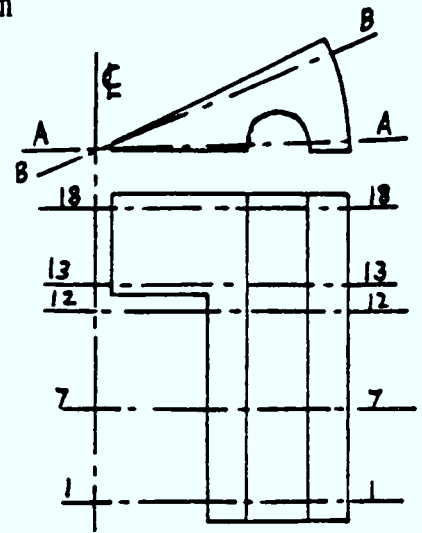
Symbols

-  Horizontal Crack
-  Radial Crack
-  Inclined Crack
-  Radial and Horizontal Cracks
-  Uncracked Gauss Point
- 

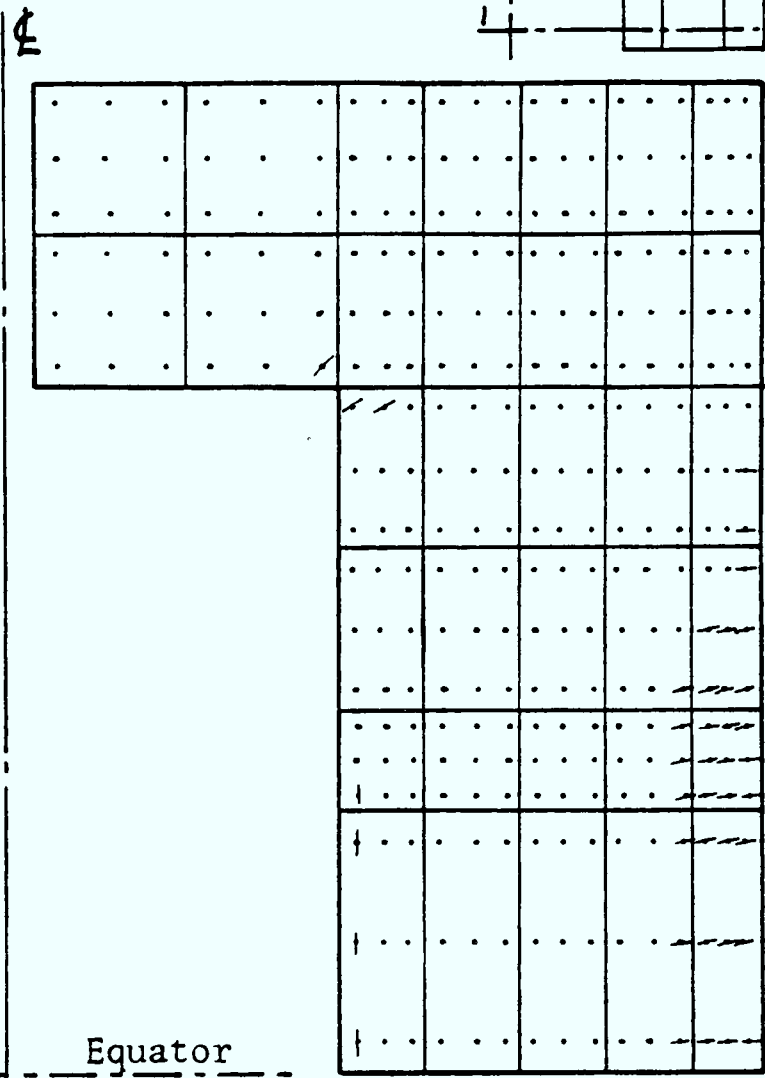
0 2 4 6 m



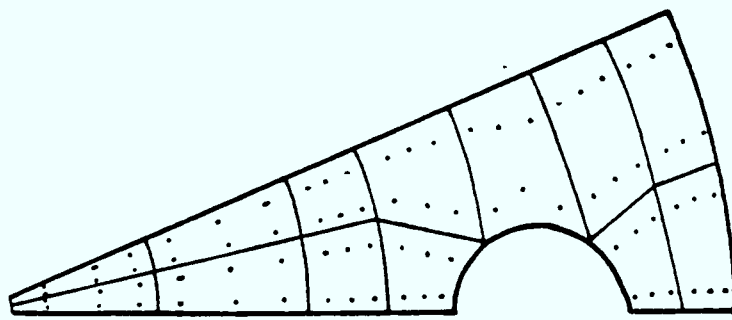
Vessel Scale



Section at AA

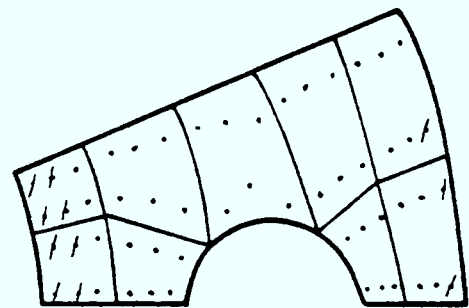


Section at BB

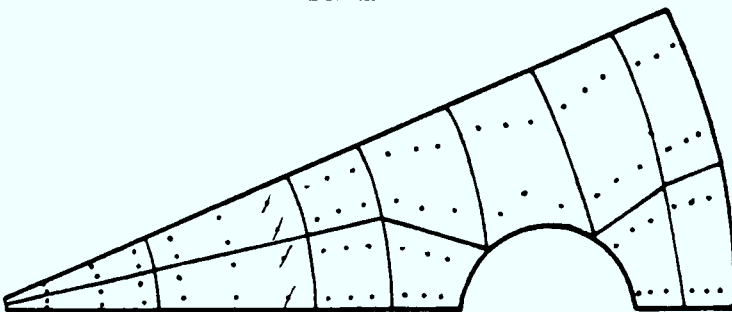


Level 18-18

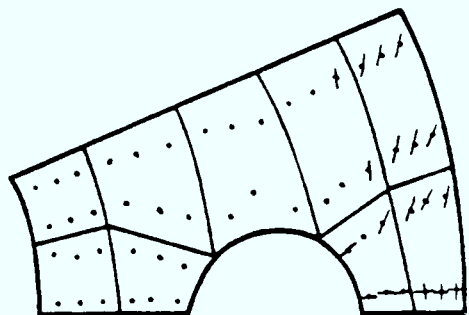
Level 12-12



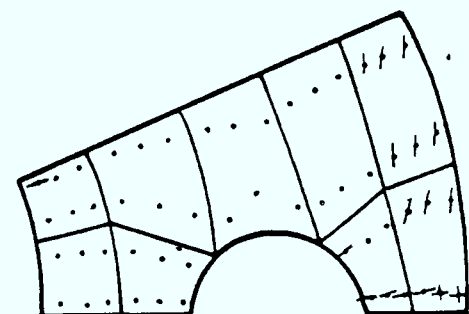
Level 7-7



Level 13-13



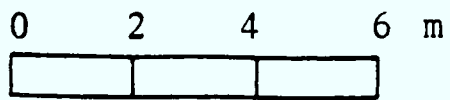
Level 1-1



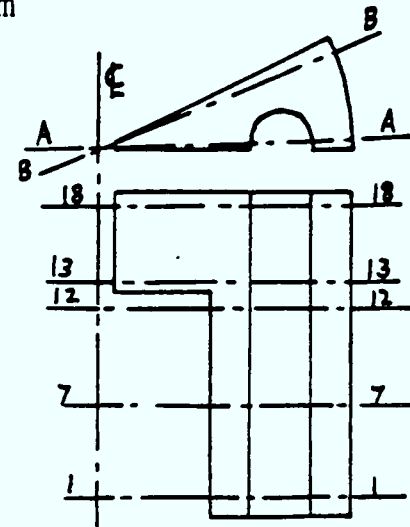
Vessel Type - Perfectly Bonded

Pressure = 14.2 N/mm²

Figure 8.37b Crack Pattern of the Vessel at Load Factor 2.5

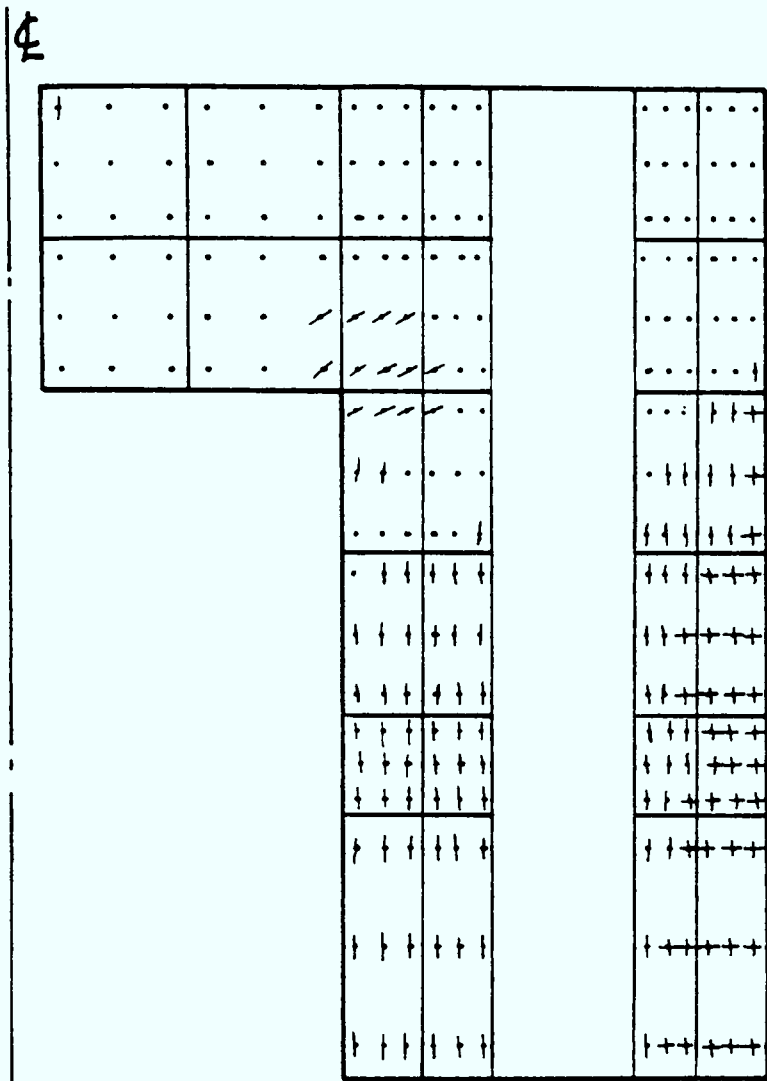


Vessel Scale

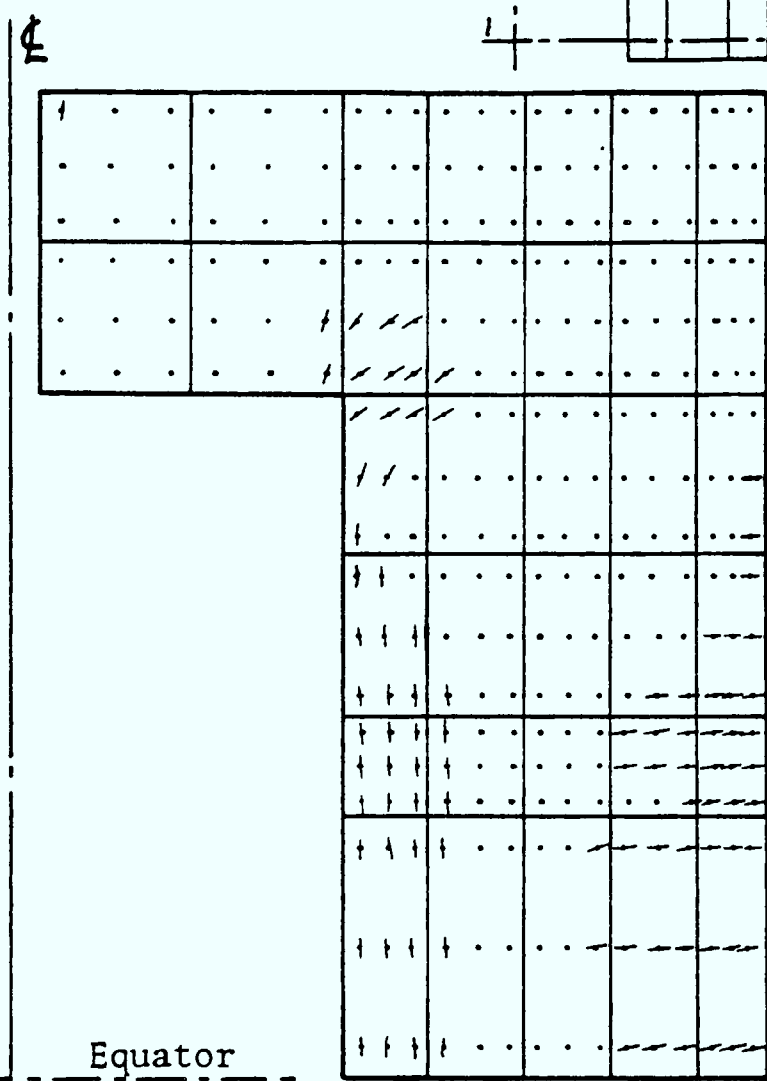


Symbols

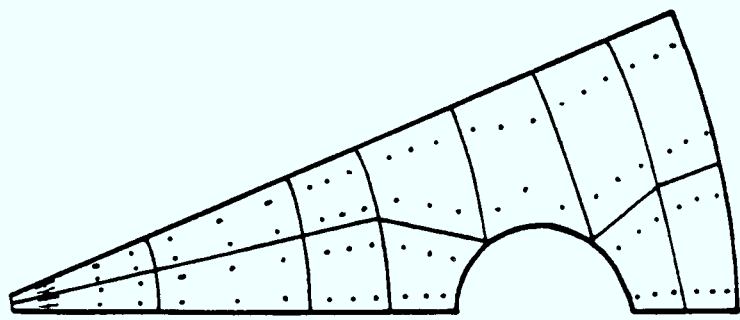
- Horizontal Crack
- Radial Crack
- Inclined Crack
- Radial and Horizontal Cracks
- Uncracked Gauss Point
-



Section at AA

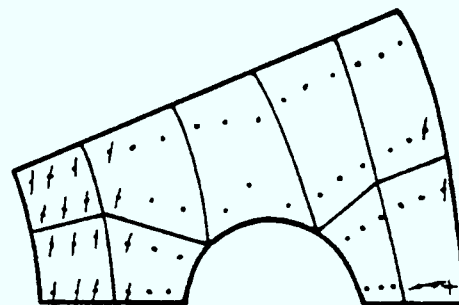


Section at BB

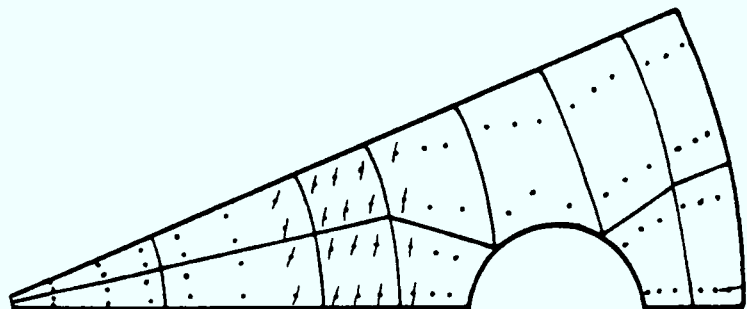


Level 18-18

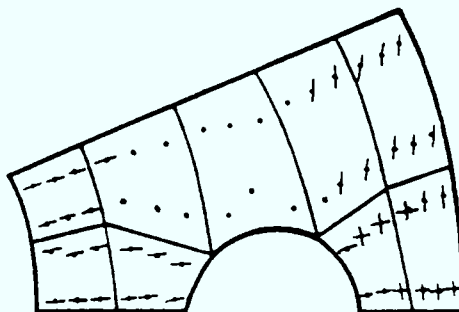
Level 12-12



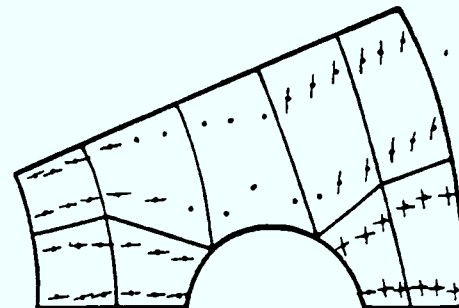
Level 7-7



Level 13-13



Level 1-1


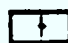






Vessel Type - Perfectly Bonded

Pressure = 17.04 N/mm²

Figure 8.37c Crack Pattern of the Vessel at Load Factor 3.0

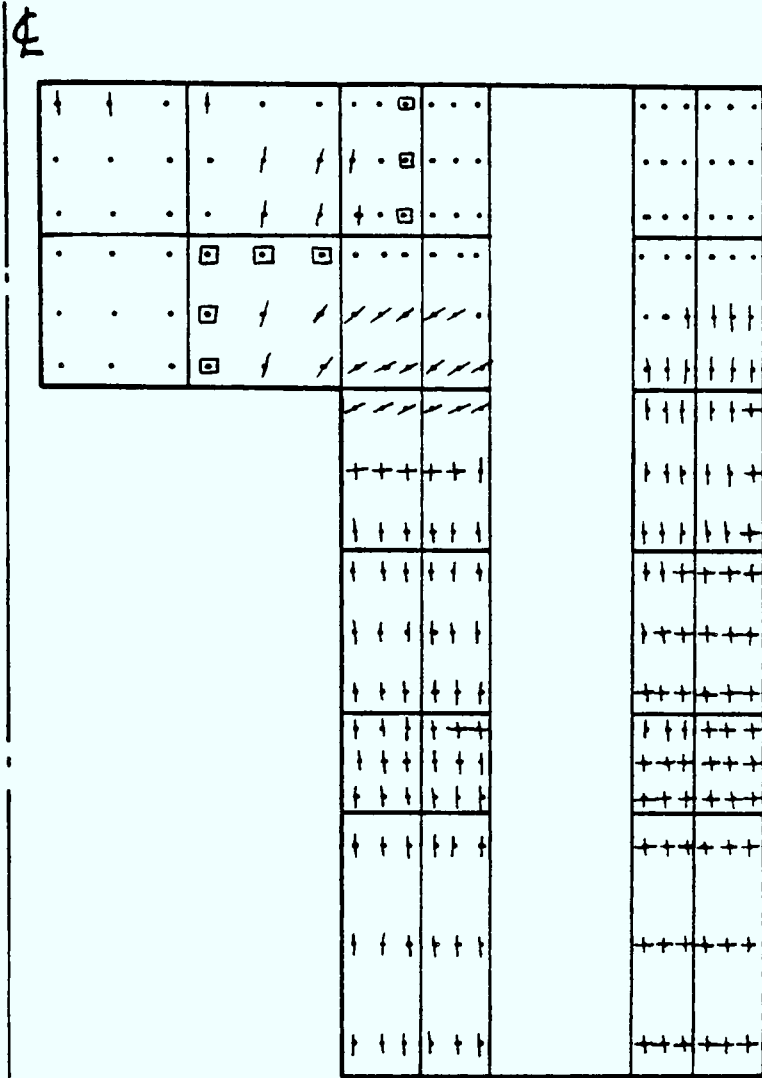
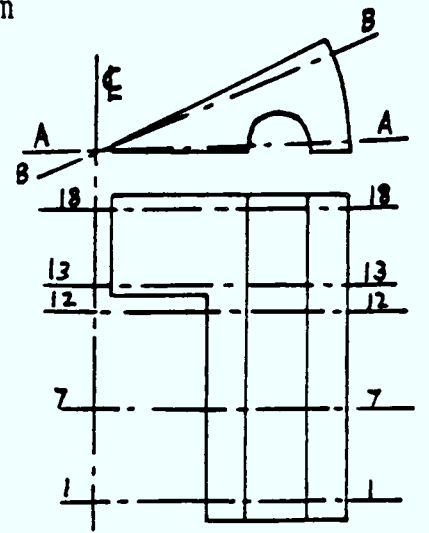
Symbols

-  Horizontal Crack
-  Radial Crack
-  Inclined Crack
-  Radial and Horizontal Crack
-  Uncracked Gauss Point
-  Compression Failure (crushing)

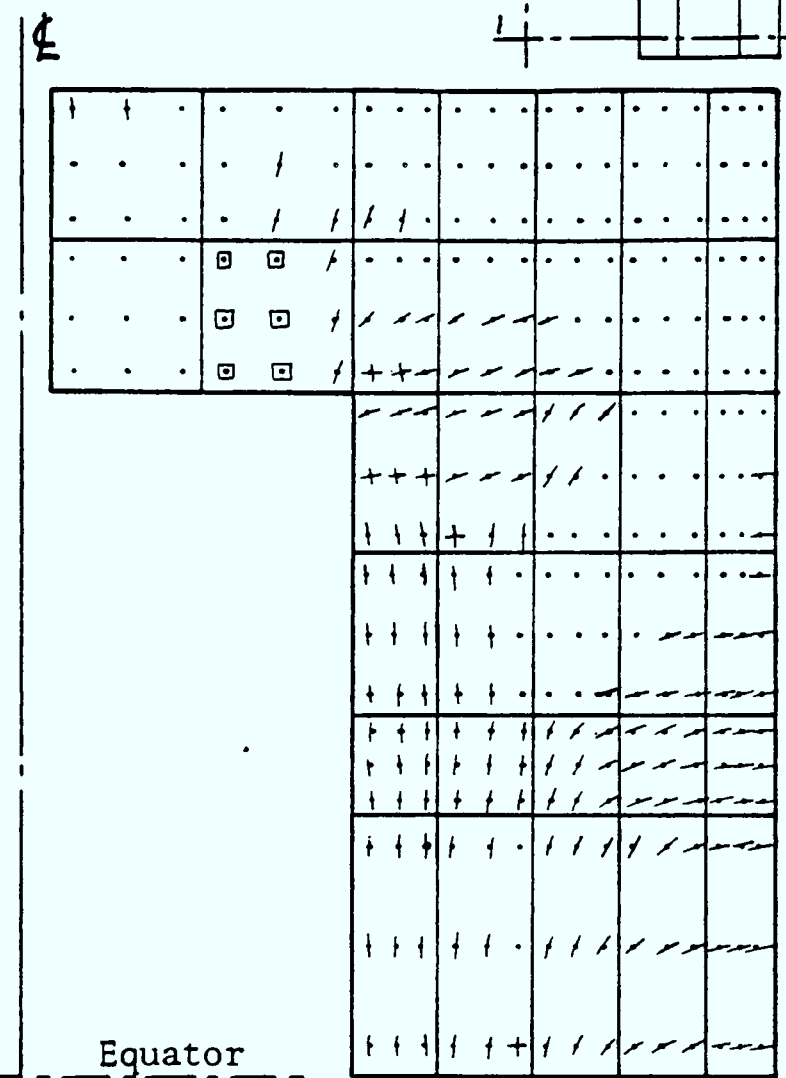
0 2 4 6 m



Vessel Scale

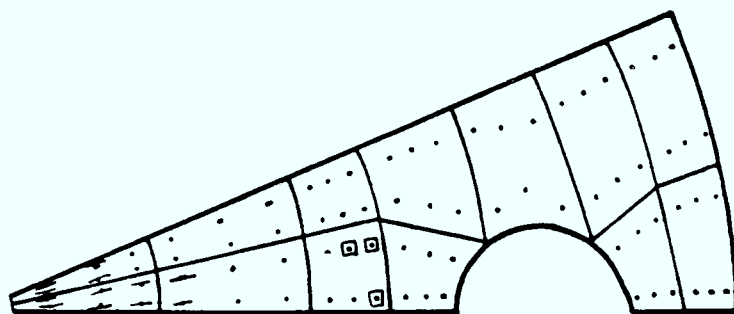


Section at AA



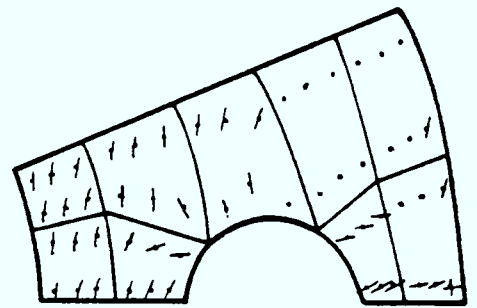
Equator

Section at BB

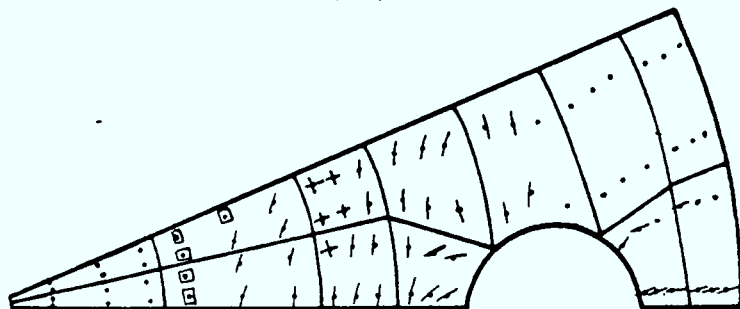
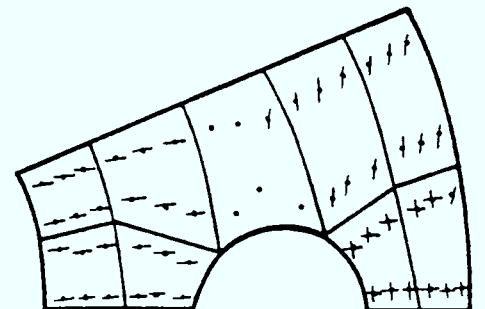


Level 18-18

Level 12-12

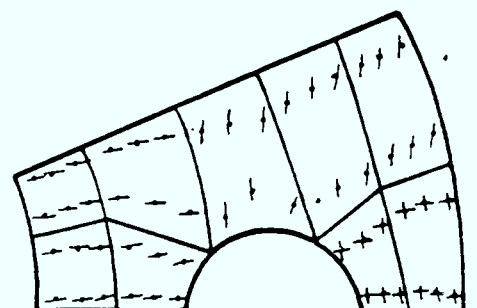


Level 7-7



Level 13-13

Level 1-1



Vessel Type - Perfectly Bonded

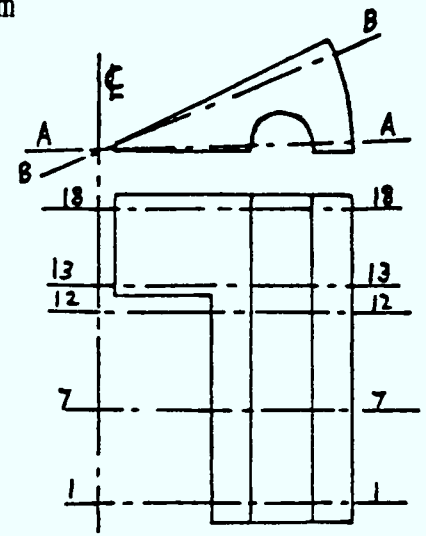
Pressure = 19.88 N/mm²

Figure 8.37d Crack Pattern of the Vessel at Load Factor 3.5

0 2 4 6 m

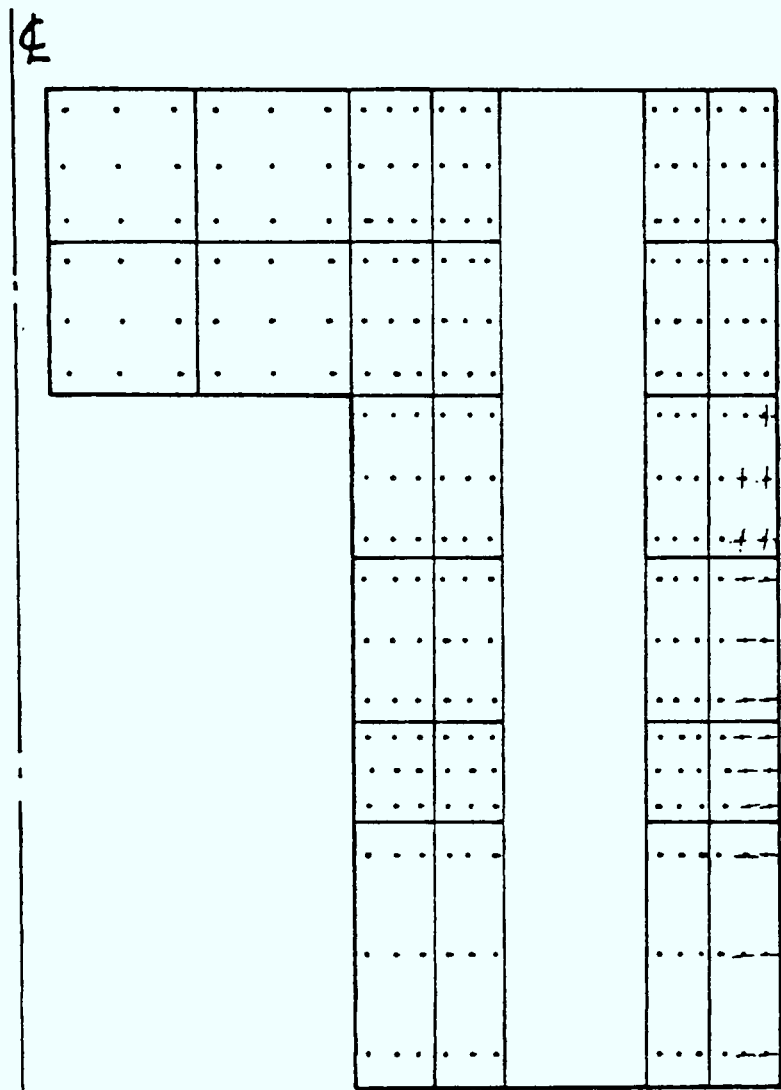


Vessel Scale

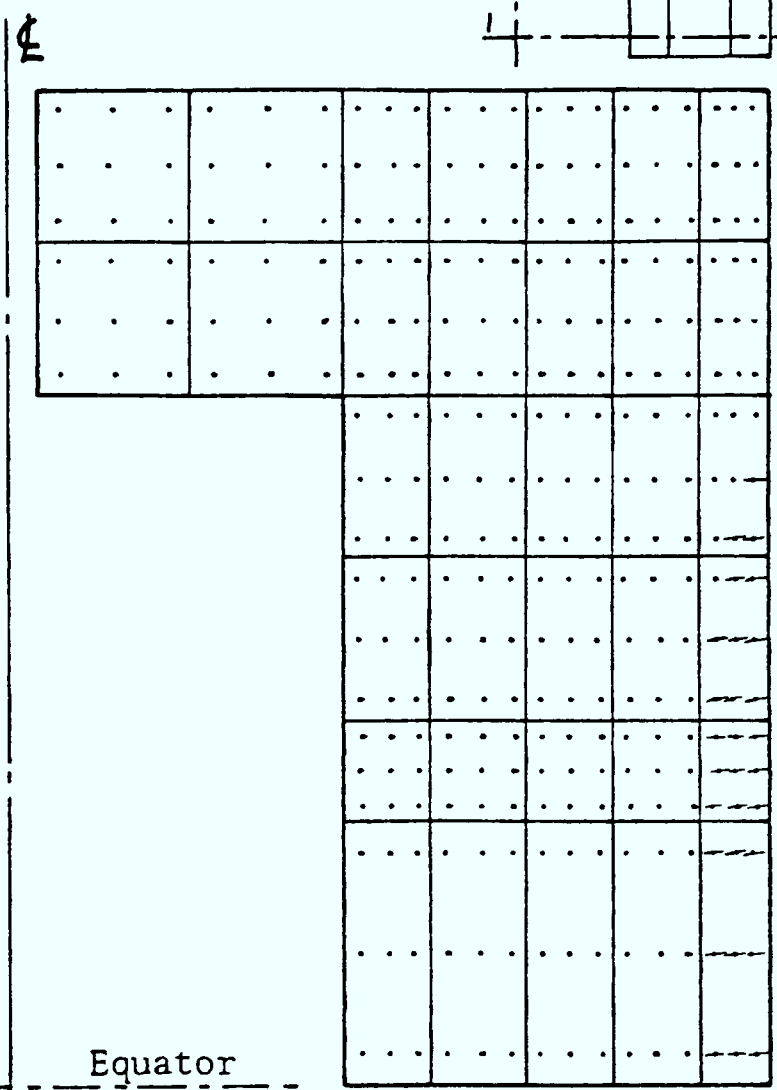


Symbols

- Horizontal Crack
- Radial Crack
- Inclined Crack
- Radial and Horizontal Cracks
- Uncracked Gauss Point
-

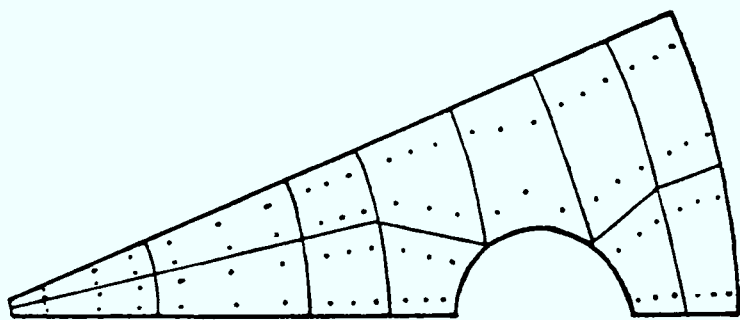


Section at AA

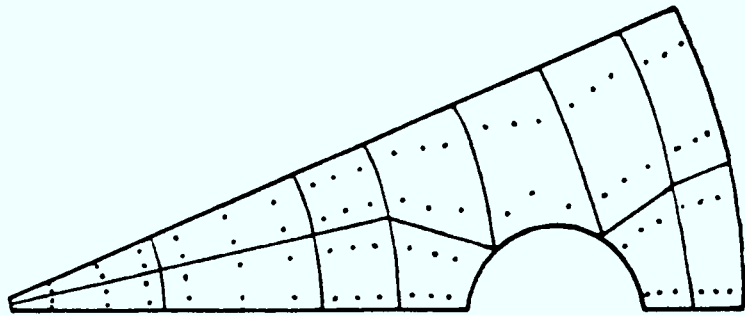


Section at BB

Equator

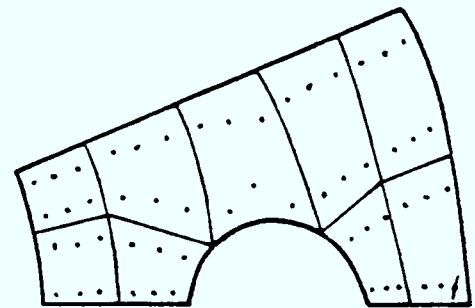


Level 18-18

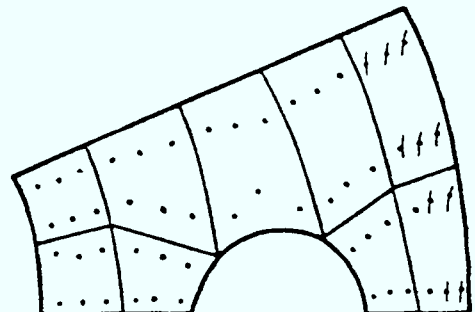


Level 13-13

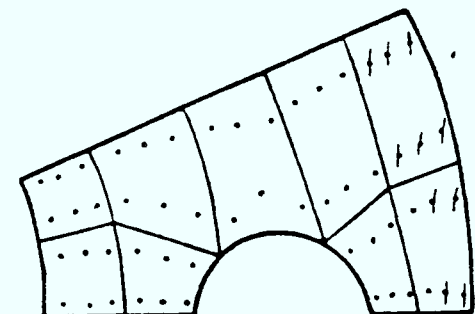
Level 12-12



Level 7-7



Level 1-1



Vessel Type - Unbonded

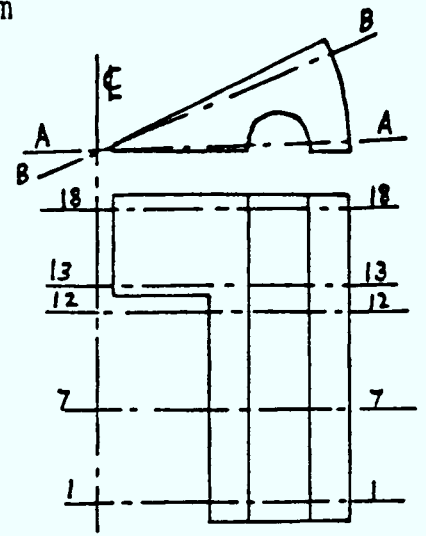
Pressure = 9.088 N/mm²

Figure 8.38 Crack Pattern of the Vessel at Load Factor 1.6

0 2 4 6 m

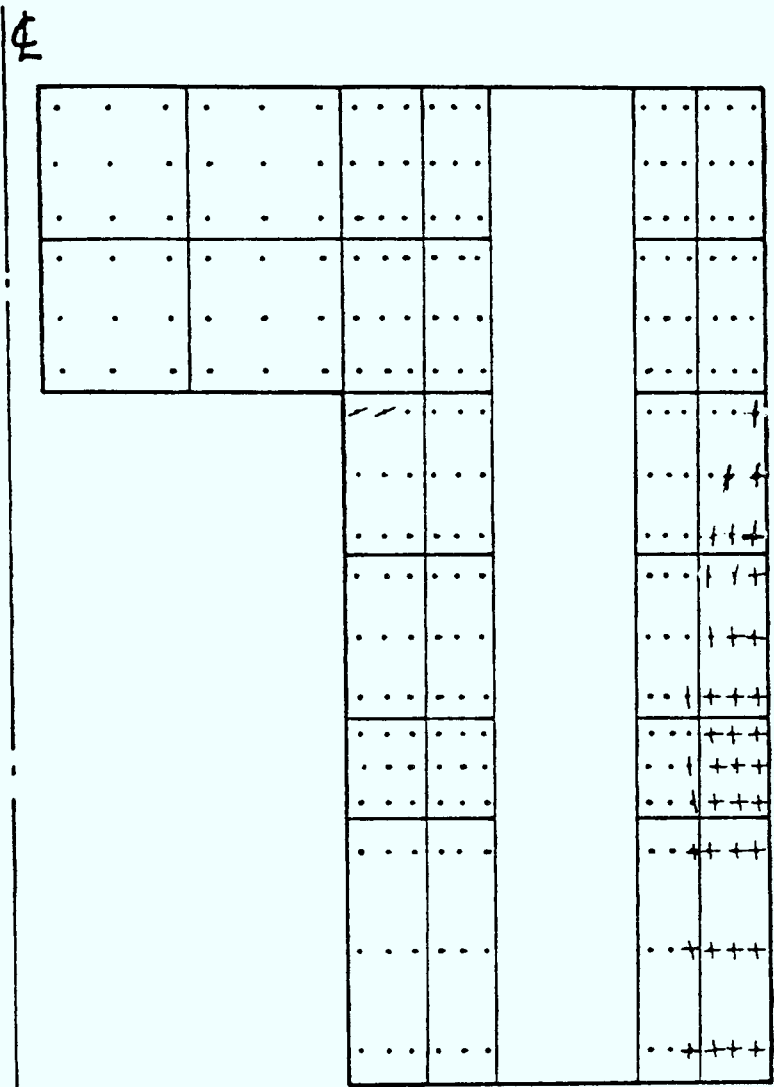


Vessel Scale

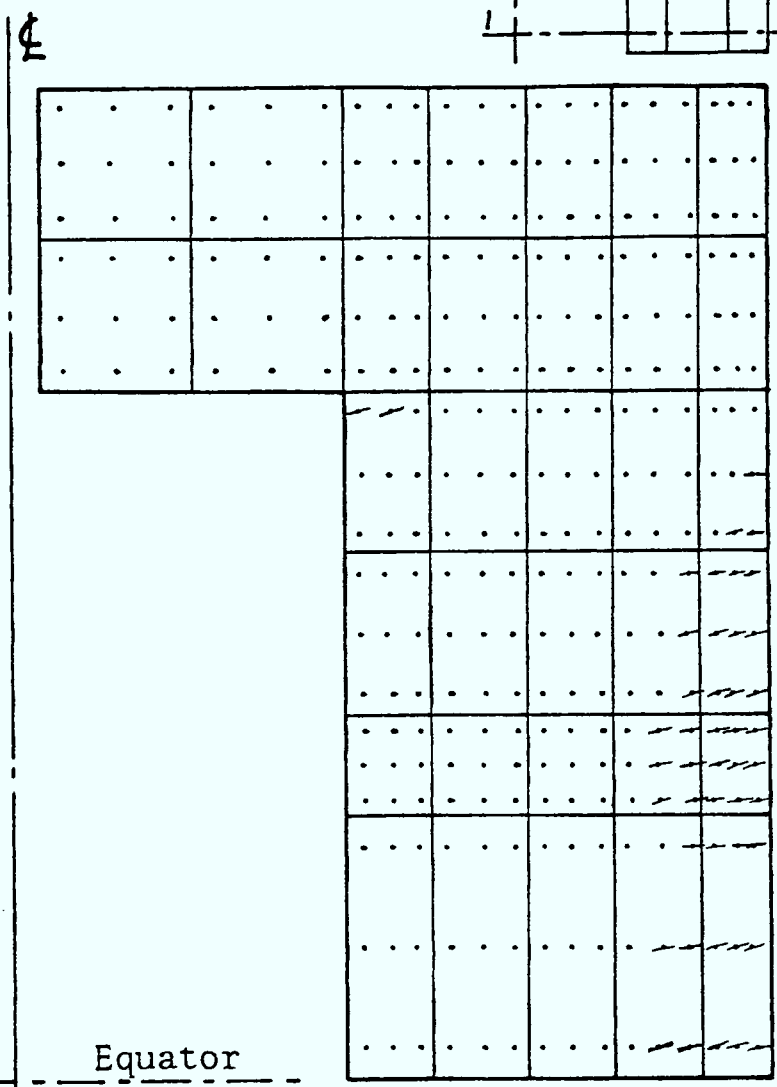


Symbols

- Horizontal Crack
- Radial Crack
- Inclined Crack
- Radial and Horizontal Cracks
- Uncracked Gauss Point
-

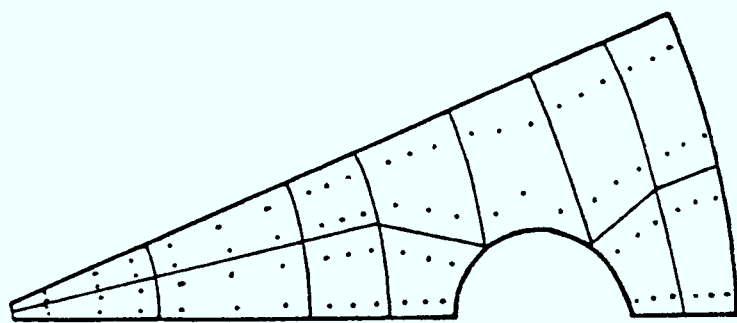


Section at AA

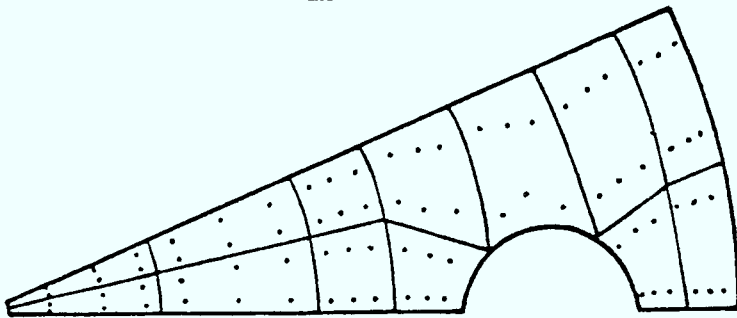


Section at BB

Equator

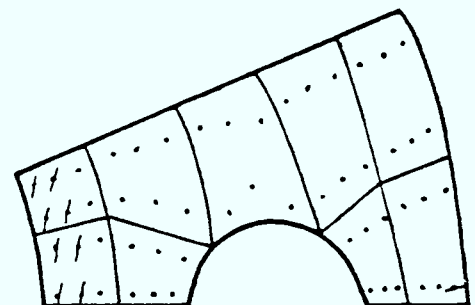


Level 18-18

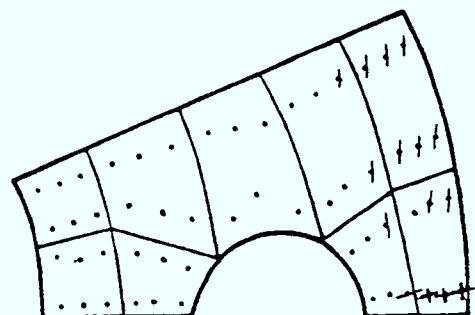


Level 13-13

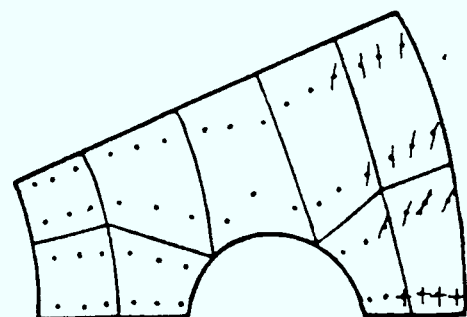
Level 12-12



Level 7-7



Level 1-1

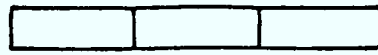


Vessel Type - Unbonded

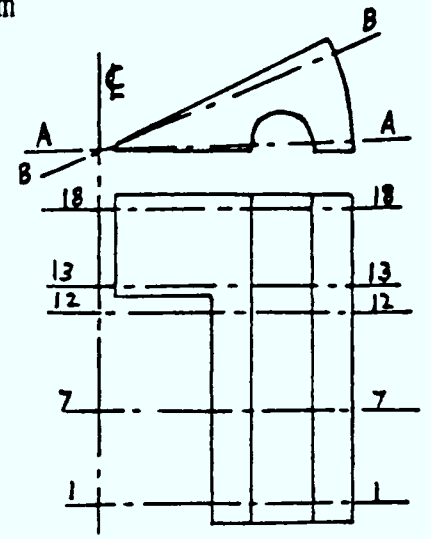
Pressure = 11.928 N/mm²

Figure 8.38a Crack Pattern of the Vessel at Load Factor 2.1

0 2 4 6 m

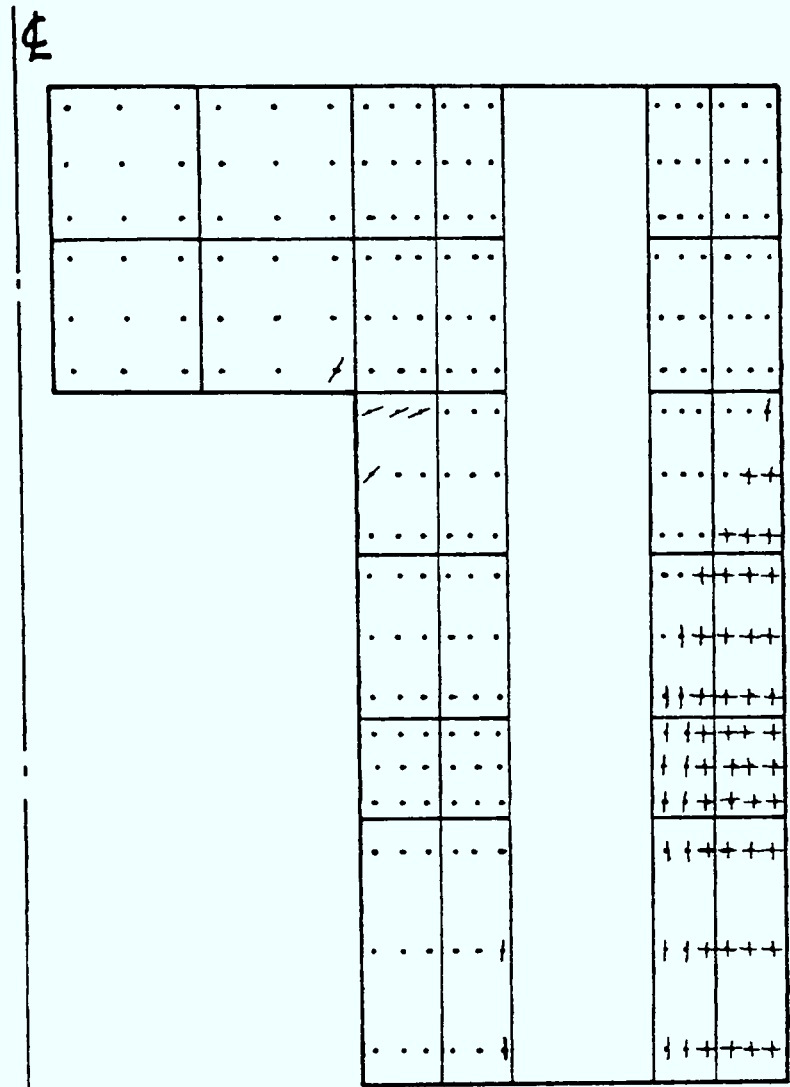


Vessel Scale

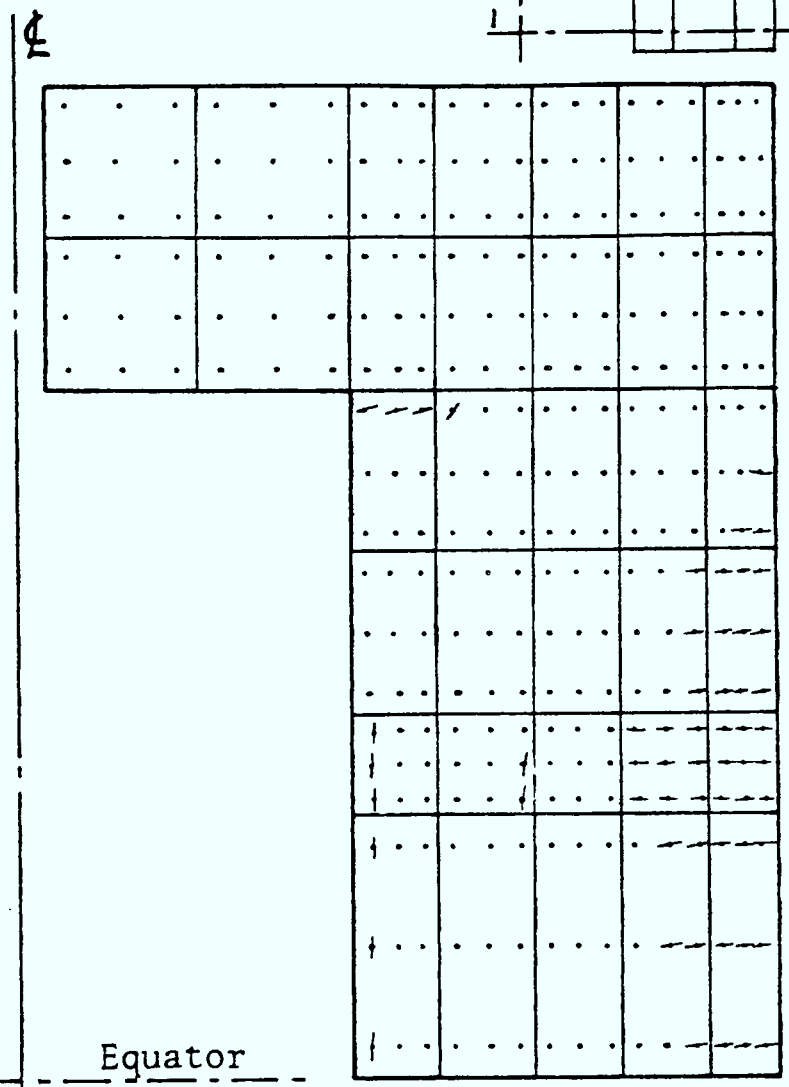


Symbols

- Horizontal Crack
- Radial Crack
- Inclined Crack
- Radial and Horizontal Cracks
- Uncracked Gauss Point
-

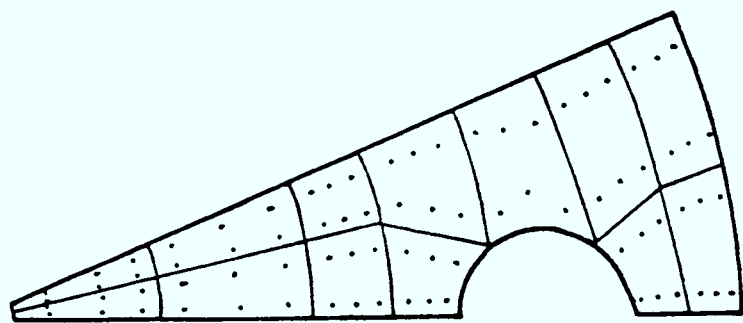


Section at AA



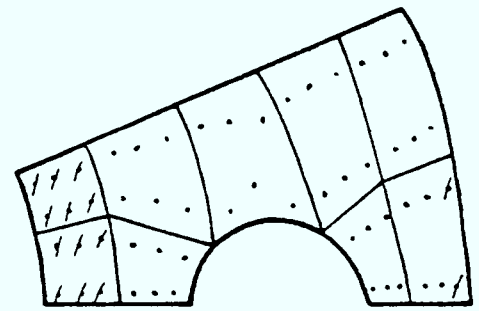
Equator

Section at BB

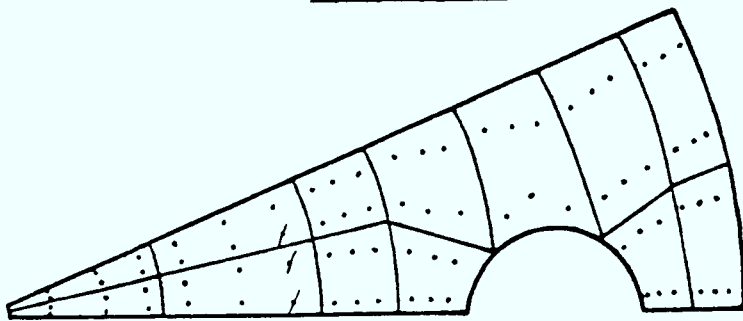
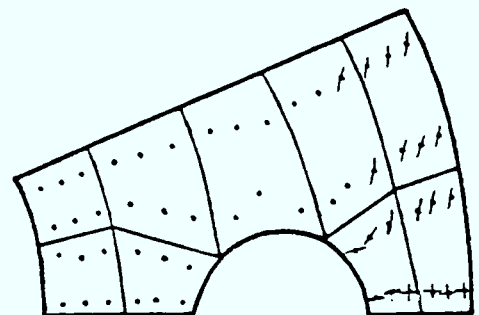


Level 18-18

Level 12-12

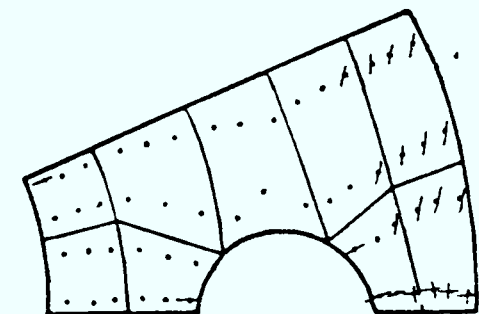


Level 7-7



Level 13-13

Level 1-1

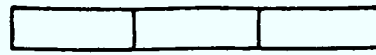


Vessel Type - Unbonded

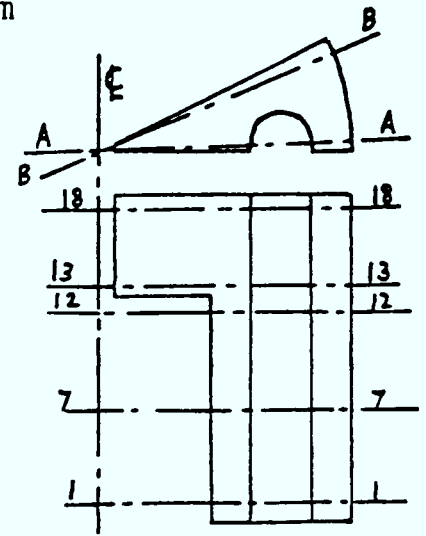
Pressure = 14.2 N/mm²

Figure 8.38b Crack Pattern of the Vessel at Load Factor 2.5

0 2 4 6 m

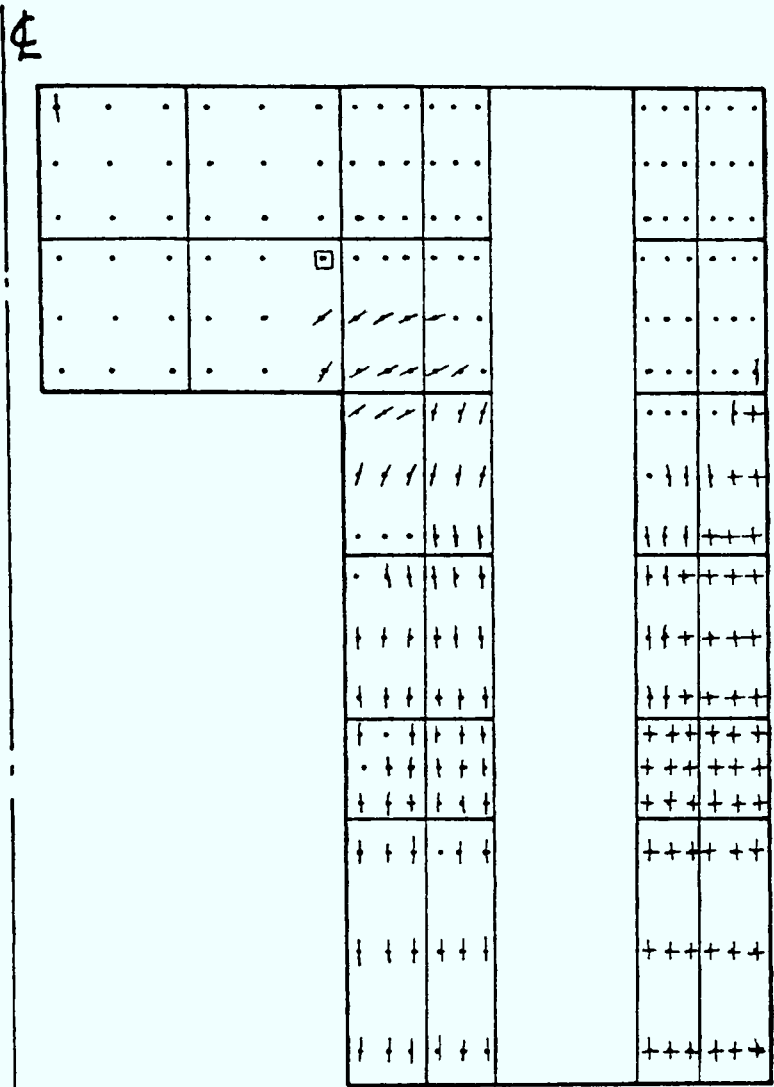


Vessel Scale

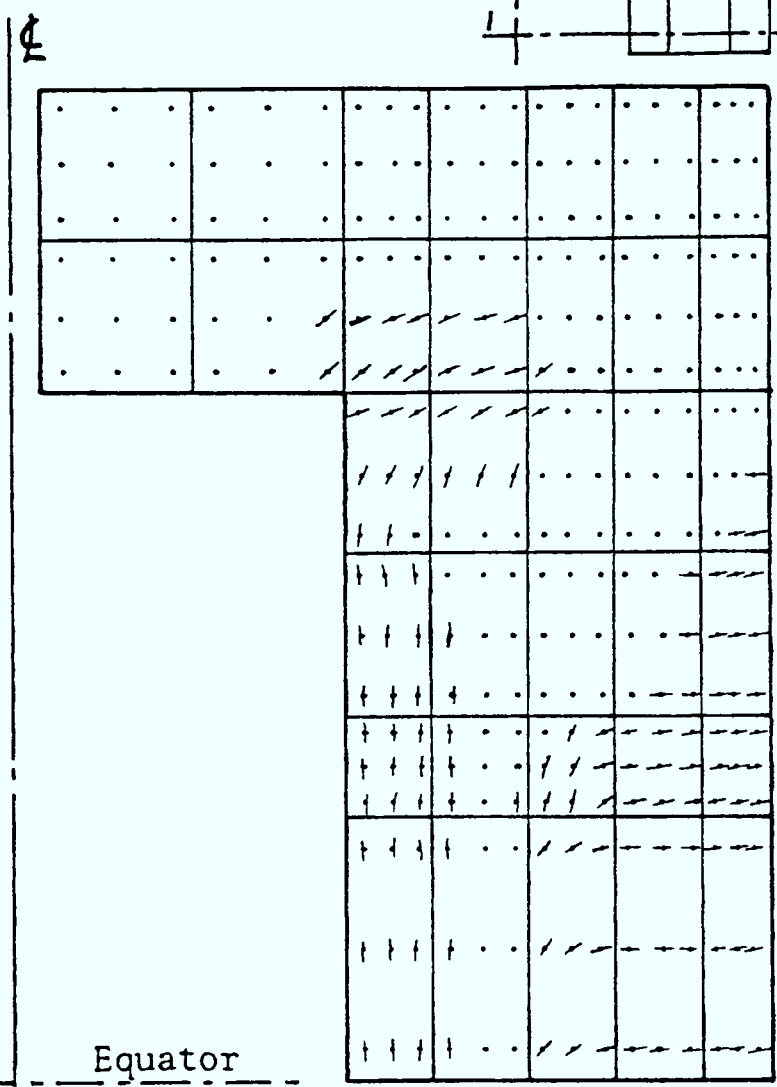


Symbols

- Horizontal Crack
- Radial Crack
- Inclined Crack
- Radial and Horizontal Cracks
- Uncracked Gauss Point
- Compression Failure (crushing)

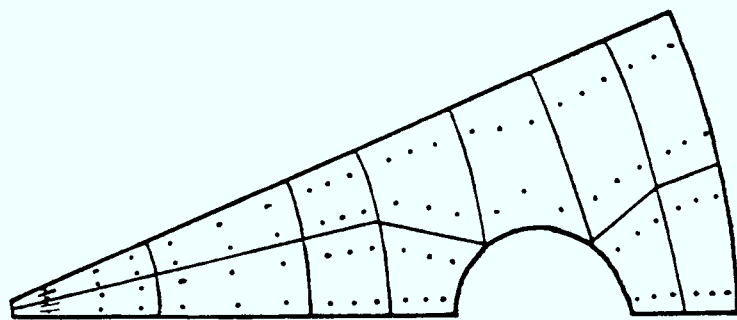


Section at AA



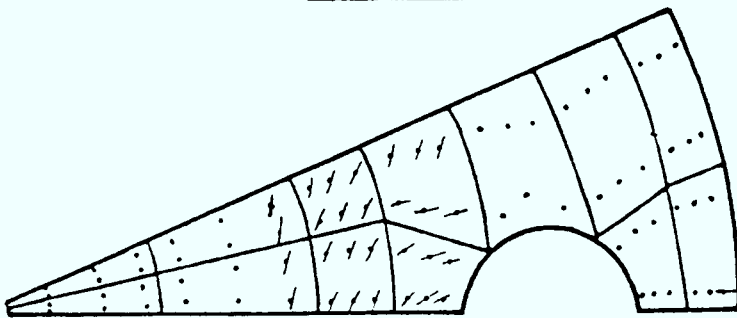
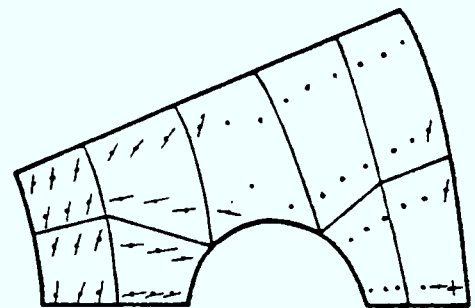
Equator

Section at BB



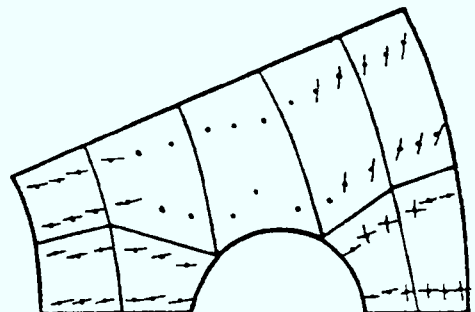
Level 18-18

Level 12-12

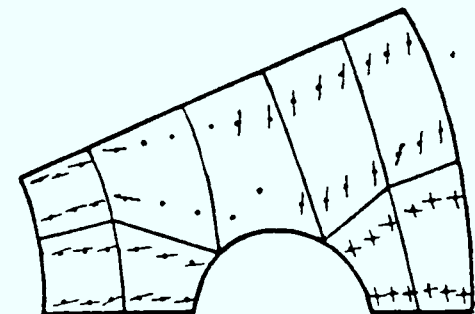


Level 13-13

Level 7-7



Level 1-1



Vessel Type - Unbonded

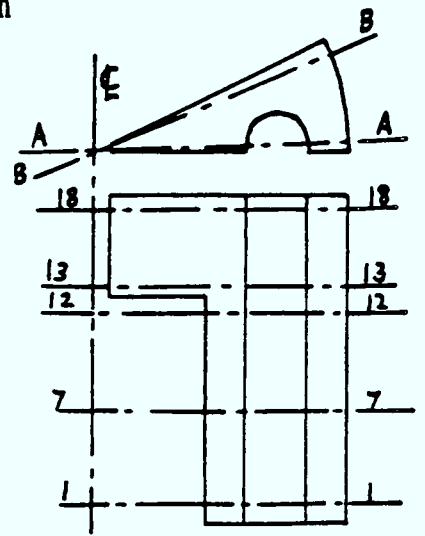
Pressure = 17.04 N/mm²

Figure 8.38c Crack Pattern of the Vessel at Load Factor 3.0

0 2 4 6 m

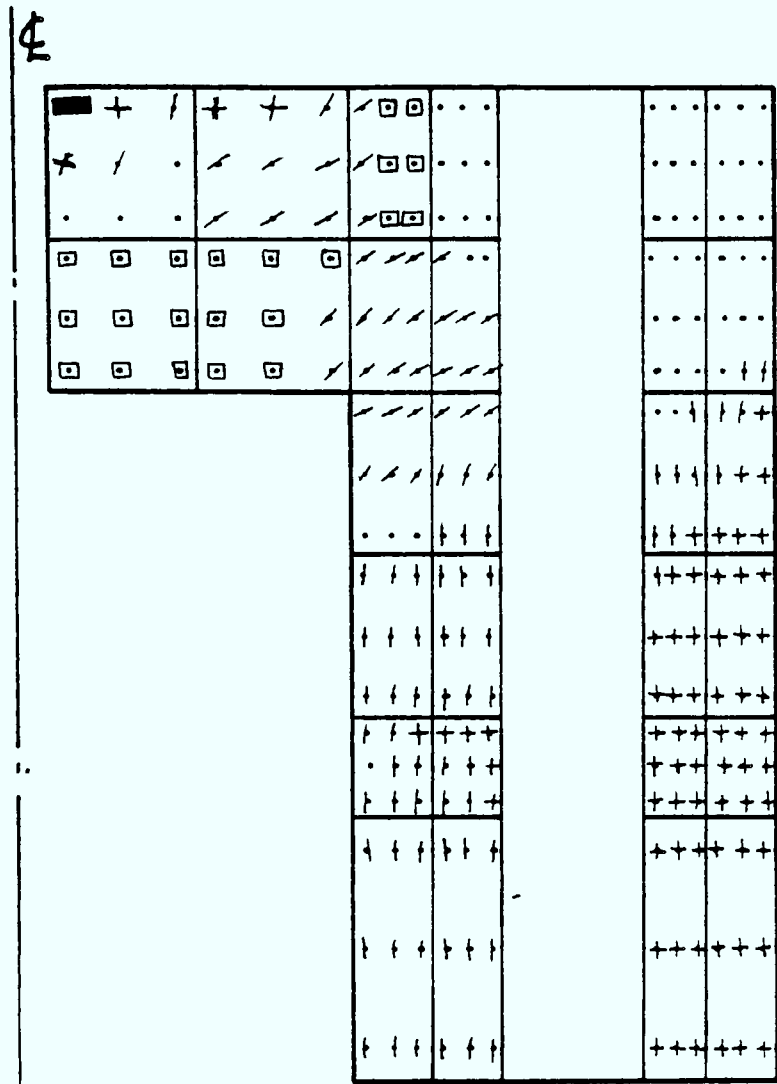


Vessel Scale

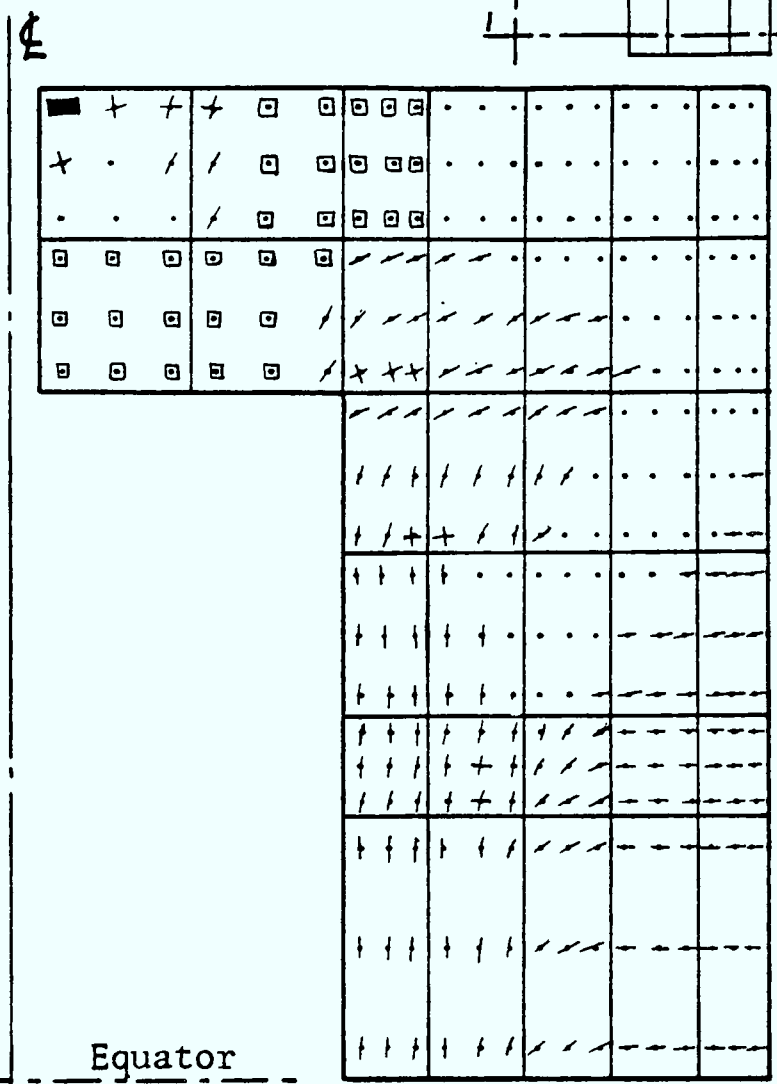


Symbols

- Horizontal Crack
- Radial Crack
- Inclined Crack
- Three Cracks
- Radial and Horizontal Cracks
- Uncracked Gauss Point
- Compression Failure (crushing)

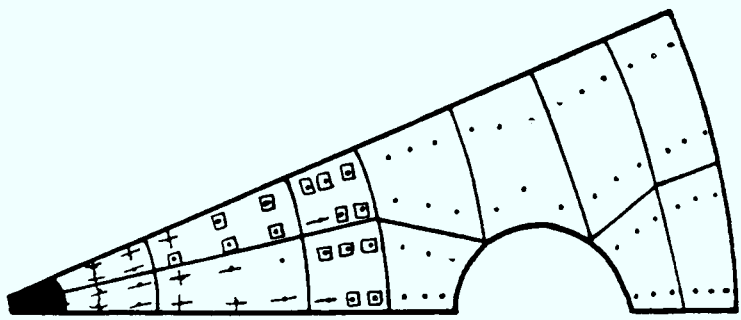


Section at AA

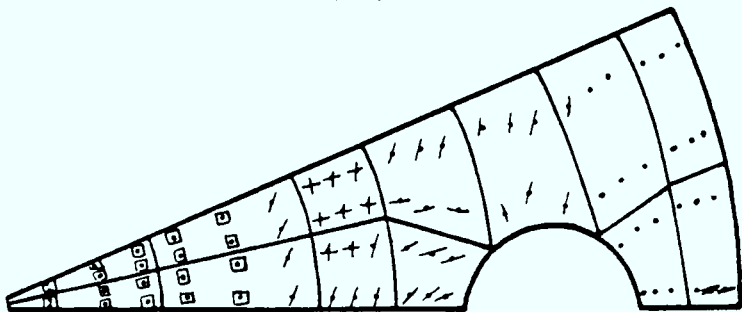


Equator

Section at BB

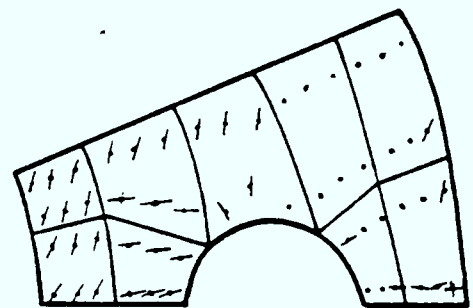


Level 18-18

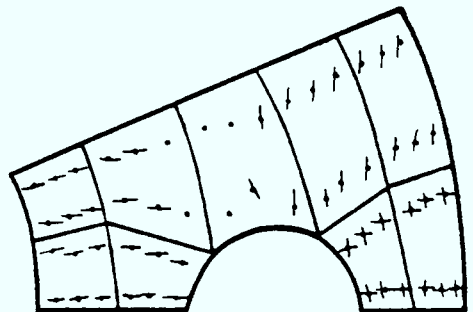


Level 13-13

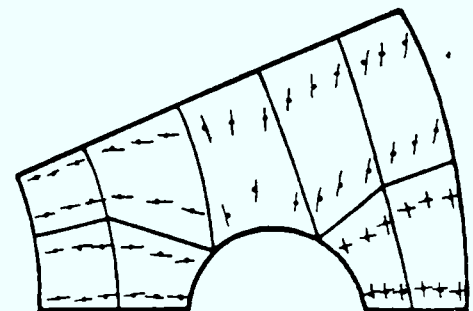
Level 12-12



Level 7-7



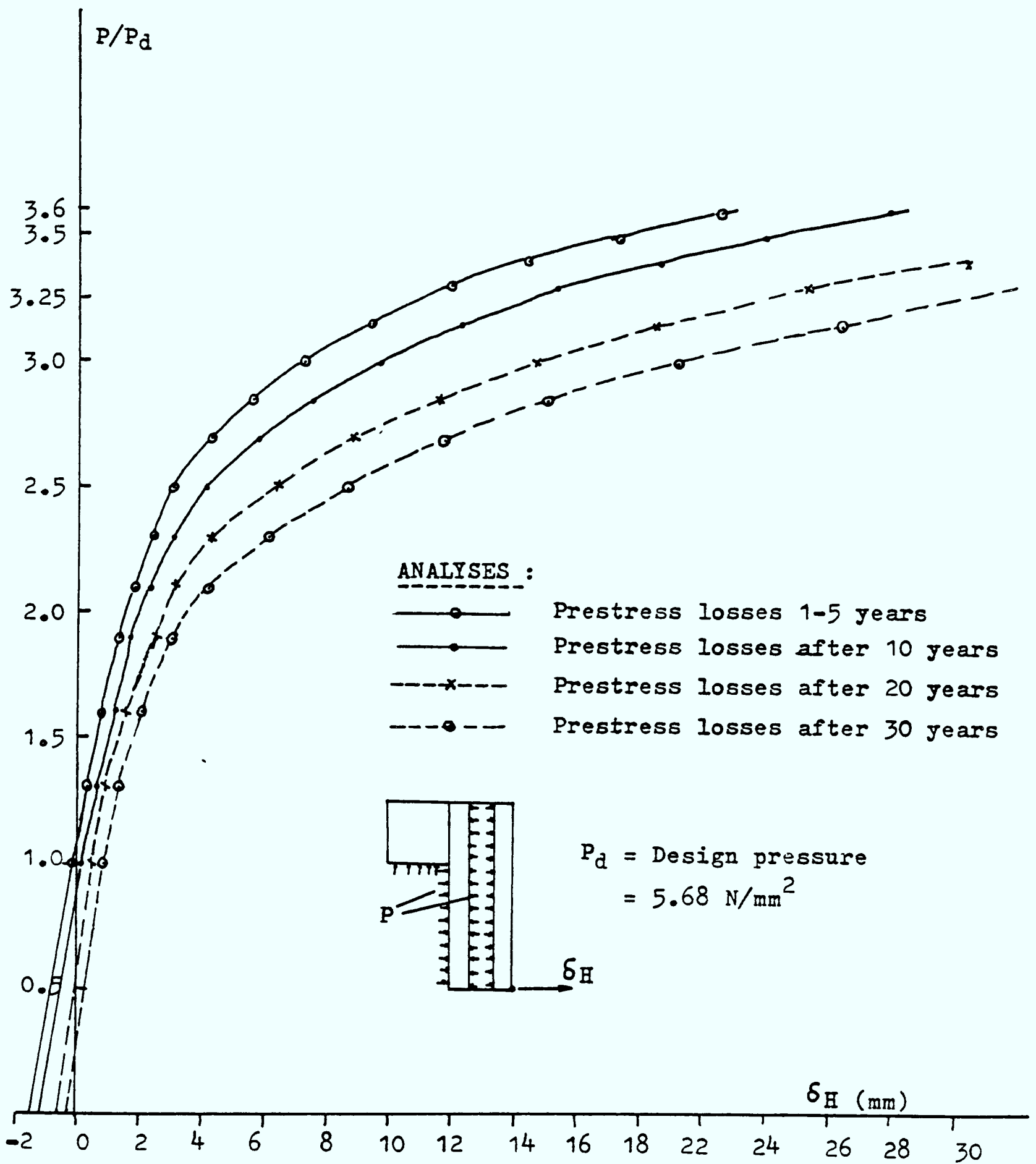
Level 1-1



Vessel Type - Unbonded

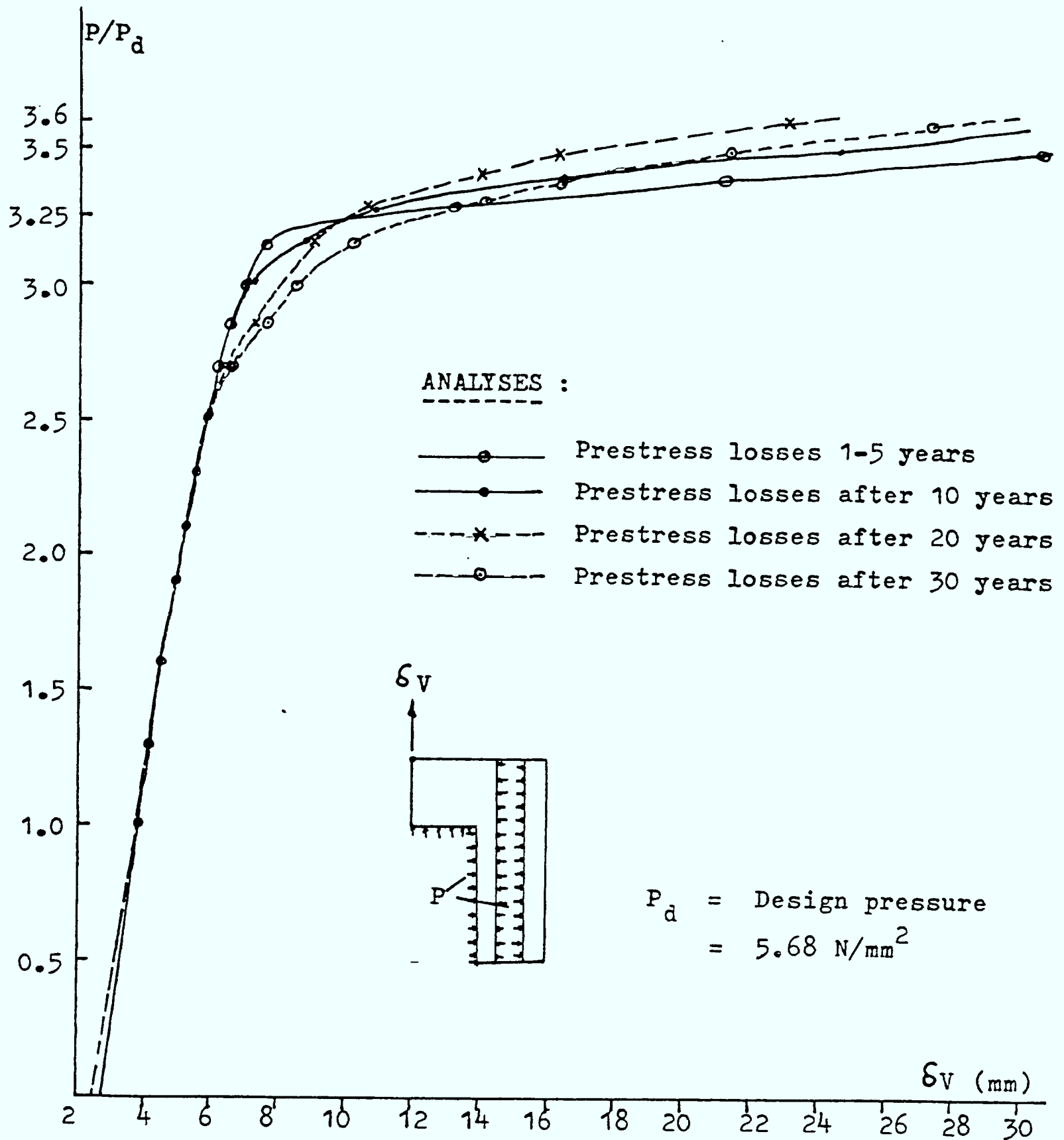
Pressure = 18.744 N/mm²

Figure 8.38d Crack Pattern of the Vessel at Load Factor 3.3



Vessel Type - Bonded Vessel with Ahmlink Element

Figure 8.39 Pressure Displacement Curves for Reactor Vessel



Vessel Type - Bonded Vessel with Ahmlink Element

Figure 8.40 Pressure Displacement Curves for Reactor Vessel

-----Deformed shape at 3.3
-----Deformed shape at 3.5

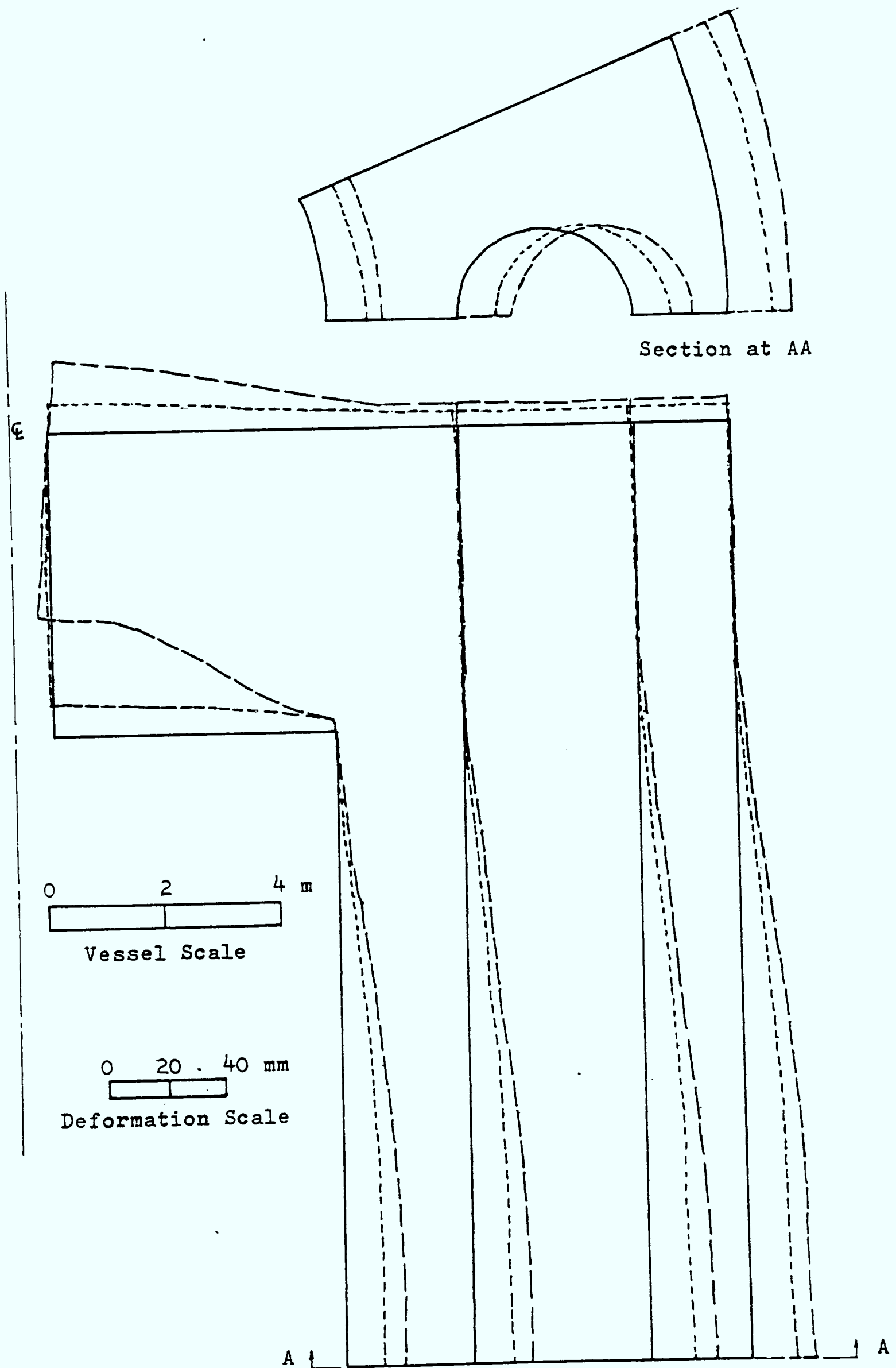


Figure 8.41 Deformed Shapes of Bonded Reactor Vessel
After Prestress Losses of 10 Years

-----Deformed shape at 3.3
-----Deformed shape at 3.5

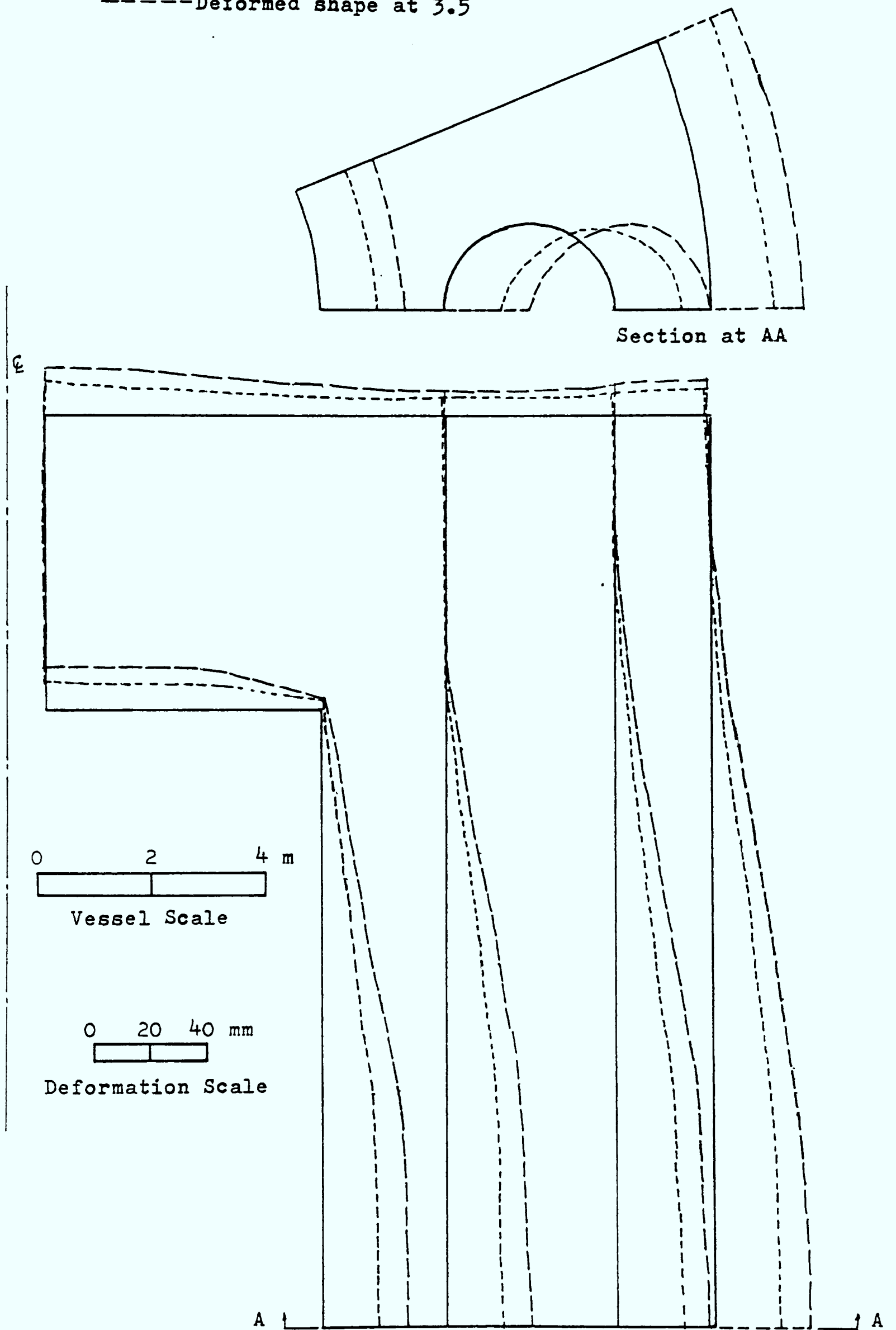
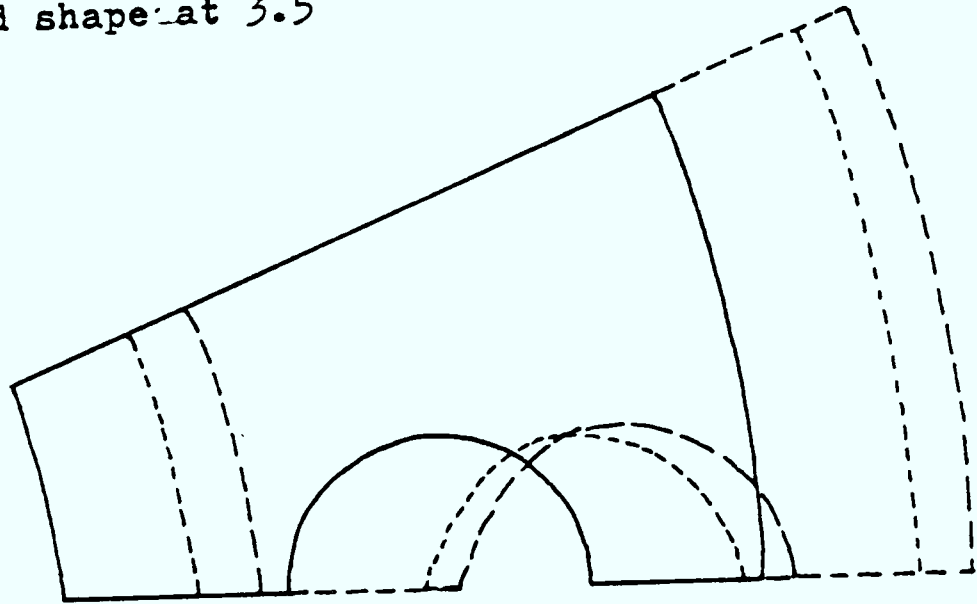


Figure 8.42 Deformed Shapes of Bonded Reactor Vessel
After Prestress Losses of 20 Years

----- Deformed shape at 3.3
----- Deformed shape at 3.5



Section at AA

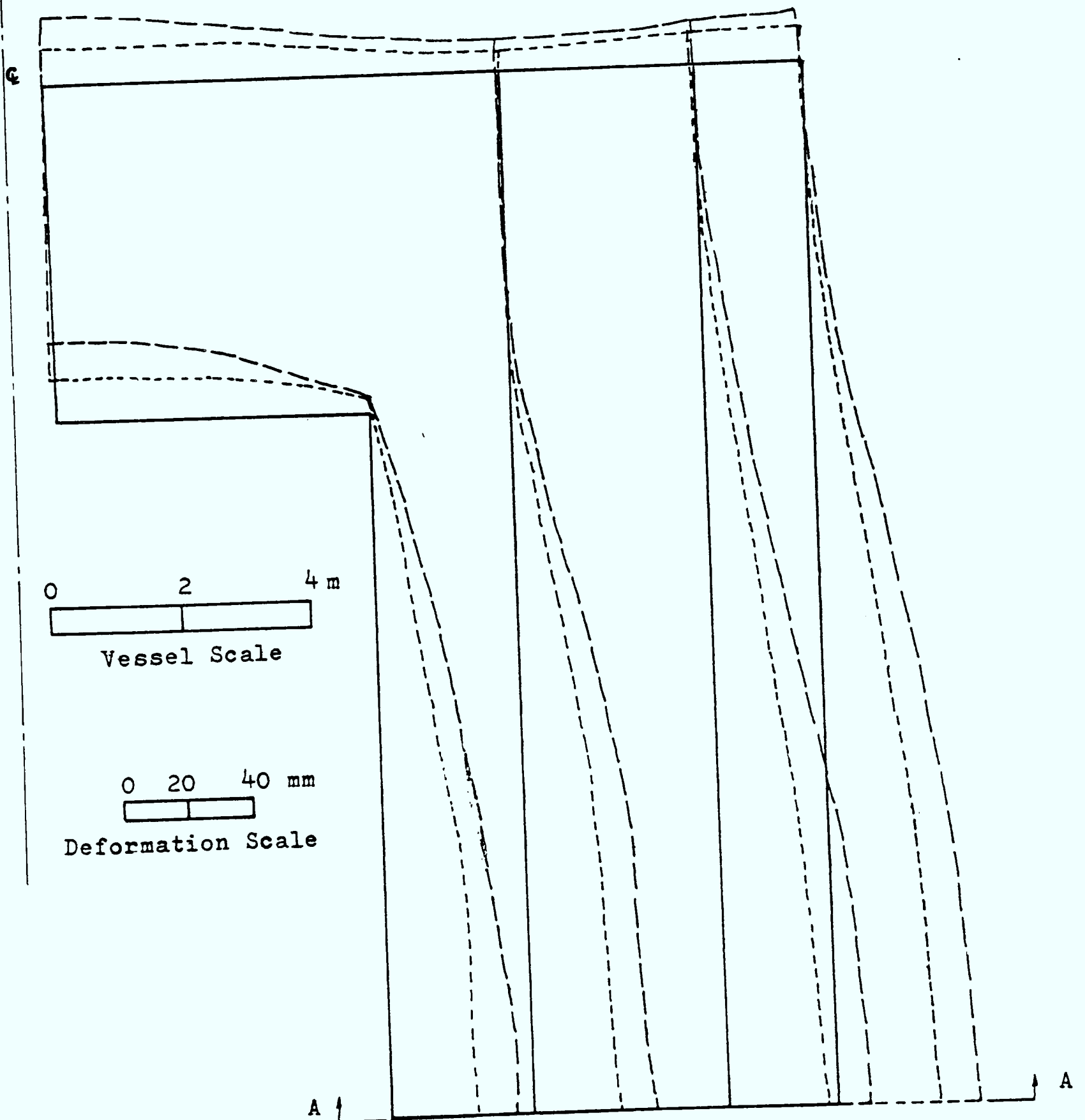
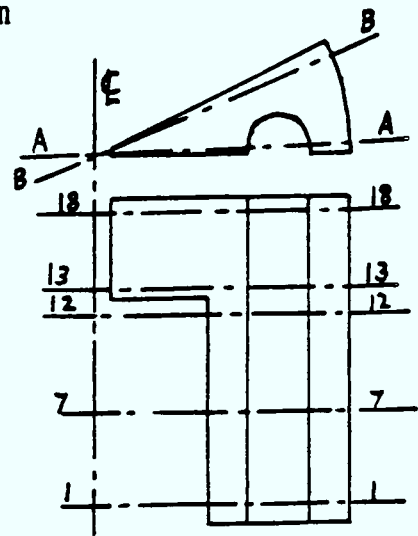


Figure 8.43 Deformed Shapes of Bonded Reactor Vessel
After Prestress Losses of 30 Years

0 2 4 6 m

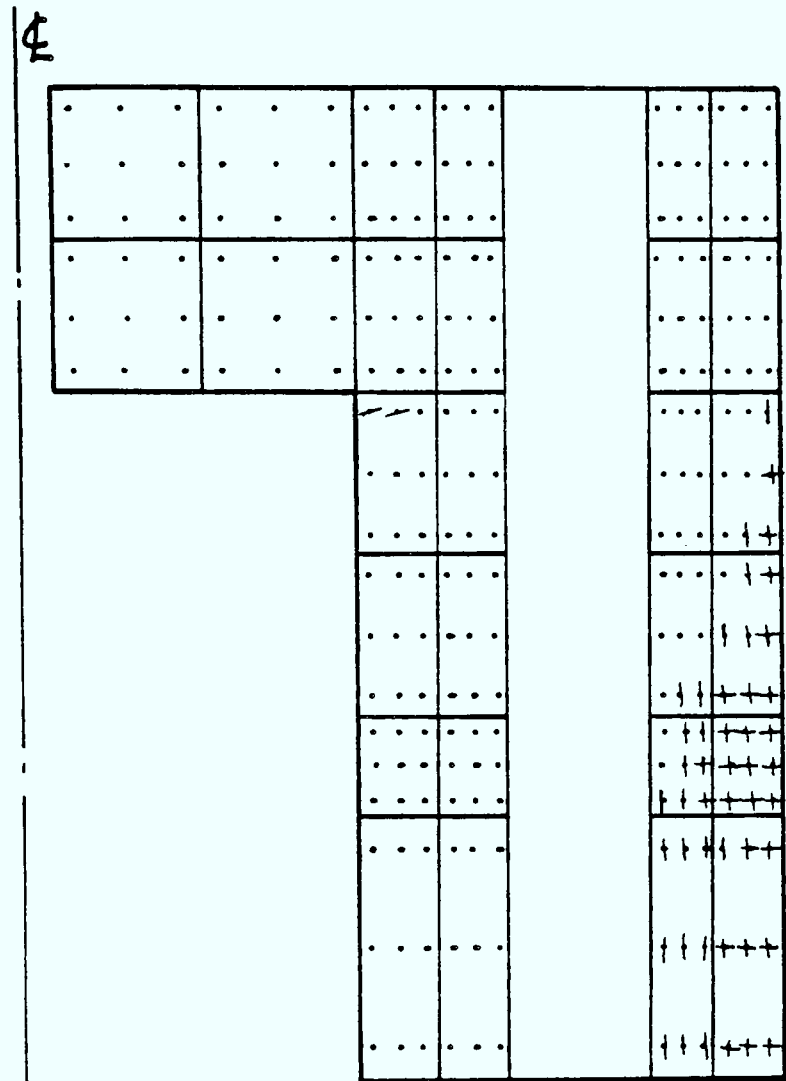


Vessel Scale

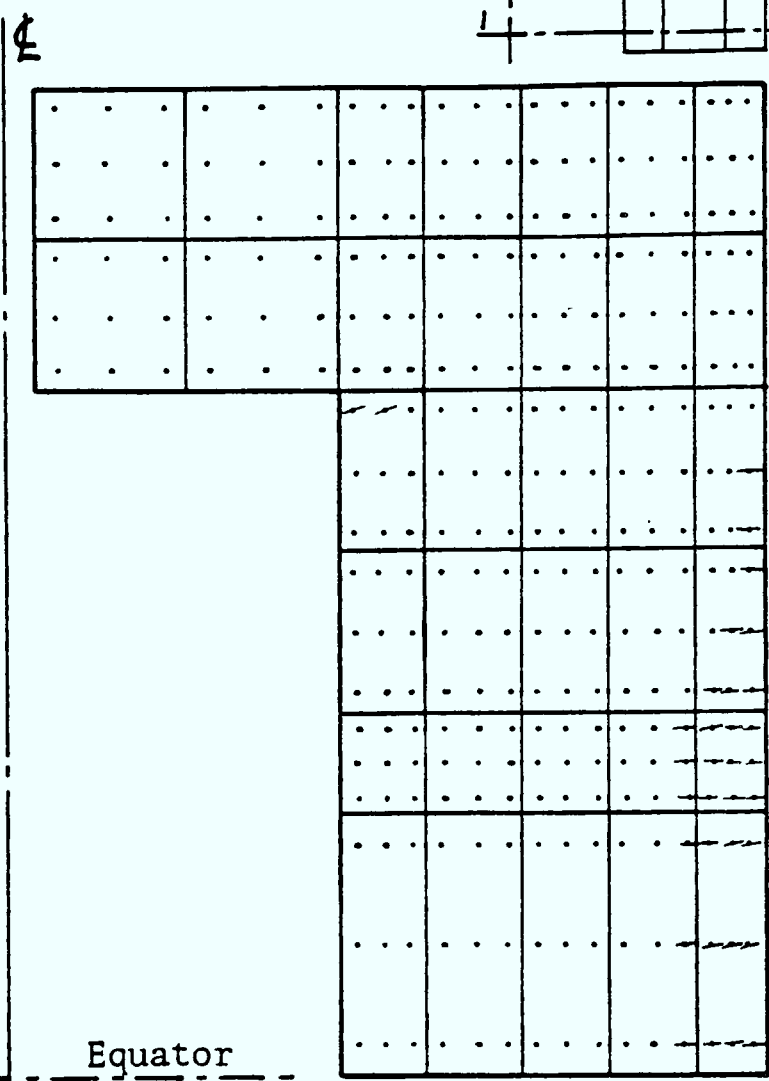


Symbols

- Horizontal Crack
- Radial Crack
- Inclined Crack
- Radial and Horizontal Cracks
- Uncracked Gauss Point
-

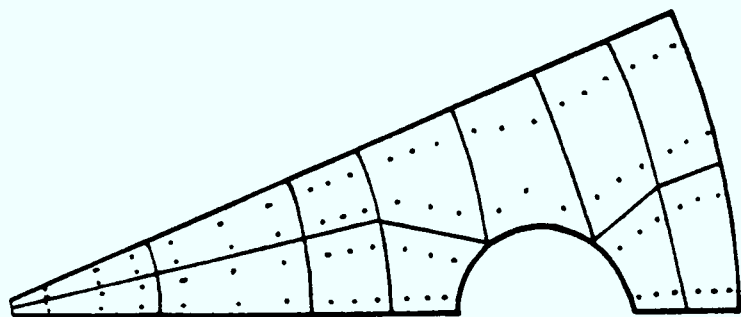


Section at AA

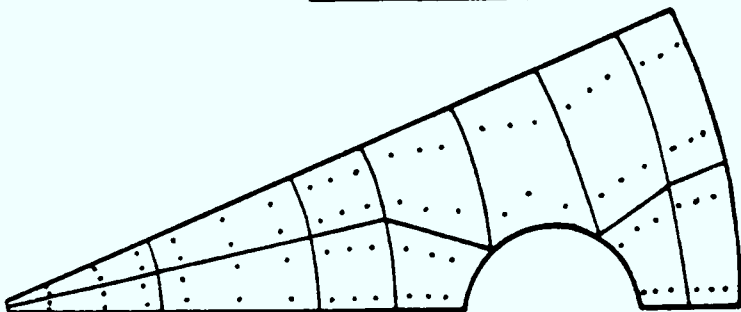


Section at BB

Equator

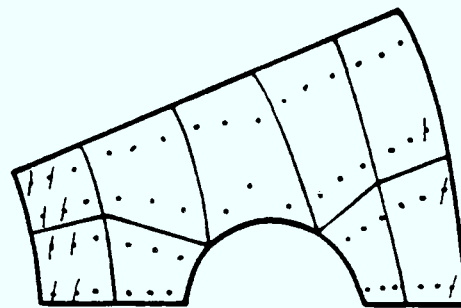


Level 18-18

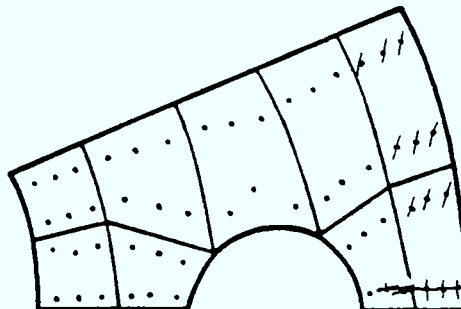


Level 13-13

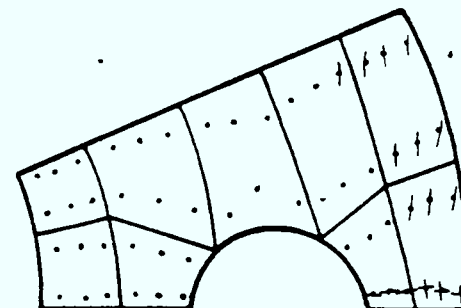
Level 12-12



Level 7-7



Level 1-1



Vessel Type -Bonded(10 Years Load)

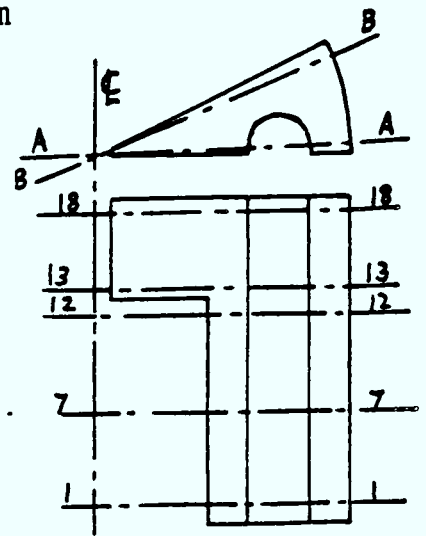
Pressure = 13.064 N/mm²

Figure 8.44 Crack Pattern of the Vessel at Load Factor 2.3

0 2 4 6 m

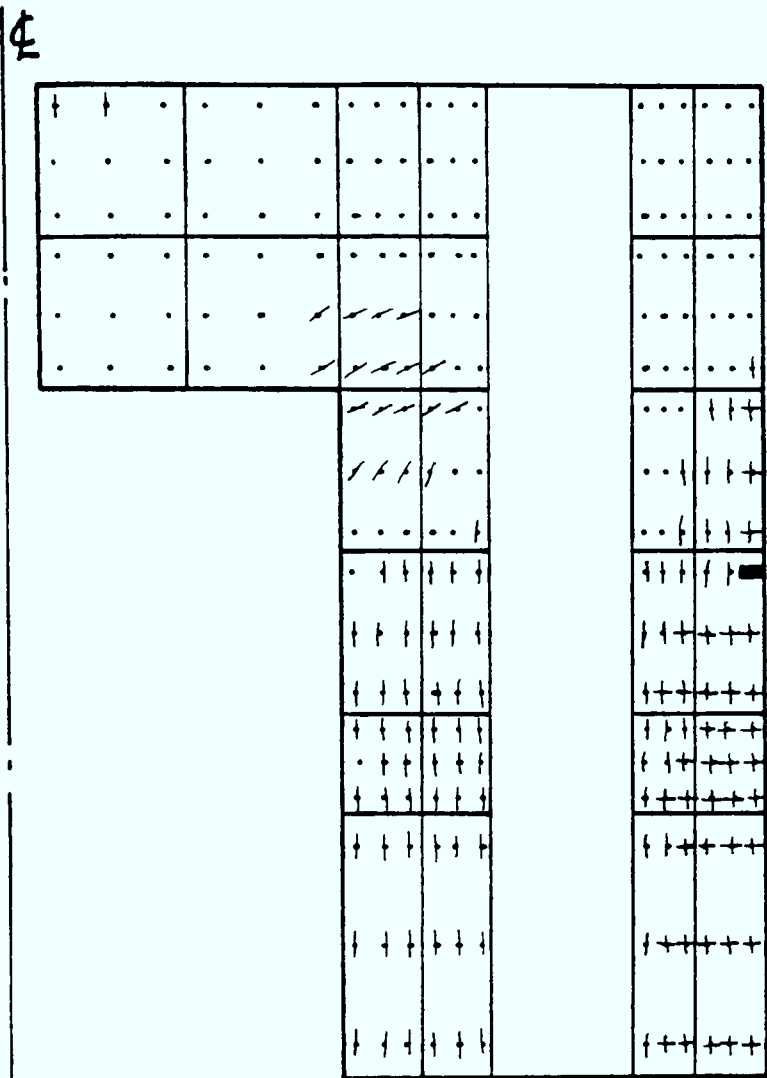


Vessel Scale

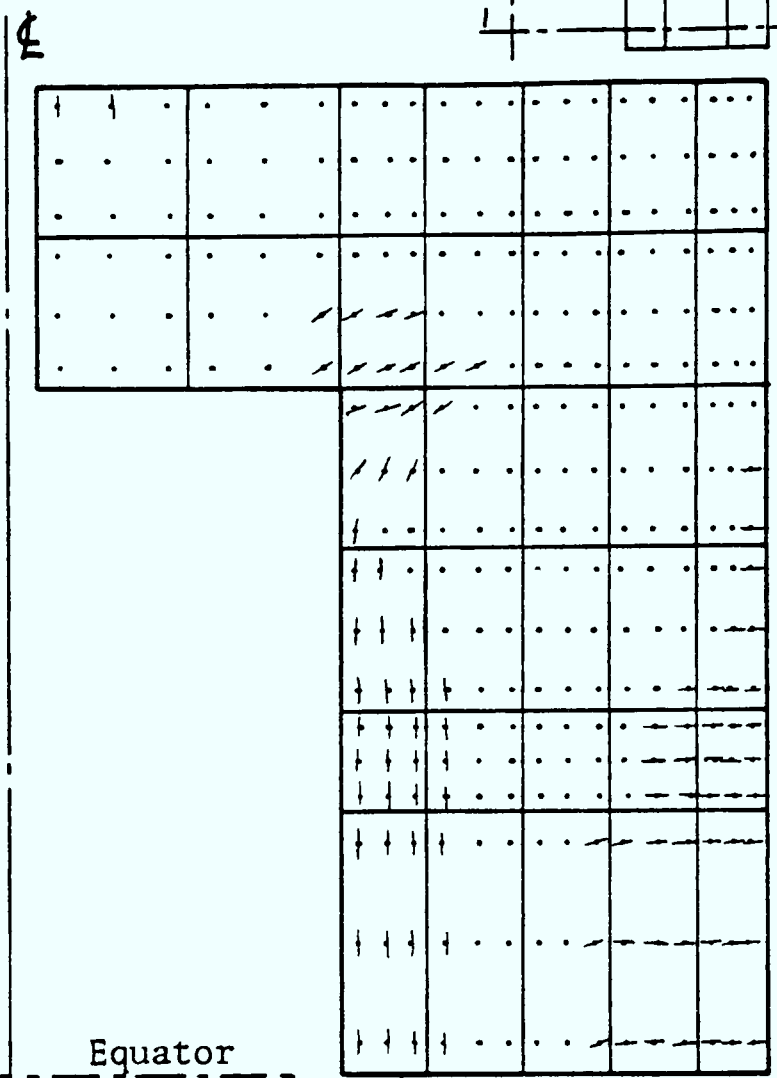


Symbols

- Horizontal Crack
- Radial Crack
- Inclined Crack
- Radial and Horizontal Cracks
- Uncracked Gauss Point
- Three Cracks

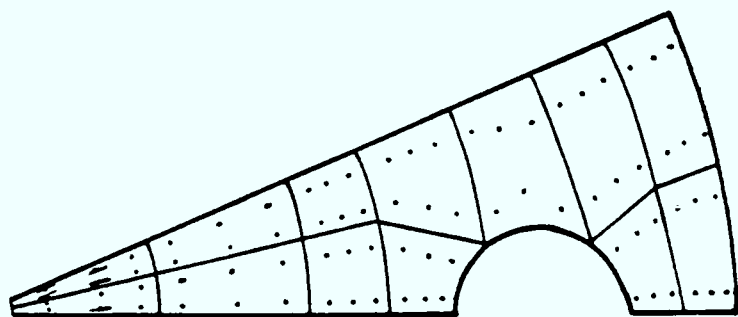


Section at AA



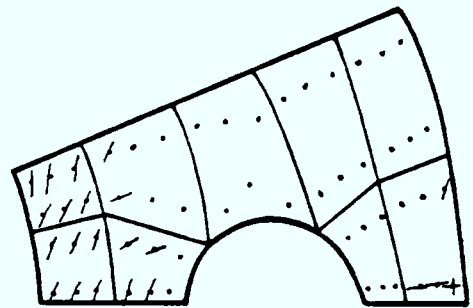
Section at BB

Equator

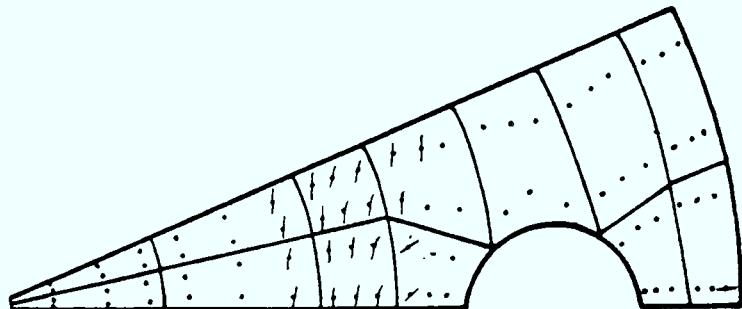
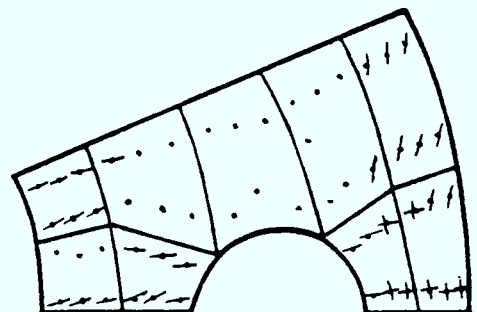


Level 18-18

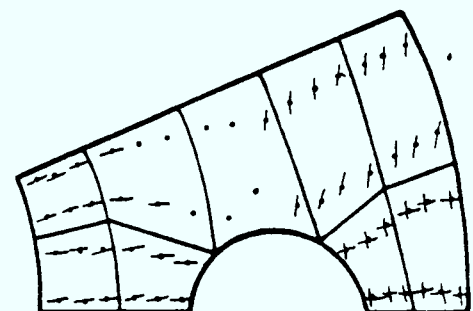
Level 12-12



Level 7-7



Level 13-13









Vessel Type - Bonded(10 Years Load) Level 1-1

Pressure = 17.04 N/mm²

Figure 8.44a Crack Pattern of the Vessel at Load Factor 3.0

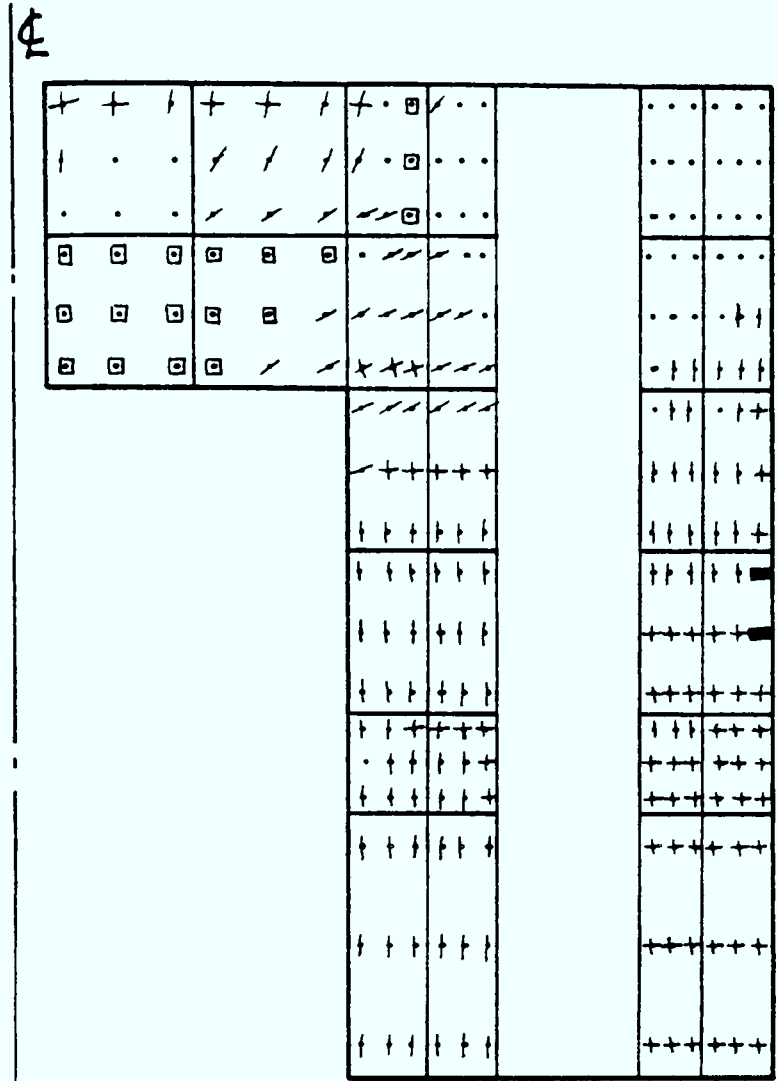
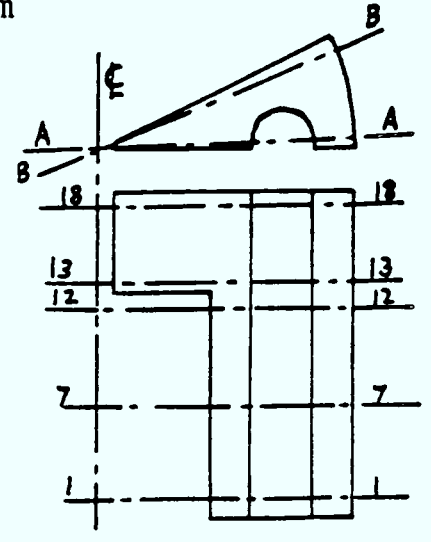
Symbols

-  Horizontal Crack
-  Radial Crack
-  Inclined Crack
-  Radial and Horizontal Cracks
-  Three Cracks
-  Compression Failure (crushing)

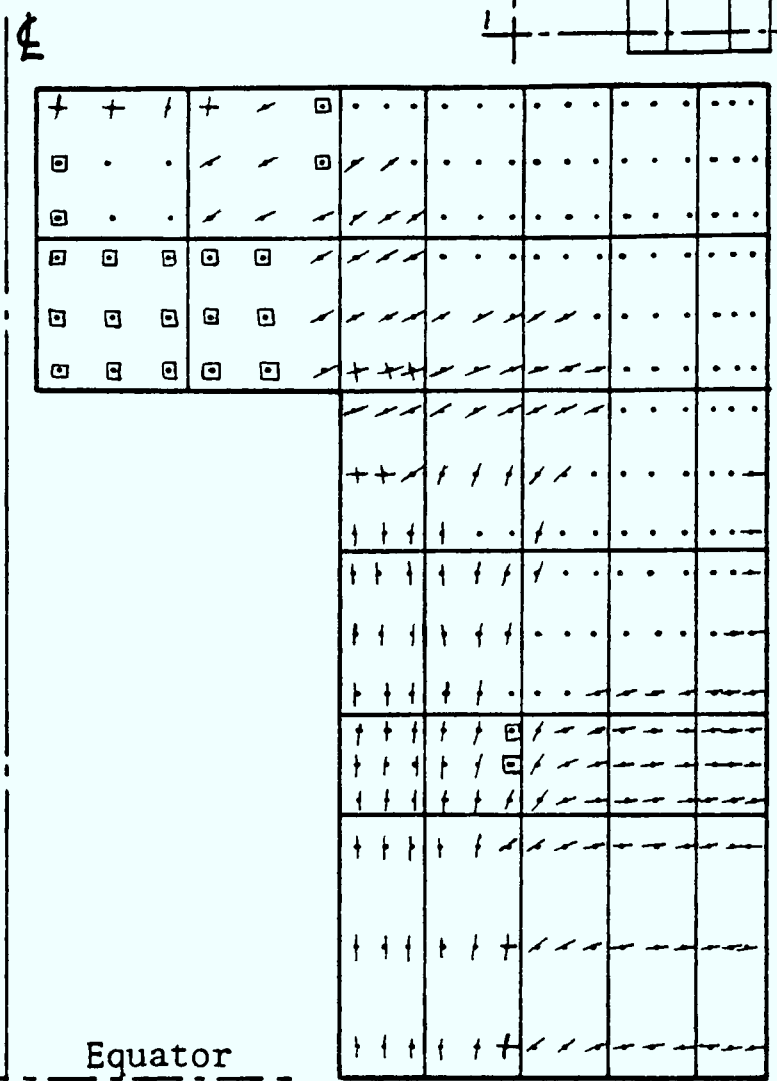
0 2 4 6 m



Vessel Scale

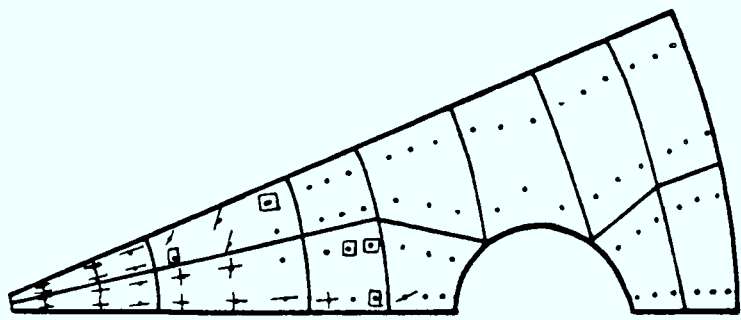


Section at AA



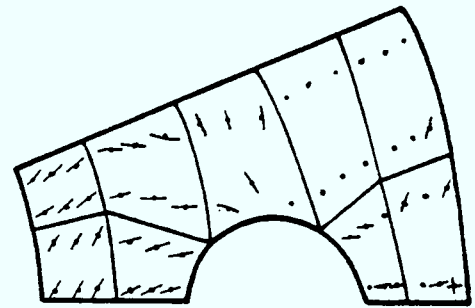
Equator

Section at BB

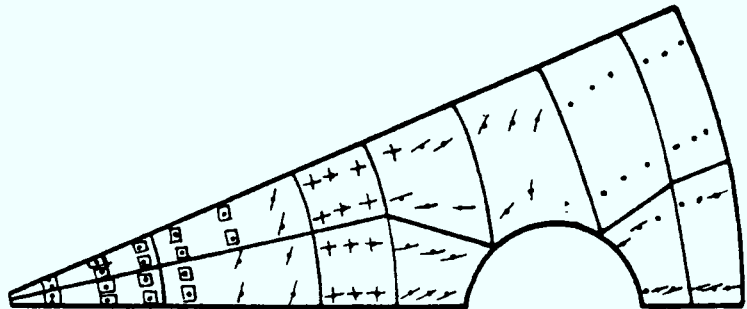


Level 18-18

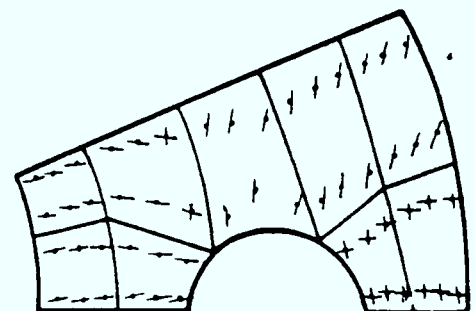
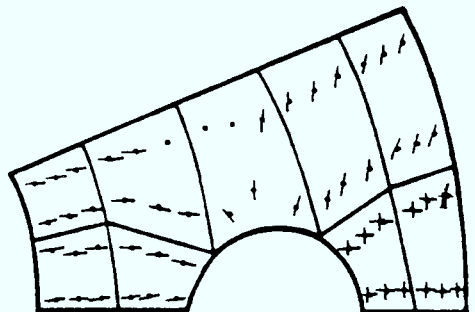
Level 12-12



Level 7-7



Level 13-13

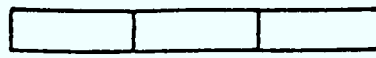


Vessel Type - Bonded (10 Years Load) Level 1-1

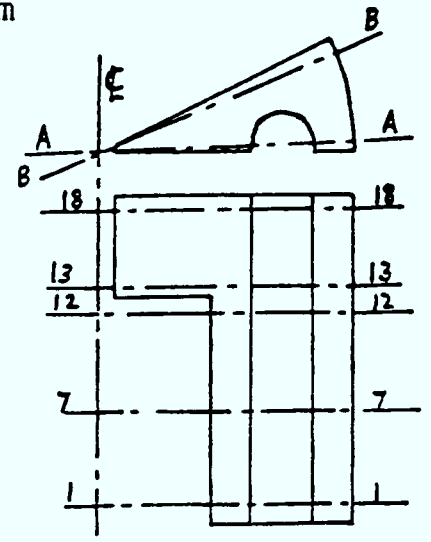
Pressure = 19.88 N/mm²

Figure 8.44b Crack Pattern of the Vessel at Load Factor 3.5

0 2 4 6 m

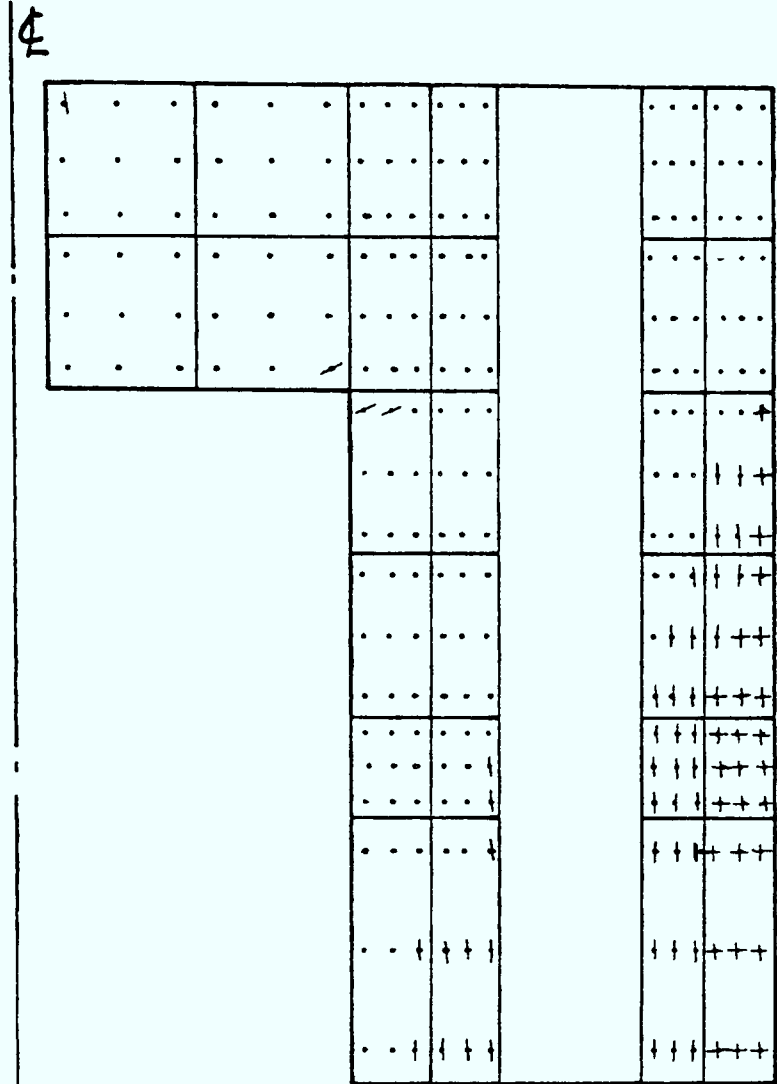


Vessel Scale

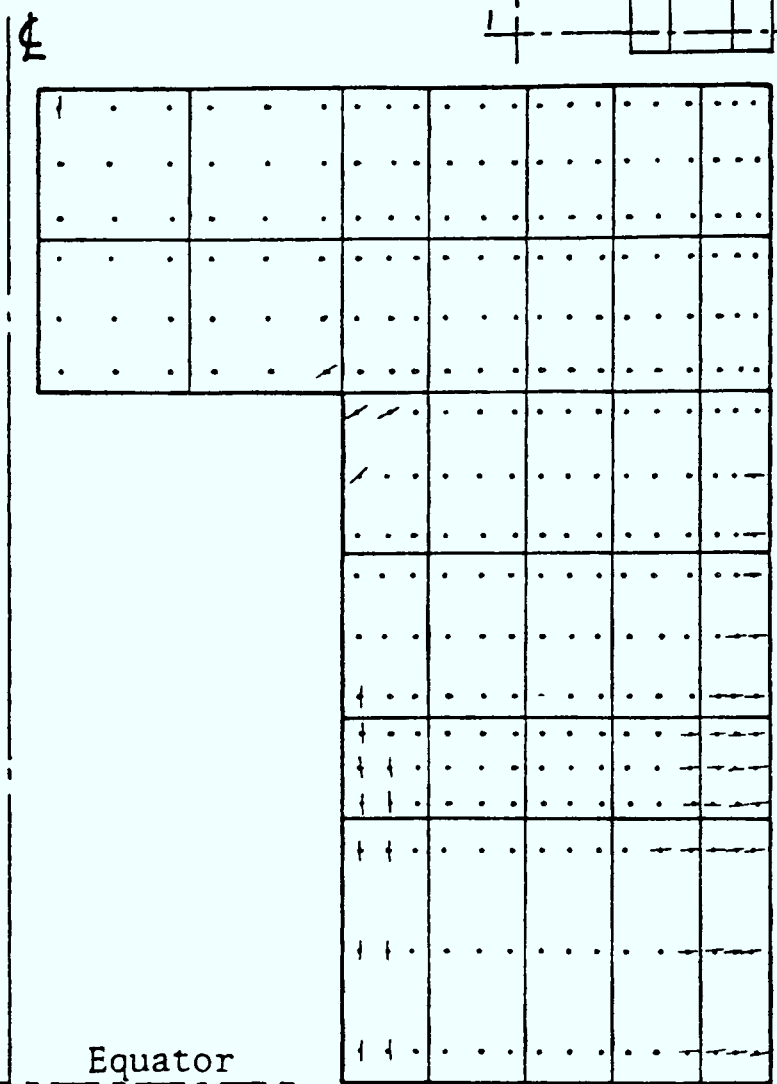


Symbols

- Horizontal Crack
- Radial Crack
- Inclined Crack
- Radial and Horizontal Cracks
- Uncracked Gauss Point
-

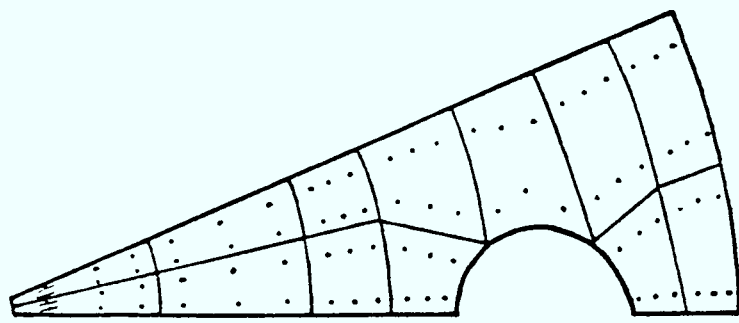


Section at AA



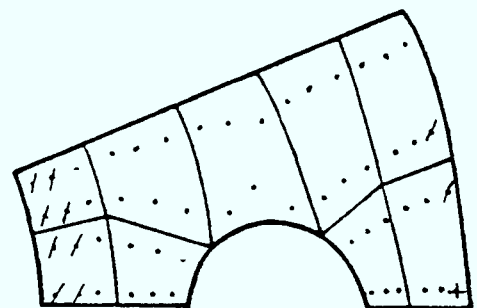
Equator

Section at BB

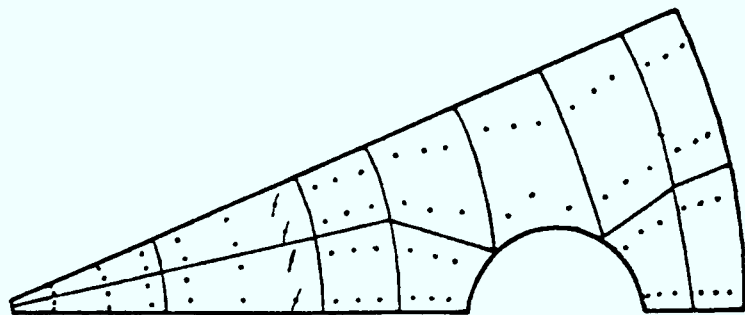
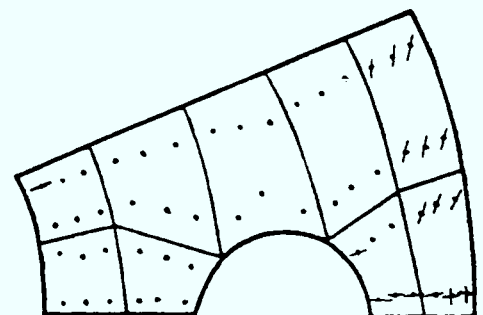


Level 18-18

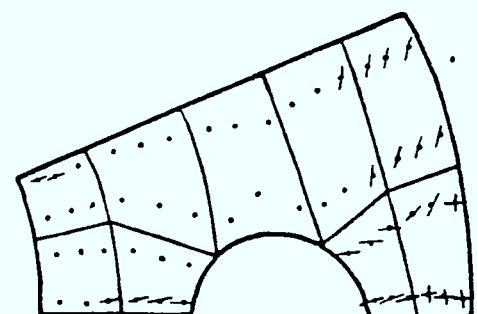
Level 12-12



Level 7-7



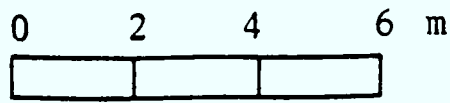
Level 13-13



Vessel Type - Bonded (20 years Load) Level 1-1

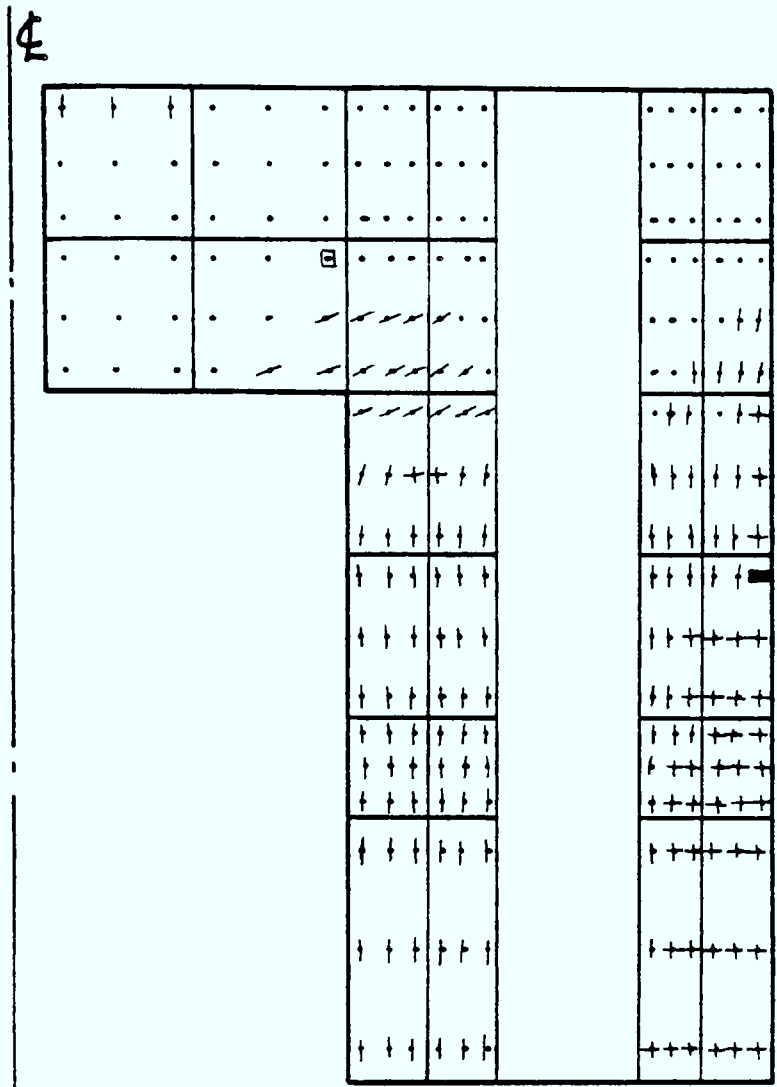
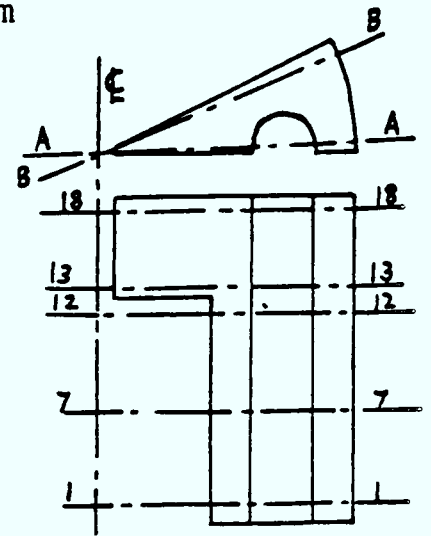
Pressure = 13.064 N/mm²

Figure 8.45 Crack Pattern of the Vessel at Load Factor 2.3

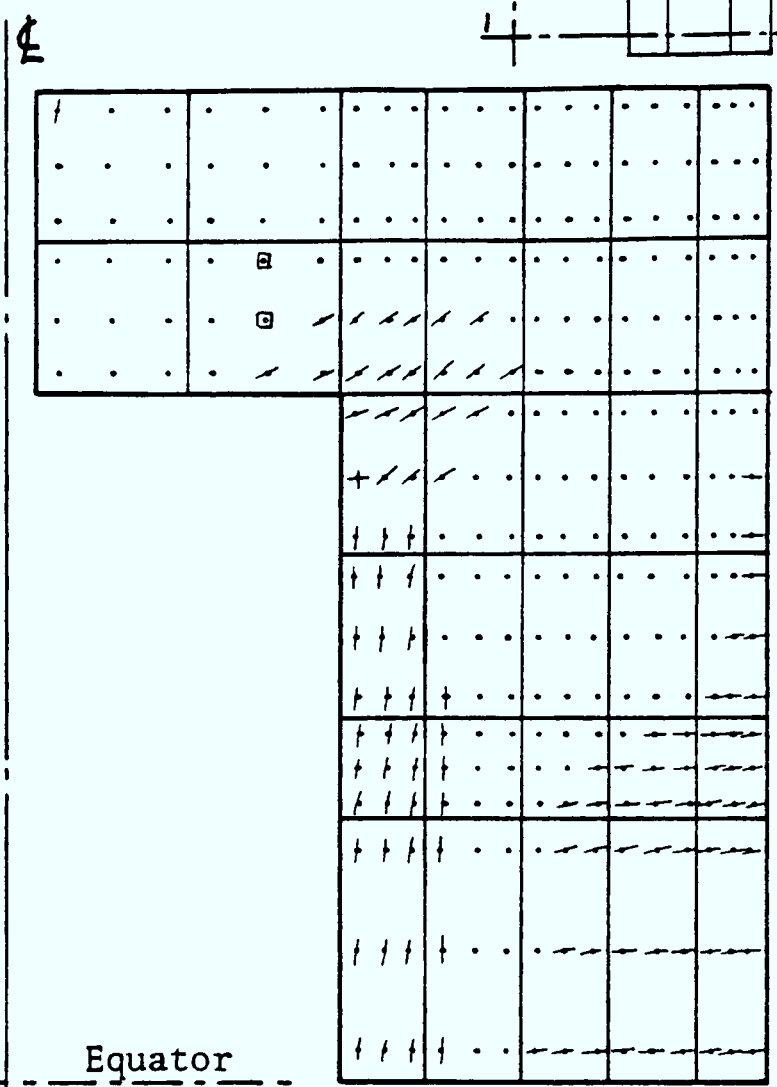


Symbols

- Horizontal Crack
- Radial Crack
- Inclined Crack
- Radial and Horizontal Cracks
- Three Cracks
- Failure in Compression (Crushing)

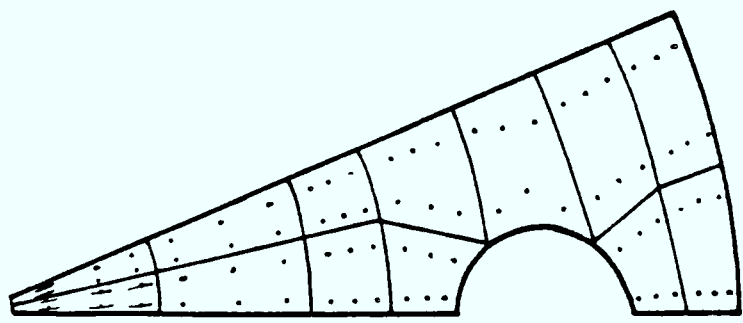


Section at AA



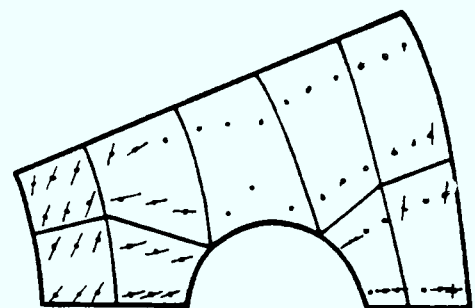
Equator

Section at BB

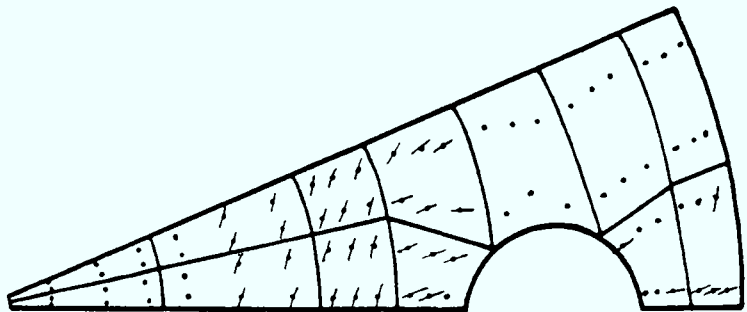


Level 18-18

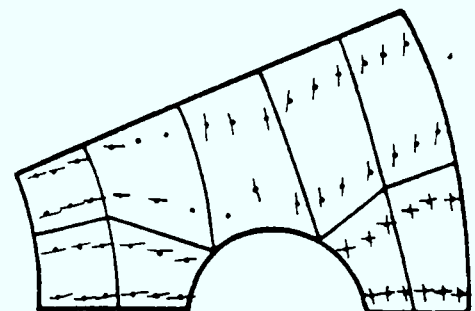
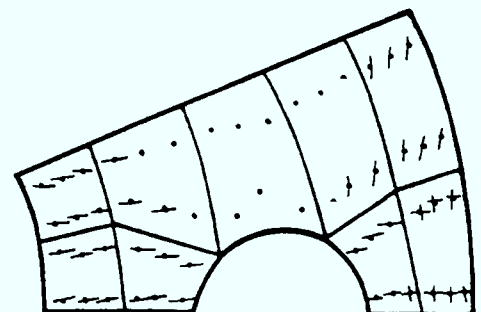
Level 12-12



Level 7-7



Level 13-13



Vessel Type - Bonded (20 Years Load) Level 1-1

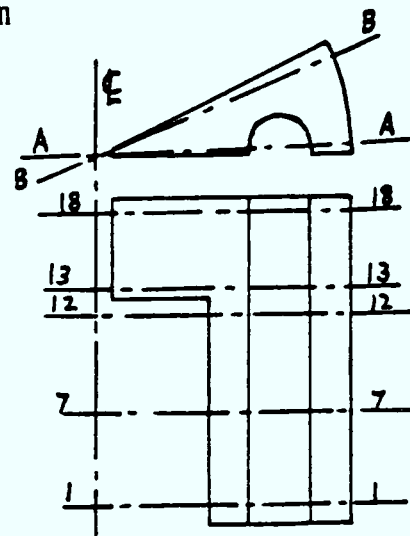
Pressure = 17.04 N/mm²

Figure 8.45a Crack Pattern of the Vessel at Load Factor 3.0

0 2 4 6 m

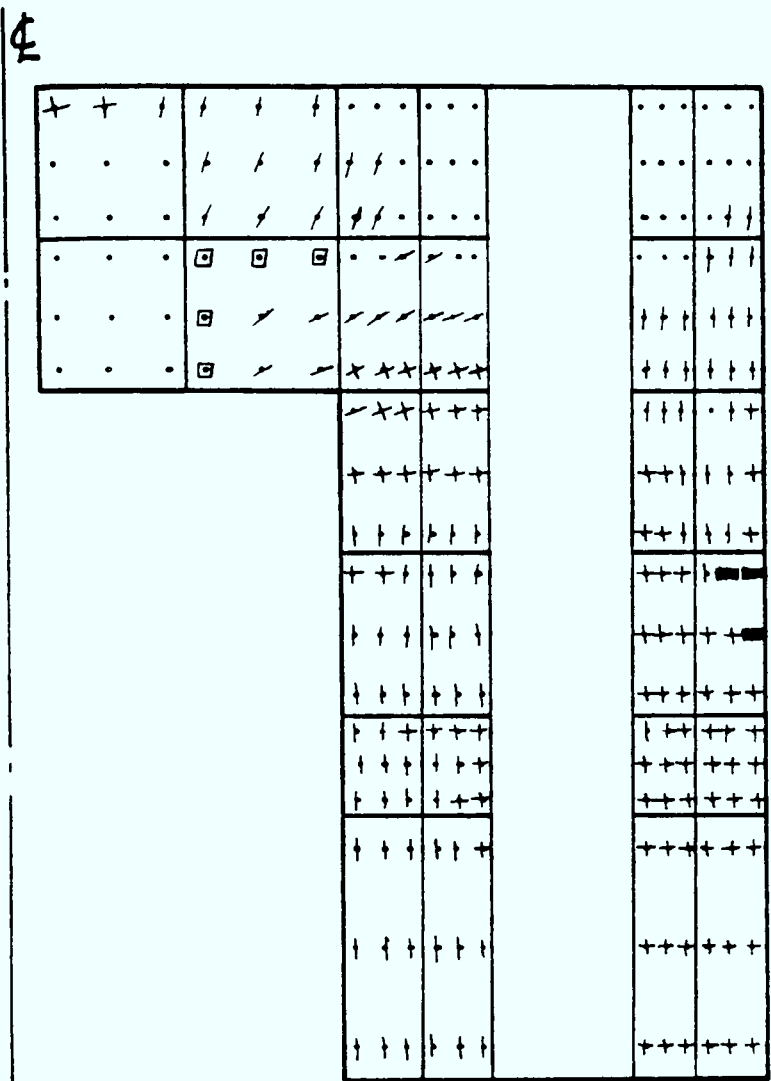


Vessel Scale

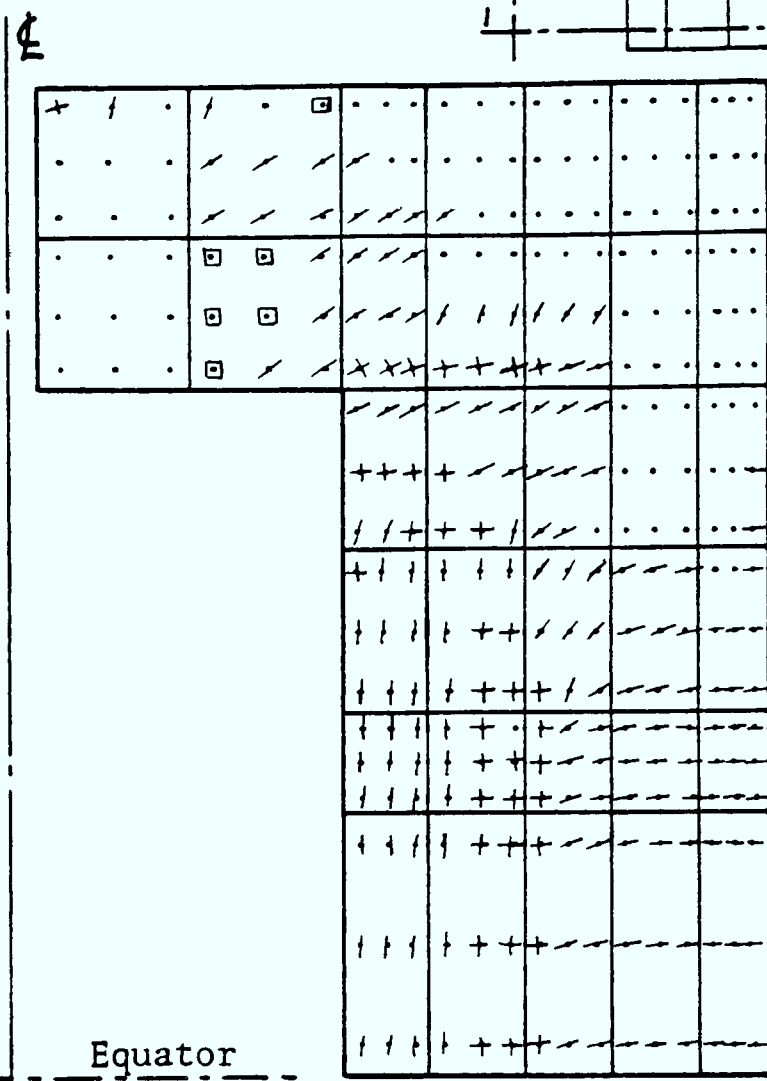


Symbols

- Horizontal Crack
- Radial Crack
- Inclined Crack
- Radial and Horizontal Cracks
- Three Cracks
- Compression Failure (crushing)

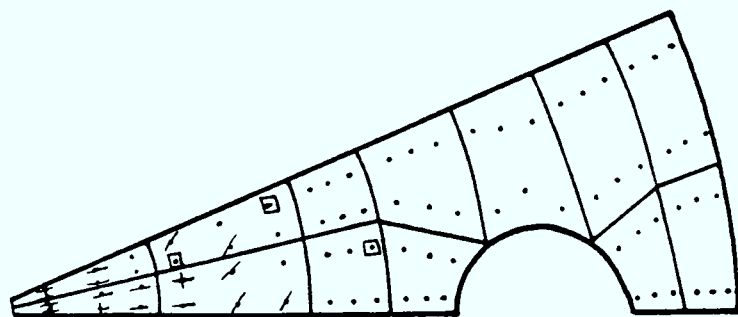


Section at AA



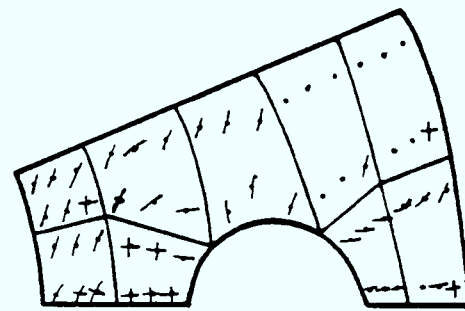
Equator

Section at BB

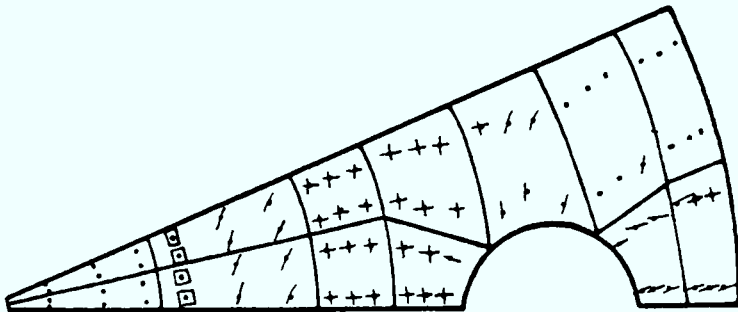


Level 18-18

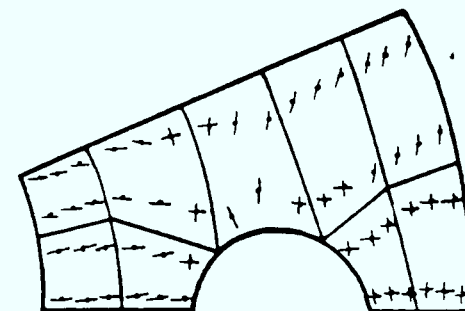
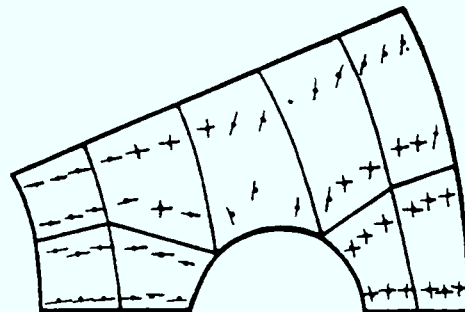
Level 12-12



Level 7-7



Level 13-13

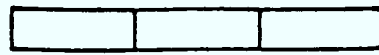


Vessel Type - Bonded (20 Years Load); Level 1-1

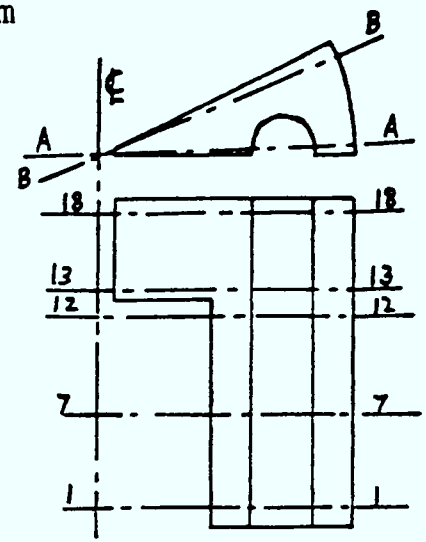
Pressure = 19.88 N/mm²

Figure 8.45b Crack Pattern of the Vessel at Load Factor 3.5

0 2 4 6 m

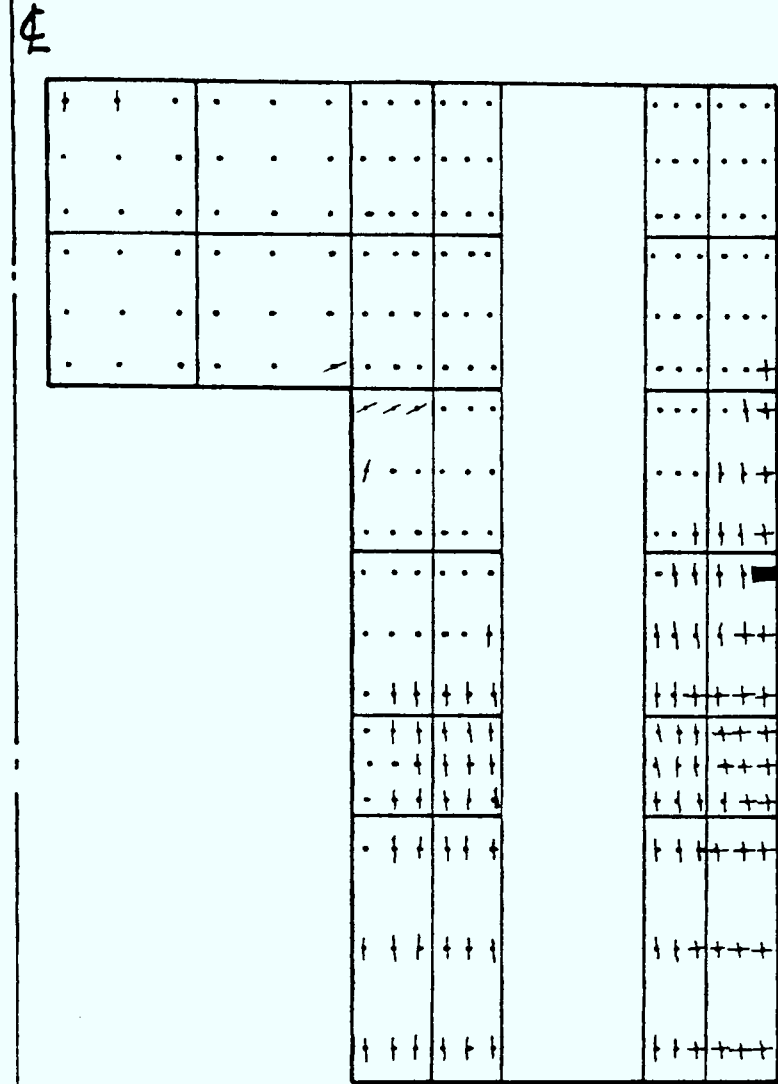


Vessel Scale

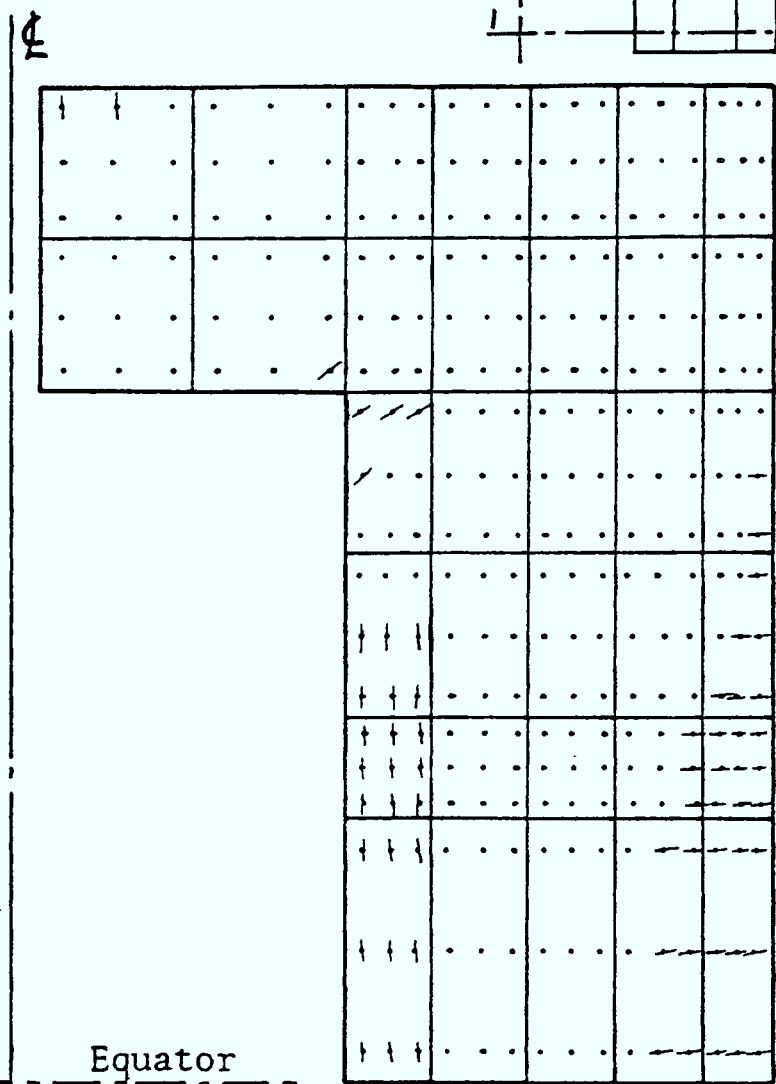


Symbols

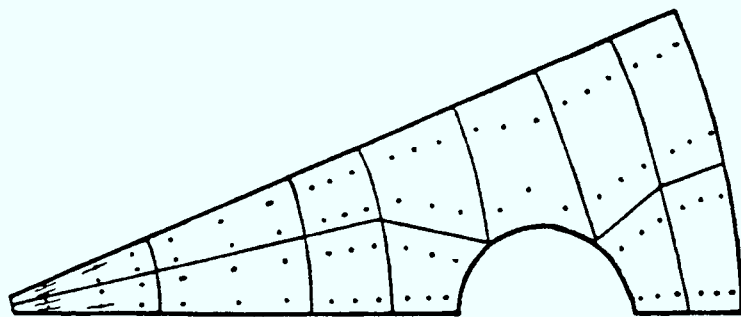
- Horizontal Crack
- Radial Crack
- Inclined Crack
- Radial and Horizontal Cracks
- Three Cracks
-



Section at AA

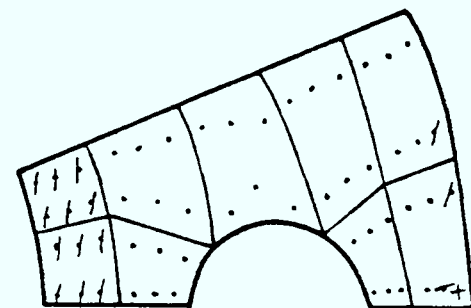


Section at BB

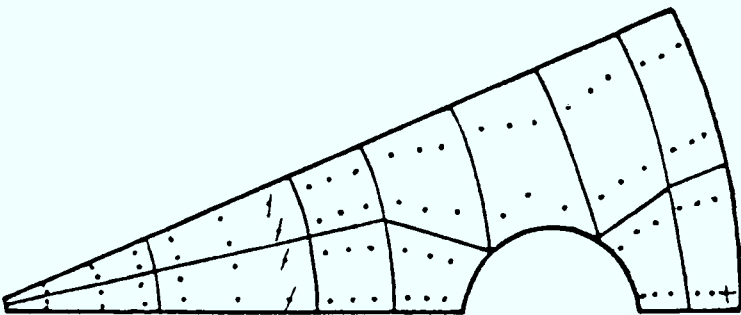


Level 18-18

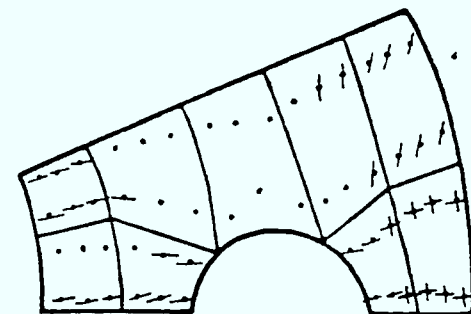
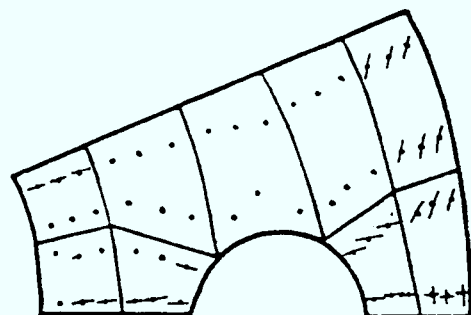
Level 12-12



Level 7-7



Level 13-13









Vessel Type - Bonded (30 Years Load) Level 1-1

Pressure = 13.064 N/mm²

Figure 8.46 Crack Pattern of the Vessel at Load Factor 2.3

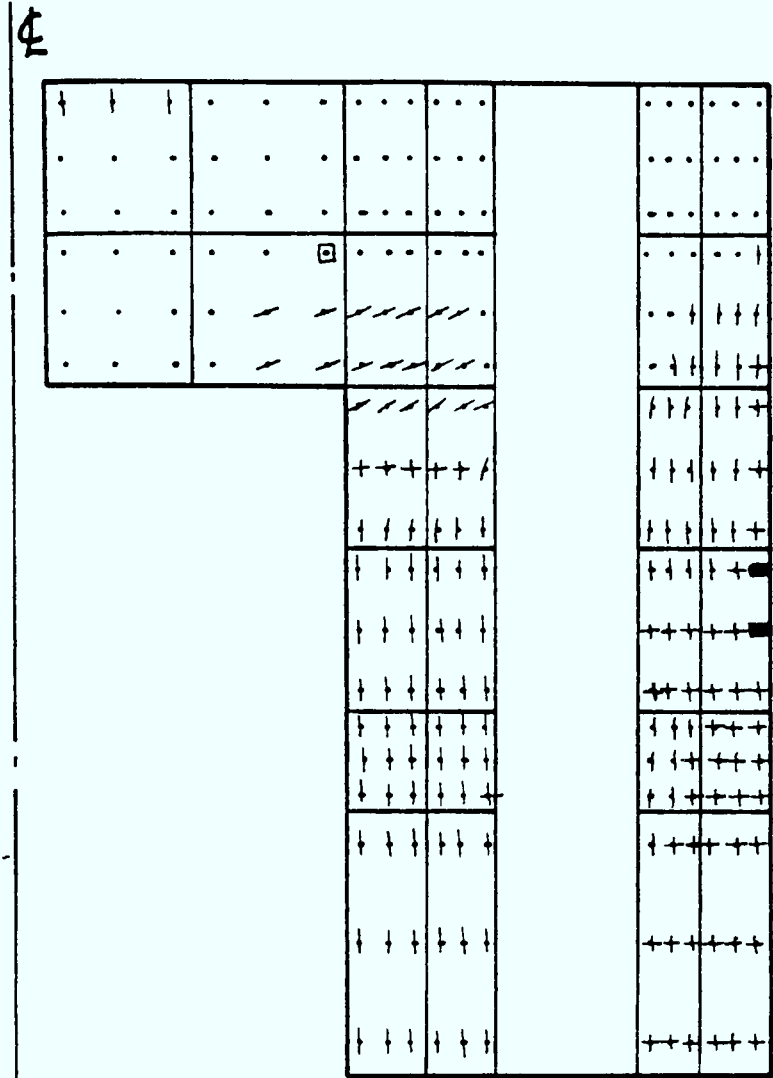
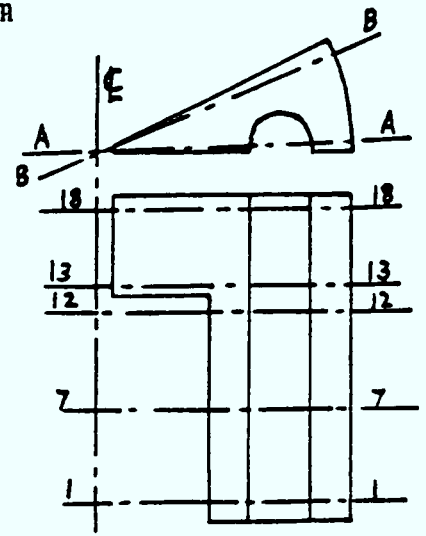
Symbols

-  Horizontal Crack
-  Radial Crack
-  Inclined Crack
-  Radial and Horizontal Cracks
-  Three Cracks
-  Compression Failure (crushing)

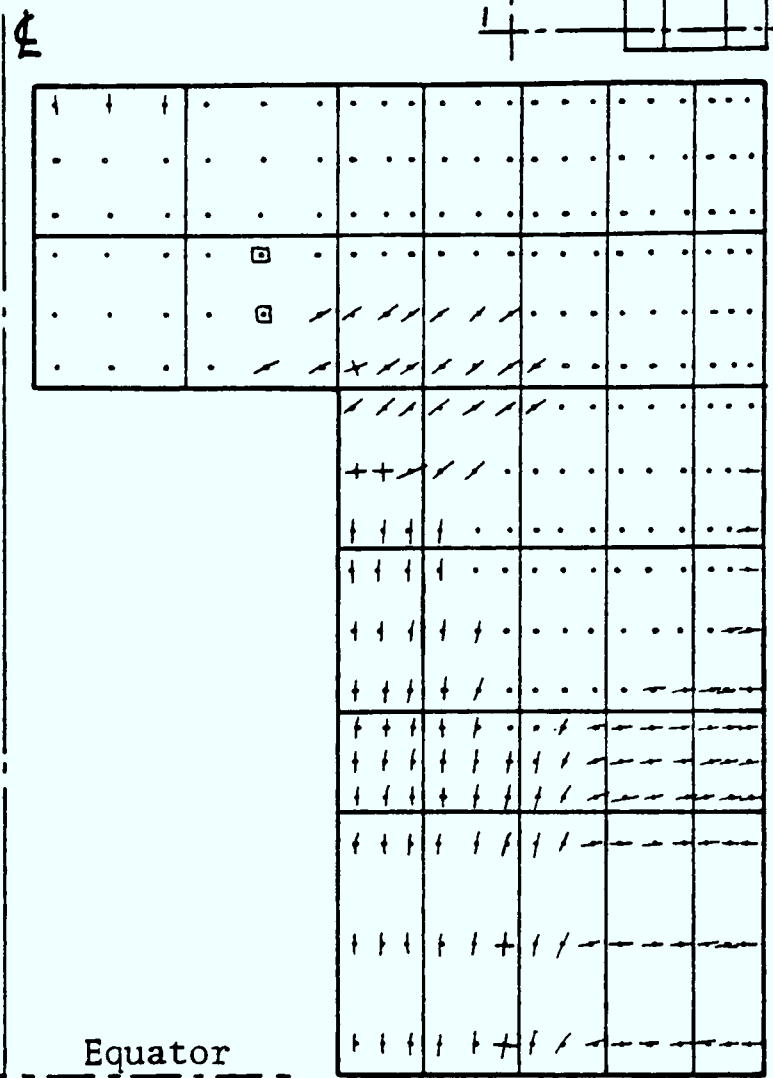
0 2 4 6 m



Vessel Scale

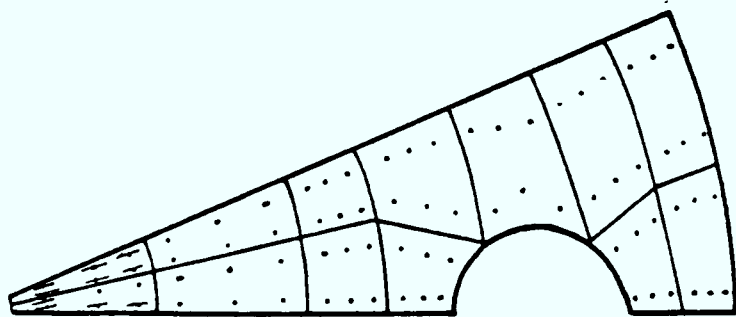


Section at AA



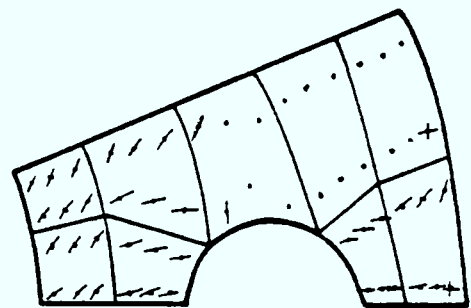
Equator

Section at BB

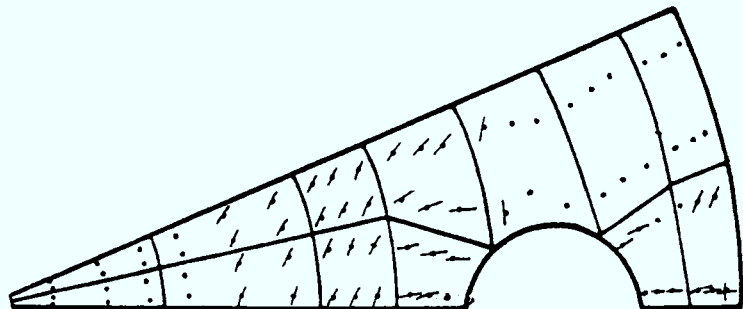


Level 18-18

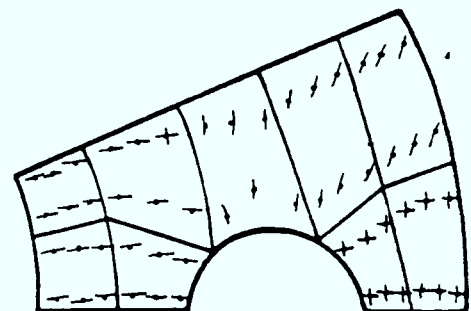
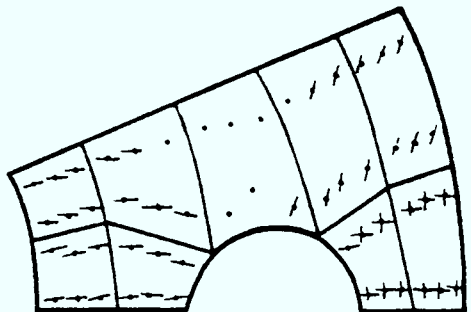
Level 12-12



Level 7-7



Level 13-13

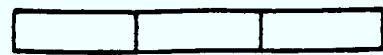


Vessel Type -Bonded(30 Years Load) Level 1-1

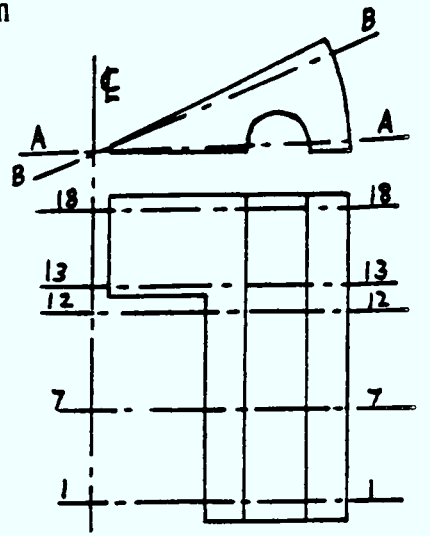
Pressure = 17.04 N/mm²

Figure 8.46a Crack Pattern of the Vessel at Load Factor 3.0

0 2 4 6 m

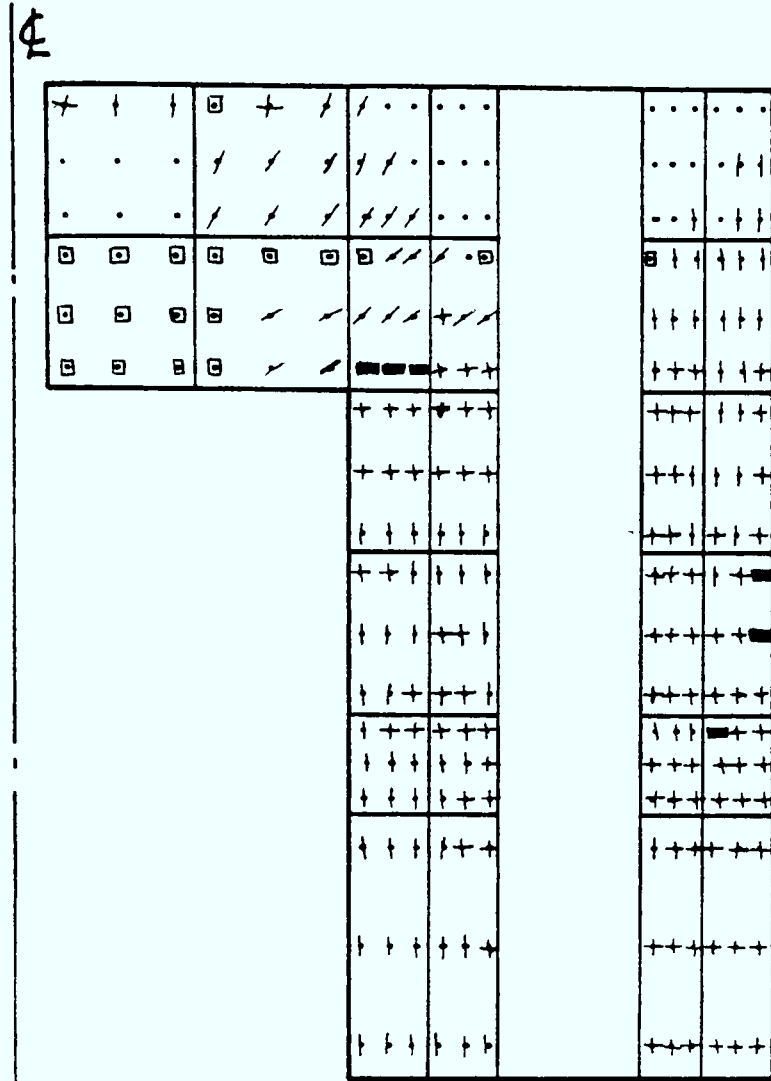


Vessel Scale

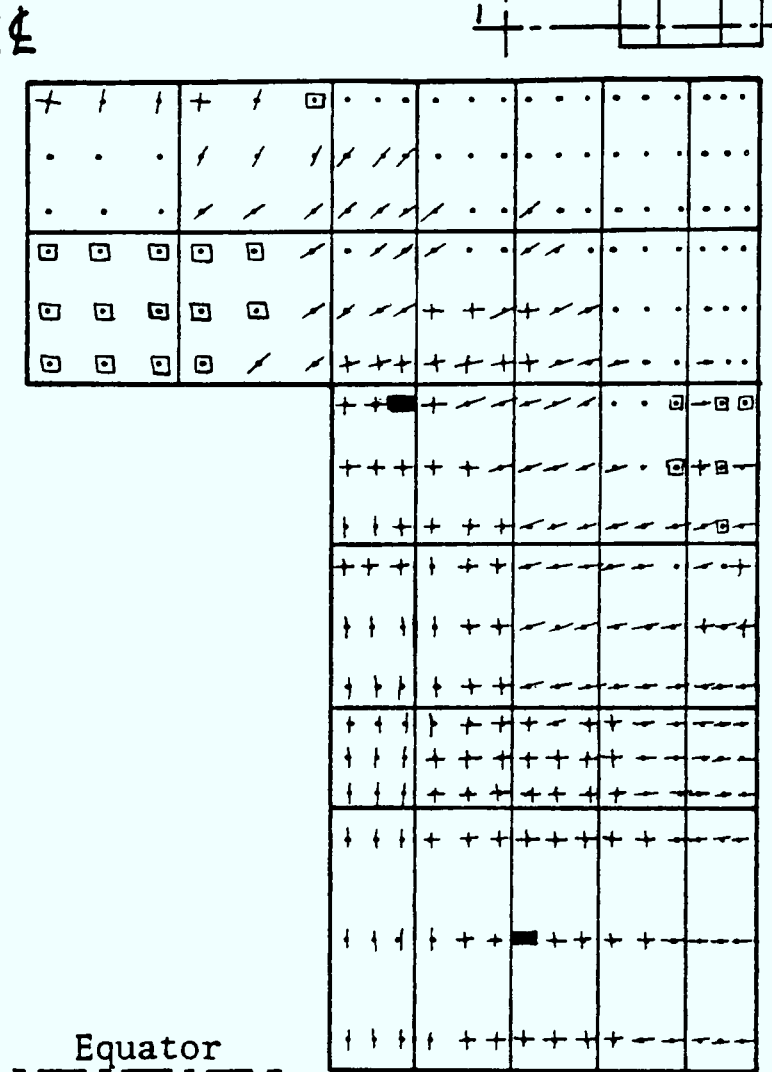


Symbols

- Horizontal Crack
- Radial Crack
- Inclined Crack
- Radial and Horizontal Cracks
- Three Cracks
- Compression failure (crushing)

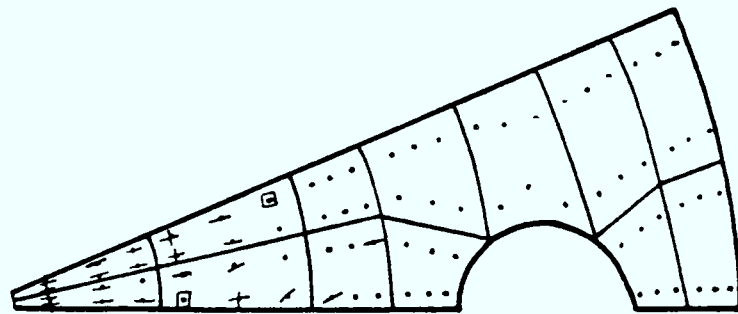


Section at AA



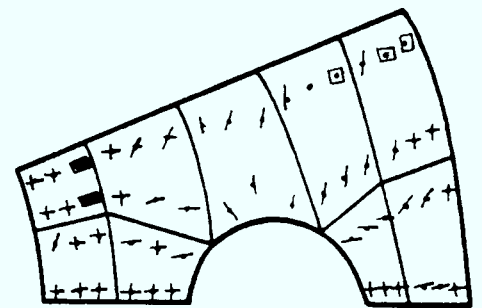
Equator

Section at BB

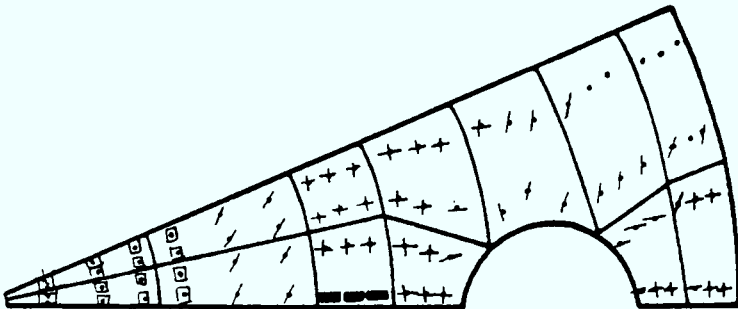


Level 18-18

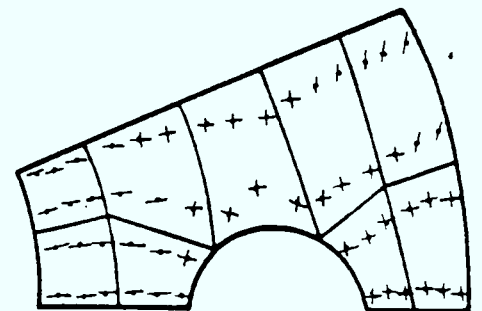
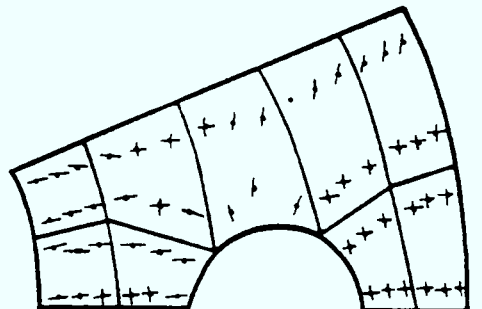
Level 12-12



Level 7-7



Level 13-13



Vessel Type - Bonded (30 Years Load), Level 1-1

Pressure = 19.88 N/mm²

Figure 8.46b Crack Pattern of the Vessel at Load Factor 3.5

CHAPTER 9

Conclusions and Recommendations

9.1. Conclusions

A generalised three-dimensional finite element analysis is presented for the time dependent non-linear behaviour of complex structures such as prestressed concrete reactor vessels. The analytical model has been successfully applied on bonded prestressed concrete slab and bonded reactor vessel.

The constitutive laws of concrete, steel and bond have been developed in this research. These constitutive laws can easily be applied to model any prestressed and reinforced concrete structures with reasonable accuracy. In addition, the constitutive laws of concrete have been extended to include creep. In the proposed analytical model the bond-slip behaviour is considered at the steel-concrete interface. However, this model is flexible enough to analyse concrete structures based on the concept of 'perfect bond' (rigid link) between the steel and the concrete.

Various non-linear solution techniques have been implemented in the finite element computer program NSARVE. Among them, the constant stiffness method (initial stress method), because of numerical stability, has shown to be suitable for the analysis of concrete vessels up to failure.

Two types of experiments have been performed. The first one is to establish a bond-slip behaviour of prestressing wires and also to obtain bond coefficients for program NSARVE as an input. The second experiment is to examine the behaviour of a bonded slab and also to validate results obtained from the analytical model. The experimental study of bond slip specimens indicates that the bond stress increases initially with a very small slip and the bond-slip relationship is

non-linear up to the maximum bond stress. The maximum bond stress reaches at a slip varying from 0.019 mm to 0.065 mm in various specimens. Beyond this, the bond stress is almost constant and is equal to its maximum value. At some stages, a scatter in the results is found. An average value of maximum bond stress 1.92 N/mm^2 and an average slip modulus of $501.5 \text{ N/mm}^2/\text{mm}$ are obtained from all the tests. Results obtained from the octagonal prestressed concrete slab shows that the load-deflection curve at the centre of the slab is linear up to 160 KN (0.064 N/mm^2) and after that it becomes non-linear due to extensive cracking. The slab finally failed at a load of 544 KN (0.218 N/mm^2). The deflected slopes along the two centre lines of the slab show that the slab failed in flexure.

A comparative study of results shows that the bonded prestressed concrete slab behaved exactly as was predicted by the analysis. The analytical ultimate load is 2.2% lower than the experimental failure load. The predicted ultimate load of bonded slab using Ahmlink elements is 1.4% lower than that using a perfect bond. A study of the slab using purely incremental method (no iterations) predicts the ultimate load 11% higher than the experimental failure load. This method is approximate and always overestimates the loads.

Various cases of vessel analyses with bonded and unbonded tendons suggest that the load carrying capacity of bonded vessel is always higher than a similar unbonded vessel. A margin of safety against failure (load factor) of 3.5 is found for the bonded vessel, while this factor is 3.3 for unbonded vessel. Therefore a difference in the margin of safety is by 6%. This suggests a very small increase in the overall load carrying capacity of the bonded vessel, as opposed to the unbonded vessel. Comparing crack patterns, load-displacement curves and deflected shapes of these two types of vessels, they indicate that the unbonded vessel is much more damaged than the bonded vessel. Even at early stages of cracking, the damage to the unbonded vessel is more in the form of ill-disposed cracking at critical zones. This suggests that in comparison with the bonded vessel, early localised cracking at lower gas pressures in unbonded vessels may cause nuclear hazards. The bonded vessel is also analysed assuming a perfect bond between the tendon and the vessel concrete, the margin

of safety for this case being 3.6, an increase of 3% on the vessel when analysed with Ahmlink elements. This is due to the fact that in perfectly bonded vessel, no slip is allowed between tendons and concrete.

Three cases of vessel analyses (Ahmlink bonded, perfectly bonded and unbonded) are also performed for 40 years of creep at normal operational conditions. The difference in results is negligible. The analyses show a considerable redistribution (relaxation) of stresses owing to the non-uniform temperature distribution through the wall and the cap. A steady state condition is reached after 10 years of creep.

After obtaining confidence by examining various results, the bonded vessel is then investigated for ultimate conditions at various stages of its life. The times chosen for the ultimate load conditions are 1-5 years, 10 years, 20 years and 30 years. The results suggest that the overall performance of 1-5 years old vessel is better than the vessel loaded at other ages. A detailed study indicates severe damage in older vessels and their deflections at failure are much too large as opposed to 1-5 year old vessel. It is also found that the failure of the 1-5 year old vessel occurred due to excessive displacement of the top cap, while the failure of the 30 year old vessel is due to excessive displacement of the wall.

It is concluded that greater faith can be put into the more reliable performance of prestressed concrete pressure vessels when tendons are bonded.

9.2. Recommendations

A numerical analysis will only predict a true non-linear behaviour provided material constitutive laws are well established. Many more experiments are needed to obtain correct material properties under variable conditions of stress and temperature.

Analytical model can be improved if more information on bond-slip behaviour is available. More sophisticated experiments are needed on large post-tensioned tendons for local bond-slip relations. Such experimental results on large post-tensioned tendons will produce even better results for vessels using the proposed analytical model. In the current analysis, the large tendons have been simulated using the data from small wires and strands.

Very little work is done on the multi-axial behaviour of concrete under cyclic and impact loads. Material laws under these loading conditions are essentially required to analyse the next generation of vessels namely the containment vessels for pressurised water reactors. This analytical model can be extended to include the effects of the following :

- (a) The impact and damage (perforation and scabbing) caused by wind generated missiles and aircraft crashes on containment vessels.
- (b) The seismic loads on and response of the containment vessels when cracked and uncracked.
- (c) The pressure and containment vessel foundation soil-structure interaction.
- (d) The loss of coolant accident within the reactor containment vessel.

REFERENCES

1. Cook, R.D. : Concepts and Applications of Finite Element Analysis.
Second edition, John Wiley and Sons, 1981.
2. Zienkiewicz, O.C. : The Finite Element in Engineering Science.
McGraw-Hill, London, 1977.
3. Martin, H.C. and Carrey, G.F. : Introduction to Finite Element
Analysis. McGraw-Hill, New York, 1973.
4. Bathe, K.J. and Wilson, E.L. : Numerical Methods in Finite Element
Analysis. Prentice-Hall Inc., Englewood Cliffs, New Jersey, 1972.
5. Desai, C.S. and Abel, J.F. : Introduction to the Finite Element
Method. Von Strand Reinhold Co., New York, 1972.
6. Ahmad, S. : Curved Finite Element in the Analysis of Solid Shell and
Plate Structures. Ph.D. Thesis, University of Wales, Swansea, 1969.
7. Clough, R.W. : Comparison of Three-dimensional Finite Elements.
Proceedings of symposium on Application of Finite Element Methods
in Civil Engineering, Vanderbilt University, 1969.
8. Ngo, D. and Scorcelis, A.C. : Finite Element Analysis of Reinforced
Concrete Beams. ACI Journal, March 1967.
9. Nilson, A.H. : Non-linear Analysis of Reinforced Concrete by Finite
Element Method. ACI Journal, September 1968.
10. Argyris, J.H. et al : Recent Development in the Finite Element
Analysis of Prestressed Concrete Reactor Vessels. Second
International Conference on Reactor Technology, Berlin, September
1973.

- 10a. Argyris, J.H. et al : Limit Load Analysis of Thick-walled Concrete Structures - A Finite Element Approach to Fracture. Computer Methods in Applied Mechanics and Engineering, 8, (1976), pp 215-243.
11. Mohraz, B. et al : Crack Development in a Prestressed Concrete Reactor as Determined by Lumped Parameter Method. Nuclear Engineering and Design, November 1970.
12. Sozen, M.A. and Paul, S.L. : Structural Behaviour of Small Scale Prestressed Concrete Reactor Vessels. Nuclear Engineering Design, 1968, pp 403-414.
13. Campbell-Allen, D. and Low, E.W.E. : Pressure Tests on End Slabs for Prestressed Concrete Pressure Vessels. Nuclear Engineering Design, 6, 1967, pp 345-359.
14. Rashid, Y.R. : Ultimate Strength Analysis of Prestressed Concrete Pressure Vessels. Nuclear Engineering Design, 7, 1968.
15. Rashid, Y.R. : Analysis of Concrete Composite Structures by the Finite Element Method, Nuclear Engineering Design, 3, 1966.
16. Launay, P. and Gachon H. : Strain and Ultimate Strength of Concrete under Triaxial Stresses. ACI Publication SP-34, Concrete for Nuclear Reactors, 1972.
17. Connor, J.J. and Sarne, Y. : Non-linear Analysis of Prestressed Concrete Reactor Pressure Vessels. 3rd International Conference on Structural Mechanics in Reactor Technology (SMIRT), 1975, London, Paper H2/2.
18. Takeda, T., Yamaguchi, T. and Imoto, K. : Inelastic Analysis of Multi-cavity PCRV under Internal Pressure. 3rd SMIRT Conference, 1975, London, Paper H2/5.

19. Phillips, D.V. et al : Finite Element Methods in the Analysis of Reactor Vessels. Nuclear Engineering Design, 20, 1972.
20. Phillips, D.V., and Zienkiewicz, O.C. : Finite Element Non-linear Analysis of Concrete Structures. Proc. of Institute of Civil Engineers, Research and Theory, Vol. 61, Part 2, 1976.
21. Bangash, Y. : Discussion on Reference 20, Paper 7865, 1976.
- 21a. Bangash, Y. : Reactor Pressure Vessel Design and Practice. Progress in Nuclear Energy, Vol. 10, No. 1, pp 69-124, 1982.
- 21b. Bangash, Y. : The Automated Three-dimensional Cracking Analysis of Prestressed Concrete Vessels, 6th SMIRT Conference, Paris, August 1981, Paper H3/2.
22. Saugy, B. et al : Three-dimensional Rupture Analysis of a Prestressed Concrete Pressure Vessel including Creep Effects. 2nd SMIRT Conference, Berlin, 1973.
23. Khan, M.H. and Saugy, B. : Evaluation of the Influence of some Concrete Characteristics on Non-linear Behaviour of Prestressed Concrete Reactor Vessel. ACI Publication, SP-34, Concrete for Nuclear Reactors, 1972.
24. William, K.J. and Wanke, E.P. : Constitutive Model for Triaxial Behaviour of Concrete, IABSE Seminar on Concrete Structures subjected to Triaxial Stresses, Part III-1, Bergamo, Italy, May 1974.
25. Kupfer, H., Hilsdorf, H.K. and Ruch, H. : Behaviour of Concrete under Biaxial Stresses. ACI Journal, Vol. 66, no. 8, 1969, pp 556-566.
26. Kupfer, H. and Gerstle, K. : Behaviour of Concrete under Biaxial Stresses, Journal of Engineering Mechanics Division, ASCE, Vol. 99, EM4, Proc. Paper 9917, August 1973, pp 552-866.

27. Chen, A.C.T. and Chen, W.F. : Constitutive Relations for Concrete. Journal of Engineering Mechanics Division, ASCE, Vol. 101, no. EM4, Proc. paper 11529, August 1975, pp 465-481.
28. Chen, A.C.T. and Chen, W.F. : Constitutive Equations and Punch Indentation of Concrete. Journal of Engineering Mechanics Division, ASCE, Vol. 101, no. EM6, Proc. paper 11809, December 1975, pp 889-906.
29. Cedolin, L., Crutzen, Y.R.J. and Dei Foli, S. : Triaxial Stress Strain Relationships for Concrete. Journal of Engineering Mechanics Division, ASCE, Vol. 103, no. EM3, Proc. paper 12969, June 1977, pp 423-439.
30. Coon, M.D. and Evans, R.J. : Incremental Constitutive Laws and their Failure Criteria with Application to Plain Concrete. International Journal of Solids and Structures, Vol. 8, no. 9, September 1972, pp 1169-1183.
31. Liu, T.C.Y., Nilson, A.H., and Slate F.O. : Biaxial Stress-Strain Relations for Concrete. Journal of Structural Division, ASCE, Vol. 98, no. ST5, Proc. paper 8905, May 1972, pp 1025-1034.
32. Liu, T.C.Y., Nilson, A.H. and Slate, F.O. : Stress-Strain Response and Fracture of Concrete in Uniaxial and Biaxial Compression. ACI Journal, 1972.
33. Romstad, K.M., Taylor, M.A. and Herrmann, L.R. : Numerical Biaxial Characterization for Concrete. Journal of Engineering Mechanics Division, ASCE, Vol. 100, no. EM5, Proc. paper 10879, October 1974, pp 935-948.
34. Saenz, L.P. : Equation for Stress Strain Curve of Concrete in Uniaxial and Biaxial Compression of Concrete. ACI Journal, Vol. 61, September 1965, pp 1229-1235.

35. Ottoson, N.S. : A Failure Criteria for Concrete. Journal of Engineering Mechanics Division, ASCE, Vol. 103, no. EM4, Proc. paper 13111, August 1977, pp 527-535.
36. Ottoson, N.S. : Constitutive Model for Short-time Loading of Concrete. Journal of Engineering Mechanics Division, ASCE, Vol. 105, no. EM1, Proc. paper 14375, February 1979, pp 127-141.
37. Ottosen, N.S. : Structural Failure of Thick-walled Concrete Elements. 4th SMIRT Conference, San Francisco, August 1977, Paper H4/3.
38. Suidan, M. and Schnobrich, W. : Finite Element Analysis of Reinforced Concrete. Journal of Structural Division, ASCE, ST10, 1973.
39. Cervenka, V. : Inelastic Finite Element Analysis of Reinforced Concrete Panels under In-plane Loads. Ph.D. Thesis, University of Colorado, Boulder, Colorado, 1970.
40. Darwin, D. and Pecknold, D.A. : Analysis of Cyclic Loading of Plane Reinforced Concrete Structures. Computer and Structures, Vol. 7, 1977, pp 137-147.
41. Darwin, D. and Pecknold, D.A. : Non-linear Biaxial Law for Concrete. Journal of Engineering Mechanics Division, ASCE, Vol. 103, no. EM2, Proc. paper 12839, April 1977, pp 229-249.
42. Elwi, A. and Murray, D.W. : A Three-dimensional Hypo-elastic Concrete Constitutive Relationship. Journal of Engineering Mechanics Division, Vol. 105, no. EM4, Proc. paper 14746, August 1979, pp 623-641.
43. Bresler, B. and Scordelis, A.C. : Shear Strength of Reinforced Concrete Beams Series II. SESM Report, No. 64-2, University of California, Berkeley, December 1964.

44. Franklin, H.A. : Non-linear Analysis of Reinforced Concrete Frames and Panels. Ph.D. Dissertation, Department of Civil Engineering, University of Colorado, Boulder, 1970.
45. Bangash, Y. : A Basis for the Design of Bonded Reinforcement in Prestressed Concrete Reactor Vessels. The Institution of Civil Engineers, paper 7478S, 1972.
46. Bangash, Y. : Movements in Prestressed Concrete Reactor Vessels. Nuclear Engineering and Design, Vol. 50, 1978, pp 463-473.
47. Bangash, Y. : Riddle of Bonded and Unbonded Tendons in Prestressed Concrete Reactor Vessels. Concrete, Vol. 8, no. 6, June 1974.
48. CP110 - British Standards.
49. Baker, A.L.L. : The Application of Triaxial Strength Theory to the Computation of Deformation and Limited Stress Values in Massive Concrete. IABSE Seminar on Concrete Structures subjected to Triaxial Loading, paper III, Bergamo, Italy, 1974.
50. Lewis, D.J., Irving, J. and Carmichael, G.D.T. : Advances in the Analysis of Prestressed Concrete Pressure Vessels. Nuclear Engineering and Design, Vol. 20, 1972, pp 543-573.
51. Zienkiewicz, O.C., Valliappan, S. and King, I.P. : Elasto-plastic Solution of Engineering Problems. Initial Stress Finite Element Approach. International Journal for Numerical Methods in Engineering, Vol. 1, no. 1, 1969, pp 75-100.
52. Nayak, G.C. et al : Elasto-plastic Analysis - A Generalisation for Various Constitutive Relations including Softening. Journal for Numerical Methods in Engineering, Vol. 5, 1972.
53. Yamada, Y. et al : Plastic Stress Strain Matrix and its Application for the Solution of Elasto-plastic Problems by the Finite Element Method. International Journal of Mechanical Science, Vol. 10, 1968.

54. Fung, Y.C. : Fundamentals of Solid Mechanics, Prictice-Hall, 1965.
55. Hill, R. : Mathematical Theory of Plasticity. Clarendon Press, 1950.
56. Mendelson, A. : Plasticity - Theory and Application. MacMillan, 1968.
57. Hodge, P.G. : The Theory of Piece-wise Linear Isotropic Plasticity. IUTAM Colloquium, Madrid, 1955.
58. Prager, W. : A New Method of Analysing Stresses and Strains in Work Hardening Plastic Solids. Trans. ASME, Journal of Applied Mechanics, 23, 1956, pp 493-496.
59. Ziegler, H. : A Modification of Prager's Hardening Rule. Quart. Applied Meth. Vol. XVII, no. 1 (1959) pp 55-65.
60. Shield, R.T. and Ziegler, H. : On Prager's Work Hardening Rule. ZAMP, Vol. 9a, no. 3, September 1958, pp 260-276.
61. Hodge, P.G. : Discussion on A New Method of Analysing Stress and Strain in Work Hardening Plastic Solids. Trans. ASME, Journal of Applied Mechanics 24 (1957), pp 482-484.
62. Haisler, W.E. : Numerical and Experimental Comparison of Plastic Work Hardening Rules. 4th SMIRT Conference, Part L4/7, 1977.
63. Bazant, Z.P. and Bhat, P.D. : Endochronic Theory of Inelasticity and Failure of Concrete. Journal of Engineering Mechanics Division, ASCE, EM4, August 1976, pp 701-721.
64. Sorenson, S.I., Arneson, A. and Bergan, P.G. : Non-linear Finite Element Analysis of Reinforced Concrete using Endochronic Theory. Conference on Non-linear Methods of Analysis, Norwegian Institute of Technology, 1978.
65. Valanis, K.C. : A Theory of Visco-plasticity without a Yield Surface. Archiwum Mechaniki Stosowanej, Vol. 3, Warsaw, 1971, pp 517-551.

66. Sandler, I.S. : On the Uniqueness and Stability of Endochronic Theory of Material Behaviour. Topical Report, no. DN001-76-C-0127, Weiclinger Assoc., New York, October 1976.
67. Hannant, D.J. : Creep and Creep Recovery of Concrete subjected to a Multi-axial Compressive Stress. ACI Journal, Vol. 66, no. 5, pp 391-394.
68. Illston, J.M. : Components of Creep in Mature Concrete. ACI Journal Vol. 65, no. 18, March 1968, pp 219-228.
69. Jordaan, I.J. : Analysis of Creep in Concrete Structure. IABSE Seminar paper III-8, Bergamo, Italy, 1974.
70. England, G.L. : Steady State Stresses in Concrete Structures subjected to Sustained Temperatures and Loads. Nuclear Engineering and Design, Vol. 3, 1966.
71. England, G.L. : Long-term Thermal Stresses in Prestressed Concrete Structures. Conference on PCPV, Institute of Civil Engineers, March 1967.
72. England, G.L. : Time-dependent Stresses in Creep Elastic Materials. A General Method of Calculation. Conference on Recent Advances in Stress Analysis, the Joint British Committee for Stress Analysis, 1968.
73. England, G.L. and Allen, S.J. : The Calculation of Time-dependent Stresses in PCRV by an Approximate Method. 1st SMIRT Conference, Berlin, September 1971.
74. England, G.L. and Phok, M. : Time-dependent Stresses in a Long Thick Cylindrical Prestressed Concrete Vessel subjected to Sustained Temperature Crossfall. Nuclear Engineering and Design, Vol. 9, 1969.

75. England, G.L. et al : Creep of Concrete - A Consistent Approach. Journal of Structural Division, ASCE, Vol. 103, no. ST3, March 1977, pp 475-491.
76. England, G.L. : The Direct Calculation of Stresses in Creeping Concrete and Concrete Structures. Conference on Structure, Solid Mechanics and Design, Southampton, Part 2, Ed. M.TE'ENI, 1969.
77. England, G.L. and Illston, J.M. : Method of Computing Stress in Concrete from History of Measured Strain. Civil Engineering and Public Review, London, Vol. 60, 1965.
78. Parrot, L.J. : Some Observations on the Components of Creep in Concrete. Magazine of Concrete Research, Vol. 22, no. 72, 1970, pp 143-148.
79. Zienkiewicz, O.C., Watson, M. and King, I.P. : A Direct Method of Visco-elastic Creep. International Journal of Mechanical Science, Vol. 10, 1968, pp 807-827.
80. Greerbaum, G.A. and Rubinstein, M.F. : Creep Analysis of Axisymmetric Bodies using Finite Elements. Nuclear Engineering and Design, Vol. 7, 1968, pp 379-397.
81. Kawamata, S., Akiyama, H. and Kuroda, T. : Creep Analysis of Boiler-podded by the Method of Sliced Substructures. 4th SMIRT Conference, 1977, paper H3/2.
- 81a. Kawamata, S. et al : The Method of Sliced Substructures in the Analysis of Boiler-podded PCPV. 3rd SMIRT Conference, 1975, paper H2/6.
82. Browne, R.D. : Properties of Concrete in Reactor Vessels. Proc. of International Conference on PCPV. The Institute of Civil Engineers, London, 1967, pp 131-151.
83. Smith, P.D., Cook, W.A. and Anderson, C.A. : Finite Element Analysis

of Prestressed Concrete Reactor Vessels. 4th SMIRT Conference 1977, paper H2/2.

84. Bazant, Z.P. : Theory of Creep and Shrinkage in Concrete Structures - A Precip of Recent Development. Mechanics Today, Vol. 2, 1975, Charter 1, pp 1-93.
85. Irving, J. and Carmichael, G.D.T. : The Assessment of Bounds on Stresses and Strains in Prestressed Concrete Reactor Pressure Vessels. Magazine of Concrete Research, Vol. 25, no. 85, December 1973.
86. Crisfield, M.A. : The Automatic Non-Linear Analysis of Stiffened Plates and Shallow Shells using Finite Elements. Proc. Institution of Civil Engineers, Part 2, 1980, 69, December, pp 801-909.
87. Lekhnitskii, S.G. : Theory of an Anisotropic Elastic Body. Holden Day, San Francisco, California, 1963.
88. Burrow, R.E.D. and Williams, A.J. : Hartlepool AGR Reactor Pressure Vessel. Nuclear Engineering International, November 1969, pp 973-980.
89. Jeager, T.A. : To Grout or not to Grout. ACI publication SP-34, 1972.
90. Edward, A.D. and Picard, A. : Bonding Properties of 1/2 inch Diameter Strand. ACI Journal, November 1972, pp 684-689.
91. Yannopoulos, P.J. : Fatigue, Bond and Cracking Characteristics of Reinforced Concrete Tension Members. Ph.D. Thesis, University of London, 1976.
92. Nilson, A.H. : Bond Stress-slip Relations in Reinforced Concrete. Report no. 345, Department of Structural Engineering, Cornell University, December 1970.

93. Rehm, G. : The Basic Principles of Bond between Steel and Concrete. Translation no. 134, Cement and Concrete Association, London, 1968, 66 pages.
94. Evans, R.H. and Robinson, G.W. : Bond Stresses in Prestress Concrete from X-ray Photographs. Proc. I.C.E. Part 1, Vol. 4, no. 2, March 1955.
95. Hanson, N.W. and Kaar, P.H. : Flexural Bond Tests of Pretensioned Prestressed Beams, ACI Journal, Vol. 55, no. 7, January 1959.
96. Dably, L.J. : Static Tests on Prestressed Concrete Beams using 7/16 inch Strands. Leigh University, Fritz Engineering Laboratory, Progress Report no. 13 on Prestressed Concrete Bridge Members, November 1956.
97. Base, G.D. : An Investigation of Transmission Length in Pretensioned Concrete. Illinois Congress of Federation Internationale de la Precontrainte, Session III, Paper no. 9, Berlin 1958, pp 603-623.
98. Ratz, E.H. et al : The Transmission of Prestressed Concrete by Bond. III Congress of Federation of Internationale de la Precontrainte, Session III, paper 10, Berlin, 1958, pp 624-640.
99. Dinshore, G.A. et al : Anchorage and Bond in Pretensioned Prestressed Concrete Members. Leigh University, Fritz Engineering Laboratory, Report No. 223-19, December 1953.
100. Ruch, H., and Rehm, G. : Tests for Determination of Transfer Lengths of Prestressing Steel. Deutscher Ausschuss fur Stahlbeton, Heft 147, Berlin, 1963, pp 1-38.
101. Kaar, P.H. et al : Influence of Concrete Strength and Strand Transfer Length. Journal of Prestressed Concrete Institute (PCI), October 1963.

102. Preston, H.K. : Characteristics of 15 percent Stronger Seven Wire Strand. PCI Journal, Vol. 8, no. 1, February 1963, pp 39-45.
103. Hanson, J.M. and Hulsbos, C.L. : Overload Behaviour of Pre-tensioned Prestressed Concrete I-beams with Web Reinforcement. Highway Record no. 76, 1965, pp 1-33.
104. Over, R.S. and Au, T. : Prestressed Transfer Bond of Pretensioned Strands in Concrete. ACI Journal, Vol. 62, no. 11, November 1965, pp 1451-1460.
105. Stocker, M.F. and Sozen, M.A. : Investigation of Prestressed Reinforced Concrete for Highway Bridges, Part V : Bond Characteristics of Prestressing Strand. University of Illinois, College of Engineering, Bulletin no. 503, 1970.
106. Lutz, L.A. and Gergely, P. : Mechanics of Bond and Slip of Deformed Bars in Concrete. ACI Journal, Vol. 64, no. 11, November 1967, pp 711-721.
- 106a. Wahla et al : Direct Measurement of Bond-slip in Reinforced Concrete. Proc. American Society Agr. Eng., 1969.
- 106b. Tanner, J.A. : An Experimental Investigation of Bond-slip in Reinforced Concrete. M.S. Thesis, Cornell University, November 1971.
107. Morris, S. and David W.J. : Bond Development Length Tests of Grouted 54 Strand Post-tensioned Tendons. ACI Journal, October 1974, pp 522-525.
108. Morris, S. : Large Post-tensioned Tendons. PCI Journal, May to June 1972.
109. Morris, S. : Grouting Tests on Large Post-tensioned Tendons for Secondary Nuclear Containment Structures. PCI Journal, March to April 1971.

110. Mattock, A.H., Yamazaki, and Kattula, B.T. : Comparative Study of Prestressed Concrete Beams with and without Bond. ACI Journal, Vol. 68, no. 2, February 1971.
111. Imoto, K. : An Analytical Method for Three-dimensional Non-linear Responses of Prestressed Concrete Nuclear Reactor Vessels. 6th SMIRT Conference, Paris, Part H3/7, 1981.
112. Naus, D.J. : Grouted and Non-grouted Tendons for Prestressed Concrete Pressure Vessels. 5th SMIRT Conference, San Francisco, Part H3/6, 1979.
- 113a. Brading, K.F. and Hills, G. : Use of Structural Models in Developing Pressure Vessel Design. Proc. Conference on Prestressed Concrete Pressure Vessels, Institution of Civil Engineers, 1968.
- 113b. Campbell-Allen, D. and Lowe, E.W.E. : The Use of Simplified Models for the Design of End Slabs. British Nuclear Energy Society, London, 1969.
114. Morgan, P.L.T. : Discussion. Proc. of Conference on Prestressed Concrete Pressure Vessels, Institution of Civil Engineers, 1968.
115. Meerwald, K. and Schwieters, G. : Testing of Perforated of Prestressed Concrete Pressure Vessel Top Slab Model. ACI Journal, Seminar on Concrete for Nuclear Reactors, Berlin, October 1970.
116. Paul, S.L. et al : Strength and Behaviour of Prestressed Concrete Vessels for Nuclear Reactors. Civil Engineering Studies, Structural Research Series no. 346, University of Illinois, July 1969.
117. Langan, D. and Garas, F.K. : Behaviour of End Slabs in Cylindrical Prestressed Concrete Pressure Vessels. 2nd SMIRT Conference, Part H3/4. 1973.

118. Langan, D. and Garas, F.K. : Capacity of Prestressed Vessels to Resist Shear. ACI Journal, Seminar on Concrete for Nuclear Reactors, SP34-12.
119. Langan, D. and Garas, F.K. : The Design of Pod Boiler Pressure Vessels with particular reference to Nuclear Power Stations. Paper H4/4, 2nd SMIRT Conference, Berlin, 1973.
120. Anderson, S.I. et al : The Scandinavian PCRV Model Project : Stress Calculation and Experimental Verification. H5/3. 2nd SMIRT Conference, Berlin, 1973.
121. Scotto, F.L. : Thin Walled 1:20 Prestressed Concrete Pressure Vessel Model for THTR Reactor Type. Paper H5/6, 2nd SMIRT Conference, Berlin, 1973.
122. Ottosen, N.S. and Andersen, S.I. : Theoretical and Experimental Studies for Optimisation of PCRV Top Closures. Part H3/6, 3rd SMIRT Conference, London, 1975.
123. Langan, D. and Smith, J.R. : 1/10th Scale Model of Hartlepool Pressure Vessel - Introduction Statement. Structural Research Laboratory, Taylor Woodrow Construction Ltd., November 1968.
124. Takeda, T. et al : Pressure Tests of PCRV Models. Paper presented at the 7th FIP International Conference, New York, May 1974.
125. Galix, T.C. et al : Crack Analysis of Multi-cavity Prestressed Concrete Reactor Vessels. Paper H4/2, 3rd SMIRT Conference, London, 1975.
126. England, G.L. and Ross, A.D. : Reinforced Concrete under Thermal Gradients. Magazine of Concrete Research, Cement and Concrete Association, Vol. 14, no. 40, March 1962, pp 5-12.

127. Nasser, K.W. and Neville, A.M. : Creep of Concrete at Elevated Temperatures. ACI Journal, Vol. 62, 1965, pp 1567-1579.
128. Hannat, D.J. : The Strain Behaviour of Concrete under Compressive Stresses at Elevated Temperatures. CERL, Note no. RD/LIN 67/66.
129. McHenry, D. : A New Aspect of Concrete and its Application to Design. Proc. American Society for Testing and Materials, Vol. 43, 1943, pp 1069-1084.
130. Ross, A.D. : Creep of Concrete under Variable Stress. ACI Journal, Vol. 54, 1958, pp 739-758.
131. England, G.L. and Jardaán, I.J. : Time-dependent and Steady State Stresses in Concrete Structures with Steel Reinforcement at Normal and Raised Temperatures. Magazine of Concrete Research, Vol. 27, no. 92, September 1975, pp 131-142.
132. Illston, J.M. and Jordaán, I.J. : Creep Prediction for Concrete under Multi-axial Stress. ACI Journal, Vol. 69, 1972, pp 158-164.
- 132a. Bangash, Y. et al : The Influence of Thermal Creep on the Operational Behaviour of Complex Structures. International Conference on Fundamental Creep and Shrinkage, Laussane, Switzerland, 1980.
133. Nayak, G.C. and Zienkiewicz, O.C. : Note on the 'Alpha' Constant Stiffness Method for Analysis of Non-linear Problems. International Journal for Numerical Methods in Engineering, 1972. pp 579-582.
134. Vallappan, S. and Doolan, T.F. : Non-linear Stress Analysis of Reinforced Concrete. Journal of the Structural Division, ASCE, Vol. 98, no. ST4, Paper 8845, April 1972, pp 885-898.
135. Schrobrich, W.C. et al : Discussion on reference 134. Journal of the Structural Division, ASCE, Vol. 98, ST10, October 1972, pp 2419-2432.

136. Lin, C. and Scordelis, A.C. : Non-linear Analysis of Reinforced Concrete Shells of General Form. Journal of the Structural Division, ASCE, ST31 March 1975, pp 2319-2432.
137. Truesdell, C. : Hypo-elasticity. Journal of Rational Mechanics Analysis, Vol. 4, 1955, pp 83-133.
138. Kotsovos, M.D. and Newman, J.B. : Behaviour of Concrete under Multi-axial Stress. ACI Journal, Vol. 74, no. 9, September 1977, pp 443-446.
139. Richart, F.E. et al : A Study of Failure under Combined Compressive Stresses. Bulletin no. 185, University of Illinois, Engineering Experiment Station, Urbana, Illinois, 1928.
140. Balmer, G.G. : Shearing Strength of Concrete under High Triaxial Stress - Computation of Mohrs Envelopes as a Curve. Structural Research Laboratory Report no. SP23, United States Department of Interior, Bureau of Reclamation, Washington D.C.
141. Chinn, J. and Zimmerman, R.M. : Behaviour of Plain Concrete under Various High Triaxial Compression Loading Conditions. Technical Report no. WL TR 64-163 (AD4684460), Air Force Weapon Laboratory, New Mexico, 1965.
142. Mills, L.L. and Zimmerman, R.M. : Compressive Strength of Plain Concrete under Multiaxial Loading Conditions. ACI Journal, Vol. 67, no. 10, October 1970, pp 802-807.
143. Sozen, M.A. and Corley, W.G. : Time-dependent Deflection of Reinforced Concrete Beams. ACI Journal, March 1966, pp 374-385.
144. Conference on Prestressed Concrete Pressure Vessels. Institution of Civil Engineers, London, 1967.

145. First International Conference on Structural Mechanics in Reactor Technology. Berlin, September 1971.
- 145a. Second International Conference on Structural Mechanics in Reactor Technology. Berlin, 1973.
- 145b. Third International Conference on Structural Mechanics in Reactor Technology. London, September 1975.
- 145c. Fourth International Conference on Structural Mechanics in Reactor Technology. San Francisco, 1977.
- 145d. Fifth International Conference on Structural Mechanics in Reactor Technology. Berlin, 1979.
- 145e. Sixth International Conference on Structural Mechanics in Reactor Technology. Paris, 1981.
146. Bartos, P. : Proc. of the International Conference on Bond in Concrete. Paisley College of Technology, Scotland, June 14th-16th 1982.
147. Javor, T. and Lazar, J. : Bond of Seven Wired Strand for Prestressed Steel. International Conference on Bond in Concrete, Paisley College of Technology, Scotland, 1982.
148. Bazant, Z.P. and Cedloin, L. : Blunt Crack Bond Propagation in Finite Element Analysis. Journal of Engineering Mechanics Division, ASCE, Vol. 105, no. EM2, April 1977, pp 297-315.
149. Hillemier, B. and Hilsdorf, H.K. : Fracture Mechanics Studies of Concrete Components. Cement and Concrete Research, Vol. 7, pp 523-536, 1977.
150. Baker, A.L.L. : A Criterion of Concrete Failure. ICE, Vol. 45, 1970, pp 269-278.

151. Baker, A.L.L. : An Analysis of Deformation and Failure Characteristics of Concrete. Magazine of Concrete Research, 11, no. 33, 1959.
152. Vile, G.W.D. : The Strength of Concrete under Short-Term Biaxial Stress. The Structure of Concrete and its Behaviour under Load. Proc. International Conference, London, 1968, pp 275-286.
153. Hanant, D.J. and Frederick, C.O. : Failure Criteria for Concrete in Compression. Magazine of Concrete Research, Vol. 20, no. 64, September 1968, pp 137-144.
154. Akroyd, T.N.W. : Concrete under Triaxial Stress. Magazine of Concrete Research, Vol. 13, no. 39, pp 111-118, November 1961.
155. FEMGEN - Interactive Mesh Generator, FEGS Ltd. Rev. 6, 1982.
156. Brading, K.F., McKillen, R.R. and Finigan, A. : Elastic and Ultimate Pressure Tests on a Tenth Scale Model of the Dungeness 'B' Concrete Pressure Vessel. Model Techniques for Prestressed Concrete Pressure Vessels, Proc. of the Conference organised by the British Nuclear Energy Society in London, 10-11 July 1969.

APPENDIX A

APPENDIX A1

A1.1 Solid Isoparametric Elements

The shape functions and their derivatives for 8, 20 and 32 noded isoparametric solid elements are given in tabulated form as follows :

A1.1.1. 8-Noded Solid Element (refer to Figure (3.1a))

TABLE A1

Node i	Shape functions $N_i(\xi, \eta, \zeta)$	Derivatives		
		$\frac{\partial N_i}{\partial \xi}$	$\frac{\partial N_i}{\partial \eta}$	$\frac{\partial N_i}{\partial \zeta}$
1	$\frac{1}{8}(1-\xi)(1-\eta)(1-\zeta)$	$-\frac{1}{8}(1-\eta)(1-\zeta)$	$-\frac{1}{8}(1-\xi)(1-\zeta)$	$-\frac{1}{8}(1-\eta)(1-\xi)$
2	$\frac{1}{8}(1+\xi)(1-\eta)(1-\zeta)$	$\frac{1}{8}(1-\eta)(1-\zeta)$	$-\frac{1}{8}(1+\xi)(1-\zeta)$	$-\frac{1}{8}(1+\xi)(1-\eta)$
3	$\frac{1}{8}(1+\xi)(1+\eta)(1-\zeta)$	$\frac{1}{8}(1+\eta)(1-\zeta)$	$\frac{1}{8}(1+\xi)(1-\zeta)$	$-\frac{1}{8}(1+\xi)(1+\eta)$
4	$\frac{1}{8}(1-\xi)(1+\eta)(1-\zeta)$	$-\frac{1}{8}(1+\eta)(1-\zeta)$	$\frac{1}{8}(1-\xi)(1-\zeta)$	$-\frac{1}{8}(1-\xi)(1+\eta)$
5	$\frac{1}{8}(1-\xi)(1-\eta)(1+\zeta)$	$-\frac{1}{8}(1-\eta)(1+\zeta)$	$-\frac{1}{8}(1-\xi)(1+\zeta)$	$\frac{1}{8}(1-\xi)(1-\eta)$
6	$\frac{1}{8}(1+\xi)(1-\eta)(1+\zeta)$	$\frac{1}{8}(1-\eta)(1+\zeta)$	$-\frac{1}{8}(1+\xi)(1+\zeta)$	$\frac{1}{8}(1+\xi)(1-\eta)$
7	$\frac{1}{8}(1+\xi)(1+\eta)(1+\zeta)$	$\frac{1}{8}(1+\eta)(1+\zeta)$	$\frac{1}{8}(1+\xi)(1+\zeta)$	$\frac{1}{8}(1+\xi)(1+\eta)$
8	$\frac{1}{8}(1-\xi)(1+\eta)(1+\zeta)$	$-\frac{1}{8}(1+\eta)(1+\zeta)$	$\frac{1}{8}(1-\xi)(1+\zeta)$	$\frac{1}{8}(1-\xi)(1+\eta)$

Node i	Shape functions $N_i(\xi, \eta, \zeta)$	Derivatives		
		$\partial N_i / \partial \xi$	$\partial N_i / \partial \eta$	$\partial N_i / \partial \zeta$
1	$\frac{1}{8}(1-\xi)(1-\eta)(1-\zeta)(-\xi-\eta-\zeta-2)$	$\frac{1}{8}(1-\eta)(1-\zeta)(2\xi+\eta+\zeta+1)$	$\frac{1}{8}(1-\xi)(1-\zeta)(2\eta+\xi+\zeta+1)$	$\frac{1}{8}(1-\xi)(1-\eta)(2\zeta+\eta+\xi+1)$
2	$\frac{1}{4}(1-\xi^2)(1-\eta)(1-\zeta)$	$-\frac{1}{2}(1-\eta)(1-\zeta)\xi$	$-\frac{1}{4}(1-\xi^2)(1-\zeta)$	$-\frac{1}{4}(1-\xi^2)(1-\eta)$
3	$\frac{1}{8}(1+\xi)(1-\eta)(1-\zeta)(\xi-\eta-\zeta-2)$	$\frac{1}{8}(1-\eta)(1-\zeta)(2\xi-\eta-\zeta-1)$	$\frac{1}{8}(1+\xi)(1-\zeta)(2\eta-\xi+\zeta+1)$	$\frac{1}{8}(1+\xi)(1-\eta)(2\zeta-\xi+\eta+1)$
4	$\frac{1}{4}(1+\xi)(1-\eta^2)(1-\zeta)$	$\frac{1}{4}(1-\eta^2)(1-\zeta)$	$-\frac{1}{2}(1+\xi)(1-\zeta)\eta$	$-\frac{1}{4}(1-\eta^2)(1+\xi)$
5	$\frac{1}{8}(1+\xi)(1+\eta)(1-\zeta)(\xi+\eta-\zeta-2)$	$\frac{1}{8}(1+\eta)(1-\zeta)(2\xi+\eta-\zeta-1)$	$\frac{1}{8}(1+\xi)(1-\zeta)(2\eta+\xi-\zeta-1)$	$\frac{1}{8}(1+\xi)(1+\eta)(2\zeta-\xi-\eta+1)$
6	$\frac{1}{4}(1-\xi^2)(1+\eta)(1-\zeta)$	$-\frac{1}{2}(1+\eta)(1-\zeta)\xi$	$\frac{1}{4}(1-\xi^2)(1-\zeta)$	$-\frac{1}{4}(1-\xi^2)(1+\eta)$
7	$\frac{1}{8}(1-\xi)(1+\eta)(1-\zeta)(-\xi+\eta-\zeta-2)$	$\frac{1}{8}(1+\eta)(1-\zeta)(2\xi-\eta+\zeta+1)$	$\frac{1}{8}(1-\xi)(1-\zeta)(2\eta-\xi-\zeta-1)$	$\frac{1}{8}(1-\xi)(1+\eta)(2\zeta-\eta+\xi+1)$
8	$\frac{1}{4}(1-\xi)(1-\eta^2)(1-\zeta)$	$-\frac{1}{4}(1-\eta^2)(1-\zeta)$	$-\frac{1}{2}(1-\xi)(1-\zeta)$	$-\frac{1}{4}(1-\eta^2)(1-\xi)$
9	$\frac{1}{4}(1-\xi)(1-\eta)(1-\zeta^2)$	$-\frac{1}{4}(1-\xi^2)(1-\eta)$	$-\frac{1}{4}(1-\xi)(1-\zeta^2)$	$-\frac{1}{2}(1-\xi)(1-\eta)\zeta$
10	$\frac{1}{4}(1+\xi)(1-\eta)(1-\zeta^2)$	$\frac{1}{4}(1-\eta)(1-\zeta^2)$	$-\frac{1}{4}(1-\xi)(1-\zeta^2)$	$-\frac{1}{2}(1+\xi)(1-\eta)\zeta$
11	$\frac{1}{4}(1+\xi)(1+\eta)(1-\zeta^2)$	$\frac{1}{4}(1+\eta)(1-\zeta^2)$	$-\frac{1}{4}(1+\xi)(1-\zeta^2)$	$-\frac{1}{2}(1+\xi)(1+\eta)\zeta$
12	$\frac{1}{4}(1-\xi)(1+\eta)(1-\zeta^2)$	$-\frac{1}{4}(1+\eta)(1-\zeta^2)$	$\frac{1}{4}(1-\xi)(1-\zeta^2)$	$-\frac{1}{2}(1-\xi)(1+\eta)\zeta$
13	$\frac{1}{8}(1-\xi)(1-\eta)(1+\zeta)(-\xi-\eta+\zeta-2)$	$\frac{1}{8}(1-\eta)(1+\zeta)(2\xi+\eta-\zeta+1)$	$\frac{1}{8}(1-\xi)(1+\zeta)(2\eta+\xi-\zeta+1)$	$\frac{1}{8}(1-\xi)(1-\eta)(2\zeta-\eta-\xi-1)$
14	$\frac{1}{4}(1-\xi^2)(1-\eta)(1+\zeta)$	$-\frac{1}{2}(1-\eta)(1+\zeta)\xi$	$-\frac{1}{4}(1-\xi^2)(1+\zeta)$	$\frac{1}{4}(1-\xi^2)(1-\eta)$
15	$\frac{1}{8}(1+\xi)(1-\eta)(1+\zeta)(\xi-\eta+\zeta-2)$	$\frac{1}{8}(1-\eta)(1+\zeta)(2\xi-\eta+\zeta-1)$	$\frac{1}{8}(1+\xi)(1+\zeta)(2\eta-\xi-\zeta+1)$	$\frac{1}{8}(1-\eta)(1+\xi)(2\zeta+\xi-\eta-1)$
16	$\frac{1}{4}(1+\xi)(1-\eta^2)(1+\zeta)$	$\frac{1}{4}(1-\eta^2)(1+\zeta)$	$-\frac{1}{2}(1+\xi)(1+\zeta)\eta$	$\frac{1}{4}(1+\xi)(1-\eta^2)$
17	$\frac{1}{8}(1+\xi)(1+\eta)(1+\zeta)(\xi+\eta+\zeta-2)$	$\frac{1}{8}(1+\eta)(1+\zeta)(2\xi+\eta+\zeta-1)$	$\frac{1}{8}(1+\xi)(1+\zeta)(2\eta+\xi+\zeta-1)$	$\frac{1}{8}(1+\xi)(1+\eta)(2\zeta+\eta+\xi-1)$
18	$\frac{1}{4}(1-\xi^2)(1+\eta)(1+\zeta)$	$-\frac{1}{2}\xi(1+\eta)(1+\zeta)$	$\frac{1}{4}(1-\xi^2)(1+\zeta)$	$\frac{1}{4}(1-\xi^2)(1+\eta)$
19	$\frac{1}{8}(1-\xi)(1+\eta)(1+\zeta)(-\xi+\eta+\zeta-2)$	$\frac{1}{8}(1+\eta)(1+\zeta)(2\xi-\eta+\zeta-1)$	$\frac{1}{8}(1-\xi)(1+\zeta)(2\eta-\xi+\zeta-1)$	$\frac{1}{8}(1-\xi)(1+\eta)(2\zeta-\xi+\eta-1)$
20	$\frac{1}{4}(1-\xi)(1-\eta^2)(1+\zeta)$	$-\frac{1}{4}(1-\eta^2)(1+\zeta)$	$-\frac{1}{2}(1-\xi)(1+\zeta)\eta$	$\frac{1}{4}(1-\xi)(1-\eta^2)$

A1.1.3. 32 Noded Solid Element (refer to Figure (3.1c))

TABLE A3

Node i	Shape functions $N_i(\xi, \eta, \zeta)$	Derivatives		
		$\frac{\partial N_i}{\partial \xi}$	$\frac{\partial N_i}{\partial \eta}$	$\frac{\partial N_i}{\partial \zeta}$
1	$\frac{9}{64}(1-\xi)(1-\eta)(1-\zeta)[\xi^2+\eta^2+\zeta^2-19/9]$	$\frac{9}{64}(1-\eta)(1-\zeta)[2\xi-3\xi^2-\eta^2-\zeta^2+\xi^2+19/9]$	$\frac{9}{64}(1-\xi)(1-\zeta)[2\eta-3\eta^2-\xi^2-\zeta^2+19/9]$	$\frac{9}{64}(1-\xi)(1-\eta)[2\zeta-3\zeta-\xi^2-\eta^2+19/9]$
2	$\frac{9}{64}(1-\xi^2)(1-3\xi)(1-\eta)(1-\zeta)$	$\frac{9}{64}(9\xi^2-3\xi-3)(1-\eta)(1-\zeta)$	$-\frac{9}{64}(1-\xi^2)(1-3\xi)(1-\zeta)$	$-\frac{9}{64}(1-\xi^2)(1-3\xi)(1-\eta)$
3	$\frac{9}{64}(1-\xi^2)(1+3\xi)(1-\eta)(1-\zeta)$	$\frac{9}{64}(3-2\xi-9\xi^2)(1-\eta)(1-\zeta)$	$-\frac{9}{64}(1-\xi^2)(1+3\xi)(1-\zeta)$	$-\frac{9}{64}(1-\xi^2)(1+3\xi)(1-\eta)$
4	$\frac{9}{64}(1+\xi)(1-\eta)(1-\zeta)[\xi^2+\eta^2+\zeta^2-19/9]$	$\frac{9}{64}(1-\eta)(1-\zeta)[3\xi^2+3\xi+\zeta^2+\eta^2-19/9]$	$\frac{9}{64}(1+\xi)(1-\zeta)[2\eta-3\eta^2-\xi^2-\zeta^2+19/9]$	$\frac{9}{64}(1+\xi)(1-\eta)[2\zeta-3\zeta-\xi^2-\eta^2+19/9]$
5	$\frac{9}{64}(1-\eta^2)(1-3\eta)(1+\xi)(1-\zeta)$	$\frac{9}{64}(1-\eta^2)(1-3\eta)(1-\zeta)$	$\frac{9}{64}(9\eta^2-2\eta-3)(1+\xi)(1-\zeta)$	$-\frac{9}{64}(1-\eta^2)(1-3\eta)(1+\xi)$
6	$\frac{9}{64}(1-\eta^2)(1+3\eta)(1+\xi)(1-\zeta)$	$\frac{9}{64}(1-\eta^2)(1+3\eta)(1-\zeta)$	$\frac{9}{64}(3-2\eta-9\eta^2)(1+\xi)(1-\zeta)$	$-\frac{9}{64}(1-\eta^2)(1+3\eta)(1+\xi)$
7	$\frac{9}{64}(1+\xi)(1+\eta)(1-\zeta)[\xi^2+\eta^2+\zeta^2-19/9]$	$\frac{9}{64}(1+\eta)(1-\zeta)[2\xi+3\xi^2+\eta^2+\zeta^2-19/9]$	$\frac{9}{64}(1+\xi)(1-\zeta)[2\eta+3\eta^2+\xi^2+\zeta^2-19/9]$	$\frac{9}{64}(1+\xi)(1+\eta)[2\zeta-3\zeta-\xi^2-\eta^2+19/9]$
8	$\frac{9}{64}(1-\xi^2)(1+3\xi)(1+\eta)(1-\zeta)$	$\frac{9}{64}(3-2\xi-9\xi^2)(1+\eta)(1-\zeta)$	$\frac{9}{64}(1-\xi^2)(1+3\xi)(1-\zeta)$	$-\frac{9}{64}(1-\xi^2)(1+3\xi)(1+\eta)$
9	$\frac{9}{64}(1-\xi^2)(1-3\xi)(1+\eta)(1-\zeta)$	$\frac{9}{64}(9\xi^2-2\xi-3)(1+\eta)(1-\zeta)$	$\frac{9}{64}(1-\xi^2)(1-3\xi)(1-\zeta)$	$-\frac{9}{64}(1-\xi^2)(1-3\xi)(1+\eta)$
10	$\frac{9}{64}(1-\xi)(1+\eta)(1-\zeta)[\xi^2+\eta^2+\zeta^2-19/9]$	$\frac{9}{64}(1+\eta)(1-\zeta)[2\xi-3\xi^2-\eta^2-\zeta^2+19/9]$	$\frac{9}{64}(1-\xi)(1-\zeta)[2\eta+3\eta^2+\xi^2+\zeta^2-19/9]$	$\frac{9}{64}(1-\xi)(1+\eta)(2\zeta-3\zeta-\xi^2-\eta^2+19/9)$
11	$\frac{9}{64}(1-\eta^2)(1+3\eta)(1-\xi)(1-\zeta)$	$-\frac{9}{64}(1-\eta^2)(1+3\eta)(1-\xi)$	$\frac{9}{64}(3-2\eta-9\eta^2)(1-\xi)(1-\zeta)$	$-\frac{9}{64}(1-\eta^2)(1+3\eta)(1-\xi)$
12	$\frac{9}{64}(1-\eta^2)(1-3\eta)(1-\xi)(1-\zeta)$	$-\frac{9}{64}(1-\eta^2)(1-3\eta)(1-\xi)$	$\frac{9}{64}(9\eta^2-2\eta-3)(1-\xi)(1-\zeta)$	$-\frac{9}{64}(1-\eta^2)(1-3\eta)(1-\xi)$
13	$\frac{9}{64}(1-\eta^2)(1-3\eta)(1-\eta)(1-\xi)$	$-\frac{9}{64}(1-\eta^2)(1-3\eta)(1-\eta)$	$-\frac{9}{64}(1-\xi)(1-\eta^2)(1-3\eta)$	$\frac{9}{64}(9\eta^2-2\eta-3)(1-\xi)(1-\eta)$
14	$\frac{9}{64}(1-\eta^2)(1-3\eta)(1-\eta)(1+\xi)$	$\frac{9}{64}(1-\eta^2)(1-3\eta)(1-\eta)$	$-\frac{9}{64}(1+\xi)(1-\eta^2)(1-3\eta)$	$\frac{9}{64}(9\eta^2-2\eta-3)(1-\eta)(1+\xi)$
15	$\frac{9}{64}(1-\eta^2)(1-3\eta)(1+\eta)(1+\xi)$	$\frac{9}{64}(1-\eta^2)(1-3\eta)(1+\eta)$	$\frac{9}{64}(1-\eta^2)(1-3\eta)(1+\eta)$	$\frac{9}{64}(1+\xi)(1+\eta)(9\eta^2-2\eta-3)$
16	$\frac{9}{64}(1-\eta^2)(1-3\eta)(1+\eta)(1-\xi)$	$-\frac{9}{64}(1-\eta^2)(1-3\eta)(1+\eta)$	$\frac{9}{64}(1-\eta^2)(1-3\eta)(1-\xi)$	$\frac{9}{64}(1+\xi)(1+\eta)(9\eta^2-2\eta-3)$
17	$\frac{9}{64}(1-\eta^2)(1+3\eta)(1-\eta)(1-\xi)$	$-\frac{9}{64}(1-\eta^2)(1+3\eta)(1-\eta)$	$-\frac{9}{64}(1-\xi)(1-\eta^2)(1+3\eta)$	$\frac{9}{64}(1-\xi)(1-\eta)(3-2\eta-9\eta^2)$
18	$\frac{9}{64}(1-\eta^2)(1+3\eta)(1-\eta)(1+\xi)$	$\frac{9}{64}(1-\eta^2)(1+3\eta)(1-\eta)$	$-\frac{9}{64}(1-\xi)(1-\eta^2)(1+3\eta)$	$\frac{9}{64}(1-\xi)(1-\eta)(3-2\eta-9\eta^2)$
19	$\frac{9}{64}(1-\eta^2)(1+3\eta)(1+\eta)(1+\xi)$	$\frac{9}{64}(1-\eta^2)(1+3\eta)(1+\eta)$	$\frac{9}{64}(1-\eta^2)(1+3\eta)(1+\eta)$	$\frac{9}{64}(1+\xi)(1+\eta)(3-2\eta-9\eta^2)$
20	$\frac{9}{64}(1-\eta^2)(1+3\eta)(1+\eta)(1-\xi)$	$-\frac{9}{64}(1-\eta^2)(1+3\eta)(1+\eta)$	$\frac{9}{64}(1-\eta^2)(1+3\eta)(1-\xi)$	$\frac{9}{64}(1+\xi)(1+\eta)(3-2\eta-9\eta^2)$
21	$\frac{9}{64}(1-\xi)(1-\eta)(1+\zeta)[\xi^2+\eta^2+\zeta^2-19/9]$	$\frac{9}{64}(1-\eta)(1+\zeta)[2\xi-3\xi^2-\eta^2-\zeta^2+19/9]$	$\frac{9}{64}(1-\xi)(1+\zeta)[2\eta-3\eta^2-\xi^2-\zeta^2+19/9]$	$\frac{9}{64}(1-\xi)(1-\eta)(2\zeta+3\zeta^2+\xi^2+\eta^2-19/9)$
22	$\frac{9}{64}(1-\xi^2)(1-3\xi)(1-\eta)(1+\zeta)$	$\frac{9}{64}(9\xi^2-2\xi-3)(1-\eta)(1+\zeta)$	$-\frac{9}{64}(1-\xi^2)(1-3\xi)(1+\zeta)$	$+\frac{9}{64}(1-\xi^2)(1-3\xi)(1-\eta)$

A1.1.3. (continued)

Node i	Shape functions $N_i(\xi, \eta, \zeta)$	Derivatives		
		$\frac{\partial N_i}{\partial \xi}$	$\frac{\partial N_i}{\partial \eta}$	$\frac{\partial N_i}{\partial \zeta}$
23	$\frac{9}{64}(1-\xi^2)(1+3\xi)(1-\eta)(1+\zeta)$	$\frac{9}{64}(3-2\xi-9\xi^2)(1-\eta)(1+\zeta)$	$-\frac{9}{64}(1-\xi^2)(1+3\xi)(1+\zeta)$	$\frac{9}{64}(1-\xi^2)(1+3\xi)(1-\eta)$
24	$\frac{9}{64}(1+\xi)(1-\eta)(1+\zeta)[\xi^2+\eta^2-19/9+\zeta^2]$	$\frac{9}{64}(1+\xi)(1-\eta)(2\xi+3\xi^2+\eta^2+\zeta^2-19/9)$	$\frac{9}{64}(1+\xi)(1+\zeta)(2\eta^2-3\eta-\xi^2-\zeta^2+19/9)$	$\frac{9}{64}(1+\xi)(1-\eta)(2\zeta+3\zeta^2+\xi^2+\eta^2-19/9)$
25	$\frac{9}{64}(1-\eta^2)(1-3\eta)(1+\xi)(1+\zeta)$	$\frac{9}{64}(1-\eta^2)(1-3\eta)(1+\zeta)$	$\frac{9}{64}(9\eta^2-2\eta-3)(1+\xi)(1+\zeta)$	$\frac{9}{64}(1-\eta^2)(1-3\eta)(1+\xi)$
26	$\frac{9}{64}(1-\eta^2)(1+3\eta)(1+\xi)(1+\zeta)$	$\frac{9}{64}(1-\eta^2)(1+3\eta)(1+\zeta)$	$\frac{9}{64}(3-2\eta-9\eta^2)(1+\xi)(1+\zeta)$	$\frac{9}{64}(1-\eta^2)(1+3\eta)(1+\xi)$
27	$\frac{9}{64}(1+\xi)(1+\eta)(1+\zeta)(\xi^2+\eta^2+\zeta^2-19/9)$	$\frac{9}{64}(1+\xi)(1+\zeta)(2\xi+3\xi^2+\eta^2+\zeta^2-19/9)$	$\frac{9}{64}(1+\xi)(1+\zeta)(2\eta+3\eta^2+\xi^2+\zeta^2-19/9)$	$\frac{9}{64}(1+\xi)(1+\eta)(2\xi+3\xi+\xi^2+\eta^2-19/9)$
28	$\frac{9}{64}(1-\xi^2)(1+3\xi)(1+\eta)(1+\zeta)$	$\frac{9}{64}(1+\eta)(1+\zeta)(3-2\xi-9\xi^2)$	$\frac{9}{64}(1-\xi^2)(1+3\xi)(1+\zeta)$	$\frac{9}{64}(1-\xi^2)(1+3\xi)(1+\eta)$
29	$\frac{9}{64}(1-\xi^2)(1-3\xi)(1+\eta)(1+\zeta)$	$\frac{9}{64}(1+\eta)(1+\zeta)(9\xi^2-2\xi-3)$	$\frac{9}{64}(1-\xi^2)(1-3\xi)(1+\zeta)$	$\frac{9}{64}(1-\xi^2)(1-3\xi)(1+\eta)$
30	$\frac{9}{64}(1-\xi)(1+\eta)(1+\zeta)(\zeta^2+\eta^2+\xi^2-19/9)$	$\frac{9}{64}(1+\eta)(1+\zeta)(2\xi-3\xi^2-\eta^2-\zeta^2+19/9)$	$\frac{9}{64}(1-\xi)(1+\zeta)(2\eta+3\eta^2+\zeta^2+\xi^2-19/9)$	$\frac{9}{64}(1-\xi)(1+\eta)(2\zeta+3\zeta^2+\xi^2+\eta^2-19/9)$
31	$\frac{9}{64}(1-\eta^2)(1+3\eta)(1-\xi)(1+\zeta)$	$-\frac{9}{64}(1-\eta^2)(1+3\eta)(1+\zeta)$	$\frac{9}{64}(3-2\eta-9\eta^2)(1-\xi)(1+\zeta)$	$\frac{9}{64}(1-\eta^2)(1+3\eta)(1-\xi)$
32	$\frac{9}{64}(1-\eta^2)(1-3\eta)(1-\xi)(1+\zeta)$	$-\frac{9}{64}(1-\eta^2)(1-3\eta)(1+\zeta)$	$\frac{9}{64}(9\eta^2-2\eta-3)(1-\xi)(1+\zeta)$	$\frac{9}{64}(1-\eta^2)(1-3\eta)(1-\xi)$

A1.1.4. Derivative Transformation and the Jacobian Matrix

With the shape functions known, the global coordinates and displacements at any point within the element can be expressed in terms of the nodal values as :

$$X = \sum_{i=1}^n N_i X_i ; \quad Y = \sum_{i=1}^n N_i Y_i ; \quad Z = \sum_{i=1}^n N_i Z_i \quad (A1.1)$$

$$U = \sum_{i=1}^n N_i U_i ; \quad V = \sum_{i=1}^n N_i V_i ; \quad W = \sum_{i=1}^n N_i W_i \quad (A1.2)$$

where n is the number of nodes on element and X_i, Y_i, Z_i and U_i, V_i, W_i are the nodal coordinates and nodal displacements respectively.

To obtain the derivatives of shape functions with respect to global coordinates, the following transformation is applied (Ref. 1) :

$$\begin{matrix} \checkmark \\ \left\{ \begin{array}{c} \frac{\partial N_i}{\partial \xi} \\ \frac{\partial N_i}{\partial \eta} \\ \frac{\partial N_i}{\partial \zeta} \end{array} \right\} \end{matrix} = \begin{matrix} \left[\begin{array}{c} \mathbf{J} \\ 3 \times 3 \end{array} \right] \end{matrix} \begin{matrix} \left\{ \begin{array}{c} \frac{\partial N_i}{\partial X} \\ \frac{\partial N_i}{\partial Y} \\ \frac{\partial N_i}{\partial Z} \end{array} \right\} \end{matrix} \quad (A1.3)$$

where i is the current node number
or

$$\begin{matrix} \left\{ \begin{array}{c} \frac{\partial N_i}{\partial X} \\ \frac{\partial N_i}{\partial Y} \\ \frac{\partial N_i}{\partial Z} \end{array} \right\} \end{matrix} = \begin{matrix} \left[\begin{array}{c} \mathbf{J} \end{array} \right] \end{matrix} \begin{matrix} \left\{ \begin{array}{c} \frac{\partial N_i}{\partial \xi} \\ \frac{\partial N_i}{\partial \eta} \\ \frac{\partial N_i}{\partial \zeta} \end{array} \right\} \end{matrix} \quad (A1.3a)$$

where $[\mathbf{J}]$ is a 3×3 Jacobian matrix and is given by :

$$\checkmark \quad \left[\mathbf{J} \right] = \begin{bmatrix} \frac{\partial X}{\partial \xi} & \frac{\partial Y}{\partial \xi} & \frac{\partial Z}{\partial \xi} \\ \frac{\partial X}{\partial \eta} & \frac{\partial Y}{\partial \eta} & \frac{\partial Z}{\partial \eta} \\ \frac{\partial X}{\partial \zeta} & \frac{\partial Y}{\partial \zeta} & \frac{\partial Z}{\partial \zeta} \end{bmatrix} \quad (A1.4)$$

$$\det \mathbf{J} = |\mathbf{J}| = \text{determinant of Jacobian} \quad (A1.4a)$$

Therefore the strain-displacement matrix B_i (Equation (3.10)) is fully defined.

A1.1.5. Nodal Forces due to Surface Pressure

In this section kinematically equivalent load is determined due to the surface pressure applied on the faces of the solid elements. The element load vector as given in Equation (3.13b) can be rewritten as :

$$\vec{P}_s^e = \int_s \tilde{N}^T \vec{p}_s d\vec{s} \quad (A1.5)$$

in which $\vec{p}_s = [p_x, p_y, p_z]^T$

\tilde{N} - element shape function matrix (A1.5a)

$d\vec{s}$ - surface area vector

The surface area vector may be expanded for the face $\xi = \pm 1$

$$d\vec{s} = d\vec{x} \times d\vec{y} \quad (A1.6)$$

and

$$d\vec{x} = \begin{bmatrix} \frac{\partial x}{\partial \xi} \\ \frac{\partial y}{\partial \xi} \\ \frac{\partial z}{\partial \xi} \end{bmatrix} d\xi \quad d\vec{y} = \begin{bmatrix} \frac{\partial x}{\partial \eta} \\ \frac{\partial y}{\partial \eta} \\ \frac{\partial z}{\partial \eta} \end{bmatrix} d\eta \quad (A1.6a)$$

From Equations (A1.6) and (A1.6a)

$$d\vec{s} = \begin{bmatrix} \frac{\partial x}{\partial \xi} \\ \frac{\partial y}{\partial \xi} \\ \frac{\partial z}{\partial \xi} \end{bmatrix} \times \begin{bmatrix} \frac{\partial x}{\partial \eta} \\ \frac{\partial y}{\partial \eta} \\ \frac{\partial z}{\partial \eta} \end{bmatrix} d\xi d\eta = \begin{bmatrix} \frac{\partial y}{\partial \xi} \frac{\partial z}{\partial \eta} - \frac{\partial z}{\partial \xi} \frac{\partial y}{\partial \eta} \\ \frac{\partial z}{\partial \xi} \frac{\partial x}{\partial \eta} - \frac{\partial x}{\partial \xi} \frac{\partial z}{\partial \eta} \\ \frac{\partial x}{\partial \xi} \frac{\partial y}{\partial \eta} - \frac{\partial y}{\partial \xi} \frac{\partial x}{\partial \eta} \end{bmatrix} d\xi d\eta \quad (A1.6b)$$

Therefore, kinematically equivalent load of Equation (A1.5) for the face where $\xi = \pm 1$ can be written as :

$$\tilde{P}_s^e = \int_{-1}^{+1} \int_{-1}^{+1} \tilde{N}^T \tilde{P}_s \begin{Bmatrix} \frac{\partial Y}{\partial \xi} \frac{\partial Z}{\partial \eta} - \frac{\partial Z}{\partial \xi} \frac{\partial Y}{\partial \eta} \\ \frac{\partial Z}{\partial \xi} \frac{\partial X}{\partial \eta} - \frac{\partial Z}{\partial \eta} \frac{\partial X}{\partial \xi} \\ \frac{\partial X}{\partial \xi} \frac{\partial Y}{\partial \eta} - \frac{\partial Y}{\partial \xi} \frac{\partial X}{\partial \eta} \end{Bmatrix} d\xi d\eta \quad (A1.7)$$

Similar expressions can be derived for the faces where $\xi = \pm 1$ and $\eta = \pm 1$. The integral of Equation (A1.7) is carried out numerically.

A1.1.6. Nodal Loads not directly on Nodes (Patch Loads)

The treatment of these loads is similar to point loads except that their values are now interpolated from the shape function values evaluated at the point where load is applied. In principle, it can be written as :

$$\tilde{P}^e = \tilde{N}^T \tilde{P}_i \quad (A1.8)$$

where $\tilde{P}_i = [P_x, P_y, P_z]^T$
 3×1

\tilde{N} - element shape function matrix (A1.8a)

$$\tilde{N} = [N_1 \tilde{I}_3, N_2 \tilde{I}_3, N_3 \tilde{I}_3, \dots, N_n \tilde{I}_3]$$

$$\tilde{I}_3 = \begin{bmatrix} 1, & 0, & 0 \\ 0, & 1, & 0 \\ 0, & 0, & 1 \end{bmatrix}$$

A1.2. Isoparametric Membrane Elements

The shape functions and their derivatives for 4, 8 and 12-noded isoparametric membrane elements are given in tabulated form as follows :

A1.2.1. 4 Noded Membrane Element (refer to Figure (3.2a)) TABLE A4

Node i	Shape functions $N_i(\xi, \eta)$	Derivatives	
		$\partial N_i / \partial \xi$	$\partial N_i / \partial \eta$
1	$\frac{1}{4}(1-\xi)(1-\eta)$	$-\frac{1}{4}(1-\eta)$	$-\frac{1}{4}(1-\xi)$
2	$\frac{1}{4}(1+\xi)(1-\eta)$	$\frac{1}{4}(1-\eta)$	$-\frac{1}{4}(1+\xi)$
3	$\frac{1}{4}(1+\xi)(1+\eta)$	$\frac{1}{4}(1+\eta)$	$\frac{1}{4}(1+\xi)$
4	$\frac{1}{4}(1-\xi)(1+\eta)$	$-\frac{1}{4}(1+\eta)$	$\frac{1}{4}(1-\xi)$

A1.2.2. 8-Noded Membrane Element (refer to Figure (3.2b)) TABLE A5

Node i	Shape functions $N_i(\xi, \eta)$	Derivatives	
		$\partial N_i / \partial \xi$	$\partial N_i / \partial \eta$
1	$\frac{1}{4}(1-\xi)(1-\eta)(-\xi-\eta-1)$	$\frac{1}{4}(1-\eta)(2\xi+\eta)$	$\frac{1}{4}(1-\xi)(2\eta+\xi)$
2	$\frac{1}{2}(1-\xi^2)(1-\eta)$	$-\xi(1-\eta)$	$-\frac{1}{2}(1-\xi^2)$
3	$\frac{1}{4}(1+\xi)(1-\eta)(\xi-\eta-1)$	$\frac{1}{4}(1-\eta)(2\xi-\eta)$	$\frac{1}{4}(1+\xi)(2\eta-\xi)$
4	$\frac{1}{2}(1-\eta^2)(1+\xi)$	$\frac{1}{2}(1-\eta^2)$	$-\eta(1+\xi)$
5	$\frac{1}{4}(1+\xi)(1+\eta)(\xi+\eta-1)$	$\frac{1}{4}(1+\eta)(2\xi+\eta)$	$\frac{1}{4}(1+\xi)(2\eta+\xi)$
6	$\frac{1}{2}(1-\xi^2)(1+\eta)$	$-\xi(1+\eta)$	$\frac{1}{2}(1-\xi^2)$
7	$\frac{1}{4}(1-\xi)(1+\eta)(-\xi+\eta-1)$	$\frac{1}{4}(1+\eta)(2\xi-\eta)$	$\frac{1}{4}(1-\xi)(2\eta-\xi)$
8	$\frac{1}{2}(1-\eta^2)(1-\xi)$	$-\frac{1}{2}(1-\eta^2)$	$-\eta(1-\xi)$

A1.2.3. 12 Noded Membrane Element (refer to Figure (3.3c)) TABLE A6

Node i	Shape functions $N_i(\xi, \eta)$	Derivatives	
		$\partial N_i / \partial \xi$	$\partial N_i / \partial \eta$
1	$\frac{9}{32}(1-\xi)(1-\eta)[\xi^2+\eta^2-10/9]$	$\frac{9}{32}(1-\eta)[2\xi-3\xi^2-\eta^2+10/9]$	$\frac{9}{32}(1-\xi)[2\eta-3\eta^2-\xi^2+10/9]$
2	$\frac{9}{32}(1-\xi)(1-\xi^2)(1-\eta)$	$\frac{9}{32}(1-\eta)(3\xi^2-2\xi-1)$	$-\frac{9}{32}(1-\xi)(1-\xi^2)$
3	$\frac{9}{32}(1-\eta)(1-\xi^2)(1+\xi)$	$\frac{9}{32}(1-\eta)(1-2\xi-3\xi^2)$	$-\frac{9}{32}(1-\xi^2)(1+\xi)$
4	$\frac{9}{32}(1+\xi)(1-\eta)[\xi^2+\eta^2-10/9]$	$\frac{9}{32}(1-\eta)[2\xi+3\xi^2+\eta^2-10/9]$	$\frac{9}{32}(1+\xi)[2\eta-3\eta^2-\xi^2-10/9]$
5	$\frac{9}{32}(1+\xi)(1-\eta^2)(1-\eta)$	$\frac{9}{32}(1-\eta^2)(1-\eta)$	$\frac{9}{32}(1+\xi)(3\eta^2-2\eta-1)$
6	$\frac{9}{32}(1+\xi)(1-\eta^2)(1+\eta)$	$\frac{9}{32}(1-\eta^2)(1+\eta)$	$\frac{9}{32}(1+\xi)(1-2\eta-3\eta^2)$
7	$\frac{9}{32}(1+\xi)(1+\eta)[\xi^2+\eta^2-10/9]$	$\frac{9}{32}(1+\eta)[2\xi+3\xi^2+\eta^2-10/9]$	$\frac{9}{32}(1+\xi)[2\eta+3\eta^2+\xi^2-10/9]$
8	$\frac{9}{32}(1+\eta)(1-\xi^2)(1+\xi)$	$\frac{9}{32}(1+\eta)(1-2\xi-3\xi^2)$	$\frac{9}{32}(1-\xi^2)(1+\xi)$
9	$\frac{9}{32}(1+\eta)(1-\xi^2)(1-\xi)$	$\frac{9}{32}(1+\eta)(3\xi^2-3\xi-1)$	$\frac{9}{32}(1-\xi^2)(1-\xi)$
10	$\frac{9}{32}(1-\xi)(1+\eta)[\xi^2+\eta^2-10/9]$	$\frac{9}{32}(1+\eta)[2\xi-3\xi^2-\eta^2+10/9]$	$\frac{9}{32}(1-\xi)[2\eta+3\eta^2+\xi^2-10/9]$
11	$\frac{9}{32}(1-\xi)(1-\eta^2)(1+\eta)$	$-\frac{9}{32}(1+\eta)(1-\eta^2)$	$\frac{9}{32}(1-\xi)(1-2\eta-3\eta^2)$
12	$\frac{9}{32}(1-\xi)(1-\eta^2)(1-\eta)$	$-\frac{9}{32}(1-\eta)(1-\eta^2)$	$\frac{9}{32}(1-\xi)(3\eta^2-2\eta-1)$

A1.2.4. The Strain-displacement Relations

With shape functions known, the global coordinates and displacements inside the element are interpolated using Equations (A1.1) and (A1.2) where, this time, n is the number of nodes on membrane elements. Thickness may also be interpolated as :

$$t = \sum_{i=1}^n N_i t_i \quad (A1.9)$$

where t_i is the nodal thickness at node i .

Assume there is a point Q on the element with local coordinate system X', Y', Z' , as shown in Figure (3.2). U', V', W' , are the local nodal freedoms in this system. The local strain field at any point using the plane stress condition may be written as :

$$\begin{aligned} \epsilon_{x'} &= \frac{\partial u'}{\partial x'} \\ \epsilon_{y'} &= \frac{\partial v'}{\partial y'} \\ \gamma_{x'y'} &= \frac{\partial u'}{\partial y'} + \frac{\partial v'}{\partial x'} \end{aligned} \quad (A1.10)$$

The local coordinate system X', Y', Z' , is established as follows. The X' axis is tangential to the local curvilinear ξ axis, the Z' axis is normal to the plane of the element and the Y' axis is calculated such that the X', Y', Z' forms a right-handed coordinate system. The matrix algebra that follows calculates the direction cosines for this coordinate system

Vector tangential to ξ on η axes in the plane of the element is written as :

$$\underline{R}_\xi = \begin{Bmatrix} \frac{\partial x}{\partial \xi} \\ \frac{\partial y}{\partial \xi} \\ \frac{\partial z}{\partial \xi} \end{Bmatrix} ; \quad \underline{R}_\eta = \begin{Bmatrix} \frac{\partial x}{\partial \eta} \\ \frac{\partial y}{\partial \eta} \\ \frac{\partial z}{\partial \eta} \end{Bmatrix} \quad (A1.11)$$

Now form a vector normal to the plane of the above vectors :

$$\underline{R}_z = \underline{R}_\xi \times \underline{R}_\eta = \begin{bmatrix} \frac{\partial Y}{\partial \xi} \frac{\partial Z}{\partial \eta} - \frac{\partial Z}{\partial \xi} \frac{\partial Y}{\partial \eta} \\ \frac{\partial Z}{\partial \xi} \frac{\partial X}{\partial \eta} - \frac{\partial X}{\partial \xi} \frac{\partial Z}{\partial \eta} \\ \frac{\partial X}{\partial \xi} \frac{\partial Y}{\partial \eta} - \frac{\partial Y}{\partial \xi} \frac{\partial X}{\partial \eta} \end{bmatrix} \quad (\text{A1.11a})$$

The direction cosines are obtained by normalising the above vectors (Z' axis vector) :

$$\hat{R}_z = \underline{R}_z / |\underline{R}_z| \quad (\text{A1.11b})$$

Now the X' axis vector

$$\hat{R}_x = \underline{R}_\xi / |\underline{R}_\xi| \quad (\text{A1.11c})$$

Finally, the Y' axis vector, $\hat{R}_y = \hat{R}_z \times \hat{R}_x$ (A1.11d)

in which $|\underline{R}_z| = \sqrt{\left(\frac{\partial X}{\partial \xi} \frac{\partial Z}{\partial \eta} - \frac{\partial Z}{\partial \xi} \frac{\partial Y}{\partial \eta}\right)^2 + \left(\frac{\partial Z}{\partial \xi} \frac{\partial X}{\partial \eta} - \frac{\partial X}{\partial \xi} \frac{\partial Z}{\partial \eta}\right)^2 + \left(\frac{\partial X}{\partial \xi} \frac{\partial Y}{\partial \eta} - \frac{\partial Y}{\partial \xi} \frac{\partial X}{\partial \eta}\right)^2}$ (A1.11e)

$$|\underline{R}_\xi| = \sqrt{\left(\frac{\partial X}{\partial \xi}\right)^2 + \left(\frac{\partial Y}{\partial \xi}\right)^2 + \left(\frac{\partial Z}{\partial \xi}\right)^2} \quad (\text{A1.11f})$$

Therefore the direction cosines matrix for the local orthogonal Cartesian system is given as :

$$\underline{R}_{3 \times 3} = \begin{bmatrix} \hat{R}_x & \hat{R}_y & \hat{R}_z \end{bmatrix} = \begin{bmatrix} R_{x'x} & R_{y'x} & R_{z'x} \\ R_{x'y} & R_{y'y} & R_{z'y} \\ R_{x'z} & R_{y'z} & R_{z'z} \end{bmatrix} \quad (\text{A1.12})$$

In order to obtain the local derivatives of Equation (A1.10), it is necessary to apply to sets of transformations. The first one is used to obtain the global derivatives as follows :

$$\underline{d}_{3 \times 3} = \begin{bmatrix} \frac{\partial x}{\partial \xi} & \frac{\partial x}{\partial \eta} & \frac{\partial x}{\partial \zeta} \\ \frac{\partial y}{\partial \xi} & \frac{\partial y}{\partial \eta} & \frac{\partial y}{\partial \zeta} \\ \frac{\partial z}{\partial \xi} & \frac{\partial z}{\partial \eta} & \frac{\partial z}{\partial \zeta} \end{bmatrix} = \underline{J}^{-1} \begin{bmatrix} \frac{\partial \xi}{\partial x} & \frac{\partial \xi}{\partial y} & \frac{\partial \xi}{\partial z} \\ \frac{\partial \eta}{\partial x} & \frac{\partial \eta}{\partial y} & \frac{\partial \eta}{\partial z} \\ 0 & 0 & 0 \end{bmatrix} \quad (\text{A1.13})$$

where

$$\tilde{J}_{3 \times 3}^T = \begin{bmatrix} \frac{\partial x}{\partial \xi} & \frac{\partial x}{\partial \eta} & R_{z'x't} \\ \frac{\partial y}{\partial \xi} & \frac{\partial y}{\partial \eta} & R_{z'y't} \\ \frac{\partial z}{\partial \xi} & \frac{\partial z}{\partial \eta} & R_{z'z't} \end{bmatrix} \quad (A1.14)$$

Since the third curvilinear coordinate does not exist in this case, it is therefore essential to substitute a thickness vector (which is normal to the middle surface) in the third column of Equation (A1.14) (see reference (6)). From this, the inverse of the 3x3 Jacobian matrix may be calculated.

Now the second transformation is used to get the local derivatives as follows :

$$\underline{d}' = \tilde{R}^T \underline{d} \tilde{R} \quad (A1.15)$$

in which

$$\underline{d}' = \begin{bmatrix} \frac{\partial u'}{\partial x'} & \frac{\partial v'}{\partial x'} & \frac{\partial w'}{\partial x'} \\ \frac{\partial u'}{\partial y'} & \frac{\partial v'}{\partial y'} & \frac{\partial w'}{\partial y'} \\ \frac{\partial u'}{\partial z'} & \frac{\partial v'}{\partial z'} & \frac{\partial w'}{\partial z'} \end{bmatrix} \quad (A1.16)$$

After carrying out the multiplication in Equation (A1.15) and also making use of Equations (A1.1) and (A1.9), the following is obtained :

$$\begin{bmatrix} \frac{\partial u'}{\partial x'} & \frac{\partial v'}{\partial x'} & \frac{\partial w'}{\partial x'} \\ \frac{\partial u'}{\partial y'} & \frac{\partial v'}{\partial y'} & \frac{\partial w'}{\partial y'} \\ \frac{\partial u'}{\partial z'} & \frac{\partial v'}{\partial z'} & \frac{\partial w'}{\partial z'} \end{bmatrix} = \sum_{i=1}^n \begin{bmatrix} d\dot{r}_1 d\dot{u}_1 & d\dot{r}_1 d\dot{u}_2 & d\dot{r}_1 d\dot{u}_3 \\ d\dot{r}_2 d\dot{u}_1 & d\dot{r}_2 d\dot{u}_2 & d\dot{r}_2 d\dot{u}_3 \\ d\dot{r}_3 d\dot{u}_1 & d\dot{r}_3 d\dot{u}_2 & d\dot{r}_3 d\dot{u}_3 \end{bmatrix} \quad (A1.17)$$

in which n = number of nodes on element

$$\begin{aligned} d\dot{r}_1 &= R_{x'x} \frac{\partial N_i}{\partial x} + R_{x'y} \frac{\partial N_i}{\partial y} + R_{x'z} \frac{\partial N_i}{\partial z} \\ d\dot{r}_2 &= R_{y'x} \frac{\partial N_i}{\partial x} + R_{y'y} \frac{\partial N_i}{\partial y} + R_{y'z} \frac{\partial N_i}{\partial z} \\ d\dot{r}_3 &= R_{z'x} \frac{\partial N_i}{\partial x} + R_{z'y} \frac{\partial N_i}{\partial y} + R_{z'z} \frac{\partial N_i}{\partial z} \end{aligned} \quad (A1.18)$$

and

$$\begin{aligned}
d\dot{u}_1 &= R_{x'x} U_i + R_{x'y} V_i + R_{x'z} W_i \\
d\dot{u}_2 &= R_{y'x} U_i + R_{y'y} V_i + R_{y'z} W_i \\
d\dot{u}_3 &= R_{z'x} U_i + R_{z'y} V_i + R_{z'z} W_i
\end{aligned}
\tag{A1.19}$$

Now from Equations (A1.10) and (A1.17)

$$\underline{\underline{\epsilon}}' = \sum_{i=1}^n \left[\begin{array}{c} d\dot{r}_1 d\dot{u}_1 \\ d\dot{r}_2 d\dot{u}_2 \\ d\dot{r}_2 d\dot{u}_1 + d\dot{r}_1 d\dot{u}_2 \end{array} \right] = \underline{\underline{B}} \underline{\underline{u}}^e
\tag{A1.20}$$

where $\underline{\underline{B}} = [\underline{\underline{B}}_1, \underline{\underline{B}}_2, \underline{\underline{B}}_3, \dots, \underline{\underline{B}}_i, \dots, \underline{\underline{B}}_n]$ (A1.21)

is the local strain-displacement matrix, and

$$\underline{\underline{u}}^e = [\underline{\underline{u}}_1, \underline{\underline{u}}_2, \underline{\underline{u}}_3, \dots, \underline{\underline{u}}_i, \dots, \underline{\underline{u}}_n]^T
\tag{A1.22}$$

is the global nodal displacement vector. For node i , $\underline{\underline{B}}_i$ and $\underline{\underline{u}}_i$ are now written as :

$$\underline{\underline{B}}_i = \begin{bmatrix} R_{x'x} d\dot{r}_1 & , & R_{x'y} d\dot{r}_1 & , & R_{x'z} d\dot{r}_1 \\ R_{y'x} d\dot{r}_2 & , & R_{y'y} d\dot{r}_2 & , & R_{y'z} d\dot{r}_2 \\ (R_{x'x} d\dot{r}_2 + R_{y'x} d\dot{r}_1), & (R_{x'y} d\dot{r}_2 + R_{y'y} d\dot{r}_1), & (R_{x'z} d\dot{r}_2 + R_{y'z} d\dot{r}_1) \end{bmatrix}
\tag{A1.23}$$

and $\underline{\underline{u}}_i = [U_i, V_i, W_i]^T$ (A1.24)

A1.3. Line Elements

A1.3.1. The Element Stiffness Matrix for 2 Noded Line Element (Figure (3.3a))

$$\underset{\sim}{K}^e = \frac{E_s A}{L} \begin{bmatrix} l_1^2 & l_1 m_1 & l_1 n_1 & -l_1^2 & -l_1 m_1 & -l_1 n_1 \\ l_1 m_1 & m_1^2 & m_1 n_1 & -l_1 m_1 & -m_1^2 & -m_1 n_1 \\ l_1 n_1 & m_1 n_1 & n_1^2 & -l_1 n_1 & -m_1 n_1 & -n_1^2 \\ -l_1^2 & -l_1 m_1 & -l_1 n_1 & l_1^2 & l_1 m_1 & l_1 n_1 \\ -l_1 m_1 & -m_1^2 & -m_1 n_1 & l_1 m_1 & m_1^2 & m_1 n_1 \\ -l_1 n_1 & -m_1 n_1 & -n_1^2 & l_1 n_1 & m_1 n_1 & n_1^2 \end{bmatrix} \quad (A1.25)$$

where

$$\begin{aligned}
 L &= \sqrt{(x_2 - x_1)^2 + (y_2 - y_1)^2 + (z_2 - z_1)^2} \\
 l_1 &= \frac{x_2 - x_1}{L} \\
 m_1 &= \frac{y_2 - y_1}{L} \\
 n_1 &= \frac{z_2 - z_1}{L}
 \end{aligned} \quad (A1.25a)$$

and E_s and A are the modulus of elasticity and cross-sectional area of the line element respectively.

A1.3.2. Isoparametric Line Elements

The shape functions and derivatives for the isoparametric line elements are given in the following :

(a) 2 noded line element (Figure (3.3a))

Shape functions	Derivatives	
$N_1 = \frac{1}{2}(1 - \xi)$	$\frac{\partial N_1}{\partial \xi} = -\frac{1}{2}$	(A1.26)
$N_2 = \frac{1}{2}(1 + \xi)$	$\frac{\partial N_2}{\partial \xi} = \frac{1}{2}$	

(b) 3 noded line element (Figure (3.3b))

Shape functions	Derivatives	
$N_1 = \frac{1}{2}(\xi - 1)\xi$	$\frac{\partial N_1}{\partial \xi} = \xi - \frac{1}{2}$	(A1.26a)
$N_2 = 1 - \xi^2$	$\frac{\partial N_2}{\partial \xi} = 2\xi$	
$N_3 = \frac{1}{2}(\xi + 1)\xi$	$\frac{\partial N_3}{\partial \xi} = \xi + \frac{1}{2}$	

(c) 4 noded line element (Figure (3.3c))

Shape functions	Derivatives	
$N_1 = \frac{1}{3}(1 - \xi)(2\xi^2 - \frac{1}{2})$	$\frac{\partial N_1}{\partial \xi} = \frac{1}{3}(4\xi - 6\xi^2 + \frac{1}{2})$	(A1.26b)
$N_2 = \frac{4}{3}(\xi^2 - 1)(\xi - \frac{1}{2})$	$\frac{\partial N_2}{\partial \xi} = \frac{4}{3}(3\xi^2 - \xi - 1)$	
$N_3 = \frac{4}{3}(1 - \xi^2)(\xi + \frac{1}{2})$	$\frac{\partial N_3}{\partial \xi} = \frac{4}{3}(1 - 3\xi^2 - \xi)$	
$N_4 = \frac{1}{3}(1 + \xi)(2\xi^2 - \frac{1}{2})$	$\frac{\partial N_4}{\partial \xi} = \frac{1}{3}(4\xi + 6\xi^2 - \frac{1}{2})$	

A1.3.3. The Strain-displacement Relation

At any point in the element local Cartesian axis X' tangential to the curvilinear ξ axis can be established. The local strain (only axial) at any point inside the element can be written as :

$$\epsilon_{x'} = \frac{\partial u'}{\partial x'} \quad (A1.27)$$

with the displacement transformation, Equation (A1.27) may be written as :

$$\epsilon_{x'} = \frac{1}{L} \left(l_1 \frac{\partial u}{\partial \xi} + m_1 \frac{\partial v}{\partial \xi} + n_1 \frac{\partial w}{\partial \xi} \right) \quad (A1.27a)$$

where l_1, m_1, n_1 are the direction cosines of the X' axis and can be written as :

$$l_1 = \frac{\partial x}{\partial \xi} / L$$

$$m_1 = \frac{\partial y}{\partial \xi} / L \quad (A1.27b)$$

$$n_1 = \frac{\partial z}{\partial \xi} / L$$

and

$$L = \sqrt{(\partial x / \partial \xi)^2 + (\partial y / \partial \xi)^2 + (\partial z / \partial \xi)^2} \quad (A1.27c)$$

$U, V,$ and W are the global nodal freedoms at any node and U' the local freedom in the X' direction. These are related by

$$U' = l_1 U + m_1 V + n_1 W \quad (A1.27d)$$

Equation (A1.27) can be written in terms of the shape function derivatives as :

$$\epsilon_{x'} = \frac{1}{L} \sum_{i=1}^n \left[l_1 \frac{\partial N_i}{\partial \xi}, m_1 \frac{\partial N_i}{\partial \xi}, n_1 \frac{\partial N_i}{\partial \xi} \right] \begin{Bmatrix} U_i \\ V_i \\ W_i \end{Bmatrix} \quad (A1.27e)$$

where n is the number of nodes on the element, or

$$\epsilon_{x'} = \underline{B} \underline{U}^e \quad (A1.28)$$

where $\underline{\underline{B}} = [\underline{\underline{B}}_1, \underline{\underline{B}}_2, \underline{\underline{B}}_3 \text{-----} \underline{\underline{B}}_i \text{-----} \underline{\underline{B}}_n]$ (A1.28a)

$$\underline{\underline{u}}^e = [\underline{\underline{u}}_1, \underline{\underline{u}}_2, \underline{\underline{u}}_3 \text{-----} \underline{\underline{u}}_i \text{-----} \underline{\underline{u}}_n]$$
 (A1.28b)

For node i

$$\underline{\underline{B}}_i = \frac{1}{L} [\ell_i \frac{\partial N_i}{\partial \xi}, m_i \frac{\partial N_i}{\partial \xi}, n_i \frac{\partial N_i}{\partial \xi}]$$
 (A1.28c)

and $\underline{\underline{u}}_i = [u_i, v_i, w_i]^T$ (A1.28d)

Therefore, the strain-displacement matrix $\underline{\underline{B}}$ (Equation (A1.28a)) is now fully defined.

A1.4. Line Element in the Body of Solid Element (Figure (3.4))

This element is useful in situations where reinforcement and prestressed steel is spread closely together in various parts of the concrete. Here, the strain-displacement relation is given in detail. The rest of the procedure leading to the stiffness matrix follows the same principle as described in Chapter 3 for isoparametric elements.

The main assumption made in this section is that the line element lies parallel to one of the curvilinear axis (ξ, η, ζ) of the parent solid element. The element may be anywhere in the solid element with maximum curvilinear coordinates $\xi = \pm 1$, $\eta = \pm 1$ and $\zeta = \pm 1$. The element uses the shape functions of the parent solid element assuming two constant curvilinear coordinates. When the element has parallel to ξ axis (see Figure (3.4)), the displacement vector inside the element can be written as :

$$\underline{u} = \underline{N}(\xi, \eta_c, \zeta_c) \underline{u}^e = \sum_{i=1}^n N_i \underline{I}_n \underline{u}_i \quad (\text{A1.29})$$

where $\underline{N}(\xi, \eta_c, \zeta_c)$ is the shape function matrix of the solid element using $\zeta = \zeta_c$, $\eta = \eta_c$ (constant). A similar expression may be written for the global coordinates. A local coordinate system X', Y', Z' , as shown in Figure (3.4) is first established. This is done as follows. Write two base vectors in the tangential direction of ξ and η

$$\underline{x}_\xi = \begin{Bmatrix} \frac{\partial x}{\partial \xi} \\ \frac{\partial y}{\partial \xi} \\ \frac{\partial z}{\partial \xi} \end{Bmatrix} \quad \underline{x}_\eta = \begin{Bmatrix} \frac{\partial x}{\partial \eta} \\ \frac{\partial y}{\partial \eta} \\ \frac{\partial z}{\partial \eta} \end{Bmatrix} \quad \text{at } \eta = \eta_c, \zeta = \zeta_c \quad (\text{A1.30})$$

A normal Z' axis vector, X' axis and Y' axis vectors are defined as

$$\underline{z}' = (\underline{x}_\xi \times \underline{x}_\eta) / |\underline{x}_\xi \times \underline{x}_\eta| \quad (\text{A1.31})$$

$$\underline{x}' = \underline{x}_\xi / |\underline{x}_\xi| \quad (\text{A1.31a})$$

$$\underline{y}' = \underline{z}' \times \underline{x}' \quad (\text{A1.31b})$$

$$\underline{R}_{3 \times 3} = [\underline{x}', \underline{y}', \underline{z}'] = \begin{bmatrix} l_1 & l_2 & l_3 \\ m_1 & m_2 & m_3 \\ n_1 & n_2 & n_3 \end{bmatrix} \quad (\text{A1.31c})$$

The local strains which contribute to the strain energy are :

$$\epsilon_{x'} = \frac{\partial u'}{\partial x'} \quad (A1.32)$$

with U' being the local axial displacement in the direction of X' axis. In this case again similar to that for the membrane elements (Appendix A1.2.), two derivative transformations are carried out :

$$\underset{3 \times 3}{\tilde{d}} = \begin{bmatrix} \frac{\partial u}{\partial x} & \frac{\partial v}{\partial x} & \frac{\partial w}{\partial x} \\ \frac{\partial u}{\partial y} & \frac{\partial v}{\partial y} & \frac{\partial w}{\partial y} \\ \frac{\partial u}{\partial z} & \frac{\partial v}{\partial z} & \frac{\partial w}{\partial z} \end{bmatrix} = \sum_{i=1}^n \left(\begin{matrix} \left[\frac{\partial N_i}{\partial x} \right]_{3 \times 1} \\ \left[\frac{\partial N_i}{\partial y} \right]_{3 \times 1} \\ \left[\frac{\partial N_i}{\partial z} \right]_{3 \times 1} \end{matrix} \begin{matrix} [u_i, v_i, w_i]_{1 \times 3} \end{matrix} \right) \quad (A1.33)$$

Now using Equations (A1.3a) and (A1.4) the following can be written :

$$\underset{3 \times 3}{\tilde{d}} = \sum_{i=1}^n \left(\begin{matrix} [U_i^{-1}]_{3 \times 1} \\ \left[\frac{\partial N_i}{\partial x} \right]_{3 \times 1} \\ \left[\frac{\partial N_i}{\partial y} \right]_{3 \times 1} \\ \left[\frac{\partial N_i}{\partial z} \right]_{3 \times 1} \end{matrix} \begin{matrix} [u_i, v_i, w_i]_{1 \times 3} \end{matrix} \right) \quad (A1.33a)$$

where n is the number of nodes on the solid element and U_i, V_i, W_i , are the global freedoms at node i .

Now write the following :

$$\underset{3 \times 3}{d'} = \underset{3 \times 3}{R}^T \underset{3 \times 3}{\tilde{d}} \underset{3 \times 3}{R} \quad (A1.34)$$

where

$$\underset{3 \times 3}{d'} = \begin{bmatrix} \frac{\partial u'}{\partial x'} & \frac{\partial v'}{\partial x'} & \frac{\partial w'}{\partial x'} \\ \frac{\partial u'}{\partial y'} & \frac{\partial v'}{\partial y'} & \frac{\partial w'}{\partial y'} \\ \frac{\partial u'}{\partial z'} & \frac{\partial v'}{\partial z'} & \frac{\partial w'}{\partial z'} \end{bmatrix} \quad (A1.34a)$$

Substitute Equations (A1.31c) and (A1.33a) into (A1.34) and carry out the multiplication and picking out the relevant strains, one obtains :

$$\epsilon_{x'} = \frac{\partial u'}{\partial x'} = \sum_{i=1}^n (\ell_1 s_1 u_i + m_1 s_1 v_i + n_1 s_1 w_i) = \underset{1 \times n}{B} \underset{n \times 1}{U}^e \quad (A1.35)$$

with

$$\underline{B} = [\underline{B}_1, \underline{B}_2, \underline{B}_3 \text{-----} \underline{B}_i \text{-----} \underline{B}_n]^T \quad (A1.36)$$

$$\underline{u}^e = [\underline{u}_1, \underline{u}_2, \underline{u}_3 \text{-----} \underline{u}_i \text{-----} \underline{u}_n]^T \quad (A1.36a)$$

For node i

$$\underline{B}_i = [l_1 s_1, m_1 s_1, n_1 s_1] \quad (A1.37)$$

$$\underline{u}_i = [u_i, v_i, w_i]^T \quad (A1.37a)$$

with

$$s_1 = l_1 \frac{\partial N_i}{\partial x} + m_1 \frac{\partial N_i}{\partial y} + n_1 \frac{\partial N_i}{\partial z} \quad (A1.38)$$

Therefore Equation (A1.36) is fully defined.

The stress is now given by :

$$\sigma_{x'} = E_s \epsilon_{x'} \quad (A1.39)$$

A1.5. Bond-linkage Stiffness Matrix

The explicit form of the bond-linkage stiffness is given below :

$$\underset{6 \times 6}{\tilde{K}_b} = \begin{bmatrix} \underset{\sim}{K}_{b11} & \underset{\sim}{K}_{b12} \\ \underset{\sim}{K}_{b21} & \underset{\sim}{K}_{b22} \end{bmatrix} \quad (A1.40)$$

where

$$\begin{aligned} K_{b12} &= \underset{\sim}{K}_{b21} = -K_{b11} \\ K_{b22} &= K_{b11} \end{aligned} \quad (A1.40a)$$

$$\underset{3 \times 3}{\tilde{K}_{b11}} = \begin{bmatrix} K_{b11} & K_{b12} & K_{b13} \\ & K_{b22} & K_{b22} \\ \text{SYM.} & & K_{b33} \end{bmatrix}$$

$$\begin{aligned} K_{b11} &= \pi dL (l^2 E_h + p^2 E_v + r^2 E_e) \\ K_{b22} &= \pi dL (m^2 E_h + q^2 E_v + s^2 E_e) \\ K_{b33} &= \pi dL (n^2 E_h + t^2 E_v) \\ K_{b12} &= \pi dL (lm E_h + pq E_v + rs E_e) \\ K_{b13} &= \pi dL (ln E_h + rt E_v) \\ K_{b23} &= \pi dL (mn E_h + st E_e) \end{aligned} \quad (A1.40b)$$

$\left. \begin{array}{l} l, m, n \\ p, q, r \\ s, t \end{array} \right\}$ - direction cosines

πdL - perimeter of the steel

APPENDIX A2

A2. Anisotropic Material Matrix

$$[D] = \begin{bmatrix} D_{11} & D_{12} & D_{13} & 0 & 0 & 0 \\ D_{21} & D_{22} & D_{23} & 0 & 0 & 0 \\ D_{31} & D_{32} & D_{33} & 0 & 0 & 0 \\ 0 & 0 & 0 & D_{44} & 0 & 0 \\ 0 & 0 & 0 & 0 & D_{55} & 0 \\ 0 & 0 & 0 & 0 & 0 & D_{66} \end{bmatrix} \quad (A2.1)$$

where

$$D_{11} = (1 - \nu_{23}\nu_{32})E_1/\nu_K$$

$$D_{22} = (1 - \nu_{13}\nu_{31})E_2/\nu_K$$

$$D_{33} = (1 - \nu_{12}\nu_{21})E_2/\nu_K$$

$$D_{12} = (\nu_{12} + \nu_{13}\nu_{32})E_2/\nu_K$$

$$D_{21} = (\nu_{21} + \nu_{23}\nu_{31})E_1/\nu_K$$

$$D_{13} = (\nu_{13} + \nu_{12}\nu_{23})E_3/\nu_K$$

$$D_{31} = (\nu_{31} + \nu_{21}\nu_{32})E_1/\nu_K$$

$$D_{23} = (\nu_{23} + \nu_{13}\nu_{21})E_3/\nu_K$$

$$D_{32} = (\nu_{32} + \nu_{31}\nu_{12})E_2/\nu_K$$

$$D_{44} = G_{12}$$

(A2.2)

$$D_{55} = G_{23}$$

$$D_{66} = G_{13}$$

$$\nu_K = 1 - \nu_{12}\nu_{21} - \nu_{13}\nu_{31} - \nu_{23}\nu_{32} - \nu_{12}\nu_{23}\nu_{31} - \nu_{21}\nu_{13}\nu_{32}$$

Due to symmetry of compliances, the following relations can be written :

$$E_1\nu_{21} = E_2\nu_{12}$$

$$E_2\nu_{32} = E_3\nu_{23} \tag{A2.3}$$

$$E_3\nu_{13} = E_1\nu_{31}$$

The values of G_{12} , G_{23} and G_{13} are calculated in terms of modulus of elasticity and Poisson's ratio as follows :

$$\begin{aligned} G_{12} &= \frac{1}{2} \left[\frac{E_1}{2(1+\nu_{12})} + \frac{E_2}{2(1+\nu_{21})} \right] \\ &= \frac{1}{2} \left[\frac{E_1}{2(1+\nu_{12})} + \frac{E_1}{2\left(\frac{E_1}{E_2} + \nu_{12}\right)} \right] \\ G_{23} &= \frac{1}{2} \left[\frac{E_2}{2(1+\nu_{23})} + \frac{E_3}{2(1+\nu_{32})} \right] \\ &= \frac{1}{2} \left[\frac{E_2}{2(1+\nu_{23})} + \frac{E_2}{2\left(\frac{E_2}{E_3} + \nu_{23}\right)} \right] \\ G_{13} &= \frac{1}{2} \left[\frac{E_3}{2(1+\nu_{31})} + \frac{E_1}{2(1+\nu_{13})} \right] \\ &= \left[\frac{E_3}{2(1+\nu_{31})} + \frac{E_3}{2\left(\frac{E_3}{E_1} + \nu_{31}\right)} \right] \end{aligned} \tag{A2.4}$$

For isotropic case :

$$E_1 = E_2 = E_3 = E$$

$$\nu_{12} = \nu_{13} = \nu_{23} = \nu_{21} = \nu_{31} = \nu_{32} = \nu$$

APPENDIX A3

A3 Inclined or Skew Boundary Supports (Figure 3.6))

It is sometimes necessary to suppress nodal freedoms of the structure in the directions other than the global X, Y, Z, axes. Such situations normally occur when analysing a wedge of a reactor vessel or its end slab. This can be accomplished by transforming the freedoms of those nodes which have skew boundary supports in the local directions. The transformations are performed at the element level or at the global level. The following gives the details of the transformation.

Inclined supports are shown in Figure (3.6). Assume that ith node has inclined support and θ is the inclination between global and local X axes. The transformation between local and global displacements at node i can be written as :

$$\begin{Bmatrix} u'_i \\ v'_i \\ w'_i \end{Bmatrix} = \begin{bmatrix} \cos\theta & \sin\theta & 0 \\ -\sin\theta & \cos\theta & 0 \\ 0 & 0 & 1 \end{bmatrix} \begin{Bmatrix} u_i \\ v_i \\ w_i \end{Bmatrix} \quad (\text{A3.1})$$

or

$$\underline{u}'_i = \underline{L}_I \underline{u}_i$$

Element transformation matrix, \underline{I} , is given by :

$$\underline{I} = \begin{bmatrix} \underline{I} & 0 & 0 & 0 & 0 \\ & \underline{I} & 0 & 0 & 0 \\ & & \underline{I} & 0 & 0 \\ \text{SYM.} & & & \underline{L}_I & 0 \\ & & & & \underline{I} \end{bmatrix} \quad (\text{A3.2})$$

Where prime quantities refer to the local coordinate system and \underline{I} is a 3x3 identity matrix, local and global load-displacement relations are written as :

$$\underline{K}' \underline{u}' = \underline{P}' \quad (\text{A3.3})$$

$$\underline{K} \underline{u} = \underline{P} \quad (\text{A3.4})$$

Local and global load and displacement transformations can be written as :

$$\begin{aligned} \underline{u}' &= \underline{T} \underline{u} & ; & & \underline{u} &= \underline{T}^T \underline{u}' \\ \underline{p}' &= \underline{T} \underline{p} & ; & & \underline{p} &= \underline{T}^T \underline{p}' \end{aligned} \quad (A3.5)$$

From the well known transformation

$$\underline{K}' = \underline{T} \underline{K} \underline{T}^T \quad (A3.6)$$

Where \underline{K} in Equation (A3.6) may be element or global stiffness matrix.

Upon expanding Equation (A3.6), one obtains :

$$\begin{array}{c} \begin{array}{|c|} \hline i \\ \hline \end{array} \begin{array}{|c|} \hline \underline{K}_{11}, \underline{K}_{12}, \underline{K}_{13}, \dots \\ \hline \end{array} \begin{array}{|c|} \hline \underline{K}_{21}, \underline{K}_{22}, \underline{K}_{23}, \dots \\ \hline \end{array} \begin{array}{|c|} \hline \dots \\ \hline \end{array} \begin{array}{|c|} \hline \underline{K}_{in} \\ \hline \end{array} \\ \hline \begin{array}{|c|} \hline \underline{L}_i^T \underline{K}_{i1}, \underline{L}_i^T \underline{K}_{i2}, \dots \\ \hline \end{array} \begin{array}{|c|} \hline \underline{L}_i^T \underline{K}_{ii} \underline{L}_i \\ \hline \end{array} \begin{array}{|c|} \hline \dots \\ \hline \end{array} \begin{array}{|c|} \hline \underline{L}_i^T \underline{K}_{in} \\ \hline \end{array} \\ \hline \begin{array}{|c|} \hline \underline{K}_{n1}, \underline{K}_{n2}, \dots \\ \hline \end{array} \begin{array}{|c|} \hline \underline{K}_{ni} \underline{L}_i^T \\ \hline \end{array} \begin{array}{|c|} \hline \dots \\ \hline \end{array} \begin{array}{|c|} \hline \underline{K}_{nn} \\ \hline \end{array} \end{array} \begin{array}{|c|} \hline \underline{u}_1 \\ \hline \underline{u}_2 \\ \hline \dots \\ \hline \underline{u}_i \\ \hline \dots \\ \hline \underline{u}_n \end{array} = \begin{array}{|c|} \hline \underline{p}_1 \\ \hline \underline{p}_2 \\ \hline \dots \\ \hline \underline{p}_i \\ \hline \dots \\ \hline \underline{p}_n \end{array} \quad (A3.7)$$

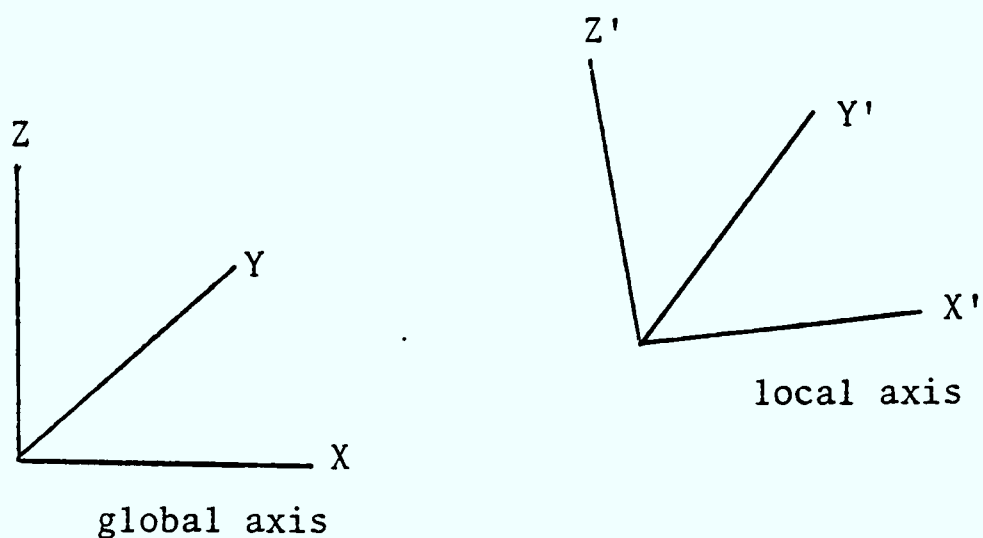
Therefore, any node which has inclined support, the equations of this node should be premultiplied by transformation matrix \underline{L}_i ; in addition to that the diagonal term should be post-multiplied by \underline{L}_i^T as given in Equation (A3.7).

Displacements calculated from equilibrium equations at i th nodes are in inclined directions. These should be transformed in global direction before stresses are calculated. The following transformation is used :

$$\underline{u}_i = \underline{L}_i^T \underline{u}'_i \quad (A3.8)$$

APPENDIX A4

A4. Stress and Strain Transformation Matrices (\underline{T}_σ , \underline{T}_ϵ)



	X	Y	Z
X'	l_1	m_1	n_1
Y'	l_2	m_2	n_2
Z'	l_3	m_3	n_3

Direction cosines of the two axes are given by :

$$\begin{aligned}
 l_1 &= \cos(X', X) & m_1 &= \cos(X', Y) & n_1 &= \cos(X', Z) \\
 l_2 &= \cos(Y', X) & m_2 &= \cos(Y', Y) & n_2 &= \cos(Y', Z) \\
 l_3 &= \cos(Z', X) & m_3 &= \cos(Z', Y) & n_3 &= \cos(Z', Z)
 \end{aligned} \tag{A4.1}$$

The following relationships can be written for local and global strain and stress vectors :

$$\begin{aligned}
 \underline{\epsilon}'_x &= \underline{T}_\epsilon \underline{\epsilon}_x \\
 \underline{\sigma}'_x &= \underline{T}_\sigma^T \underline{\sigma}_x
 \end{aligned} \tag{A4.2}$$

and also

$$\begin{aligned}
 \underline{\sigma}'_x &= \underline{T}_\sigma \underline{\sigma}_x \\
 \underline{\epsilon}_x &= \underline{T}_\epsilon^T \underline{\epsilon}'_x
 \end{aligned}$$

Where prime quantities refer to local axis, and 'T' is the transpose of the matrix. \underline{T}_ϵ , \underline{T}_σ refer to transformation for strain and stress respectively.

$$[\underline{T}_\sigma] = \begin{bmatrix} l_1^2 & m_1^2 & n_1^2 & l_1 m_1 & m_1 n_1 & l_1 n_1 \\ l_2^2 & m_2^2 & n_2^2 & l_2 m_2 & m_2 n_2 & l_2 n_2 \\ l_3^2 & m_3^2 & n_3^2 & l_3 m_3 & m_3 n_3 & l_3 n_3 \\ 2l_1 l_2 & 2m_1 m_2 & 2n_1 n_2 & l_1 m_2 + l_2 m_1 & m_1 n_2 + m_2 n_1 & l_1 n_2 + l_2 n_1 \\ 2l_2 l_3 & 2m_2 m_3 & 2n_2 n_3 & l_2 m_3 + l_3 m_2 & m_2 n_3 + m_3 n_2 & l_2 n_3 + l_3 n_2 \\ 2l_1 l_3 & 2m_1 m_3 & 2n_1 n_3 & l_1 m_3 + m_1 l_3 & m_1 n_3 + m_3 n_1 & l_1 n_3 + n_1 l_3 \end{bmatrix} \quad (A4.3)$$

$$[\underline{T}_\epsilon] = \begin{bmatrix} l_1^2 & m_1^2 & n_1^2 & 2l_1 m_1 & 2m_1 n_1 & 2l_1 n_1 \\ l_2^2 & m_2^2 & n_2^2 & 2l_2 m_2 & 2m_2 n_2 & 2l_2 n_2 \\ l_3^2 & m_3^2 & n_3^2 & 2l_3 m_3 & 2m_3 n_3 & 2l_3 n_3 \\ l_1 l_2 & m_1 m_2 & n_1 n_2 & l_1 m_2 + l_2 m_1 & m_1 n_2 + n_1 m_2 & l_1 n_2 + l_2 n_1 \\ l_2 l_3 & m_2 m_3 & n_2 n_3 & l_2 m_3 + l_3 m_2 & m_2 n_3 + n_2 m_3 & l_2 n_3 + l_3 n_2 \\ l_1 l_3 & m_1 m_3 & n_1 n_3 & l_1 m_3 + l_3 m_1 & m_1 n_3 + m_3 n_1 & l_1 n_3 + n_1 l_3 \end{bmatrix} \quad (A4.4)$$

APPENDIX A5

A5.1. Shear and Bulk Moduli Approach

In this section, a review of the material constitutive relation based on shear and bulk modulus is presented. According to this approach, concrete in a three-dimensional state of stress is considered as statically isotropic material in compression. For a moderate compression, a linear constitutive law is used. For higher compressive stresses, a non-linear stress-strain relationship is introduced. The non-linear behaviour of concrete is described by a variable shear modulus, G , expressed as a function of the second stress invariant, J_2 . The bulk modulus, K , is assumed to remain constant. This means that the volumetric dilatancy is ignored, as this effect only appears very near to failure.

A5.1.1. Constitutive Relations

The constitutive relations for concrete are written in incremental form as :

$$\Delta\sigma_m = 3K \Delta\varepsilon_m \quad (A5.1)$$

and

$$S_{ij} = 2G \Delta\varepsilon_{dij} \quad (A5.2)$$

where

$$\Delta\sigma_{ij} = \Delta S_{ij} + \delta_{ij} \Delta\sigma_m \quad (A5.3)$$

S_{ij} = deviatoric stress increment

$\Delta\sigma_m = (\Delta\sigma_{11} + \Delta\sigma_{22} + \Delta\sigma_{33})/3$ - hydrostatic stress (volumetric)

$\Delta\varepsilon_m = (\Delta\varepsilon_{11} + \Delta\varepsilon_{22} + \Delta\varepsilon_{33})/3$ - hydrostatic strain

$\Delta\varepsilon_{dij} = \Delta\varepsilon_{ij} - \delta_{ij} \Delta\varepsilon_m$ - deviatoric strain increment

δ_{ij} - Kronecker Delta (=1 for $i=j$, zero otherwise)

For numerical calculation, Equation (A5.3) is put in matrix form as :

$$\begin{bmatrix} \Delta \sigma_x \\ \Delta \sigma_y \\ \Delta \sigma_z \\ \Delta \tau_{xy} \\ \Delta \tau_{yz} \\ \Delta \tau_{zx} \end{bmatrix} = \begin{bmatrix} (K + \frac{4}{3}G), (K - \frac{2}{3}G), (K - \frac{2}{3}G), 0 & 0 & 0 \\ & (K + \frac{4}{3}G), (K - \frac{2}{3}G) & 0 & 0 & 0 \\ & & (K + \frac{4}{3}G) & 0 & 0 & 0 \\ & & & G & 0 & 0 \\ \text{SYM.} & & & & G & 0 \\ & & & & & G \end{bmatrix} \begin{bmatrix} \Delta \epsilon_x \\ \Delta \epsilon_y \\ \Delta \epsilon_z \\ \Delta \gamma_{xy} \\ \Delta \gamma_{yz} \\ \Delta \gamma_{zx} \end{bmatrix} \quad (A5.4)$$

or in short

$$\Delta \underline{\sigma} = \underline{D}_T \Delta \underline{\epsilon} \quad (A5.4)$$

where \underline{D}_T is the tangent material matrix as given in Equation (A5.4).

During loading of the structure, the shear modulus of Equation (A5.4) is assumed to vary as a logarithmic function of the second stress invariant and is expressed as follows :

$$G = G_e - \alpha \text{Log} e \frac{J_2}{J_2^e} \quad \text{for } J_2 > J_2^e \quad (A5.5)$$

$$G = G_e \quad \text{for } J_2 \leq J_2^e \quad (A5.6)$$

and $K = K_e$ - constant throughout

$$\text{where } G_e = \frac{E}{2(1+\nu)} \quad - \text{ linear-elastic shear modulus} \quad (A5.7)$$

$$K_e = \frac{E}{3(1-2\nu)} \quad - \text{ linear-elastic bulk modulus} \quad (A5.8)$$

$$J_2 = \frac{1}{2}(S_x^2 + S_y^2 + S_z^2) + \tau_{xy}^2 + \tau_{yz}^2 + \tau_{zx}^2 \quad (A5.9)$$

- second stress invariant

$$S_x = \sigma_x - \sigma_m ; \quad S_y = \sigma_y - \sigma_m ; \quad S_z = \sigma_z - \sigma_m \quad (A5.10)$$

J_2^e - limit of linearity

$$= \frac{1}{3} \sigma_c \quad (\sigma_c - \text{uniaxial compressive cylinder strength}) \quad (A5.11)$$

α is the material constant and it is determined based on the experimental data. If no experimental data is available for concrete, it is suggested that an approximate value of α is calculated using the following method :

Write a uniaxial stress-strain relationship in terms of bulk modulus, K and G, as :

$$\epsilon_u = \frac{\sigma_u}{3} \left\{ \frac{1}{3K_e} - \frac{1}{G} \right\} \quad (A5.12)$$

where K_e is defined as above. Now formulate Equation (A5.12) for rupture, that is, set $\sigma_u =$ uniaxial compressive strength and $\epsilon_u = 0.002$ to 0.003 . Therefore, G, for rupture, can be calculated using Equation (A5.12). Substitute this value of G into Equation (A5.5) from where α can be determined. Therefore the constitutive matrix (A5.4) is completely defined.

Some non-linear relations used to define Equation (A5.5) are plotted in Figure (4.15a, b, c and d). It can be seen that the variation of E, ν , G, is non-linear with stress-invariant and Equation (A5.5) reproduces a uniaxial non-linear stress curve for concrete.

APPENDIX A6

A6.1. Concrete Model based on the Endochronic Theory

The basic incremental constitutive equations of the endochronic theory are :

$$d\varepsilon_{dij} = d\varepsilon_{dij}^E + d\varepsilon_{dij}^P \quad (A6.1)$$

$$= \frac{dS_{ij}}{2G} + \frac{S_{ij}}{2G} dz \quad (A6.1a)$$

$$d\varepsilon_m = d\varepsilon_m^E + d\varepsilon_m^P \quad (A6.1b)$$

$$= \frac{d\sigma_m}{3K} + d\lambda \quad (A6.1c)$$

$$d\varepsilon_{ij} = d\varepsilon_{dij} + \delta_{ij} d\varepsilon_m$$

where

$d\varepsilon_{ij}$ - strain increment

$d\varepsilon_{dij}$ - deviatoric strain increment

$d\varepsilon_m$ - volumetric strain increment

$d\sigma_m$ - volumetric stress increment

dS_{ij} - deviatoric stress increment

$d\varepsilon_{dij}^E, d\varepsilon_{dij}^P$ - elastic and inelastic deviatoric strain increments

$d\varepsilon_m^E, d\varepsilon_m^P$ - elastic and inelastic volumetric strain increments

δ_{ij} - Kronecker Delta ($\delta_{ij} = 1$ for $i = j$, otherwise zero)

K - bulk modulus

G - shear modulus

dz - intrinsic time increment

$d\lambda$ - inelastic dilatancy increment

$$dS_{ij} = d\sigma_{ij} - \delta_{ij} d\sigma_m \quad (A6.1d)$$

The increment of intrinsic time is defined (63) in the following :

$$dz = \frac{d\eta}{z_1 F_2 \left\{ 1 + \frac{\beta_1 \eta + \beta_2 \eta^2}{1 + F_1 a_7} \right\}} \quad (A6.2)$$

$$d\eta = \left\{ \frac{a_0}{1 - (a_6 I_3(\underline{\sigma}))^{1/3}} + F_1 \right\} d\xi \quad (A6.2a)$$

$$d\xi = \sqrt{\frac{1}{2} d\varepsilon_{dij} d\varepsilon_{dij}} \quad (A6.2b)$$

$$F_1 = \frac{a_2 [1 + a_5 I_2(\underline{\sigma})] \sqrt{J_2(\underline{\varepsilon})}}{\{1 - a_1 I_1(\underline{\sigma}) - (a_3 I_3(\underline{\sigma}))^{1/3}\} (1 + a_4 I_2(\underline{\sigma}) \sqrt{J_2(\underline{\varepsilon})})} \quad (A6.2c)$$

$$F_2 = 1 + \frac{a_8}{(1 + \frac{a_9}{\eta^2}) J_2(\underline{\varepsilon})} \quad (A6.2d)$$

$I_1(\underline{\sigma})$ = first stress invariant

$I_2(\underline{\sigma})$ = second stress invariant

$I_3(\underline{\sigma})$ = third stress invariant

$J_2(\underline{\varepsilon})$ = second invariant of the deviatoric strain tensor

The shear and bulk moduli are assumed to be dependent on λ (inelastic dilatancy) and are given by :

$$G = \frac{E_0}{2(1+\nu)} \left(1 - 0.25 \frac{\lambda}{\lambda_0} \right) \quad (A6.3)$$

$$K = \frac{E_0}{3(1-2\nu)} \left(1 - 0.25 \frac{\lambda}{\lambda_0} \right) \quad (A6.3a)$$

E_0 - initial modulus of elasticity

The increment of inelastic dilatancy variable is defined as :

$$\frac{1 - \lambda/\lambda_0}{1 - c_1 I_1(\underline{\sigma})} \left\{ \left(\frac{J_2(\underline{\varepsilon})}{c_2^2 + J_2(\underline{\varepsilon})} \right)^3 + \left(\frac{\lambda}{\lambda_0} \right)^2 \right\} d\xi \quad (A6.4)$$

and $d\lambda$ is accumulated along the load path as :

$$\lambda = \sum_{\text{all load increments}} d\lambda \quad (A6.4a)$$

A set of material parameters used in Equations (A6.2) and (A6.3) have been obtained by fitting numerous test data and are defined as follows :

$$\begin{aligned}
 z_1 &= 0.0015 & a_7 &= 20.0 \\
 \beta_1 &= 30.0 & a_8 &= 0.000125 \\
 \beta_2 &= 3500.0 & a_9 &= 0.0015 \\
 a_0 &= 0.7 & \lambda_0 &= 0.001 \\
 a_1 &= 0.6/\sigma_c & c_1 &= 100/\sigma_c \\
 a_2 &= 1400 & c_2 &= 0.0005 \\
 a_3 &= 500/\sigma_c^3 & \nu &= 0.18 \\
 a_4 &= 475/\sigma_c^2 & E_0 &= (0.565 + 0.0145\sigma_c) 4730\sqrt{\sigma_c} \text{ (N/mm}^2\text{)} \\
 a_5 &= 0.8/\sigma_c^2 & &= (0.565 + 0.0001\sigma_c) 5700\sqrt{\sigma_c} \text{ (psi)} \\
 a_6 &= 0.055/\sigma_c^3 & &
 \end{aligned} \tag{A6.5}$$

where σ_c is the uniaxial compressive cylinder strength.

The above material parameters are a good approximation to the non-linear behaviour of generally used lightweight concrete. The attraction about this model is that while non-linear behaviour is simply defined by two values, i.e. σ_c and E_0 , the formulation in Equation (A6.1) is fully continuous in that no inequalities are needed to distinguish between loading and unloading for various ranges of strain.

From Equation (A6.1a) and (A6.1d) :

$$dS_{ij} + dS_{ij}^P = 2G d\varepsilon_{dij} \tag{A6.6a}$$

$$d\sigma_m + d\sigma_m^P = 3K d\varepsilon_m \tag{A6.6b}$$

where

$$dS_{ij}^P = S_{ij} dz \tag{A6.6c}$$

$$d\sigma_m^P = 3K d\lambda \tag{A6.6d}$$

let $i = 1, 2, 3 = (X, Y, Z)$

Define $\Delta\sigma_{ij} = [\Delta\sigma_x, \Delta\sigma_y, \Delta\sigma_z, \Delta\tau_{xy}, \Delta\tau_{yz}, \Delta\tau_{zx}]^T$ (A6.6e)

$$\Delta\varepsilon_{ij} = [\Delta\varepsilon_x, \Delta\varepsilon_y, \Delta\varepsilon_z, \Delta\gamma_{xy}, \Delta\gamma_{yz}, \Delta\gamma_{zx}]^T \quad (A6.6f)$$

$$I_1(\sigma) = \sigma_x + \sigma_y + \sigma_z$$

$$I_2(\sigma) = (\sigma_y \sigma_z - \tau_{yz}^2) + (\sigma_x \sigma_z - \tau_{xz}^2) + (\sigma_x \sigma_y - \tau_{xy}^2)$$

$$I_3(\sigma) = \begin{vmatrix} \sigma_x & \tau_{xy} & \tau_{xz} \\ \tau_{xy} & \sigma_y & \tau_{yz} \\ \tau_{xz} & \tau_{yz} & \sigma_z \end{vmatrix} \quad (A6.6g)$$

$$J_2(\varepsilon) = \frac{1}{2}(\varepsilon_{dx}^2 + \varepsilon_{dy}^2 + \varepsilon_{dz}^2) + \gamma_{xy}^2 + \gamma_{yz}^2 + \gamma_{zx}^2$$

$$d\varepsilon_m = (d\varepsilon_x + d\varepsilon_y + d\varepsilon_z)/3$$

For numerical analysis, the constitutive Equations (A6.6a) and (A6.6b) are to be put in matrix form. Multiply by δ_{ij} in (A6.6a) and add it in (A6.6b) :

$$(d\sigma_{ij} + \delta_{ij} d\sigma_m) + (d\sigma_{ij}^p + \delta_{ij} d\sigma_m) = 2G d\varepsilon_{ij} + 3K d\varepsilon_m \delta_{ij}$$

By definition, the above becomes :

$$d\sigma_{ij} + d\sigma_{ij}^p = 2G d\varepsilon_{ij} + 3K d\varepsilon_m \delta_{ij} \quad (A6.7)$$

$$= 2G(d\varepsilon_{ij} - \delta_{ij} d\varepsilon_m) + 3K \delta_{ij} d\varepsilon_m \quad (A6.7a)$$

$$d\sigma_{ij} + d\sigma_{ij}^p = 2G d\varepsilon_{ij} + (3K - 2G)\delta_{ij} d\varepsilon_m \quad (A6.7b)$$

Upon expanding, the above can be written in matrix form as :

$$\begin{bmatrix} \Delta\sigma_x + \Delta\sigma_x^p \\ \Delta\sigma_y + \Delta\sigma_y^p \\ \Delta\sigma_z + \Delta\sigma_z^p \\ \Delta\tau_{xy} + \Delta\tau_{xy}^p \\ \Delta\tau_{yz} + \Delta\tau_{yz}^p \\ \Delta\tau_{zx} + \Delta\tau_{zx}^p \end{bmatrix} = \begin{bmatrix} (K + \frac{4}{3}G) & (K - \frac{2}{3}G) & (K - \frac{2}{3}G) & 0 & 0 & 0 \\ & (K + \frac{4}{3}G) & (K - \frac{2}{3}G) & 0 & 0 & 0 \\ & & (K + \frac{4}{3}G) & 0 & 0 & 0 \\ & \text{SYM} & & G & 0 & 0 \\ & & & & G & 0 \\ & & & & & G \end{bmatrix} \begin{bmatrix} \Delta\varepsilon_x \\ \Delta\varepsilon_y \\ \Delta\varepsilon_z \\ \Delta\gamma_{xy} \\ \Delta\gamma_{yz} \\ \Delta\gamma_{zx} \end{bmatrix}$$

$$\text{or} \quad (\Delta \underline{\sigma} + \Delta \underline{\sigma}^P) = \underline{D}_T \Delta \underline{\varepsilon} \quad (\text{A6.8})$$

$$\text{where} \quad \Delta \underline{\sigma}^P = S_{ij} d\varepsilon + \delta_{ij} 3K d\lambda \quad (\text{A6.9})$$

Equations (A6.8) and (A6.9) along with endochronic parameters, define the material constitutive relations for concrete in compression.

A6.1.1. Extension of Endochronic Constitutive Relations for Cracking

In an uncracked situation, the concrete constitutive relations given by Equation (A6.8) are isotropic and are applicable in any coordinate system. This is rewritten in the following form :

$$\begin{Bmatrix} \Delta \sigma_x + \Delta \sigma_x^P \\ \Delta \sigma_y + \Delta \sigma_y^P \\ \Delta \sigma_z + \Delta \sigma_z^P \\ \Delta \tau_{xy} + \Delta \tau_{xy}^P \\ \Delta \tau_{yz} + \Delta \tau_{yz}^P \\ \Delta \tau_{zx} + \Delta \tau_{zx}^P \end{Bmatrix} = \begin{bmatrix} D_{11} & D_{12} & D_{13} & 0 & 0 & 0 \\ & D_{22} & D_{23} & 0 & 0 & 0 \\ & & D_{33} & 0 & 0 & 0 \\ & & & D_{44} & 0 & 0 \\ \text{SYM} & & & & D_{55} & 0 \\ & & & & & D_{66} \end{bmatrix} \begin{Bmatrix} \Delta \varepsilon_x \\ \Delta \varepsilon_y \\ \Delta \varepsilon_z \\ \Delta \gamma_{xy} \\ \Delta \gamma_{yz} \\ \Delta \gamma_{zx} \end{Bmatrix} \quad (\text{A6.10})$$

$$\begin{aligned} \text{where} \quad D_{11} &= D_{22} = D_{33} = K + 4/3G \\ D_{12} &= D_{13} = D_{23} = K - 2/3G \\ D_{44} &= D_{55} = D_{66} = G \end{aligned} \quad (\text{A6.11})$$

$$\text{or} \quad \Delta \underline{\sigma} + \Delta \underline{\sigma}^P = \underline{D}_T \Delta \underline{\varepsilon} \quad (\text{A6.12})$$

When concrete cracks, a sudden drop of tensile strength across the crack is assumed. This creates a non-equilibrium state in the structure. To maintain an equilibrium state, this released stress is redistributed to another part of the structure. The material matrix, \underline{D}_T , should also be modified to reflect the reduced stiffness across the crack. Now we write the above material constitutive relations in the crack coordinate system as :

$$\Delta \underline{\sigma}^* + \Delta \underline{\sigma}^{P*} = \underline{D}_T^* \Delta \underline{\varepsilon}^* \quad (\text{A6.13})$$

Supposing that there is one crack normal to X* direction, then concrete can no longer resist any tensile stress in that direction, i.e.

$$\Delta\sigma_x^* = 0$$

The procedure described in Chapter 4 (section 4.5.3.) is used. From the first row of Equation (A6.13) :

$$\begin{aligned} D_{11} \Delta\varepsilon_x^* + D_{12} \Delta\varepsilon_y^* + D_{13} \Delta\varepsilon_z^* &= \Delta\sigma_x^* \\ \Delta\varepsilon_x^* &= \frac{\Delta\sigma_x^*}{D_{11}} - \frac{D_{12}}{D_{11}} \Delta\varepsilon_y^* - \frac{D_{13}}{D_{11}} \Delta\varepsilon_z^* \end{aligned} \quad (A6.14)$$

Substitute Equation (A6.14) with the second and third row of Equation (A6.13) and rearrange the terms in D_T^* ; the following is obtained :

$$\begin{aligned} \Delta\sigma_y^* + \Delta\sigma_y^{P*} - \frac{D_{12}}{D_{11}} \Delta\sigma_x^{P*} &= (D_{22} - \frac{D_{12}D_{21}}{D_{11}}) \Delta\varepsilon_y^* + (D_{23} - \frac{D_{12}D_{13}}{D_{11}}) \Delta\varepsilon_z^* \\ \Delta\sigma_z^* + \Delta\sigma_z^{P*} - \frac{D_{13}}{D_{11}} \Delta\sigma_x^{P*} &= (D_{23} - \frac{D_{13}D_{12}}{D_{11}}) \Delta\varepsilon_y^* + (D_{33} - \frac{D_{13}D_{31}}{D_{11}}) \Delta\varepsilon_z^* \\ \Delta\tau_{xy}^* + \Delta\tau_{xy}^{P*} &= \beta D_{44} \gamma_{xy}^* ; \quad \Delta\tau_{yz}^* + \Delta\tau_{yz}^{P*} = D_{55} \gamma_{yz}^* ; \quad \Delta\tau_{zx}^* + \Delta\tau_{zx}^{P*} = \beta D_{66} \gamma_{zx}^* \end{aligned} \quad (A6.15)$$

Equation (A6.15) is referred to a local (crack) coordinate system. It must be transformed in the global coordinate system using Equation (4.34). If there are two cracks at one point (let it be X* and Y*) and both cracks are open, then the D_T^* matrix is modified using the same principle as described above, except that in this case a double condensation is needed (see section 4.5.3.). For all three cracks open, the concrete loses its stiffness and \underline{D}_T^* is given by :

$$\underline{D}_T^* = 0 \quad (A6.16)$$

APPENDIX A7

A7.1. Creep Strains under Multiaxial Stress

Experiments performed under various stress combinations revealed similar volumetric and deviatoric creep strain behaviour. This situation leads to stress-strain relationships for creep which are analogous to the stress-strain relationships of elasticity. Here, the normal modulus of elasticity, E , is replaced by inverse of the uniaxial creep compliance, $J(t'-\tau')$, and also the elastic Poisson's ratio is replaced by the creep Poisson's ratio. Therefore, the multiaxial creep strain may be written as (e.g. elastic equation $\epsilon_{ij} = (1+\nu)\frac{\sigma_{ij}}{E} - \nu\delta_{ij}\frac{\sigma_{kk}}{E}$) :

$$\epsilon_{ij}^c = J(t'-\tau') \{ (1+\nu_c)\sigma_{ij} - \nu_c \delta_{ij} \sigma_{kk} \} \quad (A7.1)$$

In incremental form over a pseudo time $\Delta t'$, this may be written as :

$$\Delta \epsilon_{ij}^c = \Delta J(t'-\tau') \{ (1+\nu_c)\sigma_{ij} - \nu_c \delta_{ij} \sigma_{kk} \} \quad (A7.2)$$

where $\Delta J(t'-\tau')$ is the uniaxial creep compliance over an increment of $\Delta t'$, ν_c is the creep Poisson's ratio, δ_{ij} is the Kronecker Delta. Upon expanding Equation (A7.2) and arranging it in matrix form, the following is obtained :

$$\begin{Bmatrix} \Delta \epsilon_x^c \\ \Delta \epsilon_y^c \\ \Delta \epsilon_z^c \\ \Delta \gamma_{xy}^c \\ \Delta \gamma_{yz}^c \\ \Delta \gamma_{zx}^c \end{Bmatrix} = \Delta J(t'-\tau') \begin{bmatrix} 1 & -\nu_c & -\nu_c & 0 & 0 & 0 \\ -\nu_c & 1 & -\nu_c & 0 & 0 & 0 \\ -\nu_c & -\nu_c & 1 & 0 & 0 & 0 \\ 0 & 0 & 0 & 2(1+\nu_c) & 0 & 0 \\ 0 & 0 & 0 & 0 & 2(1+\nu_c) & 0 \\ 0 & 0 & 0 & 0 & 0 & 2(1+\nu_c) \end{bmatrix} \begin{Bmatrix} \sigma_x \\ \sigma_y \\ \sigma_z \\ \tau_{xy} \\ \tau_{yz} \\ \tau_{zx} \end{Bmatrix} \quad (A7.3)$$

or in short

$$\underline{\Delta \epsilon^c} = \Delta J(t'-\tau') \underline{C} \underline{\sigma} \quad (A7.3a)$$

Following the evidence based on the experimental results, it is reasonable to assume the creep Poisson's ratio equal to the elastic Poisson's ratio (i.e. $\nu_c = \nu$.)

Basic creep equations used for numerical calculations were taken from the experimental work carried out by Illston. The coefficient of temperature dependence was obtained by processing the experimental data of Browns used by Kawamata et al. The following creep compliance function for uniaxial conditions was adopted :

$$J(t'-\tau') = \frac{1}{E} + f(\tau) \{t'-\tau'\} + Q(1 - e^{-\beta(t'-\tau')}) \quad (A7.4)$$

$$= J_E + f(\tau) J_f + J_d \quad (A7.5)$$

where $J_f = t' = [-15.37346 + 7.88977 \text{ Log}_e (t)] \times 10^{-6}$ per N/mm^2
 $Q = 14.21457 \times 10^{-6}$ per N/mm^2
 $\beta = 0.2813578 \times 10^6$ N/mm^2
 $t =$ actual time; ($\nu = \nu_c = 0.167$)

(A7.6)

and temperature function $f(T) = \frac{1}{50} (T + 30)$ where T is the temperature in degrees centigrade, in which 20°C is assumed as ambient temperature.

Now the incremental uniaxial compliance, assuming E does not vary with t' :

$$\Delta J(t'-\tau) = f(\tau) \Delta J_f + \Delta J_d \quad (A7.7)$$

$$\Delta J_f = (t'+\Delta t') - t' = 7.88977 \text{ Log}_e \left(\frac{t'+\Delta t'}{t'} \right) = \Delta t' \quad (A7.8)$$

and $\Delta J_d = J_d(t'+\Delta t') - J_d(t')$ (A7.9)

$$= (1 - e^{-\beta \Delta t'}) (Q - J_d(t')) \quad (A7.10)$$

where Q - limiting delayed elastic strain
 $J_d(t')$ - delayed elastic strain at time t'

Therefore define $Q' = (Q - Jd(t'))$ - delayed strain yet to develop,
so :

$$\Delta J_d = Q' (1 - \bar{e}^{-\beta \Delta t'}) \quad (A7.11)$$

Once the entire response of the structure is solved in pseudo time axis,
 t' , the real time, t , is then obtained from simple transformation.

A7.2. Equivalent Load due to change in Creep Strain

The creep strain (or increment of strain) in finite element analysis is treated as "initial strain". The kinematically equivalent load for such cases is defined in Chapter 3 (Equation 3.13c). This may be written using the creep strain increment of the previous section as

$$\Delta P^c = \int_{vol} \underline{\underline{B}}^T \underline{\underline{D}} \Delta \underline{\underline{\xi}}^c dvol \quad (A7.12)$$

or

$$= \int_{-1}^{+1} \int_{-1}^{+1} \int_{-1}^{+1} \underline{\underline{B}}^T \underline{\underline{D}} \Delta \underline{\underline{\xi}}^c \det J d\xi d\eta d\zeta$$

or

$$= \sum_{i=1}^{NX} \sum_{j=1}^{NY} \sum_{k=1}^{NZ} W_i W_j W_k \underline{\underline{G}} \det J \quad (A7.12a)$$

where NX, NY, NZ , are Gauss points, W_i, W_j, W_k , are the weighting coefficients and $\det J$ is the determinant of the Jacobian.

$$\underline{\underline{G}} = \underline{\underline{B}}^T \underline{\underline{D}} \Delta \underline{\underline{\xi}}^c \quad (A7.12b)$$

where $\underline{\underline{B}}$ - strain-displacement matrix
 $\underline{\underline{D}}$ - elastic or non-linear material matrix
 $\Delta \underline{\underline{\xi}}^c$ - creep strain increment of the previous section

A7.3. Equivalent Load due to Thermal Strain

The thermal strain in finite element analysis is treated as "initial strain" similar to the creep strain. The kinematically equivalent load due to temperature rise, ΔT , may be written as :

$$\underline{\Delta P}^{th} = \int_{vol} \underline{B}^T \underline{D} \underline{\Delta \varepsilon}^{th} dvol \quad (A7.13)$$

$$= \int_{-1}^{+1} \int_{-1}^{+1} \int_{-1}^{+1} \underline{B}^T \underline{D} \underline{\Delta \varepsilon}^{th} \det J d\xi d\eta d\zeta \quad (A7.13a)$$

where $\underline{\Delta \varepsilon}^{th}$ is the thermal strain increment of the material. For concrete, as for three-dimensional material, the thermal strain increment is given by :

$$\left\{ \begin{array}{c} \Delta \varepsilon_x^{th} \\ \Delta \varepsilon_y^{th} \\ \Delta \varepsilon_z^{th} \\ \Delta \gamma_{xy}^{th} \\ \Delta \gamma_{yz}^{th} \\ \Delta \gamma_{zx}^{th} \end{array} \right\}_{6 \times 1} = \left\{ \begin{array}{c} \alpha_c \Delta T \\ \alpha_c \Delta T \\ \alpha_c \Delta T \\ 0 \\ 0 \\ 0 \end{array} \right\} \quad (A7.14)$$

where α_c = coefficient of thermal expansion for concrete.

Liner steel, under plane stress condition :

$$\left\{ \begin{array}{c} \Delta \varepsilon_x^{th} \\ \Delta \varepsilon_y^{th} \\ \Delta \gamma_{xy}^{th} \end{array} \right\}_{3 \times 1} = \left\{ \begin{array}{c} \alpha_s \Delta T \\ \alpha_s \Delta T \\ 0 \end{array} \right\} \quad (A7.15)$$

where α_s = coefficient of thermal expansion for steel.

Tendons and reinforcing bars are treated as uniaxial material :

$$\left\{ \Delta \varepsilon_x^{th} \right\}_{1 \times 1} = \left\{ \alpha_s \Delta T \right\} \quad (A7.16)$$

APPENDIX B

APPENDIX B1

USER MANUAL FOR NSARVE

B1.1. Program NSARVE

In this Appendix, instructions for preparing the data decks are given. The following cards are read in :

B1.1.1. Title Card

This card is mandatory. A maximum of 80 characters are allowed. The title can be alphanumeric characters or special symbols like * , & % ... etc. Format (20A4).

B1.1.2. All or one of the following items are read on this card :

RESD - to print residuals
INPC - to run program for input check only
STRS - to print stresses, STRN - to print strains
PSTS - to print principal stresses
INDC - to print crack indicators and crack angles
ORTH - orthotropic concrete compressive model
BULK - shear and bulk modulus concrete model
ENDO - endochronic concrete model
GAUS - to print X-Y-Z coordinates at Gauss points (for solid EL)
CONR - to check convergence on residuals
COND - to check convergence on displacements
SECN - accelerated Newton-Raphson method

A maximum of 16 options (as given above) may be read on this card separated by single spaces or commas in any order. In the case of a card left blank, the default values are used. They are BULK and CONR.

Example :

BULK SECN RESD CONR STRN STRS PSTS GAUS

or

ORTH SECN STRS GAUS PSTS

The card reads as :

READ (JINP,1009) (LO (J),J-1,16)

1009 FORMAT (16(A4,1X))

B1.1.3. This card reads in the total number of nodes on the structure, the number of elements followed by the number of nodes on these elements.

READ() NNP, NTE1, NTE2, NTE3, NTE4, NNE1, NNE2, NNE3, NNE4

NNP - total number of nodes on the structure

NTE1 - number of solid elements

NTE2 - number of plane stress membrane elements

NTE3 - number of axial line elements (body elements are not included)

NTE4 - number of bond-linkage elements

NNE1, NNE2, NNE3, NNE4 - are nodes on solid, membrane, line and linkage elements respectively

FORMAT - Free format, i.e. 9 integers separated by one space or comma

B1.1.4. This card reads in the integer controlling parameters.

READ() NDF, NBC, NRF, NRS, NOGX, NOGY, NOGZ, NGX, NGY, NTYPE, NLI, NELAST, NTC1, ILOAD

NDF - number of degrees of freedom per node (always 3)

NBC - number of boundary conditions (suppressions)

NRF - number of materials for solid elements

NRS - number of materials for line elements

NOGX - number of Gauss points in XI (or local X) direction

NOGY - number of Gauss points in ETA (or local Y) direction

NOGZ - number of Gauss points in ZI (or local Z) direction

NGX, NGY - surface Gauss points for membrane elements

NTYPE - number of prestressed line elements

NLI - number of load increments

NELAST - type of analysis required
 =0 - tension cut off (cracking) and non-linear
 =1 - tension cut off (cracking) and linear elastic
 =2 - purely linear elastic

NTC1 - number of line elements inside solid elements

ILOAD - load to be factored during increments (=1 otherwise 0)

FORMAT(14IO) - free format (14 integer numbers)

B1.1.5. This card reads in controlling parameters for certain combination parameters. For example, whether incore or out of core solution, whether variable or constant stiffness method is to be used, whether creep or temperature is included. The variables read are :

READ()JRADL, INCORE, ICASE, IVARB, ICREEP, MAXWEL, ITEMLD, ITEMMP, CTEC, CTET, NITMAX

JRADL - type of coordinate system
 =1 - cylindrical
 =0 - Cartesian

INCORE - incore or out of core flag
 =1 - for incore solution
 =2 - for out of core solution

ICASE - =1 - incore
 =2 - out of core

IVARB - stiffness update flag
 =0 - constant stiffness throughout (initial stress method)
 =1 - pure Newton-Raphson method, stiffness update at each iteration
 =2 - modified Newton-Raphson method, stiffness update at every second iteration for each load increment
 =3 - modified Newton-Raphson method, stiffness update at the first iteration of each load increment

ICREEP - creep flag
 =1 - creep included
 =2 - creep not included

MAXWELL - type of creep model
 =1 - visco-elastic creep (Maxwell model)
 =0 - visco-elastic creep (Burger model)

ITEMPLD - temperature load flag
 =1 - temperature load
 =0 - no temperature

ITEMPMP - temperature dependent material property flag
 =1 - temperature dependent material property
 =0 - no temperature dependent material property

CTEC - coefficient of thermal expansion for concrete

CTET - coefficient of thermal expansion for steel

NITMAX - maximum iteration limit for any load increment

FORMAT(8I0,2F0.0,I0) - free format (8 integers, 2 reals and 1 integer)

B1.1.6. This card reads in the material and geometric property integers for each element type. Parameters read are :

READ() (LRF(J),J=1,NTE1) - ignore it if NTE1=0
 READ() (LRF(J),J=1,NTE2) - ignore it if NTE2=0
 READ() (LRF(J),J=1,NTE3) - ignore it if NTE3=0
 READ() (LRF(J),J=1,NTE4) - ignore it if NTE4=0
 READ() (LRF(J),J=1,NTC1) - ignore it if NTC1=0
 FORMAT(16I5) - fixed format, 16 integers on each card

B1.1.7. Coordinate Card

```
DO I=1,NNP
READ() X(I),Y(I),Z(I)
FORMAT(3F0.0)
```

Each card should have 3 real values (X-Y-Z coordinates) separated by one space or comma. Since there are no node numbers given on this card the program assigns node numbers in ascending order.

B1.1.8. Connectivity Relations (for each element type)

BRK8, BRK20, BRK32 (solid elements - 8, 20 and 32 nodes) :

(a) For BRK8, the connectivity relations for two elements are read on one card except in those circumstances when there are an odd number of elements in the analysis. In this case, one connectivity

is read on the last card. Therefore 16 or 8 integers as the case may be should be present separated by commas or spaces.

- (b) For BRK20 elements, one card per element is read in. The format is FORMAT(20I0) - free format, 20 integers on one card with one space between them
- (c) For BRK32 elements, two cards per element, 16 integers on each card, Fixed format. FORMAT(16I5,/,16I5)

MEM4, MEM8, MEM12 (membrane elements 4, 8, 12 nodes) :

- (a) MEM4 - two elements per card except for odd number of elements, in which case one element is read on the last card only. Free format, 8 or 4 integers per card separated by single spaces or commas.
- (b) MEM8 - two elements per card except for odd number of elements, in which case one element is read on the last card only. Free format, 16 or 8 integers per card separated by single spaces or commas.
- (c) MEM12 - connectivity of one element per card, free format and 12 integers per card separated by single spaces or commas.

FLA2, FLA3, FLA4 (axial line elements, 2, 3 and 4 nodes) :

- (a) FLA2 - 2 elements per card, free format
- (b) FLA3 - 2 elements per card, free format
- (c) FLA4 - 1 element per card, free format

LINK2 (bond linkage element, 2 nodes) :

Two elements connectivity per card, 4 integers separated by commas.

Material Properties Deck

B1.1.9. Solid Elements

Three moduli of elasticity (E1,E2,E3) and three Poisson's ratios (v1,v2,v3) are read on this card. For isotropic materials, the user should give three identical E's and V's. Six real values per card using free format. The number of cards depends on the number of NRF read on the fourth card.

B1.1.10. Material and Geometric Properties for Membrane Elements (E,V,T)

IF NTE2 .EQ. 0 THEN IGNORE THIS CARD (card number 10). Three real values on this card. These are modulus of elasticity, Poisson's ratio and membrane thickness using free format.

B1.1.11. Material and Geometric Properties for Axial Elements (E,DIA,YIELD)

IF NTE3 AND NTC1 .EQ. 0 THEN IGNORE THIS CARD (card number 11). For each section/material property (NRS of card 4) the modulus of elasticity, diameter of the bar and the yield stress must be given. Free format is used, i.e. three real values separated by commas.

B1.1.12. Properties of LINK2 Elements

IF NTE4 .EQ. 0 THEN IGNORE THIS CARD (card number 12). The first card gives the number of curve points for a specified bond-slip curve and two factors. The bond stress and slip values follow. Two real values per card, which is read in using free format. The number of the real value cards will depend on the first integer (i.e. number of curve points). The following statements are used :

```

READ()NPOINT,FACTRV,FACTRL
NPOINT - number of bond-slip curve points
FACTRV - factor for vertical bond spring
FACTRL - factor for lateral bond spring
FREE FORMAT - three values, one integer and two real values
DO 99 I=1,NPOINT
READ()BOND(I),SLIP(I)
99 CONTINUE
FORMAT(2F0.0)

```


The second card gives the length over which the link element is connected with the line and the solid element. The length is read in for each link element (NTE4 on card 3). One real value per card using free format.

B1.1.13. Boundary Conditions

Two types of boundary suppressions can be considered. The first one allows supports in the global X-Y-Z directions and the second one allows inclined support on X-Y plane (inclined an angle theta from the global X-axis). To identify that the inclined supports are present in the analysis, it is essential to read in NBC (on card 3) as -ve of the usual number of boundary conditions. For example, if there are 5 boundary supports and 1 is an inclined support at 15 degrees to the global X-axis, then -5 will identify this case. Therefore the following FORTRAN statements are given :

```
(a) IF NBC .GT. 0
      DO 99 I=1,NBC
      READ()NODE,IX,IY,IZ
      99 CONTINUE
      FORMAT(4I0) - free format, 4 integers per card

(b) IF NBC .LT. 0
      READ()THETA free format, 1 real value on this card (theta
                  should be given in degrees)
      DO 99 I=1,NBC
      READ()NODE,IX,IY,IZ
      99 CONTINUE
      FORMAT(4I0) - free format, 4 integers per card
```

B1.1.14. Non-linear Parameters

Parameters read are the uniaxial concrete cylinder strength, the limiting tensile strength, the yield stresses for prestressed and mild steel, the concrete interlocking shear factor, the concrete crushing

strain, the steel strain hardening parameter (H') and the tolerance limit for the convergence. Parameters are read as :

```
READ()CCC,CCT,YY1,YY2,BETA,ECU,HARDG,TOLREN
```

CCC - concrete cylinder strength in compression

CCT - concrete limiting tensile strength

YY1 - yield stress for prestressed tendon

YY2 - yield stress for mild steel (liner)

BETA - cracked concrete shear interlocking factor

ECU - concrete crushing strain (uniaxial)

HARDG - isotropic strain hardening parameter for steel

TOLREN - tolerance for convergence

FREE FORMAT - 8 integers with one space between them

B1.1.15. Body Element Card

IF NTC1 OF CARD 4 IS ZERO THEN IGNORE THIS CARD.

```
DO 99 I=1,NTC1
```

```
READ()IDD(I),(SG(J,I),J=1,3)
```

```
99 CONTINUE
```

Free format one integer and three real values on each card

IDD - brick element number

SG - local positions of line element inside the brick element
(local positions are the SI,ETA,ZETA coordinates)

B1.1.16. Temperature Card

Temperatures are given at the nodes. The first card reads in the number nodes at which a temperature is given and the reference temperature. The card is read as :

```
READ()NTEM,REFTEM
```

Free format - 1 integer and one real value per card

The second card reads three node numbers and their temperature values except in the case of odd number of nodes in which case one or two node numbers and their temperature values are allowed on the very last card. Free format is used.

B1.1.17. Prestress Force Card

This card is only used if NTYPE is greater than zero. This card reads the prestressing force in the steel line elements using free format. One real value only.

B1.1.18. Creep Solution Times Card

This card is only used if ICREEP on card 5 is non-zero. The card reads the incremental solution times in days for each load increment. Three times are read on each card using free format. A negative value on the card terminates the reading of solution times. The same sequence should be repeated for the next load increment if there is more than one load increment.

```
DO 99 I=1,NLI
READ()TIME1,TIME2,TIME3
FREE FORMAT
99 CONTINUE
```

Let us suppose a creep solution is required at 1YEAR,5YEARS,20YEARS, 25YEARS and 30YEARS time periods, and there is only one load increment.

The following two cards will be sufficient :

```
365.0 1465.0 5475.0
1825.0 1825.0 -0.77
```

B1.1.19. Output Card

This card reads integer number to control the printing of the output for each load increment and creep solution times. The columns 1 - 50 are used for the load increment and the columns 51 - 80 for creep solution times. 50 load increments and 30 creep solution times are allowed.

```
READ() (IOUTP(J)J=1,80)
FORMAT(80I1)
```

If value read on a particular column is 1 then output for that load increment is suppressed whilst if it is 0 then it is printed. For example 1101, means that output is suppressed for load increment 1,2 and 4 only. Output is printed for each creep solution time.

B1.1.20. Incremental Load Factors (Pseudo Times)

This card reads incremental load factors at which a solution is attempted. The card is not needed if ILOAD (card 5) is zero. The number of factors is equal to the number of load increments. Three factors are read per card using free format.

```
DO 99 I=1,NLI
READ()T1,T2,T3
FREE FORMAT
99 CONTINUE
```

B1.1.20. External Loads

Five types of loads may be applied :

- (a) Pressure loads
- (b) Point loads
- (c) Patch loads (loads not directly at nodes)
- (d) Self weight
- (e) Thermal loads

The first card in this section gives the load controlling parameters i.e. type of loading to be applied on the structure. The card reads :

```
READ()NFACTES,NCONC,NPATCH,ROH,TEMFAC
FREE FORMAT - 3 integers and 2 real values on this card
```

where

- NFACTES - number of faces for brick elements where pressure is applied
- NCONC - number of point loads on nodes
- NPATCH - number of point loads not directly on nodes
- ROH - density of the material
- TEMFAC - factor for thermal loads

(a) Pressure Loads

Constant and variable pressure loads may be applied on the faces of brick elements. This card deck is not used if NFACES=0. For each face, the following cards are read :

READ() IEL,NF,NS

FREE FORMAT - 3 integers per card

where

IEL - brick element number

NF - face number where pressure is applied

NS - =0 - constant pressure, =1 - variable pressure

The face numbering scheme is as follows

FACE NUMBER 1, WHERE XI = +1

FACE NUMBER 2, WHERE ETA = +1

FACE NUMBER 3, WHERE ZI = +1

FACE NUMBER 4, WHERE XI = -1

FACE NUMBER 5, WHERE ETA = -1

FACE NUMBER 6, WHERE ZI = -1

This card is read depending on the value of NS :

(i) IF NS=0 (CONSTANT PRESSURE)

READ() PRESS

FREE FORMAT - 1 real value per card

(ii) IF NS=1 (VARIABLE PRESSURE) NODAL PRESSURE ON THE FACE OF THE ELEMENT

MUST BE READ

8 node brick - 4 real values per card

20 node brick - 8 real values per card

32 node brick - 12 real values per card

Positive pressure acts in the positive directions of XI, ETA and ZI axes.

(b) Point Loads

IF NCONC=0 THIS CARD IS NOT USED. For each point load, node number and three global X-Y-Z loads are read. The card reads :

READ()NODE,XLOAD,YLOAD,ZLOAD

FREE FORMAT - 1 integer and 3 real values per card

For example, at node 56 load is 0.66 in -Z direction 56 0.0 0.0 -0.66 will be necessary.

(c) Patch Loads

Patch loads are similar to point loads except that they are not applied on nodes. The nodal values are calculated using the shape function of brick elements. This card reads

READ() IEL,XG,YG,ZG,XLOAD,YLOAD,ZLOAD

FREE FORMAT - 1 integer and 6 real values

where

IEL - brick element number

XG,YG,ZG - local position of load in local XI,ETA,ZI directions

XLOAD,YLOAD,ZLOAD - global loads in X,Y,Z directions

(d) Self Weight

IF RHO=0, THIS CARD IS NOT USED. In this case the density (RHO) is read at the beginning of the section. The load is calculated as gravity load and is applied in the -ve global Z- direction.

(e) Thermal Loads

IF TEMFAC=0.0 THIS CARD IS NOT USED. Thermal loads are calculated element by element. The elements on which temperatures may be applied are BRICKS, MEMBRANES, AXIAL LINE and BODY elements. A total or a factor of the total temperature may be applied. For example TEMFAC can be 0.1 or 0.5 etc. then incremental thermal strain = TEMFAC*(TEMP-REFTEM)

where TEMP - total temperature, and REFTEM - reference temperature.

B1.2. Test Examples

B1.2.1. Square Braced Frame

The square braced frame shown in Figure (8.1) was analysed to validate the elasto-plastic capability of line elements. The frame was modelled using 2-node line (axial) elements. There are six line elements and four nodes. The geometric and material property details are given in Figure (8.1). Total load is 150 kN was applied at node 4 in 6 increments. For each load increment, equilibrium iterations were performed. The example was analysed using three solution procedures : pure Newton Raphson method, the modified Newton Raphson method and the Initial Stress Method (see Chapter 6). The pure Newton Raphson method was proved to be the best for this particular example. Convergence was checked on residual loads and a tolerance of 3×10^{-2} was used. Load-deflection curve at node 4 is shown in Figure (8.1c). Yielding of the diagonal line element (element 5) occurs at the load =81kN after which the displacements increase rapidly with increasing load. Unloading and reloading test was also performed on this example. The load was slowly taken off and then reapplied. An elastic unloading/reloading behaviour was observed (see Figure 8.1c)), as would be expected. The computed results are almost identical to those from analytical solutions.

B1.2.2. Elasto-Plastic Analysis of Thick-Walled Cylinder

The thick cylinder shown in Figure 8.2. subjected to internal pressure was analysed to test the elastic and elasto-plastic response of membrane elements. The same example was analysed by others (52, 152) The analytical solution under plane strain condition ($\epsilon_z = 0$) is given by Hill (55). Figure (8.2) gives the finite element mesh along with the geometric and material properties. 1/4 of the cylinder was assumed to obey the Von Mises yield criterion with elastic perfectly plastic response. A 3x3 Gauss integration rule was used. Modified Newton Raphson method was used with the stiffness updated at each load increment and the iteration was terminated when the norm of the residual loads became less than 0.01.

The internal pressure was applied in small increments. The solution was obtained at pressures 0.63p, 0.7p, 0.8p and 1p, where p being the internal pressure. These pressures were chosen such that one layer of integration points across the radius yielded at one time. The yielding starts from the inner radius of the cylinder and moves towards the outer radius. The spread of plasticity with increasing internal pressure is shown in Figure (8.3a). The elastic theoretical solution is given by the following equations :

$$\sigma_r = -p \left(\frac{b^2/r^2 - 1}{b^2/a^2 - 1} \right) \quad ; \quad \sigma_\theta = p \left(\frac{b^2/r^2 + 1}{b^2/a^2 - 1} \right)$$

where a, b are the inner and outer radii and r being the radius where stresses are calculated. In this example a = 1.0, b = 2.0, therefore

$$\sigma_r = p/3 (1 - 4/r^2) \quad ; \quad \sigma_\theta = p/3 (1 + 4/r^2)$$

Analytical solution	Computed solution
$\sigma_r = -1.813525$	-1.819
$\sigma_\theta = 3.3865$	3.411

Elastic stresses compare favourably with the analytical solution. Figure (8.3b) shows the analytical and computed internal pressure (normalised) versus outside radial displacement. Results are in good agreement.

B1.2.3. Elastic Analysis of Cantilever Beam

20-node brick element was used to analyse a cantilever beam. Full details are given in Figure (8.4.). Elastic analysis was performed and results were compared with the conventional beam theory of strength of materials. According to this theory the tip deflection is given by $(\frac{WL^3}{3EI})$ and the theoretical value of 0.0028444 was obtained. Two integration rules were used to integrate the solid elements. These were a 2x2x3 and a 3x3x3 integration grids. The results obtained from the analysis for the tip deflection are :

- (i) = 0.002849 for 2x2x3 integration
- (ii) = 0.002831 for 3x3x3 integration

The results compare favourably with the theoretical result. The results of 3x3x3 integration grid are rather stiff and by reducing the integration the element gives better results in bending.

B1.2.4. Reinforced Concrete Beam Analysis

A simply supported beam (Figure (8.5.)) was analysed under ultimate load conditions. This beam was experimentally tested in reference (143) (Beam C3). Due to symmetry, only a half of the beam was modelled using 10 concrete elements (8-node brick) and 20 steel elements (2 node line elements) placed at the bottom of the beam. Figure (8.5c) gives the full details of material and geometric properties and finite element mesh. The total load was applied in one step. The mid-span deflection computed in the analysis was 6.731 mm but the measured deflection in the test (143) was 7.874 mm. The computed results show a rigid model than the real structure. The cracks and the reinforcement stresses, as obtained from the analysis are shown in Figure (8.5.). This example was analysed with both variable stiffness method (where the stiffness matrix was updated at every iteration) and the constant stiffness method. With variable stiffness method, the results converged in five iterations and with the constant stiffness method it required 27 iterations. Convergence was checked on residuals and a tolerance of 3×10^{-2} was used. All three compressive concrete models were tested with this example, i.e. the orthotropic model, the shear and bulk modulus model and the endochronic theory model. The results obtained with all three models were approximately the same. This is not surprising, because the main non-linearity in this example was due to cracking. The mid-span deflection of this example can be improved by taking two elements through the thickness of the beam. This will result in more Gauss points through the thickness and cause more cracks which will make the beam deflect more.

B1.2.5. Simply Supported Reinforced Concrete Beam

The simply supported reinforced concrete beam was experimentally tested by Bresler and Scordelis (43). The beam is shown in Figure (8.6.). This example was chosen for the analysis to demonstrate the non-linear model (cracking and high compression) of concrete. Due to symmetry, only $\frac{1}{2}$ of the beam was analysed. The finite element mesh (using 8 node solid and the body axial line elements - shown by broken lines), the geometric and material property details are shown in Figure (8.6.).

A 2x2x2 Gauss point integration rule was applied for brick elements. A maximum principal stress criterion for cracking and an orthotropic concrete model was used for compression. The total load was applied in 19 increments (see load-deflection curve of Figure (8.7.)) and equilibrium iterations were performed. Figure (8.7.) gives the plot of the experimental load-deflection and the one analysed by the present model - the comparison between the two is reasonably close. Other results (44, 64) which were analysed using different models are also shown in the same figure for comparison.

Figure (8.6.) shows the experimentally obtained crack pattern just before the failure at a total load of 249.2 KN and the failure plane is indicated by the broken lines. The computed crack patterns at load levels 215.2 KN and 245 KN are also shown. The failure as indicated by the experiment is not observed by the computed crack pattern. This could perhaps be improved if 20 node bricks were used with finer mesh through the thickness of the beam. The example demonstrates the application of the non-linear method.

1 TITLE - CANTILEVER BEAM USING SOLID 20-NODED ELEMENT
PROGRAMME CONTROLLING PARAMETERS

```

-----
COMP STPS PSTG STRA INDC
TOTAL NUMBER OF ELEMENTS = 2
TOTAL NO. OF NODAL POINTS = 32
NUMBER OF SOLID ELEMENTS = 20
NUMBER OF MEMBRANE ELEMENTS = 0
NUMBER OF LINE ELEMENTS = 0
NO. OF LINE ELEMENTS INSIDE THE SOLID ELEMENT = 0
NUMBER OF BOND LINKAGE ELEMENTS = 0
NO. OF NODES ON SOLID ELEMENT = 20
NO. OF NODES ON MEMBRANE ELEMENT = 0
NO. OF NODES ON LINE ELEMENT = 0
NO. OF NODES ON LINKAGE ELEMENT = 0
NO. OF DEGREES OF FREEDOM PER NODE = 3
NO. OF BOUNDARY CONDITIONS = 8
NO. OF MATERIALS FOR SOLID ELEMENTS = 1
NO. OF MATERIALS FOR LINE ELEMENTS = 0
NO. OF INTEGRATION PTS. FOR SOLID ELEMENT = 27
NO. OF INTEGRATION PTS. FOR MEMBRAN ELEMENT = 1
NO. OF PRESTRESSED LINE ELEMENTS = 0
TOTAL NUMBER OF LOAD INCREMENTS = 1
TYPE OF ANALYSIS (0=NL-TC,1=TC,2=ELASTIC) = 2
CO-ORDINATE SYSTEM FLAG (1-CYLDR.,0-CARTESIAN) = 0
INCORE SOLUTION COUNTER (1-INCORE,0-CUTCORE) = 1
ICASE = 1
STIFFNESS UPDATE FLAG (0-CONST,1-VARS,2-KT2,3-KT1) = 0
CREEP SOLN COUNTER (0-NO CREEP,1-CREEP INCLUDED) = 0
TYPE OF CREEP MODEL (1-MAXWELL,0-BURGER MODEL) = 0
COEFFICIENT OF THERMAL EXPANSION (CONCRETE) = 0.000000000
COEFFICIENT OF THERMAL EXPANSION (STEEL) = 0.000000000
TEMPERATURE LOAD FLAG (IF ITEMLO=1) = 0
TEMPERATURE DEPENDENT MATERIAL PROP. FLAG = 0
MAXIMUM ITERATION FOR A LOAD INCREMENT = 6
CONCRETE COMPRESSION CRITERIA (0-ORTH,1-ENDO,2-BULK) = 2
    
```

1	NODES	X-COORDINATE	Y-COORDINATE	Z-COORDINATE
	1	0.000	0.000	0.000
	2	0.000	1.500	0.000
	3	0.000	3.000	0.000
	4	0.000	3.000	2.500
	5	0.000	3.000	2.500
	6	0.000	0.000	5.000
	7	0.000	1.500	5.000
	8	0.000	3.000	5.000
	9	5.000	0.000	0.000
	10	5.000	3.000	0.000
	11	5.000	0.000	5.000
	12	5.000	3.000	5.000
	13	10.000	0.000	0.000
	14	10.000	1.500	0.000
	15	10.000	3.000	0.000
	16	10.000	0.000	2.500
	17	10.000	3.000	2.500
	18	10.000	0.000	5.000
	19	10.000	1.500	5.000
	20	10.000	3.000	5.000
	21	15.000	0.000	0.000
	22	15.000	3.000	0.000
	23	15.000	0.000	5.000
	24	15.000	3.000	5.000
	25	20.000	0.000	0.000
	26	20.000	1.500	0.000
	27	20.000	3.000	0.000
	28	20.000	0.000	2.500
	29	20.000	3.000	2.500
	30	20.000	0.000	5.000
	31	20.000	1.500	5.000
	32	20.000	3.000	5.000

**STIFFNESS REFORMED AT INCR. 1 ITERATION 1
 ENTER IN FORNEG
 EXIT FROM FORNEG
 ENTER IN RECOMP
 EXIT FROM RECOMP
 1 PRINT OUT AT THE END OF LOAD INCREMENT NO.- 1 AND TIME - 0.00(DAYS)

CODE	NO. OF ITERATIONS REQUIRED TO CONVERGE = 1			X - LOAD	Y - LOAD	Z - LOAD
	X - DISPL.	Y - DISPL.	Z - DISPL.			
1	0.0000E 00	0.0000E 00	0.0000E 00			
2	0.0000E 00	0.0000E 00	0.0000E 00			
3	0.0000E 00	0.0000E 00	0.0000E 00			
4	0.0000E 00	0.0000E 00	0.0000E 00			
5	0.0000E 00	0.0000E 00	0.0000E 00			
6	0.0000E 00	0.0000E 00	0.0000E 00			
7	0.0000E 00	0.0000E 00	0.0000E 00			
8	0.0000E 00	0.0000E 00	0.0000E 00			
9	-0.2108E-03	-0.3344E-04	-0.2442E-03			
10	-0.1955E-03	-0.1305E-04	-0.2425E-03			
11	-0.1989E-03	-0.1292E-04	-0.2426E-03			
12	-0.2103E-03	-0.3373E-04	-0.2440E-03			
13	-0.3934E-03	-0.4610E-04	-0.8696E-03			
14	-0.3841E-03	-0.3777E-04	-0.8747E-03			
15	-0.3723E-03	-0.2993E-04	-0.8685E-03			
16	-0.1027E-04	-0.3921E-04	-0.8549E-03			
17	-0.1072E-04	-0.3853E-04	-0.8546E-03			
18	-0.2717E-03	-0.3358E-04	-0.8706E-03			
19	-0.3833E-03	-0.3819E-04	-0.8767E-03			
20	-0.3928E-03	-0.4601E-04	-0.8713E-03			
21	-0.4958E-03	-0.8317E-04	-0.1775E-02			
22	-0.4709E-03	-0.7207E-04	-0.1774E-02			
23	-0.4705E-03	-0.7221E-04	-0.1772E-02			
24	-0.4961E-03	-0.8459E-04	-0.1772E-02			
25	-0.5377E-03	-0.1261E-03	-0.2810E-02			
26	-0.5225E-03	-0.1233E-03	-0.2809E-02			
27	-0.5099E-03	-0.1204E-03	-0.2816E-02			
28	-0.1396E-04	-0.1256E-03	-0.2821E-02			
29	-0.1379E-04	-0.1216E-03	-0.2820E-02			
30	-0.5171E-03	-0.1248E-03	-0.2832E-02	0.000000E 00	0.000000E 00	-0.166700E 00
31	-0.5317E-03	-0.1238E-03	-0.2831E-02	0.000000E 00	0.000000E 00	-0.566700E 00
32	-0.5450E-03	-0.1227E-03	-0.2831E-02	0.000000E 00	0.000000E 00	-0.166700E 00

B21

APPENDIX B2

B2.1. Subroutine Listings

```

SUBROUTINE NSARVE
C*****
C
C----- WRITTEN BY MASROOR AHMAD IN JUNE 1977
C----- DIVISION OF STRUCTURES OF THAMES POLYTECHNIC
C----- LONDON, S.E.18
C
C*****
$INSERT COMMON.FE
REAL FZA
COMMON FZA(700000)
LOGICAL STIF
C----- NOTE THAT DIMENSION OF FZA AND MOT MUST BE SAME
MOT = 700000
C
C*****
C
C----- THREE DIMENSIONAL NON-LINEAR ANALYSIS OF REACTOR
C----- VESSEL INCLUDING CRACKING AND NON LINEAR BOND SLIP
C----- BEHAVIOUR ALSO TEMPERATURE AND CREEP EFFECTS
C
C----- ISOPARAMETRIC SOLID ELEMENTS REPRESENT THE
C----- VESSEL CONCRETE, MEMBRANE ELEMENTS REPRESENT
C----- STEEL LINER, LINE ELEMENTS REPRESENT PRESTRE-
C----- SSING AND REINFORCED STEEL AND LINKAGE ELEM-
C----- ENT REPRESENTS NON-LINEAR BOND
C*****
C----- STIFFNESS UPDATE OPTIONS -
C-----
C----- IVARB = 0 - CONSTANT STIFFNESS (MODIFIED NEWTON RAPHSON M
C----- (KO - OPTION)
C----- = 1 - VARIABLE STIFFNESS (NEWTON RAPHSON METHOD)
C----- (KT - OPTION)
C----- = 2 - STIFFNESS UPDATED AT THE SECOND ITERATION
C----- OF EACH LOAD INCREMENT (KT2 - OPTION)
C----- = 3 - STIFFNESS UPDATED AT THE FIRST ITERATION
C----- OF EACH LOAD INCR (KT1-OPTION)
C-----
C----- CREEP ANALYSIS
C-----
C----- ICREEP = 1 - CREEP OF CONCRETE INCLUDED IN THE ANALYSIS
C----- = 0 - CREEP NOT INCLUDED
C-----
C----- MAXWEL = 1 - MAXWELL CONCRETE CREEP MODEL
C----- = 2 - BURGER CREEP MODEL
C-----
C----- EQUATION ASSEMBLY AND SOLUTION OPTIONS -
C-----
C----- ICASE =1 AND INCORE=1 - INCORE ASSEMBLY AND SOLUTION
C----- =1 AND =0 - OUT OF CORE ASSEMBLY AND SOLN.
C----- (2*NHBD*NHBD MINM. CORE STORAGE)
C-----
C----- ICASE = 2 AND INCORE = 0 -BIG OUT OF CORE ASSEMBLY AND
C-----
C----- JRADL = 1 - CYLINDRICAL CO-ORDINATE SYSTEM
C----- = 0 - CARTESIAN CO-ORDINATE SYSTEM
C-----
C----- NELAST= 2 - ELASTIC ANALYSIS
C----- NELAST= 1 - ELASTIC + TENSION CUT-OFF
C----- = 0 - NON-LINEAR ANALYSIS
C-----
C----- NBC = NEGATIVE - INCLINED SUPPORT IN DIRN. THETA
C-----
C----- IOUTP(NLR) = 0 - OUTPUT FOR LOAD INCR. 'NLR'
C----- = 1 - OUTPUT SUPPRESSED FOR LOAD_INCR. 'NLR'
C*****

```

```

C                                     = 1 = OUTPUT SUPPRESSED FOR LOAD_INCR. 'NLR'
C*****
C
C-----
C          INITIALISE READ AND WRITE CHANNEL NOS.
C          ( MACHINE DEPENDENT)
C
C          JINP=5
C          JOUT=6
C
C          NQ1=INTS(11)
C          NQ2=INTS(12)
C          NQ3=INTS(13)
C          NQ4=INTS(14)
C          NQ5=INTS(15)
C          NQ6=INTS(16)
C          NQ7=INTS(17)
C
C-----
C          INPUT DATAS
C
C          CALL INPUT
C-----
C          INITIALISE VARIABLES
C          DISMAX=0.0
C          NLR=0
C          NKAR=0
C          NCREP=0
C          STIF=.TRUE.
C
C          CALL INITL
C
C-----
C          PUT ZERO INFORMATION ON FILE NQ7
C          REWIND NQ7
C          DO 112 I=1,NTE1
C          WRITE(NQ7)((ECT(J,JK),J=1,6),JK=1,NGF)
C          1      ,((ETU(J,JK),J=1,3),JK=1,NGF)
C          2      ,((CWI(J,JK),J=1,3),JK=1,NGF)
C          112 CONTINUE
C-----
C          CALC. GAUSS POINT VALUES
C          CALL GAUSS
C-----
C          CALC. TOTAL LOADS TO BE FACTORED DURING LOAD INCREMENTS
C          CALL LOADIF
C
C-----
C          CALC. INFORMATION FOR OUT OF CORE ASSEMBLY
C          AND SOLUTION
C          IF(ICASE.EQ.1)GO TO 110
C          NEQ1B=(MOT-1)/(2*(NHBD+2))
C          IF(NEQ1B.GT.NEQ)NEQ1B=NEQ
C          NEQ2B=NEQ1B*2
C          NBLK=(NEQ-1)/NEQ1B +1
C          GO TO 120
C          110 CONTINUE
C
C          NNODE=NHBD/NDF
C          NEQ1B=NNODE*NDF
C          NEQ2B=2*NEQ1B
C          NBLK=NEQ/NEQ1B
C          NEXTR=NEQ-NBLK*NEQ1B
C          IF(NEXTR.GT.0)NBLK=NBLK+1
C          IF(INCORE.EQ.0)GO TO 115
C          NBLK=1
C          NEQ1B=NEQ
C          NEQ2B=NEQ
C          NNODE=NNF
C          115 CONTINUE
C          120 CONTINUE
C          NTL=NEQ2B*NHBD
C          IF(NTL.GT.MOT)CALL ERROR

```

```

C-----
C
C 11 CONTINUE
C
C      IF(NKAR.EQ.1)GO TO 29
C-----      NEXT LOAD INCREMENT
C      NLR=NLR+1
C      LCREEP=0
C      IF(NLR .GT. NLI)GO TO 100
C      CALL LODINC
C
C      IF(INPCK.NE.0)GO TO 100
C      NITER=0
C      HFACT=1.0
C      EFACT=0.0
C 29 CONTINUE
C
C-----      STIFFNESS FORMATION
C
C-----      CALC. STIFFNESS MATRIX + ASSEMBLE + DECOMPOSE
C
C      IF(.NOT. STIF)GO TO 31
C      CALL STIFDEC(FZA,NBLK,NEQ1B,NEQ2B,NNODE,MOT)
C 31 CONTINUE
C      IF(IVARB.EQ.0)STIF=.FALSE.
C
C-----      ITERATIONS FOR A LOAD INCREMENT
C
C 33 CONTINUE
C      NITER=NITER+1
C-----      LIMIT ON NO. OF ITERATIONS
C      IF(NITER.GT.NITMAX)GO TO 93
C
C-----      RESOLVE FORCE VECTOR AND BACK SUBSTITUTE
C
C      CALL SOLVE(FZA,NBLK,NEQ1B,NEQ2B,MOT)
C
C-----      CALC. UPDATED STRESSES AND RESIDUALS
C
C-----      CALL ACCELERATION ROUTINE IF REQUESTED
C      IF(ISECNF.EQ.1)CALL ACCNEW
C      CALL TOSTRS
C      NCREP=0
C
C      IF(NELAST.EQ.2)GO TO 92
C      IF(LCREEP.NE.0)GO TO 92
C
C-----      TEST FOR CONVERGENCE
C      CALL CONVER(EXCESS,RESID,VAL2,DISPT,DISPI,VAL1)
C      IF(IFCONV.EQ.1)GO TO 135
C-----      RESIDUAL CONVERGENCE CHECK
C      IF(VAL2.LT.TOLREN)GO TO 92
C      GO TO 136
C 135 CONTINUE
C-----      DISPLACEMENT CONVERGENCE CHECK
C      IF(VAL1.LT.TOLREN)GO TO 92
C 136 CONTINUE
C
C      IF(IVARB.EQ.0)GO TO 33
C
C      IF(IVARB.EQ.3)GO TO 33
C      NKAR=1
C      STIF=.FALSE.
C      IF(IVARB.EQ.2 .AND. NITER.EQ.1)STIF=.TRUE.
C      IF(IVARB.EQ.1)STIF=.TRUE.
C      GO TO 11
C

```

```

C
C 93 CONTINUE
C
C WRITE(JOUT,1000)NLR,NITER
1000 FORMAT(//,20X,'MAXIMUM ITERATIONS REACHED',4X,
1 'LOAD INCR.',I5,4X,'ITERATIONS',I5).
C
C
C
C 92 CONTINUE
C----- INITIALISE EQUIV. STRESS/STRAIN AT THE
C          END OF LOAD INCR. TO BE USED FOR
C          LOADING OR UNLOADING
C CALL EQVINT
C
C CALL OUTPUT
C
C----- IF ANY OF THE DISPLACEMENT EXCEEDS THE SPECIFIED VALUE,UMAX
C----- STOP THE ANALYSIS
C          UMAX=100.0
C          DO 170 J=1,NEQ
C          IF(RABS(UU(J)).GT.UMAX)DISMAX=UU(J)
170 CONTINUE
C          IF(RABS(DISMAX).GT.UMAX)WRITE(JOUT,1012)DISMAX,UMAX
1012 FORMAT(////,5X,'***PROGRAMME STOPED BECAUSE OF MAXIMUM',
1 'CALCULATED DISPL.',F10.5 ' EXCEEDS THE MAX.',
2 ' SPECIFIED DISPL.',F10.5)
C          IF(RABS(DISMAX).GT.UMAX)GO TO 100
C          IF(ICREEP.EQ.0)GO TO 190
C
C----- CREEP OF CONCRETE
C
C LCREEP=LCREEP+1
C IF(CRTIME(LCREEP,NLR).LE.0.0) GO TO 190
C DTIME=CRTIME(LCREEP,NLR)
C TIME=TIME+DTIME
C NCREP=1
C
C CALL CCREEP
C
C NITER=0
C HFACT=1.0
C EFACT=0.0
C TEMFAC=0.0
C GO TO 31
190 CONTINUE
C NKAR=0
C STIF=.FALSE.
C IF(IVARB.EQ.1 .OR. IVARB.EQ.3)STIF=.TRUE.
C GO TO 11
C
C 100 CONTINUE
C
C IF(INPCK.NE.0)WRITE(JOUT,1009)
1009 FORMAT(//,20X,'**USER REQUESTED TERMINATION**',/20X,30(1H-))
C
C----- END OF THE PROGRAMME
C
C RETURN
C END

```

SUBROUTINE ACCNEW

```

C
C----- THIS ROUTINE CALCULATES THE MODIFIED INCR. DISPL.
C----- BASED ON A CORRECTION DUE TO CURRENT AND OLD RESIDUALS
C----- THIS METHOD IS CALLED SECANT-NEWTON METHOD. THE
C----- CONVERGENCE IS FASTER IF USED WITH MODIFIED N-R PROCEDURE.
C
$INSERT COMMON.FE
C
      IF(NITER.EQ.1)GO TO 20
C----- CALC. ACCELERATION FACTORS
      AFACT=0.0
      BFACT=0.0
      CFACT=0.0
      DO 10 J=1,NEQ
      RESDIF=F(J)-FO(J)
      AFACT=AFACT+UO(J)*PO(J)
      BFACT=BFACT+UO(J)*RESDIF
      CFACT=CFACT+U(J)*RESDIF
10 CONTINUE
C----- FACTORS H AND E
      HFACT = -AFACT/BFACT
      EFACT = HFACT*(1.0-CFACT/BFACT)-1.0
C
      20 CONTINUE
      WRITE(JOUT,1901)NITER,ISECNF,HFACT,EFACT
1901 FORMAT(' **ACCNEW-NITER,ISECNF,HFACT,EFACT',2I5,2E12.4)
C----- COPY CURRENT RESIDUALS INTO OLD RESIDUALS
      DO 30 J=1,NEQ
      FO(J)=F(J)
30 CONTINUE
C----- UPDATE THE DISPLACEMENT INCR. AND STORE IT IN F
      DO 40 J=1,NEQ
      F(J)=HFACT*U(J)+EFACT*UO(J)
C----- PUT CURRENT DISPL. AS OLD DISPL.
      UO(J)=F(J)
40 CONTINUE
C----- CHECK THAT NEWTON CUT-OUT FACTOR REQUIRED
      DISU=0.0
      DISUO=0.0
      DISUUO=0.0
C----- NORMS OF DISPL.
      DO 50 J=1,NEQ
      DISU=DISU+F(J)*F(J)
      DISUO=DISUO+U(J)*U(J)
      DISUUO=DISUUO+U(J)*F(J)
50 CONTINUE
      DISU=RSQRT(DISU)
      DISUO=RSQRT(DISUO)
C
      THETA=DISUUO/(DISU*DISUO)
C
      WRITE(JOUT,1902)THETA,EFACT
1902 FORMAT(' **ACCNEW-THETA,EFACT',2E12.4)
      IF(THETA.LT.0.25)GO TO 70
      IF(RABS(EFACT).GT.2.0)GO TO 70

```

```

C----- FOR NO CUTOUT FACTOR, COPY P INTO U
      DO 60 J=1,NEQ
      U(J)=P(J)
      60 CONTINUE
      GO TO 90
      70 CONTINUE
C----- SECANT NEWTON CUTOUT FACTOR (NO ACCELERATION ALLOWED)
C
      DO 80 J=1,NEQ
      UO(J)=U(J)
      80 CONTINUE
      WRITE(6,1900)HFACT,EFACT
      1900 FORMAT(' **SECANT NEWTON CUTOUT FACTORS-H =',E12.4,
      1          2X,'E = ',E12.4)
C----- SET H AND E SUCH THAT THE ORIGINAL NEWTON-RAPHSON PROCEDURI
C----- IS APPLIED
      HFACT=1.0
      EFACT=0.0
      90 CONTINUE
      RETURN
      END
OK,

```